

JOURNAL OF SCIENCE



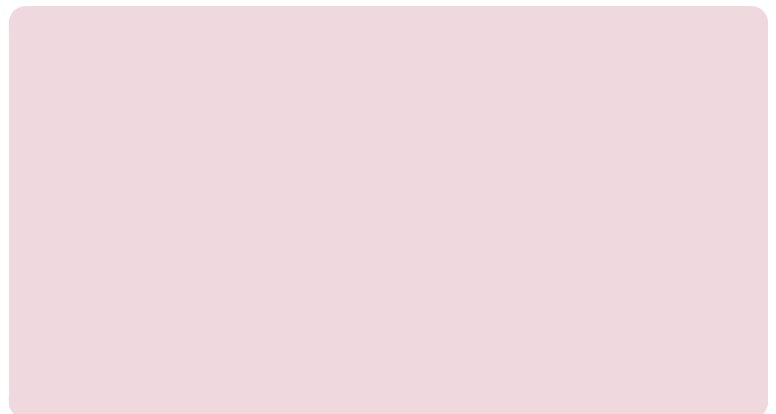
SAKARYA UNIVERSITY

Sakarya University Journal of Science



SAKARYA
UNIVERSITY

e-issn: 2147-835X



Sakarya University Journal of Science
Volume: 23 Issue: 5 October 2019
Editorial Boards

Editor-in-Chief

Emrah Doğan, Civil Engineering, Sakarya University (Turkey)
email: emrahd@sakarya.edu.tr

Editors

Ahmet Çağatay Çilingir, Mechanical Engineering, Sakarya University (Turkey)
email: cilingir@sakarya.edu.tr

Alparslan Serhat Demir, Industrial Engineering, Sakarya University (Turkey)
email: alparslanserhat@sakarya.edu.tr

Beytullah Eren, Environmental Engineering, Sakarya University (Turkey)
email: beren@sakarya.edu.tr

Cüneyt Bayılmış, Computer Science, Sakarya University (Turkey)
email: cbayilmis@sakarya.edu.tr

Ertan Bol, Civil Engineering, Sakarya University (Turkey)
email: ebol@sakarya.edu.tr

Kerem Küçük, Computer Science, Kocaeli University (Turkey)
email: kkucuk@kocaeli.edu.tr

Mehmet Nebioğlu, Chemistry, Sakarya University (Turkey)
email: nebioglu@sakarya.edu.tr

Meral Demirtaş, Meteorology Engineering, Ondokuz Mayıs University (Turkey)
email: mdemirtas@omu.edu.tr

Naci Çağlar, Civil Engineering, Sakarya University (Turkey)
email: caglar@sakarya.edu.tr

Sadık Bağcı, Physics, Sakarya University (Turkey)
email: sbagci@sakarya.edu.tr

Serkan Zeren, Mechatronics Engineering, Kocaeli University (Turkey)
email: serkan.zeren@kocaeli.edu.tr

Şevket Gür, Mathematics, Sakarya University (Turkey)
email: sgur@sakarya.edu.tr

Zafer Barlas, Metallurgical and Materials Engineering, Sakarya University of Applied Sciences (Turkey)
email: barlas@sakarya.edu.tr

Editorial Board

Ahmet Aygün, Environmental Engineering, Bursa Technical University (Turkey)
email: ahmet.aygun@btu.edu.tr

Ali Çoruh, Physics, Sakarya University (Turkey)
email: coruh@sakarya.edu.tr

Ali Pınar, Civil Engineering, Boğaziçi University (Turkey)
email: pinara@boun.edu.tr

Ali Sarıbiyık, Civil Engineering, Sakarya University of Applied Sciences (Turkey)
email: alisaribiyik@sakarya.edu.tr

Azim Gökçe, Metallurgical and Materials Engineering, Sakarya University of Applied Sciences (Turkey)
email: azimg@sakarya.edu.tr

Barış Yüce, Industrial Engineering, University of Exeter (England)
email: b.yuce@exeter.ac.uk

Bengü Bayram, Mathematics, Balıkesir University (Turkey)
email: benguk@balikesir.edu.tr

Berrin Denizhan, Industrial Engineering, Sakarya University (Turkey)
email: denizhan@sakarya.edu.tr

Çiğdem Gündüz, Mathematics, Kocaeli University (Turkey)
email: caras@kocaeli.edu.tr

Dilek Angın, Food Engineering, Sakarya University (Turkey)
email: angin@sakarya.edu.tr

Emrah Evren Kara, Mathematics, Düzce University (Turkey)
email: eevrenkara@duzce.edu.tr

Emre Tabar, Physics, Sakarya University (Turkey)
email: etabar@sakarya.edu.tr

Erman Aslan, Mechanical Engineering, Istanbul University (Turkey)
email: erman.aslan@istanbul.edu.tr

Esra Erkuş Duman, Mathematics, Gazi University (Turkey)
email: eerkusduman@gmail.com

Giglou Abolfazl, Civil Engineering, Uidaho University (USA)
email: abolfazl@uidaho.edu

Habibullah Uzun, Environmental Engineering, Marmara University (Turkey)
email: habibullah.uzun@marmara.edu.tr

Halil Yiğit, Computer Science, Kocaeli University (Turkey)
email: halilyigit@kocaeli.edu.tr

Hüseyin Aksoy, Biology, Sakarya University (Turkey)
email: haksoy@sakarya.edu.tr

Ipek Güleç, Mathematics, Hacettepe University (Turkey)
email: ipek@hacettepe.edu.tr

İdris Cesur, Mechanical Engineering, Sakarya University of Applied Sciences (Turkey)
email: icesur@sakarya.edu.tr

İlkay Şişman, Chemistry, Sakarya University (Turkey)
email: isisman@sakarya.edu.tr

İnan Keskin, Civil Engineering, Karabük University (Turkey)
email: inankeskin@karabuk.edu.tr

Jamal Khatib, Civil Engineering, University of Wolverhampton (England)
email: j.m.khatib@wlv.ac.uk

Kadriye Ergün, Industrial Engineering, Balıkesir University (Turkey)
email: kergun@balikesir.edu.tr

Kasım Serbest, Mechatronics Engineering, Sakarya University of Applied Sciences (Turkey)
email: kserbest@subu.edu.tr

Mahmut Özacar, Chemistry, Sakarya University (Turkey)
email: mozacar@sakarya.edu.tr

Maryna Van De Venter, Biochemistry and Microbiology, Nelson Mandela University (Germany)
email: maryna.vandeventer@nmmu.ac.za

Mehmet Ozen, Mathematics, Sakarya University (Turkey)
email: ozen@sakarya.edu.tr

Murat Tuna, Chemistry, Sakarya University (Turkey)
email: tuna@sakarya.edu.tr

Murat Utkucu, Civil Engineering, Sakarya University (Turkey)
email: mutkucu@sakarya.edu.tr

Mustafa Alkan, Mathematics, Akdeniz University (Turkey)
email: alkan@akdeniz.edu.tr

Mustafa Yılmaz, Biology - Vegetative and Animal Production, Sakarya University of Applied Sciences (Turkey)
email: mustafayilmaz@sakarya.edu.tr

Nazan Deniz Yön, Biology, Sakarya University (Turkey)
email: ndyon@sakarya.edu.tr

Necati Olgun, Mathematics, Gaziantep University (Turkey)
email: olgun@gantep.edu.tr

Nesrin Güler, Statistics, Sakarya University (Turkey)
email: nesring@sakarya.edu.tr

Osman Kırtel, Civil Engineering, Sakarya University of Applied Sciences (Turkey)
email: okirtel@sakarya.edu.tr

Özer Uygun, Industrial Engineering, Sakarya University (Turkey)
email: ouygun@sakarya.edu.tr

Özgül Keleş, Metallurgical and Materials Engineering, Istanbul Technical University (Turkey)
email: ozgulkeles@itu.edu.tr

Öznur Özkan, Mathematics, Başkent University (Turkey)
email: oznur@baskent.edu.tr

Peter Claisse, Civil Engineering, Coventry University (England)
email: pete@claisse.info

Ramazan Meral, Biosystem Engineering, Bingöl University (Turkey)
email: rmeral@bingol.edu.tr

Salima Saib, Physics, University of M'sila (Algeria)
email: salima_saib@yahoo.fr

Sema Salur, Mathematics, Rochester University (England)
email: sema.salur@rochester.edu

Sezgin Aydın, Physics, Gazi University (Turkey)
email: sezginaydin@gazi.edu.tr

Sezgin Kaçar, Electrical and Electronics Engineering, Sakarya University of Applied Sciences (Turkey)
email: skacar@sakarya.edu.tr

Shivam Tripathi, Civil Engineering, Purdue University (USA)
email: shiva@iitk.ac.in

Tijen Talas Oğraş, Biology - Genetic Engineering, Tubitak (Turkey)
email: tijen.ogras@tubitak.gov.tr

Uğur Çalığülü, Metallurgical and Materials Engineering, Fırat University (Turkey)
email: ugurcaligulu@gmail.com

Vezer Ayhan, Mechanical Engineering, Sakarya University of Applied Sciences (Turkey)
email: vayhan@sakarya.edu.tr

SAKARYA UNIVERSITY JOURNAL OF SCIENCE
CONTENTS
Volume: 23 - Issue: 5 (OCTOBER 2019)

RESEARCH ARTICLES

1	A New Glassy Carbon Surface Covered With 1-(2-Benzothiazolyl)-3-Methyl Pyrazol-5-One And Its Characterization Demet Uzun	707--713
2	Coefficient Inequalities For Janowski Type Close-To-Convex Functions Associated With Ruscheweyh Derivative Operator Öznur Özkan Kılıç	714--717
3	Asymptotically J_Σ -Equivalence Of Sequences Of Sets Uğur Ulusu, Esra Gülle	718--723
4	A New Approximation To Classify The Liquids Measured In Microwave Frequency Range Turgut Ozturk	724--730
5	On Generalized Tribonacci Octonions Arzu Özkoç Öztürk	731--735
6	Effects Of Glass Fiber Reinforcement To Tensile Strength In Epoxy Matrix Granular Composite Materials Hüseyin Onur Öztürk, Yaşar Kahraman	736--743
7	Metallographic Aspects Investigation Of Penstock Materials In Hydroelectric Power Plants And Penstock Maintenance Methods Gökhan Kahraman, Yahya Taşgın	744--748
8	Numerical And Experimental Investigation Of Bending Behavior Of Pre-Stressed Aluminum Tube Seçil Ekşi, Kenan Genel	749--754
9	A Preliminary Study On Salt Tolerance Of Some Barley Genotypes Ali Doğru, Merve Yılmaz Kaçar	755--762
10	Absolute Almost Weighted Summability Methods Mehmet Ali Sarıgöl	763--766
11	A Bayesian Parameter Estimation Approach To Response Surface Optimization In Quality Engineering Elif Kozan, Onur Köksoy	767--774
12	Experimental And Statistical Investigation Of Surface Roughness In Turning Of Aisi 4140 Steel Harun Akkuş	775--781
13	Landslide Susceptibility Assessment Using Skyline Operator And Majority Voting Alev Mutlu, Furkan Goz, Kubra Koksall, Arzu Erener	782--787
14	On Fuhrmann'S Theorem In Abstract Spaces Nilgün Sönmez	788--791
15	A New Class Of S-Type $X(U,V;L_P(E))$ Operators Pınar Zengin Alp, Merve İlkhan	792--800
16	A New Type Of Canal Surface In Euclidean 4-Space E^4 İlim Kişi, Günay Öztürk, Kadri Arslan	801--809
17	Batch And Column Studies For Removal Of Sulphate From Real Wastewater Using Ion Exchange Resin Tijen Ennil Bektas, Filiz Eren	810--816

18	Chromium-Aluminide Coatings Via Pack Cementation Method On Inconel 718 Alloy And Fe-Cr-Ni Superalloy Tuba Yener	817--823
19	Determination Of Anticancer And Antibacterial Activities Of Disubstituted Tacrine Derivatives Salih Ökten, Ali Aydın, Ahmet Tutar	824--830
20	Key Mechanical Design Performance Features And Mechanical Characterization Of Poly-Crystallized Bi ₂ .1Sr ₂ .0-Xtixca1.1Cu ₂ .00y Superconducting Ceramic Cuprates Tahsin Turgay, Yusuf Zalaoğlu, Gürcan Yıldırım	831--839
21	Mechanochemical Conversion Of Domestic Celestite Mineral To Src ₂ O ₄ In The Ammonium Oxalate Media Mert Zorağa	840--847
22	Heat Transfer Analysis Of Different Thermal Oils In Parabolic Trough Solar Collectors With Longitudinal Sinusoidal Internal Fin Burak Kurşun	848--858
23	Implementation Of Dormand-Prince Based Chaotic Oscillator Designs In Different Iq-Math Number Standards On Fpga İsmail Koyuncu, Halil İbrahim Şeker	859--868
24	Experimental Research Of Energy Consumption Of Austenitizing Heat-Treated Casting Fittings In Pipe Threading Burak Öztürk	869--878
25	A Study Of Symmetrical And Unsymmetrical Short Circuit Fault Analyses In Power Systems Faruk Yalçın, Yılmaz Yıldırım	879--895
26	X-Ray Radiography Of Micro-Alloyed Steel Joined By Submerged Arc Welding Mustafa Türkmen	896--901
27	Production And Characterization Of Carbon-Kevlar-Aramid Reinforced Layer Composites With Vartm Method Yahya Taşgın, Engin Şahin	902--907
28	Determination Of Fuel Type For Optimal Performance And Emission In A Ci Engine Used Biodiesel And Its Blends Via Multi-Criteria Decision Making Sinan Erdoğan, Mustafa Kemal Balki, Cenk Sayın	908--915
29	An Experimental Study On Extraction Of Sugar From Carob Using With Taguchi Method Ufuk Durmaz, Mehmet Berkant Özel	916--923
30	Effect Of Wet Soil On Thermal Performance Of Air-Fluid Ground Heat Exchanger For Heating Ufuk Durmaz, Orhan Yalçınkaya, Ozlem Bablak Ergun, Mustafa Ozdemir	924--928
31	Some Notes On Odd Or Even Indexed Fibonacci And Lucas Sequences Alparslan Kargın, Emre Kişi, Halim Özdemir	929--933
32	The Effect Of Gibbs Factor On Transient Analysis In Underground Power Cables Yılmaz Uyaroğlu, Selçuk Emiroğlu	934--941
33	Thermo-Hydraulic Effects Of Vortex Generator Pairs In A Crossflow Channel With A Transverse-Jet Flow Besir Kok	942--963
34	Imposed Source Current Predictive Control For Battery Charger Applications With Active Damping Mustafa Gökdağ, Ozan Gülbudak	964--971

35	Effect Of Reduction Ratio Below Austenite Recrystallization Stop Temperature On Mechanical Properties Of An Api X70M Psl2 Line Pipe Steel Ramazan Tütük, Mustafa Merih Arıkan, Eyüp Sabri Kayalı	972--981
36	Some Connections Between Various Classes Of Analytic Functions Associated With The Power Series Distribution Serkan Çakmak, Sibel Yalçın, Şahsene Altınkaya	982--985
37	Optimized Analytical Solution Of Platform Panel Radiative Area Dimensioning Of Geostationary Communications Satellites: A Practical Approach Murat Bulut, Nedim Sözbir	986--992
38	Effect Of Rapidly Annealing Process On Mgb2 Superconducting Wires Fırat Karaboğa	993--1004
39	Stability And Hopf Bifurcation In Three-Dimensional Predator-Prey Models With Allee Effect İlknur Kuşbeyzi Aybar	1005--1011
40	Hermite-Hadamard Type Inequalities For Exponentially P-Convex Stochastic Processes Serap Özcan	1012--1018

JOURNAL OF SCIENCE



SAKARYA UNIVERSITY

Sakarya University Journal of Science

ISSN 1301-4048 | e-ISSN 2147-835X | Period Bimonthly | Founded: 1997 | Publisher Sakarya University |
<http://www.saujs.sakarya.edu.tr/>

Title: A New Glassy Carbon Surface Covered With 1-(2-Benzothiazolyl)-3-Methyl Pyrazol-5-One And Its Characterization

Authors: Demet Uzun

Received: 2018-08-01 00:00:00

Accepted: 2019-01-15 00:00:00

Article Type: Research Article

Volume: 23

Issue: 5

Month: October

Year: 2019

Pages: 707-713

How to cite

Demet Uzun; (2019), A New Glassy Carbon Surface Covered With 1-(2-Benzothiazolyl)-3-Methyl Pyrazol-5-One And Its Characterization. Sakarya University Journal of Science, 23(5), 707-713, DOI: 10.16984/saufenbilder.450117

Access link

<http://www.saujs.sakarya.edu.tr/issue/44066/450117>

New submission to SAUJS

<http://dergipark.gov.tr/journal/1115/submission/start>

A new glassy carbon surface covered with 1-(2-benzothiazolyl)-3-methyl pyrazol-5-one and its characterization

Demet Uzun^{*1}

Abstract

1-(2-benzothiazolyl)-3-methyl pyrazol-5-one (B3MP) was electrochemically covered on a glassy carbon (GC) electrode surface in nonaqueous medium. Properties of B3MP film were investigated by cyclic voltammetry (CV), electrochemical impedance spectroscopy (EIS) and fourier transform infrared spectroscopy (FTIR). The number of electron transferred was calculated as 0.66 indicating that a single electron transfer process was carried out and the modification mechanism of B3MP via electrochemical oxidation on the GC electrode was suggested.

Keywords: Electrochemical modification, Impedance spectroscopy, Glassy carbon electrode.

1. INTRODUCTION

Pyrazolone derivatives have a major role in the synthesis of many drugs in the fields of pharmaceuticals [1]. In addition to their analgesics and antipyretics impacts, they possess biological properties such as antimicrobial [2], antitumor [3], anti-inflammatory [4]. They have also been utilized as analytical reagents [5] to extract and separate different metal ions [6]. Their applications have been found in other areas, such as sensors [7-8].

The synthesis of pyrazole and pyrazolone derivatives have considered by chemists because of they are reported as a new class of corrosion inhibitors [9]. It has also been reported that there are many hetarylazopyrazolone derivatives which posses different chromophoric groups [10]. It was demonstrated that some dyes such as pyrazolone derivatives can be used in protection of optical record systems and optical filters [11]. Besides their well known dying properties, these type of hetarylazo dyes have taken a great interest by their

usage in non-textile applications, especially in high technology due to their near-infrared absorbing properties [12].

Covering carbon surfaces with organic molecules via covalent grafting has been became more interesting because of their applications in the area of materials science and electrochemical analysis [13]. These grafted molecules containing different functional groups were brought stability to the surfaces, so chemical and electrochemical methods have been developed to prepare new modified carbon surfaces [14].

In this study, an organic molecule which is a pyrazolone derivative, namely B3MP, was used as a modifier for the first time to develop a modified glassy carbon electrode via electrochemical method. The properties of developed electrode was investigated by electrochemical and spectroscopic methods which are CV and EIS.

* demetuzun@gazi.edu.tr

¹ Gazi University, Faculty of Science, Department of Chemistry, 06500, Ankara/Turkey ORCID: 0000-0002-7090-6516

2. EXPERIMENTAL

2.1. Apparatus and Chemicals

A CHI 660B Electrochemical Workstation was used for CV and EIS measurements. A conventional three-electrode system was used. Working electrode was a glassy carbon (GC) electrode (BAS Model), the reference electrode was an Ag/Ag⁺ (0.01 M) used in nonaqueous medium and an Ag/AgCl/KCl (sat.) used in aqueous medium. A Pt wire was used as the counter electrode. FTIR measurements of B3MP and B3MP film on GC surface were made with a Thermo Scientific Nicolet IS5 with a grazing angle and ATR (Attenuated Total Reflectance) accessories.

As supporting electrolyte, 1.0 mM ferrocyanide/1.0 mM ferricyanide (1/1) mixture with 0.1 M KCl was prepared for EIS measurements. The frequency range from 100 kHz to 0.01 kHz was selected to perform EIS data. The ac amplitude was 5 mV and the electrode potential was 0.215 V, the formal potential of ferrocyanide/ferricyanide redox couple.

Analytical grade reagents were used in the study. Tetrabutylammonium tetrafluoroborate (TBATFB), get from Merck, was used for the supporting electrolyte in nonaqueous medium. Acetonitrile (ACN) as a solvent was provided from Sigma-Aldrich. ACN containing 0.1 M TBATFB was used to prepare ferrocene solution (1×10^{-3} M).

Aqueous solutions were prepared and polished electrodes were cleaned with ultra pure quality of water (18.3 M Ω) (Millipore Corp. Bedford, MA (USA)).

3. RESULTS AND DISCUSSION

3.1. Effect of Scan Rate on The Oxidation Peak Current of B3MP

The scan rate's effect on the oxidation peak current of B3MP at the GC surface (Figure 1) was studied by CV in ACN containing 0.1 M TBATFB in the range of 25–150 mV s⁻¹. A plot of logarithm of the

oxidation peak current vs. logarithm of scan rate (inset of Figure 1) gave a straight line with a slope of 0.8229 (R²=0.991) showing that the electrooxidation of B3MP at the GC surface is adsorption-controlled electrode reaction. Cathodic peak was not observed in the reverse scan, displaying that the charge transfer is electrochemically irreversible in the electrode process.

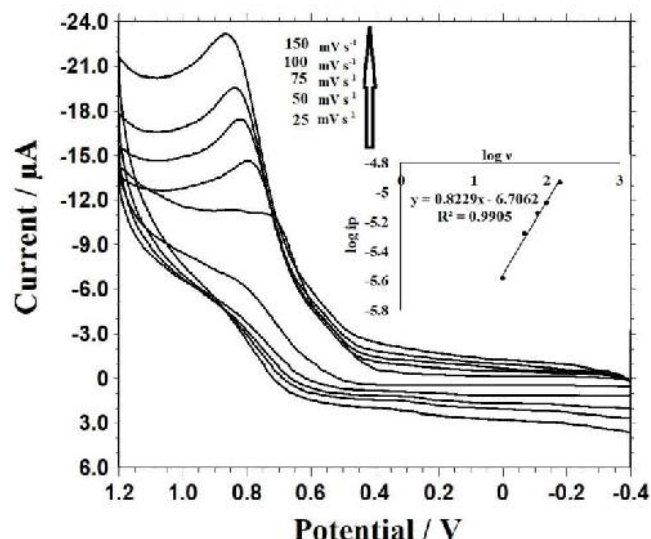


Figure 1. CVs of 1 mM B3MP at GC electrode in ACN containing 0.1 M TBATFB with different scan rates (25, 50, 75, 100, and 150 mV s⁻¹) vs. Ag/Ag⁺ (0.01 M) Inset: The plot of logarithm of peak current vs. logarithm of scan rate.

It was noticed that while the scan rate was increased, the anodic peak potential (E_p) at about 0.7 V was shifted to positive direction (Figure 2) [15]. As for an adsorption-controlled and totally irreversible electrode process, E_p is defined by the following equation [16],

$$E_p = E^{o'} + \frac{2.303 RT}{\alpha n F} \log \frac{RTk^o}{\alpha n F} + \frac{2.303 RT}{\alpha n F} \log v \quad (1)$$

E_p vs. logarithm of scan rate was linear according to the equation:

$$E_p (\text{V}) = 0.1799 \log v + 0.4777 \quad (R^2 = 0.9879) \quad (2)$$

The αn value was calculated as 0.33 from the slope of the E_p vs. log v plot ($2.303 RT / \alpha n F$) using the Laviron's equation [16]. In irreversible electrode process, α is assumed as 0.5 [17]. Hence, the number of electrons in the reaction was calculated to be $0.66 \approx 1$ indicating that a single electron transfer process was carried out between B3MP and GC electrode in the redox reaction.

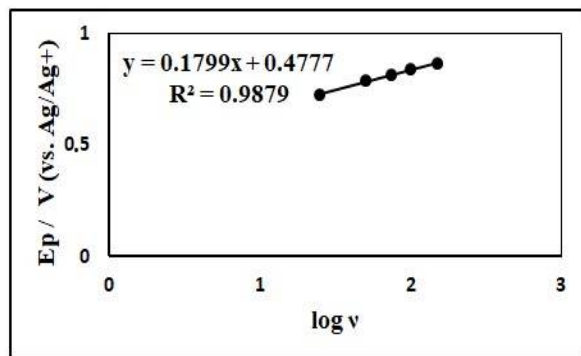


Figure 2. The plot of peak potential vs. logarithm of scan rate.

3.2. Preparation of B3MP-GC Electrode

In the first step of the electrode modification, a bare GC electrode was polished with 0.05 μm alumina slurry. Polished electrode were sonicated in ultra-pure water and then with ACN for 5 min, respectively. Then, GC electrode was rinsed with ACN.

The multi cyclic voltammograms (CVs) for 1 mM B3MP at GC surface in nonaqueous solution (in ACN containing 0.1 M TBATFB) vs. Ag/Ag^+ (0.01 M) are shown in Figure 3. An irreversible oxidation peak (at 0.7 V) was decreased until the 20th cycle in the potential range of -0.4 V and 1.2 V with a scan rate of 100 mV s^{-1} . The GC surface was passivated [18] and became stable state in this cycle due to inhibition of electrode surface by covalent modification resulting of the reaction between -OH and the sp^2 carbon atoms on the GC surface [13]. After modification, the passivation of the surfaces is significant to protect the materials against corrosive impacts. Also, passivation of the surface due to film is advantage for using B3MP-GC in the positive potential region processes [19].

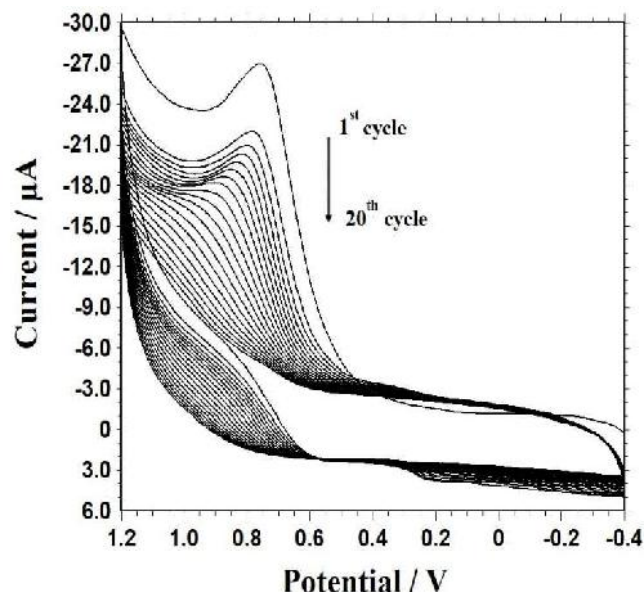


Figure 3. The cyclic voltammetric sweeps of 1 mM B3MP solution prepared in ACN containing 0.1 M TBATFB at GC electrode vs. Ag/Ag^+ (0.01 M), scan rate is 100 mV s^{-1} .

3.3. Electrochemical Characterization of the B3MP-GC Surface Using Redox Probes

B3MP-GC surface was firstly characterized by electrochemical method using redox probes that are ferricyanide and ferrocene. For this purpose the CVs of redox probes were taken at the bare GC and B3MP-GC covered with different scan cycles shown in Figure 4(a) and Figure 4(b), respectively. Figure 4 showed that redox peaks' currents were decreased and disappeared in ferricyanide. The completely blocking was occurred at 20 cycle that is why it was chosen as optimum condition for the prepare of the modified electrode. The completely blockage of oxidation and reduction of mentioned ferricyanide redox probe is a reliable indication of B3MP layer formation on the surface of GC electrode. Whereas, the results showed that there was no completely blocking effect for ferrocene. This distinguished difference in electrochemical behaviors between ferricyanide and ferrocene at the B3MP-GC electrode should be due to the electrostatic effects of the carrying charges of the electrochemical probes and the surface charges of the B3MP layers at the GC surface [20].

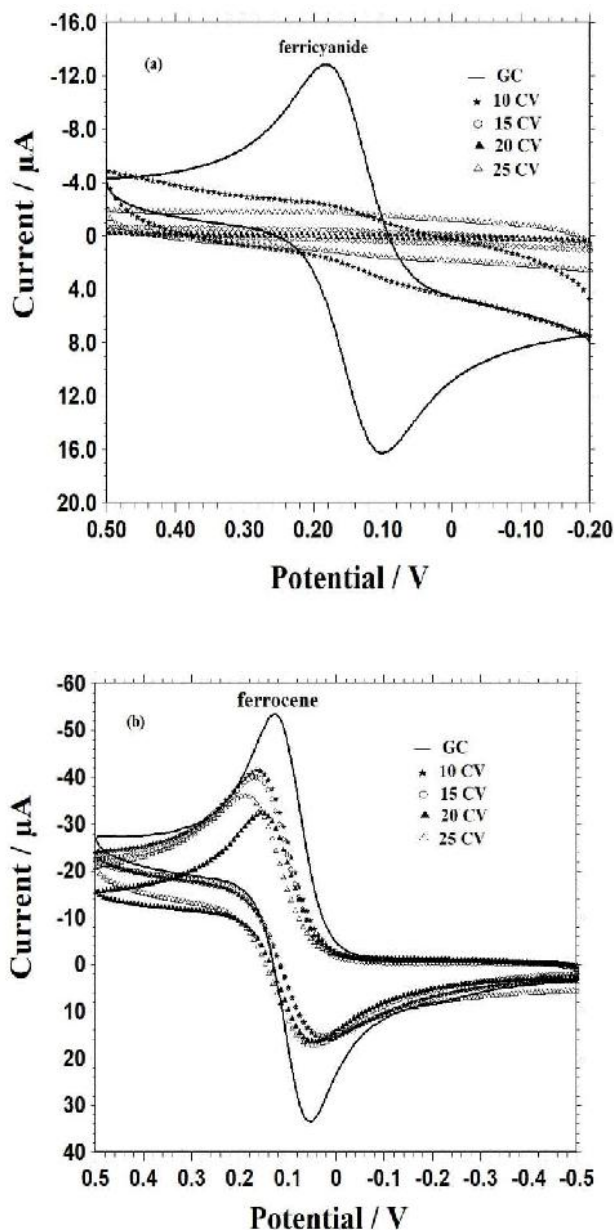
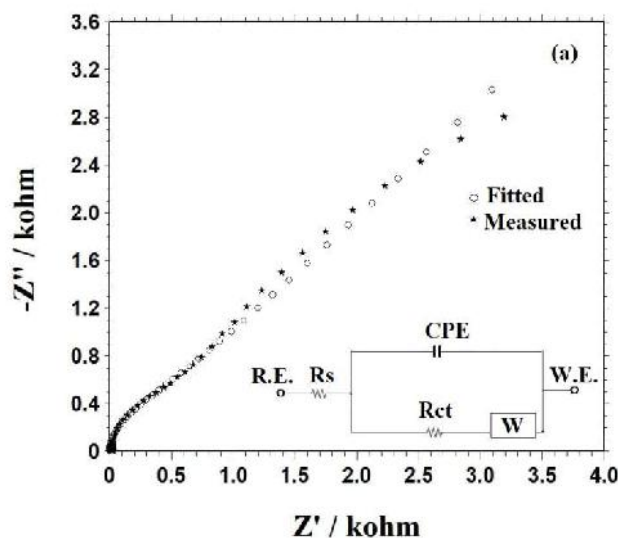


Figure 4. CVs of 1 mM (a) ferricyanide (in 0.1 M KCl) vs. Ag/AgCl/KCl (sat.) and (b) ferrocene (in ACN containing 0.1 M TBATFB) vs. Ag/Ag⁺ at the bare GC and B3MP-GC electrodes, scan rate is 100 mV s⁻¹.

3.4. EIS Characterization of the B3MP-GC Surface

EIS is a powerful and sensitive method to learn about the features of electrode's surfaces [21]. Figure 5 shows the Nyquist plots for the bare GC and the B3MP-GC surfaces. Bare GC shows almost a straight line impedance plot at the low frequency region with a small semicircle at the high frequency region. But a high semicircle is observed for the B3MP-GC at the high frequency region, showing that the electron transfer is

blocked between redox couple and the B3MP-GC. The equivalent circuits for bare GC and B3MP-GC are shown inset of Figure 5(a) and (b), respectively. An electrolyte solution resistance (R_s), a constant phase element (CPE), charge-transfer resistance (R_{ct}) and the Warburg resistance (w) resulting from the diffusion of ions from the bulk of the electrolyte to the interface are presented in this equivalent circuit [22]. CPE and R_{ct} values were found by fitting the impedance spectra using this equivalent circuit. R_{ct} values were calculated for redox couple at bare GC and the B3MP-GC as 0.38 k Ω and 21 k Ω , respectively. The charge transfer resistance' value at the B3MP-GC is higher than at the bare GC, hence it can be said that the passivation of the film is possible on B3MP-GC. The values of CPE for GC and B3MP-GC are found to be 0.2 μ F and 0.07 μ F, respectively. The Warburg resistance of the bare GC and B3MP-GC surfaces is 26.9 and 4.7, respectively. The surface coverage (θ) of the B3MP film can be calculated from equation $\theta=1-R_{ct}^0/R_{ct}$ [23]. The obtained surface coverage is 98.2%. This value is accepted for a dense film.



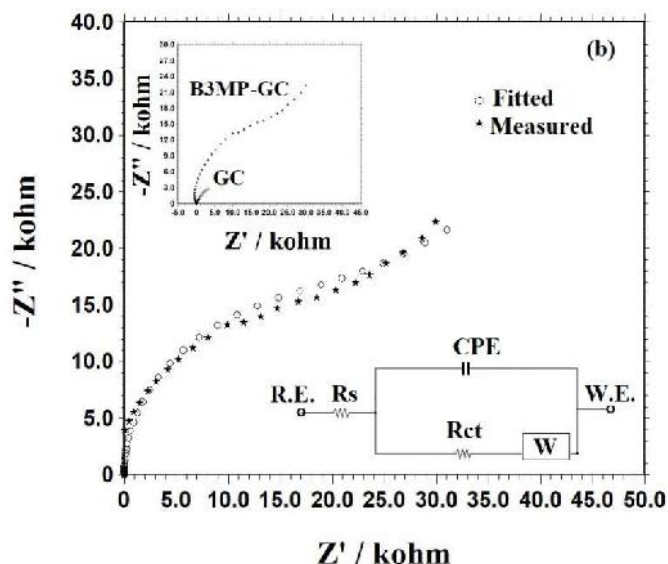


Figure 5. Nyquist plots for (a) bare GC and (b) B3MP-GC in 1 mM ferrocyanide/ferricyanide containing 0.1 M KCl. The Randle's equivalent circuit models for each electrode are at the bottom on the right hand side. Frequency range is 100 kHz-0.01 kHz with 5 mV wave amplitude at a formal potential of 0.215 V.

3.5. FTIR spectrum of the B3MP-GC surface

The IR data were used to characterize B3MP-GC surface and investigate the coupling sites. IR spectra of solid B3MP and B3MP film on the GC surface were recorded and compared with each other to see the differences between them. The IR of solid B3MP (curve a) and RAIRS spectra of B3MP film (curve b) were presented in Figure 6.

The heteroaromatic compound with N-H group, stretching vibration was appeared at 3136 cm^{-1} while it was disappeared at GC surface. This significant change in the N-H band of B3MP film on the GC surface recommends that the N-H group plays a role in the modification process of the GC surface.

The C-H stretching vibrations on aromatic ring were exhibited in B3MP at the regions $3070\text{-}3052\text{ cm}^{-1}$ but these vibrations weren't observed in surface spectrum suggesting that there were π - π interactions between the aromatic ring and the graphitic rings systems of the GC [24]. Aliphatic C-H bands were also recorded at $2872\text{-}2991\text{ cm}^{-1}$ for solid B3MP and $2843\text{-}2960\text{ cm}^{-1}$ for surface film [6].

The infrared bands from B3MP in the solid state observed at 1650 and 1622 cm^{-1} were assigned to C=O stretching and C=C stretching, respectively [6]. Surface spectrum has a broad and weak band with a frequency shift in this region at about 1619 cm^{-1} in the surface spectrum assigned to C=C group but it was not correctly detected because of overlapping. C=O band wasn't observed in the surface spectrum.

C=N stretching vibration [6] was observed at 1596 and 1521 cm^{-1} in solid B3MP spectrum and only one band at 1517 cm^{-1} in the surface spectrum. The strong band observed at 1229 cm^{-1} in solid B3MP spectrum was assigned to C-N stretching vibration. It was weakly observed at 1222 cm^{-1} in surface spectrum.

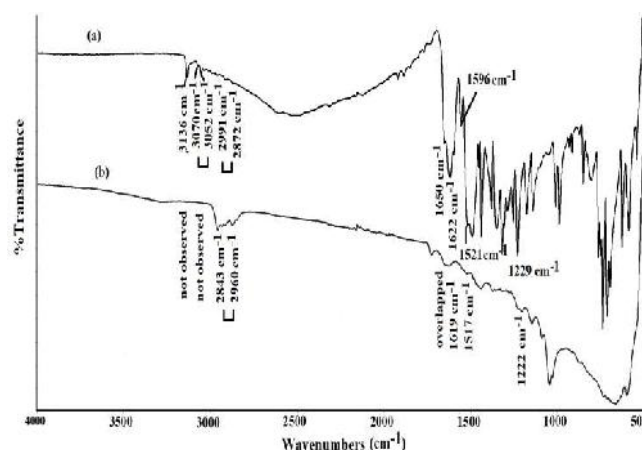


Figure 6. IR spectrum of (a) solid B3MP and (b) B3MP film on the GC surface

All mentioned above showed that the B3MP was covered to surface. The modification mechanism was proposed from the scan rate, CV and FTIR results, shown in Figure 7. According to that the -NH group in B3MP molecule was oxidized first with one-electron generating radical cation [25]; then the radical cation delocalized in the heteroaromatic ring and -OH radical cation was occurred and the radical cation reacted with the GC surface forming C-O-C linkages with giving one H^+ [26-28].

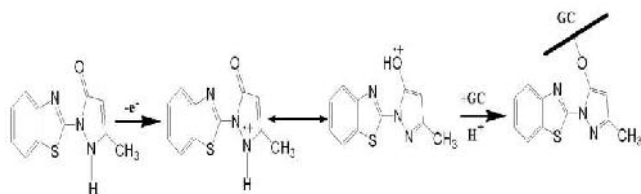


Figure 7. The proposed modification mechanism of GC with B3MP.

4. CONCLUSIONS

In this paper, B3MP was firstly covered to GC electrode via electrochemical method in nonaqueous medium to develop a new electrode. The properties of new surface were evaluated by CV, EIS and FTIR. From the EIS results, B3MP-GC showed a high surface coverage value (98.2%) as a result of increasing charge transfer resistance for redox couple. The electrochemical coverage mechanism of B3MP to the GC surface has been also investigated. It was supposed that the B3MP was covered to GC surface from its $-OH$ group with releasing one electron. This modified electrode can be used in the corrosion studies because of its high electro-inactive property and also in diverse applications such as energy storage, sensing, etc.

REFERENCES

- [1] K. Brune, "The early history of non-opioid analgesics," *Acute Pain*, vol. 1, pp. 33–40, 1997.
- [2] S. M. Sondhi, S. Kumar, N. Kumar, P. Roy, "Synthesis anti-inflammatory and anticancer activity evaluation of some pyrazole and oxadiazole derivatives," *Medicinal Chemistry Research*, vol. 21, no. 10, pp. 3043–3052, 2012.
- [3] A. Zaoui, L. Hammal, N. Bennamane, S. Merabtene, B. Nedjar-Kolli, "A catalytic method for the synthesis of pyrazolone derivatives using heteropolyacids and study of the antibacterial activity," *International Journal of Pharmaceutical, Chemical and Biological Sciences*, vol. 3, no. 3, pp. 732–737, 2013.
- [4] E. Bagdatli, E. Altuntas, U. Sayin, "Synthesis and structural characterization of new oxovanadium(IV) complexes derived from

azo-5-pyrazolone with prospective medical importance," *Journal of Molecular Structure*, vol. 1127, pp. 653–661, 2017.

- [5] N.V. Trofimov, N.N. Nekhaer, N.A. Kanaev, A.I. Busev, "Pyrazolone derivatives as analytical redox-reagents. Determination of cerium and hydrogen peroxide with bis-(1-phenyl-3-methylpyrazolone-5)," *Zhurnal Analiticheskoy Khimii*, vol. 37, pp.1445–1451, 1982.
- [6] E. Aktan, B. Çatıkkaş, "Infrared and Raman spectra, DFT investigation of the tautomerism, conformational equilibrium, structure and vibrational assignment of 1-(2-benzothiazolyl)-3-methyl pyrazol-5-one," *Vibrational Spectroscopy*, vol. 67, pp. 92–100, 2013.
- [7] T. Ito, C. Goto, K. Noguchi, "Lanthanoid ion-selective solvent polymeric membrane electrode based on 1-phenyl-3-methyl-4-octadecanoyl-5-pyrazolone," *Analytica Chimica Acta*, vol. 443, pp. 41–51, 2001.
- [8] V. Kumar Gupta, S. Jain, S. Chandra, "Chemical sensor for lanthanum(III) determination using aza-crown as ionophore in poly(vinyl chloride) matrix," *Analytica Chimica Acta*, vol. 486, pp. 199–207, 2003.
- [9] A. S. Fouda, A. A. Al-Sarawy, E. E. El-Katori "Pyrazolone derivatives as corrosion inhibitors for C-steel in hydrochloric acid solution," *Desalination*, vol. 201, pp. 1–13, 2006.
- [10] M.S. Yen, I. J. Wang, "A facile syntheses and absorption characteristics of some monoazo dyes in bis-heterocyclic aromatic systems part I: syntheses of polysubstituted-5-(2-pyrido-5-yl and 5-pyrazolo-4-yl)azo-thiophene derivatives," *Dyes and Pigments*, vol. 62, pp. 173–180, 2004.
- [11] H. Bach, K. Anderle, Th. Fuhrmann, J. H. Wendorff, "Biphoton-induced refractive index change in 4-Amino-4'-nitroazobenzene/polycarbonate," *The Journal of Physical Chemistry*, vol. 100, pp. 4135–4140, 1996.
- [12] E. Aktan, N. Ertan, T. Uyar, "Synthesis, characterization and theoretical study of new hetarylazopyrazolone dyes and investigation of their absorption spectra," *Journal of Molecular Structure*, vol. 1060, pp. 215–222, 2014.

- [13] D. Morales-Martínez, F. J. González, "Reversible reorganization of alkyl ester groups grafted on glassy carbon electrode: Induction by a redox probe," *Electrochemistry Communications*, vol. 62, pp. 21–23, 2016.
- [14] V. Georgakilas, M. Otyepka, A. B. Bourlinos, V. Chandra, N. Kim, K. C. Kemp, P. Hobza, R. Zboril, K. S. Kim, "Functionalization of graphene: Covalent and non-covalent approaches, derivatives and applications," *Chemical Reviews*, vol. 112, pp. 6156–6214, 2012.
- [15] L. Arrue, T. Barra, M. B. Camarada, X. Zarate, E. Schott, "Electrochemical and theoretical characterization of the electro-oxidation of dimethoxycurcumin," *Chemical Physics Letters*, vol. 677, pp. 35–40, 2017.
- [16] E. Laviron, "Adsorption, autoinhibition and autocatalysis in polarography and in linear potential sweep voltammetry," *Journal of Electroanalytical Chemistry and Interfacial Electrochemistry*, vol. 52, no. 3, pp. 355–393, 1974.
- [17] Y. Li, Y. Gao, Y. Cao, H. Li, "Electrochemical sensor for bisphenol A determination based on MWCNT/melamine complex modified GCE," *Sensors and Actuators B*, vol. 171–172, pp. 726–733, 2012.
- [18] S. Bouden, G. Trippé-Allard, J. Ghilane, H. Randriamahazaka, "Electrochemical immobilization of redox active molecule based ionic liquid," *Electrochemistry Communications*, vol. 58, pp. 65–68, 2015.
- [19] D. Uzun, H. Arslan, A. Balaban Gündüzalp, E. Hasdemir, "Preparation of modified glassy carbon surface with N-(1-H-indole-3yl) methylene thiazole-2-amine and its characterization," *Surface & Coatings Technology*, vol. 239, pp. 108–115, 2014.
- [20] Y. Chen, L.-R. Guo, W. Chen, X.-J. Yang, B. Jin, L.-M. Zheng, X.-H. Xia, "3-mercaptopropylphosphonic acid modified gold electrode for electrochemical detection of dopamine," *Bioelectrochemistry*, vol. 75, pp. 26–31, 2009.
- [21] H. Chen, J.-H. Jiang, Y. Huang, T. Deng, J.-S. Li, G.-L. Shen, R.-Q. Yu, "An electrochemical impedance immunosensor with signal amplification based on Au-colloid labeled antibody complex," *Sensors and Actuators B*, vol. 117, pp. 211–218, 2006.
- [22] M. Khoshroo, A. A. Rostami, "Characterization of the organic molecules deposited at gold surface by the electrochemical reaction of diazonium salts," *Journal of Electroanalytical Chemistry*, vol. 647, pp. 117–122, 2010.
- [23] R. Zhang, G.-D. Jin, D. Chen, X.-Y. Hu, "Simultaneous electrochemical determination of dopamine, ascorbic acid and uric acid using poly(acid chrome blue K) modified glassy carbon electrode," *Sensors and Actuators B*, vol. 138, pp. 174–181, 2009.
- [24] D. Deletioğlu, E. Hasdemir, A.O. Solak, Z. Üstündağ, R. Güzel, Preparation and characterization of poly(indole-3-carboxaldehyde) film at the glassy carbon surface, *Thin Solid Films*. 519 (2010) 784–789.
- [25] R. N. Goyal, N. Kumar, N. K. Singhal, "Oxidation chemistry and biochemistry of indole and effect of its oxidation product in albino mice," *Bioelectrochemistry and Bioenergetics*, vol. 45, pp. 47–53, 1998.
- [26] R. S. Deinhammer, M. Ho, J. W. Anderegg, M. D. Porter, "Electrochemical oxidation of amine-containing compounds: A route to the surface modification of glassy carbon electrodes," *Langmuir*, vol. 10, pp. 1306–1313, 1994.
- [27] Y. Li, X. Lin, "Simultaneous electroanalysis of dopamine, ascorbic acid and uric acid by poly (vinyl alcohol) covalently modified glassy carbon electrode," *Sensors and Actuators B*, vol. 115, pp. 134–139, 2006.
- [28] V. K. Gupta, M. L. Yolac, N. Atar, A. Osman Solak, L. Uzun, Z. Üstündağ, "Electrochemically modified sulfisoxazole nanofilm on glassy carbon for determination of cadmium(II) in water samples," *Electrochimica Acta*, vol. 105, pp. 149–156, 2013.

JOURNAL OF SCIENCE



SAKARYA UNIVERSITY

Sakarya University Journal of Science

ISSN 1301-4048 | e-ISSN 2147-835X | Period Bimonthly | Founded: 1997 | Publisher Sakarya University |
<http://www.saujs.sakarya.edu.tr/>

Title: Coefficient Inequalities For Janowski Type Close-To-Convex Functions Associated With Ruscheweyh Derivative Operator

Authors: Öznur Özkan Kılıç

Received: 2019-01-10 00:00:00

Accepted: 2019-01-28 00:00:00

Article Type: Research Article

Volume: 23

Issue: 5

Month: October

Year: 2019

Pages: 714-717

How to cite

Öznur Özkan Kılıç; (2019), Coefficient Inequalities For Janowski Type Close-To-Convex Functions Associated With Ruscheweyh Derivative Operator. Sakarya University Journal of Science, 23(5), 714-717, DOI: 10.16984/saufenbilder.511321

Access link

<http://www.saujs.sakarya.edu.tr/issue/44066/511321>

New submission to SAUJS

<http://dergipark.gov.tr/journal/1115/submission/start>

Coefficient Inequalities for Janowski Type Close-to-Convex Functions Associated with Ruscheweyh Derivative Operator

Öznur Özkan Kılıç*¹

ABSTRACT

The aim of this paper is to introduce a new subclasses of the Janowski type close-to-convex functions defined by Ruscheweyh derivative operator and obtain coefficient bounds belonging to this class.

Keywords: Univalent Function, Subordination, Close-to-Convex Function, Ruscheweyh Derivative Operator

1. INTRODUCTION

Let \mathcal{A} denote the class of functions of the form

$$f(z) = z + \sum_{n=2}^{\infty} a_n z^n$$

which are analytic in the open unit disk

$$\Delta = \{z \in \mathbb{C} : |z| < 1\}.$$

Let \mathcal{S} denote the subclasses of \mathcal{A} which are univalent in Δ .

An analytic function f is subordinate to an analytic function F , written as $f < F$ or

$f(z) < F(z)$, if there exists a Schwarz function $\omega: \Delta \rightarrow \Delta$ with $\omega(0) = 0$ and $|\omega(z)| < 1$ satisfying $f(z) = F(\omega(z))$. In particular, if F is univalent in Δ , we have the following equivalence:

$$f(z) < F(z) \Leftrightarrow [f(0) = F(0) \wedge f(\Delta) = F(\Delta)].$$

The Hadamard product or convolution of two functions $f(z) = z + \sum_{n=2}^{\infty} a_n z^n \in \mathcal{A}$ and

$g(z) = z + \sum_{n=2}^{\infty} b_n z^n \in \mathcal{A}$, denoted by $f * g$, is defined by

$$(f * g)(z) = z + \sum_{n=2}^{\infty} a_n b_n z^n$$

for $z \in \Delta$.

In 1975, Ruscheweyh [5] introduced a linear operator $\mathcal{D}^\delta: \mathcal{A} \rightarrow \mathcal{A}$ defined by

$$\begin{aligned} \mathcal{D}^\delta f(z) &= \frac{z}{(1-z)^{\delta+1}} * f(z) \\ &= z + \sum_{n=2}^{\infty} \varphi_n(\delta) a_n z^n \end{aligned}$$

with

$$\varphi_n(\delta) = \frac{(\delta+1)_{n-1}}{(n-1)!}$$

* Corresponding Author

¹ Baskent University, Statistics and Computer Science Program, Ankara, Turkey ORCID: 0000-0003-4209-9320

for $\delta > -1$ and $(a)_n$ is Pochhammer symbol defined by

$$(a)_n = \frac{\Gamma(a+n)}{\Gamma(a)}$$

$$= \begin{cases} 1 & \text{if } n = 0 \\ a(a+1)\cdots(a+n-1) & \text{if } n \in \mathbb{N} \end{cases}$$

for $a \in \mathbb{C}$ and $\mathbb{N} = \{1,2,3,\dots\}$.

Notice that

$$\mathcal{D}^0 f(z) = f(z),$$

$$\mathcal{D}^1 f(z) = zf'(z)$$

and

$$\mathcal{D}^m f(z) = \frac{z(z^{m-1}f(z))^m}{m!}$$

$$= z + \sum_{n=2}^{\infty} \frac{\Gamma(n+m)}{\Gamma(m+1)(n-1)!} a_n z^n$$

for all $\delta = m \in \mathbb{N}_0 = \{0,1,2,\dots\}$.

In geometric function theory, various subclasses defined by Ruscheweyh derivative operator were studied.

Let \mathcal{S}^* and \mathcal{C} be the usual subclasses of functions which members are univalent, starlike and convex in Δ , respectively. We also denote $\mathcal{S}^*(\alpha)$ and $\mathcal{C}(\alpha)$ the class of starlike functions of order α and the class of convex functions of order α , for $0 \leq \alpha < 1$, respectively. Note that $\mathcal{S}^* = \mathcal{S}^*(0)$ and $\mathcal{C} = \mathcal{C}(0)$.

In 1973, Janowski [2] introduced the classes by $\mathcal{S}^*(A, B)$ and $\mathcal{C}(A, B)$

$$\mathcal{S}^*(A, B) = \left\{ f \in \mathcal{A} : \frac{zf'(z)}{f(z)} < \frac{1 + Az}{1 + Bz} \right\}$$

and

$$\mathcal{C}(A, B) = \left\{ f \in \mathcal{A} : 1 + \frac{zf''(z)}{f'(z)} < \frac{1 + Az}{1 + Bz} \right\}$$

for $-1 \leq B < A \leq 1$, $z \in \Delta$. Note that

$$\mathcal{S}^*(\alpha) = \mathcal{S}^*(1 - 2\alpha, -1), \quad \mathcal{S}^* = \mathcal{S}^*(1, -1) \quad \text{and}$$

$$\mathcal{C}(\alpha) = \mathcal{C}(1 - 2\alpha, -1), \quad \mathcal{C} = \mathcal{C}(1, -1).$$

A function $f \in \mathcal{A}$ is said to be close-to-star if and only if there exists $g \in \mathcal{S}^*$ such that $\Re\{f(z)/g(z)\} > 0$ for all $z \in \Delta$. Also, a function $f \in \mathcal{A}$ is said to be close-to-convex if and only if there exists $g \in \mathcal{C}$ such that $\Re\{f'(z)/g'(z)\} > 0$ for all $z \in \Delta$. The classes of close-to-star and close-to-convex functions denote by \mathcal{CS}^* and \mathcal{CC} , respectively. The class of close-to-star functions was introduced by Reade in [4] and the class of close-to-convex functions was introduced by Kaplan in [3]. Similarly, we denote by $\mathcal{CS}^*(\gamma)$ and $\mathcal{CC}(\gamma)$ the classes of close-to-star functions of order γ and close-to-convex functions of order γ , for $0 \leq \gamma < 1$, respectively. Note that $\mathcal{CS}^* = \mathcal{CS}^*(0)$ and $\mathcal{CC} = \mathcal{CC}(0)$.

The class of Janowski type close-to-starlike functions in Δ , denoted by $\mathcal{CS}^*(A, B)$, is defined by

$$\mathcal{CS}^*(A, B) = \left\{ f \in \mathcal{A} : \frac{f(z)}{g(z)} < \frac{1 + Az}{1 + Bz}, g \in \mathcal{S}^* \right\}$$

for $-1 \leq B < A \leq 1$, $z \in \Delta$. Similarly, the class of Janowski type close-to-convex functions in Δ , denoted by $\mathcal{CC}(A, B)$, is defined by

$$\mathcal{CC}(A, B) = \left\{ f \in \mathcal{A} : \frac{f'(z)}{g'(z)} < \frac{1 + Az}{1 + Bz}, g \in \mathcal{C} \right\}$$

for $-1 \leq B < A \leq 1$, $z \in \Delta$. The classes are introduced by Reade [4] in 1955.

Definition 1.1. The class of Janowski type functions defined by Ruscheweyh derivative operator in Δ , denoted by $\mathcal{J}_{\mathcal{R}}(\delta, \beta, A, B)$, is defined by

$$\mathcal{J}_{\mathcal{R}}(\delta, \beta, A, B) = \left\{ f \in \mathcal{A} : \frac{\mathcal{D}^\delta f(z)}{\mathcal{D}^\beta g(z)} < \frac{1 + Az}{1 + Bz}, \right.$$

$$\left. g \in \mathcal{S}^* \right\}$$

for $\delta, \beta > -1$, $-1 \leq B < A \leq 1$, $z \in \Delta$.

We need the following lemma to obtain our results.

Lemma 1.2. [1] If the function $p(z)$ of the form

$$p(z) = 1 + \sum_{n=1}^{\infty} p_n z^n$$

is analytic in Δ and

$$p(z) < \frac{1 + Az}{1 + Bz}$$

then $|p_n| \leq A - B$, for $n \in \mathbb{N}, -1 \leq B < A \leq 1$.

2. MAIN RESULTS AND THEIR CONSEQUENCES

We begin by finding the estimates on the coefficient $|a_n|$ for functions in the class $\mathcal{J}_{\mathcal{R}}(\delta, \beta, A, B)$.

Theorem 2.1. If the function $f(z) \in \mathcal{A}$ be in the class $\mathcal{J}_{\mathcal{R}}(\delta, \beta, A, B)$, then

$$|a_n| \leq \frac{n \varphi_n(\beta) + (A-B) \sum_{m=1}^{n-1} m \varphi_m(\beta)}{\varphi_n(\delta)}. \quad (2.1)$$

Proof. Let $f(z) \in \mathcal{J}_{\mathcal{R}}(\delta, \beta, A, B)$. Then, there are analytic functions $g(z) = z + \sum_{n=2}^{\infty} b_n z^n \in \mathcal{S}^*$, ω is a Schwarz function and

$p(z) = 1 + \sum_{n=1}^{\infty} p_n z^n$ as in Lemma 1.2 such that

$$\frac{\mathcal{D}^{\delta} f(z)}{\mathcal{D}^{\beta} g(z)} = \frac{1 + A\omega(z)}{1 + B\omega(z)} = p(z) \quad (2.2)$$

for $z \in \Delta$. Then (2.2) can be written as

$$\mathcal{D}^{\delta} f(z) = p(z) \cdot \mathcal{D}^{\beta} g(z)$$

or

$$\begin{aligned} z + \sum_{n=2}^{\infty} \varphi_n(\delta) a_n z^n \\ = z + \sum_{n=2}^{\infty} \sum_{m=1}^n \varphi_{n-m+1}(\beta) b_{n-m+1} p_{m-1} \end{aligned}$$

Equating the coefficients of like powers of z , we obtain

$$\varphi_2(\delta) a_2 = \varphi_2(\beta) b_2 + p_1,$$

$$\varphi_3(\delta) a_3 = \varphi_2(\beta) b_2 p_1 + \varphi_3(\beta) b_3 + p_2,$$

and

$$\begin{aligned} \varphi_n(\delta) a_n &= \varphi_n(\beta) b_n + \varphi_{n-1}(\beta) b_{n-1} p_1 \\ &+ \varphi_{n-2}(\beta) b_{n-2} p_2 + \dots + p_{n-1}. \end{aligned}$$

By using Lemma 1.2 and $g \in \mathcal{S}^*$, we get

$$\varphi_n(\delta) |a_n| \leq n \varphi_n(\beta) + (A - B) \sum_{m=1}^{n-1} m \varphi_m(\beta)$$

and this inequality is equivalent to (2.1).

Corollary 2.2. If the function $f(z) \in \mathcal{A}$ be in the class $\mathcal{CS}^*(A, B)$, then

$$|a_n| \leq n + \frac{(A-B)(n-1)n}{2}.$$

Proof. In Theorem 2.1, we take $\delta = 0, \beta = 0$.

Corollary 2.3. If the function $f(z) \in \mathcal{A}$ be in the class $\mathcal{CS}^*(\gamma)$, then

$$|a_n| \leq n + (1 - \gamma)(n - 1)n.$$

Proof. In Theorem 2.1, we take $\delta = 0, \beta = 0$,

$$A = 1 - 2\gamma, B = -1.$$

Corollary 2.4. If the function $f(z) \in \mathcal{A}$ be in the class \mathcal{CS}^* , then

$$|a_n| \leq n^2.$$

Proof. In Theorem 2.1, we take $\delta = 0, \beta = 0$,

$$A = 1, B = -1.$$

Corollary 2.5. If the function $f(z) \in \mathcal{A}$ be in the class $\mathcal{CC}(A, B)$, then

$$|a_n| \leq 1 + \frac{(A-B)(n-1)}{2}.$$

Proof. In Theorem 2.1, we take $\delta = 1, \beta = 0$.

Corollary 2.6. If the function $f(z) \in \mathcal{A}$ be in the class $\mathcal{CC}(\gamma)$, then

$$|a_n| \leq 1 + (1 - \gamma)(n - 1).$$

Proof. In Theorem 2.1, we take $\delta = 1, \beta = 0$,

$$A = 1 - 2\gamma, B = -1.$$

Corollary 2.7. If the function $f(z) \in \mathcal{A}$ be in the class \mathcal{CC} , then

$$|a_n| \leq n.$$

Proof. In Theorem 2.1, we take $\delta = 1$, $\beta = 0$,

$$A = 1, B = -1.$$

We note that Results in Corollary 2.4 and Corollary 2.7 were proved by Reade in 1955.

(See [4])

REFERENCES

- [1] R. M. Goel, B. C. Mehrok, "A subclass of starlike functions with respect to symmetric points," *Tamkang Journal of Mathematics*, vol. 13, no. 1, pp. 11–24, 1982.
- [2] W. Janowski, "Some extremal problems for certain families of analytic functions," *Annales Polonici Mathematici*, 28, pp. 297-326, 1973.
- [3] W. Kaplan, "Close-to-convex schlicht functions," *The Michigan Mathematical Journal*, vol.1, no.2, pp. 169-185, 1952.
- [4] M. O. Reade, " On close-to-convex univalent functions," *The Michigan Mathematical Journal*, vol. 3, no. 1, pp. 59-62, 1955.
- [5] S. Ruscheweyh, "New criteria for univalent functions," *Proceedings of the American Mathematical Society*, vol. 49, no. 1, pp. 109- 115, 1975.

JOURNAL OF SCIENCE



SAKARYA UNIVERSITY

Sakarya University Journal of Science

ISSN 1301-4048 | e-ISSN 2147-835X | Period Bimonthly | Founded: 1997 | Publisher Sakarya University |
<http://www.saujs.sakarya.edu.tr/>

Title: Asymptotically J_{Σ} -Equivalence of Sequences of Sets

Authors: Uğur Ulusu, Esra Gülle

Received: 2019-01-08 00:00:00

Accepted: 2019-03-01 00:00:00

Article Type: Research Article

Volume: 23

Issue: 5

Month: October

Year: 2019

Pages: 718-723

How to cite

Uğur Ulusu, Esra Gülle; (2019), Asymptotically J_{Σ} -Equivalence of Sequences of Sets. Sakarya University Journal of Science, 23(5), 718-723, DOI: 10.16984/saufenbilder.509863

Access link

<http://www.saujs.sakarya.edu.tr/issue/44066/509863>

New submission to SAUJS

<http://dergipark.gov.tr/journal/1115/submission/start>

Asymptotically \mathcal{J}_σ -Equivalence of Sequences of Sets

Uğur Ulusu^{*1}, Esra Gülle²

Abstract

In this study, we introduce the concepts of Wijsman asymptotically \mathcal{J} -invariant equivalence ($W_{\mathcal{J}\sigma}^L$), Wijsman asymptotically strongly p -invariant equivalence ($[W_{V_\sigma}^L]_p$) and Wijsman asymptotically \mathcal{J}^* -invariant equivalence ($W_{\mathcal{J}^*}^L$). Also, we investigate the relationships among the concepts of Wijsman asymptotically invariant equivalence, Wijsman asymptotically invariant statistical equivalence, $W_{\mathcal{J}\sigma}^L$, $[W_{V_\sigma}^L]_p$ and $W_{\mathcal{J}^*}^L$.

Keywords: asymptotically equivalence, \mathcal{J} -convergence, invariant convergence, sequences of sets, Wijsman convergence

1. INTRODUCTION AND BACKGROUND

Let σ be a mapping of the positive integers into themselves. A continuous linear functional ψ on ℓ_∞ , the space of real bounded sequences, is said to be an invariant mean or a σ -mean if it satisfies following conditions:

- * $\psi(s) \geq 0$, when the sequence $s = (s_n)$ has $s_n \geq 0$ for all n ,
- * $\psi(e) = 1$, where $e = (1,1,1,\dots)$ and
- * $\psi(s_{\sigma(n)}) = \psi(s_n)$ for all $s \in \ell_\infty$.

The mappings σ are assumed to be one-to-one and such that $\sigma^m(n) \neq n$ for all positive integers n and m , where $\sigma^m(n)$ denotes the m th iterate of the mapping σ at n . Thus, ψ extends the limit functional on c , the space of convergent sequences, in the sense that $\psi(s) = \lim s$ for all $s \in c$.

Mursaleen [4] defined the concept of strongly σ -convergent sequence. Then, using a positive real number p , Savaş [9] generalized the concept of strongly σ -convergent sequence. Following, Savaş and Nuray [10] defined the concept of lacunary σ -statistically convergent sequence.

The idea of \mathcal{J} -convergence which is based on the structure of the ideal \mathcal{J} of subsets of the set \mathbb{N} (natural numbers) was introduced by Kostyrko *et al.* [2].

$\mathcal{J} \subseteq 2^{\mathbb{N}}$ which is a family of subsets of \mathbb{N} is called an ideal if it satisfies following conditions:

- * $\emptyset \in \mathcal{J}$,
- * For each $X, Y \in \mathcal{J}$ we have $X \cup Y \in \mathcal{J}$,
- * For each $X \in \mathcal{J}$ and each $Y \subseteq X$ we have $Y \in \mathcal{J}$.

* Corresponding Author egulle@aku.edu.tr

¹ Afyon Kocatepe University, Analysis and Functions Theory, Afyon, Turkey ORCID: 0000-0001-7658-6114

² Afyon Kocatepe University, Analysis and Functions Theory, Afyon, Turkey ORCID: 0000-0001-5575-2937

Let $\mathcal{J} \subseteq 2^{\mathbb{N}}$ be an ideal. If $\mathbb{N} \notin \mathcal{J}$, then \mathcal{J} is called non-trivial and if $\{n\} \in \mathcal{J}$ for each $n \in \mathbb{N}$, then a non-trivial ideal \mathcal{J} is called admissible.

All ideals considered in this study are assumed to be admissible.

An admissible ideal $\mathcal{J} \subset 2^{\mathbb{N}}$ is said to satisfy the property (AP) if for every countable family of mutually disjoint sets $\{X_1, X_2, \dots\}$ belonging to \mathcal{J} there exists a countable family of sets $\{Y_1, Y_2, \dots\}$ such that the symmetric difference $X_j \Delta Y_j$ is a finite set for $j \in \mathbb{N}$ and $Y = (\bigcup_{j=1}^{\infty} Y_j) \in \mathcal{J}$.

$\mathcal{F} \subseteq 2^{\mathbb{N}}$ which is a family of subsets of \mathbb{N} is called a filter if it satisfies following conditions:

- * $\emptyset \notin \mathcal{F}$,
- * For each $X, Y \in \mathcal{F}$ we have $X \cap Y \in \mathcal{F}$,
- * For each $X \in \mathcal{F}$ and each $Y \supseteq X$ we have $Y \in \mathcal{F}$.

For any ideal there is a filter $\mathcal{F}(\mathcal{J})$ corresponding with \mathcal{J} , given by

$$\mathcal{F}(\mathcal{J}) = \{M \subset \mathbb{N} : (\exists X \in \mathcal{J})(M = \mathbb{N} \setminus X)\}.$$

A sequence $s = (s_n)$ is said to be \mathcal{J} -convergent to L if for every $\gamma > 0$, the set

$$B_\gamma = \{n : |s_n - L| \geq \gamma\}$$

belongs to \mathcal{J} . It is denoted by $\mathcal{J} - \lim s_n = L$.

A sequence $s = (s_n)$ is said to be \mathcal{J}^* -convergent to L if there exists a set $M = \{m_1 < m_2 < \dots < m_n < \dots\} \in \mathcal{F}(\mathcal{J})$ such that

$$\lim_{n \rightarrow \infty} s_{m_n} = L.$$

It is denoted by $\mathcal{J}^* - \lim s_n = L$.

Recently, the concepts of σ -uniform density of a subset B of the set \mathbb{N} and corresponding \mathcal{J}_σ -convergence for real sequences were introduced by Nuray *et al.* [5].

Let $B \subseteq \mathbb{N}$ and

$$s_m = \min_n |B \cap \{\sigma(n), \sigma^2(n), \dots, \sigma^m(n)\}|,$$

$$S_m = \max_n |B \cap \{\sigma(n), \sigma^2(n), \dots, \sigma^m(n)\}|.$$

If the following limits exists

$$\underline{\mathcal{V}}(B) = \lim_{m \rightarrow \infty} \frac{s_m}{m}, \quad \overline{\mathcal{V}}(B) = \lim_{m \rightarrow \infty} \frac{S_m}{m},$$

then they are called a lower σ -uniform density and an upper σ -uniform density of the set B , respectively.

If $\underline{\mathcal{V}}(B) = \overline{\mathcal{V}}(B)$, then $\mathcal{V}(B) = \underline{\mathcal{V}}(B) = \overline{\mathcal{V}}(B)$ is called the σ -uniform density of B .

The class of all $B \subseteq \mathbb{N}$ with $\mathcal{V}(B) = 0$ is denoted by \mathcal{J}_σ .

A sequence $s = (s_n)$ is said to be \mathcal{J}_σ -convergent to L if for every $\gamma > 0$, the set

$$B_\gamma = \{n : |s_n - L| \geq \gamma\}$$

belongs to \mathcal{J}_σ , i.e., $\mathcal{V}(B_\gamma) = 0$. It is denoted by $\mathcal{J}_\sigma - \lim s_n = L$.

Let Z be any non-empty set. The function $g: \mathbb{N} \rightarrow P(Z)$ is defined by $g(i) = C_i \in P(Z)$ for each $i \in \mathbb{N}$, where $P(Z)$ is power set of Z . The sequence $\{C_i\} = (C_1, C_2, \dots)$, which is the range's elements of g , is said to be set sequences.

The concept of convergence for real sequences has been extended by many researchers to concepts of convergence for set sequences. The one of these such extensions considered in this study is the concept of Wijsman convergence (see, [6, 7]).

Let (Z, d) be a metric space. For any point $z \in Z$ and any non-empty subset C of Z , the distance from z to C is defined by

$$\rho(z, C) = \inf_{c \in C} d(z, c).$$

Throughout the study, we take (Z, d) be a metric space and C, C_i, D_i be any non-empty closed subsets of Z .

A sequence $\{C_i\}$ is said to be Wijsman convergent to C if for each $z \in Z$,

$$\lim_{i \rightarrow \infty} \rho(z, C_i) = \rho(z, C).$$

A sequence $\{C_i\}$ is said to be Wijsman invariant convergent to C if for each $z \in Z$

$$\lim_{n \rightarrow \infty} \frac{1}{n} \sum_{i=1}^n \rho(z, C_{\sigma^i(m)}) = \rho(z, C),$$

uniformly in $m = 1, 2, \dots$.

Let $0 < p < \infty$. A sequence $\{C_i\}$ is said to be Wijsman strongly p -invariant convergent to C if for each $z \in Z$

$$\lim_{n \rightarrow \infty} \frac{1}{n} \sum_{i=1}^n |\rho(z, C_{\sigma^i(m)}) - \rho(z, C)|^p = 0,$$

uniformly in m .

A sequence $\{C_i\}$ is said to be Wijsman invariant statistical convergent to C if for every $\gamma > 0$ and each $z \in Z$

$$\lim_{n \rightarrow \infty} \frac{1}{n} |\{i \leq n: |\rho(z, C_{\sigma^i(m)}) - \rho(z, C)| \geq \gamma\}| = 0,$$

uniformly in m .

In [3], Marouf introduced the concept of asymptotically equivalence for real sequences. Then, this concept has been development by several researchers.

Two nonnegative sequences $s = (s_n)$ and $t = (t_n)$ are said to be asymptotically equivalent if

$$\lim_{n \rightarrow \infty} \frac{s_n}{t_n} = 1.$$

It is denoted by $s \sim t$.

The concept of asymptotically equivalence for real sequences has been firstly extended by Ulusu and Nuray [11] to concept of asymptotically equivalence (Wijsman sense) for set sequences. Similar concepts can be seen in [1, 8].

For any non-empty closed subsets $C_i, D_i \subseteq Z$ such that $\rho(z, C_i) > 0$ and $\rho(z, D_i) > 0$ for each $z \in Z$, the sequences $\{C_i\}$ and $\{D_i\}$ are said to be asymptotically equivalent (Wijsman sense) if for each $z \in Z$,

$$\lim_{i \rightarrow \infty} \frac{\rho(z, C_i)}{\rho(z, D_i)} = 1.$$

It is denoted by $C_i \sim D_i$.

As an example, consider the following sequences:

$$C_i = \{(x, y): x^2 + y^2 + 2ix = 0\},$$

$$D_i = \{(x, y): x^2 + y^2 - 2ix = 0\}.$$

Since

$$\lim_{i \rightarrow \infty} \frac{\rho(z, C_i)}{\rho(z, D_i)} = 1,$$

the sequences $\{C_i\}$ and $\{D_i\}$ are asymptotically equivalent (Wijsman sense), i.e., $C_i \sim D_i$.

The term $\rho(z; C_i, D_i)$ is defined as follows:

$$\rho(z; C_i, D_i) = \begin{cases} \frac{\rho(z, C_i)}{\rho(z, D_i)}, & z \notin C_i \cup D_i \\ L, & z \in C_i \cup D_i. \end{cases}$$

Two sequences $\{C_i\}$ and $\{D_i\}$ are said to be asymptotically invariant equivalent (Wijsman sense) of multiple L if for each $z \in Z$

$$\lim_{n \rightarrow \infty} \frac{1}{n} \sum_{i=1}^n \rho(z; C_{\sigma^i(m)}, D_{\sigma^i(m)}) = L,$$

uniformly in m . It is denoted by $C_i \overset{wv_\sigma^L}{\sim} D_i$.

Two sequences $\{C_i\}$ and $\{D_i\}$ are said to be asymptotically invariant statistical equivalent (Wijsman sense) of multiple L if for every $\gamma > 0$ and each $z \in Z$

$$\lim_{n \rightarrow \infty} \frac{1}{n} |\{i \leq n: |\rho(z; C_{\sigma^i(m)}, D_{\sigma^i(m)}) - L| \geq \gamma\}| = 0,$$

uniformly in m . It is denoted by $C_i \overset{ws_\sigma^L}{\sim} D_i$.

The set of all asymptotically invariant statistical equivalent (Wijsman sense) sequences is denoted by WS_σ^L .

From now on, for short, we use $\rho_z(C)$, $\rho_z(C_i)$ and $\rho_z(C_i, D_i)$ instead of $\rho(z, C)$, $\rho(z, C_i)$ and $\rho(z; C_i, D_i)$, respectively.

2. MAIN RESULTS

Definition 2.1 Two sequences $\{C_i\}$ and $\{D_i\}$ are said to be Wijsman asymptotically J -invariant equivalent or Wijsman asymptotically J_σ -

equivalent of multiple L if for every $\gamma > 0$ and each $z \in Z$, the set

$$B_{\gamma,z}^{\sim} := \{i: |\rho_z(C_i, D_i) - L| \geq \gamma\}$$

belongs to J_{σ} , that is, $\mathcal{V}(B_{\gamma,z}^{\sim}) = 0$. In this case,

we write $C_i \stackrel{W_{J\sigma}^L}{\sim} D_i$ and if $L = 1$, simply Wijsman asymptotically J -invariant equivalent.

The set of all Wijsman asymptotically J_{σ} -equivalent sequences will be denoted by $W_{J\sigma}^L$.

Theorem 2.2 Let $\rho_z(C_i) = \mathcal{O}(\rho_z(D_i))$. If $C_i \stackrel{W_{J\sigma}^L}{\sim} D_i$, then $C_i \stackrel{WV_{J\sigma}^L}{\sim} D_i$.

Proof. Let $m, n \in \mathbb{N}$ are arbitrary and $\gamma > 0$ is given. Now, we calculate

$$T_z(m, n) := \left| \frac{1}{m} \sum_{i=1}^m \rho_z(C_{\sigma^i(n)}, D_{\sigma^i(n)}) - L \right|.$$

Then, for each $z \in Z$ we have

$$T_z(m, n) \leq T_z^1(m, n) + T_z^2(m, n)$$

where

$$T_z^1(m, n) := \frac{1}{m} \sum_{\substack{i=1 \\ |\rho_z(C_{\sigma^i(n)}, D_{\sigma^i(n)}) - L| \geq \gamma}}^m |\rho_z(C_{\sigma^i(n)}, D_{\sigma^i(n)}) - L|$$

and

$$T_z^2(m, n) := \frac{1}{m} \sum_{\substack{i=1 \\ |\rho_z(C_{\sigma^i(n)}, D_{\sigma^i(n)}) - L| < \gamma}}^m |\rho_z(C_{\sigma^i(n)}, D_{\sigma^i(n)}) - L|.$$

For each $z \in Z$ and every $n = 1, 2, \dots$, it is obvious that $T_z^2(m, n) < \gamma$. Since $\rho_z(C_i) = \mathcal{O}(\rho_z(D_i))$, there exists an $R > 0$ such that

$$|\rho_z(C_{\sigma^i(n)}, D_{\sigma^i(n)}) - L| \leq R$$

for each $z \in Z$ ($i = 1, 2, \dots; n = 1, 2, \dots$). So, this implies that

$$\begin{aligned} T_z^1(m, n) &\leq \frac{R}{m} |\{1 \leq i \leq m: |\rho_z(C_{\sigma^i(n)}, D_{\sigma^i(n)}) - L| \geq \gamma\}| \\ &\leq R \frac{\max\{|\{1 \leq i \leq m: |\rho_z(C_{\sigma^i(n)}, D_{\sigma^i(n)}) - L| \geq \gamma\}|}{m} \\ &= R \frac{S_m}{m}. \end{aligned}$$

Then, due to our hypothesis, $C_i \stackrel{WV_{J\sigma}^L}{\sim} D_i$.

Definition 2.3 Let $0 < p < \infty$. Two sequences $\{C_i\}$ and $\{D_i\}$ are said to be Wijsman asymptotically strongly p -invariant equivalent of multiple L if for each $z \in Z$

$$\lim_{n \rightarrow \infty} \frac{1}{n} \sum_{i=1}^n |\rho_z(C_{\sigma^i(n)}, D_{\sigma^i(n)}) - L|^p = 0,$$

uniformly in m . In this case, we write $C_i \stackrel{[W_{V\sigma}^L]^p}{\sim} D_i$ and if $L = 1$, simply Wijsman asymptotically strongly p -invariant equivalent.

Theorem 2.4 If $C_i \stackrel{[W_{V\sigma}^L]^p}{\sim} D_i$, then $C_i \stackrel{W_{J\sigma}^L}{\sim} D_i$.

Proof. Let $C_i \stackrel{[W_{V\sigma}^L]^p}{\sim} D_i$ and $\gamma > 0$ is given. For each $z \in Z$, we can write

$$\begin{aligned} &\sum_{i=1}^m |\rho_z(C_{\sigma^i(n)}, D_{\sigma^i(n)}) - L|^p \\ &\geq \sum_{i=1}^m |\rho_z(C_{\sigma^i(n)}, D_{\sigma^i(n)}) - L|^p \\ &\quad |\rho_z(C_{\sigma^i(n)}, D_{\sigma^i(n)}) - L| \geq \gamma \\ &\geq \gamma^p |\{1 \leq i \leq m: |\rho_z(C_{\sigma^i(n)}, D_{\sigma^i(n)}) - L| \geq \gamma\}| \\ &\geq \gamma^p \max_n |\{1 \leq i \leq m: |\rho_z(C_{\sigma^i(n)}, D_{\sigma^i(n)}) - L| \geq \gamma\}| \\ &\text{and so} \\ &\frac{1}{m} \sum_{i=1}^m |\rho_z(C_{\sigma^i(n)}, D_{\sigma^i(n)}) - L|^p \\ &\geq \gamma^p \frac{\max\{|\{1 \leq i \leq m: |\rho_z(C_{\sigma^i(n)}, D_{\sigma^i(n)}) - L| \geq \gamma\}|}{m} \\ &= \gamma^p \frac{S_m}{m}, \end{aligned}$$

for all n . This implies that $\lim_{m \rightarrow \infty} \frac{S_m}{m} = 0$ and

consequently $C_i \stackrel{W_{J\sigma}^L}{\sim} D_i$.

Theorem 2.5 Let $\rho_z(C_i) = \mathcal{O}(\rho_z(D_i))$. If $C_i \stackrel{W_{J\sigma}^L}{\sim} D_i$, then $C_i \stackrel{[W_{V\sigma}^L]^p}{\sim} D_i$.

Proof. Let $\rho_z(C_i) = \mathcal{O}(\rho_z(D_i))$ and $\gamma > 0$ is given. Also, we suppose that $C_i \stackrel{W_{J\sigma}^L}{\sim} D_i$. By assumption, we have $\mathcal{V}(B_{\gamma,z}^{\sim}) = 0$. Since

$\rho_z(C_i) = \mathcal{O}(\rho_z(D_i))$, there exists an $R > 0$ such that

$$|\rho_z(C_{\sigma^i(n)}, D_{\sigma^i(n)}) - L| \leq R$$

for each $z \in Z$ ($i = 1, 2, \dots; n = 1, 2, \dots$).

Then, for each $z \in Z$ we get

$$\begin{aligned} & \frac{1}{m} \sum_{i=1}^m |\rho_z(C_{\sigma^i(n)}, D_{\sigma^i(n)}) - L|^p \\ &= \frac{1}{m} \sum_{\substack{i=1 \\ |\rho_z(C_{\sigma^i(n)}, D_{\sigma^i(n)}) - L| \geq \gamma}}^m |\rho_z(C_{\sigma^i(n)}, D_{\sigma^i(n)}) - L|^p \\ & \quad + \frac{1}{m} \sum_{\substack{i=1 \\ |\rho_z(C_{\sigma^i(n)}, D_{\sigma^i(n)}) - L| < \gamma}}^m |\rho_z(C_{\sigma^i(n)}, D_{\sigma^i(n)}) - L|^p \\ & \leq R \frac{\max\{i \leq m: |\rho_z(C_{\sigma^i(n)}, D_{\sigma^i(n)}) - L| \geq \gamma\}}{m} + \gamma^p \\ & \leq R \frac{S_m}{m} + \gamma^p, \end{aligned}$$

for all n . Hence, for each $z \in Z$ we have

$$\lim_{m \rightarrow \infty} \frac{1}{m} \sum_{i=1}^m |\rho_z(C_{\sigma^i(n)}, D_{\sigma^i(n)}) - L|^p = 0.$$

This completes the proof.

Considering the Theorem 2.4 and Theorem 2.5 together we can give the following corollary:

Corollary 2.6 Let $\rho_z(C_i) = \mathcal{O}(\rho_z(D_i))$. Then, $C_i \stackrel{W_{J_\sigma}^L}{\sim} D_i$ if and only if $C_i \stackrel{[W_{V_\sigma}^L]^p}{\sim} D_i$.

Now, without proof, we shall state a theorem that gives a relation between $W_{J_\sigma}^L$ and WS_σ^L .

Theorem 2.7 $C_i \stackrel{W_{J_\sigma}^L}{\sim} D_i \Leftrightarrow C_i \stackrel{WS_\sigma^L}{\sim} D_i$.

Definition 2.8 Two sequences $\{C_i\}$ and $\{D_i\}$ are said to be Wijsman asymptotically J^* -invariant equivalent or Wijsman asymptotically J_σ^* -equivalent of multiple L if and only if there exists a set $M = \{m_1 < m_2 < \dots < m_i < \dots\} \in \mathcal{F}(J_\sigma)$ such that for each $z \in Z$,

$$\lim_{i \rightarrow \infty} \rho_z(C_{m_i}, D_{m_i}) = L.$$

In this case, we write $C_i \stackrel{W_{J_\sigma^*}^L}{\sim} D_i$ and if $L = 1$, simply Wijsman asymptotically J_σ^* -equivalent.

Theorem 2.9 If $C_i \stackrel{W_{J_\sigma^*}^L}{\sim} D_i$, then $C_i \stackrel{W_{J_\sigma}^L}{\sim} D_i$.

Proof. Let $C_i \stackrel{W_{J_\sigma^*}^L}{\sim} D_i$. Then, there exists a set $H \in J_\sigma$ such that for $M = \mathbb{N} \setminus H = \{m_1 < m_2 < \dots < m_i < \dots\}$ and each $z \in Z$,

$$\lim_{i \rightarrow \infty} \rho_z(C_{m_i}, D_{m_i}) = L. \quad (2.1)$$

Given $\gamma > 0$. By (2.1), there exists an $i_0 \in \mathbb{N}$ such that

$$|\rho_z(C_{m_i}, D_{m_i}) - L| < \gamma,$$

for each $i > i_0$. Hence, for every $\gamma > 0$ and each $z \in Z$ it is obvious that

$$\{i \in \mathbb{N}: |\rho_z(C_i, D_i) - L| \geq \gamma\} \subset H \cup \{m_1 < m_2 < \dots < m_{i_0}\}. \quad (2.2)$$

Since J_σ is admissible, the set on the right-hand side of (2.2) belongs to J_σ . Therefore, $C_i \stackrel{W_{J_\sigma}^L}{\sim} D_i$.

The converse of Theorem 2.9 holds if J_σ has property (AP).

Theorem 2.10 Let J_σ has property (AP). If $C_i \stackrel{W_{J_\sigma}^L}{\sim} D_i$, then $C_i \stackrel{W_{J_\sigma^*}^L}{\sim} D_i$.

Proof. Suppose that J_σ satisfies condition (AP).

Let $C_i \stackrel{W_{J_\sigma}^L}{\sim} D_i$. Then, for every $\gamma > 0$ and each $z \in Z$ we have

$$\{i: |\rho_z(C_i, D_i) - L| \geq \gamma\} \in J_\sigma.$$

Put

$$X_1 = \{i: |\rho_z(C_i, D_i) - L| \geq 1\}$$

and

$$X_n = \{i: \frac{1}{n} \leq |\rho_z(C_i, D_i) - L| < \frac{1}{n-1}\},$$

for $n \geq 2$ ($n \in \mathbb{N}$). Obviously, $X_i \cap X_j = \emptyset$ for each $z \in Z$ and $i \neq j$. By condition (AP), there exists a sequence of $\{Y_n\}_{n \in \mathbb{N}}$ such that $X_j \Delta Y_j$ are

finite sets for $j \in \mathbb{N}$ and $Y = (\bigcup_{i=1}^\infty Y_j) \in \mathcal{J}_\sigma$. It is enough to prove that for $G = \mathbb{N} \setminus Y$ and each $z \in Z$, we have

$$\lim_{\substack{i \rightarrow \infty \\ i \in G}} \rho_z(C_i, D_i) = L. \tag{2.3}$$

Let $\delta > 0$. Choose $n \in \mathbb{N}$ such that $\frac{1}{n+1} < \delta$. Hence, for each $z \in Z$

$$\{i: |\rho_z(C_i, D_i) - L| \geq \delta\} \subset \bigcup_{j=1}^{n+1} X_j.$$

Since $X_j \Delta Y_j$ ($j = 1, 2, \dots, n + 1$) are finite sets, there exists an $i_0 \in \mathbb{N}$ such that

$$\left(\bigcup_{j=1}^{n+1} Y_j\right) \cap \{i: i > i_0\} = \left(\bigcup_{j=1}^{n+1} X_j\right) \cap \{i: i > i_0\}. \tag{2.4}$$

If $i > i_0$ and $i \notin Y$, then $i \notin \bigcup_{j=1}^{n+1} Y_j$ and by (2.4), $i \notin \bigcup_{j=1}^{n+1} X_j$. But then, for each $z \in Z$ we get

$$|\rho_z(C_i, D_i) - L| < \frac{1}{n+1} < \delta$$

and so (2.3) holds. Consequently, we have $C_i \overset{W_{\mathcal{J}_\sigma}^L}{\sim} D_i$.

3. REFERENCES

[1] Ö. Kişi and F. Nuray, “On $S_\lambda^L(\mathcal{J})$ -asymptotically statistical equivalence of sequences of sets,” *ISRN Mathematical Analysis*, vol. 2013, Article ID 602963, 6 pages, 2013. doi:10.1155/2013/602963

[2] P. Kostyrko, W. Wilczyński, and T. Šalát, “ \mathcal{J} -convergence,” *Real Anal. Exchange*, vol. 26, no. 2, pp. 669–686, 2000.

[3] M. Marouf, “Asymptotic equivalence and summability,” *Int. J. Math. Math. Sci.*, vol 16, no. 4, pp. 755–762, 1993.

[4] M. Mursaleen, “Matrix transformation between some new sequence spaces,” *Houston J. Math.*, vol. 9, no. 4, pp. 505–509, 1983.

[5] F. Nuray, H. Gök, and U. Ulusu, “ \mathcal{J}_σ -convergence,” *Math. Commun.*, vol.16, pp. 531–538, 2011.

[6] F. Nuray and B. E. Rhoades, “Statistical convergence of sequences of sets,” *Fasc. Math.*, vol. 49, pp. 87–99, 2012.

[7] N. Pancaroğlu and F. Nuray, “On invariant statistically convergence and lacunary invariant statistically convergence of sequences of sets,” *Progress in Applied Mathematics*, vol. 5, no. 2, pp. 23–29, 2013.

[8] N. Pancaroğlu, F. Nuray, and E. Savaş, “On asymptotically lacunary invariant statistical equivalent set sequences,” *AIP Conf. Proc.*, vol. 1558, no. 1, pp. 780–781, 2013. doi:10.1063/1.4825609

[9] E. Savaş, “Strongly σ -convergent sequences,” *Bull. Calcutta Math.*, vol. 81, pp. 295–300, 1989.

[10] E. Savaş and F. Nuray, “On σ -statistically convergence and lacunary σ -statistically convergence,” *Math. Slovaca*, vol. 43, no. 3, pp. 309–315, 1993.

[11] U. Ulusu and F. Nuray, “On asymptotically lacunary statistical equivalent set sequences,” *Journal of Mathematics*, vol. 2013, Article ID 310438, 5 pages, 2013. doi:10.1155/2013/310438

JOURNAL OF SCIENCE



SAKARYA UNIVERSITY

Sakarya University Journal of Science

ISSN 1301-4048 | e-ISSN 2147-835X | Period Bimonthly | Founded: 1997 | Publisher Sakarya University |
<http://www.saujs.sakarya.edu.tr/>

Title: A New Approximation To Classify The Liquids Measured in Microwave Frequency Range

Authors: Turgut Ozturk

Received: 2018-12-12 00:00:00

Accepted: 2019-03-05 00:00:00

Article Type: Research Article

Volume: 23

Issue: 5

Month: October

Year: 2019

Pages: 724-730

How to cite

Turgut Ozturk; (2019), A New Approximation To Classify The Liquids Measured in Microwave Frequency Range. Sakarya University Journal of Science, 23(5), 724-730, DOI: 10.16984/saufenbilder.495640

Access link

<http://www.saujs.sakarya.edu.tr/issue/44066/495640>

New submission to SAUJS

<http://dergipark.gov.tr/journal/1115/submission/start>

A New Approximation to Classify the Liquids Measured in Microwave Frequency Range

Turgut Ozturk*¹

Abstract

Different classification techniques have been proposed to analyze the measurement results in order to show that the liquids measured in the microwave frequency range can be separated. Furthermore, it has been shown that the proposed process can be applied successfully with different liquid quantities. Furthermore, the effect of different type containers has been demonstrated. In this context, five different liquids have been measured between 0.8-5 GHz in this study, by using ring resonator method. Thus, the ability of the proposed model has been demonstrated by the success of the measurement method and classification techniques.

Keywords: classification, liquids, ring-resonator method, transmission parameter, PCA, k-means

1. INTRODUCTION

The dielectric parameters can be used for quality control process. Because, each sector wants to know the structure of the material they use and follow the content change. Recent studies have shown the wide range of applications of liquids in science and industry by their characterization [1], [2]. Monitoring changes suffered during the processing of a product is important for the quality-control process. Therefore, the preliminary information about the preferred sample will facilitate the next steps. For example, the change in grape juice or fresh milk that is converted into another product can be explained by the analysis results obtained in raw condition.

The complex permittivity of high-loss liquids was measured in the frequency band of mm wave and wine analysis was performed. The reason for preferring the mm wave frequency band is that the complex permittivity of water reaches its maximum values in this frequency range. In addition, when the amount of water is increased in this study, the change in the complex permittivity (ϵ) of the mixture (wine and musts) has been shown for wine quality [3]. A new method has been proposed to analyze the dielectric effects at four different single-frequency measurements by positioning two sensor antennas in a linear fashion in order to determine the impurities in aqueous substances [4]. In addition, a Group Method of Data

* Corresponding Author: turgut.ozturk@btu.edu.tr

¹ Bursa Technical University, Electrical-Electronics Engineering, Bursa, Turkey. ORCID: 0000-0002-0749-5849

Handling (GMDH), which is a kind of neural network, has been used to predict the permittivity values by using the correlation process [5].

Many measurement methods can be used in microwave and millimeter wave frequency bands to determine the complex permittivity of the liquids or solids [3], [6], [7]. Ring Resonator Method (RRM) is used to obtain the dielectric properties of any materials. In this context, this process can also be applied for quality control of a product. Thus, a brief review of the contributes of permittivity measurement, which is related to the molecular structure, can be repeated. A non-destructive measurement of the permittivity can be used for the desired purpose after developing the most appropriate model and algorithm after performing measurement methods [8]. Since the complex permittivity is sensitive to the ionic content of the material and the water, it is possible to understand the structural change of the measured material [9], [10]. The quality structure of asphalt pavements was investigated by measuring the permittivity value between 7-17 GHz [11]. The permittivity of liquids as well as solids can be calculated non-destructively with the aid of the S_{11} reflection coefficient [12], [13]. On the other hand, the permittivity of mixture was extracted by considering the aggregation of solute and solvent molecules in the liquids using mixing rules [14].

In recent studies, it has been observed that machine learning methods are frequently used in characterization and classification processes. This approach may be particularly useful in the production of a new material or in the determination of properties of a material. In this context, 3D materials are used to characterize metallic materials in order to lead texture analysis, and the results are analyzed by Failure analysis method [15]. The color and texture properties used in existing algorithms as well as the lighting conditions supported by the thermal image and the effect of color diversity on the identification of materials have been successfully demonstrated [16]. With a different approach, nearly 400 organic molecules have been analyzed, by presenting three different algorithms for predicting viscosity at room temperature, taking

into consideration hydrogen bonds as another attractive feature [17]. Furthermore, various methods (principal component analysis and k-means etc.) have been presented to analyze the multivariate data in engineering applications [18], [19]. Besides that, artificial neural networks or genetic algorithms approaches have been used for classification, however, they need training process [19]–[21]. Therefore, PCA and K-means algorithms were selected for proposed model.

This paper presents a method to collect the transmission parameter of liquids in different quantities and distinguish them according to whether they are reliable or not. A successful classification and identification have been made by evaluating the various liquids among themselves without the need for any reference measurements. Furthermore, it has been shown that the intended target can be achieved by varying the amount of liquids. Moreover, the containers which will not absorb the samples are selected to avoid the absorption effects of liquid with container. In this context, the liquids are distinguished successfully by proposed measurement and classification approaches.

2. MEASUREMENT SPECTROSCOPY AND CLASSIFICATION TECHNIQUES

RRM can be used to characterize the materials as well as they performed for oscillators and filters in microwave. RRM has wide application areas such as radar detectors, modern medicine, wireless mobile communications, and military facilities [22]. RRM consists of a microstrip line with two feed lines and coupling gaps as shown in Figure 1. The measurement process is very short for this method. Therefore, the simple of measuring process makes the method easy to use.

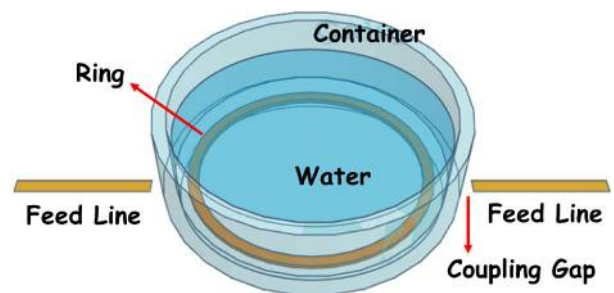


Figure 1. Presentation of RRM with a container

For this measurement process, a container (made by glass and teflon) is placed to contact with ring as shown in Figure 1. Before measurement process, ring resonator is calibrated. The transmission coefficient is measured by using ring antenna with a vector network analyzer [23]. This method is a non-destructive, although it is not non-contactless. The liquids as well as solids can be measured by using RRM [24], [25]. Therefore, it can be used to measure the liquids.

The Principle Components (PCs) of PCA are achieved by eigenvalue decomposition of correlation or covariance matrix of predictive variables. The PCs can be computed using statistical software, after the variables and data set are composed. Hence, the outputs of eigen vectors (linear coefficients) are provided along with standard and mean deviation of each variables. By this way, the PCs are computed for regression process. A sample can be identified using a few components instead of thousands of variables [26].

The problem can be defined as determining the k (integer) points in R^d (d -dimensional space), called centers, in n data points for K-means technique. Hence, the distance of mean squared from every data point to nearest center. This process is called squared error distortion. The number of clusters should be pre-specified in data set. The appropriate cluster number is determined by a trial and error process and this is a blind side due to it makes more difficult the clustering process. Therefore, a set might be adopted instead of a single default K . Because, the reflection of specific characteristic of reasonable large data set is very important to achieve a good clustering [18].

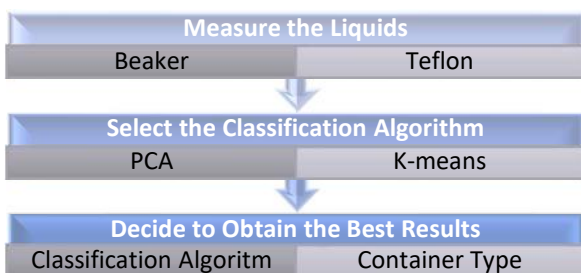


Figure 2. The flowchart of proposed model

The proposed model can be summarized with three steps: Measure the liquids with different quantities, use the classification algorithms, and determine the container and classification techniques to obtain the best results. The types of algorithms and containers used in this study are shown as seen in Figure 2.

3. RESULTS AND DISCUSSION

The transmission parameter can be used as a determinative property. Hence, the differences of measured liquids can be exposed using characteristic indication of liquids. As mentioned above, two different classification techniques were used to classify the liquids which were measured in two different containers by using RRM between 0.8-5 GHz. These classification techniques can explore the differences of S_{21} parameter as shown in Figure 3.

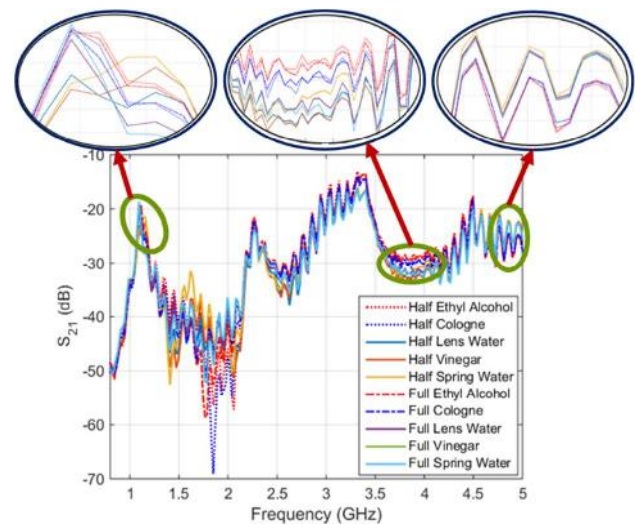


Figure 3. S_{21} parameter of liquids in beaker container between 0.8-5 GHz using RRM

Although this classification process is difficult, the used techniques can be clutched the changes which were specified using zoom regions in Figure 3. It is not possible to make the distinction by using S_{21} parameters at first glance. But the cologne and ethyl alcohol samples are dissociated in zoom regions as shown in Figure 3. The measured liquids by using RRM were sorted as 1) Half-Ethyl Alcohol 2) Half-Cologne 3) Half-Lens Water 4) Half-Vinegar 5) Half-Spring Water 6) Full-Ethyl Alcohol 7) Full-Cologne 8) Full-Lens Water 9) Full-Vinegar 10) Full-Spring Water.

With the number of measured liquid samples, the number of data collected by the VNA in the RRM spectroscopy system (0.8-5 GHz) is very large (as 201 points). For this reason, K-means and PCA classification are applied to the algorithms which are successful in multivariate data analysis. To show the separation of liquids, firstly PCA algorithm was performed for the measurement of beaker container as seen in Figure 4.

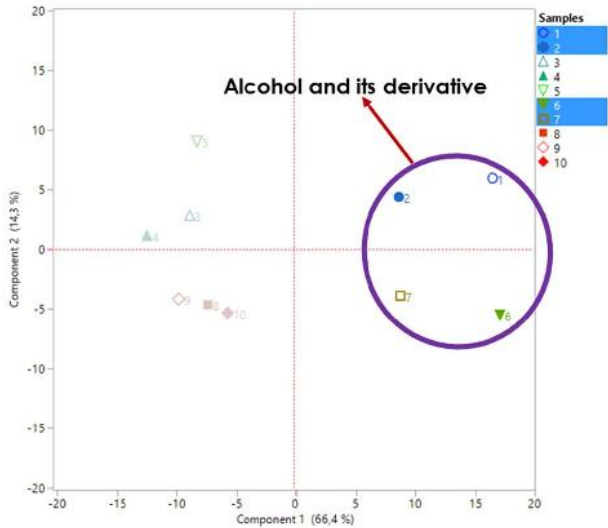


Figure 4. Clustering of liquids measured in beaker container for PCA algorithm

In fact, although a successful classification process has taken place, it may be desired that the unsafe group appear more clearly. The k-means algorithm was used as an alternative to PCA algorithm and the results of PCA were confirmed. After entering the number of possible groups by the user, the results are achieved as shown in Figure 5.

Using K-means algorithm, the distance between the safe and unsafe groups has become more prominent and there are also two different colors for the two groups that have arisen due to the structure of the algorithm used. In this way, the intended groups are reached as safe (green) and unsafe (red) groups. The same liquids were measured using teflon container to repeat the results obtained in the beaker container in a different container and to verify the results. As in the beaker container, the results were first analyzed by PCA algorithm and the separation was obtained as seen in Figure 6.

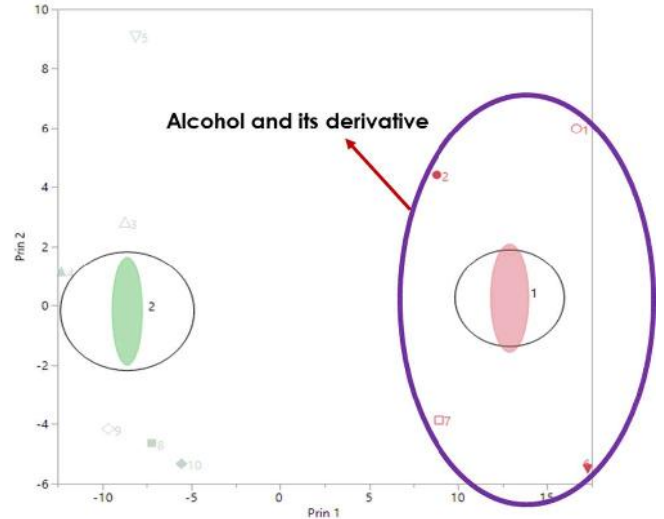


Figure 5. Clustering of liquids measured in beaker container for K-means algorithm

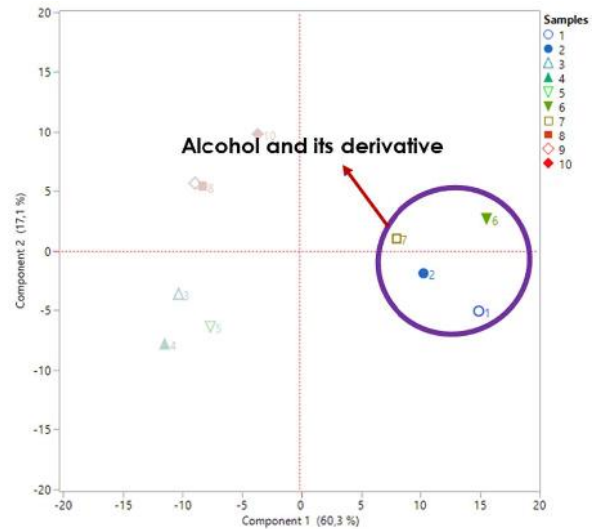


Figure 6. Clustering of liquids measured in teflon container for PCA algorithm

Finally, the measurements made in teflon container were analyzed by K-means algorithm and a successful classification was obtained as in beaker container. The distance between the groups has become more pronounced as shown in Figure 7.

The preferred classification techniques differ from other algorithms, and can classify more materials, especially as they reduce the size of the data. Therefore, the locations of used parameters (pin and component) in figures show where the groups will be located eventually. It should be considered the average distance from the main

points; the groups are composed after the characteristic analysis of each sample in data set. In addition, to present the homogeneous data set of this study, two components and two pins were used.

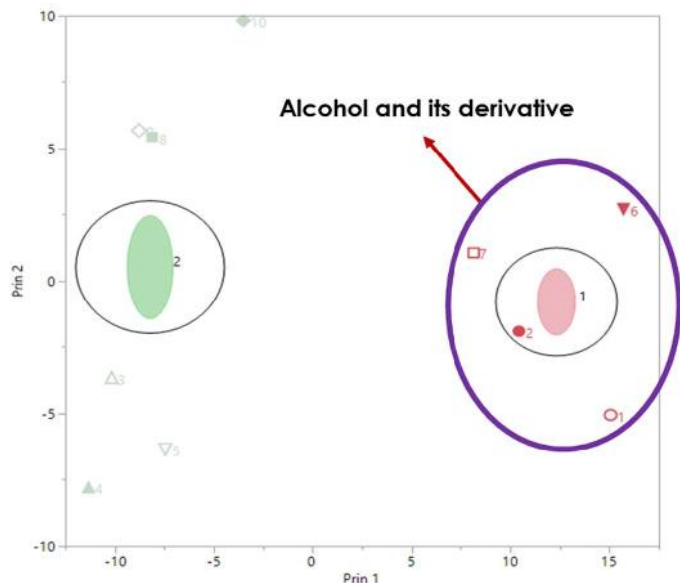


Figure 7. Clustering of liquids measured in teflon container for K-means algorithm

The measurement results of liquids in beaker and teflon containers were analyzed with different quantities. The classification process has been done with high accuracy using multivariate data algorithm. K-means algorithm was found to be better than PCA, when the results are examined. It was determined that the amount of liquid in the container partially affected the classification process. The number of liquid types measured in this study eliminates this negative situation. However, in order to obtain a better classification result, the best of the multivariate data algorithms should be determined when the liquid type is too high.

4. CONCLUSION

It has been shown that without the need for any additional process, it is possible to have information about a liquid with the assistance of other parameter predicted using an available parameter. Furthermore, different quantities of liquids have been measured by RRM between 0.8-5 GHz to demonstrate the ability of recognition of samples using two different classification

techniques. The results show that a spectroscopy system will be able to develop to detect unknown and hazardous liquids. However, studies should be focused to identify different types of fluids that occur with molecular interactions. Thus, it may be possible to identify mixed liquids. On the other hand, a new classification algorithm can be tried to classify the liquids.

REFERENCES

- [1] N. T. Cherpak, A. A. Barannik, Y. V. Prokopenko, T. A. Smirnova, and Y. F. Filipov, "A New Technique of Dielectric Characterization of Liquids," in *Nonlinear Dielectric Phenomena in Complex Liquids*, Dordrecht: Kluwer Academic Publishers, 2004, pp. 63–76.
- [2] T. Ozturk, "Characterization of Liquids Using Electrical Properties in Microwave and Millimeter Wave Frequency Bands," *J. Nondestruct. Eval.*, vol. 38, no. 1, p. 11, Mar. 2019.
- [3] B. Lucic et al., "Correlation of liquid viscosity with molecular structure for organic compounds using different variable selection methods," *Arkivoc*, vol. 2002, no. 4, p. 45, Jul. 2002.
- [4] S. Kim, J. Kwak, and B. Ko, "Automatic Classification Algorithm for Raw Materials using Mean Shift Clustering and Stepwise Region Merging in Color," *J. Broadcast Eng.*, vol. 21, no. 3, pp. 425–435, May 2016.
- [5] T. Ghorbanpour, A. Ghanadzadeh Gilani, and S. Fallahi, "Experimental measurement, excess parameters, and analysis of permittivity data for (primary diols + ketones) binary systems," *J. Mol. Liq.*, vol. 260, pp. 403–414, Jun. 2018.
- [6] T. Ozturk, A. Elhawil, İ. Uluer, and M. T. Guner, "Development of extraction techniques for dielectric constant from free-space measured S-parameters between 50 and 170 GHz," *J. Mater. Sci. Mater.*

- Electron., vol. 28, no. 15, pp. 11543–11549, Aug. 2017.
- [7] T. Ozturk, M. Hudlička, and İ. Uluer, “Development of Measurement and Extraction Technique of Complex Permittivity Using Transmission Parameter S₂₁ for Millimeter Wave Frequencies,” *J. Infrared, Millimeter, Terahertz Waves*, vol. 38, no. 12, pp. 1510–1520, Dec. 2017.
- [8] I. Matiss, “Multi-element capacitive sensor for non-destructive measurement of the dielectric permittivity and thickness of dielectric plates and shells,” *NDT E Int.*, vol. 66, pp. 99–105, Sep. 2014.
- [9] M. Fares, Y. Fargier, G. Villain, X. Derobert, and S. P. Lopes, “Determining the permittivity profile inside reinforced concrete using capacitive probes,” *NDT E Int.*, vol. 79, pp. 150–161, Apr. 2016.
- [10] G. Villain, A. Ihamouten, and X. Dérobert, “Determination of concrete water content by coupling electromagnetic methods: Coaxial/cylindrical transition line with capacitive probes,” *NDT E Int.*, vol. 88, no. July 2016, pp. 59–70, Jun. 2017.
- [11] M.-K. Olkkonen, “Permittivity scanning of asphalt in a transmission configuration across 7–17 GHz employing a phase compensation method,” *NDT E Int.*, vol. 83, pp. 143–151, Oct. 2016.
- [12] Z. Li, A. Haigh, C. Soutis, A. Gibson, and R. Sloan, “A Simulation-Assisted Non-destructive Approach for Permittivity Measurement Using an Open-Ended Microwave Waveguide,” *J. Nondestruct. Eval.*, vol. 37, no. 3, p. 39, Sep. 2018.
- [13] Y. Jiang, Y. Ju, and L. Yang, “Nondestructive In-situ Permittivity Measurement of Liquid Within a Bottle Using an Open-Ended Microwave Waveguide,” *J. Nondestruct. Eval.*, vol. 35, no. 1, p. 7, Mar. 2016.
- [14] A. A. Amooey, “Improved mixing rules for description of the permittivity of mixtures,” *J. Mol. Liq.*, vol. 180, pp. 31–33, Apr. 2013.
- [15] P. Saponaro, S. Sorensen, A. Kolagunda, and C. Kambhamettu, “Material classification with thermal imagery,” in *IEEE Conference on Computer Vision and Pattern Recognition (CVPR)*, 2015, vol. 07–12–June, pp. 4649–4656.
- [16] T. Bhattacharjee, J. Wade, and C. Kemp, “Material Recognition from Heat Transfer given Varying Initial Conditions and Short-Duration Contact,” in *Robotics: Science and Systems XI*, 2015.
- [17] M. X. Bastidas-Rodríguez, “Fractographic classification in metallic materials by using 3D processing and computer vision techniques,” *Rev. Fac. Ing.*, vol. 25, no. 43, pp. 83–96, 2016.
- [18] T. Kanungo et al., “An Efficient k -Means Clustering Algorithm: Analysis and Implementation,” *IEEE Trans. Pattern Anal. Mach. Intell.*, vol. 24, no. 7, pp. 881–892, 2002.
- [19] T. Ozturk, “Classification of measured unsafe liquids using microwave spectroscopy system by multivariate data analysis techniques,” *J. Hazard. Mater.*, vol. 363, pp. 309–315, Feb. 2019.
- [20] S. Ozturk, E. Kayabasi, E. Celik, and H. Kurt, “Determination of lapping parameters for silicon wafer using an artificial neural network,” *J. Mater. Sci. Mater. Electron.*, vol. 29, no. 1, pp. 260–270, Jan. 2018.
- [21] E. Kayabasi, S. Ozturk, E. Celik, and H. Kurt, “Determination of cutting parameters for silicon wafer with a Diamond Wire Saw using an artificial neural network,” *Sol. Energy*, vol. 149, pp. 285–293, Jun. 2017.
- [22] G. E. Chatzarakis and T. Education, “Review of Different Ring Resonator Coupling Methods,” in *Proceedings of the 9th WSEAS International Conference on*

Telecommunications and Informatics, 2010, pp. 227–231.

- [23] M. Fishel, P. Koehn, and E. Rosen, “Comparison of ring resonator relative permittivity measurements to ground penetrating radar data,” May 2014.
- [24] L. Su, J. Mata-Contreras, P. Velez, and F. Martin, “Estimation of the complex permittivity of liquids by means of complementary split ring resonator (CSRR) loaded transmission lines,” in 2017 IEEE MTT-S International Microwave Workshop Series on Advanced Materials and Processes for RF and THz Applications (IMWS-AMP), 2017, pp. 1–3.
- [25] A. Kulkarni and V. Deshmukh, “Dielectric Properties Measurement Using Ring Resonator,” *Int. J. Sci. Res.*, vol. 4, no. 4, pp. 2361–2364, 2015.
- [26] M. Ringnér, “What is principal component analysis?,” *Nat. Biotechnol.*, vol. 26, no. 3, pp. 303–304, 2008.

JOURNAL OF SCIENCE



SAKARYA UNIVERSITY

Sakarya University Journal of Science

ISSN 1301-4048 | e-ISSN 2147-835X | Period Bimonthly | Founded: 1997 | Publisher Sakarya University |
<http://www.saujs.sakarya.edu.tr/>

Title: on Generalized Tribonacci Octonions

Authors: Arzu Özkoç Öztürk

Received: 2019-02-11 00:00:00

Accepted: 2019-03-06 00:00:00

Article Type: Research Article

Volume: 23

Issue: 5

Month: October

Year: 2019

Pages: 731-735

How to cite

Arzu Özkoç Öztürk; (2019), on Generalized Tribonacci Octonions. Sakarya University Journal of Science, 23(5), 731-735, DOI: 10.16984/saufenbilder.525320

Access link

<http://www.saujs.sakarya.edu.tr/issue/44066/525320>

New submission to SAUJS

<http://dergipark.gov.tr/journal/1115/submission/start>

On Generalized Tribonacci Octonions

Arzu Özkoç Öztürk^{*1}

Abstract

In this paper, we introduce generalized tribonacci octonion sequence which is a generalization of the third order recurrence relations. We investigate many identities which are created by using generalized tribonacci sequence. We get different results for these classes of octonions, comprised recurrence relation, summation formulas, Binet formula, norm value and generating function.

Keywords: Tribonacci octonion, Binet formula, Generalized Tribonacci sequence

1. INTRODUCTION

Tribonacci numbers which are described as

$$T_n = T_{n-1} + T_{n-2} + T_{n-3} \quad (1.1)$$

for $n \geq 4$, with initial conditions $T_1 = 1$, $T_2 = 1$ and $T_3 = 2$.

The generalized tribonacci sequence is the generalization of the sequences tribonacci, Padovan, Narayana and third order Jacobsthal sequences. The generalized Tribonacci sequence V_n defined as

$$V_n = rV_{n-1} + sV_{n-2} + tV_{n-3}, n \geq 3,$$

where $V_0 = a$, $V_1 = b$, $V_2 = c$ are arbitrary integers and r, s, t are real numbers. Its characteristic equation is $x^3 - rx^2 - sx - t = 0$ and it has one real and two conjugate complex

roots of it are $\alpha = \frac{r}{3} + A + B$, $\omega_1 = \frac{r}{3} + \varepsilon A + \varepsilon^2 B$ and $\omega_2 = \frac{r}{3} + \varepsilon^2 A + \varepsilon B$ where

$$A = \left(\frac{r^3}{27} + \frac{rs}{6} + \frac{t}{2} + \sqrt{\Delta} \right)^{\frac{1}{3}},$$

$$B = \left(\frac{r^3}{27} + \frac{rs}{6} + \frac{t}{2} + \sqrt{\Delta} \right)^{\frac{1}{3}},$$

with $\Delta = \frac{r^3 t}{27} - \frac{r^2 s^2}{108} + \frac{rst}{6} - \frac{s^3}{27} + \frac{t^2}{4}$ and

$$\varepsilon = -\frac{1}{2} + \frac{i\sqrt{3}}{2}.$$

It has Binet formula

$$V_n = \frac{P\alpha^n}{(\alpha - \omega_1)(\alpha - \omega_2)} - \frac{Q\omega_1^n}{(\alpha - \omega_1)(\omega_1 - \omega_2)}$$

* Corresponding Author: arzuozkoc@duzce.edu.tr

¹ Düzce University, Department of Mathematics, Düzce, Turkey. ORCID: 0000-0002-2196-3725

$$+ \frac{R\omega_2^n}{(\alpha - \omega_2)(\omega_1 - \omega_2)} \quad (1.2)$$

where $P = c - (\omega_1 + \omega_2)b + \omega_1\omega_2a$, $Q = c - (\alpha + \omega_2)b + \alpha\omega_2a$ and $R = c - (\alpha + \omega_1)b + \alpha\omega_1a$.

In Clifford algebra, octonions are a normed division algebra with eight dimensions over the real numbers larger than the quaternions. For α_i and $\beta_i \in \mathbb{R}$ ($i = 0, 1, \dots, 7$), the field of octonion

$$\alpha = \sum_{s=0}^7 \alpha_s e_s \text{ and } \beta = \sum_{s=0}^7 \beta_s e_s$$

is an eight-dimensional non-commutative and non-associative (but satisfy a weaker form of a associativity) algebra generated by eight base elements e_0, e_1, \dots, e_6 and e_7 which satisfy the non-commutative and non-associative multiplication rules. Afterwards the Fibonacci octonion numbers are given in [1]. For $n \geq 0$ the Fibonacci octonion numbers that are given for the n -th classic Fibonacci F_n number are defined by the following recurrence relation:

$$O_n = \sum_{s=0}^7 F_{n+s} e_s.$$

Also the sum and subtract of m and n are

$$m \pm n = \sum_{s=0}^7 (\alpha_s \pm \beta_s) e_s$$

where $m \in \mathbb{Q}$ can be written as, respectively.

$$\bar{m} = \alpha_0 - \sum_{s=0}^7 \alpha_s e_s$$

is the conjugate of m and this operation provides $\bar{\bar{m}} = m, \overline{m+n} = \bar{m} + \bar{n}$ and $\overline{m \cdot n} = \bar{m} \cdot \bar{n}$ for all $m, n \in \mathbb{Q}$. The norm of an octonion is defined

$$Nr^2(m \cdot n) = Nr^2(m)Nr^2(n) \text{ and}$$

$$(m \cdot n)^{-1} = m^{-1} \cdot n^{-1}.$$

Octonions are alternative but not commutative and not associative, $m \cdot (m \cdot n) = m^2 \cdot n$, $(m \cdot$

$$n) \cdot n = m \cdot n^2, (m \cdot n) \cdot m = m \cdot (n \cdot m) = m \cdot n \cdot m$$

where \cdot is the product on the octonions.

We give a definition of generalized tribonacci sequence which is a generalization of tribonacci numbers. Also we consider generalized tribonacci octonions which contain tribonacci, Padovan, Narayana octonions. In our work, we introduce for finding special identities of generalized tribonacci octonions. We motivate by their results in [2], [3] and [4]. In [3], they studied Horadam octonions. In [5], they considered Padovan and Pell-Padovan quaternions which is the third order quaternions. In our mind, with generalized tribonacci sequence V_n helped us for construct the recurrence relations of the generalized tribonacci octonions. The generalized tribonacci octonions $O_{V,n}$ are the example of the third order octonions with $n \geq 3$,

$$O_{V,n} = \sum_{k=0}^7 V_{n+k} e_k \quad (1.3)$$

where V_n is the n -th generalized tribonacci sequence. Generalized tribonacci sequence was examined in detail [6], [7] and it was shown that this sequence is used to generalize all the third order linear recurrence relations on octonions.

Note that, the second order linear recurrence octonion sequences for example in [8], they defined modified Pell and Modified k -Pell octonions and in [9], authors studied Pell octonions. Moreover in [10], (p, q) -Fibonacci octonions are obtained which is the same results in [3] but the initial conditions are $F_0(p, q) = 0$ and $F_1(p, q) = 1$, also in [11]. Another octonionic sequence was devoted to studying Jacobsthal and Jacobsthal-Lucas octonions in [12]. Furthermore in [13], they derived third-order Jacobsthal quaternions, now we expand all third order recurrence octonion sequences in one recurrence relations. New identities and relations were introduced in [14], which is on tribonacci quaternions. Also in [15], authors considered the bicomplex generalized tribonacci quaternions. Generalized tribonacci octonions were studied in [16], we expect to find octonions in a new third order recurrence concepts.

2. GENERALIZED TRIBONACCI OCTONIONS

The generalized tribonacci octonions $O_{V,n}$ are the example of sequences defined by a recurrence relation for $n \geq 3$,

$$O_{V,n} = rO_{V,n-1} + sO_{V,n-2} + tO_{V,n-3} \quad (2.1)$$

with the initial conditions of

$$O_{V,0} = \sum_{k=0}^7 V_k e_k = V_0 e_0 + V_1 e_1 + \dots + V_7 e_7$$

$$O_{V,1} = \sum_{k=0}^7 V_{1+k} e_k = V_1 e_0 + V_2 e_1 + \dots + V_8 e_7$$

and

$$O_{V,2} = \sum_{k=0}^7 V_{2+k} e_k = V_2 e_0 + V_3 e_1 + \dots + V_9 e_7$$

Theorem 2.1 Binet Formula for the generalized Tribonacci octonions $O_{V,n}$ are

$$O_{V,n} = \frac{P\alpha^* \alpha^n}{(\alpha - w_1)(\alpha - w_2)} - \frac{Qw_1^* w_1^n}{(\alpha - w_1)(w_1 - w_2)} + \frac{Rw_2^* w_2^n}{(\alpha - w_2)(w_1 - w_2)}$$

where

$$\alpha^* = e_0 + \alpha e_1 + \alpha^2 e_2 + \dots + \alpha^7 e_7$$

$$w_1^* = e_0 + w_1 e_1 + w_1^2 e_2 + \dots + w_1^7 e_7$$

$$w_2^* = e_0 + w_2 e_1 + w_2^2 e_2 + \dots + w_2^7 e_7.$$

Proof. Using the definition of the (1.3) and Binet formula for the generalized tribonacci numbers (1.2), we have

$$O_{V,n} = V_n e_0 + V_{n+1} e_1 + \dots + V_{n+7} e_7 = \left(\frac{P\alpha^* \alpha^n}{(\alpha - w_1)(\alpha - w_2)} - \frac{Qw_1^* w_1^n}{(\alpha - w_1)(w_1 - w_2)} + \frac{Rw_2^* w_2^n}{(\alpha - w_2)(w_1 - w_2)} \right) e_0$$

$$+ \left(\frac{P\alpha^* \alpha^{n+1}}{(\alpha - w_1)(\alpha - w_2)} - \frac{Qw_1^* w_1^{n+1}}{(\alpha - w_1)(w_1 - w_2)} + \frac{Rw_2^* w_2^{n+1}}{(\alpha - w_2)(w_1 - w_2)} \right) e_1 + \dots + \left(\frac{P\alpha^* \alpha^{n+7}}{(\alpha - w_1)(\alpha - w_2)} - \frac{Qw_1^* w_1^{n+7}}{(\alpha - w_1)(w_1 - w_2)} + \frac{Rw_2^* w_2^{n+7}}{(\alpha - w_2)(w_1 - w_2)} \right) e_7.$$

Then make some arrangement,

$$O_{V,n} = \frac{P}{(\alpha - w_1)(\alpha - w_2)} (\alpha^n e_0 + \alpha^{n+1} e_1 + \dots + \alpha^{n+7} e_7) - \frac{Q}{(\alpha - w_1)(w_1 - w_2)} (w_1^n e_0 + w_1^{n+1} e_1 + \dots + w_1^{n+7} e_7) + \frac{R}{(\alpha - w_2)(w_1 - w_2)} (w_2^n e_0 + w_2^{n+1} e_1 + \dots + w_2^{n+7} e_7),$$

so

$$O_{V,n} = \frac{P\alpha^* \alpha^n}{(\alpha - w_1)(\alpha - w_2)} - \frac{Qw_1^* w_1^n}{(\alpha - w_1)(w_1 - w_2)} + \frac{Rw_2^* w_2^n}{(\alpha - w_2)(w_1 - w_2)}.$$

Theorem 2.2 [16] (Generating Function) The generating function for $O_{V,n}$ is

$$\sum_{n=0}^{\infty} O_{V,n} x^n = \frac{\left\{ \begin{array}{l} O_{V,0} + [O_{V,1} - rO_{V,0}]x \\ + [O_{V,2} - rO_{V,1} - sO_{V,0}]x^2 \end{array} \right\}}{1 - rx - sx^2 - tx^3}.$$

Proof. To compute generating function $O_{V,n}$ $\sum_{n=0}^{\infty} O_{V,n} x^n$

$$= O_{V,0} + O_{V,1}x + O_{V,2}x^2 + \dots + O_{V,n}x^n + \dots$$

then using the equations of $-rx \sum_{n=0}^{\infty} O_{V,n} x^n$, $-sx^2 \sum_{n=0}^{\infty} O_{V,n} x^n$ and $-tx^3 \sum_{n=0}^{\infty} O_{V,n} x^n$,

$$\left\{ \begin{array}{l} \sum_{n=0}^{\infty} O_{V,n} x^n - rx \sum_{n=0}^{\infty} O_{V,n} x^n \\ -sx^2 \sum_{n=0}^{\infty} O_{V,n} x^n - tx^3 \sum_{n=0}^{\infty} O_{V,n} x^n \end{array} \right\} = O_{V,0} + (O_{V,1} - rO_{V,0})x + (O_{V,2} - rO_{V,1} - sO_{V,0})x^2$$

$$\begin{aligned}
 &+(O_{V,3} - rO_{V,2} - sO_{V,1} - tO_{V,0})x^3 \\
 &+ \dots + (O_{V,n} - rO_{V,n-1} - sO_{V,n-2} - tO_{V,n-3})x^n \\
 &+ \dots
 \end{aligned}$$

So,

$$\begin{aligned}
 &\sum_{n=0}^{\infty} O_{V,n}x^n(1 - rx - sx^2 - tx^3) \\
 &= O_{V,0} + [O_{V,1} - rO_{V,0}]x + [O_{V,2} - rO_{V,1} - sO_{V,0}]x^2
 \end{aligned}$$

we get the result.

Then we can give the following theorem relative to summation formulas.

Theorem 2.3 The sum of the first n –terms of the octonion sequence $O_{V,n}$ is given by;

$$\sum_{l=0}^n O_{V,l} = \frac{\left\{ \begin{array}{l} (r+s-1)O_{V,0} + (r-1)O_{V,1} - O_{V,2} \\ +tO_{V,n-2} + (s+t)O_{V,n-1} + (r+s+t)O_{V,n} \end{array} \right\}}{r+s+t-1}$$

Proof. Note that, applying (2.1), we deduce that

$$\begin{aligned}
 n = 3 &\Rightarrow O_{V,3} = rO_{V,2} + sO_{V,1} + tO_{V,0} \\
 n = 4 &\Rightarrow O_{V,4} = rO_{V,3} + sO_{V,2} + tO_{V,1} \\
 &\dots \tag{2.2}
 \end{aligned}$$

$$\begin{aligned}
 n = n - 1 &\Rightarrow O_{V,n-1} = rO_{V,n-2} + sO_{V,n-3} + tO_{V,n-4} \\
 n = n &\Rightarrow O_{V,n} = rO_{V,n-1} + sO_{V,n-2} + tO_{V,n-3}.
 \end{aligned}$$

If we sum of both sides of (2.2), then we obtain

$$\begin{aligned}
 &O_{V,3} + \dots + O_{V,n} \\
 &= r \sum_{l=0}^n O_{V,l} + s \sum_{l=0}^n O_{V,l} + t \sum_{l=0}^n O_{V,l}. \tag{2.3}
 \end{aligned}$$

If we make necessary regulations, (2.3) becomes

$$\begin{aligned}
 &(r+s+t-1) \sum_{l=0}^n O_{V,l} \\
 &= \left\{ \begin{array}{l} (r+s-1)O_{V,0} + (r-1)O_{V,1} \\ +tO_{V,n-2} + (s+t)O_{V,n-1} + (r+s+t)O_{V,n} \end{array} \right\}
 \end{aligned}$$

as we claimed.

We formulate the norm value for the generalized tribonacci octonions.

Theorem 2.4 The norm value for generalized tribonacci octonions $O_{h,n}(x)$ is given by

$$\begin{aligned}
 Nr^2(O_{V,n}) &= P^2\alpha^{2n}(w_1 - w_2)^2\underline{\alpha} + Q^2w_1^{2n}(\alpha \\
 &-w_2)^2\underline{w_1} + R^2w_2^{2n}(\alpha - w_1)^2\underline{w_2} + 2RP(w_1 - \\
 &w_2)(\alpha - w_1)(\alpha w_2)^n\underline{\alpha w_2} - 2PQ(\alpha w_1)^n(w_1 - \\
 &w_2)(\alpha - w_2)\underline{\alpha w_1} - 2RQ(\alpha - w_1)(\alpha - \\
 &w_2)(w_1 w_2)^n\underline{w_1 w_2}
 \end{aligned}$$

where

$$\underline{\alpha} = 1 + \alpha^2 + \alpha^4 + \alpha^6 + \alpha^8 + \alpha^{10} + \alpha^{12} + \alpha^{14}$$

$$\underline{w_1} = 1 + w_1^2 + w_1^4 + w_1^6 + w_1^8 + w_1^{10} + w_1^{12} + w_1^{14}$$

$$\underline{w_2} = 1 + w_2^2 + w_2^4 + w_2^6 + w_2^8 + w_2^{10} + w_2^{12} + w_2^{14}$$

$$\underline{\alpha w_1} = 1 + \alpha w_1 + (\alpha w_1)^2 + (\alpha w_1)^3 + (\alpha w_1)^4$$

$$+(\alpha w_1)^5 + (\alpha w_1)^6 + (\alpha w_1)^7$$

$$\underline{\alpha w_2} = 1 + \alpha w_2 + (\alpha w_2)^2 + (\alpha w_2)^3 + (\alpha w_2)^4$$

$$+(\alpha w_2)^5 + (\alpha w_2)^6 + (\alpha w_2)^7$$

$$\underline{w_1 w_2} = \left\{ \begin{array}{l} 1 + w_1 w_2 + (w_1 w_2)^2 + (w_1 w_2)^3 \\ + (w_1 w_2)^4 + (w_1 w_2)^5 \\ + (w_1 w_2)^6 + (w_1 w_2)^7 \end{array} \right\}.$$

Proof. Note that by the norm definition,

$$Nr^2(O_{V,n}) = \sum_{l=0}^n V_{n+l}^2$$

also

$$V_n = \frac{P\alpha^n(w_1 - w_2) - Qw_1^n(\alpha - w_2) + Rw_2^n(\alpha - w_1)}{(\alpha - w_1)(w_1 - w_2)(\alpha - w_2)}$$

where

$$\delta = (\alpha - w_1)(w_1 - w_2)(\alpha - w_2).$$

Then

$$\begin{aligned} \delta^2 V_n^2 &= P^2 \alpha^{2n} (w_1 - w_2)^2 - 2PQ \alpha^n w_1^n (w_1 - w_2) (\alpha - w_2) \\ &+ Q^2 w_1^{2n} (\alpha - w_2)^2 + 2RP \alpha^n (w_1 - w_2) w_2^n (\alpha - w_1) \\ &- 2RQ w_1^n w_2^n (\alpha - w_2) (\alpha - w_1) + R^2 w_2^{2n} (\alpha - w_1)^2 \end{aligned}$$

so

$$\begin{aligned} \delta^2 N r^2 (O_{V,n}) &= P^2 \alpha^{2n} (w_1 - w_2)^2 - 2PQ \alpha^n w_1^n (w_1 - w_2) \\ &(\alpha - w_2) + Q^2 w_1^{2n} (\alpha - w_2)^2 + 2RP \alpha^n \\ &(w_1 - w_2) w_2^n (\alpha - w_1) - 2RQ w_1^n w_2^n (\alpha - w_2) (\alpha - w_1) \\ &+ R^2 w_2^{2n} (\alpha - w_1)^2 + \dots + P^2 \alpha^{2n+14} (w_1 - w_2)^2 \\ &+ Q^2 w_1^{2n+14} (\alpha - w_2)^2 + R^2 w_2^{2n+14} (\alpha - w_1)^2 \\ &+ 2RP \alpha^{n+7} (w_1 - w_2) w_2^{n+7} (\alpha - w_1) - 2PQ \alpha^{n+7} w_1^{n+7} \\ &(w_1 - w_2) (\alpha - w_2) - 2RQ w_1^{n+7} w_2^{n+7} (\alpha - w_2) (\alpha - w_1). \end{aligned}$$

Moreover, we done extra calculations so the result is clear.

3. REFERENCES

[1] O. Keçilioğlu, I. Akkus, ‘*The Fibonacci Octonions*,’ *Advances in Applied Clifford Algebras* 25 (2015), 151-158.

[2] G. Cerda-Morales, ‘*The third order Jacobsthal Octonions: Some Combinatorial Properties*,’ *An.St. Univ.Ovidius Constanta*, 26(3), 2018.

[3] A. Karataş, S. Halıcı, ‘*Horadam Octonions*,’ *An. S t. Univ. Ovidius Constant A.* 25(3)(2017), 97-106.

[4] G. Cerda-Morales, ‘*On a Generalization of Tribonacci Quaternions*,’ *Mediterranean Journal of Mathematics* 14:239 (2017), 1–12.

[5] D. Tascı, ‘*Padovan and Pell-Padovan Quaternions*,’ *Journal of Science and Arts*, 1(42)2018, 125-132.

[6] C.C. Yalavigi, ‘*Properties of Tribonacci Numbers*,’ *Fibonacci Q.* 10(3), (1972), 231–246.

[7] A.G. Shannon, A.F. Horadam, ‘*Some Properties of Third-order Recurrence Relations*,’ *Fibonacci Q.* 10(2), (1972), 135–146.

[8] P Catarino, ‘*The Modified Pell and Modified k-Pell Quaternions and Octonions*,’ *Advances in Applied Clifford Algebras* 26, (2016):577-590.

[9] A. Szynal-Liana, I. Włoch, ‘*The Pell Quaternions and the Pell Octonions*,’ *Advances in Applied Clifford Algebras* 26 (2016), 435–440.

[10] A. Ipek, C. Cimen, ‘*On (p, q) Fibonacci Octonions*.’ *Mathematica Aeterna*, 6(6)(2016), 923-932.

[11] A. Özkoç Öztürk, A. Porsuk, ‘*Some Remarks Regarding the (p, q) -Fibonacci and Lucas Octonion Polynomials*,’ *Universal Journal of Mathematics and Applications*, 1 (1) (2018), 46-53.

[12] C.B. Cimen, A. Ipek, ‘*On Jacobsthal and Jacobsthal-Lucas Octonions*,’ *Mediterranean Journal of Mathematics*, 14:37 (2017), 1–13.

[13] G. Cerda-Morales, ‘*Identities for Third Order Jacobsthal Quaternions*,’ *Advances in Applied Clifford Algebras* 27(2) (2017), 1043–1053.

[14] I. Akkus, G. Kizilaslan, ‘*On Some Properties of Tribonacci Quaternions*,’ arXiv:1708.05367.

[15] C. Kızılateş, P. Catarino and N. Tuglu, ‘*On the Bicomplex Generalized Tribonacci Quaternions*,’ *Mathematics*, 7 (1) (2019), 80.

[16] G. Cerda-Morales, ‘*The Unifying Formula for all Tribonacci-type Octonions Sequences and Their Properties*,’ arxiv.org/abs/1807.04140.

JOURNAL OF SCIENCE



SAKARYA UNIVERSITY

Sakarya University Journal of Science

ISSN 1301-4048 | e-ISSN 2147-835X | Period Bimonthly | Founded: 1997 | Publisher Sakarya University |
<http://www.saujs.sakarya.edu.tr/>

Title: Effects of Glass Fiber Reinforcement To Tensile Strength in Epoxy Matrix Granular Composite Materials

Authors: Hüseyin Onur Öztürk, Yaşar Kahraman

Received: 2018-10-12 00:00:00

Accepted: 2019-03-07 00:00:00

Article Type: Research Article

Volume: 23

Issue: 5

Month: October

Year: 2019

Pages: 736-743

How to cite

Hüseyin Onur Öztürk, Yaşar Kahraman; (2019), Effects of Glass Fiber Reinforcement To Tensile Strength in Epoxy Matrix Granular Composite Materials.

Sakarya University Journal of Science, 23(5), 736-743, DOI:

10.16984/saufenbilder.469746

Access link

<http://www.saujs.sakarya.edu.tr/issue/44066/469746>

New submission to SAUJS

<http://dergipark.gov.tr/journal/1115/submission/start>

Effects of glass fiber Reinforcement to Tensile Strength in Epoxy Matrix Granular Composite Materials

Hüseyin Onur Öztürk^{*1}, Yaşar Kahraman²

ABSTRACT

Conventional metal materials are used in every field in industrial applications, but contemporary requirements such as energy savings, environmental factors and carbon footprint increase the importance of composite materials in the industry. This study aims to develop a composite construction material for machine tools that allows easy molding, has lower-cost molding materials compared to existing systems, and requires relatively less finish machining given the comparable materials and systems used in the construction of machine tools. The study examines the effects of fiberglass reinforcement on the tensile strength of the composite material, and the reasons for these effects.

Keywords: granular composites, mineral casting, epoxy granite, machine construction

1. INTRODUCTION

Due to their high vibration dampening capacity, epoxy matrix granular composite materials are today used in special CNC machine tools for precision machining. They are not used in the bodies of conventional machine tools because columns and beams with much broader cross-sections are required to achieve the required tensile strength compared to metal bodies (Figure1).



Figure 1. Sample machine tool bodies produced using epoxy matrix granular composite materials

Thus, the cost of materials limits their use and applications. In granular composite materials, it is important that the matrix material and the

* Corresponding Author: h.onurozturk89@gmail.com

¹ Sakarya University, Faculty of Engineering, Department of Mechanical Engineering, Sakarya/Turkey

² Sakarya University, Faculty of Engineering, Department of Mechanical Engineering, Sakarya/Turkey

reinforcement materials form a suitable interface. Therefore, the granular material should be distributed homogeneously in the matrix, and the matrix material between the granules should have optimum saturation to display the required mechanical properties. In granular composite materials, the basic components of granules and the matrix material are connected with an adhesion bond, which is formed as the matrix material solidifies. The composite material to be developed in this study uses resin as the matrix material, and basalt granules and silica sand grains as the granule materials (Figure 2.). Basalt and silica grains have very low densities when compared with materials such as steel or aluminum, and they help create a light and rigid structure in composite materials. In addition, basalt and silica granules can be used in the composite structure to be developed after some mechanical processing, without undergoing any chemical or thermal treatment.



Figure 2. (a) Basalt granules and (b) silica sand grains

1.1 Problem Statement

The disadvantage of using granule materials is that they do not form a cohesion bond with the matrix material. Basalt granules and silica grains create a highly rigid composite structure throughout the material, forming an adhesion bond with the matrix material of epoxy, but the fragility of the material also increases, causing a rapid break as a result of crack propagation. The proposed solution is to increase the tensile strength of the material by creating a fibrous structure by reinforcing the material with 'S' glass fiberglass to support the composite structure. In addition, as it was subjected to tensile force, an examination was made of the effect of the fiberglass reinforcement on the tensile strength of the material.

2. MOLD DESIGN AND MATERIAL PREPARATION

2.1. Mold Design

Bisphenol A based epoxy resin was used as the epoxy matrix material. When designing molds, the priority criteria are that the mold release agent and the mold are resistant to the 60°C exothermic reaction that takes place as the epoxy matrix material is cured, and do not undergo any deformation that would affect the size of the specimens. Other design parameters taken into account are that the mold should be economic, easy to process and reusable (Figure3).



Figure 3. Molds for the tensile test specimens

Water soluble liquid polyvinyl alcohol was used as the mold release agent, which allows the formation of 0.05 mm and 0.08 mm film layers. The compound used as the mold release agent is water soluble, and can be easily removed by rinsing or wiping the product once it is taken out of the mold, without leaving any traces. The molds and specimens were prepared in accordance with the ASTM D638 TYPE 3 standard.

2.2. Material Preparation

Prior to molding, granule materials are washed and dried. If they are not removed, dust particles on basalt granules prevent the adhesion bond that is expected to form between the basalt granules and the matrix material. Dust particles on basalt granules, which form a barrier preventing the adhesion bond, must be removed prior to mixing basalt granules with silica particles and the matrix material. Bisphenol A epoxy matrix material

consists of two components, the resin and the activator. For ideal curing, it is important to follow the ideal mixing ratio recommended by the producer. As the two components are mixed to achieve the ideal mixture, air bubbles form throughout the material (Figure 4).



Figure 4. (a) Matrix resin with air bubbles and (b) matrix resin with air bubbles removed

If these air bubbles are not removed from the matrix material, air inside the bubbles expands because of the heat generated during curing, causing the bubbles to become larger and creating air pockets in the composite structure. These air pockets decrease the strength of the composite material, and create discontinuities in the composite material. Air bubbles that form prior to the curing process should be removed from the matrix material using the vacuum method to prevent any harmful effects. CO₂ laser cutting machine was used to cut the S glass fiberglass fabric used for reinforcement down to appropriate size (Figure 5).

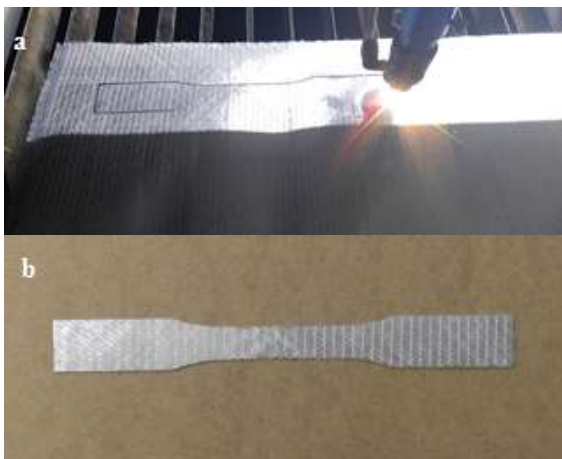


Figure 5. (a) Cutting S glass with CO₂ laser and (b) sample fiberglass fabric reinforcement cut with laser

The high precision of laser cutting makes it much easier to place the reinforcement fiberglass into the mold. In addition, compared to other mechanical cutting methods, it does not change the knitting form of the reinforcement S glass fiberglass fabric, ensuring that all layers in the specimens have a smooth and equivalent structure. Warps and wefts on the fabric can be deformed when cutting methods other than laser cutting are used, and thus, any differences that might form between layers can lead to misleading results.

3. CREATING THE COMPOSITE STRUCTURE

For efficient results to be obtained, which can be used in finite element analyses and quantitative calculations, molding should produce the ideal composite structure (Figure 6).

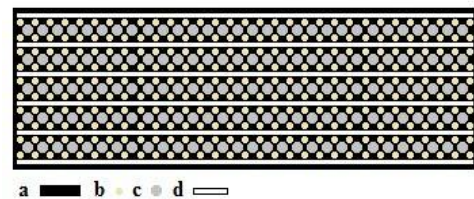


Figure 6. View of the ideal layered composite structure, (a) epoxy bisphenol, the matrix material, (b) silica sand particles, (c) basalt granules, (d) S glass fiberglass reinforcement fabric

To obtain equidistant layers, the height of each layer was controlled during molding to make the material structure as close to the ideal composite structure as possible. For the homogenous distribution of the granules, they were spread as layers inside the mold. During granule spreading, the molds are mounted on a vibration machine specially designed for molding (Figure 7).



Figure 7. Vibration molding machine

The vibration machine ensures that the basalt granules inside the mold make small movements, eventually settling in places appropriate for their size in the matrix. Silica sand particles, on the other hand, which are smaller compared to basalt granules, fill the potential spaces between basalt granules that might form due to the surface tension of the matrix material, with the effect of vibration and gravity. The frequency of the vibration transferred to the molds by the machine can be varied between 0 and 400 hertz, using the frequency drive on the machine. We have experimented with different frequency values to observe the movements of basalt and silica sand particles inside the matrix. Based on this observation, the most appropriate frequency values for the movement of the particles was selected.

4. TENSILE TESTS

The DARTEC tensile test machine with a capacity of 250 KN was used for the tensile tests (Figure 8).



Figure 8. Tensile testing machine and test specimen

To carry out the tensile tests using the machine, the ASTM D638 standard and the sizes of the tensile test specimens were specified, and tensile tests were conducted with a speed of 1.5mm/sec, following the standard. A total of 50 specimens, with 5 identical specimens in each group, were subjected to tensile testing (Figure 9).



Figure 9. Tensile test specimens

Tensile test specimens were given names in accordance with their contents to facilitate the easy recognition of their contents during and after the tests and interpretation following the tests (Table 10).

Table 10. Material contents of tensile test specimens, ratio of volumes

Specimen code	Epoxy resin ratio	Basalt and quartz granule ratio	Fiberglass ratio
12S	12%	88%	*
14S	14%	86%	*
16S	16%	84%	*
18S	18%	82%	*
20S	20%	80%	*
12F	12%	78%	10%
14F	14%	76%	10%
16F	16%	74%	10%
18F	18%	72%	10%
20F	20%	70%	10%

The letters S and F in the names of the specimens indicate the fiberglass content of the tensile test specimens. The letter S indicates that the tensile test specimen does not contain fiberglass reinforcement. Specimens with the letter F in their names, on the other hand, contain fiberglass reinforcement. The two-digit numbers preceding the letters S and F indicate the ratio of the volume of epoxy matrix material to the total volume of the tensile test specimen.

5. RESULTS AND DISCUSSION

Graphs were created using open-source Libreoffice software, based on data obtained from the tensile tests, to visualize the results of tensile tests for specimens with and without fiberglass reinforcement. In specimens without fiberglass reinforcement, material ductility and tensile strength increased in parallel with the increase in the ratio of epoxy matrix material (Figure 11.).

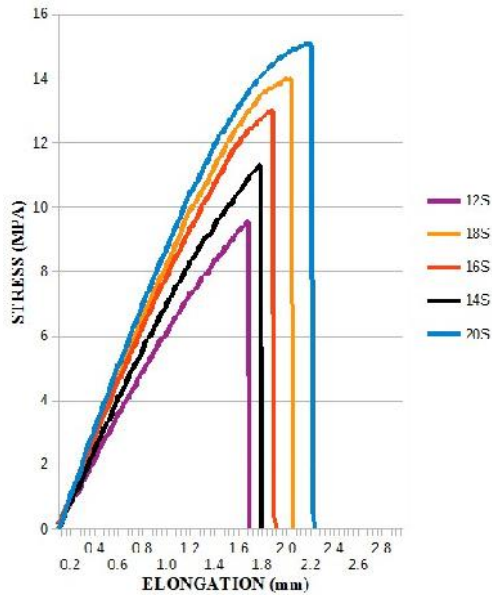


Figure 11. Tensile test graph for specimens without fiberglass reinforcement

With their rigid structure, granules added to the matrix increase the rigidity and fragility of the composite structure. As the ratio of the matrix material increases, so does the amount of matrix material between granules, making the composite structure more ductile. As the distance between granules increases, crack formation and propagation speeds decline. Because the matrix material and the granules form only an adhesion bond and because matrix material ratios above 20% cause the matrix material inside the mold to separate from the composite material and accumulate on the surface, further increase in the ratio of matrix material does not make an additional contribution in terms of strength. In specimens without fiberglass reinforcement, the upper limit of 20% for the ratio of matrix material generates the maximum strength value (Figure 12).

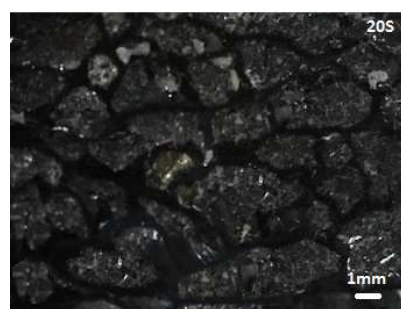


Figure 12. Cross section views of the specimens without fiberglass reinforcement

With the effect of fiberglass reinforcement, material behavior in specimens with fiberglass

reinforcement was very different when compared with specimens without fiberglass reinforcement (Figure 13).

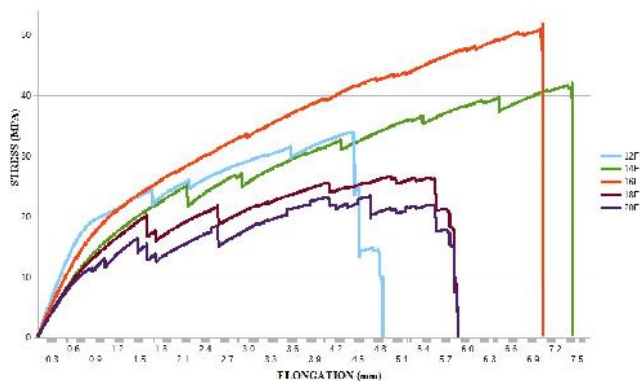


Figure 13. Tensile test graph for specimens with fiberglass reinforcement

Comparing specimens with the same ratio of matrix material, the strength of specimens with fiberglass reinforcement were as high as 4 times the strength of the specimens without fiberglass reinforcement. The intermittent structure of the graph for specimens with fiberglass is a result of fiber breaks. The tensile test graph shows that, as a result of fiber breaks, the elongation ratio increases in specimens with fiberglass reinforcement, as fiberglass reinforcement increases unit elongation amount. Because fiberglass reinforcement is in the form of layers, matrix material between granules located between two granule layers plays a bigger role in increasing strength. Maximum strength is observed in 16F specimens because the distribution of the surfaces that form effective adhesion bonds becomes closest to the ideal in 16F specimens. The matrix material in 12F and 14F specimens is not well-distributed enough for the formation of sufficient adhesion bonds. During the tensile tests, the materials make crunchy separation sounds as they are deformed. 18F and 20F specimens, on the other hand, have a larger amount of matrix material between granules (Figure 14.).

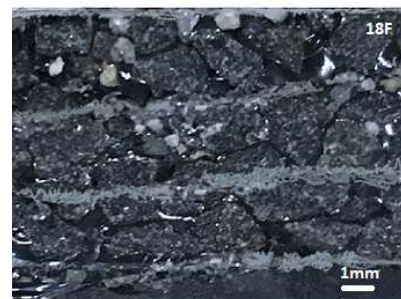


Figure 14. Cross section views of the specimens with fiberglass reinforcement

There is less sound during the tensile tests, and the sounds generated are similar to the soft sounds heard during the tensile tests of polymer based materials as they break. Specimens are expected

to display increased ductile behavior in this case, but granules separate and prevent further ductile behavior. Because basalt granules separate from the structure due to their nature, cross section photographs of the specimens were not successful.

6. OVERALL RESULTS

In this study, specimens with and without fiberglass reinforcement were subjected to tensile tests with a speed of 1.5 mm/sec. Specimens with fiberglass reinforcement were observed to have a tensile strength that was high as 4 times the strength of the specimens without fiberglass reinforcement (Figure 15).

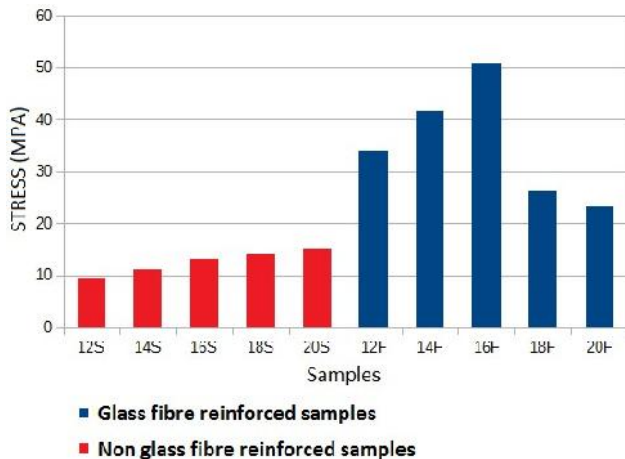


Figure 15. Comparative tensile test graph for specimens with and without fiberglass reinforcement

Specimens with fiberglass reinforcement displayed ductile behavior, whereas specimens without fiberglass reinforcement had high rigidity and no breaking elongation, with the specimens breaking almost without any elongation. During the tensile test, fiberglass fibers broke first as a result of tension, and as the matrix material and fiberglass fibers stretched and the matrix material saturated the fiberglass fibers more fully, the unit elongation amount of the composite material increased. The composite material developed cannot undergo an effective cutting process. However, machining allowance can be left and material removal from the surface can be undertaken following molding. The rigid

structure created by granules can be supported with fiberglass reinforcement, making it possible to produce thinner beams and columns for machine tool bodies, and have lighter and highly strong machine tool body parts as a result.

5. REFERENCES

- [1] Kaw A. K. (2006), *Mechanics of composite materials*. Boca Raton: Taylor & Francis.
- [2] R. Butcher, C.-E. Rousseau, and H. Tippur, "A functionally graded particulate composite preparation, measurements and failure analysis," *Acta Materialia*, vol.47, no. 1, pp. 259-268, 1998.
- [3] J. D. Suh and D. G. Lee, "Design and manufacture of hybrid polymer concrete bed for high-speed CNC milling machine", *International Journal of Mechanical Material Design*, vol. 4, pp. 113-121. 2008.
- [4] H. V. Rama Krishna, S. Padma Priya, S. K. Rai, A. Varada Rajulu, "Tensile, Impact, and Chemical Resistance Properties of Granite Powder-Epoxy Composites", *Journal of Reinforced Plastics and Composites*, vol. 24, pp. 451-460. 2005.
- [5] A. P. Filho and F. L. Nito, "Behavior of granite epoxy beams subjected to mechanical vibrations", *Materials Research*, vol. 13 no. 4, pp. 497-503. 2010.
- [6] A. P. Filho, F. Shimabukuro, "Characterization of Compression Strength of Granite- epoxy Composites Using Design of Experiments", *Materials Research*, vol. 11, no. 4, pp.399-404. 2008.
- [7] P. A. McKeown and G. H. Morgan, "Epoxy granite: a structural material for precision machines," *Precision Engineering*, vol. 1, no. 4, pp. 227-229, 1979.
- [8] W. P. Lin and H. T. Hu "Parametric Study on the Failure of Fiber-Reinforced Composite Laminates under Biaxial Tensile Load" *Journal of Composite Materials*, vol. 36, no.12, pp. 1481 – 1503, 2002.

- [9] K., P., Roysarkar and M. K. Banerjee. Synthetic Composite: A Non-Conventional Material for Machine Tool Structures., *Procs. of the 20th AIMTDR Conference*, BIT, Ranchi, pp. 117-124, 2002.
- [10] Wenfeng Bai, “Study on vibration alleviating properties of glass fiber reinforced polymer concrete through orthogonal tests”, *Journal of Materials and Design*, vol. 30, pp. 1417-1421, 2009.
- [11] P. Mani, A. K. Gupta, and S. Krishnamoorthy, “Comparative study of epoxy and polyester resin-based polymer concretes,” *International Journal of Adhesion and Adhesives*, vol.7, no.3, pp. 157–163, 1987.
- [12] Akash. D.A, Thyagaraj. N.R, Sudev. L.J, "Experimental Study of Dynamic Behavior of Hybrid Jute/Sisal Fibre Reinforced Polyester Composites", *International Journal of Science and Engineering Applications* Volume 2 Issue 8. pp.170-172, 2013.
- [13] Iqbal Mokhtar, Mohd Yazid Yahya and Mohammed Rafiq Abdul Kadir, "Mechanical Characterization of Basalt/HDPE Composite under In-Vitro Condition", *Polymer-Plastics Technology and Engineering*, vol.52, pp.1007–1015, 2013.
- [14] Kari S., Berger H., Gabbert U., “Numerical evaluation of effective material properties of randomly distributed short cylindrical fiber composites”, *Computational Material Science*, Vol. 39, pp. 198–204., 2007.
- [15] Hashin Z., “Thin interphase imperfect interface in elasticity with application to coated fiber composites”, *Journal of Mech Phys Solids*, vol. 50, pp. 2509-2537., 2002.
- [16] Ramos R. R., Sabina F.J., Diaz R.G., Castillero J.B. “Closed-form expressions for the effective coefficients of fiber reinforced composite with transversely isotropic constituents. I: Elastic and square symmetry”, *Mech Mater*, vol. 33, pp. 223-235., 2001.
- [17] Erbe, T., Krol, J. and Theska, R., “Mineral casting as material for machine base-frames of precision machines”, *Twenty-third Annual Meeting of the American Society for Precision Engineering and Twelfth ICPE*, Portland, Oregon, 2008.

JOURNAL OF SCIENCE



SAKARYA UNIVERSITY

Sakarya University Journal of Science

ISSN 1301-4048 | e-ISSN 2147-835X | Period Bimonthly | Founded: 1997 | Publisher Sakarya University |
<http://www.saujs.sakarya.edu.tr/>

Title: Metallographic Aspects Investigation of Penstock Materials in Hydroelectric Power Plants And Penstock Maintenance Methods

Authors: Gökhan Kahraman, Yahya Taşgın

Received: 2019-02-26 15:52:05

Accepted: 2019-03-09 14:19:14

Article Type: Research Article

Volume: 23

Issue: 5

Month: October

Year: 2019

Pages: 744-748

How to cite

Gökhan Kahraman, Yahya Taşgın; (2019), Metallographic Aspects Investigation of Penstock Materials in Hydroelectric Power Plants And Penstock Maintenance Methods. Sakarya University Journal of Science, 23(5), 744-748, DOI: 10.16984/saufenbilder.532674

Access link

<http://www.saujs.sakarya.edu.tr/issue/44066/532674>

New submission to SAUJS

<http://dergipark.gov.tr/journal/1115/submission/start>

Metallographic Aspects Investigation of Penstock Materials in Hydroelectric Power Plants and Penstock Maintenance Methods

Gökhan Kahraman^{*1}, Yahya Taşgın²

Abstract

Hydroelectric power plants are renewable energy sources and have little impact on the environment. Therefore, it is one of the most preferred energy sources in the world. In parallel with this situation, it is very important that the hydroelectric power plants are maintained, their failures are prevented or permanently removed. One of the most important parts of hydroelectric power plants is penstock pipes. Along with the snail part of the power plant, the penstock supplies the pressurized water to the turbine wheel for energy production. In the power plants that have been producing energy for many years, the maintenance and material properties of penstock are very important. In this study, one of the most important equipment of hydroelectric power plants, pressurized water pipes (penstock) and chemical components have been examined in macro and micro structure and their maintenance is investigated. In the metallographic study on the samples taken from two different regions of the penstock pipe; the perlitic structure, which has a homogeneous distribution into the ferritic structure forming the matrix, is determined and supported by analyzes. This study will help to ensure that all hydroelectric power plants operate smoothly in terms of penstock.

Keywords: Renewable energy, Hydroelectric Power Plants, Penstock, Metallographic Survey

1. INTRODUCTION

Hydroelectric power plants are the most important renewable energy source of the world's electricity supply due to their low environmental impact, low operating and maintenance costs. Hydroelectricity is one of the sustainable clean energy sources and suitable for environmental legislation such as Kyoto Protocol. Hydroelectric power plants do not produce greenhouse gas emissions, because they do not use fuel and do not pollute the air. They contribute to global warming prevention activities.

Around 16% of the world's electricity production is provided by hydroelectric power [1].

The amount of energy to be produced from the water source in hydroelectric power plants depends on the net head and the flow rate of the water. According to these two main parameters, the type of turbine to be used is determined. Turbine types are classified in two main categories as impulse turbines and reaction turbines [2]. Impulse turbines include pelton and reaction turbines include Francis, Kaplan turbines[3]. In all turbine types, the pipes that convey the pressurized

* Corresponding Author gokhankahraman@munzur.edu.tr

¹ Department of Mechanical Engineering, Munzur University, 62000 Tunceli, Turkey ORCID: 0000-0002-8365-2447

² Department of Mechanical Engineering, Munzur University, 62000 Tunceli, Turkey ORCID: 0000-0002-0902-336X

water for energy production are called as penstock. Therefore, manufacturing and calculation of penstock is very important. The risk of any explosion and perforation can cause enormous cost damage to hydroelectric power plant facilities. There are many studies on penstock pipes in the literature [4] [5] [6] [7]. Lucas et al. have conducted fatigue analysis in penstock because of variable water velocities in pumped power plants [8]. Kumar and Singal have solved the problem of material selection of penstock for small hydroelectric power plants by using Multiple Attribute Decision Making (MADM) method [9]. Kawamura et al. have studied metallographic and physical materials of the penstock of hydroelectric power plants that have been producing energy for many years [10]. Leon and Zhu have performed a dimensional analysis to determine the optimum penstock diameter and optimum flow in impulse and reaction turbines [11]. By calculating the optimum diameter of the penstock used in small-scale hydroelectric power plants, Alexander and Giddens have analyzed the cost of the penstock pipe diameter according to cost [12]. Bulloch and Callagy have conducted corrosion, fatigue and crack analysis in the penstock of a 25 MW hydroelectric power plant [13].

2. MATERIAL AND METHOD

In hydroelectric power plants, the pressure pipes between the dam lake or the loading pool and the turbines are called as penstock. Penstock pipes are manufactured by bending steel sheets and welding them together. The steel sheets must be ductile. St 37, St 42 and St 52 steel sheets are used in the manufacture of penstock pipes. The yield boundaries of these plates vary between 21-36 (kp/mm²) and the breakage boundaries vary between 22-27%. The materials used for the penstock pipes manufacture must have the ability to withstand the pulling, bending, cracking stresses, and the inner surfaces of the penstock, which are manufactured, must be covered with a

protective coating against corrosion and they must be smooth. In addition, the joints of penstock pipes should be assembled with gaskets against water tightness and must have a structure that tolerates stresses that may occur during temperature changes. Depending on the topography of the plant or in hydroelectric power plants having high hydraulic head, the length of the penstock can be very long. This significantly affects the initial investment cost of the plant. For this reason, optimum diameter calculation is very important in penstock pipes. In high hydraulic head power plants, it is necessary to calculate the wall thicknesses and connection parts of the penstock according to high static and dynamic stresses [14]. Figure 1 shows the penstock of a hydroelectric power plant.



Figure 1. Penstock pipes

The maintenance of the penstock pipes used for many years under pressure and the examination of the material structures are of great importance in terms of the prevention of any possible damage in the dams. The maintenance levels of the penstock pipes are given below.

- Visible areas of penstock pipes should be visually inspected once a week.
- Long penstock pipes are sealed by sealing material at certain distances. The reason for this is the expansion of the penstock due to the temperature difference caused by the seasons. Due to any maintenance in the turbine,

pressurized water in penstock is discharged. Empty penstock pipes seals get dry under the sun. Therefore, it is necessary to keep water continuously in the seals of empty penstock pipes.

- The wall thickness of the penstock pipes increases as a result of the pressure from the dam body to the turbine snail. Penstock thickness must be measured by ultrasonic method once a year. Measured values should be recorded by creating an archive and the values measured every year should be compared with the previous year.
- Internal and external parts of penstock pipes should be sanded and painted with epoxy paint in certain periods depending on corrosion.

2.1. Metallographic Survey

As a result of the metallographic studies on the samples taken from two different points of the penstock it is observed that in the optical images given in Figure 2, the main structure (matrix) is formed by ferrite (yellow regions) and disconnected black areas in the structure are perlite. Images taken at different magnifications enabled the detection of grain boundaries as a result of etching. The perlite contained in the ferritic structure positively affects many properties of ferrite, which contains very low carbon content (0.008%). Chemical and mechanical properties of the material;

C: 0,22 P: 0,04 Mn: 0,6 Al: 0,02 Tensile strength: 490-630 Mpa, Yielding point: 335 Mpa

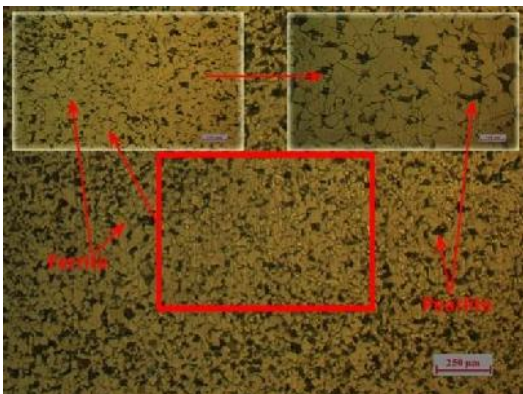


Figure 2. Optical images of the sample one at different magnifications.

When we examine the SEM images at different magnifications in Figure 3, it is evident that the ferritic structure forming the matrix is the black regions. The styliform white areas are composed of perlite, a two-phase structure with coverglass gathering the iron and cementite phases.

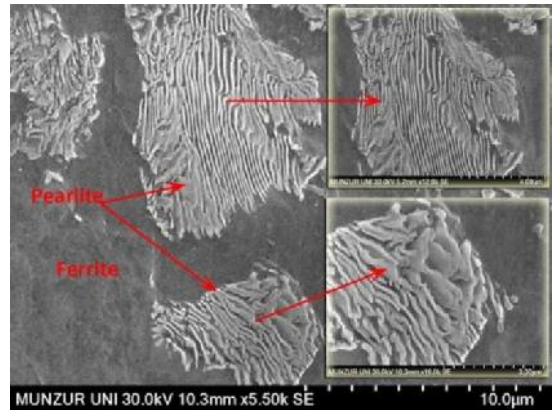


Figure 3. SEM images of the sample one at different magnifications.

In Figure 4, regional and point EDS analyzes are given. In the analysis we have obtained from the overall structure, it is seen that the matrix is composed of 96.18% Fe as a result of the different coloring we made for each element, while the portions of other elements are very small. When we examine the spectrum peaks, C, Mg and Si compounds are composed of Fe and Mn.

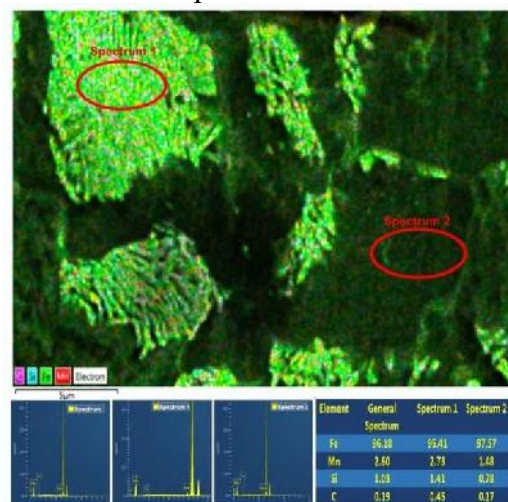


Figure 4. Demonstration of regional and spot EDS analysis of the sample one.

When we examined the metallographic images of the sample from the second region as it can be

observed in Figure 5 at different optical magnifications, ferritic structure is in the ferritic structure disorganizedly (Yellow regions Ferrite, Black regions Ferrite)

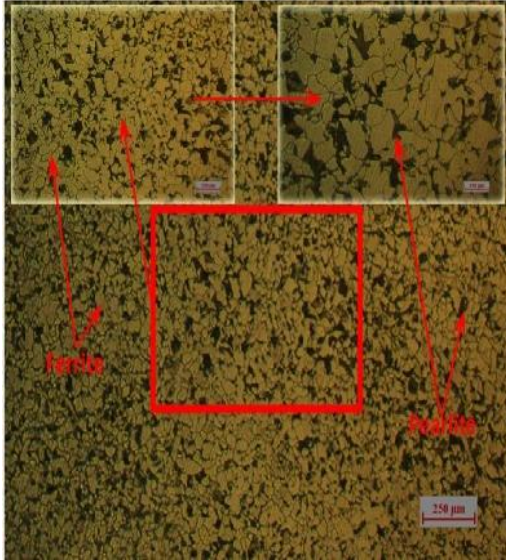


Figure 5. SEM images of the sample two at different magnifications.

When we examine the SEM images shown in Figure 6, it is seen that this hypoeutectoid structure consisting of ferritic and perlitic structure, as seen in the sample one, consists of a few cementite phases.

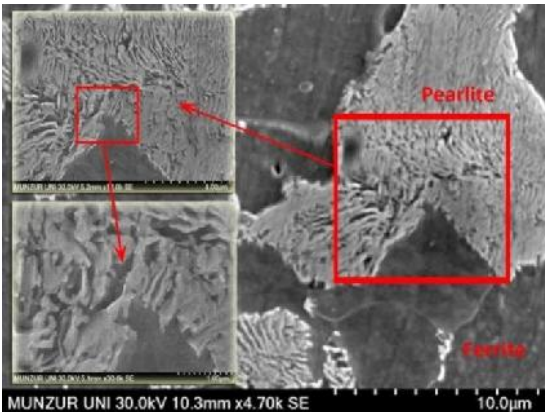


Figure 6. Optical images of sample two at different magnifications.

In the image we examined in Figure 7, regional and point EDS analyzes are given. The structure, which contains over 95% Fe, consists of ferrite in dark areas and Pearlite in light green areas. In the peaks obtained from EDS analyzes, it contains a second compound formed by C, Mn and Si as well as the compound consisting of Fe and Mn.

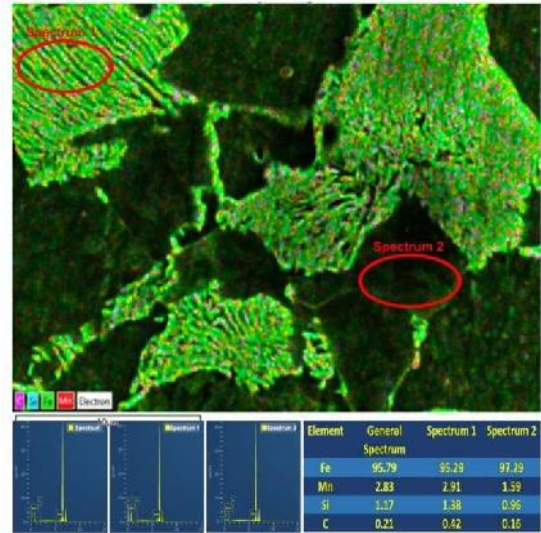


Figure 7. Demonstration of regional and point EDS analysis of sample two.

3. CONCLUSION

Penstock pipes are one of the most important parts of hydroelectric power plants. According to the net head of the dam their pressure varies between 5 and 25 bar. This pressure can cause huge loss of life and property in any penstock pipe burst. Hydroelectric power plants, which are the most important renewable energy source of the countries and which generate huge economic income, may not produce electricity for years due to failures and penstock pipe accidents. Therefore, they cause huge financial losses for countries. The results obtained in this study are given below,

- 1)The maintenance process of penstock pipes in hydroelectric power plants is investigated.
- 2)A sample is taken from the penstock of a hydroelectric power plant and analyzed from two different points and examined metallographically.
- 3)As a result of the investigations, it is evident that the general structure is ferrite, and the coverglass formed by the combination of iron and cementite phases creates perlitic structure.
- 4)It is found that a small amount of Mn, Si, C and low carbon steel are present in the material containing more than 95% Fe.

REFERENCES

- [1] World Energy Council, 2016.
- [2] U. Dorji , R. Ghomashchi, “Hydro turbine failure mechanisms,” *Engineering Failure Analysis*, vol. 44, pp. 136–147, 2014.
- [3] M.K. Padhy, R.P. Saini, “A review on silt erosion in hydro turbines,” *Renew Sustain Energy Rev*, vol. 12, pp. 1975–1986, 2007.
- [4] A. Adamkowski, “Case study: lapino power plant penstock failure,” *J. Hydraul. Eng.*, Vol. 127 pp. 547–555, 2000.
- [5] F. Kawamura, “Fracture toughness of long-term used SS41 and welding joint”, Master Thesis, Kagawa University, 2005.
- [6] C.K. Sanathanan, “Accurate low order model for hydraulic turbine-penstock,” *IEEE Trans Energy Convers*, vol. 2 pp. 196-200, 1987.
- [7] G.M. Lucas, J.I. Sarasua, J.A.S. Fernandez, J.R. Wilhelmi, “Power-frequency control of hydropower plants with long penstocks in isolated systems with wind generation,” *Renewable Energy*, vol. 83, pp. 245-255, 2015.
- [8] G.M. Lucas, J.L.P. Diaz, M. Chazarra, J.L. Sarasua, G. Cavazzini, G. Pavesi, G. Ardizzon, “Risk of penstock fatigue in pumped-storage power plants operating with variable speed in pumping mode,” *Renewable Energy*, vol. 133, pp. 636-646, 2019.
- [9] R. Kumar, S.K. Singal, “Penstock material selection in small hydropower plants using MADM methods,” *Renewable and Sustainable Energy Reviews*, vol. 52 pp. 240–255, 2015.
- [10] F. Kawamura, M. Miura, R. Ebara, K. Yanase, “Material strength of long-term used penstock of a hydroelectric power plant,” *Case Studies in Structural Engineering*, vol. 6, pp. 103–114, 2016.
- [11] A.S. Leon, L. Zhu, “A dimensional analysis for determining optimal discharge and penstock diameter in impulse and reaction water turbines,” *Renewable Energy*, vol. 71, pp. 609-615, 2014.
- [12] K.V. Alexander, E.P. Giddens, “Optimum penstocks for low head microhydro schemes,” *Renewable Energy*, vol. 33, pp. 507–519, 2008.
- [13] J.H. Bulloch, A.G. Callagy, “An detailed integrity assessment of a 25 MW hydroelectric power station penstock,” *Engineering Failure Analysis*, vol. 17, pp. 387–393, 2010.
- [14] H. Başeşme, *Hidroelektrik santraller ve Hidroelektrik santral tesisleri*, 2003.

JOURNAL OF SCIENCE



SAKARYA UNIVERSITY

Sakarya University Journal of Science

ISSN 1301-4048 | e-ISSN 2147-835X | Period Bimonthly | Founded: 1997 | Publisher Sakarya University |
<http://www.saujs.sakarya.edu.tr/>

Title: Numerical And Experimental Investigation of Bending Behavior of Pre-Stressed Aluminum Tube

Authors: Seçil Ekşi, Kenan Genel

Received: 2019-02-18 00:00:00

Accepted: 2019-03-11 00:00:00

Article Type: Research Article

Volume: 23

Issue: 5

Month: October

Year: 2019

Pages: 749-754

How to cite

Seçil Ekşi, Kenan Genel; (2019), Numerical And Experimental Investigation of Bending Behavior of Pre-Stressed Aluminum Tube . Sakarya University Journal of Science, 23(5), 749-754, DOI: 10.16984/saufenbilder.528549

Access link

<http://www.saujs.sakarya.edu.tr/issue/44066/528549>

New submission to SAUJS

<http://dergipark.gov.tr/journal/1115/submission/start>

Numerical and Experimental Investigation of Bending Behavior of Pre-Stressed Aluminum Tube

Seçil EKŞİ^{*1}, Kenan GENEL²

Abstract

The effect of the pre-stress and internal Pa6 (cast-polyamide) material on the bending behavior of the aluminum tube is investigated experimentally. Finite element studies have been carried out to better understand the effect of pre-stress on the cross-section of tube and to shed light on the experimental studies. From the simulation studies, it was concluded that the effect of the pre-stress on the load carrying capacity of the tube is limited. After finite element studies, experimental studies were performed. In experimental studies, the lower cross-section of the tube was subjected to 175 MPa stress corresponding to 93% of the yield strength of the material. The tensile stress in the tube during the loading is reduced by applying pressure to the lower cross section of the tube beam. In addition, a change in the load carrying capacity of the tube was investigated using a Pa6 ring to delay local buckling. As a result of the experiments, it was found that the pre-stress significantly improved the bending behavior of the tube in the elastic region, while reducing buckling displacement. Application of both pre-stress and internally reinforcement enhanced bending performance of the tube in both elastic and plastic regions. Load carrying capacity of pre-stressed and internally reinforced tube was increased 1.67 times according to the base tube.

Keywords: pre-stress 1, tube 2, bending 3, finite element analysis 4

1. INTRODUCTION

It is known that pre-stressing is widely used in the construction sector. In reinforced concrete structures, the concrete is given a pre-stress to reduce the tensile stress in concrete under service loads or to a certain extent. Pre-stressing is also

used in bridges, steel structure, underwater structures, prefabricated structures, towers, beams, buildings, etc. There are many studies on pre-stressed materials and structure used in the construction sector [1-4]. Zhu et. all investigated bending behavior of aluminum I-beams with carbon fiber reinforced plastic (CFRP) tendons by

* Corresponding Author: eksi@sakarya.edu.tr

¹ Sakarya University, Mechanical Engineering Department, Sakarya, Turkey. ORCID: 0000-0002-1404-718X

² Sakarya University, Mechanical Engineering Department, Sakarya, Turkey. ORCID: 0000-0003-0994-2806

pre-stressed. They report that pre-stress increase the bending rigidity and decreases the flexure. Improvement in yield load is at a level of 33.3%. Maximum improvement in failure load of aluminum beam is about 52.3% [1].

There are limited number of studies on pre-stressed tube beams. Bending, impact and wear behavior of pre-stressed tube structures are investigated in some studies (5-8). Zeinoddini and his friends investigated the behavior of axially pre-loaded steel tubes subjected to lateral impacts experimentally and numerically. They reported that axially pre-loads decrease the lateral impact loads [5]. Firouzsaları and Showkati investigated bending behavior of pre-compressed specimens under local lateral loads experimentally and numerically. They found good correlation between numerical simulation and experimental study. As a result of their study they reported that the final tube strength and the amount of absorbed energy depends on axial compressive preloading. When axial compressive preloading increase, final tube strength and absorbed energy capability decrease under lateral loads [6]. Zhi and his friends studied on axially preloaded circular steel tubes subjected to transverse low-velocity impact experimentally. Bending behavior and lateral collapse capacity of tubes are enhanced with axial tension. Axial compression has a significant effect on collapse capacity of tubes [7]. Guan and his friends investigated the impact wear behavior of Inconel 690 alloy tubes with initial pre-compressive stress load. They reported that tube deflection decreased with increasing pre-stress. Contact peak force, wear scar areas and material rigidity increased with increasing pre-stress. Absorbed energy capacity of tubes gradually decreased before the reaching the equilibrium [8].

In this paper, we present effect of the pre-stress and internal Pa6 material reinforcement on the bending behavior of the aluminum tube.

2. SIMULATION STUDY

Three-point bending simulations of the aluminum tube were performed with using

Ansyz 16. Analyzes were carried out using a quarter-symmetric model of the tube. 10580 20-node Solid 95 quadratic elements and 44318 nodes are used in analyses for the aluminum tube, supports and the loading punch. Contact mechanics between the support/beam and punch/beam interfaces, CONTA174 3-D8-node contact elements are used. The coefficient of friction between the contacting surfaces is taken as 0.2.

The diameter of the tube used in the analyses is 31 mm, the wall thickness is 1 mm and the length is 270 mm. Yield and tensile strength of aluminum tube are 187 MPa and 247 MPa, respectively. The pre-stress process is defined by applying pressure to the lower and quadrant sections from the two ends of the tube structure. The application of constant pressure to the lower sections of the tube beam is shown in Figure 1 together with boundary conditions.

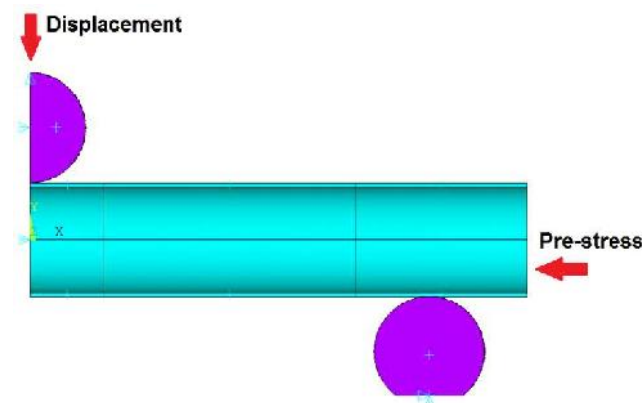


Figure 1. Finite element model and boundary conditions of pre-stressed tube

3. EXPERIMENTAL STUDY

The apparatus for pre-stress application to the tube is designed (Figure 2). In this apparatus, the load is applied to the tube body with of steel wires located between the load cell and the nut. One side of the tube is placed on the cover which is fixed

on the main body. The steel tension wire passing through the tube (\varnothing 6 mm) is connected to the torque bolt at the other end of the assembly. Here the bolt is tightened using the torque spanner so that the gap of the wire is taken, and then the bolt movement is continued until the specified loads value is read in the load cell. For a given tube diameter, foreseen load and therefore for the pre-stress in the section, a torque value must be read in the torque spanner. The tube fixed at one end will be compressed from the other end to the desired torque with the bolt-nut connection, then moved to the three-point bending tester by separating it with the detachable caps shown in the picture on the frame. The diameter, wall thickness and length of the aluminum tube used in the experiments are as follows; 30 mm, 1 mm and 270 mm. The material of the aluminum tube is 6063-T6. Yield strength is 187 MPa and tensile strength is 247 MPa.

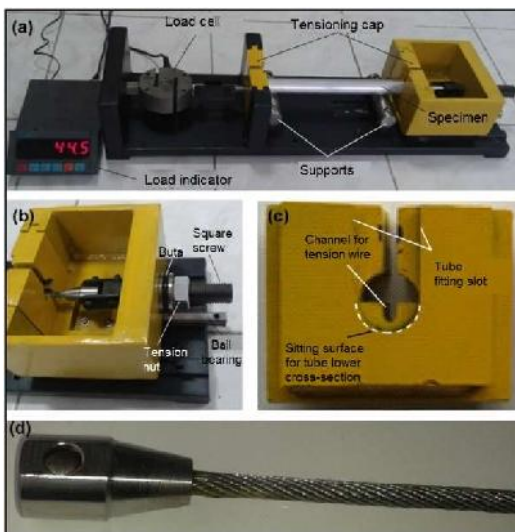


Figure 2. The pre-stress apparatus: (a) General view, (b) Detail view of the drive side, (c) Clamping covers (d) 6 mm diameter steel wire and conical head used in the tensioning process

The test on the three-point bending test machine with the pre-stress device is given in Figure 3.



Figure 3. Test on three point bending machine with pre-stress device

4. SIMULATION RESULTS

The load-displacement curves of tubes obtained from finite element analyses are shown in Figure 4. When the figure is examined, it is seen that when 100 MPa pre-stress is applied to the lower half section of tube, the load carrying capacity of the tube decreases, the buckling displacement value decreases, and the rigidity increases slightly. When pre-stress is applied to the lower quarter section of tube, the load carrying capacity is slightly increased compared to base tube. Bending rigidity and energy absorbing capacity of the tube structure increased in the elastic region.

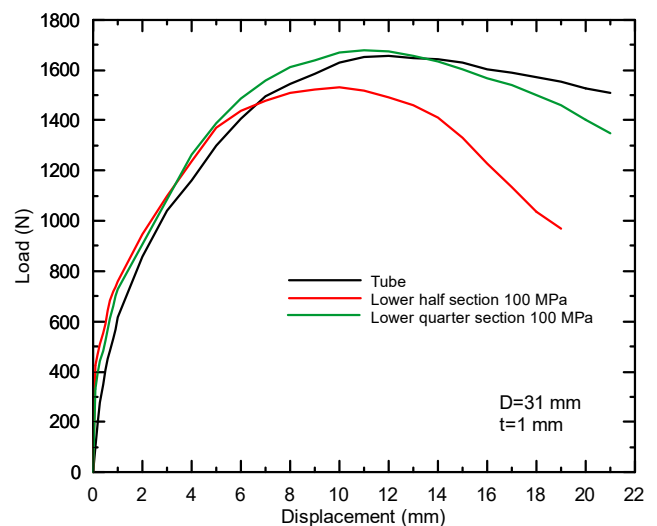


Figure 4. Load-displacement curves obtained from quarter and half section pre-stressed tubes analyses

The results of the analyses carried out at different pre-stress values applied to the lower quadrant of tube are given in Figure 5.

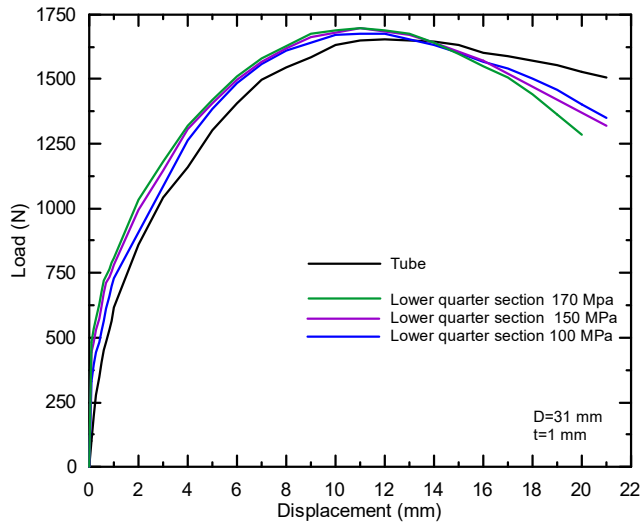


Figure 5. Load-displacement curves obtained from quarter section pre-stressed tubes analyses

When the values of the pre-stress at lower quarter section of tube is changed, it is seen that the load carrying capacity and rigidity of tube changed insignificantly. When a comparison is made between the models with the 100 MPa pre-stress at the lower half section of tube and the base tube model, yield stress in the lower wall of tube is seen in base tube at 12 mm displacement and the buckling takes place. In the pre-stressed tube, the buckling displacement decreased to 9 mm, but in the lower wall, the yield displacement increased to 14 mm.

The von-Mises stress distribution for the pre-stressed (lower half section 100 MPa) and the base tube models for the displacements (9 and 12 mm) at which the greatest load is obtained in the models is given in Figure 6. When these stress distributions are compared, the distinction between stresses in the lower wall is remarkable. Considering that the yield strength of the tube material is 187 MPa, it is understood that the yield in the pre-stressed tube occurs only in the upper half of the section.

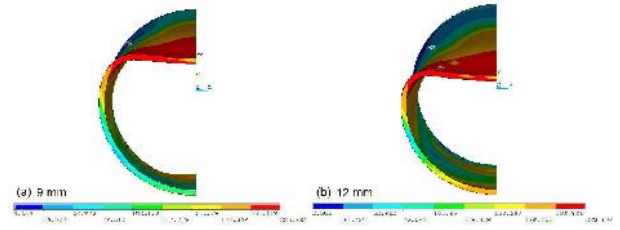


Figure 6. (a) Stress distribution (displacement 9 mm) in pre-stressed model (lower half section 100 MPa), (b) Stress distribution (displacement 12 mm) in base tube model

5. EXPERIMENTAL RESULTS

In the simulation studies, the application of pre-load to quarter-section was performed by defining the pressure directly to the forehead of tube. However, in the experimental study, it is not possible to apply the pre-stress on the steel cord to the lower quadrant homogeneously. Because it passes very close to the bottom wall of the cord. This is an obstacle to perform the experiment. Accordingly, experiments were planned for the application of the pre-stress to the lower half-section of the tube. Diameter of tube used in experiments is 30 mm with 1 mm thickness. In three point bending tests, Pa6 ring was placed to the tube in order to prevent the local deformation on the surface of tube. Width of Pa6 ring was determined equal to the diameter of the mandrel (D:30 mm). The ring was prepared as a tight fit. Loads applied to the tube structure did not exceed the yield strength in the wall. Loads did not cause buckling. The optimal upper stress value was determined as 175 MPa for the initial preload of 7745 N. The axial load on the tube lower cross section through the steel cord and the bending load applied to the tube during the experiment to obtain the pre-stress is obtained simultaneously with the two load cell is given in Figure 7. Initially, the pressure of 175 MPa is applied to the bottom wall of the tube with the steel cord under the pre-load of 7745 N. With increasing displacement, the displacement value of 4.6 mm is reached in 8080 N. The tensile stress at this load value is 177.3 MPa, which is less than yield strength of aluminum (187 MPa)

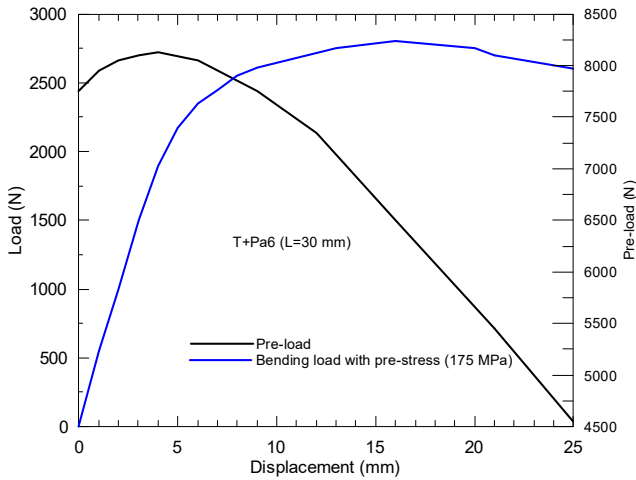


Figure 7. Pre load and bending load – displacement curves

The pre-loading value of the cord quickly decreases with increasing displacement and the bending load starts to emerge because the movement in the pre loading equipment is limited in the channel where the cord moves. The load measurement on the cord was stopped by interfering to the experiment.

The results of experiments are given in Figure 8. Pre-stress did not provide a significant improvement on base tube structure. The maximum load carrying value of tube structure with Pa6 ring, which has an initial pre-stress value of 175 MPa, increased slightly to 2808 N with an increase compared to the non-pre-stress state (2717 N). Bending rigidity of tube structure has increased significantly. Energy absorbing capability of tube has also increased. When the buckling displacement values are examined, the buckling displacement is smaller relative to the non-pre-stressed tube structure. Although improvement has been achieved with respect to the previous pre-stressed condition. It is expected that the buckling displacement will be slightly smaller than the non-stressed condition.

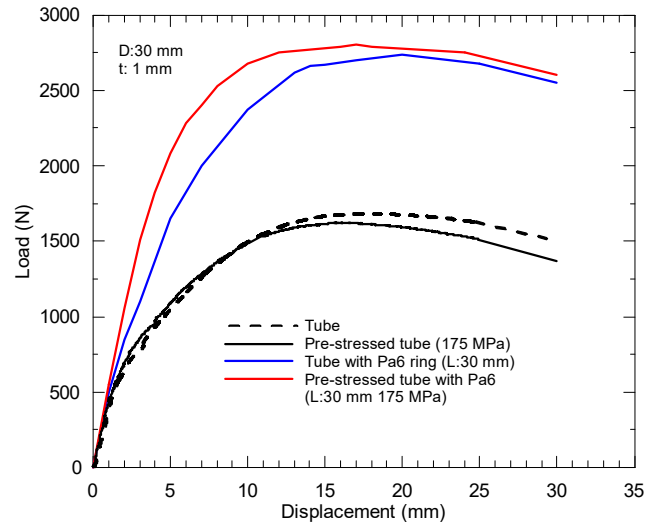


Figure 8. Load-displacement curves of pre-stressed / non-pre stressed and pre-stressed reinforced / non-reinforced tube structures with Pa6 ring

In order to produce a tube with a pre-stressed practical arrangement which can be used in practice, the most simple and light application of the above apparatus is designed as in Figure 9 below.

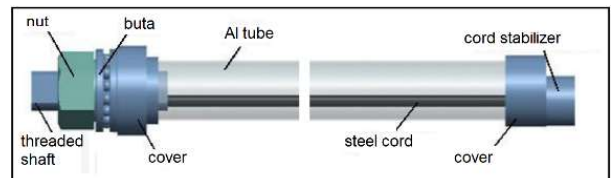


Figure 9. Tube-mounted portable device design for pre-stress application

The minimum weight of this portable design is 610 g for cases where the covers are made of aluminum. Taking into account the obtained load carrying capacity, it is clear that the specific load carrying capacity ($2808/610 =$) will get a very small value of 4.6. Therefore, the improvement in light weight and load carrying behavior is extremely limited.

6. CONCLUSIONS

The contribution of the applied pre-stress to the load carrying capacity of the tube beam is insignificant and reduces buckling displacement. The pre-stress application with internal reinforcement increases the bending rigidity of the structure in the elastic region and provides some improvement in the load carrying capacity (F_{max}). On the other hand, there was no improvement in terms of specific load carrying capacity, but a decrease of 75% was observed. Load carrying capacity of pre-stressed and internally reinforced tube was increased 1.67 times according to the non-pre stressed internal reinforced tube. It has been found from numerous experiments and obtained results that the improvement provided if a polymeric part equivalent to the additional weight used for the application of the pre-stress is partially inserted into the tube structure is highly preferred over the pre-stress case. It has thus been understood that pre-stress application enhances the rigidity of the elastic region provided that the inner Pa6 ring is used, but this method is expensive and is not very preferred because of the difficulty of the practice.

Acknowledgments

The work described in this paper is supported by TUBITAK (The Scientific and Technological Research Council of Turkey) under project number 110M054.

7. REFERENCES

[1] P. Zhu, H. Fan and Y. Zhou, "Flexural behavior of aluminum I-beams strengthened by pre-stressed CFRP tendons", *Construction and Building Materials*, vol.122, pp. 607– 618, 2016.

[2] E. Bernat-Maso, L. Gil, L. Mercedes and C. Escrig, "Mechanical properties of pre-stressed fabric-reinforced cementitious matrix composite

(PFRCM)", *International Journal of Impact Engineering*, vol. 35, pp. 1267–1279, 2008.

[3] S. Liu, D. Zhu, G. Li, Y. Yao, Y. Ou, C. Shi and Y. Du, "Flexural response of basalt textile reinforced concrete with pre-tension and short fibers under low-velocity impact loads", *Construction and Building Materials*, vol.169, pp.859–876,2018.

[4] B. Anshari, Z.W. Guan, A. Kitamori, K. Jung and K. Komatsu, "Structural behaviour of glued laminated timber beams pre-stressed by compressed wood", *Construction and Building Materials*, vol. 29, pp. 24–32, 2012.

[5] M. Zeinoddini, J.E. Harding and G.A.R. Parke, "Axially pre-loaded steel tubes subjected to lateral impacts (a numerical simulation) ", *International Journal of Impact Engineering*, vol. 35, pp. 1267–1279, 2008.

[6] S. E. Firouzsalar and H. Showkati, "Behavior of pre-compressed tubes subjected to local loads", *Ocean Engineering*, vol. 65, pp. 19–31, 2013.

[7] X-D. Zhia, R. Zhanga, F. Fana and C. Huanga, "Experimental study on axially preloaded circular steel tubes subjected to low-velocity transverse impact", *Thin-Walled Structures*, vol.130, pp.161–175, 2018.

[8] H-D. Guan, Z-B. Cai, Y-P. Ren, J-Y. Jing, W-J. Wang and M-H. Zhu, "Impact-fretting wear behavior of Inconel 690 alloy tubes effected by pre-compressive stress", *Journal of Alloys and Compounds*, vol.724, pp. 910–920, 2017.

JOURNAL OF SCIENCE



SAKARYA UNIVERSITY

Sakarya University Journal of Science

ISSN 1301-4048 | e-ISSN 2147-835X | Period Bimonthly | Founded: 1997 | Publisher Sakarya University |
<http://www.saujs.sakarya.edu.tr/>

Title: A Preliminary Study on Salt Tolerance of Some Barley Genotypes

Authors: Ali Doğru, Merve Yılmaz Kaçar

Received: 2017-12-26 00:00:00

Accepted: 2019-03-12 00:00:00

Article Type: Research Article

Volume: 23

Issue: 5

Month: October

Year: 2019

Pages: 755-762

How to cite

Ali Doğru, Merve Yılmaz Kaçar; (2019), A Preliminary Study on Salt Tolerance of Some Barley Genotypes. Sakarya University Journal of Science, 23(5), 755-762,

DOI: 10.16984/saufenbilder.371055

Access link

<http://www.saujs.sakarya.edu.tr/issue/44066/371055>

New submission to SAUJS

<http://dergipark.gov.tr/journal/1115/submission/start>



A preliminary study on salt tolerance of some barley genotypes

Ali Doğru^{*1}, Merve Yılmaz Kaçar²

Abstract

In this study, salt (NaCl) tolerance of five barley genotypes (Avcı-2002, Aydanhanım, Bülbül-89, Orza-96, Tarm-92) was investigated. These genotypes were exposed to different salt concentrations (0 mM (control), 100 mM, 200 mM and 300 mM) and then some basic growth parameters (root length, shoot length total plant length, fresh weight, dry weight) were determined on the 18 d old plants. Tolerance indices for each genotype were calculated on the basis of root and shoot length. Salt stress significantly inhibited root and shoot growth in all genotypes, except for genotype Bülbül-89. Inhibition degree of root and shoot growth was found to be proportional to the salt concentrations applied. Maximum inhibitory effect of salinity on root and shoot growth was observed in genotype Avcı-2002 at maximum salinity level (300 mM), while Bülbül-89 was less affected by the same level of salinity. In addition, salt stress disturbed water relation in barley genotypes dependent on the organ type, as demonstrated by more severe inhibition in shoot fresh weight as compared to root fresh weight. These results may show that salt stress reduced translocation of water from roots to shoots rather than water uptake from growth medium in barley genotypes used in this study. Changes in dry weight of roots and shoots indicated that salt stress more severely reduced biomass accumulation in roots in barley genotypes. The calculated tolerance indices demonstrated that Bülbül-89 is the most tolerant barley genotype to salinity, while Avcı-2002 was the most susceptible one.

Keywords: Barley, *Hordeum vulgare*, salt tolerance, tolerance indices

1. INTRODUCTION

Salinity is one of the major problems restricting agricultural production, especially in arid and semi-arid areas [1]. The concept of soil salinity indicates the amount of soluble salts present in the

soil in the unit volume [2]. Soluble salts are the natural components of the soil and many of them are nutrients necessary for plants. However, the accumulation of these salts in the soil prevents the cultivation of the crop plants and reduces agricultural yield. The reason for this is that high salt concentrations are toxic to plants and cause

* Corresponding Author: adogru@sakarya.edu.tr

¹ Sakarya University, Department of Biology, Sakarya, Turkey. ORCID: 0000 0003 0060 4691

² Sakarya University, Department of Biology, Sakarya, Turkey. ORCID: 0000 0002 5402 8178

the physicochemical structure of the soil to deteriorate [3]. One of the most important causes of soil salinity is the release of various types of soluble salts such as Na^+ , Ca^{+2} , Mg^{+2} , sulfate and carbonate from the parent rocks by the influence of climatic factors and to participate in soil structure [4]. Another source of salt accumulation in agricultural land is the height of the groundwater. As the groundwater rises, the salts found in the lower layers of the soil come out of the upper layers and the soil fertility starts to decrease [5]. Sodium chloride (NaCl) is the most important salt compound that causes salinity in the soil. It is also the most toxic type of salt for plants because of its high solubility [5].

Salinity is one of the most important problems of the earth [7]. Approximately 1.5 million hectares of our country's land are also facing salinity problems [8]. According to the latest estimates, over 800 million hectares of agricultural land in the world are affected by salinity [9]. This amount corresponds to more than 6% of the total agricultural land on the earth. The danger of salinization is continuously increasing for our fertile soils that can still be cultivated.

Soluble salts in the soil can be easily taken up by plants. Salt stress could damage plants in different ways. High soil salinity, for example, may reduce the osmotic potential of the soil solution and cause physiological drought for plants. In addition, salt stress reduces the growth rate of plants by disrupting mineral nutrition. Finally, Na^+ and Cl^- ions may represent specific toxic effects for plant growth and development [10, 11]. All of these factors lead to multiple negative effects on plant growth and development at the physiological, biochemical and molecular levels. For example, it has been reported that salinity reduces plant growth by slowing down mitosis in the meristematic cells [12, 13]. Hasanuzzaman et al. (2009) found that salt stress significantly reduced total plant height and leaf area in rice plants [14]. Guan et al. (2011), on the other hand, have demonstrated that salt stress significantly reduced total plant height, number of side branches as well as shoot thickness in *Suaeda salsa* [15]. Salt stress also affects fresh and dry weights of various organs in plants. For example, salt stress has been found to reduce the total plant dry weight in *Raphanus sativus* [16]. Leidi and Saiz (1997)

observed that salt stress reduced dry weight in cotton plant [17]. Kurban et al. (1999) have reported that low salt concentrations (50 mM) increased total plant weight in *Alhagi pseudoalhagi* while higher salt concentrations (200 and 300 mM) caused lower plant weight [18]. However, cultivated plants exhibit a wide variation in susceptibility to salt stress. It has been well known that plants are more susceptible to salt stress at the early seedling stage [19].

It has been reported that the salts found in the soil could be removed by washing after the drainage system has been provided [20]. However, this method is impractical because of being expensive. The second and most economical method for reclaiming these areas is to select and cultivate salt tolerant plant species and genotypes [21]. In environments containing high concentrations of various soluble salts, the ability of plants to grow and complete their life cycle is known as salt tolerance [22]. It has been determined that salt tolerance of barley varies depending on genotypes.

Accordingly, the aim of this study is to examine the effects of salt (NaCl) stress in some growth parameters of five different barley genotypes [Avcı-2002 (six-row feed barley), Aydanhanım (two-row malting barley), Bülbül-89 (two-row feed barley), Orza-96 (two-row feed barley) and Tarm-92 (two-row feed barley)] which are commonly grown in Turkey. In addition, tolerance indices were calculated in order to determine the variation between barley genotypes in terms of salt tolerance.

2. MATERIAL AND METHODS

2.1. Plant Material, Growth Conditions and Experimental Design

Seeds of barley cultivars (*Hordeum vulgare* L. cvs. Avcı-2002, Aydanhanım, Bülbül-89, Orza-96 and Tarm-92) were obtained from Field Crops Central Research Institute, Ankara, Turkey. All seed samples were surface sterilized in 5% sodium hypochlorite solution for 10 minutes before sowing. After washing in distilled water, three seeds of each cultivar were sown in plastic pots (14 cm in diameters) containing perlite. The experiment was performed in a controlled growth

chamber (25/20 °C day-night temperature) under a PPFD of 200 $\mu\text{mole m}^{-2} \text{s}^{-1}$ light intensity, with a photoperiod of 16 h and 50±5 relative humidity. The perlite moisture was maintained at field capacity for 12 days (d), after which some of the pots from each cultivar were exposed to salt stress (100, 200 and 300 mM NaCl) for 6 d. The control plants were watered for additional 6 d with Hoagland nutrient solution. At the 18th d of the experiment, plants were harvested and morphological measurements were performed immediately.

2.2. Determination of root and shoot length

Measurements of root and shoot length were done with a millimetric ruler on 7 plants from each treatment and 3 independent replicates (n=21). The longest root was taken into consideration for measurement. Root length, shoot length and total plant length were expressed as cm plant⁻¹.

2.3. Determination of fresh and dry weight

After harvesting, fresh weights (FW) of roots and shoots were determined separately (7 plants from each treatment and 3 independent replicates; n=21). Dry weight (DW) of roots and shoots was measured after drying in hot-air oven at 80 °C for 2 d. The fresh and dry weight of roots and shoots were expressed as g plant⁻¹.

2.4. Calculation of tolerance indices

Tolerance indices (TI) were calculated on the basis of root length (RL) and shoot length (SL) according to the following formula [23]:

$$TI (\%) = (RL \text{ or } SL_{NaCl} / RL \text{ or } SL_{control}) \times 100$$

According to the calculated tolerance indices for each salt concentration applied, five different barley genotypes were scored between one and five. One score was given to the genotype with minimum tolerance indices while five score was given to the genotype with maximum tolerance indices. Then, the scores obtained for each salt concentration for each genotype were added to obtain the total score [24].

2.5. Statistical analysis

The experimental design was a complete randomised block with three independent replicates. The significance of difference between controls and applications (mean values) was determined by one-way ANOVA at 95% confidence level by using SPSS 11.0 statistical program for Windows. Means and s.e. values represent seven replicates (n=7) for all measurements.

3. RESULTS AND DISCUSSION

Decreased growth rate in plant species has been considered as one of the most obvious effects of salt stress [25]. Growth ability of plants under salt stress has been used as a common screening criterion to determine salt tolerance degree of plant genotypes [22]. In addition, identification of plant species and genotypes that are tolerant to high soil salinity is very important for reclamation of salinized areas for agricultural purposes [26]. In our study, it was observed that salt stress decreased root growth of all barley genotypes significantly, except for genotype Bülbul-89, as compared to controls (Figure 1A) (P<0.05). Also, our results showed that inhibition degree of growth in roots was proportional to the salt concentrations applied. The inhibitory effect of salt stress on root growth was observed in all barley genotypes used in this study. However, root growth in Avcı-2002 was found to be the most susceptible to salt concentrations, while Bülbul-89 was the most tolerant genotype because of insignificant decrease in root growth as a result of salt applications. Root growth in Avcı-2002 and Bülbul-89 was inhibited by 33% and 15% at 300 mM salt application, as compared to controls, respectively. Similarly, salt stress decreased shoot growth rate in barley genotypes in a concentration dependent manner as well (Figure 1B). Furthermore, our results showed that roots and shoots of barley genotypes used in this study represented considerable variation with respect to salinity tolerance and sensitivity. In Aydanhanım, for example, root growth was found to be more sensitive to salt stress while shoot growth was more tolerant. In Bülbul-89 and Orza-96, on the other hand, shoot growth was sensitive

and root growth was tolerant to salinity. These results are in accordance with the findings of Zaimoğlu and Doğru [27], who reported that sensitivity and/or tolerance degree of different maize genotypes may show great variation under saline conditions. Similarly, root and shoot growth was decreased more severely as the salt concentration increased in our study, as indicated by Pessaraki et al. [28] in *Distichlis spicata* plants. It has been reported that salt stress could reduce mitotic activity in the meristematic cells in plants, depending on the plant species, genotype, salt concentration and exposure time [29]. Accordingly, we may conclude that mitotic activity in the salt-stressed barley genotypes used in this study showed considerable variation in an organ dependent manner. Total plant length, on the other hand, was found to be significantly lower than respective controls in all salt-stressed barley genotypes, possibly due to cumulative effect of decreased root and shoot growth (Figure 1C).

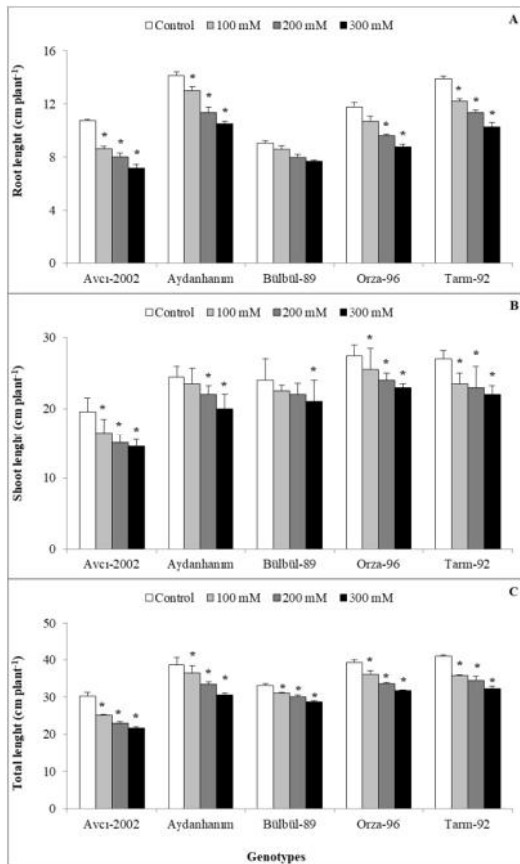


Figure 1. The effect of salt stress on (A) root length, (B) shoot length and (C) total length in barley genotypes (Significant differences from controls ($P < 0.05$) are marked

with an asterisk. Abbreviations and statistical evaluations are the same for the following figures and table(s)).

Genotype Avcı-2002 had the lowest tolerance indices in root and shoot among all barley cultivars used in this study. This showed that meristematic cells located in the root and shoot tips were highly sensitive to salinity (Table 1). Bülbül-89, on the other hand, represented the highest tolerance indices in roots and shoots and was found to be the most salt tolerant barley genotype (Table 1). Total score, calculated on the basis of root and shoot length, confirmed our results as well. It was 6 for Avcı-2002 and displayed the highest salt-induced damage, while Bülbül-89 was less affected by salinity and maintained root and shoot growth, with a 29 of total score (Table 1). Shannon and Grieve [30] reported that one of the most important physiological growth parameters used to determine differences in salt tolerance between different plant species and genotypes is the growth rate of root and shoot. Anjum [31] has exposed two different *Citrus* rootstocks (Cleopatra and Troyer) to 40 and 80 mM salt stress and concluded that Cleopatra is more tolerant to salinity because of maintaining root and shoot growth under saline conditions. Several studies have demonstrated that salt stress decreased plant growth by causing hormonal imbalance [18], physiological drought [19], ion toxicity [4], enzyme inactivation [20], inhibition of protein synthesis [21] and oxidative stress [22]. However, these probabilities remained to be investigated in our study.

Our results showed that salt stress did not significantly affect fresh weight of roots in Avcı-2002, Aydanhanım and Orza-96 (Figure 2A) ($P > 0.05$). However, in Bülbül-89 and Tarm-92, especially higher salt concentrations (200 and 300 mM) led to the relatively and significantly lower fresh weight in roots as compared to controls ($P < 0.05$). The lower level of root fresh weight indicates severe impairment of water uptake from growth medium in Bülbül-89 and Tarm-92. Shoot fresh weight, however, was more severely and significantly affected by salt stress in barley cultivars except for Aydanhanım (Figure 2B) ($P < 0.05$) when compared to respective controls and root fresh weights.

Table 1. Tolerance indices and total scores of barley cultivars under salt stress

Genotypes	Root			Shoot			Total score
	Tolerance indices (%)			Tolerance indices (%)			
	100 mM	200 mM	300 mM	100 mM	200 mM	300 mM	
Avcı-2002	80,4 (1)*	74,5 (1)	66,7 (1)	84,6 (1)	76,9 (1)	74,4 (1)	6**
Aydanhanım	92,1 (4)	80,6 (2)	74,6 (3)	95,9 (5)	89,8 (4)	81,6 (3)	21
Bülbül-89	94,8 (5)	88,3 (5)	85,1 (5)	93,8 (4)	91,7 (5)	87,5 (5)	29**
Orza-96	90,6 (3)	81,7 (3)	74,3 (2)	92,7 (3)	87,3 (3)	83,6 (4)	18
Tarm-92	87,8 (2)	81,8 (4)	73,8 (4)	87,0 (2)	85,2 (2)	81,5 (2)	16

* Values in the parenthesis indicate the scores given according to tolerance indices

** The highest score indicates the lowest damage and the lowest score indicates the highest damage

Therefore, changes in root and shoot fresh weights clearly indicated that salt stress affected water relations between barley plants and environment, depending on the salt concentration, organ type and genotype.

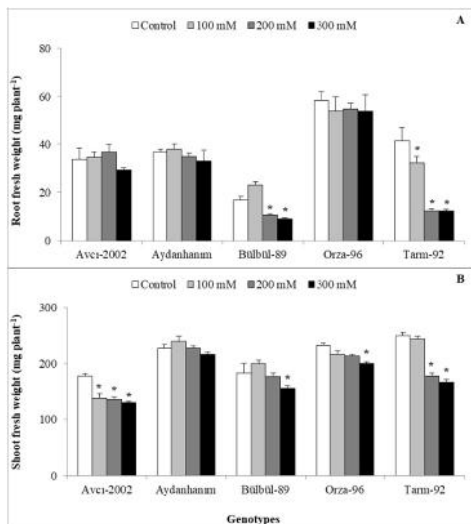


Figure 2. The effect of salt stress on (A) root fresh weight and (B) shoot fresh weight in barley genotypes

It has been reported that adjustment of water balance in the tissues of plants under biotic and abiotic stresses is a very important factor in terms of stress tolerance [32]. Several studies have

indicated that decreases in the osmotic potential and water content in salt-sensitive plant species and genotypes are more prominent than tolerant species and genotypes [33]. In addition, it has been well known that fresh weight and water content in leaves is the most reliable suggestive indicator about physiological status in the salt-stressed plants [34]. Consequently, we may conclude that Avcı-2002, represented the lowest shoot fresh weight, is the most salt susceptible genotypes used in our study while Bülbül-89 was the most tolerant barley genotypes to salinity among others, with the highest shoot fresh weight. Similar to fresh weight, dry weights of barley genotypes were also affected by salt stress. Root dry weight was significantly lowered in Avcı-2002, Aydanhanım and Tarm-92 as compared to controls (Figure 3A) ($P < 0.05$). In Bülbül-89 and Orza-96, however, it was not changed significantly as a result of salt applications ($P > 0.05$). Shoot dry weight was found to be less affected in barley genotypes and only higher salt concentrations (200 and 300 mM) reduced shoot dry weight in Tarm-92 significantly (Figure 3B) ($P < 0.05$). Obviously, our results showed that salt stress inhibited root metabolism more severely than leaves in barley cultivars used in this study, causing reduced biomass accumulation. The decrease in biomass accumulation in plants under salt stress has mostly been attributed to ion imbalance [12]. Davenport et al. [35] and Munns and Tester [36], for example, have stated that salt stress decreased photosynthetic activity and biomass in plants by reducing activities of some enzymes which are responsible for carbon fixation and pigment synthesis as a result of Na^+ accumulation in plant tissues.

In summary, our preliminary study showed that there is a broad variation between barley cultivars in terms of salt tolerance. We found that salt stress reduced root and shoot growth rate more severely than other physiological growth parameters evaluated in this study. Tolerance indices, calculated on the basis of root and shoot length, indicated that Bülbül-89 is the most salt-tolerant barley genotype and Avcı-2002 is the most susceptible one.

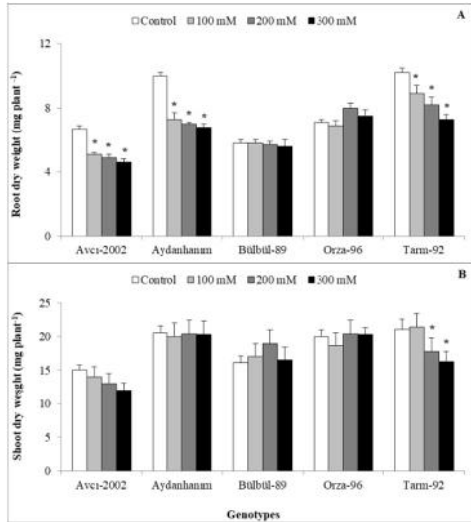


Figure 3. The effect of salt stress on (A) root dry weight and (B) shoot dry weight in barley genotypes

Aydanhanım, Orza-96 and Tarm-92, on the other hand, were found to be moderately tolerant to salinity. Fresh and dry weight of roots and shoots showed that salt stress affected water relation and biomass accumulation in barley plants depending on the genotype, salt concentration and organ type. However, we believe that changes in root and shoot growth rate in barley genotypes under salt stress may be used as a more reliable criterion for salt tolerance selection. In this study we have only identified the most salt-susceptible and salt-tolerant barley genotypes. Our future aim is to investigate the physiological and biochemical basis of salt responses of these two genotypes and our detailed experiments have been still continuing.

REFERENCES

- [1] P. Rengasamy, "World salinization with emphasis on Australia," *Journal of Experimental Botany*, vol. 57, pp. 1017–1023, 2006.
- [2] N. Y. Bolat, "Doğal ekosistemde bulunan mikoriza türlerinin kültür bitkilerine adaptasyonunun sağlanması," Yüksek Lisans Tezi, Çukurova Üniversitesi, Fen Bilimleri Enstitüsü, s. 14, 2006.
- [3] H. Tuncay, "Söke ovası tuzlu ve sodyumlu toprakların ıslahında esas olacak özelliklerin tespitine dair çalışmalar," Ege Üniversitesi Ziraat Fakültesi Yayınları, Bornova, İzmir, 1978.
- [4] B. Seçkin, "Tuzluluk stresinin bazı arpa (*Hordeum* ssp.) türleri üzerindeki fizyolojik ve biyokimyasal etkilerinin araştırılması," Doktora Tezi, Ege Üniversitesi, Fen Bilimleri Enstitüsü, pp. 15-38, 2010.
- [5] A. Ergene, "Toprak Bilgisi," Atatürk Üniversitesi Ziraat Fakültesi Yayınları, Erzurum, 1982.
- [6] A. Cesur, "Tuzlu koşullarda çimlendirilen arpa köklerinde hücre döngüsü, mitotik indeks ve kromozom yapısına H₂O₂ ön muamelesinin etkileri," Yüksek Lisans Tezi, Süleyman Demirel Üniversitesi, Fen Bilimleri Enstitüsü, pp. 1-3, 2007.
- [7] K. Çavuşoğlu, "Geleneksel hormonlarla son yıllarda bulunan bazı hormonların ve büyüme düzenleyicilerinin yüksek sıcaklık ve tuz (NaCl) stresleri altındaki arpa ve turp tohumlarının çimlenmesi üzerindeki etkilerinin karşılaştırılması," Doktora Tezi, Süleyman Demirel Üniversitesi, Fen Bilimleri Enstitüsü, pp. 1-5, 2006.
- [8] I. Öncel and Y. Keleş, "Tuz stresi altındaki buğday genotiplerinde büyüme, pigment içeriği ve çözünen madde kompozisyonunda değişimler," *Cumhuriyet Üniversitesi, Fen-Edebiyat Fakültesi, Fen Bilimleri Dergisi*, vol. 23, no. 2, 2002.
- [9] Anonymous, "FAO Land and Plant Nutrition Management Service," <http://www.fao.org/ag/ag/agll/spush>, 2008.
- [10] M. Ashraf, "Breeding for salinity tolerance in plants," *Critical Review of Plant Sciences*, vol. 13, pp. 17–42, 1994.
- [11] H. Marschner, "Mineral Nutrition of Higher Plants," Academic Press, London 1995.
- [12] R. Munns, "Comparative physiology of salt and water stress," *Plant Cell and Environment*, vol. 25, pp. 239–250, 2002.

- [13] J. C. Papp, M. C. Ball and N. Terry, “A comparative study of the effects of NaCl salinity on respiration, photosynthesis, and leaf extension growth in *Beta vulgaris* L. (sugar beet),” *Plant Cell and Environment*, vol. 6, no. 8, pp. 675-677, 1983.
- [14] M. Hasanuzzaman, M. Fujita, M. N. Islam, K. U. Ahamed and K. Nahar, “Performance of four irrigated rice varieties under different levels of salinity stress,” *International Journal of Integrative Biology*, vol. 6, pp. 85–90, 2009.
- [15] B. Guan, J. Yu, X. Chen, W. Xie and Z. Lu, “Effects of salt stress and nitrogen application on growth and ion accumulation of *Suaeda salsa* plants,” *International Conference of Remote Sensing, Environment and Transportation Engineering*, pp. 8268-8272, 2011.
- [16] L. F. M. Marcelis and J. van Hooijdonk, “Effect of salinity on growth, water use and nutrient use in radish (*Raphanus sativus* L.),” *Plant and Soil*, vol. 215, pp. 57–64, 1999.
- [17] E. O. Leidi and J. F. Saiz, “Is salinity tolerance related to Na acculamation in upland cotton seedlings,” *Plant and Soil*, vol. 190, pp. 67-75, 1997.
- [18] H. Kurban, H. Saneoka, K. Nehira, R. Adilla, G. S. Premachandra and K. Fujita, “Effect of salinity on growth, photosynthesis and mineral composition in leguminous plant *Alhagi pseudoalhagi* (Bieb.),” *Soil Science and Plant Nutrition*, vol. 45, pp. 851–862, 1999.
- [19] E. R. Lamond and A. D. Whitney, “Management soline and sodik soils, cooperative extension service,” Kansas State University, Kansas, U.S.A., 1991.
- [20] M. Ayyıldız, “Sulama suyu kalitesi ve tuzluluk problemleri”, Ankara Üniversitesi Ziraat Fakültesi Yayınları Ders Kitabı, Ankara, pp. 244-250, 1983.
- [21] M. N. Khalid, H. F. Iqbal, A. Tahir and A. N. Ahmad, “Germination potential of chickpeas (*Cicer arietinum* L.) under saline conditions,” *Pakistan Journal of Biological Sciences*, vol. 4, no. 4, pp. 395-396, 2001.
- [22] A. K. Parida, A. B. Das, “Salt tolerance and salinity effects on plants: a review,” *Ecotoxicology and Environmental Safety*, vol. 60, pp. 324-349, 2005.
- [23] S. A. Bağcı, H. Ekiz and A. Yılmaz, “Determination of the salt tolerance of some barley genotypes and the characteristics affecting tolerance,” *Turkish Journal of Agriculture and Forestry*, vol. 27, pp. 253-260, 2003.
- [24] B. Ayhan, Y. Ekmekçi and D. Tanyolaç, “Erken fide evresindeki bazı mısır çeşitlerinin ağır metal (kadmiyum ve kurşun) stresine karşı dayanıklılığının araştırılması,” *Anadolu Üniversitesi Bilim ve Teknoloji Dergisi*, vol. 8, no. 2, pp. 411-422, 2007.
- [25] P. E. Verslues, M. Agarwal, S. K. Agarwal, J. Zhu and J. K. Zhu, “Methods and concepts in quantifying resistance to drought, salt and freezing, abiotic stresses that affect plant water status,” *Plant Journal*, vol. 45, pp. 523–539, 2006.
- [26] M. Ashraf and P. J. C. Harris, “Potential biochemical indicators of salinity tolerance in plants,” *Plant Science*, vol. 166, pp. 3-16, 2004.
- [27] S. Zaimoğlu and A. Doğru, “Farklı Mısır Genotiplerinde Tuz Stresinin Bazı Büyüme Parametreleri ve Fotosentetik Aktivite Üzerindeki Etkileri,” *23. Ulusal Biyoloji Kongresi*, pp. 270, 2016.
- [28] M. Pessarakli, K. B. Marcum and D. M. Kopec, “Growth response of desert saltgrass under salt stres, turfgrass landscape and urban IPM research summary,” Cooperative Extension, Agricultural Experiment Station, The

University of Arizona, Tuscon AZ1246 series, 70-73, 2001.

- [29] R. Munns, "Comparative physiology of salt and water stress," *Plant Cell and Environment*, vol. 25, pp. 239–250, 2002.
- [30] M. C. Shannon and C. M. Grieve, "Tolerance of vegetable crops to salinity," *Scientia Horticulturae*, vol. 78, pp. 5–38, 1999.
- [31] M. A. Anjum, "Effect of NaCl concentrations in irrigation water on growth and polyamine metabolism in two citrus rootstocks with different levels of salinity tolerance," *Acta Physiologia Plantarum*, vol. 30, pp. 43–52, 2008.
- [32] H. J. Bohnert, D. E. Nelson and R. G. Jensen, "Adaptation to environmental stresses," *Plant Cell*, vol. 7, pp. 1099-1111, 1995.
- [33] M. M. F. Mansour, "Protection of plasma membrane of onion epidermal cells by glycinebetaine and proline against NaCl stress," *Plant Physiology and Biochemistry*, vol. 36, pp. 767–772, 1998.
- [34] M. M. F. Mansour, K.H.A. Salama, F.Z.M. Ali, and A.F.A. Hadid, "Cell and plant responses to NaCl in *Zea mays* L. cultivars differing in salt tolerance," *General and Applied Plant Physiology*, vol. 31, pp. 29-41, 2005.
- [35] R. Davenport, R. James, A. Zakrisson-Plogander, M. Tester and R. Munns, "Control of sodium transport in durum wheat," *Plant Physiology*, vol. 137, pp. 807-818, 2005.
- [36] R. Munns and M. Tester, "Mechanisms of salinity tolerance," *Annual Review of Plant Biology*, vol. 59, pp. 651-681, 2008

JOURNAL OF SCIENCE



SAKARYA UNIVERSITY

Sakarya University Journal of Science

ISSN 1301-4048 | e-ISSN 2147-835X | Period Bimonthly | Founded: 1997 | Publisher Sakarya University |
<http://www.saujs.sakarya.edu.tr/>

Title: Absolute Almost Weighted Summability Methods

Authors: Mehmet Ali Sarıgöl

Received: 2019-01-31 16:17:44

Accepted: 2019-03-18 08:33:49

Article Type: Research Article

Volume: 23

Issue: 5

Month: October

Year: 2019

Pages: 763-766

How to cite

Mehmet Ali Sarıgöl; (2019), Absolute Almost Weighted Summability Methods.

Sakarya University Journal of Science, 23(5), 763-766, DOI:

10.16984/saufenbilder.520449

Access link

<http://www.saujs.sakarya.edu.tr/issue/44066/520449>

New submission to SAUJS

<http://dergipark.gov.tr/journal/1115/submission/start>

Absolute almost weighted summability methods

Mehmet Ali Sarıgöl*¹

Abstract

In this paper, we introduce absolute almost weighted convergent series and treat with the classical results of Bor [3-4] and also study some relations between this method and the well known spaces.

Keywords: Absolute summability, almost summability, weighted mean, equivalence methods

1. INTRODUCTION

Let ℓ_∞ be the subspace of all bounded sequences of w , the set of all sequences of complex numbers. A sequence $(x_n) \in \ell_\infty$ said to be almost convergent to γ if all of its Banach limits (see, [1]) are equal to γ . Lorentz [8] proved that the sequence (x_n) is almost convergent to γ if and only if

$$\frac{1}{m+1} \sum_{v=0}^m x_{n+v} \rightarrow \gamma \text{ as } m \rightarrow \infty \text{ uniformly in } n \quad (1.1)$$

Let $\sum a_v$ be a given infinite series with s_n as its n -th partial sum and (p_n) be a sequence of positive real numbers such that, $P_{-1} = p_{-1}$,

$$P_n = p_0 + p_1 + \dots + p_n \rightarrow \infty \text{ as } n \rightarrow \infty. \quad (1.2)$$

The series $\sum a_v$ is said to be summable $|\bar{N}, p_n|_k$, $k \geq 1$, if (see, [2])

$$\sum_{n=1}^{\infty} \left(\frac{P_n}{p_n} \right)^{k-1} |T_n - T_{n-1}|^k < \infty, \quad (1.3)$$

where

$$T_n = \frac{1}{P_n} \sum_{v=0}^n p_v s_v,$$

which reduces to the absolute Cesàro summability $|C, 1|_k$ in Flett [5]'s notation in the special case $p_n = 1$ for $n \geq 0$. Many papers concerning the summability $|\bar{N}, p_n|_k$ was published by several authors (see, [2-3], [5-7], [10-15]). For example, it is well known that the classical results of Bor [2,3] give sufficient conditions for the equivalence of the summability methods $|C, 1|_k$ and $|\bar{N}, p_n|_k$ as follows.

Theorem 1.1. Let (p_n) be a sequence of positive real numbers such that

$$(i) np_n = O(P_n) \text{ and } (ii) P_n = O(np_n). \quad (1.4)$$

Then, $\sum a_v$ is summable $|C, 1|_k$ if and only if it is summable $|\bar{N}, p_n|_k$, $k \geq 1$.

2. MAIN RESULTS

The main purpose of this paper is to derive an absolute almost weighted summability from the absolute weighted summability just as absolute almost convergence emerges out of the concept of absolute convergence and to discuss Theorem 1.1 for new summability method. Also, we study some relations

* Corresponding Author msarigol@pau.edu.tr

¹ University of Pamukkale, Denizli-20017, Turkey ORCID: 0000-0002-9820-1024

between this method and between some known spaces. Now for the sequence of partial sums (s_n) of the series $\sum a_v$ we define $T_m(n)$ by

$$T_{-1} = s_{n-1}, \quad T_m(n) = \frac{1}{P_m} \sum_{v=0}^m p_v s_{n+v}, m \geq 0.$$

Then, it is easily seen that

$$T_m(n) - T_{m-1}(n) = \begin{cases} a_n, & m = 0 \\ \frac{p_m}{P_m P_{m-1}} \sum_{v=1}^m P_{v-1} a_{n+v}, & m \geq 1 \end{cases}$$

So we give the following definition.

Definition 2.1. Let $\sum a_v$ be an infinite series with partial sum s_n and (p_n) be a sequence of positive real numbers satisfying (1.2). The series $\sum a_v$ is said to be absolute almost weighted summable $|f(\bar{N}), p_m|_k, k \geq 1$, if

$$\sum_{m=0}^{\infty} \left(\frac{P_m}{p_m}\right)^{k-1} |\Delta T_{m-1}(n)|^k < \infty \quad (2.1)$$

uniformly in n , where $\Delta T_{-1}(n) = 0, \Delta T_{m-1}(n) = T_{m-1}(n) - T_m(n)$ for $m, n \geq 0$.

Note that, for $p_m = 1$ (resp. $k = 1$), it reduces to the absolute almost Cesàro summability $|f(C), 1|_k$ (resp. $\hat{\ell}$, given by Das et al [4]). Further, it is clear that every $|f(\bar{N}), p_m|_k$ summable series is also summable $|\bar{N}, p_n|_k$, but the converse is not true.

Before discussing a similar of Theorem 1.1 for the new method, we study a relation between this method and the space ℓ_k of all k -absolutely convergent series.

Theorem 2.2. Let (p_n) be a sequence of positive numbers satisfying the condition $P_n = O(p_n)$. If $\sum |a_v|^k < \infty$, then it is summable $|f(\bar{N}), p_m|_k, k \geq 1$. If $k = 1$, then the condition is omitted.

To prove this theorem, we require the following lemma of Maddox [9].

Lemma 2.3. If $\sum_m |b_m(n)| < \infty$ for each n and $\sum_m |b_m(n)| \rightarrow 0$ as $n \rightarrow \infty$, then $\sum_m |b_m(n)|$ is uniformly convergent in n .

Proof of Theorem 2.2. Since the proof is easy for $k = 1$, it is omitted. Now, for $k > 1$, it follows from Hölder's inequality that

$$\sum_{m=0}^{\infty} \left(\frac{P_m}{p_m}\right)^{k-1} |\Delta T_{m-1}(n)|^k$$

$$\begin{aligned} &\leq |a_n|^k + \sum_{m=1}^{\infty} \frac{p_m}{P_m P_{m-1}^k} \left(\sum_{v=1}^m \left| \frac{P_{v-1}}{p_v} p_v a_{n+v} \right| \right)^k \\ &\leq |a_n|^k \\ &+ \sum_{m=1}^{\infty} \frac{p_m}{P_m P_{m-1}} \sum_{v=1}^m \left(\frac{P_{v-1}}{p_v}\right)^k p_v |a_{n+v}|^k \left(\frac{1}{P_{m-1}} \sum_{v=1}^m p_v\right)^{k-1} \\ &= O(1) \left\{ |a_n|^k + \sum_{v=1}^{\infty} \left(\frac{P_{v-1}}{p_v}\right)^k p_v |a_{n+v}|^k \sum_{m=v}^{\infty} \frac{p_m}{P_m P_{m-1}} \right\} \\ &= O(1) \left\{ |a_n|^k + \sum_{v=1}^{\infty} \left(\frac{P_{v-1}}{p_v}\right)^k \frac{p_v}{P_{v-1}} |a_{n+v}|^k \right\} \\ &= O(1) \left\{ |a_n|^k + \sum_{v=1}^{\infty} |a_{n+v}|^k \right\} \\ &= O(1) \left\{ \sum_{v=n}^{\infty} |a_v|^k \right\} \rightarrow 0 \text{ as } n \rightarrow \infty. \end{aligned}$$

Thus the proof is completed by Lemma 2.3.

Theorem 2.4. Let (p_n) satisfy the conditions of Theorem 1.1. If, as $m \rightarrow \infty$,

$$L_m(n) = \frac{1}{P_m} \sum_{v=1}^m (P_v - (v+1)p_v) \rightarrow 0$$

uniformly in n , then it is summable $|f(\bar{N}), p_m|_k$ whenever $\sum a_v$ is summable $|f(C), 1|_k, k \geq 1$.

Theorem 2.5. Let (p_n) satisfy the conditions of Theorem 1.1. If, as $m \rightarrow \infty$,

$$R_m(n) = \frac{1}{m} \sum_{v=1}^m \left((v+1) - \frac{P_v}{p_v} \right) y_v(n) \rightarrow 0$$

uniformly in n , then, it is summable $|f(C), 1|_k$ whenever $\sum a_v$ is summable $|f(\bar{N}), p_m|_k, k \geq 1$.

Proof of Theorem 2.4. We define the sequences $(x_m(n))$ and $(y_m(n))$ by

$$x_0(n) = a_n, x_m(n) = \frac{1}{m(m+1)} \sum_{v=1}^m v a_{n+v} \quad (2.3)$$

and

$$y_0(n) = a_n, y_m(n) = \frac{p_m}{P_m P_{m-1}} \sum_{v=1}^m P_{v-1} a_{n+v} \quad (2.4)$$

Suppose that $\sum a_v$ is summable $|f(C), 1|_k$. Then,

$$\sum_{m=1}^{\infty} m^{k-1} |x_m(n)|^k < \infty$$

and the remaining term tends to zero uniformly in n , respectively. By using Abel's summations we write

$$\begin{aligned} y_m(n) &= \frac{p_m}{P_m P_{m-1}} \sum_{v=1}^m \frac{P_{v-1}}{v} v a_{n+v} \\ &= \frac{p_m}{P_m P_{m-1}} \left[\sum_{v=1}^{m-1} \Delta \left(\frac{P_{v-1}}{v} \right) v(v+1) x_v(n) \right. \\ &\quad \left. + \frac{P_{m-1}}{m} m(m+1) x_m(n) \right] \\ &= \frac{p_m}{P_m P_{m-1}} \sum_{v=1}^{m-1} (P_v - (v+1)p_v) x_v(n) \\ &\quad + \frac{(m+1)p_m}{P_m} x_m(n) \\ &= y_m^{(1)}(n) + y_m^{(2)}(n), \text{ say.} \end{aligned}$$

Now, by Minkowski's inequality, it is sufficient to show that the remaining term, as $j \rightarrow \infty$,

$$\sum_{m=j}^{\infty} \left(\frac{P_m}{p_m} \right)^{k-1} |y_m^{(r)}(n)|^k \rightarrow 0 \text{ uniformly in } n,$$

for $r = 1, 2$. By applying Hölder inequality for $k > 1$ (clearly for $k = 1$) we have, from the hypotheses of the theorem

$$\begin{aligned} &\sum_{m=j}^{\infty} \left(\frac{P_m}{p_m} \right)^{k-1} |y_m^{(1)}(n)|^k \\ &= O(1) \sum_{m=j}^{\infty} \frac{p_m}{P_m P_{m-1}} \left(\sum_{v=1}^{j-1} + \sum_{v=j}^{m-1} \right) \\ &\quad |(P_v - (v+1)p_v) x_v(n)|^k \end{aligned}$$

$$\begin{aligned} &= O(1) \sum_{m=j}^{\infty} \frac{p_m}{P_m P_{m-1}} \left\{ |P_{j-1} L_{j-1}(n)|^k \right. \\ &\quad \left. + \left| \sum_{v=j}^{m-1} (P_v - (v+1)p_v) x_v(n) \right|^k \right\} \\ &= O(1) \left\{ |P_{j-1} L_{j-1}(n)|^k \sum_{m=j}^{\infty} \frac{p_m}{P_m P_{m-1}} \right. \\ &\quad \left. + \sum_{m=j+1}^{\infty} \frac{p_m}{P_m P_{m-1}} \left(\sum_{v=j}^{m-1} v p_v |x_v(n)| \right)^k \right\} \\ &= O(1) \left\{ |L_{j-1}(n)|^k \right. \\ &\quad \left. + \sum_{m=j+1}^{\infty} \frac{p_m}{P_m P_{m-1}} \sum_{v=j}^{m-1} v^k p_v |x_v(n)|^k \left(\sum_{v=0}^{m-1} \frac{p_v}{P_{m-1}} \right)^{k-1} \right\} \\ &= O(1) \left\{ |L_{j-1}(n)|^k + \sum_{v=j}^{\infty} v^k p_v |x_v(n)|^k \sum_{m=v+1}^{\infty} \frac{p_m}{P_m P_{m-1}} \right\} \\ &= O(1) \left\{ |L_{j-1}(n)|^k + \sum_{v=j}^{\infty} \frac{v p_v}{P_v} v^{k-1} |x_v(n)|^k \right\} \\ &= O(1) \left\{ |L_{j-1}(n)|^k \sum_{v=j}^{\infty} v^{k-1} |x_v(n)|^k \right\} \rightarrow 0 \text{ as } j \rightarrow \infty, \end{aligned}$$

uniformly in n .

Also, by using $m p_m = O(P_m)$ we get

$$\begin{aligned} &\sum_{m=j}^{\infty} \left(\frac{P_m}{p_m} \right)^{k-1} |y_m^{(2)}(n)|^k \\ &= \sum_{m=j}^{\infty} \left| \frac{(m+1)p_m}{P_m} x_m(n) \right|^k \\ &= O(1) \sum_{m=j}^{\infty} (m)^{k-1} |x_m(n)|^k \rightarrow 0 \end{aligned}$$

uniformly in n , which completes the proof of part (i).

The proof of Theorem 2.5 is proved by changing the roles of " p_n " and "1".

Also the following results are directly obtained by Lemma 2.3.

Theorem 2.6. Let (p_n) be a sequence of positive numbers satisfying the conditions of Theorem 1.1. If

$$\sum_{m=0}^{\infty} (m + 1)^{k-1} |x_m(n)|^k \rightarrow 0 \text{ as } n \rightarrow \infty$$

or

$$\sum_{m=0}^{\infty} \left(\frac{P_m}{p_m}\right)^{k-1} |y_m(n)|^k \rightarrow 0 \text{ as } n \rightarrow \infty$$

holds, then a series $\sum a_v$ is summable $|f(C), 1|_k$ and $|f(\bar{N}), p_m|_k$, $k \geq 1$, where the sequences $(x_m(n))$ and $(y_m(n))$ are as in (2.3) and (2.4).

Proof. By following the lines of the proof of Theorem 2.4, we have

$$\sum_{m=1}^{\infty} \left(\frac{P_m}{p_m}\right)^{k-1} |y_m(n)|^k = O(1) \left\{ \sum_{v=1}^{\infty} v^{k-1} |x_v(n)|^k \right\}$$

and also

$$\sum_{m=1}^{\infty} m^{k-1} |x_m(n)|^k = O(1) \left\{ \sum_{v=1}^{\infty} \left(\frac{P_v}{p_v}\right)^{k-1} |y_v(n)|^k \right\}$$

which completes the proof together with Lemma 2.3.

REFERENCES

- [1] S. Banach, "Theorie des operations lineaires", Warsaw, 1932.
- [2] H. Bor, "On two summability methods", Math. Proc. Camb. Phil. Soc., vol.97, pp.147-149, 1985.
- [3] H. Bor, "A note on two summability methods", Proc. Amer. Math. Soc., vol.98, pp. 81-84, 1986.
- [4] G. Das, B. Kuttner and S. Nanda, "Some sequence suquences", Trans. Amer. Math. Soc., vol. 283, pp.729-739, 1984.
- [5] T.M. Flett, "On an extension of absolute summability and some theorems of Littlewood and Paley," Proc. London Math. Soc., vol. 7, pp.113-141, 1957.
- [6] G.C. Hazar and F. Gökce, "On summability methods $|A_f|_k$ and $|C, 0|_k$ ", Bull. Math. Anal. Appl., vol. 8 (1), pp.22-26, 2016.
- [7] G.C.H. Güleç, "Summability factor relations between absolute weighted and Cesàro means", Math Meth Appl Sci., Special Issue, pp. 1-5, 2018 (Doi: 10.1002/mma.5399).
- [8] G.G. Lorentz, "A contribution to the theory of divergent sequences", Acta Math., vol. 80, pp. 167-190, 1948.
- [9] I.J. Maddox, "Elements of Functional Analysis", Cambridge Univ. Press, 1970.
- [10] M.A. Sarıgöl, "Necessary and sufficient conditions for the equivalence of the summability methods", Indian J. Pure Appl. Math., vol. 22, pp. 483-489, 1991.
- [11] M.A. Sarıgöl, "On absolute weighted mean summability methods", Proc. Amer. Math. Soc., vol. 115, pp.157-160, 1992.
- [12] M.A. Sarıgöl, "On inclusion relations for absolute weighted mean summability", J. Math. Anal. Appl., vol.181, pp. 762-767, 1994.
- [13] M.A. Sarıgöl and H. Bor, "Characterization of absolute summability factors", J. Math. Anal. Appl., vol. 195, pp. 537-545, 1995.
- [14] M.A. Sarıgöl, "On the local properties of factored Fourier series", Appl. Math. Comp., vol. 216, pp. 3386-3390, 2010.
- [15] M.A. Sarıgöl, "Matrix transformations on fields of absolute weighted mean summability", Studia Sci. Math. Hungarica, vol. 48 (3), pp. 331-341, 2011.

JOURNAL OF SCIENCE



SAKARYA UNIVERSITY

Sakarya University Journal of Science

ISSN 1301-4048 | e-ISSN 2147-835X | Period Bimonthly | Founded: 1997 | Publisher Sakarya University |
<http://www.saujs.sakarya.edu.tr/>

Title: A Bayesian Parameter Estimation Approach To Response Surface Optimization in Quality Engineering

Authors: Elif Kozan, Onur K ksoy

Received: 2018-11-20 15:07:54

Accepted: 2019-03-19 14:53:12

Article Type: Research Article

Volume: 23

Issue: 5

Month: October

Year: 2019

Pages: 767-774

How to cite

Elif Kozan, Onur K ksoy; (2019), A Bayesian Parameter Estimation Approach To Response Surface Optimization in Quality Engineering. Sakarya University Journal of Science, 23(5), 767-774, DOI: 10.16984/saufenbilder.485785

Access link

<http://www.saujs.sakarya.edu.tr/issue/44066/485785>

New submission to SAUJS

<http://dergipark.gov.tr/journal/1115/submission/start>

A Bayesian Parameter Estimation Approach to Response Surface Optimization in Quality Engineering

Elif Kozan^{*1}, Onur Köksoy²

Abstract

In recent years, Bayesian analyses have become increasingly popular for solving industrial related problems. This paper illustrates the use of Bayesian methods in response surface methodology (RSM) in the context of “off-line quality” improvement. RSM and Bayesian Linear Regression - an approach which uses the prior information to make a more efficient inference - are considered together. Results from different estimators are compared for the first time ever. Bayesian linear regression uses the prior information in the high uncertainty state of the response function to make more efficient and more realistic inferences than can be obtained with classical regression. Several different values of the prior distribution of the parameter and uncertainty analysis will be presented for comparative purposes. The effect of the change in the prior information and variances will be illustrated by using an example from the literature.

Keywords: Response surface methodology, Bayesian regression, off-line quality control, experimental design, WinBUGS

1. INTRODUCTION

In general, the Bayesian approach is a special form of Bayes’ theorem, which was first introduced by Thomas Bayes [1]. Subsequently Laplace [16] presented the general form of Bayes’ theorem. In the 20th century, Laplace’s studies have received considerable attention from authors such as Keynes [11], Ramsey [21], and Savage [22]. Jeffreys [10] made some important contributions to the fundamental theory of Bayesian statistics. Metropolis et al. [17] introduced the Metropolis-Hastings algorithm. Along with new technologies in computer sciences, this algorithm has been used to overcome the computational difficulties connected with integrals of problems involving Bayesian models. Hasting [8] introduced the Monte Carlo method for evaluating integrals as a

major tool for practical Bayesian inference. In addition, the development of techniques such as Markov chain Monte Carlo (MCMC) has greatly increased the applicability of the Bayesian approach. Goldstein [6] applied the Bayesian approach to regression problems.

The development of fast computers made necessary calculations faster and pioneered the use of the Bayesian approach for a wide range of applications. Also, a review of the literature reveals that the estimation step becomes more powerful and more realistic when using prior model information. In Bayesian inference, the Bayes’ risk function includes both a posterior model of unknown parameters given the observation and a cost of error function. By minimizing this risk function, one easily obtains the point estimators

* Corresponding Author 1986elif@gmail.com

¹ Ege University, Faculty of Science, Department of Statistics, B-Block, 35100, Bornova, Izmir, Turkey 0000-0002-8267-074X

² Ege University, Faculty of Science, Department of Statistics, B-Block, 35100, Bornova, Izmir, Turkey 0000-0003-2634-0794

using Bayesian methodology. A couple of different methods are available for Bayesian estimation, including maximum a posteriori (MAP), minimum mean square error (MMSE), and Markov chain Monte Carlo algorithms.

By utilizing Bayesian philosophy with a focus on quality purposes in RSM, it seems more realistic results might be obtained by comparison with the results of classical regression. Taguchi [12,25] presented a robust design method based on statistical experimental design and quality engineering concepts. This method, along with Taguchi's philosophy, received a great deal of attention, but it seemed to have some statistical shortcomings. Box [2] has criticized Taguchi's method and revealed its shortcomings. Based on his criticism, RSM, first presented by Box and Wilson [3], was popularized in the early 1990s as a tool for improving the quality. Vining and Myers [13,14,15,27] proposed an alternative off-line quality improvement approach (i.e., dual response approach) by combining RSM and the good properties of Taguchi's method. This novel approach to RSM has become popular and is widely quoted in the literature.

There are some studies available related to the Bayesian approach for estimates of response surface model parameters. Steinberg[23] presented a Bayesian approach to empirical regression modeling in which the response function was represented by a power series expansion in Hermite polynomials. Chen[4] used Bayesian hierarchical regression modelling approach to dual response surface. Moreover, Bayesian analysis provides inference about the uncertainty of the model parameters. Chen and Ye[5] applied the Bayesian hierarchical model on dual response surface to partially replicated designs and the performance of the Bayesian model was compared with least squares methods by using simulated data under various mean and variance models. Peterson et al.[20] presented a Bayesian predictive approach to multiresponse optimization experiments. Quesada et al. [24] presented a Bayesian approach and consist of maximizing the posterior predictive probability that the process satisfies a set of constraints on the responses. Türkşen's study [26] was analyzed of response

surface model parameters, which was obtained by using Bayesian approach and fuzzy approach, through interval analysis.

This study aims to apply Bayesian estimation methods to RSM with a focus area of quality improvement. The research will consider various Bayesian estimates and investigate their effects of using a prior model on the mean and variance responses. Different estimators generate different solutions depending on the influence of the selected prior information.

The rest of this paper is organized as follows: In the following section a brief overview of selected Bayesian estimation methods is presented. An estimation process of common regression coefficients of data modeling, linked to a discussed Bayesian estimation method, is put forward in Section 3. The next section illustrates the findings and offers a brief discussion of experimental design, including Bayesian analyses to RSM. Finally, the paper ends with a conclusion.

2. BAYESIAN PARAMETER ESTIMATION

In terms of the Bayesian approach, point estimation of a parameter vector θ is usually the mean of the posterior distribution based on minimization of the following Bayesian conditional risk function:

$$R(\hat{\theta}|\mathbf{y}) = \int_{\theta} C(\hat{\theta}, \theta) f(\theta|\mathbf{y}) d\theta \quad (2.1)$$

where $C(\hat{\theta}, \theta)$ is the cost function and $f(\theta|\mathbf{y})$ is the posterior density of θ , given an observation vector \mathbf{y} . More methods to find Bayesian estimators will be presented. The reader is referred to Vaseghi (2000) for details.

2.1. Maximum a posteriori estimation (MAP)

The MAP method is based on maximization of the posterior distribution. According to this method, the cost function is assumed to be uniformly distributed, defined as,

$$C(\hat{\theta}, \theta) = 1 - \delta(\hat{\theta}, \theta) \quad (2.2)$$

where $\delta(\hat{\theta}, \theta)$ is the Kronecker delta function. Then, the conditional risk function is given by,

$$R(\hat{\theta}|\mathbf{y})_{MAP} = \int_{\theta} (1 - \delta(\hat{\theta}, \theta))f(\theta|\mathbf{y})d\theta \quad (2.3)$$

By using equation (2.3), when the posterior function $f(\theta|\mathbf{y})$ attains a maximum, the minimum Bayesian risk can be achieved (see Figure 2.1 in [28]). Hence, the MAP estimator is given in equation (2.4). Here, the MAP estimator is the mode of the posterior distribution.

$$\hat{\theta}_{MAP} = \operatorname{argmax}_{\theta} f(\theta|\mathbf{y}) = \operatorname{argmax}_{\theta} [f(\mathbf{y}|\theta) f(\theta)] \quad (2.4)$$

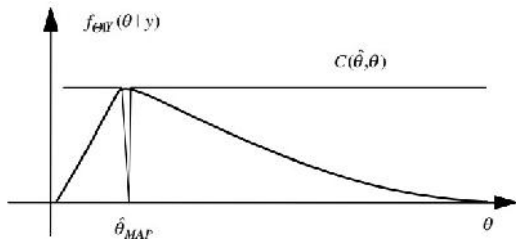


Figure 2.1 The Bayesian cost function for the MAP estimate

2.2. Minimum mean square error estimation (MMSE)

The MMSE method minimizes the mean square error cost function. The conditional risk function is

$$R(\hat{\theta}|\mathbf{y})_{MMSE} = E((\hat{\theta} - \theta)^2|\mathbf{y}) = \int_{\theta} (\hat{\theta} - \theta)^2 f(\theta|\mathbf{y})d\theta \quad (2.5)$$

By minimizing equation (2.5) with respect to parameter θ , the MMSE estimator is obtained as

$$\hat{\theta}_{MMSE} = \int_{\theta} \theta f(\theta|\mathbf{y})d\theta \quad (2.6)$$

Figure 2.2, taken from [28], illustrates the mean square error cost function and the Bayesian estimate:

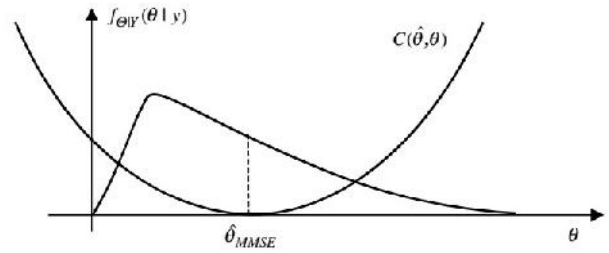


Figure 2.2 Bayesian cost function graph for the MMSE estimate

2.3. Estimation of parameters using MCMC by WinBUGS

As the third estimation strategy, the posterior distribution is obtained by the MCMC method in WinBUGS, which was created in the 1990s as a free software package. WinBUGS uses Gibbs sampling as a special case of the Metropolis-Hastings algorithm.

Let $f(\theta_j | \theta_{\setminus j}, \mathbf{y})$ be the full conditional posterior distribution, where θ is the parameter vector such as $\theta_{\setminus j} = (\theta_1, \dots, \theta_{j-1}, \theta_{j+1}, \dots, \theta_d)^T$ and $\mathbf{y} = (y_1, y_2, \dots, y_n)^T$ be the vector of length n of the response data. For a particular state of the chain $\theta^{(t)}$, the new parameter values have been obtained by Gibbs sampling as follows [19]:

$$\begin{aligned} \theta_1^{(t)} &\sim f(\theta_1 | \theta_2^{(t-1)}, \theta_3^{(t-1)}, \dots, \theta_p^{(t-1)}, \mathbf{y}), \\ \theta_2^{(t)} &\sim f(\theta_2 | \theta_1^{(t)}, \theta_3^{(t-1)}, \dots, \theta_p^{(t-1)}, \mathbf{y}), \\ \theta_3^{(t)} &\sim f(\theta_3 | \theta_1^{(t)}, \theta_2^{(t)}, \dots, \theta_p^{(t-1)}, \mathbf{y}), \\ \theta_p^{(t)} &\sim f(\theta_p | \theta_1^{(t)}, \theta_2^{(t)}, \dots, \theta_{p-1}^{(t)}, \mathbf{y}) \end{aligned}$$

After these generations, the Monte Carlo error might be observable. This error represents the standard error of the estimation made by the Markov chain algorithm. Therefore the iteration continues until this error becomes less than 0.05 (e.g., as small as possible).

3. BAYESIAN ESTIMATION OF REGRESSION MODELS

Bayesian estimation and data modeling constitute a useful method, as it can be used in a wide range of areas, including signal processing, computer vision processes, genome data analysis, and industrial applications.

Regression modeling defines the functional relationship between a dependent random variable and another set of independent variables. Let $\mathbf{y} = (y_1, \dots, y_n)^T$ be the n -dimensional column vector, and let \mathbf{X} be the $n \times p$ matrix whose i^{th} row is x_i . Then the classical regression assumption is

$$\{\mathbf{y}|\mathbf{X}, \boldsymbol{\beta}, \sigma^2\} \sim \text{multivariate normal}(\mathbf{X}\boldsymbol{\beta}, \sigma^2\mathbf{I}) \tag{3.1}$$

where \mathbf{I} and σ^2 are the $p \times p$ identity matrix and variance of the model, respectively. The sampling density of the data, as a function of parameter vector $\boldsymbol{\beta}$, is

$$p\{\mathbf{y}|\mathbf{X}, \boldsymbol{\beta}, \sigma^2\} \propto e^{\{-\frac{1}{2\sigma^2}[\mathbf{y}^T\mathbf{y} - 2\boldsymbol{\beta}^T\mathbf{X}^T\mathbf{y} + \boldsymbol{\beta}^T\mathbf{X}^T\mathbf{X}\boldsymbol{\beta}]\}} \tag{3.2}$$

if $\boldsymbol{\beta} \sim \text{multivariate normal}(\boldsymbol{\beta}_0 = \boldsymbol{\beta}_{\text{prior}}, \boldsymbol{\Sigma}_0 = \boldsymbol{\Sigma}_{\text{prior}})$, then

$$p(\boldsymbol{\beta}|\mathbf{y}, \mathbf{X}, \sigma^2) \propto p(\mathbf{y}|\boldsymbol{\beta}, \mathbf{X}, \sigma^2)p(\boldsymbol{\beta}) = e^{\{\boldsymbol{\beta}^T(\boldsymbol{\Sigma}_0^{-1}\boldsymbol{\beta}_0 + \frac{\mathbf{X}^T\mathbf{y}}{\sigma^2}) - \frac{1}{2}\boldsymbol{\beta}^T(\boldsymbol{\Sigma}_0^{-1} + \frac{\mathbf{X}^T\mathbf{X}}{\sigma^2})\boldsymbol{\beta}\}} \tag{3.3}$$

This result seemed to be proportional to a multivariate normal density, with

$$\boldsymbol{\Sigma}_{MMSE}^* = \text{var}(\boldsymbol{\beta}|\mathbf{y}, \mathbf{X}, \sigma^2) = (\boldsymbol{\Sigma}_0^{-1} + \frac{\mathbf{X}^T\mathbf{X}}{\sigma^2})^{-1} \tag{3.4}$$

and

$$\boldsymbol{\beta}_{MMSE}^* = E(\boldsymbol{\beta}|\mathbf{y}, \mathbf{X}, \sigma^2) = (\boldsymbol{\Sigma}_0^{-1} + \frac{\mathbf{X}^T\mathbf{X}}{\sigma^2})^{-1}(\boldsymbol{\Sigma}_0^{-1}\boldsymbol{\beta}_0 + \mathbf{X}^T\mathbf{y}/\sigma^2) \tag{3.5}$$

$$= \boldsymbol{\Sigma}_{MMSE}^* (\boldsymbol{\Sigma}_{\text{prior}}^{-1}\boldsymbol{\beta}_{\text{prior}} + (\frac{\mathbf{X}^T\mathbf{X}}{\sigma^2})\boldsymbol{\beta}_{\text{classical}})$$

If the elements of the prior precision matrix $\boldsymbol{\Sigma}_0^{-1}$ are small, then the conditional expectation

$E(\boldsymbol{\beta}|\mathbf{y}, \mathbf{X}, \sigma^2)$ is approximately equal to the least squares estimate (known as MMSE). Also, the MAP estimators are defined as follows (see [9]):

$$\boldsymbol{\beta}_{MAP}^* = (\boldsymbol{\Sigma}_{\text{prior}}^{-1}\sigma^2 + \mathbf{X}^T\mathbf{X})^{-1}\mathbf{X}^T\mathbf{X}\boldsymbol{\beta}_{\text{classical}} + (\boldsymbol{\Sigma}_{\text{prior}}^{-1}\sigma^2 + \mathbf{X}^T\mathbf{X})^{-1}\sigma^2\boldsymbol{\Sigma}_{\text{prior}}^{-1}\boldsymbol{\beta}_{\text{prior}} \tag{3.6}$$

and the variance-covariance matrix is

$$\boldsymbol{\Sigma}_{MAP}^* = (\boldsymbol{\Sigma}_{\text{prior}}^{-1}\sigma^2 + \mathbf{X}^T\mathbf{X})^{-1}\mathbf{X}^T\sigma^2((\boldsymbol{\Sigma}_{\text{prior}}^{-1}\sigma^2 + \mathbf{X}^T\mathbf{X})^{-1}\mathbf{X}^T)^T. \tag{3.7}$$

4. BAYESIAN APPROACH TO RESPONSE OPTIMIZATION

Let us consider the experiment discussed in [7],[18]. The study involves three factors, namely $X_1, X_2,$ and X_3 . The goal is to find the combination of factor levels that maximizes the amount (in grams) of crystal growth. Table 4.1 presents the experimental data.

When RSM applies to the experimental setup, the second order estimated response surface is

$$\hat{Y}_{\text{classical}} = 97.58 + 1.36X_2 - 1.49X_3 - 12.06X_2^2 - 9.23X_3^2 \tag{4.1}$$

According to this model, the optimum response is found at $\hat{Y}_{\text{max}} = 97.68$ grams, which is illustrated in Figure 4.1 when the coded variables are $x_2 = 0.05646$ and $x_3 = -0.08097$.

Table 4.1 A central composite design of three variables

Run	x_1	x_2	x_3	y	Run	x_1	x_2	x_3	y
1	-1	-1	-1	66	11	0	-1.682	0	68
2	-1	-1	1	70	12	0	1.682	0	63
3	-1	1	-1	78	13	0	0	-1.682	65
4	-1	1	1	60	14	0	0	1.682	82
5	1	-1	-1	80	15	0	0	0	113
6	1	-1	1	70	16	0	0	0	100
7	1	1	-1	100	17	0	0	0	118
8	1	1	1	75	18	0	0	0	88
9	-1.682	0	0	100	19	0	0	0	100
10	1.682	0	0	80	20	0	0	0	85

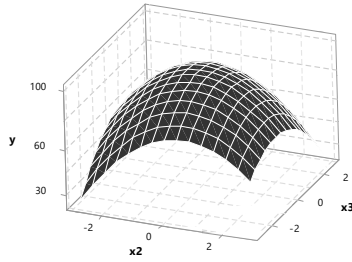


Figure 4.1 Response surface graph of maximum growth

4.1 Bayesian MMSE estimator approach to response optimization

Let the unknown β parameter for the prior distribution of the model be $\beta \sim \text{Normal}(\beta_{\text{prior}}, \Sigma_{\text{prior}})$. Consider different prior means and variances on the parameters. For example the parameters β have a multivariate normal prior distribution as used by Gilmour and Mead [7] with mean $\beta_{\text{prior}} = [100, 0, 0, -6, -6]$ and diagonal variance matrix with each element on the diagonal being 10. For illustration $\sigma^2 = 1$ was assumed [7]. Another assumption for mean $\beta_{\text{prior}} = [110, 0, 0, -6, -6]$ and diagonal variance matrix with each element on the diagonal being 1 also $\sigma^2 = 158,7$ was assumed. These assumptions were used in combination with each other. Also, the classical coefficient vector from the classical regression is given as $\beta_{\text{classical}}$. In Bayesian MMSE, the expected value model of the posterior distribution can be found by using equation (3.5), as follows:

$$\beta_{\text{MMSE}}^* = \begin{bmatrix} 97.56355 \\ 1.35119 \\ -1.48318 \\ -12.02238 \\ -9.21221 \end{bmatrix}$$

and using equation (3.4),

$$\Sigma_{\text{MMSE}}^* = \begin{bmatrix} 0.11793 & 0 & 0 & -0.05016 & -0.05016 \\ 0 & 0.07268 & 0 & 0 & 0 \\ 0 & 0 & 0.07268 & 0 & 0 \\ -0.05016 & 0 & 0 & 0.06795 & 0.00587 \\ -0.05016 & 0 & 0 & 0.00587 & 0.06795 \end{bmatrix}$$

Using these results, the optimum response is found to be $\hat{Y}_{\text{max}} = 97.66$ grams when the coded variables are $x_2 = 0.05619$, and $x_3 = -0.08050$.

However, if one uses the classical regression estimator $\sigma^2 = 158.7$ rather than $\sigma^2 = 1$ in the MMSE estimation process, the optimum response becomes $\hat{Y}_{\text{max}} = 97.48$ with $x_2 = 0.03221$, and $x_3 = -0.04136$.

4.2 Bayesian MAP estimator approach to response optimization

Second, consider the MAP estimator. For instance, the prior information is chosen as $\beta'_{\text{prior}} = [110, 0, 0, -6, -6]$ and the classical variance estimator is $\sigma^2 = 158.7$. The other assumptions mentioned in the previous section are applied for this estimator and the results are given in the final summary Table 4.3. In Bayesian MAP, by using the given prior information, the expected value model of the posterior distribution can be found by using equation (3.6), as follows:

$$\beta_{\text{MAP}}^* = \begin{bmatrix} 108.12898 \\ 0.10830 \\ -0.11888 \\ -7.66978 \\ -7.40964 \end{bmatrix} \quad \text{and using equation (3.7),}$$

$$\Sigma_{\text{MAP}}^* = \begin{bmatrix} 0.08364 & 0 & 0 & 0.04764 & 0.04764 \\ 0 & 0.07324 & 0 & 0 & 0 \\ 0 & 0 & 0.07324 & 0 & 0 \\ -0.04764 & 0 & 0 & 0.10452 & 0.02099 \\ -0.04764 & 0 & 0 & 0.02099 & 0.10452 \end{bmatrix}$$

Using these results, the optimum response is found as $\hat{Y}_{\text{max}} = 108.13$ grams when the coded variables are $x_2 = 0.00706$, and $x_3 = -0.00802$.

4.3 Using MCMC by WinBUGS approach to response optimization

Finally, by using WinBUGS for the in prior informations. For instance $\beta_{\text{prior}} = [110, 0, 0, -6, -6]$ and $\sigma^2 = 158.7$; the WinBUGS output is presented in Table 4.2. The other assumptions mentioned in section 4.1 are applied for this problem and the results are given in the final summary Table 4.3. Examining the model parameters in the output, the autocorrelation is a way of measuring the independence of the simulated values. According to Figure 4.2, no autocorrelation exists for the model parameters.

Table 4.2 Posterior summaries of the regression parameters

node	mean	sd	MC error	2.5%	median	97.5%	start	sample
beta1	173.1	2.361	0.04592	58.81	173.1	107.8	1001	5000
beta2	-3.043	2.206	0.04354	-9.847	-3.043	4.811	1001	5000
beta3	-11.35	2.137	0.04305	-15.53	-11.35	-7.145	1001	5000
beta4	-13.03	2.161	0.04004	-14.21	-13.03	-8.742	1001	5000

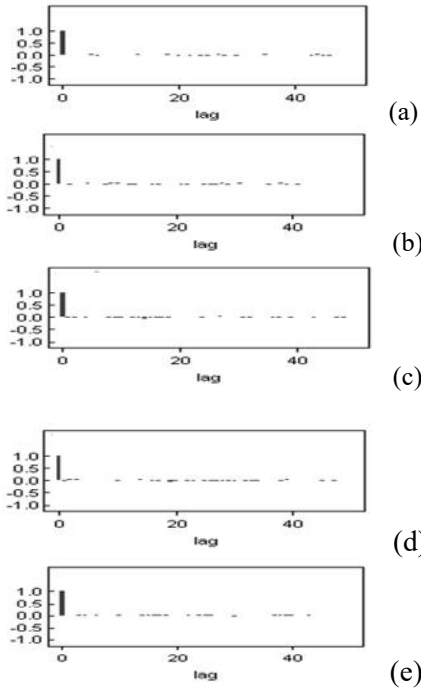


Figure 4.2 Plots for the autocorrelation functions of the chains: (a) β_0 , (b) β_1 , (c) β_2 , (d) β_3 , (e) β_4

Using these Bayesian regression coefficients obtained by WinBUGS, the optimum response is found as $\hat{Y}_{max} = 103.12$ grams when the coded variables are $x_2 = 0.02731$, and $x_3 = -0.03230$.

The output in Figure 4.3 gives a trace of the actual values of the chain and information about simulation convergences. It seems the Markov chain quickly converges to the final distribution. Also, according to the Kernel density plots with 3000 sample sizes in Figure 4.4, one realizes that the posterior distributions of the parameters are close to the normal density.

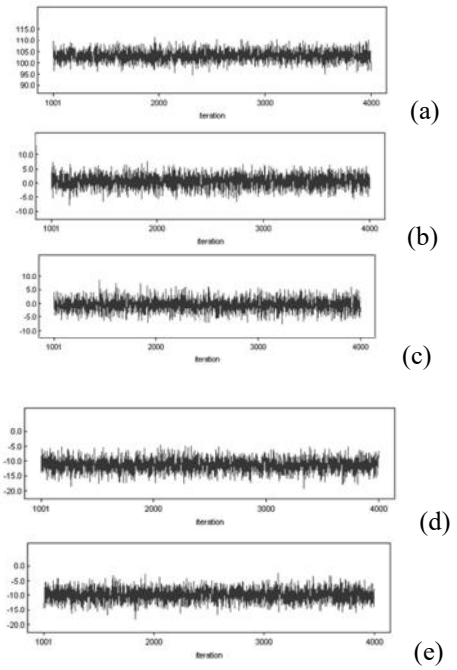


Figure 4.3 Convergence plots for the parameter chains: (a) β_0 , (b) β_1 , (c) β_2 , (d) β_3 , (e) β_4

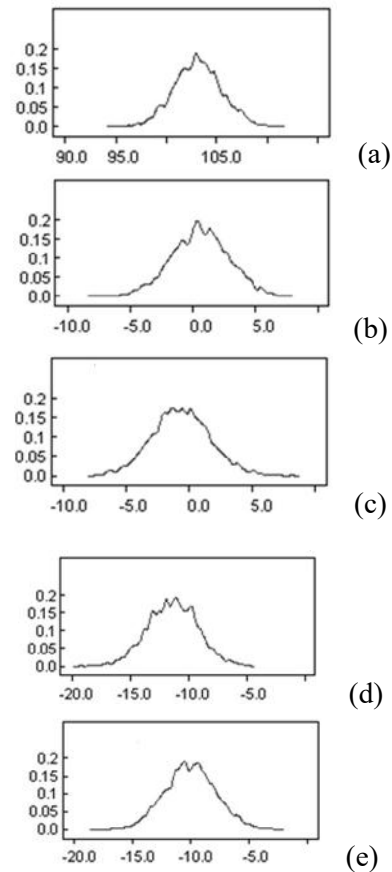


Figure 4.4 Plots for the posterior pdfs of the parameter chains: (a) β_0 , (b) β_1 , (c) β_2 , (d) β_3 , (e) β_4

4.4. Final summary

The summary results about the mean and the variance of posterior distributions and the optimum response values based on different prior information are given in Table 4.3

Table 4.3. Optimum response values for different prior information and different variance

Prior Expectation	Prior Variance Σ_{prior} (diagonal)	Variance	Bayesian Regression with RSM			
			Response (MMSE)	Response(MA P)	Response (WinBUGS)	
$\beta_{prior} = [100, 0, 0, -6, -6]$	1	$\sigma^2 = 158.7$	99.16	99.16	99.14	
	10		97.48	97.48	97.5	
$\beta_{prior} = [110, 0, 0, -6, -6]$	1		108.14	108.14	108.1	
	10		103.10	103.13	103.12	
$\beta_{prior} = [100, 0, 0, -6, -6]$	1		$\sigma^2 = 1$	97.52	97.52	97.52
	10			97.66	97.66	97.66
$\beta_{prior} = [110, 0, 0, -6, -6]$	1	98.55		98.55	98.54	
	10	97.78		97.78	97.78	

5. CONCLUSION

In this article, the application of Bayesian methods to RSM is studied. Bayesian regression estimators are obtained by using various priors and two different variance assumptions (see Table 4.3). These estimators are utilized as Bayesian regression estimators and their posterior information is revealed. Then, RSM is applied to such posterior information and a comparison is made between these emerging results and the results obtained by classical RSM.

According to the comparison results, where the situations of the prior variance (Σ_{prior} diagonal) are smaller, then the estimated Bayesian responses are generally bigger than the classical responses. However, the higher prior expected value (β_{prior}) assigns, the higher estimated Bayesian responses compared with the classical method. In other words, the prior information must be chosen carefully, otherwise this leads to

different solutions rather than the one obtained by the classical response surface method.

REFERENCES

- [1] T. Bayes, "An essay towards solving a problem in the doctrine of chances", R soc Lond Philos Trans., vol.5, no.3, pp. 370–418, 1763.
- [2] G.E.P. Box, " Discussion of 'off-Line quality control, parameter design, and the Taguchi method by R.N. Kacker", Journal of Quality Technology, vol.17, pp. 189-190, 1985.
- [3] G.E.P. Box and K.B. Wilson, "On the experimental attainment of optimum conditions", Journal of the Royal Statistical Society, vol.13, no.B ,pp. 1-45, 1951.
- [4] Y. Chen, "Bayesian Hierarchical Modelling of Dual Response Surfaces" , Ph.D. thesis , Virginia Polytechnic Institute and State University, 2005
- [5] Y. Chen and K. Ye, "Bayesian Hierarchical Modeling on Dual Response Surfaces in Partially Replicated Designs", Quality Technology & Quantitative Management, vol.6, No.4, pp.371-389, 2009
- [6] M. Goldstein, "Bayesian analysis of regression problems", Biometrika, vol. 63, no.1, pp. 51-58, 1976.
- [7] S.G. Gilmour and R. Mead, "A Bayesian design criterion for locating the optimum point on a response surface", Statistics & Probability Letters vol.64, no.3, pp. 235-242, 2003.
- [8] W.K. Hasting, "Monte Carlo sampling methods using Markov chains and their applications", Biometrika vol.57, no.1, pp. 97-109, 1970.
- [9] P.D Hoff., "A First Course in Bayesian Statistical Methods", Springer, New York, 2009.

- [10] H. Jeffreys, "Theory of Probability", The Clarendon Press, Oxford, 1939.
- [11] J.M. Keynes, "A Treatise on Probability", St Martin's, London, 1921.
- [12] O.Köksoy ve F.Z. Muluk, "Taguchi'nin Tasarım ve Analizlerine Eleştiriler", I. Ulusal Kalite Fonksiyon Göçerimi Sempozyumu, Nisan, İzmir, 2002
- [13] O. Köksoy, and N. Doganaksoy, "Joint Optimization of Mean and Standart deviation in Response Surface Experimentation", Journal of Quality Technology, vol.35, no.3, pp.239-252, 2003
- [14] O.Köksoy, ve F.Z. Muluk, "Solution to the Taguchi's Problem with Correlated Responses, Gazi University Journal of Science, vol.27, no.1, pp.59-70, 2004
- [15] O. Köksoy and S.S Fan, 2012, "An Upside-down Normal Loss Function-based Method for Quality Improvement", Engineering Optimization, vol.44, no.8, pp.935-945, 2012
- [16] P.S Laplace, "Memoir on the probability of causes of events", Mémoires de Mathématique et de Physique, Tome Sixième, English translation by S. M. Stigler 1986, Statist. Sci. vol.1, no.19, pp. 364–378, 1774.
- [17] N. Metropolis, A.W. Rosenbluth, M.N. Rosenbluth, A.H.Teller and E. Teller , "Equation of state calculations by fast computing machines," Journal of Chemical Physics, vol.21, no.6, pp. 1087-1092,1953.
- [18] D.C Montgomery, "Design and Analysis of Experiments (5th edition)", John Willey & Sons, New York, 2001.
- [19] I.Ntzoufras, "Bayesian Modeling Using WinBUGS", John Wiley & Sons, New Jersey, 2009.
- [20] J. J. Peterson, G.M. Quesada and E.Castillo, " A Bayesian Reliability Approach to Multiple Response Optimization with Seemingly Unrelated Regression Models", Quality Technology & Quantitative Management, vol.6, No.4, pp.353-369, 2009
- [21] F.P. Ramsey, "Truth and probability (1926), in Ramsey, F.P",. The Foundations of Mathematics and Other Logical Essays, Harcourt, Brace and Company, New York, pp. 156-198,1931.
- [22] L.J. Savage, "The theory of statistical decision", Journal of the American Statistical Association, vol. 46,pp. 55–67,1951.
- [23] D. M. Steinberg, "A Bayesian Approach to Flexible Modeling of Multivariate Response Functions", Journal of Multivariate Analysis, vol.34, pp.157-172 , 1990
- [24] G.M. Quesada, E. Castillo and J.J Peterson, "A Bayesian Reliability Approach to Multiple Response Optimization in the Presence of Noise Variables", Journal of Applied Statistics, vol.31, no.3, pp.251-270, 2004.
- [25] G.Taguchi , "System of Experimental Design: Engineering Methods to Optimize Quality and Minimize Cost", White Plains, New York, 1987.
- [26] Ö. Türkşen, "Analysis of Response Surface Model Parameters with Bayesian Approach and fuzzy Approach",International Journal of Uncertainty, Fuzziness and Knowledge-Based Systems, vol.24 no.1, pp.109-122, 2016.
- [27] G.G Vining and R.H. Myers, "Combining Taguchi and response surface philosophies: A dual response approach", Journal of Quality Technology vol.22,no.1, pp. 38-45,1990.
- [28] S.Vaseghi, "Advanced Digital Signal Processing and Noise Reduction", John Wiley & Sons, New York, 2000.

JOURNAL OF SCIENCE



SAKARYA UNIVERSITY

Sakarya University Journal of Science

ISSN 1301-4048 | e-ISSN 2147-835X | Period Bimonthly | Founded: 1997 | Publisher Sakarya University |
<http://www.saujs.sakarya.edu.tr/>

Title: Experimental And Statistical Investigation of Surface Roughness in Turning of
A1S1 4140 Steel

Authors: Harun Akkuş

Received: 2018-11-30 15:12:02

Accepted: 2019-03-20 09:42:41

Article Type: Research Article

Volume: 23

Issue: 5

Month: October

Year: 2019

Pages: 775-781

How to cite

Harun Akkuş; (2019), Experimental And Statistical Investigation of Surface
Roughness in Turning of A1S1 4140 Steel. Sakarya University Journal of Science,
23(5), 775-781, DOI: 10.16984/saufenbilder.490668

Access link

<http://www.saujs.sakarya.edu.tr/issue/44066/490668>

New submission to SAUJS

<http://dergipark.gov.tr/journal/1115/submission/start>

Experimental and Statistical Investigation of Ra in Turning of AISI 4140

Harun AKKUŞ*¹

Abstract

In this study, 48 HRC hardness AISI 4140 is turned on in different cutting parameters and cooling environment. The Taguchi L₉ test design was developed based on the three-level cutting speed (V), feed rate (f), depth of cut (a) and cooling environment parameters. According to the L₉ experimental design, the mean surface roughness (Ra) values were measured. Chip form occurring during turning is photographed. The S/N (Signal/Noise) ratios of the Taguchi experiment design in the Minitab program have been determined. According to the experimental results, the most significant effect on the Ra from the four factors was found in the hand made by the depth of cut. In ANOVA, it was respectively determined that depth of cut, cutting speed, feed rate and cooling environment affected 95% confidence in Ra value. It has been found that the repeat experiments for the optimum parameters yielded about 90% accuracy compared to the Taguchi estimate.

Keywords: AISI 4140, turning, surface roughness, chip formation, optimization

1. INTRODUCTION

Recently, improvements in the resulting cutting insert and machine tools has enabled the material to be processed to form hardened. The production of the material in the hardened state provides the following advantages; reduction in processing time, reduction in the number of machine tools required, reduction in processing costs, better surface quality, reduction in finish operations, removal of degradation caused by heat treatment, production of complex parts, etc. [1,2]

The goal in machining is to bring a workpiece to the desired geometry and to provide the desired surface qualities in the workpiece [3]. To create this geometry, the production engineer must determine factors such as the appropriate material, tool, cooling environment, cutting parameters, and looms. An important part of

machining is turning. The turning operation is a cylindrical shaping operation designed to take up a piece of material through a rotating material. Today, there are different studies about turning [4,5]. Surface roughness, tool wear, vibration, acoustic emission, force values resulting from turning are the main issues of today's articles [6-9]. These values are studied experimentally, simulated and statistically [10,11].

Taguchi optimization method, presently the most commonly preferred method optimization. Taguchi method; with a low-cost development cycle, aims to improve product performance in system and process design. This method is an experimental and analytical approach that determines the most efficient parameters on total performance. The Taguchi method provides a design that covers the whole process with a few experiments [12-15]. This saves time and money.

* Corresponding Author: harunakkus@windowslive.com (ORCID Number: 0000-0002-9033-309X)

¹ Automotive Technology Program, Technical Sciences Vocational School, Amasya University, Amasya, Turkey

One of the important parameters in machining is surface quality [16]. Surface roughness is considerably influential on piston-cylinder mechanisms, bearings, gears et al. [17]. Surface texture is used as an effective factor in machining. Surface roughness or texture is the most commonly used quality indicator [18]. Experimental, statistical, artificial intelligence methods and surface topography of surface roughness have been studied in many studies [19,20]. The factors affecting the surface roughness are cutting speed, feed rate, depth of cut, cooling medium, material hardness, material type, tool tip, ambient temperature, humidity etc. [21]. The common aim of these studies is to obtain the optimum surface roughness and determine the best parameters for the factors affecting surface roughness. The two most important parameters affecting the roughness of the surface are the feed rate and insert geometry [22-24].

In this study, the Ra values of the AISI 4140 steel were measured and the chip formation were photographed. Taguchi L₉ orthogonal array is used as experimental design. Obtained surface roughness values were determined by Taguchi analysis. Estimated by the constructed Taguchi model and experimentally investigated for accuracy.

2. EXPERIMENTAL DESIGN

In this study AISI 4140 workpiece material was used. AISI4140 is steel which used to crankshaft, crank arms, axle shaft and sleeve, automobile and aircraft construction, gear and wheel making, on construction and agricultural machinery, on machine tools, such as bolts, nuts and studs, high strength steel suitable for surface hardening. The residue on the surface of the test material was cleaned before the heat treatment was applied. The material was heated at 700 °C for one hour and then cooled to air and normalization was applied. It was then heated to 830 °C and cooled in oil for one hour. BMS Digirock RSR hardness tester was measured at an average of 48 HRC.

For the experiments, the steel material was cut at Ø80x180 mm. Dimension differences and surface layer on the surface of the material after heat treatment have been removed on the lath.

Experiments were carried out on the ACE Micromatic Designers LT-20C lathe counter at the Amasya University Machine Laboratory. In the experiments Sandvik DDJNR 2525M 15 tool holder, Sandvik DNMG 15 06 08-PM 4325 insert was used. The

processing distance is 100 mm. Figure 1 shows the lathe, tool holder and insert used in the experiments.



Figure 1. Test sample in the lathe, inserts and tool holder

Three different cutting parameters (V - f - a) and cooling environment were determined. The cutting parameters was determined according to the manufacturers catalog. The cooling environment is also defined as three parameters: dry, liquid and air. These cut-off parameters and the cooling environment are given in Table 1. In the 32 °C temperature of the dry cutting environment, the liquid environment was cooled by the counter's own coolant pump with 50 lpm of spray amount and with boron oil mixed water and for the air environment compressed air is used at a pressure of 15 bar with a 200 liter capacity air compressor.

Table 1. Cutting parameters

Parameters	Units	Level 1	Level 2	Level 3
V	m/min.	300	345	390
f	mm/rev.	0,15	0,30	0,45
a	mm	1	3	5
Cooling environment	-	Dry	Air	Liquid

Taguchi L₉ orthogonal array was created by Minitab statistical program. Taguchi is profitable in terms of cost and time. Ra values were measured with Mitutoyo SJ-210 surface roughness tester.

The experiments were performed as seven replicates. Ra values were averaged. Since the blade used in this study has four corners, the cutting edge is used differently in each process. Table 2 shows the experimental list generated by the L₉ test design and the average Ra values obtained.

3. RESULTS

3.1. Evaluating Results with Taguchi

Optimum cutting conditions for Ra were determined by choosing the smaller-the-better S/N ratio in the

Taguchi optimization method. S / N ratios, level values calculated. The obtained S / N ratios are given in Table 2.

Table 2. Ra values and S/N ratios.

Case no	V (m/min)	f (mm/rev)	a (mm)	Cooling enviroment	Ra (μm)	S/N
1	300	0,15	1	Dry	0,74	2,6154
2	300	0,30	3	Air	3,25	-10,2377
3	300	0,45	5	Liquid	5,74	-15,1782
4	345	0,15	3	Liquid	4,92	-13,8393
5	345	0,30	5	Dry	4,38	-12,8295
6	345	0,45	1	Air	4,49	-13,0449
7	390	0,15	5	Air	5,67	-15,0717
8	390	0,30	1	Liquid	3,53	-10,9555
9	390	0,45	3	Dry	7,27	-17,2307

The most important criterion used in the Taguchi method is the S / N ratio. The optimum cutting conditions were determined according to the point where the S / N ratio was the maximum. According to this method, in Table 2, in the orthogonal array L₉, the optimum cutting parameters were obtained as Ra of 2,6154 S/N for Ra.

The optimum surface roughness value will be reached in first level for V , first level for f , first level for a and first level for cutting environment. The level values given in Table 3 of Figure 2 are given graphically. After this, the optimum cutting conditions of the experiments to be carried out under the same conditions can be determined and interpreted according to the level values of the cutting speed, feed rate, depth of cut and cooling environment factors specified in Table 3 and Figure 2.

In this case, the first level of the V factor, the first level of the f factor, the first level of the a factor and the first level of the cooling environment are shown in Figure 2 and Table 3. Therefore, the optimum cutting conditions determined under the same conditions for the experiments to be performed will be 300 m/min for V , 0,15 mm/rev for f , 1 mm of a and dry cooling environment. In Table 3, the order of effect of the cutting parameters on the surface roughness is obtained as a , V , f and cooling environment.

Table 3. The order of importance of the parameters for Ra

Level	V	f	a	Cooling enviroment
1	-7,6	-8,765	-7,128	-9,148
2	-13,238	-11,341	-13,769	-12,785
3	-14,419	-15,151	-14,36	-13,324
Delta	6,819	6,386	7,231	4,176
Rank	2	3	1	4

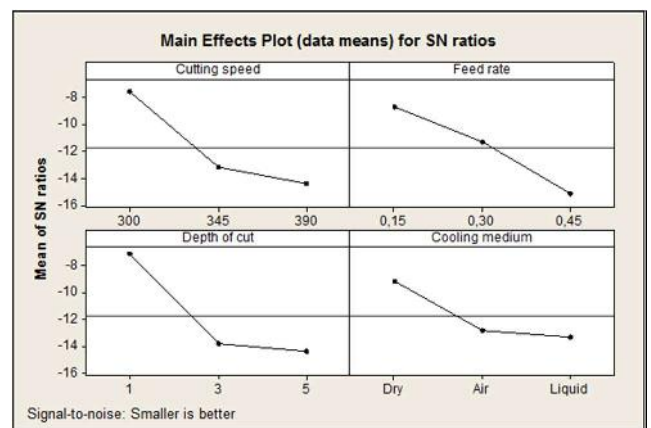


Figure 2. Data means for S/N ratios

While the optimum cutting conditions were determined from the S/N ratio obtained by Taguchi method, the relationship between the cutting parameters and the variance analysis was determined. The relationship between S/N- V , f , a and cooling environment is evaluated. The S/N ANOVA analysis results are shown in Table 4-8. According to the results of ANOVA, p

<0.01 or $p < 0,05$ should be at significance level. According to these results, the most meaningful value is depth of cut. a , V and f were effective at 95% confidence level.

Table 4. The interaction S/N – V for Ra

Source	DF	SS	MS	F	P
V	2	7,68	3,84	1,17	0,0318
Error	6	19,71	3,28		
Total	8	27,38			

Table 5. The interaction S/N – f for Ra

Source	DF	SS	MS	F	P
f	2	8,7	4,35	1,4	0,0373
Error	6	18,68	3,11		
Total	8	27,38			

Table 6. The interaction S/N – a for Ra

Source	DF	SS	MS	F	P
a	2	10,46	5,23	1,86	0,0236
Error	6	16,92	2,82		
Total	8	27,38			

Table 7. The interaction S/N – cooling medium for Ra

Source	DF	SS	MS	F	P
Cooling environment	2	0,54	0,27	0,06	0,0942
Error	6	26,84	4,47		
Total	8	27,38			

Taguchi aims to reduce the number of experimental design experiments and to arrive at the correct result in a short time. The prediction experiments conducted in this study were conducted to prove the closeness of the Taguchi estimate, which was not considered time and cost. At the end of the Taguchi analysis, estimates for the levels given in Table 8 were performed. In Table 8 show that Taguchi's estimate, test result and the absolute error between these results is given as a percentage. In the light of these results, Taguchi realized the prediction with about 90% accuracy of the experimental results.

Table 8. Estimate and experimental test results so absolute error

V	f	a	Cooling environment	Experiment Ra	Taguchi Ra	Absolute difference	Absolute error %
300	0,15	5	Dry	2,814	3,083	0,269	9,559
345	0,3	3	Air	4,198	4,603	0,405	9,647
390	0,45	1	Liquid	6,195	5,643	0,552	8,910

3.2. Turning Result Occurring Chip Structures

In Fig. 3, sawdust structures are shown in the experiments. According to the test design, the chip forms obtained in the processes are evaluated according to ISO 3685. Table 10 gives the names of the chip structures that have been formed. According to the

results obtained by Debnath et al. (2016), tool wear and chip structure are directly related to each other. They found that cutting speed (43,1%), depth of cut (35,8%), cooling medium (13,7%) and advance (7,2%) effect on tool wear were obtained. As the depth of cut increases, Arc chips-loose chips form. In the processes performed in liquid air and air-cooled environment, fracture occurs in the chip formation due to pressure effect.

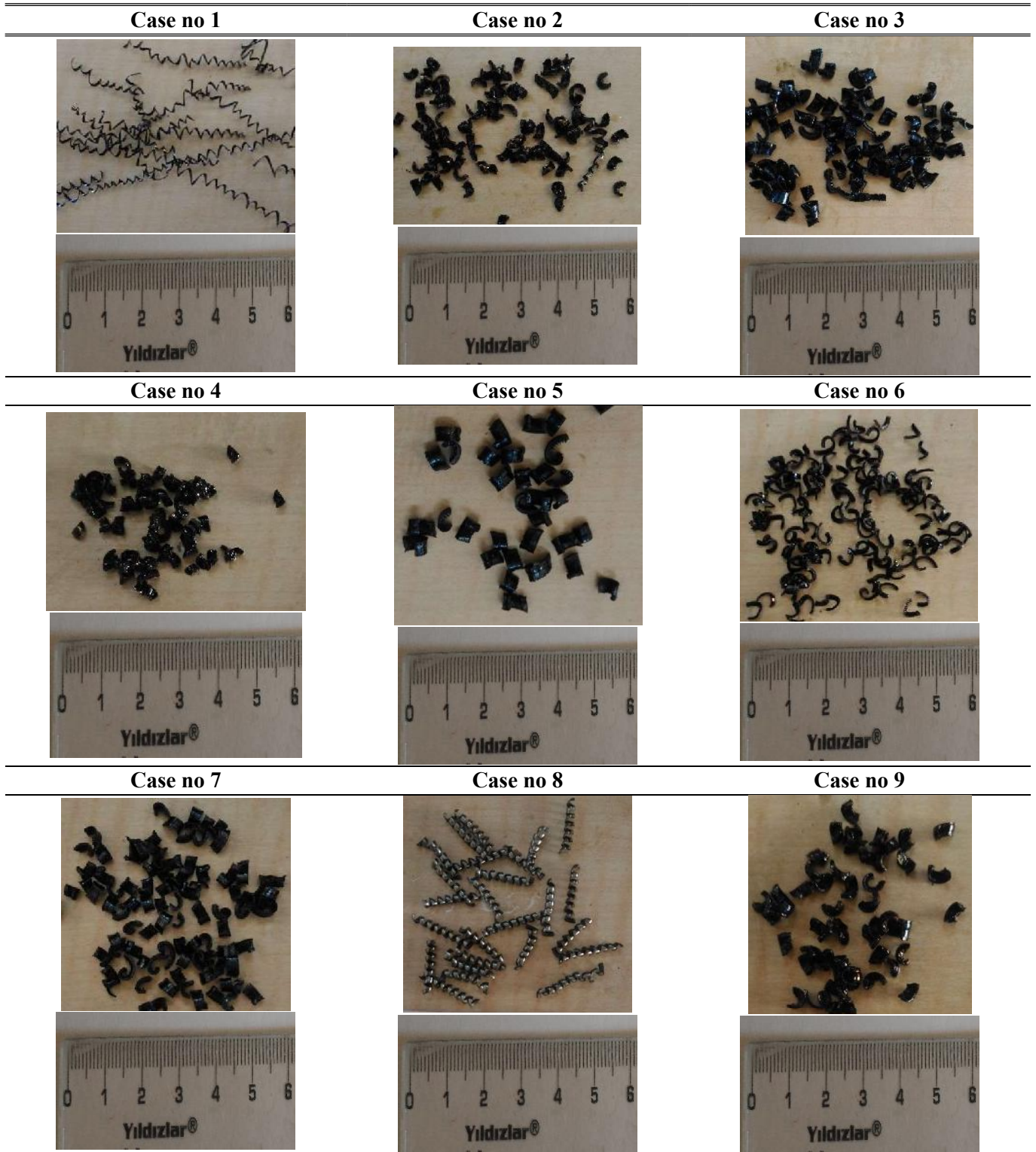


Figure 3. Photographs of chip formation from experiments

Table 9. Chip formation according to ISO 3685

Case number	V (m/min.)	f (mm/rev.)	a (mm)	Cooling enviroment	ISO 3685 chip formation
1	300	0,15	1	Dry	Tubular chips-Long
2	300	0,30	3	Air	Arc chips-Loose
3	300	0,45	5	Liquid	Arc chips-Loose
4	345	0,15	3	Liquid	Arc chips-Loose
5	345	0,30	5	Dry	Arc chips-Loose
6	345	0,45	1	Air	Arc chips-Connected
7	390	0,15	5	Air	Tubular chips-Short
8	390	0,30	1	Liquid	Arc chips-Loose
9	390	0,45	3	Dry	Arc chips-Loose

4. CONCLUSIONS AND RECOMMENDATIONS

In this study, the turning operation was performed using the Taguchi experiment design to determine the optimum cutting parameters for Ra values.

L_9 orthogonal array was obtained by using Taguchi method in MINITAB statistical packet program for three levels of V , f , a and cooling medium as independent variables. In this case, 9 experiments were performed instead of 81 experiments with full factorial design. Experiments performed on the orthogonal array L_9 yielded the S/N of the final Ra. Using the smaller-the-better equation, the maximum value of S/N was searched. Optimum cutting parameters are obtained with maximum S/N ratio. The lowest surface roughness value in the turning operation was obtained at a V of 300 m / min., f of 0,15 mm/rev., a 1 mm and a dry cutting environment corresponding to the 2,6154 S/N.

By applying ANOVA to the S/N ratios, the relationship levels of the cutting parameters over the Ra were obtained. According to the ANOVA analysis, it was concluded that the determined factors (V - f - a -cooling medium) had a 95% confidence level. The most effective parameter from the cutting conditions was the depth of the cut.

Taguchi estimation and the experimental result shows that the design with Taguchi is about 90% accurate.

In future studies, different materials, different tips, different processing methods, different cooling liquids, different hardness values can be used in experiments. Wear, force, vibration, acoustic emission can be measured. Different statistical methods and models can be used.

5. REFERENCES

- [1] Z. Hessainia, A. Belbah, M.A. Yallese, T. Mabrouki, J. F. Rigal, "On the prediction of surface roughness in the hard turning based on cutting parameters and tool vibrations", *Measurement*, 46(5), 1671-1681, 2013
- [2] M. Mia, N.R. Dhar, "Prediction of surface roughness in hard turning under high pressure coolant using artificial neural network", *Measurement*, 92, 464-474, 2016
- [3] Y. Yamane, T. Ryutaro, S. Tadanori, I.M. Ramirez, Y. Keiji, "A new quantitative evaluation for characteristic of surface roughness in turning", *Precision Engineering*, 50, 20-26, 2017
- [4] G.S. Ahmed, S.S. H. Quadri, M. S. Mohiuddin, "Optimization of feed and radial force in turning process by using Taguchi design approach", *Materials Today: Proceedings*, 2(4-5), 3277-328, 2015
- [5] D. Deepak, B. Rajendra, "Optimization of Machining Parameters for Turning of Al6061 using Robust Design Principle to minimize the surface roughness", *Procedia Technology*, 24, 372-378, 2016
- [6] D.M. D'Addona, S.J. Raykar, "Analysis of surface roughness in hard turning using wiper insert geometry", *Procedia CIRP*, 41, 841-846, 2016
- [7] E.G. Plaza, P.N. López, "Application of the wavelet packet transform to vibration signals for surface roughness monitoring in CNC turning operations", *Mechanical Systems and Signal Processing*, 98, 902-919, 2018
- [8] X. Yue, M. Xu, W. Du, C. Chu, "Effect of cutting edge radius on surface roughness in

- diamond tool turning of transparent MgAl₂O₄ spinel ceramic”, *Optical Materials*, 71, 129-135, 2017
- [9] S. Debnath, M.M. Reddy, Q.S. Yi, “Influence of cutting fluid conditions and cutting parameters on surface roughness and tool wear in turning process using Taguchi method”, *Measurement*, 78, 111-119, 2016
- [10] S. Ramesh, L. Karunamoorthy, K. Palanikumar, “Measurement and analysis of surface roughness in turning of aerospace titanium alloy (gr5)”, *Measurement*, 45(5), 1266-1276, 2012
- [11] P. Zhang, Z. Liu, “Modeling and prediction for 3D surface topography in finish turning with conventional and wiper inserts”, *Measurement*, 94, 37-45, 2016
- [12] İ. Asiltürk, H. Akkuş, “Determining the effect of cutting parameters on surface roughness in hard turning using the Taguchi method”, *Measurement*, 44(9), 1697-1704, 2011
- [13] Agrawal, S. Goel, W.B. Rashid, M. Price, “Prediction of surface roughness during hard turning of AISI 4340 steel (69 HRC), *Applied Soft Computing*, 30, 279-286, 2015
- [14] M. Nalbant, H. Gökkaya, G. Sur, “Application of Taguchi method in the optimization of cutting parameters for surface roughness in turning”, *Materials & Design*, 28 (4), 1379-1385, 2007
- [15] İ. Tekaüt, M. Günay, U. Şeker, “Optimization of cutting parameters and chip breaker form by Taguchi method in turning operations”, *6th International Advanced Technologies Symposium*, 127-131, 2011
- [16] Torres, I. Puertas, C.J. Luis, “Surface roughness analysis on the dry turning of an Al-Cu alloy”, *Procedia engineering*, 132, 537-544, 2015
- [17] T. Asakura, “Surface roughness measurement”, *Speckle metrology*, 11-49, 1978
- [18] M. Tomov, M. Kuzinovski, P. Cichosz, “Modeling and prediction of surface roughness profile in longitudinal turning”, *Journal of Manufacturing Processes*, 24, 231-255, 2016
- [19] J. Chen, Q. Zhao, “A model for predicting surface roughness in single-point diamond turning”, *Measurement*, 69, 20-30, 2015
- [20] T. Mikołajczyk, K. Nowicki, A. Bustillo, D.Y. Pimenov, “Predicting tool life in turning operations using neural networks and image processing”, *Mechanical Systems and Signal Processing*, 104, 503-513, 2018
- [21] G.M.A. Acayaba, P.M. Escalona, “Prediction of surface roughness in low speed turning of AISI316 austenitic stainless steel”, *CIRP Journal of Manufacturing Science and Technology*, 11, 62-67, 2015
- [22] J.C. Pereira, R.G. Ruiz, “Influencia de los parámetros de corte y geometría de la herramienta en la rugosidad superficial obtenida en operaciones de torneado del bronce SAE 40”, *Revista Ingeniería*, 14(3), 77-85, 2007
- [23] S. Chandraker, “Taguchi analysis on cutting force and surface roughness in turning MDN350 steel”, *Materials Today: Proceedings*, 2(4-5), 3388-3393, 2015
- [24] C.L. He, W.J. Zong, Z.M. Cao, T. Sun, “Theoretical and empirical coupled modeling on the surface roughness in diamond turning” *Materials & Design*, 82, 216-222, 2015

JOURNAL OF SCIENCE



SAKARYA UNIVERSITY

Sakarya University Journal of Science

ISSN 1301-4048 | e-ISSN 2147-835X | Period Bimonthly | Founded: 1997 | Publisher Sakarya University |
<http://www.saujs.sakarya.edu.tr/>

Title: Landslide Susceptibility Assessment Using Skyline Operator And Majority Voting

Authors: Alev Mutlu, Furkan Goz, Kubra Koksal, Arzu Erener

Received: 2018-11-07 13:04:26

Accepted: 2019-03-20 10:44:41

Article Type: Research Article

Volume: 23

Issue: 5

Month: October

Year: 2019

Pages: 782-787

How to cite

Alev Mutlu, Furkan Goz, Kubra Koksal, Arzu Erener; (2019), Landslide Susceptibility Assessment Using Skyline Operator And Majority Voting. Sakarya University Journal of Science, 23(5), 782-787, DOI: 10.16984/saufenbilder.479801

Access link

<http://www.saujs.sakarya.edu.tr/issue/44066/479801>

New submission to SAUJS

<http://dergipark.gov.tr/journal/1115/submission/start>

Landslide Susceptibility Assessment using Skyline Operator and Majority Voting

Alev Mutlu^{*1}, Furkan Goz², Kubra Koksal³, Arzu Erener⁴

ABSTRACT

Landslide susceptibility assessment is the problem of determining the likelihood of a landslide to occur in a particular area based on the geological and morphological properties of the area. In this study, we propose a method wherein skyline operator is used to model landslides and majority voting is used to assess landslide susceptibility. Experiments conducted on a real life data set showed that the proposed method achieves 83.07% classification accuracy and is superior over most commonly used techniques for landslide susceptibility assessment such as logistic regression, support vector machines and artificial neural network.

Keywords: Landslide Susceptibility Assessment, Majority Voting, Skyline Operator

1. INTRODUCTION

Modeling and assessing natural hazards is a challenging and active research problem. Studies regarding natural hazards such as earthquakes [1,2], floods [3,4], and volcanic activities [5,6] have been proposed. In this study, we focus on landslides and propose a landslide modeling and landslide susceptibility assessment method based on the skyline operator and majority voting principle.

Landslide is a natural phenomenon defined as the outward and downward movement of soil making materials. According to UN Office for Disaster Risk Reduction, landslides are among the top five most frequent natural hazards and caused some 130000 deaths and US\$ 50 billion economic loss [7]. Landslide susceptibility assessment is the problem of determining the likelihood of a landslide to occur in a particular area based on morphological and geological properties of the area [8]. In literature, there exist numerous studies regarding landslide susceptibility assessment. However, these studies mainly differ by means of study area rather than the underlying

landslide modeling and susceptibility assessment techniques. Bivariate and multivariate statistical methods, decision trees, support vector machines, and neural networks are among the most frequently applied techniques in landslide susceptibility assessment.

In this study, we propose a hybrid method based on the skyline operator and majority voting principle for landslide susceptibility assessment. Given properties of landslide occurring zones, the skyline operator is utilized to retrieve skyline points that define the minimum values of landslide triggering factors. To assess landslide susceptibility of a zone, a two-step majority voting is implemented. In the first step, properties of a test zone are compared against each skyline point. A skyline point votes *yes* for the test instance if majority of the features of the test instance have greater values than those of the skyline point, otherwise the skyline point votes *no*. In the second step, votes for *yes* and *no* are counted and the final decision is made according to the majority of the votes. The proposed method primarily distinguishes from state-of-the-art methods by the following aspects:

^{1*} Corresponding Author

¹Kocaeli University, Faculty of Engineering, Department of Computer Engineering, alev.mutlu@kocaeli.edu.tr

²Kocaeli University, Faculty of Engineering, Department of Computer Engineering, furkan.goz@kocaeli.edu.tr

³Kocaeli University, Faculty of Engineering, Department of Computer Engineering, 150201172@kocaeli.edu.tr

⁴Kocaeli University, Faculty of Engineering, Department of Geomatic Engineering, arzu.erenner@kocaeli.edu.tr

- It requires only positive data (properties of landslide occurring areas) to model landslides,
- As to our knowledge there is no other study that utilizes skyline operator in landslide susceptibility assessment,
- The method can be categorized as a hybrid rather than an ensemble.

Performance of the proposed method is evaluated on a real life dataset regarding Savsat region of Turkey. Savsat is a landslide intensive area located in the eastern part of Turkey and has been subject to several studies [9–12]. Experimental results based on 10-fold cross validation showed that the proposed method achieves 83.07% accuracy. When compared to the applications of support vector machines, neural networks, and logistic regression on the same dataset, the proposed method achieves higher accuracy and almost the same accuracy results when compared to decision trees.

The rest of the paper is organized as follows. In Section 2, we briefly introduce methods used for landslide susceptibility assessment and introduce the techniques used in this study. In Section 3 we introduce the proposed method. In Section 4 we first describe the study area and later discuss the experimental findings. Section 5 concludes the paper.

2. BACKGROUND

In this section, we first summarize some of the most commonly used techniques for landslide susceptibility assessment and later introduce the methods used in this study.

Bivariate statistics involve determining the relationship between two variables, generally called dependent and independent. Multivariate statistics, on the other hand, aim to figure out the relationship between one dependent variable and multiple independent variables [13]. In the case of landslide susceptibility assessment, the dependent variable indicates whether a landslide is present or absent, and independent variables are values of the landslide triggering factors. Weights of evidence [14, 15] and frequency ratio [14, 16] are two of the most commonly employed bivariate statistical methods and logistic regression [10, 17] is the most commonly used multivariate statistical method in landslide susceptibility assessment.

Support vector machines are supervised learning algorithms that map labeled instances in a space and construct hyperplanes such that they are as far as from the nearest training data of any class. To predict the

class for a test instance, it is mapped into the same space and class label of the hyperplane it falls into is assigned. In case of landslide susceptibility assessment, landsliding and non-landsliding zones are plotted on an n -dimensional space, where n is the number of landslide triggering factors, and support vector machine models are built [18–20].

In literature there also exist decision tree-based methods for landslide susceptibility assessment. Such models represent the learning model as a tree like structure where each internal node is condition and leaf nodes are class labels and conjunction of test conditions from root to a leaf form a classification rule. In case of landslide susceptibility assessment, conditions are tests on values of landslide triggering factors [18, 21].

Neural networks are computational models that mimic the human brain. These models are formed of input, output, and hidden layers. Neurons at each layer are connected to those at the next layer. In case of landslide susceptibility assessment problem, neurons of the input layer indicate values of landslide triggering factors and neurons of the output layer indicate the presence or absence of a landslide [16].

In literature there are hybrid studies proposed for landslide susceptibility assessment that utilize Naïve Bayes Trees [22], Random Forest [23], neuro-fuzzy inference [24].

In this study skyline operator is utilized to model landslides. Skyline operator is concerned with retrieving objects, called *skyline points*, from a set of objects such that the retrieved objects are not dominated by any other object in the set. The skyline operator is implemented in domains such as recommendation [25, 26], scientometrics [27, 28].

Object p is said to dominate object q , denoted as $p < q$, if p is as good as q in all dimensions and better in at least one dimension. Domination operator is formulated in (1) for objects with d dimensions where \geq operator means as good as or better and operator $>$ means better. Goodness of an object is determined based on some utility function that is monotone on all attributes of the objects.

$$p < q \leftrightarrow \forall i \{1, 2, \dots, d\} p_i \geq q_i \wedge \exists j \in \{1, 2, \dots, d\} p_j > q_j \quad (1)$$

Skyline points of a set consist of objects that are not dominated by any other object in the set. The skyline operator is formulated in (2) and its SQL extension is provided in (3).

$$S_p = \{p \mid p \in P \wedge \nexists q \in P : q < p\} \quad (2)$$

SELECT ... FROM ... WHERE ... GROUP BY ... HAVING ...

(3)

SKYLINE OF $d_1[MIN|MAX], \dots, d_n[MIN|MAX]$

To assess landslide susceptibility in the proposed method, majority voting principle is implemented. Trained on the same data set, different classifiers may assign different class labels for a particular test instance. In majority voting, votes of individual classifiers for a test instance is counted and prediction with the highest vote is assigned to the test instance. Majority voting principle can be formulated as in (4) where h_1, h_2, \dots, h_N are individual classifiers, w_1, w_2, \dots, w_N are weights that sum to 1 and $I(\cdot)$ is indicator function.

$$c(x) = \operatorname{argmax}_i + \sum_{j=1}^N w_j (h_j(x) = 1) \quad (4)$$

3. THE PROPOSED METHOD

The proposed method consists of three main steps: data preprocessing, model building, and landslide susceptibility assessment. In the following subsections we present these steps.

3.1 Data Preprocessing

In literature there is no consensus on the exact set of landslide triggering factors. In this study, similar to [10], aspect, slope, soil-map, altitude, erosion, land-use, distance to fault, depth of soil, distance to drainage, distance to road, and lithology are considered as landslide triggering factors. Data related to landslide triggering factors are usually obtained from different organizations in raw format; hence the data needs to be preprocessed. The data-preprocessing step in this study involves discretization, weight assignment, and data cleaning.

3.1.1 Discretization

In this step features that come from continuous domain are discretized using equal width binning. In equal width binning method, data to be discretized is firstly sorted and then partitioned into intervals of almost equal width. The equal width binning method is formulated in (5) where w is width of an interval; k is the number intervals determined a priori, min and max are, respectively, the smallest and largest value in the data set. Intervals boundaries are defined as $[-\infty, min + w], (min + w, min + 2w], \dots (min + (k-1)w, \infty]$.

$$k = \frac{\max - \min}{w} \quad (5)$$

In the proposed method aspect, slope, altitude, erosion, distance to fault, depth of soil, distance to drainage, distance to road are the features that have continuous values.

3.1.2 Weight Assignment

After discretization, each discrete value is assigned with a weight that indicates its effect on landslide occurrence. In this study, weights are assigned using Frequency ratio (FR) model. FR model is formulated in (6) where the numerator indicates the fraction of the zones with landslides and discrete value i (N_{Li}) over the total number of landsliding zones (N_i). The denominator indicates the fraction of the number of landsliding zones with any value of the feature that i belongs to over total number of zones of the study area. $FR = 1$ is assumed to be average, FR values less than 1 indicate low correlation between landslide occurrence and the value under consideration, and vice versa. The weight of i is the natural logarithm of its frequency ratio (7).

$$FR_i = \frac{N_{Li}/N_{Li}}{\sum N_{Li}/\sum N_{Li}} \quad (6)$$

$$w_i = \ln(FR_i) \quad (7)$$

Weight of a feature value indicates its effect on landslide occurrence. The higher weight indicates more effect.

3.1.3 Data Cleaning

After the discretization and class weight calculation steps, feature vectors with exactly the same values in every feature position but class label may be generated. We consider such representations as inconsistent and remove them. Discretization and weight assignment may also generate repetitive feature vectors, such repeating vectors are also removed from the training data in data cleaning step.

3.2 Model Building

In this study, skyline operator is used to model landslides. For this purpose, representations of only landslide occurring zones are considered and skyline operator is used to find dominating feature vectors with the lowest features values. Hence (3) is implemented with *MIN* keyword. In this study we assume that each skyline point is a model that defines the minimum values a feature vector should have in order to represent a landslide-zone.

In Table 1 we provide 10 vectors each indicating properties of a landslide zone. The first 11 attributes represent different characteristics of a zone and the last attribute is the class label.

Table 1. Example training dataset

L1	[0, 2, 1, 5, 1, 2, 3, 2, 7, 0, 3, 1]
L2	[0, 3, 3, 4, 3, 1, 4, 5, 8, 0, 6, 1]
L3	[0, 3, 2, 6, 2, 4, 4, 3, 7, 5, 9, 1]
L4	[0, 3, 3, 3, 1, 3, 2, 3, 8, 4, 4, 1]
L5	[0, 3, 3, 6, 3, 2, 5, 4, 9, 1, 4, 1]
L6	[0, 4, 6, 6, 3, 2, 4, 7, 8, 0, 3, 1]
L7	[0, 6, 8, 9, 6, 5, 7, 4, 8, 4, 7, 1]
L8	[0, 3, 3, 3, 2, 1, 2, 4, 4, 0, 2, 1]
L9	[0, 5, 4, 7, 3, 2, 6, 3, 9, 4, 4, 1]
L10	[0, 7, 6, 4, 2, 4, 7, 4, 6, 2, 4, 1]

The skyline operator will return L1, L4, and L8 as skyline points.

3.3 Landslide Susceptibility Assessment

To assess landslide susceptibility of a test zone a two-step majority voting mechanism is implemented. In the first step, feature vector representing the test zone is compared against each skyline point. A skyline point votes *yes* if majority of feature values representing the test zone are greater than the values of the skyline otherwise it votes *no*. In the second step, votes for *yes* and *no* are counted, and the final decision is made according to the majority of the votes.

In Table 2, we list the properties of the skyline points discovered in the previous section and two test instances.

Table 2. Example test dataset

L1	[0, 2, 1, 5, 1, 2, 3, 2, 7, 0, 3, 1]
L4	[0, 3, 3, 3, 1, 3, 2, 3, 8, 4, 4, 1]
L8	[0, 3, 3, 3, 2, 1, 2, 4, 4, 0, 2, 1]
T1	[0, 1, 2, 4, 0, 2, 1, 1, 4, 0, 2, 0]

For T1, L1 will vote *no* (7 features have smaller values), L4 will vote *no* (10 features have smaller values), and L8 will vote *yes* (5 features have smaller values). The final decision will be *no*.

4. EXPERIMENTS

To evaluate the performance of the proposed method, a real life dataset describing highly landslide intensive

area namely Savsat is used. Savsat is town in north east of Turkey located between 42°24'N and 42°50'N latitudes and 41°12'E and 41°37'E longitudes. The area has been subject to several landslide studies including [9, 10, 21]. Figure 1 shows the study area. Landslides indicated with yellow are dormant and landslide indicated with blue are active.

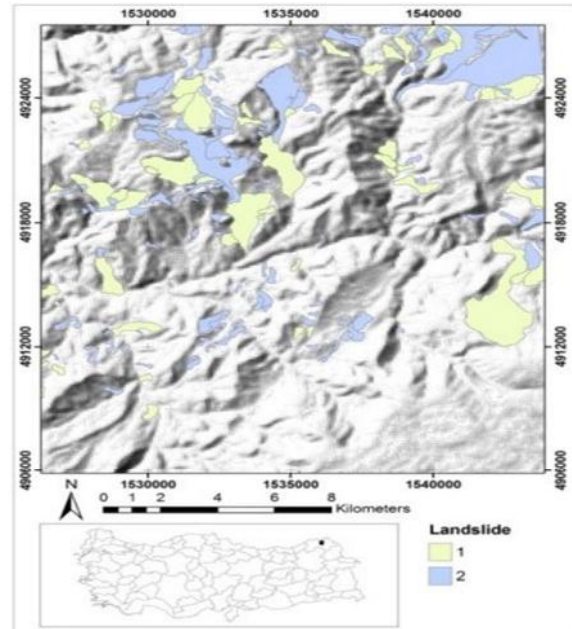


Figure 1. Map of the study area, yellow areas represent dormant landslides, blue areas represent active landslides

The dataset describing the area are obtained from the General Directorate of Mineral Research and Exploration (MRE) of Turkey. The dataset describing the area consists of properties of 13645 zones. Each zone is described using eleven features and a class label. Eight of the features are from continuous domain and the remaining three are from categorical domain.

Table 3 lists the attributes discretized, the number of bins, and bin width. Soil depth and erosion are the remaining two features that are discretized. Soil depth is discretized into four bins as follows: very deep (depth > 90 cm), deep (90 >= depth > 50 cm), shallow (50 >= depth > 20 cm) and shallow (20 >= depth >= 0 cm). Erosion is also discretized into 4 bins, namely none or low, medium, high, and very high. The bin widths are consistent with those recommended in literature [10, 14, 30].

After the data cleaning step, the size of the data set is reduced to 9762 instances, 6329 of which describe landslide safe zones and the remaining 3433 zones describe landslide-occurring zones.

Table 3. Properties of discretized attributes

Feature name	Value range	Num. of bins	Bin width
Aspect	[-1, 360]	8	45
Slope	[0, 52]	9	5
Altitude	[697, 3000]	5	500
Distance to fault	[0, ∞]	9	500
Distance to drainage	[0, ∞]	8	100
Distance to road	[0, ∞]	8	100

In Table 4 we report the predictive accuracy achieved by the proposed method, logistic regression, support vector machines, neural network, and decision trees. The reference models are built using Weka tool [31]. The reported results are obtained via 10-fold cross validation. On the average, the skyline operator retrieved 160 skyline points at each fold.

Table 4. Accuracy results

Method Name	Accuracy
Logistic Regression	77.13%
Support Vector Machine	76.35%
Neural Network	80.48%
Decision Tree	84.22%
The Proposed Method	83.07%

As the results show, the proposed method is superior over the reference studies other than decision support tree based model.

5. CONCLUSION

In this study we introduced a method based on the skyline operator and majority voting principle for landslide susceptibility assessment. In the proposed method the skyline operator is utilized to discover skylines that describe land- slide models, and majority voting is used to assess landslide susceptibility of a test instance. Experiments on a real life data set describing properties of a highly landslide intensive area namely Savsat show that the proposed method is superior over most commonly used methods in landslide susceptibility assessment such as logistic regression, support vector machines and neural networks. The proposed method performs slightly worse than decision tree based model, 83.07% vs. 84.22%.

Landslides usually occur in large areas. Hence a factor that has a high effect in a particular part of a landslide may have low effect in another part of the landslide. As a feature work we plan to extend the proposed method to handle such situations.

REFERENCES

- [1] A. Morales-Esteban, F. Martínez-Álvarez, A. Troncoso, J. Justo, C. Rubio-Escudero, "Pattern recognition to forecast seismic time series", *Expert Systems with Applications*, vol. 37, no. 12, pp. 8333-8342, 2010.
- [2] K. Asim, F. Martínez-Álvarez, A. Basit, T. Iqbal, "Earthquake magnitude prediction in Hindukush region using machine learning techniques", *Natural Hazards*, vol. 85, no. 1, pp. 471-486, 2016.
- [3] H. Cloke, F. Pappenberger, "Ensemble flood forecasting: A review", *Journal of Hydrology*, vol. 375, no. 3-4, pp. 613-626, 2009.
- [4] B. Bhattacharya, D. Solomatine, "Neural networks and M5 model trees in modelling water level–discharge relationship", *Neurocomputing*, vol. 63, pp. 381-396, 2005.
- [5] H. Langer, S. Falsaperla, A. Messina and S. Spampinato, "Performance of a new multistation alarm system for volcanic activity based on neural network techniques", in *Second European Conference on Earthquake Engineering and Seismology*, 2014.
- [6] J. Parra, O. Fuentes, E. Anthony, V. Kreinovich, "Use of Machine Learning to Analyze and – Hopefully – Predict Volcano Activity", *Acta Polytechnica Hungarica*, vol. 14, no. 3, 2017.
- [7] UNISDR: "Landslide Hazard and Risk Assessment", Unisdr.org. [Online]. Available: https://www.unisdr.org/files/52828_03landslidehazardandriskassessment.pdf. [Accessed: 31- Aug- 2018].
- [8] F. Dai, C. Lee, Y. Ngai, "Landslide risk assessment and management: an overview", *Engineering Geology*, vol. 64, no. 1, pp. 65-87, 2002.
- [9] E. Topsakal, T. Topal, "Slope stability assessment of a re-activated landslide on the Artvin-Savsat junction of a provincial road in Meydancik, Turkey", *Arabian Journal of Geosciences*, vol. 8, no. 3, pp. 1769-1786, 2014.
- [10] A. Erener, A. Mutlu, H. Sebnem Düzgün, "A comparative study for landslide susceptibility mapping using GIS-based multi-criteria decision analysis (MCDA), logistic regression (LR) and association rule mining (ARM)", *Engineering Geology*, vol. 203, pp. 45-55, 2016.

- [11] C. Ozgen, "An Investigation of landslide at km:12+ 200 od Artvin-Savsat junction-Meydancik Provincial road", PhD thesis, Middle East Technical University (2012).
- [12] P. Temel, "Evaluation of potential run-of river hydropower plant using multicriteria decision making in terms of environmental and social aspect", PhD thesis, Middle East Technical University (2015).
- [13] J. Isotalo, "Basics of Statistics", [Online] Available: <https://www.mv.helsinki.fi/home/jmisotal/BoS.pdf> [Accessed: 2019-01-17]
- [14] Q. Ding, W. Chen, H. Hong, "Application of frequency ratio, weights of evidence and evidential belief function models in landslide susceptibility mapping", *Geocarto International*, pp. 1-21, 2016.
- [15] C. Xu, X. Xu, F. Dai, J. Xiao, X. Tan, R. Yuan, "Landslide hazard mapping using GIS and weight of evidence model in Qingshui River watershed of 2008 Wenchuan earthquake struck region", *Journal of Earth Science*, vol. 23, no. 1, pp. 97-120, 2012.
- [16] B. Pradhan, S. Lee, "Landslide susceptibility assessment and factor effect analysis: backpropagation artificial neural networks and their comparison with frequency ratio and bivariate logistic regression modeling", *Environmental Modelling & Software*, vol. 25, no. 6, pp. 747-759, 2010.
- [17] L. Wang, M. Guo, K. Sawada, J. Lin, J. Zhang, "Landslide susceptibility mapping in Mizunami City, Japan: A comparison between logistic regression, bivariate statistical analysis and multivariate adaptive regression spline models", *CATENA*, vol. 135, pp. 271-282, 2015.
- [18] B. Pradhan, "A comparative study on the predictive ability of the decision tree, support vector machine and neuro-fuzzy models in landslide susceptibility mapping using GIS", *Computers & Geosciences*, vol. 51, pp. 350-365, 2013.
- [19] B. Feizizadeh, M. Roodposhti, T. Blaschke, J. Aryal, "Comparing GIS-based support vector machine kernel functions for landslide susceptibility mapping", *Arabian Journal of Geosciences*, vol. 10, no. 5, 2017.
- [20] D. Kumar, M. Thakur, C. Dubey and D. Shukla, "Landslide susceptibility mapping & prediction using Support Vector Machine for Mandakini River Basin, Garhwal Himalaya, India", *Geomorphology*, vol. 295, pp. 115-125, 2017.
- [21] H. Saito, D. Nakayama, H. Matsuyama, "Comparison of landslide susceptibility based on a decision-tree model and actual landslide occurrence: The Akaishi Mountains, Japan", *Geomorphology*, vol. 109, no. 3-4, pp. 108-121, 2009.
- [22] A. Shirzadi, D. T. Bui, B. T. Pham, K. Solaimani, K. Chapi, A. Kaviani, H. Shahabi, I. Revhaug, "Shallow landslide susceptibility assessment using a novel hybrid intelligence approach", *Environmental Earth Sciences*, vol. 76, no. 2, 2017.
- [23] H. R. Pourghasemi, K. Norman, "Random forests and evidential belief function-based landslide susceptibility assessment in Western Mazandaran Province, Iran", *Environmental Earth Sciences*, vol. 75, no. 3, 2016.
- [24] I. N. Aghdam, P. Biswajeet, M. Panahi, "Landslide susceptibility assessment using a novel hybrid model of statistical bivariate methods (FR and WOE) and adaptive neuro-fuzzy inference system (ANFIS) at southern Zagros Mountains in Iran", *Environmental Earth Sciences*, vol. 76 no.6, 2017.
- [25] K. Kodama, Y. Iijima, X. Guo and Y. Ishikawa, "Skyline queries based on user locations and preferences for making location-based recommendations", *International Workshop on Location Based Social Networks*, 2009
- [26] J. Yang et al, "Finding superior skyline points for multidimensional recommendation applications", *World Wide Web*, vol. 15, no. 1, pp. 33-60, 2012
- [27] G. Stoupas et al, "Rainbow ranking: an adaptable, multidimensional ranking method for publication sets", *Scientometrics*, vol. 118, no. 1, pp. 147-160, 2018
- [28] A. Sidiropoulos, "Gazing at the skyline for star scientists", *Journal of Informatics*, vol. 10, no. 3, 2016.
- [30] E. Topsakal, "An Investigation of landslide at km:12+ 200 od Artvin-Savsat junction-Meydancik Provincial road", PhD thesis, Middle East Technical University, (2012).
- [31] Weka 3: Data Mining Software in Java, [Online] Available: <https://www.cs.waikato.ac.nz/ml/weka/> [Accessed: 2018-04-10].

JOURNAL OF SCIENCE



SAKARYA UNIVERSITY

Sakarya University Journal of Science

ISSN 1301-4048 | e-ISSN 2147-835X | Period Bimonthly | Founded: 1997 | Publisher Sakarya University |
<http://www.saujs.sakarya.edu.tr/>

Title: on Fuhrmann'S Theorem in Abstract Spaces

Authors: Nilgün Sönmez

Received: 2019-01-27 21:54:06

Accepted: 2019-03-21 15:05:03

Article Type: Research Article

Volume: 23

Issue: 5

Month: October

Year: 2019

Pages: 788-791

How to cite

Nilgün Sönmez; (2019), on Fuhrmann'S Theorem in Abstract Spaces. Sakarya University Journal of Science, 23(5), 788-791, DOI: 10.16984/saufenbilder.518403

Access link

<http://www.saujs.sakarya.edu.tr/issue/44066/518403>

New submission to SAUJS

<http://dergipark.gov.tr/journal/1115/submission/start>

On Fuhrmann's Theorem in Abstract Spaces

Nilgün SÖNMEZ

Abstract

We prove that Fuhrmann's Theorem holds on every Ptolemaic space.

Keywords: Fuhrmann's theorem, Ptolemy's theorem, Ptolemaic space , Abstract space

1. INTRODUCTION

The classical Fuhrmann's Theorem, [2], states that if P is an inscribed hexagon in the plane R^2 with oriented vertices p_1, \dots, p_6 and d denotes the Euclidean distance in R^2 , then

$$\begin{aligned} & d(p_1, p_4) \cdot d(p_2, p_5) \cdot d(p_3, p_6) = \\ & d(p_1, p_2) \cdot d(p_3, p_4) \cdot d(p_5, p_6) + \\ & d(p_1, p_6) \cdot d(p_2, p_3) \cdot d(p_4, p_5) + \\ & d(p_1, p_2) \cdot d(p_4, p_5) \cdot d(p_3, p_6) + \\ & d(p_2, p_3) \cdot d(p_5, p_6) \cdot d(p_1, p_4) + \\ & d(p_3, p_4) \cdot d(p_2, p_5) \cdot d(p_1, p_6). \end{aligned} \quad (1)$$

The classical Fuhrmann's Theorem follows as an elementary corollary of Ptolemy's theorem in R^2 , proved by the Ancient Greek mathematician Claudius Ptolemaeus (Ptolemy) of Alexandria almost 1800 years ago.

2. PRELIMINARIES

Theorem 1 (*Ptolemy's Theorem in R^2*) Given an inscribed quadrilateral $Q = (p_1, p_2, p_3, p_4)$ then

$$\begin{aligned} & d(p_1, p_3) \cdot d(p_2, p_4) = d(p_1, p_2) \cdot d(p_3, p_4) + \\ & d(p_1, p_4) \cdot d(p_2, p_3). \end{aligned} \quad (2)$$

Now, Fuhrmann's Theorem may be proved as follows: We apply Theorem 1 to the quadrilaterals

$$Q_1 = (p_1, p_2, p_4, p_5), Q_2 = (p_2, p_3, p_4, p_6)$$

$$Q_3 = (p_1, p_4, p_5, p_6), Q_4 = (p_1, p_2, p_5, p_6),$$

to obtain the relations

$$\begin{aligned} & d(p_1, p_4) \cdot d(p_2, p_5) = d(p_1, p_2) \cdot d(p_4, p_5) + \\ & d(p_2, p_4) \cdot d(p_1, p_5), \end{aligned} \quad (3)$$

$$\begin{aligned} & d(p_2, p_4) \cdot d(p_3, p_6) = d(p_2, p_3) \cdot d(p_4, p_6) + \\ & d(p_3, p_4) \cdot d(p_2, p_6), \end{aligned} \quad (4)$$

$$\begin{aligned} & d(p_1, p_5) \cdot d(p_4, p_6) = d(p_1, p_4) \cdot d(p_5, p_6) + \\ & d(p_4, p_5) \cdot d(p_1, p_6), \end{aligned} \quad (5)$$

$$\begin{aligned} & d(p_1, p_5) \cdot d(p_2, p_6) = d(p_1, p_2) \cdot d(p_5, p_6) + \\ & d(p_2, p_5) \cdot d(p_1, p_6). \end{aligned} \quad (6)$$

We multiply (3) by $d(p_3, p_6)$ to obtain

$$\begin{aligned} & d(p_1, p_4) \cdot d(p_2, p_5) \cdot d(p_3, p_6) = \\ & d(p_1, p_2) \cdot d(p_4, p_5) \cdot d(p_3, p_6) + \\ & d(p_2, p_4) \cdot d(p_1, p_5) \cdot d(p_3, p_6) \end{aligned}$$

using (4)

$$\begin{aligned}
 & d(p_1, p_4) \cdot d(p_2, p_5) \cdot d(p_3, p_6) \\
 &= d(p_1, p_2) \cdot d(p_4, p_5) \cdot d(p_3, p_6) \\
 &+ d(p_1, p_5) \cdot (d(p_2, p_3) \cdot d(p_4, p_6)) \\
 &+ d(p_3, p_4) \cdot d(p_2, p_6)) \\
 &= d(p_1, p_2) \cdot d(p_4, p_5) \cdot d(p_3, p_6) \\
 &+ d(p_1, p_5) \cdot d(p_2, p_3) \cdot d(p_4, p_6) \\
 &+ d(p_1, p_5) \cdot d(p_3, p_4) \cdot d(p_2, p_6).
 \end{aligned}$$

We now use (5) and (6) for the last two terms to obtain

$$\begin{aligned}
 & d(p_1, p_4) \cdot d(p_2, p_5) \cdot d(p_3, p_6) = \\
 & d(p_1, p_2) \cdot d(p_4, p_5) \cdot d(p_3, p_6) + \\
 & d(p_2, p_3) \cdot (d(p_1, p_4) \cdot d(p_5, p_6) + \\
 & d(p_4, p_5) \cdot d(p_1, p_6)) + \\
 & d(p_3, p_4) \cdot (d(p_1, p_2) \cdot d(p_5, p_6) + \\
 & d(p_2, p_5) \cdot d(p_1, p_6))
 \end{aligned}$$

and Fuhrmann's Theorem follows.

It is therefore clear that Fuhrmann's Theorem does not rely on the Euclidean space itself but rather on its Ptolemaic property, see Definition 1 of Ptolemaic spaces below. This property is intuitive and has been generalised to more abstract spaces, for example see [1,3], [4], among a great variety of other references on Ptolemaic spaces.

Let (X, d) be a metric space and suppose there is remote point which we shall denote by ω . We consider the one point compactification of (X, d) : $\tilde{X} = X \cup \{\omega\}$ and \tilde{d} is defined on $\tilde{X} \times \tilde{X}$ by

$$\tilde{d}(x, y) = \begin{cases} d(x, y) & \text{if } x, y \in X, \\ +\infty & \text{if } x \in X, y = \omega, \\ +\infty & \text{if } x = \omega, y \in X, \\ 0 & \text{if } x = y = \omega. \end{cases}$$

To lighten the notation, we will drop the tildes and henceforth (X, d) shall denote the compactified space with the extended metric.

Definition 1 The space (X, d) is called Ptolemaic if for every p_1, p_2, p_3, p_4 pairwise distinct points of X , the following relation holds:

$$d(p_1, p_3) \cdot d(p_2, p_4) \leq d(p_1, p_2) \cdot d(p_3, p_4) + d(p_1, p_4) \cdot d(p_2, p_3). \tag{7}$$

Definition 2 A Ptolemaic circle c in X is a curve homeomorphic to S^1 such that for every

p_1, p_2, p_3, p_4 pairwise distinct points on c Equation (2) holds.

It turns out that a variety of nice spaces are Ptolemaic. For instance, the extended Euclidean space $\overline{R^n} = R^n \cup \{\infty\}$ with the extended Euclidean metric is Ptolemaic and its Ptolemaic circles are the usual Euclidean circles as well as the straight lines. This space of course may be identified via stereographic projection with the sphere S^n and the metric is identified to the chordal metric. The sphere S^n is in turn identified to the boundary of R^{n+1} which is the usual Euclidean space, the first among the \mathbf{K} -hyperbolic spaces $H_{\mathbf{K}}^n$, where \mathbf{K} can be the set of the real numbers R , the set of the complex numbers C , the set of quaternions \mathbf{H} and the set of octonions \mathbf{O} (the latter only for $n = 2$). The boundaries of those spaces may be identified to what is called the generalised Heisenberg group $h_{\mathbf{K}}$ together with a point at infinity ∞ . There is a natural metric defined on those spaces, the so-called Korányi metric d_h . Now, it is known (see for instance [4]) that all spaces $\partial H_{\mathbf{K}}^n$ endowed with the extension to infinity of the Korányi metric d_h are Ptolemaic and have Ptolemaic circles.

3. MAIN RESULT

Theorem 2 Fuhrmann's Theorem holds on every Ptolemaic circle on the boundary of $H_{\mathbf{K}}^n$.

Let $\overline{R^n}$ be the extended Euclidean space; that is

$$\overline{R^n} = R^n \cup \{\infty\}.$$

We will denote the Korányi metric $d_h = d$ in $\overline{R^n}$, by requiring

$$d(p, \infty) = +\infty, \text{ if } p \neq \infty, d(\infty, \infty) = 0$$

and let $p = (p_1, p_2, p_3, p_4) \in \overline{R^n}$ be arbitrary. There are six distances in $(0, +\infty]$ involved:

$$d(p_i, p_j), \quad i, j = 1, \dots, 4, i \neq j$$

We adopt the convention: $(+\infty): (+\infty) = 1$, and to p we associate the cross-ratio $|X^d|(p)$ defined by

$$|X^d|(p) = \frac{d(p_4, p_2)}{d(p_4, p_1)} \cdot \frac{d(p_3, p_1)}{d(p_3, p_2)} = \frac{d(p_5, p_4)}{d(p_5, p_1)} \cdot \frac{d(p_2, p_1)}{d(p_2, p_4)} = \frac{x_5 - x_4}{x_4 - x_2}$$

[5].

For every $i, j, k, l = 1, \dots, 4$, such that $p_i, p_j, p_k, p_l \in \overline{R^n}$ are pairwise disjoint, the following symmetry conditions are clearly satisfied:

$$\begin{aligned} |X^d|(p)(p_i, p_j, p_k, p_l) &= |X^d|(p)(p_j, p_i, p_l, p_k) \\ &= |X^d|(p)(p_k, p_l, p_i, p_j) \\ &= |X^d|(p)(p_k, p_l, p_j, p_i). \end{aligned}$$

Let now $p = (p_1, p_2, p_3, p_4) \in \overline{R^n}$ and set

$$\begin{aligned} |X_1^d|(p) &= |X^d|(p)(p_1, p_2, p_3, p_4), \\ |X_2^d|(p) &= |X^d|(p)(p_1, p_3, p_2, p_4). \end{aligned}$$

[5]. The cross-ratios of all possible permutations of points of p are functions of $|X_1^d|(p)$ and $|X_2^d|(p)$.

We apply it to the quadrilaterals

$$\begin{aligned} Q_1 &= (p_1, p_2, p_4, p_5), Q_2 = (p_2, p_3, p_4, p_6) \\ Q_3 &= (p_1, p_4, p_5, p_6), Q_4 = (p_1, p_2, p_5, p_6). \end{aligned}$$

We assume that

$$\begin{aligned} p_1 &= \infty, p_2 = (x_2, 0, u), p_3 = (x_3, 0, u), \\ p_4 &= (x_4, 0, u), p_5 = (x_5, 0, u), \\ p_6 &= (0, 0, u) \end{aligned}$$

where $x_5 > x_4 > x_3 > x_2 > 0$.

We now use (3). Then:

$$\begin{aligned} |X_1^d|(p) &= |X^d|(p)(p_1, p_2, p_4, p_5) \\ &= \frac{d(p_5, p_2)}{d(p_5, p_1)} \cdot \frac{d(p_4, p_1)}{d(p_4, p_2)} \\ &= \frac{x_5 - x_2}{x_4 - x_2} \end{aligned}$$

and

$$|X_2^d|(p) = |X^d|(p)(p_1, p_4, p_2, p_5)$$

The p_2 and p_4 separate p_1 and p_5 since $|X_1^d|(p) - |X_2^d|(p) = 1$. We now use (4). Then:

$$\begin{aligned} |X_1^d|(p) &= |X^d|(p)(p_2, p_3, p_4, p_6) \\ &= \frac{d(p_6, p_3)}{d(p_6, p_2)} \cdot \frac{d(p_4, p_2)}{d(p_4, p_3)} \\ &= \frac{x_3}{x_2} \cdot \frac{x_4 - x_2}{x_4 - x_3} \end{aligned}$$

and

$$\begin{aligned} |X_2^d|(p) &= |X^d|(p)(p_2, p_4, p_3, p_6) \\ &= \frac{d(p_6, p_4)}{d(p_6, p_2)} \cdot \frac{d(p_3, p_2)}{d(p_3, p_4)} \\ &= \frac{x_4}{x_2} \cdot \frac{x_3 - x_2}{x_3 - x_4} \\ &= -\frac{x_4}{x_2} \cdot \frac{x_3 - x_2}{x_4 - x_3} \end{aligned}$$

The p_2 and p_6 separate p_3 and p_4 since $|X_1^d|(p) + |X_2^d|(p) = 1$. We now use (5). Then:

$$\begin{aligned} |X_1^d|(p) &= |X^d|(p)(p_1, p_4, p_5, p_6) \\ &= \frac{d(p_6, p_4)}{d(p_6, p_1)} \cdot \frac{d(p_5, p_1)}{d(p_5, p_4)} \\ &= -\frac{x_4}{x_5 - x_4} \end{aligned}$$

and

$$\begin{aligned} |X_2^d|(p) &= |X^d|(p)(p_1, p_5, p_4, p_6) \\ &= \frac{d(p_6, p_5)}{d(p_6, p_1)} \cdot \frac{d(p_4, p_1)}{d(p_4, p_5)} \\ &= \frac{x_5}{x_5 - x_4} \end{aligned}$$

The p_4 and p_5 separate p_1 and p_6 since $|X_2^d|(p) - |X_1^d|(p) = 1$. We now use (6). Then:

$$|X_1^d|(p) = |X^d|(p)(p_1, p_2, p_5, p_6)$$

$$\begin{aligned}
 &= \frac{d(p_6, p_2)}{d(p_6, p_1)} \cdot \frac{d(p_5, p_1)}{d(p_5, p_2)} \\
 &= -\frac{x_2}{x_5 - x_2}
 \end{aligned}$$

and

$$\begin{aligned}
 |X_2^d|(p) &= |X^d|(p)(p_1, p_5, p_2, p_6) \\
 &= \frac{d(p_6, p_5)}{d(p_6, p_1)} \cdot \frac{d(p_2, p_1)}{d(p_2, p_5)} \\
 &= \frac{x_5}{x_5 - x_2}
 \end{aligned}$$

The p_1 and p_6 separate p_2 and p_5 since $|X_1^d|(p) + |X_2^d|(p) = 1$.

4. CONCLUSION

Fuhrmann's theorem is satisfied in abstract Ptolemaic spaces.

5. REFERENCES

- [1] H. S. M. Coxeter and S. L. Greitzer, "Geometry Revisited," Washington, DC: Math. Assoc. Amer., pp. 42–43, 1967.
- [2] W. Fuhrmann, "Synthetische Beweise Planimetrischer Sätze," Berlin, pp. 61, 1890.
- [3] R.A. Johnson, "Modern Geometry: An Elementary Treatise on the Geometry of the Triangle and the Circle," Boston, MA: Houghton Mifflin, pp. 65-66, 1929.
- [4] I. D. Platis, "Cross-ratios and the Ptolemaean Inequality in Boundaries of Symmetric Spaces of Rank 1," *Geometriae Dedicata*, vol. 169, pp. 187–208, 2014.
- [5] I. D. Platis and V. Schroeder, "Möbius Rigidity of Invariant Metrics in Boundaries of Symmetric Spaces of Rank 1," *Monatshefte für Mathematic*, vol. 183, no. 2, pp. 357–373, 2017.

JOURNAL OF SCIENCE



SAKARYA UNIVERSITY

Sakarya University Journal of Science

ISSN 1301-4048 | e-ISSN 2147-835X | Period Bimonthly | Founded: 1997 | Publisher Sakarya University |
<http://www.saujs.sakarya.edu.tr/>

Title: A New Class of S-Type $X(U,V;L_P(E))$ Operators

Authors: Pinar Zengin Alp, Merve İlkan

Received: 2019-01-25 12:49:57

Accepted: 2019-03-25 22:00:11

Article Type: Research Article

Volume: 23

Issue: 5

Month: October

Year: 2019

Pages: 792-800

How to cite

Pinar Zengin Alp, Merve İlkan; (2019), A New Class of S-Type $X(U,V;L_P(E))$ Operators. Sakarya University Journal of Science, 23(5), 792-800, DOI: 10.16984/saufenbilder.517762

Access link

<http://www.saujs.sakarya.edu.tr/issue/44066/517762>

New submission to SAUJS

<http://dergipark.gov.tr/journal/1115/submission/start>

A New Class Of s-TYPE $X(u, v, l_p(E))$ Operators

Pınar Zengin Alp^{*1}, Merve İlkan²

Abstract

In this paper, we define a new class of s-type $X(u, v; l_p(E))$ operators, $L_{u,v,E}$. Also we show that this class is a quasi-Banach operator ideal and we study on the properties of the classes which are produced via different types of s-numbers.

Keywords: operator ideals, s-numbers, block sequence spaces.

1. INTRODUCTION

Operator ideal theory is an important subject of functional analysis. There are many different ways of constructing operator ideals, one of them is using s-numbers. Some equivalents of s-numbers are Kolmogorov numbers, Weyl numbers and approximation numbers. Pietsch defined in [1] the concept of s-number sequence to combine all s-numbers in one definition. After some revisions on this definition s-number sequence is presented in [2], [3].

In this paper, by \mathbb{N} and \mathbb{R}^+ we denote the set of all natural numbers and nonnegative real numbers, respectively.

A finite rank operator is a bounded linear operator whose dimension of the range space is finite [4].

Let X and Y be real or complex Banach spaces. The space of all bounded linear operators from X to Y and the space of all bounded linear operators between any two arbitrary Banach spaces are denoted by $\mathcal{L}(X, Y)$ and \mathcal{L} , respectively.

An s-number sequence is a map $s = (s_n): \mathcal{L} \rightarrow \mathbb{R}^+$ which assigns every operator $T \in \mathcal{L}$ to a non-negative scalar sequence $(s_n(T)_{n \in \mathbb{N}})$ if the following conditions hold for all Banach spaces X, Y, X_0 and Y_0 :

(S1) $\|T\| = s_1(T) \geq s_2(T) \geq \dots \geq 0$ for every $T \in \mathcal{L}(X, Y)$,

* Corresponding Author: pinarzenginalp@gmail.com

¹ Düzce University, Department of Mathematics, Düzce, Turkey. ORCID: 0000-0001-9699-7199

² Düzce University, Department of Mathematics, Düzce, Turkey. ORCID: 0000-0002-0831-1474

(S2) $s_{m+n-1}(S + T) \leq s_m(T) + s_n(T)$ for every $S, T \in \mathcal{L}(X, Y)$ and $m, n \in \mathbb{N}$,

(S3) $s_n(RST) \leq \|R\|s_n(S)\|T\|$ for some $R \in \mathcal{L}(Y, Y_0)$, $S \in \mathcal{L}(X, Y)$ and $T \in \mathcal{L}(X_0, X)$, where X_0, Y_0 are arbitrary Banach spaces,

(S4) If $\text{rank}(T) \leq n$, then $s_n(T) = 0$,

(S5) $s_n(I: l_2^n \rightarrow l_2^n) = 1$, where I denotes the identity operator on the n -dimensional Hilbert space l_2^n , where $s_n(T)$ denotes the n -th s -number of the operator T [5].

As an example of s -numbers $a_n(T)$, the n -th approximation number, is defined as

$$a_n(T) = \inf\{\|T - A\| : A \in \mathcal{L}(X, Y), \text{rank}(A) < n\},$$

where $T \in \mathcal{L}(X, Y)$ and $n \in \mathbb{N}$ [6].

Let $T \in \mathcal{L}(X, Y)$ and $n \in \mathbb{N}$. The other examples of s -number sequences are given in the following, namely Gelfand number ($c_n(T)$), Kolmogorov number ($d_n(T)$), Weyl number ($x_n(T)$), Chang number ($y_n(T)$), Hilbert number ($h_n(T)$), etc. For the definitions of these sequences we refer to [4], [7]. In the sequel there are some properties of s -number sequences.

When any metric injection $J \in \mathcal{L}(Y, Y_0)$ is given and an s -number sequence $s = (s_n)$ satisfies $s_n(T) = s_n(JT)$ for all $T \in \mathcal{L}(X, Y)$ the s -number sequence is called injective [3].

Proposition 1. The number sequences $(c_n(T))$ and $(x_n(T))$ are injective [3].

When any metric surjection $S \in \mathcal{L}(X_0, X)$ is given and an s -number sequence $s = (s_n)$ satisfies $s_n(T) = s_n(TS)$ for all $T \in \mathcal{L}(X, Y)$ the s -number sequence is called surjective [3].

Proposition 2. The number sequences $(d_n(T))$ and $(y_n(T))$ are surjective [3].

Proposition 3. Let $T \in \mathcal{L}(X, Y)$. Then $h_n(T) \leq x_n(T) \leq c_n(T) \leq a_n(T)$ and $h_n(T) \leq y_n(T) \leq d_n(T) \leq a_n(T)$ [3].

Lemma 1. Let $S, T \in \mathcal{L}(X, Y)$, then $|s_n(T) - s_n(S)| \leq \|T - S\|$ for $n = 1, 2, \dots$ [1].

A sequence space is defined as any vector subspace of ω , where ω is the space of real valued sequences.

The Cesaro sequence space ces_p is defined as $ces_p = \{x = (x_k) \in \omega : \sum_{n=1}^{\infty} \left(\frac{1}{n} \sum_{k=1}^n |x_k|\right)^p < \infty\}$

where $1 < p < \infty$ [8], [9], [10].

If an operator $T \in \mathcal{L}(X, Y)$ satisfies $\sum_{n=1}^{\infty} (a_n(T))^p < \infty$ for $0 < p < \infty$, it is defined as an l_p type operator in [6] by Pietsch. Then Constantin defined a new class named ces - p type operators, via Cesaro sequence spaces. If an operator $T \in \mathcal{L}(X, Y)$ satisfies $\sum_{n=1}^{\infty} \left(\frac{1}{n} \sum_{k=1}^n a_n(T)\right)^p < \infty$, $1 < p < \infty$, it is called ces - p type operator. The class of ces - p type operators includes the class of l_p type operators [11]. Later on Tita [12] proved that the class of l_p type operators and ces - p type operators are coincides. Some other generalizations of l_p type operators were examined in [4], [13], [14], [15].

Continuous linear functionals on X are compose the dual of X which is denoted by X' . Let $x' \in X'$ and $y \in Y$, then the map $x' \otimes y: X \rightarrow Y$ is defined by

$$(x' \otimes y)(x) = x'(x)y, x \in X.$$

A subcollection \mathfrak{I} of \mathcal{L} is called an operator ideal if every component $\mathfrak{I}(X, Y) = \mathfrak{I} \cap \mathcal{L}(X, Y)$ satisfies the following conditions:

i) if $x' \in X'$, $y \in Y$, then $x' \otimes y \in \mathfrak{I}(X, Y)$,

ii) if $S, T \in \mathfrak{I}(X, Y)$, then $S + T \in \mathfrak{I}(X, Y)$,

iii) if $S \in \mathfrak{I}(X, Y)$, $T \in \mathcal{L}(X_0, X)$ and $R \in \mathcal{L}(Y, Y_0)$, then $RST \in \mathfrak{I}(X_0, Y_0)$ [2].

Let \mathfrak{I} be an operator ideal and $\alpha: \mathfrak{I} \rightarrow \mathbb{R}^+$ be a function on \mathfrak{I} . Then, if the following conditions satisfied:

i) If $x' \in X'$, $y \in Y$, then $\alpha(x' \otimes y) = \|x'\| \|y\|$,

ii) there exists a constant $c \geq 1$ such that $\alpha(S + T) \leq c[\alpha(S) + \alpha(T)]$,

iii) if $S \in \mathfrak{S}(X, Y)$, $T \in \mathcal{L}(X_0, X)$ and $R \in \mathcal{L}(Y, Y_0)$, then $\alpha(RST) \leq \|R\| \alpha(S) \|T\|$

α is called a quasi-norm on the operator ideal \mathfrak{S} [2].

For special case $c = 1$, α is a norm on the operator ideal \mathfrak{S} .

If α is a quasi-norm on an operator ideal \mathfrak{S} , it is denoted by $[\mathfrak{S}, \alpha]$. Also if every component $\mathfrak{S}(X, Y)$ is complete with respect to the quasinorm α , $[\mathfrak{S}, \alpha]$ is called a quasi-Banach operator ideal.

Let $[\mathfrak{S}, \alpha]$ be a quasi-normed operator ideal and $J \in \mathcal{L}(Y, Y_0)$ be a metric injection. If for every operator $T \in \mathcal{L}(X, Y)$ and $JT \in \mathfrak{S}(X, Y_0)$ we have $T \in \mathfrak{S}(X, Y)$ and $\alpha(JT) = \alpha(T)$, $[\mathfrak{S}, \alpha]$ is called an injective quasi-normed operator ideal. Furthermore, let $[\mathfrak{S}, \alpha]$ be a quasi-normed operator ideal and $Q \in \mathcal{L}(X_0, X)$ be a metric surjection. If for every operator $T \in \mathcal{L}(X, Y)$ and $TQ \in \mathfrak{S}(X, Y_0)$ we have $T \in \mathfrak{S}(X, Y)$ and $\alpha(TQ) = \alpha(T)$, $[\mathfrak{S}, \alpha]$ is called a surjective quasi-normed operator ideal [2].

Let T' be the dual of T . An s-number sequence is called symmetric if $s_n(T) \geq s_n(T')$ for all $T \in \mathcal{L}$. If $s_n(T) = s_n(T')$ the s-number sequence is said to be completely symmetric [2].

For every operator ideal \mathfrak{S} , the dual operator ideal denoted by \mathfrak{S}' is defined as

$$\mathfrak{S}'(X, Y) = \{T \in \mathcal{L}(X, Y) : T' \in \mathfrak{S}(Y', X')\},$$

where T' is the dual of T and X' and Y' are the duals of X and Y , respectively.

An operator ideal \mathfrak{S} is called symmetric if $\mathfrak{S} \subset \mathfrak{S}'$ and is called completely symmetric if $\mathfrak{S} = \mathfrak{S}'$ [2].

Let $E = (E_n)$ be a partition of finite subsets of positive integers such that

$$\max E_n < \max E_{n+1}$$

for $n = 1, 2, \dots$. Foroutannia, in [16] defined the sequence space $l_p(E)$ as

$$l_p(E) = \left\{ x = (x_n) \in \omega : \sum_{n=1}^{\infty} \left| \sum_{j \in E_n} x_j \right|^p < \infty \right\},$$

where $(1 \leq p < \infty)$ with the seminorm $\|x\|_{p,E}$ which defined in the following way:

$$\|x\|_{p,E} = \left(\sum_{n=1}^{\infty} \left| \sum_{j \in E_n} x_j \right|^p \right)^{\frac{1}{p}}$$

For example if $E_n = \{2n - 1, 2n\}$ for all n , then $x = (x_n) \in l_p(E)$ if and only if $\sum_{n=1}^{\infty} |x_{2n-1} + x_{2n}|^p < \infty$. It is obvious that $\|\cdot\|_{p,E}$ cannot be a norm, since if $x = (1, -1, 0, 0, \dots)$ and $E_n = \{2n - 1, 2n\}$ for all n then $\|x\|_{p,E} = 0$ while $x \neq \theta$. In the special case $E_n = \{n\}$ for $n = 1, 2, \dots$, we have $l_p(E) = l_p$ and $\|x\|_{p,E} = \|x\|_p$.

For more information about block sequence spaces we refer to [17], [18].

2. MAIN RESULTS

Let $u = (u_n)$ and $v = (v_n)$ be positive real number sequences. In this section we give the definition of the sequence space $X(u, v; l_p(E))$ as follows:

$$X(u, v; l_p(E)) = \left\{ x \in \omega : \sum_{n=1}^{\infty} \left(u_n \sum_{j \in E_n} v_j x_j(T) \right)^p < \infty \right\}$$

An operator $T \in \mathcal{L}(X, Y)$ is in the class of $L_{u,v;E}(X, Y)$ if

$$\sum_{n=1}^{\infty} \left(u_n \sum_{j \in E_n} v_j s_j(T) \right)^p < \infty, \quad (1 \leq p < \infty)$$

The class of all s-type $X(u, v; l_p(E))$ operators are denoted by $L_{u,v;E}$.

Theorem 1. The class $L_{u,v;E}$ is an operator ideal for $1 \leq p < \infty$ where $v_{2k-1} + v_{2k} \leq M v_k$, ($M > 0$) and $\sum_{n=1}^{\infty} (u_n)^p < \infty$.

Proof.

$$\begin{aligned} \sum_{n=1}^{\infty} \left(u_n \sum_{j \in E_n} v_j s_j(x' \otimes y) \right)^p &= (u_1 v_1 s_1(x' \otimes y))^p \\ &= u_1^p v_1^p \|x' \otimes y\|^p \\ &= u_1^p v_1^p \|x'\|^p \|y\|^p < \infty \end{aligned}$$

Since the rank of the operator $x' \otimes y$ is one, $s_n(x' \otimes y) = 0$ for $n \geq 2$. Therefore $x' \otimes y \in L_{u,v;E}$.

Let $S, T \in L_{u,v;E}$. Then

$$\sum_{n=1}^{\infty} \left(u_n \sum_{j \in E_n} v_j s_j(S) \right)^p < \infty, \quad \sum_{n=1}^{\infty} \left(u_n \sum_{j \in E_n} v_j s_j(T) \right)^p < \infty$$

To show that $S + T \in L_{u,v;E}(X, Y)$, we begin with

$$\begin{aligned} \sum_{n=1}^{\infty} \left(u_n \sum_{j \in E_n} v_j s_j(S + T) \right)^p &\leq \sum_{n=1}^{\infty} \left(u_n \sum_{j \in E_n} v_{2j-1} s_{2j-1}(S + T) \right. \\ &\quad \left. + u_n \sum_{j \in E_n} v_{2j} s_{2j}(S + T) \right)^p \\ &\leq \sum_{n=1}^{\infty} \left(u_n \sum_{j \in E_n} (v_{2j-1} \right. \\ &\quad \left. + v_{2j}) s_{2j-1}(S + T) \right)^p \\ &\leq \sum_{n=1}^{\infty} \left(M u_n \sum_{j \in E_n} v_j (s_j(S) + s_j(T)) \right)^p \end{aligned}$$

By using Minkowski inequality;

$$\begin{aligned} \left(\sum_{n=1}^{\infty} \left(u_n \sum_{j \in E_n} v_j s_j(S + T) \right)^p \right)^{\frac{1}{p}} &\leq M \left(\sum_{n=1}^{\infty} \left(u_n \sum_{j \in E_n} v_j s_j(S) \right)^p \right)^{\frac{1}{p}} \\ &\quad + M \left(\sum_{n=1}^{\infty} \left(u_n \sum_{j \in E_n} v_j s_j(T) \right)^p \right)^{\frac{1}{p}} < \infty \end{aligned}$$

Hence $S + T \in L_{u,v;E}(X, Y)$.

Let $R \in \mathcal{L}(Y, Y_0)$, $S \in L_{u,v;E}(X, Y)$ and $T \in \mathcal{L}(X_0, X)$

$$\begin{aligned} \sum_{n=1}^{\infty} \left(u_n \sum_{j \in E_n} v_j s_j(RST) \right)^p &\leq \sum_{n=1}^{\infty} \left(u_n \sum_{j \in E_n} \|R\| \|T\| v_j s_j(S) \right)^p \\ &\leq \|R\|^p \|T\|^p \sum_{n=1}^{\infty} \left(u_n \sum_{j \in E_n} v_j s_j(S) \right)^p < \infty \end{aligned}$$

So $RST \in L_{u,v;E}(X_0, Y_0)$.

Therefore $L_{u,v;E}$ is an operator ideal.

Theorem 2. $\|T\|_{u,v;E} = \frac{(\sum_{n=1}^{\infty} (u_n \sum_{j \in E_n} v_j s_j(T))^p)^{\frac{1}{p}}}{u_1 v_1}$ is a quasi-norm on the operator ideal $L_{u,v;E}$.

Proof.

$$\begin{aligned} \frac{(\sum_{n=1}^{\infty} (u_n \sum_{j \in E_n} v_j s_j(x' \otimes y))^p)^{\frac{1}{p}}}{u_1 v_1} &= \frac{(u_1^p v_1^p \|x' \otimes y\|^p)^{\frac{1}{p}}}{u_1 v_1} = \|x' \otimes y\| \\ &= \|x'\| \|y\|. \end{aligned}$$

Since rank of the operator $x' \otimes y$ is one, $s_n(x' \otimes y) = 0$ for $n \geq 2$. Therefore $\|x' \otimes y\|_{u,v;E} = \|x'\| \|y\|$.

Let $S, T \in L_{u,v;E}$. Then

$$\begin{aligned} \sum_{j \in E_n} v_j s_j(S + T) &\leq \sum_{j \in E_n} v_{2j-1} s_{2j-1}(S + T) + \sum_{j \in E_n} v_{2j} s_{2j}(S + T) \\ &\leq \sum_{j \in E_n} (v_{2j-1} + v_{2j}) s_{2j-1}(S + T) \\ &\leq M \sum_{j \in E_n} v_j (s_j(S) + s_j(T)) \end{aligned}$$

By using Minkowski inequality;

$$\begin{aligned} & \left(\sum_{n=1}^{\infty} \left(u_n \sum_{j \in E_n} v_j s_j(S+T) \right)^p \right)^{\frac{1}{p}} \\ & \leq M \left(\sum_{n=1}^{\infty} \left(u_n \sum_{j \in E_n} v_j s_j(S) \right)^p \right)^{\frac{1}{p}} \\ & \quad + M \left(\sum_{n=1}^{\infty} \left(u_n \sum_{j \in E_n} v_j s_j(T) \right)^p \right)^{\frac{1}{p}} < \infty \end{aligned}$$

Hence $\|S+T\|_{u,v;E} \leq M(\|S\|_{u,v;E} + \|T\|_{u,v;E})$.

Let $R \in \mathcal{L}(Y, Y_0)$, $S \in L_{u,v;E}(X, Y)$ and $T \in \mathcal{L}(X_0, X)$

$$\begin{aligned} & \left(\sum_{n=1}^{\infty} \left(u_n \sum_{j \in E_n} v_j s_j(RST) \right)^p \right)^{\frac{1}{p}} \\ & \leq \left(\sum_{n=1}^{\infty} \left(u_n \sum_{j \in E_n} \|R\| \|T\| v_j s_j(S) \right)^p \right)^{\frac{1}{p}} \\ & \leq \|R\| \|T\| \left(\sum_{n=1}^{\infty} \left(u_n \sum_{j \in E_n} v_j s_j(S) \right)^p \right)^{\frac{1}{p}} < \infty \end{aligned}$$

Hence

$$\|RST\|_{u,v;E} \leq \|R\| \|T\| \|S\|_{u,v;E}.$$

Therefore $\|T\|_{u,v;E}$ is a quasi-norm on $L_{u,v;E}$.

Theorem 3. Let $1 \leq p < \infty$. $[L_{u,v;E}, \|T\|_{u,v;E}]$ is a quasi-Banach operator ideal.

Proof: Let X, Y be any two Banach spaces and $1 \leq p < \infty$. The following inequality holds

$$\|T\|_{u,v;E} = \frac{\left(\sum_{n=1}^{\infty} (u_n \sum_{j \in E_n} v_j s_j(T))^p \right)^{\frac{1}{p}}}{u_1 v_1} \geq \|T\|$$

for $T \in L_{u,v;E}$.

Let (T_m) be a Cauchy in $L_{u,v;E}(X, Y)$. Then for every $\varepsilon > 0$ there exists $n_0 \in \mathbb{N}$ such that

$$\|T_m - T_l\|_{u,v;E} < \varepsilon \tag{2.1}$$

For all $m, l \geq n_0$. It follows that

$$\|T_m - T_l\| \leq \|T_m - T_l\|_{u,v;E} < \varepsilon.$$

Then (T_m) is a Cauchy sequence in $\mathcal{L}(X, Y)$. $\mathcal{L}(X, Y)$ is a Banach space since Y is a Banach space. Therefore $\|T_m - T\| \rightarrow 0$ as $m \rightarrow \infty$ for $T \in \mathcal{L}(X, Y)$. Now we show that $\|T_m - T\|_{u,v;E} \rightarrow 0$ as $m \rightarrow \infty$ for $T \in L_{u,v;E}(X, Y)$.

The operators $T_l - T_m, T - T_m$ are in the class $\mathcal{L}(X, Y)$ for $T_m, T_l, T \in \mathcal{L}(X, Y)$.

$$|s_n(T_l - T_m) - s_n(T - T_m)| \leq \|T_l - T_m - (T - T_m)\| = \|T_l - T\|$$

Since $T_l \rightarrow T$ as $l \rightarrow \infty$ that is $\|T_l - T\| < \varepsilon$ we obtain

$$s_n(T_l - T_m) \rightarrow s_n(T - T_m) \text{ as } l \rightarrow \infty. \tag{2.2}$$

It follows from (2.1) that the statement

$$\|T_m - T_l\|_{u,v;E} = \frac{\left(\sum_{n=1}^{\infty} (u_n \sum_{j \in E_n} v_j s_j(T_m - T_l))^p \right)^{\frac{1}{p}}}{u_1 v_1} < \varepsilon$$

holds for all $m, l \geq n_0$. We obtain from (2.2) that

$$\frac{\left(\sum_{n=1}^{\infty} (u_n \sum_{j \in E_n} v_j s_j(T_m - T))^p \right)^{\frac{1}{p}}}{u_1 v_1} < \varepsilon \text{ as } l \rightarrow \infty.$$

Hence we have $\|T_m - T\|_{u,v;E} < \varepsilon$ for all $m \geq n_0$.

Finally we show that $T \in L_{u,v;E}(X, Y)$,

$$\begin{aligned} \sum_{n=1}^{\infty} \left(u_n \sum_{j \in E_n} v_j s_j(T) \right)^p &\leq \sum_{n=1}^{\infty} \left(u_n \sum_{j \in E_n} v_{2j-1} s_{2j-1}(T) \right. \\ &\quad \left. + u_n \sum_{j \in E_n} v_{2j} s_{2j}(T) \right)^p \\ &\leq \sum_{n=1}^{\infty} \left(u_n \sum_{j \in E_n} (v_{2j-1} \right. \\ &\quad \left. + v_{2j}) s_{2j-1}(T - T_m + T_m) \right)^p \\ &\leq M \sum_{n=1}^{\infty} \left(u_n \sum_{j \in E_n} v_j (s_j(T - T_m) + s_j(T_m)) \right)^p \end{aligned}$$

By using Minkowski inequality; since $T_m \in L_{u,v,E}(X, Y)$ for all m and $\|T_m - T\|_{u,v,E} \rightarrow 0$ as $m \rightarrow \infty$, we have

$$\begin{aligned} &M \left(\sum_{n=1}^{\infty} \left(u_n \sum_{j \in E_n} v_j (s_j(T - T_m) + s_j(T_m)) \right)^p \right)^{\frac{1}{p}} \\ &\leq M \left(\sum_{n=1}^{\infty} \left(u_n \sum_{j \in E_n} v_j (s_j(T - T_m)) \right)^p \right)^{\frac{1}{p}} \\ &\quad + M \left(\sum_{n=1}^{\infty} \left(u_n \sum_{j \in E_n} v_j (s_j(T_m)) \right)^p \right)^{\frac{1}{p}} < \infty \end{aligned}$$

which means that $T \in L_{u,v,E}(X, Y)$.

Proposition 1. The inclusion $L_{u,v,E}^p \subseteq L_{u,v,E}^q$ holds for $1 < p \leq q < \infty$.

Proof: Since $l_p \subseteq l_q$ for $1 < p \leq q < \infty$ we have $L_{u,v,E}^p \subseteq L_{u,v,E}^q$.

Let $\mu = (\mu_n(T))$ be one of the sequences $a = (a_n(T))$, $c = (c_n(T))$, $d = (d_n(T))$, $x = (x_n(T))$, $y = (y_n(T))$ and $h = (h_n(T))$. Then we define the space $L_{u,v,E}^{(\mu)}$ and the norm $\|T\|_{u,v,E}^{(\mu)}$ as follows:

$$L_{u,v,E}^{(\mu)}(X, Y) = \left\{ T \in \mathcal{L}(X, Y) : \sum_{n=1}^{\infty} \left(u_n \sum_{j \in E_n} v_j (\mu_j(T)) \right)^p < \infty \right\},$$

$(1 < p < \infty)$

and

$$\|T\|_{u,v,E}^{(\mu)} = \frac{\left(\sum_{n=1}^{\infty} \left(u_n \sum_{j \in E_n} v_j \mu_j(T) \right)^p \right)^{\frac{1}{p}}}{\left(\sum_{n=1}^{\infty} (u_n)^p \right)^{\frac{1}{p}} v_1}.$$

Theorem 4. Let $1 < p < \infty$. The quasi-Banach operator ideal $[L_{u,v,E}^{(s)}, \|T\|_{u,v,E}^{(s)}]$ is injective, if s-number sequence is injective.

Proof. Let $1 < p < \infty$ and $T \in \mathcal{L}(X, Y)$ and $I \in \mathcal{L}(Y, Y_0)$ be any metric injection. Suppose that $IT \in L_{u,v,E}^{(s)}(X, Y_0)$. Then

$$\sum_{n=1}^{\infty} \left(u_n \sum_{j \in E_n} v_j s_j(IT) \right)^p < \infty$$

Since $s = (s_n)$ is injective, we have

$$s_n(T) = s_n(IT) \text{ for all } T \in \mathcal{L}(X, Y), n = 1, 2, \dots \quad (2.3)$$

Hence we get

$$\sum_{n=1}^{\infty} \left(u_n \sum_{j \in E_n} v_j s_j(T) \right)^p = \sum_{n=1}^{\infty} \left(u_n \sum_{j \in E_n} v_j s_j(IT) \right)^p < \infty$$

Thus $T \in L_{u,v,E}^{(s)}(X, Y)$ and we have from (2.3)

$$\begin{aligned} \|IT\|_{u,v,E}^{(s)} &= \frac{\left(\sum_{n=1}^{\infty} \left(u_n \sum_{j \in E_n} v_j s_j(IT) \right)^p \right)^{\frac{1}{p}}}{\left(\sum_{n=1}^{\infty} (u_n)^p \right)^{\frac{1}{p}} v_1} \\ &= \frac{\left(\sum_{n=1}^{\infty} \left(u_n \sum_{j \in E_n} v_j s_j(T) \right)^p \right)^{\frac{1}{p}}}{\left(\sum_{n=1}^{\infty} (u_n)^p \right)^{\frac{1}{p}} v_1} = \|T\|_{u,v,E}^{(s)} \end{aligned}$$

Hence the operator ideal $[L_{u,v,E}^{(s)}, \|T\|_{u,v,E}^{(s)}]$ is injective.

Corollary 1. Since the number sequences $(c_n(T))$ and $(x_n(T))$ are injective, the quasi-

Banach operator ideals $[L_{u,v,E}^{(c)}, \|T\|_{u,v,E}^{(c)}]$ and $[L_{u,v,E}^{(x)}, \|T\|_{u,v,E}^{(x)}]$ are injective [3].

Theorem 5. Let $1 < p < \infty$. The quasi-Banach operator ideal $[L_{u,v,E}^{(s)}, \|T\|_{u,v,E}^{(s)}]$ is surjective, if s -number sequence is surjective.

Proof. Let $1 < p < \infty$ and $T \in \mathcal{L}(X, Y)$ and $S \in \mathcal{L}(X_0, X)$ be any metric injection. Suppose that $TS \in L_{u,v,E}^{(s)}(X_0, Y)$. Then

$$\sum_{n=1}^{\infty} \left(u_n \sum_{j \in E_n} v_j s_j(TS) \right)^p < \infty.$$

Since $s = (s_n)$ is surjective, we have

$$s_n(T) = s_n(TS) \text{ for all } T \in \mathcal{L}(X, Y), n = 1, 2, \dots \quad (2.4)$$

Hence we get

$$\sum_{n=1}^{\infty} \left(u_n \sum_{j \in E_n} v_j s_j(T) \right)^p = \sum_{n=1}^{\infty} \left(u_n \sum_{j \in E_n} v_j s_j(TS) \right)^p < \infty.$$

Thus $T \in L_{u,v,E}^{(s)}(X, Y)$ and we have from (2.4)

$$\begin{aligned} \|TS\|_{u,v,E}^{(s)} &= \frac{\left(\sum_{n=1}^{\infty} \left(u_n \sum_{j \in E_n} v_j s_j(TS) \right)^p \right)^{\frac{1}{p}}}{\left(\sum_{n=1}^{\infty} (u_n)^p \right)^{\frac{1}{p}} v_1} \\ &= \frac{\left(\sum_{n=1}^{\infty} \left(u_n \sum_{j \in E_n} v_j s_j(T) \right)^p \right)^{\frac{1}{p}}}{\left(\sum_{n=1}^{\infty} (u_n)^p \right)^{\frac{1}{p}} v_1} = \|T\|_{u,v,E}^{(s)}. \end{aligned}$$

Hence the operator ideal $[L_{u,v,E}^{(s)}, \|T\|_{u,v,E}^{(s)}]$ is surjective.

Corollary 2. Since the number sequences $(d_n(T))$ and $(y_n(T))$ are surjective, the quasi-Banach operator ideals $[L_{u,v,E}^{(d)}, \|T\|_{u,v,E}^{(d)}]$ and $[L_{u,v,E}^{(y)}, \|T\|_{u,v,E}^{(y)}]$ are surjective [3].

Theorem 6. Let $1 < p < \infty$. Then the following inclusion relations hold:

- i. $L_{u,v,E}^{(a)} \subseteq L_{u,v,E}^{(c)} \subseteq L_{u,v,E}^{(x)} \subseteq L_{u,v,E}^{(h)}$
- ii. $L_{u,v,E}^{(a)} \subseteq L_{u,v,E}^{(d)} \subseteq L_{u,v,E}^{(y)} \subseteq L_{u,v,E}^{(h)}$.

Proof. Let $T \in L_{u,v,E}^{(a)}$. Then

$$\sum_{n=1}^{\infty} \left(u_n \sum_{j \in E_n} v_j s_j(T) \right)^p < \infty$$

where $1 < p < \infty$. And from Proposition 3, we have;

$$\begin{aligned} \sum_{n=1}^{\infty} \left(u_n \sum_{j \in E_n} v_j h_j(T) \right)^p &\leq \sum_{n=1}^{\infty} \left(u_n \sum_{j \in E_n} v_j x_j(T) \right)^p \\ &\leq \sum_{n=1}^{\infty} \left(u_n \sum_{j \in E_n} v_j c_j(T) \right)^p \\ &\leq \sum_{n=1}^{\infty} \left(u_n \sum_{j \in E_n} v_j a_j(T) \right)^p \\ &< \infty \end{aligned}$$

and

$$\begin{aligned} \sum_{n=1}^{\infty} \left(u_n \sum_{j \in E_n} v_j h_j(T) \right)^p &\leq \sum_{n=1}^{\infty} \left(u_n \sum_{j \in E_n} v_j y_j(T) \right)^p \\ &\leq \sum_{n=1}^{\infty} \left(u_n \sum_{j \in E_n} v_j d_j(T) \right)^p \\ &\leq \sum_{n=1}^{\infty} \left(u_n \sum_{j \in E_n} v_j a_j(T) \right)^p \\ &< \infty. \end{aligned}$$

So it is shown that the inclusion relations are satisfied.

Theorem 7. The operator ideal $L_{u,v,E}^{(a)}$ is symmetric and the operator ideal $L_{u,v,E}^{(h)}$ is completely symmetric for $1 < p < \infty$.

Proof. Let $1 < p < \infty$.

3. REFERENCES

Firstly, we prove that the inclusion $L_{u,v,E}^{(a)} \subseteq (L_{u,v,E}^{(a)})'$ holds. Let $T \in L_{u,v,E}^{(a)}$. Then

$$\sum_{n=1}^{\infty} \left(u_n \sum_{j \in E_n} v_j a_j(T) \right)^p < \infty.$$

It follows from [2] $a_n(T') \leq a_n(T)$ for $T \in \mathcal{L}$. Hence we get

$$\sum_{n=1}^{\infty} \left(u_n \sum_{j \in E_n} v_j a_j(T') \right)^p \leq \sum_{n=1}^{\infty} \left(u_n \sum_{j \in E_n} v_j a_j(T) \right)^p < \infty.$$

Therefore $T \in (L_{u,v,E}^{(a)})'$. Thus $L_{u,v,E}^{(a)}$ is symmetric.

Now we prove that the equation $L_{u,v,E}^{(h)} = (L_{u,v,E}^{(h)})'$ holds. It follows from [3] that $h_n(T') = h_n(T)$ for $T \in \mathcal{L}$. Then we can write

$$\sum_{n=1}^{\infty} \left(u_n \sum_{j \in E_n} v_j h_j(T') \right)^p = \sum_{n=1}^{\infty} \left(u_n \sum_{j \in E_n} v_j h_j(T) \right)^p.$$

Hence $L_{u,v,E}^{(h)}$ is completely symmetric.

Theorem 8 Let $1 < p < \infty$. The equation $L_{u,v,E}^{(c)} = (L_{u,v,E}^{(d)})'$ and the inclusion relation $L_{u,v,E}^{(d)} \subseteq (L_{u,v,E}^{(c)})'$ holds. Also, the equation $L_{u,v,E}^{(d)} = (L_{u,v,E}^{(c)})'$ holds for any compact operators.

Proof. Let $1 < p < \infty$. For $T \in \mathcal{L}$ we have from [3] that $c_n(T) = d_n(T')$ and $c_n(T') \leq d_n(T)$. Also, if T is a compact operator, then the equality $c_n(T') = d_n(T)$ holds. Thus the proof is clear.

Theorem 9 $L_{u,v,E}^{(x)} = (L_{u,v,E}^{(y)})'$ and $L_{u,v,E}^{(y)} = (L_{u,v,E}^{(x)})'$ hold.

Proof. Let $1 < p < \infty$. For $T \in \mathcal{L}$ we have from [3] that $x_n(T) = y_n(T')$ and $y_n(T) = x_n(T')$. Thus the proof is clear.

[1] A. Pietsch, "s-Numbers of operators in Banach spaces," *Studia Mathematica*, vol. 51, no. 3, pp. 201-223, 1974.

[2] A. Pietsch, "Operator Ideals," VEB Deutscher Verlag der Wissenschaften, Berlin, 1978.

[3] A. Pietsch, "Eigenvalues and s-numbers," Cambridge University Press, New York, 1986.

[4] A. Maji, P.D. Srivastava, "On operator ideals using weighted Cesàro sequence space," *Journal of the Egyptian Mathematical Society*, vol. 22, no. 3, pp. 446-452, 2014.

[5] B. Carl, A. Hinrichs, "On s-numbers and Weyl inequalities of operators in Banach spaces," *Bulletin of the London Mathematical Society*, vol. 41, no. 2, pp. 332-340, 2009.

[6] A. Pietsch, "Einige neu Klassen von Kompakten linearen Abbildungen," *Romanian Journal of Pure and Applied Mathematics*, vol. 8, pp. 427-447, 1963.

[7] J. Burgoyne, "Denseness of the generalized eigenvectors of a discrete operator in a Banach space," *Journal of Operator Theory*, vol. 33, pp. 279-297, 1995.

[8] S. Saejung, "Another look at Cesaro sequence spaces," *Journal of Mathematical Analysis and Applications*, vol. 366, no. 2, pp. 530-537, 2010.

[9] J. S. Shiue, "On the Cesaro sequence spaces," *Tamkang Journal of Mathematics*, vol. 1, no. 1, pp. 19-25, 1970.

[10] N. Şimşek, V. Karakaya, H. Polat, "Operators ideals of generalized modular spaces of Cesaro type defined by weighted means," *Journal of Computational Analysis and Applications*, vol. 19, no. 1, pp. 804-811, 2015.

[11] G. Constantin "Operators of ces-p-type," *Atti Della Accademia Nazionale dei Lincei Rendiconti-classe di Scienze Fisiche-Matematiche & Naturali*, vol. 52, no. 6, pp.875-878, 1973.

[12] N. Tita, "On Stolz mappings," *Mathematica Japonica*, vol. 26, no. 4, pp. 495–496, 1981.

[13] E. E. Kara, M. İlkhán, "On a new class of s-type operators," *Konuralp Journal of Mathematics*, vol. 3, no. 1, pp. 1-11, 2015.

[14] A. Maji, P.D. Srivastava, "Some class of operator ideals," *International Journal of Pure and Applied Mathematics*, vol. 83, no. 5, pp. 731-740, 2013.

[15] A. Maji, P.D. Srivastava, "Some results of operator ideals on s-type $|A, p|$ operators," *Tamkang Journal of Mathematics*, vol. 45, no. 2, pp. 119-136, 2014.

[16] D. Foroutannia, "On the block sequence space $lp(E)$ and related matrix transformations," *Turkish Journal of Mathematics*, vol. 39, pp. 830-841, 2015.

[17] H Roopaei, D Foroutannia, "The norm of certain matrix operators on new difference sequence spaces," *Jordan Journal of Mathematics and Statistics*, vol. 8, no. 3, pp. 223 - 237, 2015.

[18] H. Roopaei, D Foroutannia, "A new sequence space and norm of certain matrix operators on this space," *Sahand Communications in Mathematical Analysis (SCMA)*, vol. 3, no. 1, pp. 1-12, 2016.

JOURNAL OF SCIENCE



SAKARYA UNIVERSITY

Sakarya University Journal of Science

ISSN 1301-4048 | e-ISSN 2147-835X | Period Bimonthly | Founded: 1997 | Publisher Sakarya University |
<http://www.saujs.sakarya.edu.tr/>

Title: A New Type of Canal Surface in Euclidean 4-Space E^4

Authors: İlim Kişi, Günay Öztürk, Kadri Arslan

Received: 2019-02-08 14:24:10

Accepted: 2019-03-27 09:01:34

Article Type: Research Article

Volume: 23

Issue: 5

Month: October

Year: 2019

Pages: 801-809

How to cite

İlim Kişi, Günay Öztürk, Kadri Arslan; (2019), A New Type of Canal Surface in Euclidean 4-Space E^4 . Sakarya University Journal of Science, 23(5), 801-809,

DOI: 10.16984/saufenbilder.524471

Access link

<http://www.saujs.sakarya.edu.tr/issue/44066/524471>

New submission to SAUJS

<http://dergipark.gov.tr/journal/1115/submission/start>

İlim Kişi^{*1}, Günay Öztürk², Kadri Arslan³

ABSTRACT

We give, with its sample, a new type of canal surface constructed by means of the parallel transport frame of its spine curve in Euclidean 4-space IE^4 . We investigate the curvature features of this surface with respect to the principal curvature functions according to parallel transport frame. Further, we give certain results about Weingarten type canal and tube surfaces. Finally, we give the visualizations of projections of this new type of canal surface in IE^3 for various radius functions.

Keywords: Gaussian curvature, mean curvature, parallel transport frame, Weingarten surface

1. INTRODUCTION

Given a space curve γ called spine curve, a canal surface associated to this curve is defined as a surface swept by a family of spheres of varying radius $r(u)$. If $r(u)$ is constant, the canal surface is a tubular (tube, pipe) surface.

Actually, the concept of canal surface is a generalization of an offset of a planar curve. In [11], do Carmo gives some geometrical properties of tube surfaces and by means of these surfaces proves the theorems named as Fenchel's theorem and the Fary-Milnor theorem.

Apart from being used in pure mathematics, canal surfaces are widely used in many areas especially in CAGD, e.g. construction of blending surfaces, i.e. canal surface with a rational radius, shape reconstruction or robotic path planning (see, [21, 23]). Canal surfaces are also useful in visualising

long thin objects such as poles, 3D fonts, brass instruments, or visceral organs of the body.

Tori, Dupin cyclids in [22] and tube surfaces in [18] are the special types of the canal surfaces.

Given a surface M in an Euclidean 3-space IE^3 and its two principal curvatures κ_1 and κ_2 , M is a Weingarten surface under the condition that there is a smooth relation $U(\kappa_1, \kappa_2) = 0$. If K and H denote respectively the Gaussian and the mean curvatures of M , $U(\kappa_1, \kappa_2) = 0$ refers to $\Phi(K, H) = 0$, which is equivalent to $\frac{\partial(K, H)}{\partial(u, v)} = K_u H_v - K_v H_u = 0$. Also, if the surface satisfies the equation $aK + bH = c$ for the non-zero real numbers a, b, c , then it is called as a linear Weingarten surface [20].

Frenet-Serret frame gives way to the study of curves in classical differential geometry in

* Corresponding Author

¹ Kocaeli University, Faculty of Arts and Sciences, Mathematics, (ilim.ayvaz@kocaeli.edu.tr) ORCID: 0000-0002-4785-8165

² İzmir Demokrasi University, Faculty of Arts and Sciences, Mathematics, ORCID: 0000-0002-1608-0354

³ Uludağ University, Faculty of Arts and Sciences, Mathematics, ORCID: 0000-0002-1440-7050

Euclidean space. However, the Frenet frame can not be constructed at the points in which curvature vanishes. Hence, an alternative frame is needed. In [6], Bishop defines a new frame for a curve and calls it Bishop frame, which is well defined even if the curve's second derivative in 3-dimensional Euclidean space vanishes. In [6, 16], the advantages of the Bishop frame and the comparison of Bishop frame with the Frenet frame in Euclidean 3-space are given. Euclidean 4-space IE^4 has the same problem as Euclidean 3-space. That is, one of the i -th ($1 < i < 4$) derivatives of the curve may be zero.

In [14], using the similar idea, authors consider such curves and construct an alternative frame. They give parallel transport frame of a curve in IE^4 . They generalize the notion which is well known in Euclidean 3-space for 4-dimensional Euclidean space IE^4 .

In [1-5, 8, 10, 12, 15, 19, 25], authors give some characteristic properties of surfaces in IE^4 . Furthermore, in [9, 17] authors consider canal surfaces in IE^4 .

In the present study, we consider a canal surface constructed with parallel transport frame of its spine curve in Euclidean 4-space IE^4 .

This paper is organized as in the following: Section 2 gives certain preliminaries of a curve and a surface in IE^4 . Section 3 introduces a new type of canal surface and give some curvature conditions of this surface in IE^4 . Section 4 gives some visualizations of projections of canal surfaces in IE^3 for various radius functions. The figures presented in this paper are generated via the Maple programme.

2. BASIC CONCEPTS

Given a unit speed curve $\gamma : I \subseteq \mathbb{R} \rightarrow IE^4$ for an interval I in \mathbb{R} , the derivative formulas of Frenet frame are

$$\begin{bmatrix} T' \\ N' \\ B_1' \\ B_2' \end{bmatrix} = \begin{bmatrix} 0 & \kappa & 0 & 0 \\ -\kappa & 0 & \tau & 0 \\ 0 & -\tau & 0 & \sigma \\ 0 & 0 & -\sigma & 0 \end{bmatrix} \begin{bmatrix} T \\ N \\ B_1 \\ B_2 \end{bmatrix},$$

where $\{T, N, B_1, B_2\}$ is the Frenet frame of γ , and κ , τ and σ are principal curvature functions related to this frame of the curve γ , respectively.

In [14], authors use the same tangent vector $T(s)$ as in Frenet frame for the first vector, and for the other vectors of the new frame they use relatively parallel vector fields $M_1(s)$, $M_2(s)$, and $M_3(s)$ to construct an alternative frame. They call this frame a parallel transport frame along the curve γ . Then they give the following theorem for a parallel transport frame.

Theorem 2.1. [14] Let $\{T, N, B_1, B_2\}$ be the Frenet frame and $\{T, M_1, M_2, M_3\}$ the parallel transport frame along a unit speed curve $\gamma : I \subseteq \mathbb{R} \rightarrow IE^4$. The relation between these frames may be expressed as

$$\begin{aligned} T &= T, \\ N &= \cos \theta(s) \cos \psi(s) M_1 \\ &+ (-\cos \varphi(s) \sin \psi(s) + \sin \varphi(s) \sin \theta(s) \cos \psi(s)) M_2 \\ &+ (\sin \varphi(s) \sin \psi(s) + \cos \varphi(s) \sin \theta(s) \cos \psi(s)) M_3, \\ B_1 &= \cos \theta(s) \sin \psi(s) M_1 \\ &+ (\cos \varphi(s) \cos \psi(s) + \sin \varphi(s) \sin \theta(s) \sin \psi(s)) M_2 \\ &+ (-\sin \varphi(s) \cos \psi(s) + \cos \varphi(s) \sin \theta(s) \sin \psi(s)) M_3, \\ B_2 &= -\sin \theta(s) M_1 + \sin \varphi(s) \cos \theta(s) M_2 \\ &+ \cos \varphi(s) \cos \theta(s) M_3, \end{aligned} \quad (1)$$

where θ , ψ and φ are the Euler angles. Then the alternative parallel frame equations are

$$\begin{bmatrix} T' \\ M_1' \\ M_2' \\ M_3' \end{bmatrix} = \begin{bmatrix} 0 & k_1 & k_2 & k_3 \\ -k_1 & 0 & 0 & 0 \\ -k_2 & 0 & 0 & 0 \\ -k_3 & 0 & 0 & 0 \end{bmatrix} \begin{bmatrix} T \\ M_1 \\ M_2 \\ M_3 \end{bmatrix}, \quad (2)$$

where k_1, k_2, k_3 are principal curvature functions according to parallel transport frame of the curve γ and their expressions are as follows:

$$\begin{aligned} k_1 &= \kappa_1 \cos \theta \cos \psi, \\ k_2 &= \kappa_1 (-\cos \phi \sin \psi + \sin \phi \sin \theta \cos \psi), \\ k_3 &= \kappa_1 (\sin \phi \sin \psi + \cos \phi \sin \theta \cos \psi), \end{aligned}$$

where

$$\begin{aligned} \theta' &= \frac{\sigma}{\sqrt{\kappa^2 + \tau^2}}, \\ \psi' &= -\tau - \sigma \frac{\sqrt{\sigma^2 - (\theta')^2}}{\sqrt{\kappa^2 + \tau^2}}, \\ \phi' &= -\frac{\sqrt{\sigma^2 - (\theta')^2}}{\cos \theta}, \end{aligned}$$

and the following equalities

$$\begin{aligned} \kappa &= \sqrt{k_1^2 + k_2^2 + k_3^2}, \\ \tau &= -\psi' + \phi' \sin \theta, \\ \sigma &= \frac{\theta'}{\sin \psi}, \\ \phi' \cos \theta + \theta' \cot \psi &= 0 \end{aligned}$$

are hold.

Given a regular surface M in IE^4 with the parametrization $X(u, v) : (u, v) \in D \subset IE^2$, at any point $p=X(u, v)$, the vectors X_u and X_v span the tangent space of M . Then the first fundamental form's coefficients are computed as

$$E = \langle X_u, X_u \rangle, \quad F = \langle X_u, X_v \rangle, \quad G = \langle X_v, X_v \rangle. \quad (3)$$

Here, \langle , \rangle is the Euclidean dot product. For the regularity of the surface patch $X(u, v)$, $W^2 = EG - F^2 \neq 0$.

At any point p in M , there is a decomposition $T_p IE^4 = T_p M + T_p^\perp M$, where $T_p^\perp M$ is the orthogonal component of $T_p M$ in IE^4 . Let $\tilde{\nabla}$ be the Riemannian connection of IE^4 . Then the induced Riemannian connection on M for any

given local vector fields X_1, X_2 tangent to M is defined as

$$\nabla_{X_i} X_j = (\tilde{\nabla}_{X_i} X_j)^T, \quad (4)$$

where T represents the tangential component.

Let $\chi(M)$ and $\chi^\perp(M)$ be the spaces of the smooth vector fields tangent and normal to M , respectively. The second fundamental map is defined as follows:

$$\begin{aligned} h : \chi(M) \times \chi(M) &\rightarrow \chi^\perp(M) \\ h(X_i, X_j) &= \tilde{\nabla}_{X_i} X_j - \nabla_{X_i} X_j, \quad 1 \leq i, j \leq 2. \end{aligned} \quad (5)$$

This map is well-defined, symmetric, and bilinear.

Proposition 2.2. [7] Let M be a surface in IE^4 given with the parametrization $X(u, v)$. If the coefficient of the first fundamental form $F=0$, the second fundamental form of M becomes

$$\begin{aligned} h(X_u, X_u) &= X_{uu} - \frac{1}{E} \langle X_{uu}, X_u \rangle X_u + \frac{1}{G} \langle X_{uv}, X_u \rangle X_v, \\ h(X_u, X_u) &= X_{uv} - \frac{1}{E} \langle X_{uv}, X_u \rangle X_u - \frac{1}{G} \langle X_{uv}, X_v \rangle X_v, \\ h(X_u, X_u) &= X_{vv} + \frac{1}{E} \langle X_{uv}, X_v \rangle X_u - \frac{1}{G} \langle X_{vv}, X_v \rangle X_v. \end{aligned} \quad (6)$$

Proposition 2.3. [7] Let M be a surface in IE^4 given with the parametrization $X(u, v)$. Then for the basis X_u, X_v of $T_p(M)$ the Gaussian curvature and the mean curvature vector of M are defined as follows respectively,

$$K = \frac{1}{W^2} (\langle h(X_u, X_u), h(X_v, X_v) \rangle - \langle h(X_u, X_v), h(X_u, X_v) \rangle) \quad (7)$$

and

$$\tilde{H} = \frac{1}{2W^2} (Eh(X_v, X_v) - 2Fh(X_u, X_v) + Gh(X_u, X_u)), \quad (8)$$

where $W^2 = EG - F^2$.

3. CANAL SURFACE ACCORDING TO PARALLEL TRANSPORT FRAME IN IE^4

In [13], authors give the following parametrization for a canal surface:

$$M : X(u, v) = \gamma(u) + r(u)(B_1(u) \cos v + B_2(u) \sin v),$$

where $\gamma = \gamma(u)$ is a space curve parametrized by

arclength with the Frenet frame $\{T(u), N(u), B_1(u), B_2(u)\}$.

Using the similar idea, we give the following parametrization:

$$M: X(u, v) = \gamma(u) + r(u)(M_2(u) \cos v + M_3(u) \sin v), \quad (9)$$

where $r(u)$ is a differentiable function and $\{T(u), M_1(u), M_2(u), M_3(u)\}$ is parallel transport frame of the curve γ in IE^4 .

Corollary 3.1. Let $\{T, N, B_1, B_2\}$ be the Frenet frame and $\{T, M_1, M_2, M_3\}$ the parallel transport frame along a unit speed curve $\gamma = \gamma(s) : I \rightarrow IE^4$. Then, the parallel transport frame vectors can be given as follows:

$$\begin{aligned} T &= T, \\ M_1 &= \cos \theta(u) \cos \psi(u)N \\ &+ \cos \theta(u) \sin \psi(u)B_1 - \sin \theta(u)B_2, \\ M_2 &= (-\cos \phi(u) \sin \psi(u) + \sin \phi(u) \sin \theta(u) \cos \psi(u))N \\ &+ (\cos \phi(u) \cos \psi(u) + \sin \phi(u) \sin \theta(u) \sin \psi(u))B_1 \\ &+ \sin \phi(u) \cos \theta(u)B_2, \\ M_3 &= (\sin \phi(u) \sin \psi(u) + \cos \phi(u) \sin \theta(u) \cos \psi(u))N \\ &+ (-\sin \phi(u) \cos \psi(u) + \cos \phi(u) \sin \theta(u) \sin \psi(u))B_1 \\ &+ \cos \phi(u) \cos \theta(u)B_2. \end{aligned}$$

Proof. If the equations (1) is written in the matrix form, the transition matrix is obtained as follows:

$$\begin{bmatrix} 1 & 0 & 0 & 0 \\ 0 & \cos \theta \cos \psi & -\cos \phi \sin \psi + \sin \phi \sin \theta \cos \psi & \sin \phi \sin \psi + \cos \phi \sin \theta \cos \psi \\ 0 & \cos \theta \sin \psi & \cos \phi \cos \psi + \sin \phi \sin \theta \sin \psi & -\sin \phi \cos \psi + \cos \phi \sin \theta \sin \psi \\ 0 & -\sin \theta & \sin \phi \cos \theta & \cos \phi \cos \theta \end{bmatrix}.$$

By calculating the inverse of this transition matrix, we write the desired result.

Example 3.2. Consider the unit speed curve $\gamma(u) = (a \cos cu, a \sin cu, b \cos du, b \sin du)$ in IE^4 , where $a^2c^2 + b^2d^2 = 1$. Then the canal surface associated to the spine curve γ in IE^4 has the following parametrization

$$\begin{aligned} X(u, v) = & \left\{ a \cos cu + \frac{r(u)}{4\kappa} \left\{ (ac^2 \cos cu + \sqrt{3}\kappa bd \sin cu - 2\sqrt{3}bd^2 \cos cu) \cos v \right. \right. \\ & \left. \left. + (-\sqrt{3}ac^2 \cos cu - 3\kappa bd \sin cu - 2bd^2 \cos cu) \sin v \right\}, \right. \\ & a \sin cu + \frac{r(u)}{4\kappa} \left\{ (ac^2 \sin cu - \sqrt{3}\kappa bd \cos cu - 2\sqrt{3}bd^2 \sin cu) \cos v \right. \\ & \left. \left. + (-\sqrt{3}ac^2 \sin cu + 3\kappa bd \cos cu - 2bd^2 \sin cu) \sin v \right\}, \right. \\ & b \cos du + \frac{r(u)}{4\kappa} \left\{ (bd^2 \cos du - \sqrt{3}\kappa ac \sin du + 2\sqrt{3}ac^2 \cos du) \cos v \right. \\ & \left. \left. + (-\sqrt{3}bd^2 \cos du + 3\kappa ac \sin du + 2ac^2 \cos du) \sin v \right\}, \right. \\ & \left. b \sin du + \frac{r(u)}{4\kappa} \left\{ (bd^2 \sin du + \sqrt{3}\kappa ac \cos du + 2\sqrt{3}ac^2 \sin du) \cos v \right. \right. \\ & \left. \left. + (-\sqrt{3}bd^2 \sin du - 3\kappa ac \cos du + 2ac^2 \sin du) \sin v \right\} \right\} \end{aligned}$$

where $\kappa = \sqrt{k_1^2 + k_2^2 + k_3^2}$, $0 \leq u \leq 2\pi$, a, b, c, d are real constants and $c, d > 0$.

The tangent space of M is spanned by the vectors

$$\begin{aligned} X_u &= fT + r' \cos v M_2 + r' \sin v M_3, \\ X_v &= -r \sin v M_2 + r \cos v M_3, \end{aligned} \quad (10)$$

where

$$f(u, v) = 1 - k_2(u)r(u) \cos v - k_3(u)r(u) \sin v. \quad (11)$$

Thus, the coefficients of the first fundamental form become

$$\begin{aligned} E &= \langle X_u, X_u \rangle = f^2 + (r')^2, \\ F &= \langle X_u, X_v \rangle = 0, \\ G &= \langle X_v, X_v \rangle = r^2. \end{aligned} \quad (12)$$

Proposition 3.3. Let M be a canal surface according to parallel transport frame given with the parametrization (9) in IE^4 . Then for all $p \in M$, the surface patch of M is regular if and only if $r^2(f^2 + (r')^2) \neq 0$.

Proof. Assume that the surface patch is regular. Then from the equations (12), $W^2 = r^2(f^2 + (r')^2) \neq 0$. Conversely, if the condition holds, it is easy to see that the surface patch is regular.

The second partial derivatives of $X(u, v)$ are expressed as follows:

$$\begin{aligned} X_{uu} &= gT + fk_1M_1 + (fk_2 + r'' \cos v)M_2 + (f(k_3 + r'' \sin v)M_3, \\ X_{uv} &= f_vT - r' \sin v M_2 + r' \cos v M_3, \\ X_{vv} &= -r \cos v M_2 - r \sin v M_3 \end{aligned} \quad (13)$$

where

$$g = g(u, v) = f_u(u, v) - k_2(u)r'(u) \cos v - k_3(u)r'(u) \sin v. \quad (14)$$

Hence, from the equations (10) and (13), we get

$$\begin{aligned} \langle X_{uu}, X_u \rangle &= ff_u + r'r'', \\ \langle X_{uv}, X_u \rangle &= ff_v, \\ \langle X_{uv}, X_v \rangle &= rr', \\ \langle X_{uv}, X_v \rangle &= 0. \end{aligned} \tag{15}$$

Further, by the use of the equations (10), (12), and (15), the second fundamental form of M becomes

$$\begin{aligned} h(X_u, X_u) &= \frac{1}{r(f^2 + (r')^2)} (f^2 r'(f - 1) - rr'(fr'' - gr'))T \\ &\quad + fk_1 M_1 \\ &\quad + \frac{f \cos v}{r(f^2 + (r')^2)} (f^2 - f^3 + r(fr'' - gr'))M_2 \\ &\quad + \frac{f \sin v}{r(f^2 + (r')^2)} (f^2 - f^3 + r(fr'' - gr'))M_3, \end{aligned} \tag{16}$$

$$h(X_u, X_v) = \frac{f_v r'}{f^2 + (r')^2} (r'T - f \cos v M_2 - f \sin v M_3) \tag{17}$$

$$h(X_v, X_v) = \frac{fr}{f^2 + (r')^2} (r'T - f \cos v M_2 - f \sin v M_3). \tag{18}$$

From the equations (15)-(17), we get the following result:

Proposition 3.7. Let M be a canal surface according to parallel transport frame given with the parametrization (9) in IE^4 . Then the Gaussian curvature of M at point p is

$$K = \frac{1}{r^2(f^2 + (r')^2)^2} (f^4 - f^3 - fr(fr'' - gr') - f_v^2(r')^2). \tag{19}$$

As a consequence of (19), we obtain the following result:

Corollary 3.8. Let M be a tube surface with constant $r = r(u)$. Then the Gaussian curvature of M becomes

$$K = -\frac{k_2 \cos v + k_3 \sin v}{fr} = \frac{f - 1}{fr^2}. \tag{20}$$

Proposition 3.9. Let M be a canal surface according to parallel transport frame given with the parametrization (9) in IE^4 . If γ is a straight line, then the Gaussian curvature of M at point p is

$$K = -\frac{r''}{r(1 + (r')^2)^2}. \tag{21}$$

Proof. Let γ be a straight line. Then the curvatures k_1, k_2, k_3 of γ are identically zero. By (11) and (14), we find $f=1, g=0$ which shows that the equation (21) holds.

Corollary 3.10. Let M be a canal surface according to parallel transport frame given with the parametrization (9) in IE^4 . When γ is a straight line, the surface M is flat if and only if r is a linear function of the form $r(u)=au+b$ for some real constants a, b.

Proposition 3.11. Let M be a canal surface according to parallel transport frame given with the parametrization (9) in IE^4 . Then the mean curvature vector of M at point p is

$$\begin{aligned} \bar{H} &= \frac{1}{2r(f^2 + (r')^2)^2} \{ (fr'(f^2 + (r')^2) - rr'(fr'' - gr') - f^2 r'(1 - f))T \\ &\quad + frk_1(f^2 + (r')^2)M_1 \\ &\quad + (-f^2 \cos v(f^2 + (r')^2) + f^3 \cos v(1 - f) + fr(fr'' - gr') \cos v)M_2 \\ &\quad + (-f^2 \sin v(f^2 + (r')^2) + f^3 \sin v(1 - f) + fr(fr'' - gr') \sin v)M_3 \}. \end{aligned} \tag{22}$$

Proof. Substituting the equations (16)-(18) into (6), we obtain the vector given in (22).

Corollary 3.12. Let M be a canal surface according to parallel transport frame given with the parametrization (9) in IE^4 . Then the mean curvature of M at point p is

$$H = \frac{1}{2r(f^2 + (r')^2)^{3/2}} \left(\begin{aligned} &f^2(f^2 + (r')^2)^2 - 2fr'^2(fr'' - gr') \\ &- 2f^3(f^2 + (r')^2)(1 - f) + r^2(fr'' - gr')^2 \\ &+ 2f^2r(fr'' - gr') + f^4(1 - f)^2 \\ &+ f^2r^2k_1^2(f^2 + (r')^2) - 4f^3r(fr'' - gr') \end{aligned} \right)^{1/2}.$$

Corollary 3.13. Let M be a tube surface with constant $r = r(u)$. Then the mean curvature vector of M becomes

$$\bar{H} = \frac{1}{2fr} (rk_1 M_1 + \cos v(-2f + 1)M_2 + \sin v(-2f + 1)M_3). \tag{23}$$

Corollary 3.14. Let M be a tube surface with constant $r = r(u)$. Then the mean curvature of M at point p is

$$H = \frac{1}{2fr} (4f^2 - 4f + r^2 k_1^2 + 1)^{1/2}. \quad (24)$$

Proposition 3.15. Let M be a canal surface according to parallel transport frame given with the parametrization (9) in IE^4 . If γ is a straight line, then the mean curvature vector of M at point p is

$$\bar{H} = \frac{1 + (r')^2 - rr''}{2r(1 + (r')^2)^{3/2}} (r'T - \cos v M_2 - \sin v M_3). \quad (25)$$

Proof. Let γ be a straight line. Then the curvatures k_1, k_2, k_3 of γ are identically zero. By (11) and (14), we find $f=1, g=0$ which shows that the equation (25) holds.

Corollary 3.16. Let M be a canal surface according to parallel transport frame given with the parametrization (9) in IE^4 . If γ is a straight line, then the mean curvature of M at point p is

$$H = \frac{1 + (r')^2 - rr''}{2r(1 + (r')^2)^{3/2}}. \quad (26)$$

Proposition 3.17. Let M be a canal surface according to parallel transport frame given with the parametrization (9) in IE^4 . If γ is a straight line, the surface M is minimal if and only if

$$2r + 2\sqrt{r^2 - c_1^2} = e^{\frac{u+c_2}{c_1}}.$$

Proof. Let M is minimal. Then from the equation (26), $1 + (r')^2 - rr'' = 0$. If we take $r' = p(u)$, the last equation becomes

$$\frac{dr}{r} = \frac{pdp}{p^2 + 1}. \quad (27)$$

The solution of the equation (27) is as follows:

$$r^2 = c_1^2(p^2 + 1).$$

Again taking $p(u) = r'$, we obtain the following ordinary differential equation:

$$\frac{dr}{\sqrt{r^2 - c_1^2}} = \frac{du}{c_1}.$$

Integrating both sides of the last equation, we get the solution.

As a consequence of (25), we obtain the following result:

Proposition 3.18. Let M be a tube surface with constant $r = r(u)$. If γ is a straight line, the mean curvature vector of M at point p is

$$\bar{H} = \frac{1}{2r} (-\cos v M_2 - \sin v M_3).$$

Corollary 3.19. Let M be a tube surface with constant $r = r(u)$. If γ is a straight line, M has constant mean curvature of the form

$$H = \frac{1}{2r}.$$

Proposition 3.20. Let M be a tube surface with constant $r = r(u)$ in IE^4 . If γ is a straight line, then M is a Weingarten surface.

Proof. Considering the equations (21) and (26), we see that K and H are the functions of the variable u . Thus

$$K_v = 0 = H_v,$$

which means $K_u H_v - K_v H_u = 0$.

Proposition 3.21. Let M be a tube surface with constant $r = r(u)$ in IE^4 . M is a Weingarten surface if and only if one of the three conditions holds:

- i) The first curvature function of the spine curve γ vanishes, i.e., $k_1 = 0$.
- ii) The first curvature function of the spine curve γ is constant, i.e., $(k_1)_u = 0$.
- iii) For the second and the third curvatures of the spine curve γ , the equation

$$\frac{k_3(u)}{k_2(u)} = \tan v = c, \quad c \in \mathbb{R}$$

holds.

Proof. By using the equations (20) and (24), we obtain

$$K_u = \frac{f_u}{f^2 r^2}, \quad K_v = \frac{f_v}{f^2 r^2}, \quad (28)$$

and

$$H_u = \frac{1}{4f^2 r^2} \left\{ \begin{array}{l} fr(4f^2 - 4f + r^2 k_1^2 + 1)^{-1/2} (8ff_u - 4f_u + 2r^2 k_1(k_1)_u) \\ - 2f_u r(4f^2 - 4f + r^2 k_1^2 + 1)^{1/2} \end{array} \right\}$$

$$H_v = \frac{1}{4f^2 r^2} \left\{ \begin{array}{l} fr(4f^2 - 4f + r^2 k_1^2 + 1)^{-1/2} (8ff_v - 4f_v) \\ - 2f_v r(4f^2 - 4f + r^2 k_1^2 + 1)^{1/2} \end{array} \right\}. \quad (29)$$

Thus,

$$K_u H_v - K_v H_u = 0 \Leftrightarrow k_1(k_1)_u f_v = 0,$$

which yields the expected result.

Proposition 3.22. Let M be a tube surface with constant $r = r(u)$. If γ is a straight line, M is a linear Weingarten surface.

Proof. Assume that M is a tube surface with constant $r = r(u)$ in IE^4 and γ is a straight line.

Then we know that $K=0$ and $H = \frac{1}{2r}$. For the non-zero real numbers a, b, c , we get

$$a \cdot 0 + b \cdot \frac{1}{2r} = c,$$

which has the solution $(a, 2rc, c)$, $a, c \in \mathbb{R} - \{0\}$.

4. VISUALIZATION

Canal surfaces are very popular in geometric modeling. In this section, we visualize the surfaces given with the patch

$$X(u, v) = (x(u, v), y(u, v), z(u, v), w(u, v))$$

in IE^4 by the use of Maple program. We plot the graph of the projection of the given surface by using maple plotting command

$$\text{plot3d}([x, y, z + w], u = a..b, v = c..d). \quad (30)$$

After than, we construct some 3D geometric shape models by using the canal surfaces defined in Example 3.2. for the following values;

a) $r(u) = 2u + 6$,

b) $r(u) = u^2$,

c) $r(u) = \cos(u^2)$.

We plot the graph of the projection of these surfaces in IE^3 by the use of plotting command (30). (see, Figure 1, Figure 2, Figure 3).

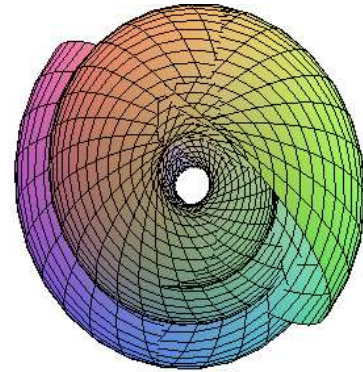


Figure 1: Canal surface with $r(u) = 2u + 6$

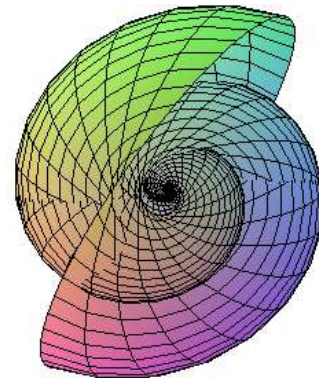


Figure 2: Canal surface with $r(u) = u^2$

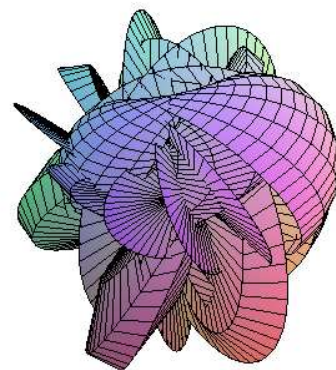


Figure 3: Canal surface with $r(u) = \cos(u^2)$

REFERENCES

- [1] K. Arslan, B. (Kılıç) Bayram, B. Bulca, G. Öztürk, "On translation surfaces in 4-dimensional Euclidean space," *Acta et Commentationes Universitatis Tartuensis de Mathematica*, vol. 20, no. 2, pp. 123-133, 2016.
- [2] K. Arslan, B. Bayram, B. Bulca, G. Öztürk, "Generalized rotation surfaces in IE^4 ," *Results in Mathematics*, vol. 61, pp. 315-327, 2012.
- [3] K. Arslan, B. Bulca, B. (Kılıç) Bayram, G. Öztürk, "Normal transport surfaces in Euclidean 4-space IE^4 ," *Differential Geometry-Dynamical Systems*, vol. 17, pp. 13-23, 2015.
- [4] P. Bayard and F. Sanchez-Bringas, "Geometric invariants of surfaces in IR^4 ," *Topology and its Applications*, vol. 159, no. 2, pp. 405-413, 2012.
- [5] B. Bayram, B. Bulca, K. Arslan, and G. Öztürk, "Superconformal ruled surfaces in IE^4 ," *Mathematical Communications*, vol. 14, pp. 235-244, 2009.
- [6] L.R. Bishop, "There is more than one way to frame a curve," *Amer. Math. Monthly*, vol. 82, pp. 246-251, 1975.
- [7] B. Bulca, "A characterization of surfaces in IE^4 ," PhD, Uludag University, Bursa, Turkey, 2012.
- [8] B. Bulca and K. Arslan, "Surfaces given with the Monge patch in IE^4 ," *Journal of Mathematical Physics, Analysis, Geometry*, vol. 9, no. 4, pp. 435-447, 2013.
- [9] B. Bulca, K. Arslan, B. Bayram, and G. Öztürk, "Canal surfaces in 4-dimensional Euclidean space," *An International Journal of Optimization and Control: Theories and Applications*, vol. 7, no. 1, pp. 83-89, 2017.
- [10] B. Bulca, K. Arslan, B. Bayram, and G. Öztürk, "Spherical product surfaces in IE^4 ," *Analele Stiintifice ale Universitatii Ovidius Constanta*, vol. 20, no. 1, pp. 41-54, 2012.
- [11] P.M. Do Carmo, "Differential Geometry of Curves and Surfaces", Englewood Cliffs, NJ, USA: Prentice-Hall, 1976.
- [12] G. Ganchev and V. Milousheva, "General rotational surfaces in the 4-dimensional Minkowski space," *Turkish Journal of Mathematics*, vol. 38, pp. 883-895, 2014.
- [13] R.O. Gal and L. Pal, "Some notes on drawing twofolds in 4-dimensional Euclidean Space," *Acta Universitatis Sapientiae, Informatica*, vol. 1, no. 2, pp. 125-134, 2009.
- [14] F. Gökçelik, Z. Bozkurt, İ. Gök, F.N. Ekmekçi and Y. Yaylı, "Parallel transport frame in 4-dimensional Euclidean space IE^4 ," *Caspian J. of Math. Sci.*, vol. 3, pp. 91-103, 2014.
- [15] E. İyigün, K. Arslan, G. Öztürk, "A characterization of Chen surfaces in IE^4 ," *Bulletin of the Malaysian Mathematical Sciences Society*, vol. 31, pp. 209-215, 2008.
- [16] M.K. Karacan and B. Bükçü, "On natural curvatures of Bishop frame," *Journal of Vectorial Relativity*, vol. 5, pp. 34-41, 2010.
- [17] İ. Kişi and G. Öztürk, "A new approach to canal surface with parallel transport frame," *International Journal of Geometric Methods in Modern Physics*, vol. 14, no. 2, pp. 1-16, 2017.
- [18] T. Maekawa, N.M. Patrikalakis, T. Sakkalis and G. Yu, "Analysis and applications of pipe surfaces," *Computer-Aided Geometric Design*, vol. 15, pp. 437-458, 1998.
- [19] G. Öztürk, B. Bulca, B. (Kılıç) Bayram, K. Arslan, "Meridian surfaces of Weingarten type in 4-dimensional Euclidean space IE^4

- ,” *Konuralp Journal of Mathematics*, vol. 4, no. 1, pp. 239-245, 2016.
- [20] S.J. Ro and D.W. Yoon, “Tubes of Weingarten types in a Euclidean 3-Space,” *Journal of the Chungcheong Mathematical Society*, vol. 22, pp. 359-366, 2009.
- [21] U. Shani and D.H. Ballard, “Splines as embeddings for generalized cylinders,” *Computer Vision Graphics and Image Processing*, vol. 27, pp. 129-156, 1984.
- [22] C.K. Shene, “Blending two cones with Dupin cyclids,” *Computer-Aided Geometric Design*, vol. 15, pp. 643-673, 1998.
- [23] L. Wang, C.L. Ming, and D. Blackmore, “Generating sweep solids for NC verification using the SEDE method,” *Proceedings of the Fourth Symposium on Solid Modeling and Applications*; 14-16 May 1995; Atlanta, Georgian: pp. 364-375.
- [24] Z. Xu, R. Feng, and J.G. Sun, “Analytic and algebraic properties of canal surfaces,” *Journal of Computational and Applied Mathematics*,” vol. 195, pp. 220-228, 2006.
- [25] Y.C. Wong, “Contributions to the theory of surfaces in a 4-space of constant curvature,” *Trans. Amer. Math. Soc.*, vol. 59, no. 3, pp. 467-507, 1946.

JOURNAL OF SCIENCE



SAKARYA UNIVERSITY

Sakarya University Journal of Science

ISSN 1301-4048 | e-ISSN 2147-835X | Period Bimonthly | Founded: 1997 | Publisher Sakarya University |
<http://www.saujs.sakarya.edu.tr/>

Title: Batch And Column Studies For Removal of Sulphate From Real Wastewater Using Ion Exchange Resin

Authors: Tijen Ennil Bektas, Filiz Eren

Received: 2019-03-11 14:00:49

Accepted: 2019-03-27 12:52:45

Article Type: Research Article

Volume: 23

Issue: 5

Month: October

Year: 2019

Pages: 810-816

How to cite

Tijen Ennil Bektas, Filiz Eren; (2019), Batch And Column Studies For Removal of Sulphate From Real Wastewater Using Ion Exchange Resin. Sakarya University Journal of Science, 23(5), 810-816, DOI: 10.16984/saufenbilder.538174

Access link

<http://www.saujs.sakarya.edu.tr/issue/44066/538174>

New submission to SAUJS

<http://dergipark.gov.tr/journal/1115/submission/start>

Batch and Column Studies for Removal of Sulphate from Real Wastewater Using Ion Exchange Resin

Tijen Ennil Bektaş^{*1}, Filiz Eren²

Abstract

In this study, sorption potential of anion exchange resin (Lewatit Monoplus M600) to remove sulphate from real wastewater was investigated. Kinetic studies were performed in batch experiments. A comparison of kinetic models applied to the sorption of sulphate onto resin was evaluated for the "infinite solution volume model" and "unreacted core model". Rate-determining step is the liquid film control step of the unreacted core model. When pH values increased above 9, more than 80% sulphate removal was observed. Column sorption-elution experiments were performed for the removal of the sulphate from the wastewater by resin. The Thomas and the Yoon-Nelson models were applied to experimental data to determine the characteristic column parameters.

Keywords: Sulphate, anion-exchange resin, wastewater, kinetic models, column performance

1. INTRODUCTION

Sulfate is one of the most important ions involved in a natural way the surrounding waters. All natural waters contain varying amounts of sulphate. Some industrial wastewaters have a high sulphate content. When wastewater is discharged without treatment, it increases the amount of sulphate in natural waters. Sulfate compounds are important pollutants with the problems such as taste, odor, toxicity and corrosion which are

formed at the end of various reactions. Since the sulphate causes diarrhea, it should not be more than the values specified in the standards. World Health Organization (WHO) determined the sulphate concentration in drinking water to be 500 mg / L [1]. The American Environmental Protection Agency (EPA) determined this value as 250 mg / L [2]. In Turkey, according to the Water Pollution Control Regulations (SKKY), the

* Corresponding Author: ennilb@gmail.com

¹ Çanakkale Onsekiz Mart University, Chemical Engineering Department, Çanakkale, Turkey. ORCID: 0000-0001-9180-3623

² Eskişehir Osmangazi University, Chemical Engineering Department, Eskişehir, Turkey. ORCID:0000-0002-7302-8659

amount of sulphate in the wastewater should not exceed 200 mg / L [3].

Accumulator industry, leather and paper industry, fertilizer production, metal processing industry, petroleum refinery, boron operation, textile and explosive industry produces wastewater containing a large amount of sulphate ions. Sulphate can be removed from the wastewater by many methods such as adsorption [4], ion exchange [5], membrane process [6], biological reduction [7] and chemical precipitation [8-10].

There are 930.000 tons / year product capacity in Kırka Boron Plant. The products produced in this plant are tinkal, boraxpentahydrate, anhydrous borax and calcined tinkal. Water is used in the first washing process of the boron mine. In addition, after the ore is subjected to other processes, plenty of water is released. These waters are kept in settling ponds. At Eti Maden Kırka Bor Plant, approximately 400.000 tons / year of waste is produced. These wastes, which cause environmental problems, contain high levels of sulfate ions.

In this study, sulphate removal from Kırka Boron wastewater was investigated by using strong basic anion exchange resin (Lewatit MonoPlus M600). The studies were carried out in two parts as batch and continuous system. Different kinetic models were applied to both systems.

2. MATERIALS AND METHODS

First of all, the wastewater obtained from Eti Kırka Boron was analyzed and given in Table 1. Lewatit MonoPlus M 600 is a strongly basic, gelular anion exchange resin with beads of uniform size based on a styrene-divinylbenzene copolymer. it was kindly supplied by Ökotek Chem., Turkey. The characteristics of the resin are given in Table 2.

Table 1. Characterization of wastewater

pH=9.79	
Analysis type	Amount
Boron(mg/L)	3800
Sulphate(mg/L)	885
Suspended solids (mg/L)	243
The amount of solids precipitated (mL/L)	1.7
COD (mg/L)	600
pH	9.79

For the batch kinetic study, 500 mL wastewater with 5 g resin was mixed using a magnetic stirrer at 20 °C. Samples were taken at certain time intervals and sulphate analysis was performed. Standard analysis method (450 nm wavelength) was used for sulphate analysis in Hach DR-4000 spectrophotometer. The time to equilibrium was found and different kinetic models defined for heterogeneous systems were applied to experimental data. In addition, experiments were carried out at different pH values to investigate the effect of initial pH change on sulfate removal. For this purpose, the pH of the wastewater was set to 4, 7, 9 and 11. 50 mL of wastewater and 0.5 g of resin at different pH levels were contacted at a temperature of 25 °C in a shaking water bath for a period of time.

Table 2. Properties of Lewatit MonoPlus M 600

Ionic form	Cl ⁻
Functional group	Quaternary amine, type II
Structure	Gel type beads
Mean bead size (mm)	0.6 (+/- 0.05)
Bulk density (g/L)	700
Density approx. (g/mL)	1.1
Maximum operating temperature (°C)	30
Total capacity (min. solution/L resin)	1.25
pH range	0-11

The column experiments were performed in a glass column (0.7 cm internal diameter and 15 cm length). Glass wool was placed in the bottom of the column and then packed with a definite wet settled volume of the resin (2 mL). The wastewater solution was fed to the column at a flow rate of 6.5 mL / min using a peristaltic pump (Atto SJ 1211 Model). From the outlet of the column, each successive 3 mL fractions of the effluent were collected using a fraction collector (Spectral Chrom CF-1). Breakthrough curve was obtained by analysis of each fraction by the spectrophotometer. Column studies were terminated when the column reached exhaustion. The column experimental set up is shown in Fig. 1. The column elution experiments were carried out with a 0.5 M NaCl solution at a flow rate of 6.5 mL / min and the elution curve was plotted. The sorption data obtained were evaluated according to Thomas and Yoon Nelson models. Model coefficients and sorption capacities were calculated.

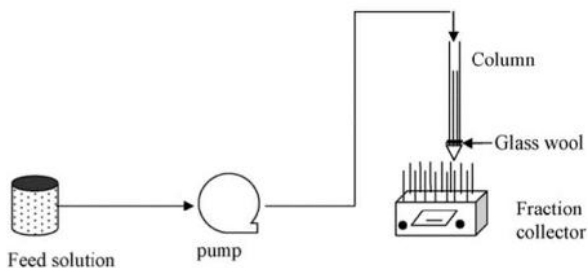


Figure 1. Experimental system

3. RESULTS AND DISCUSSION

3.1. Batch Study

3.1.1. Kinetic Models of Ion Exchange

The ion exchange between ions in the solution and the ions in the resin is defined by a heterogeneous process. There are four basic steps in the sorption process with the resin particle.

- 1) Transport of the ion in solution from the bulk solution to the outer film surrounding the resin particle.

- 2) Transport of ion from liquid film to outer surface centers of resin (diffusion in liquid film).
- 3) Ion diffusion within the pores of the resin.
- 4) Chemical reaction in internal surface centers.

There are two models in the definition of ion exchange mechanisms: "infinite solution volume model" and "unreacted core model" [11].

In the infinite solution volume model, the ions in the solution enter and react to the resin particle at different speeds and at different locations. The chemical exchange reaction at the fixed charge of the resin is usually assumed to be too fast to affect the overall exchange rate [11, 12].

Particle diffusion control is given by the following equation [13, 14]:

$$-\ln(1-x^2)=2kt \text{ where } k=D_r\pi^2/r_o^2 \quad (1)$$

Film diffusion control is given as follows [18-19]:

$$-\ln(1-x)=K_{li} t \text{ where } K_{li}=3DC/r_oC_r \quad (2)$$

In the unreacted core model, the reaction occurs at the outer skin of the resin particle. There is no change in the volume of resin particles as the reaction proceeds. In contrast, a solid layer of ash is formed. For spherical particles, the relationship between time (t) and fractional conversion (x) are as follows [11, 13-15]:

When the fluid film controls the rate:

$$x=3C_{A0}K_mAt/ar_o C_{s0} \quad (3)$$

When the reacted layer controls the rate:

$$[3-3(1-x)^{2/3}-2x]=6D_{e,r}C_{A0}t/ar_o^2C_{s0} \quad (4)$$

When the chemical reaction controls the rate:

$$[1-(1-x)^{1/3}]=k_s C_{A0}t/r_o \quad (5)$$

The results of the experiment are shown in Fig. 2 for the effect of the contact time for the removal of sulphate from wastewater. Five kinetic models were applied to fit the kinetic data of the resin. Fig. 3 and 4 show the functions of these kinetic models versus time.

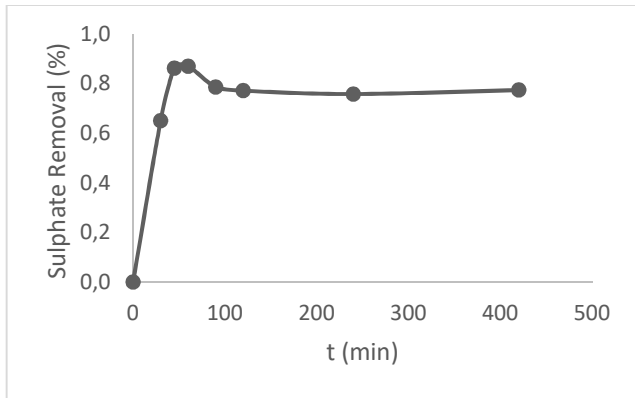


Figure 2. Effect of contact time on sulphate removal

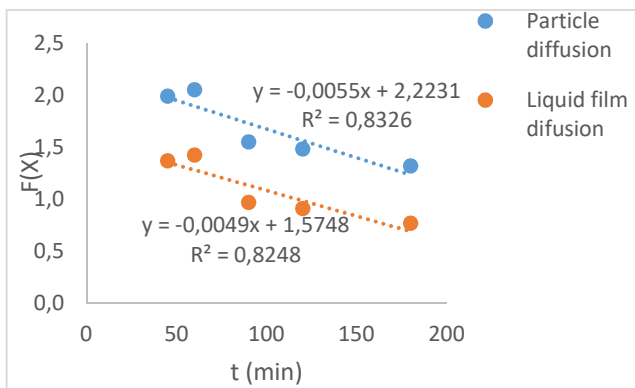


Figure 3. Kinetic behavior of resin based on infinite solution volume model

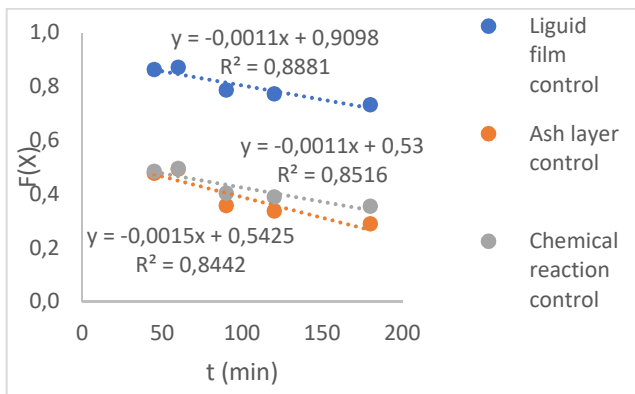


Figure 4. Kinetic behavior of resin based on unreacted core model

Since the resin reached equilibrium after about 180 minutes, the data obtained at contact times larger than 180 minutes were neglected. The data obtained from the removal of the sulphate in the wastewater by the resin mostly corresponds to the liquid film control step of unreacted core model.

3.1.2. Effect of Initial pH

The effect of pH on the removal of sulphate is shown in Fig. 5. Experimental results showed that the best sulphate removal from wastewater was obtained at pH 11. The higher-valued, larger atomic weight and smaller diameter are primarily retained by the ion exchange resin. The sulfate ions at pH 11 were more preferred in the competition with other ions.

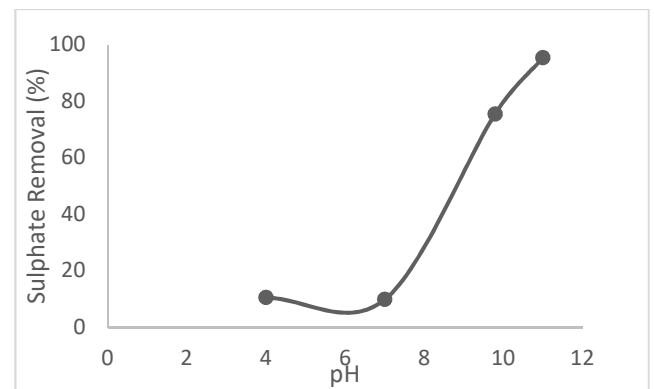


Figure 5. Effect of initial pH on sulphate removal

3.2. Column Study

The data obtained from sorption and elution experiments in the column are shown in Fig.6 and 7. As seen from the Fig. 6, the breaking point was reached when 30 ml of wastewater passed through the column. After this point, the concentration of sulfate in the effluent has increased continuously. When approximately 500 mL of wastewater was passed, the initial sulfate concentration was observed in the output stream.

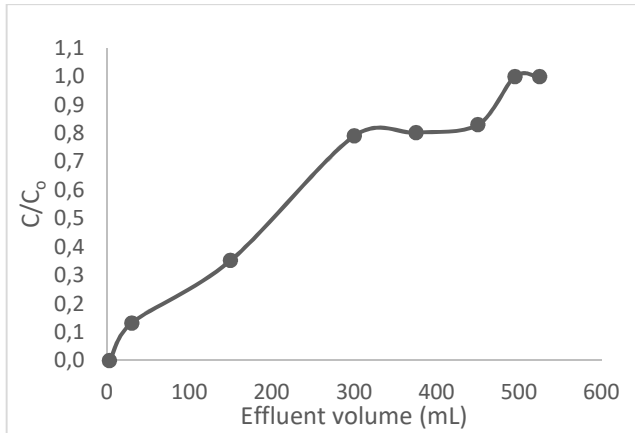


Figure 6. Breakthrough curve for the removal of sulphate

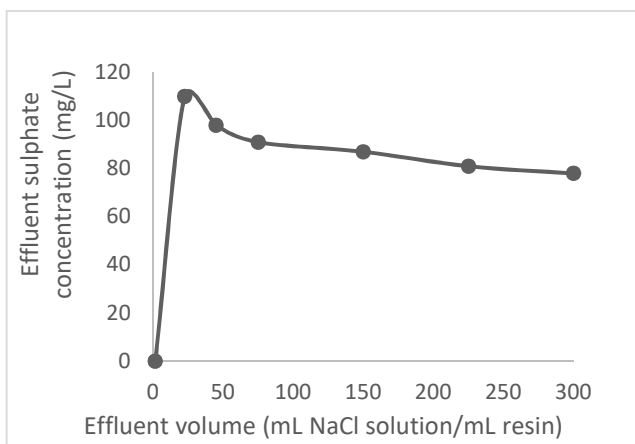


Figure 7. Elution curve

The breakthrough curve is usually expressed in terms of sorbed sulphate concentration ($C_{\text{sor}}=C_0-C$) or normalized concentration defined as the ratio of effluent sulphate concentration to inlet sulphate concentration (C/C_0) as a function of time (t) or volume of effluent (V) for a given bed height. Total sorbed sulphate quantity (maximum column capacity q_0 =mg sulphate/g resin) in the column was calculated from Eq. 1 [16]:

$$q_0 = \int_0^{V_T} \frac{(C_0 - C)dV}{m} \quad (1)$$

where m is the mass of the resin (g). The capacity value q_0 was obtained by graphical integration. The column capacity values of the resin are given in Table 3.

Table 3. Column performance of Lewatit MonoPlus M 600

Total capacity		Breakthrough capacity		Elution efficiency (%)
mg/mL resin	mg/g resin	mg/mL resin	mg/g resin	
96.7	128.9	0.741	0.988	26.8

3.2.1. The Thomas and Yoon-Nelson Models

Successful design of a column sorption process requires estimation of the breakthrough curve. In addition, the maximum sorption capacity of a sorbent is also required in the column design. The sorption data from column studies were analyzed using the Thomas model. This model gives reasonable accuracy in predicting breakthrough curves under different operating conditions. The Thomas model is suitable when the ion exchange mechanism is not controlled by internal and external diffusion.

This model is expressed linearly with the following equation [17]

$$\ln\left(\frac{C_0}{C} - 1\right) = \frac{K_T q_0 m}{q} - \frac{K_T C_0}{q} V \quad (2)$$

The kinetic coefficient K_T and sorption capacity of the bed q_0 can be determined from a plot of $\ln[(C_0/C)-1]$ against time (t) (Fig.8).

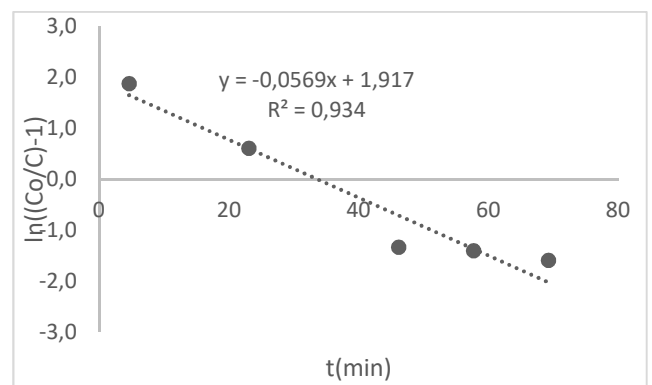


Figure 8. The Thomas Model for sulphate removal from wastewater by resin

The Yoon-Nelson model was developed by in Yoon and Nelson 1984 to describe the adsorption breakthrough curves. This model is not only less complicated than other models, but also requires no detailed data concerning the characteristics of the sorbate, the type of the sorbent, and the physical properties of the sorption bed [18]. The linearized form of the this model is given as follows:

$$\ln\left(\frac{C}{C_0 - C}\right) = K_{YN}t - \tau K_{YN} \quad (2)$$

The values of K_{YN} and τ can be calculated from a plot of $\ln(C/C_0 - C)$ against time (t) (Fig. 9).

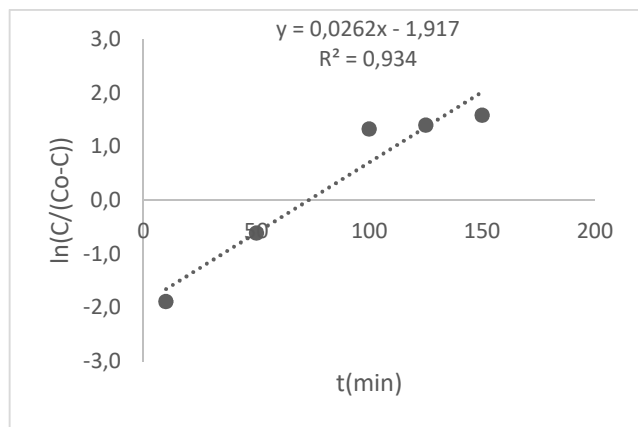


Figure 9. The Yoon-Nelson Model for sulphate removal from wastewater by resin

The parameters of both models are calculated and given in Table 4. Comparing the values of R^2 both the Thomas and Yoon-Nelson models can be used to describe the behavior of the sorption of sulphate in a column.

Table 4. The Thomas and Yoon- Nelson parameters for sulphate removal

Thomas Model			Yoon-Nelson Model		
K_T (mL/mg min)	q_0 (mg/g)	R^2	K_{YN} (min ⁻¹)	τ (min)	R^2
4.2×10^{-4}	1.35×10^4	0.934	0.024	73.17	0.934

4. CONCLUSIONS

Batch and column experiments were conducted to examine sulfate removal from wastewater by an anion exchange resin. Although the amount of

sulphate contained in the wastewater of Kirka Boron is quite high, 80% removal is achieved with relatively low amount of resin. The liquid film control is the best kinetic model to describe the sorption process. The best sulphate removal was observed at pH 11. The total and breaking capacity of the resin was calculated for wastewater. Elution efficiency with NaCl was low. A different regenerant solution may be tried to increase efficiency. The column experimental data were fitted well to the Thomas and Yoon-Nelson models.

List of Symbols

a	stoichiometric coefficient
C	total concentration of both exchanging species, M
C_{A0}	concentration of species A in bulk solution, M
C_{so}	concentration of solid reactant at the bead's unreacted core, M
D	diffusion coefficient in solution phase, m ² s ⁻¹
$D_{e,r}$	diffusion coefficient in solid phase, m ² s ⁻¹
D_r	diffusion coefficient in solution phase, m ² s ⁻¹
k_s	reaction constant based on surface, ms ⁻¹
K_{li}	rate constant for film diffusion (infinite solution volume condition), Ls ⁻¹
K_{mA}	mass transfer coefficient of species A through the liquid film, ms ⁻¹
K_T	Thomas rate constant, mL(min mg) ⁻¹
K_{YN}	Yoon-Nelson rate constant, min ⁻¹
τ	Time required for 50% adsorbate breakthrough, min
X	fractional attainment of equilibrium or extent of resin conversion

5. REFERENCES

- [1] WHO, "Sulfate in drinking water," Guidelines for Drinking Water Quality, 2004.

- [2] US EPA, "Health effects from exposure to high levels of sulfate in drinking water study," 1999.
- [3] Regulation For Water Pollution Control, Official Gazette Published, No: 25687, 31/12/2004.
- [4] C. Namasivayam and D. Sangeetha, "Application of coconut coir pith for the removal of sulfate and other anions from water," *Desalination*, vol. 219, no. 1, pp. 1-13, 2008.
- [5] F. İncetan, "Removal of natural organic matters and sulfate from surface from surface water sources by MIEX resin" Master Thesis, Erciyes University, Institute of Science, Department of Environmental Engineering, 2011.
- [6] A. Karabacak, "Sulphate removal by nanofiltration from water" Master Thesis, Middle East Technical University, Institute of Science, Department of Environmental Engineering, 2010.
- [7] X. Wang, Y. Song and J. Mai, "Combined fenton oxidation and aerobic biological processes for treating a surfactant wastewater containing abundant sulfate," *Journal of Hazardous Materials*, vol. 160, pp. 344-348, 2008.
- [8] D. Duranoğlu, "Sulfate removal from wastewater by chemical precipitation method," *Journal of Engineering and Natural Sciences*, vol. 30, pp. 39-55, 2011.
- [9] P. G. Klepetsanis and P.G. Koutsoukos, "Precipitation of calcium sulfate dehydrate at constant calcium activity," *J. Cryst. Growth*, vol. 98, pp. 480-486, 1989.
- [10] I. Kabdaşlı, A. Bilgin and O. Tünay, "Sulphate control by ettringite precipitation in textile industry wastewaters," *Environmental Technology*, vol. 37, no.4, pp. 446-451, 2016.
- [11] O. Levenspiel, "Chemical Reaction Engineering", 1 Edn, Wiley, New York, 1972.
- [12] J. L. Cortina and A. Warshawsky, "Developments - in solid-liquid extraction by solvent impregnated resins," *Ion Exchange and Solvent Extraction*, L.A. Marinsky and Y. Marcus (Eds.), Vol. 13, Marcel Dekker, Inc, New York, 1997.
- [13] J. L. Cortina, A. Warshawsky, N. Kahara, V. Kappel, C.H. Sampaio and R. M.Kautzmann, "Kinetics of gold cyanide extraction using ion-exchange resins containing piperazine functionality," *React. Funct. Polym.*, vol. 54, pp. 25-35, 2003.
- [14] M. Badruk, N. Kabay, M. Demircioglu, H. Mordoğan and U. Ipekoglu, "Removal of boron from wastewater of geothermal power plant by selective ion-exchange resins. I. Batch sorption-elution studies," *Separ. Sci. Technol.*, vol. 34, pp. 2553-2569, 1999.
- [15] R. Boncukoğlu, A. E. Yılmaz, M. M. Kocakerim and M. Çopur, "An empirical model for kinetics of boron removal from boron-containing wastewaters by ion exchange in a batch reactor," *Desalination*, vol. 160, pp. 159-166, 2004.
- [16] Z. Aksu and F. Gönen, "Biosorption of phenol by immobilized activated sludge in continuous packed bed: prediction of breakthrough curves," *Process Biochem.*, vol. 39, pp. 599-613, 2004.
- [17] H. C. Thomas, "Heterogeneous ion exchange in a flowing system," *J. Am. Chem. Soc.*, vol. 66, pp. 1664-1666, 1944.
- [18] Y. H. Yoon and J. H. Nelson, "Application of gas adsorption kinetics. I. A theoretical model for respirator cartridge service time," *Am. Ind. Hyg. Assoc. J.*, vol. 45, pp.509-516, 1984.

JOURNAL OF SCIENCE



SAKARYA UNIVERSITY

Sakarya University Journal of Science

ISSN 1301-4048 | e-ISSN 2147-835X | Period Bimonthly | Founded: 1997 | Publisher Sakarya University |
<http://www.saujs.sakarya.edu.tr/>

Title: Chromium-Aluminide Coatings Via Pack Cementation Method on Inconel 718 Alloy And Fe-Cr-Ni Superalloy

Authors: Tuba Yener

Received: 2018-12-11 16:23:45

Accepted: 2019-04-08 11:17:11

Article Type: Research Article

Volume: 23

Issue: 5

Month: October

Year: 2019

Pages: 817-823

How to cite

Tuba Yener; (2019), Chromium-Aluminide Coatings Via Pack Cementation Method on Inconel 718 Alloy And Fe-Cr-Ni Superalloy. Sakarya University Journal of Science, 23(5), 817-823, DOI: 10.16984/saufenbilder.495407

Access link

<http://www.saujs.sakarya.edu.tr/issue/44066/495407>

New submission to SAUJS

<http://dergipark.gov.tr/journal/1115/submission/start>

Chromium-Aluminide Coatings on Inconel 718 Alloy and Fe-Cr-Ni SuperAlloy

Tuba YENER *

Abstract

In this study, it is investigated the low-temperature chromium aluminide coatings on a FeCrNi-base superalloy and Inconel 718 by pack cementation method. Pack-aluminizing diffusion coating was applied at 800°C during 4 and 6 hours. The chromium-aluminizing powder packs were prepared using aluminium and chromium powders as a source for depositing aluminium and chromium, Al₂O₃ powder as an inert filler and ammonium chloride NH₄Cl as an activator. SEM (scanning electron microscope) EDS with energy dispersive X-ray spectrometer and XRD were used to characterize the coating layers. SEM analysis revealed that coating layers were homogenous, compact and nonporous and there was a good bonding at the interface of the coating and matrix. Layer thickness variation was changed from 11 to 18 µm measured from the surface to the matrix. The hardness of the coating layer increased to 1000 HVN while the hardness of the matrix was 340 HVN with the increasing process time.

Keywords: Low Temperature pack Aluminizing, Chromising, layer thickness, hardness.

1. INTRODUCTION

Steel has a widespread use in many industrial areas including transportation and general engineering and construction. Galvanized steel is mainly used for corrosion protection on the industry in order to resist corrosion [1]. However, since it is a expensive method, research has focused on cheaper and more durable coatings. The pack cementation technique an alternative technique can be applied to form hard and protective aluminide coatings on alloy steels [2], [3].

The need for coatings to upgrade surface properties such as abrasion and corrosion

resistance, friction, oxidation and is increasing day by day [4], [5]. To resist oxidation at elevated temperatures, many superalloy part, such as turbine blades and nozzle guiding fins, are generally of interest in the diffusion aluminide coatings [6]. The formation of the protective alumina scale (especially under cyclic loading conditions) during high temperature exposures is preferred due to the strong interdiffusion between aluminide coatings and superalloy substrate [7], [8]. Various metals and alloys that produce single or multi-component metal diffusion coatings and composite layers are an important for protecting the components from oxidation, aqueous corrosion and corrosion at high temperature [9]. High

* Corresponding Author: tcerezci@sakray.edu.tr
Sakarya University, Metallurgy and Materials Department, Sakarya, Tukiye. ORCID: 0000-0002-2908-8507

temperature protective coatings for Ni-based superalloys widely used in aircraft engines and industrial gas turbines. It is necessary to increase working life in oxidizing and corrosion environments. The formation of the protective slow-growing α -alumina layer on the coating surface plays a key role in obtaining the necessary protection. Such coatings are obtained by coatings containing high concentrations of Al provided by aluminum-rich phases [3]. In this context, the Cr element which also forms a protective oxide can also be selected [10]. The diffusion aluminide coatings are usually formed by exposing the superalloy to an Al-rich gas medium at elevated temperatures to provide alpha diffusion to the substrate or to allow for diffusion of nickel from the substrate [3].

Diffusion aluminising and chromising of iron and steel has been a subject of high interest in relatively early published journals [9]. In the present work, aluminium-chromium coatings are applied on the two types of metallic alloys surface (Inconel 718 commercial alloy and the other one is Fe-Cr-Ni super alloy). In addition this, it is aimed to form Al-Cr coatings by using pack cementation process at relatively lower temperatures

1.1. Materials and Experiments

The commercial Inconel 718 and Fe-Cr-Ni superalloys were used as a substrate for coating, and their compositions are listed in Table 1.

Table 1. Chemical composition of Inconel 718 alloy and Fe-Cr-Ni super alloy

Element (Wt. %)	Al	Cr	Fe	Co	Ni	Mo	Si
Inconel 718	1.8	22.2	1.18	11	54	9.6	-
Fe-Cr-Ni Superalloy	0.36	21.54	54.6	-	21.28	-	2.22

Substrate samples with the dimensions of 10 mm×10 mm×8 mm were utilized in this work. The samples were ground up to 800 grit SiC emery paper, washed with acetone, ultrasonically cleaned in ethanol for 10 min and dried. 20 g of powder mixture containing 20% metallic Al, 10% metallic

Cr, 5% NH_4Cl , 65% Al_2O_3 was used. Chloride salts commonly used for package cementation; NH_4Cl , NaCl and AlCl_3 [11]. The salt considered for this article is NH_4Cl . For an appropriate pack cementation operation, the amount of halide activator controlled in the range of 1% to 5% [11]. Thus, the addition of halide salts in the packages was chosen to be 5% by weight.

In pack aluminising process, the substrates were immersed in pack powders charged into a alumina crucible, which was covered with alumina powder over the lid was closed. The pack was then loaded into an open atmosphere furnace. The aluminising process temperature were applied at 800°C for 4 and 6 hours for both of the alloys. The microstructure and chemical composition of the cross-section of the coated specimens were analysed using scanning electron microscopy (SEM, Model JEOL JSM-6060, Japan) with energy dispersive spectroscopy (EDS). X-Ray diffraction (XRD, Model D/MAX-B/2200/PC, Rigaku Co., Japan) was used to identify phases formed in the surface layer of as-coated specimens with a wavelength of 1.5418 Å Cu-K α source radiation over a 2θ range of 10–80°. The microhardness of the test materials was measured using by a Vickers indentation technique with a diamond indenter a load of 0.98 N using Leica WMHT-Mod model Vickers hardness instrument. Hardness was measured along the cross sections of the samples and measurements were obtained using a 10-s holding duration. The hardness results were obtained by taking the average of 5 values.

2. RESULTS AND DISCUSSION

2.1. SEM-EDS Analyses

SEM micrographs of cross sectioned Inconel 718 and Fe-Cr-Ni super alloy aluminised and chromised at 800°C for 4 and 6 hours are given in Figure 1. It was observed that chromium-aluminide layer is dense, compact and it is silvery metallic appearance. Furthermore, when compared to the inconel 718, it is seen that the coating interface on the super alloy is layered but the inconel has a flat interface. The cracks in the

outermost layer are formed during grinding and polishing, showing the brittleness of the aluminide layer [12]. The average layer thickness obtained is approximately the same both of the inconel and super alloy, in addition, it is seen that the coating interfaces are quite smooth for Inconel 718 alloy.

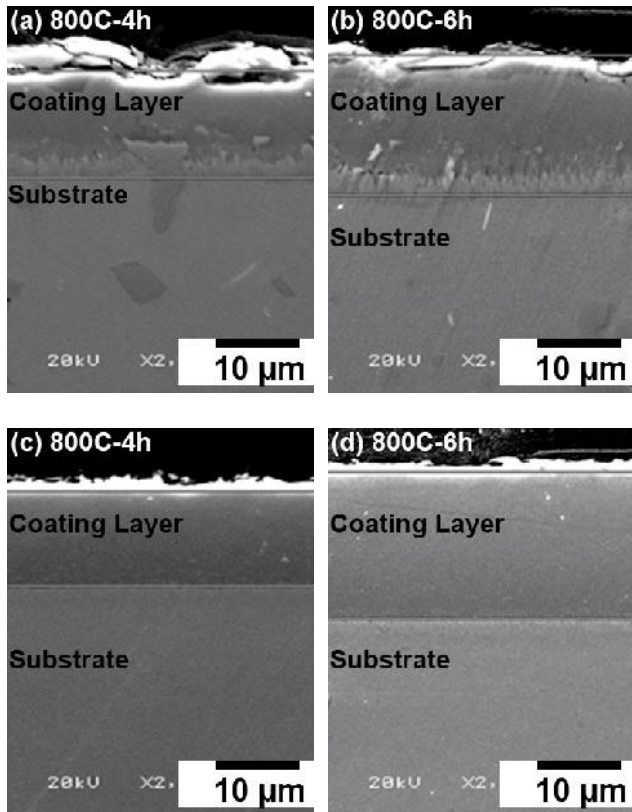


Figure 1. SEM Micrographs of Fe-Cr-Ni super alloy chromium-aluminized at 800°C (a) 2h, (b) 4h and Inconel 718 alloy 800 °C (c) 2h, (d) 4h.

For further analysis of aluminide layer, the SEM-Map study was performed and they are given in Figure 2 and Figure 3. It is seen that the coatings deposited on the super alloy is more brittle whereas Inconel 718 alloy remains much more intact. This can be resulted from the differences in the intermetallics phases formed on the coating. Another result that may be associated with this can be the hardness values of the coating.

Looking at SEM-MAP (Figure 2, Figure 3) analyses; at the coating surface, chromium deposition is more intense in the super alloy based coating. This is also supported by EDS analysis in Figure 4. Diffusion zone intensively contains Cr in the aluminised-chromised super alloy in Figure 2.

Whereas in Figure 3 almost no interface (transition zone) can be existed in Inconel 718 alloy.

2.2. Hardness and Layer Thickness

The microhardness measurements, at 400 μm depth from surface are shown in Figure 5. The hardness of aluminide layer is much higher than that of substrate due to the formation intermetallic phases. Especially, higher aluminisation temperatures cause higher hardness because of formation of fully dense and thicker aluminide coating layer [12]. However chromium can increase the hardness and brittleness of the aluminide layer thanks to the presence of interstitial compounds such as Al_8Cr in the surface layer as it can be seen from XRD analyses (Figure 7).

When the hardness values and the layer thickness graphs (Figure 5) obtained from coating surface toward the center are taken into consideration; it is evident that the hardness and the layer thickness increased with processing time and temperature as it can be seen in Figure 6. With the formation of the coating layer, a high hardness increment at 800°C-6h was reached to about 1000 HV for Inconel 718 and 900 HV for super alloy. This can be attributed to formation of the intermetallics such as Ni_2Al_3 , Al_8Cr_5 coatings during the pack aluminising process.

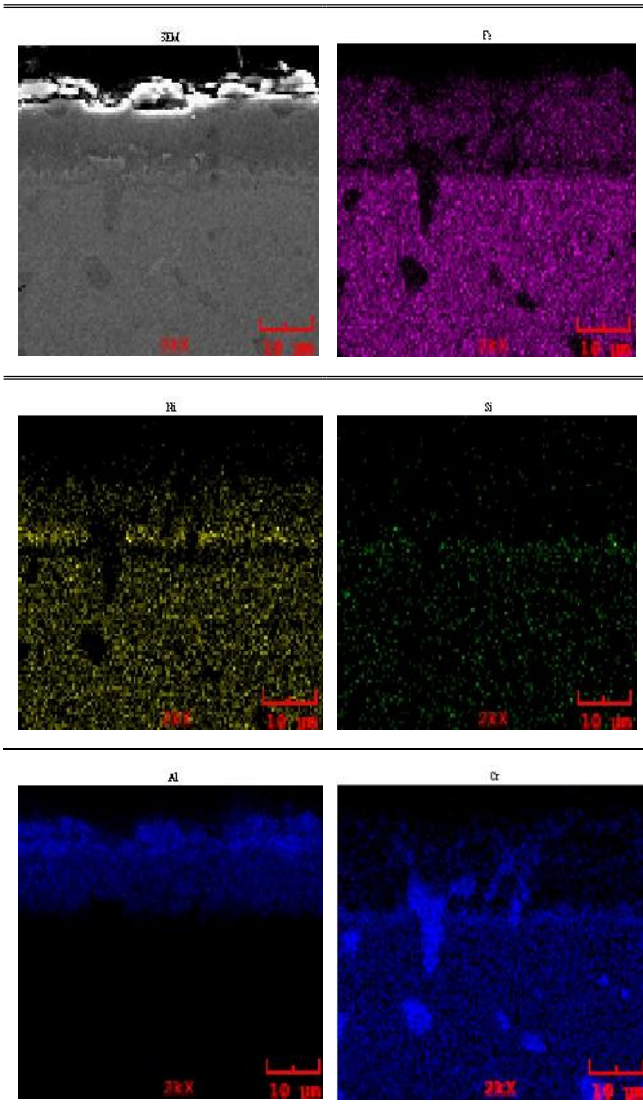


Figure 2. SEM-MAP analyses of 800°C-6h, Al-Cr deposited Super Alloy sample

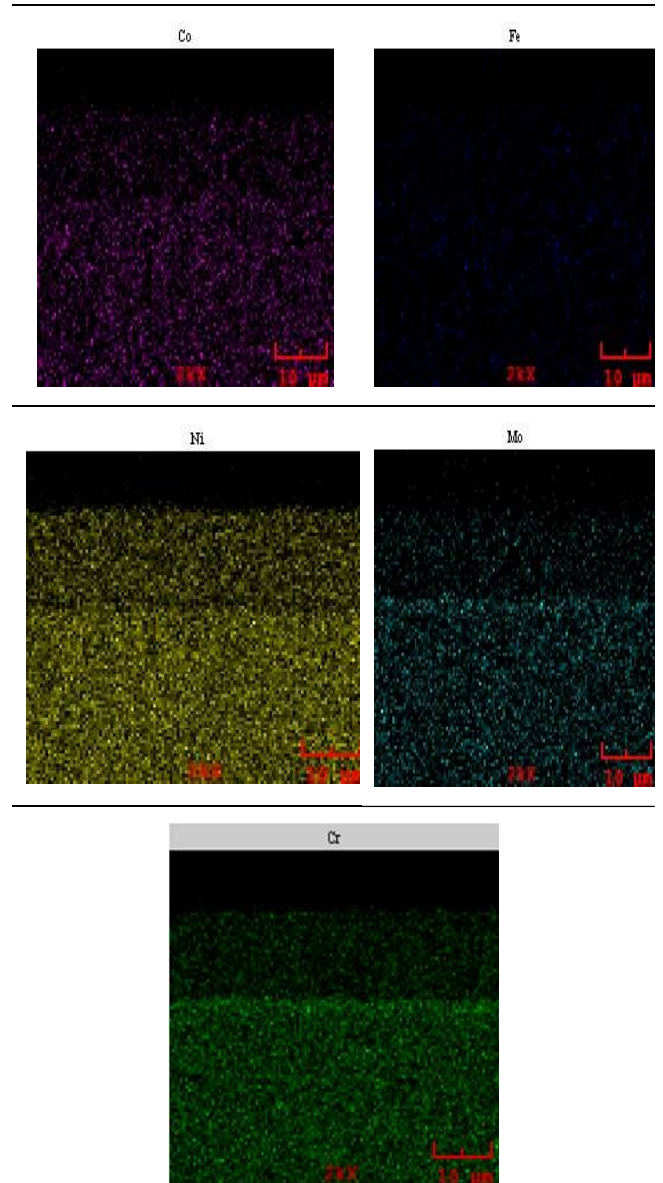
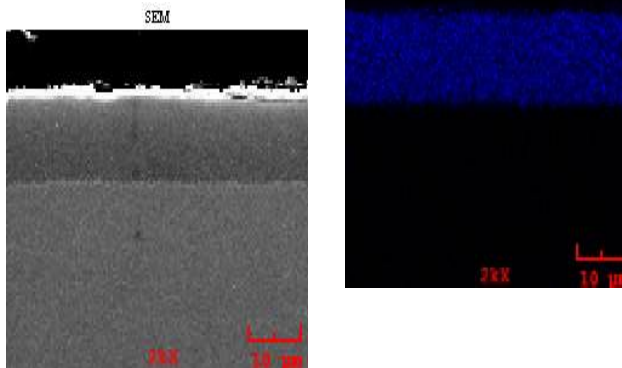


Figure 3. SEM-MAP analyses of 800°C-6h, Al-Cr deposited Inconel 718 sample.

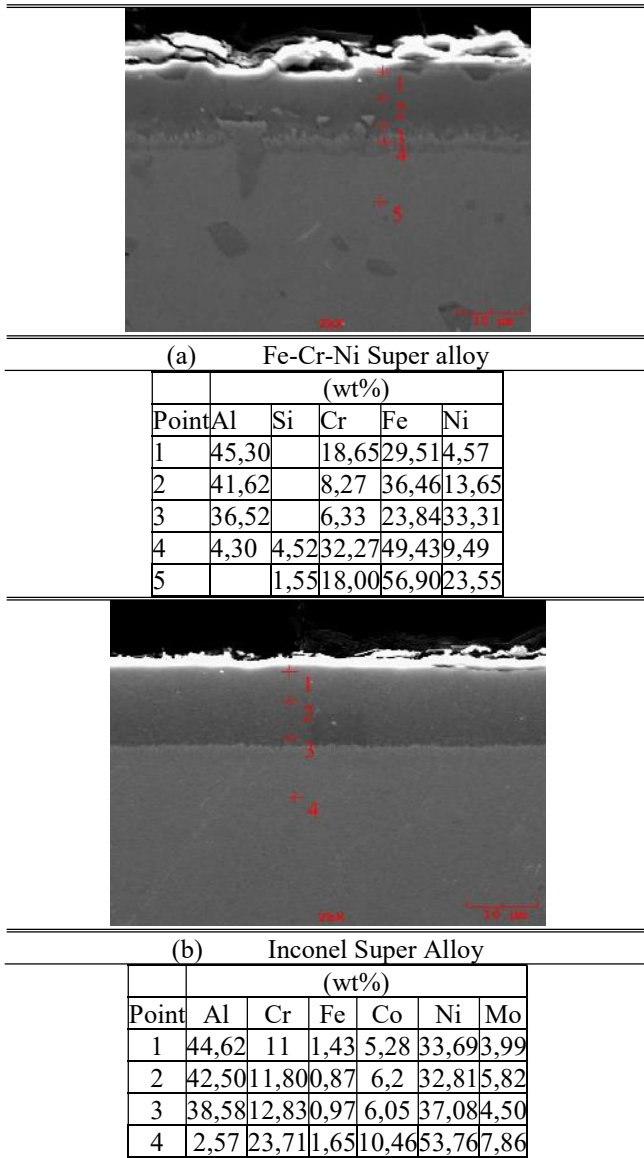


Figure 4. SEM-EDS Analyses of 800°C-4h Al-Cr coatings.

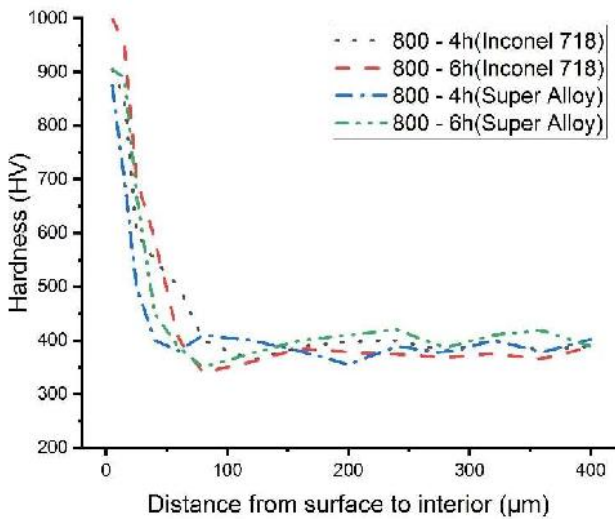


Figure 5. Hardness graphs of Inconel 718 and Super Alloy from surface to interior

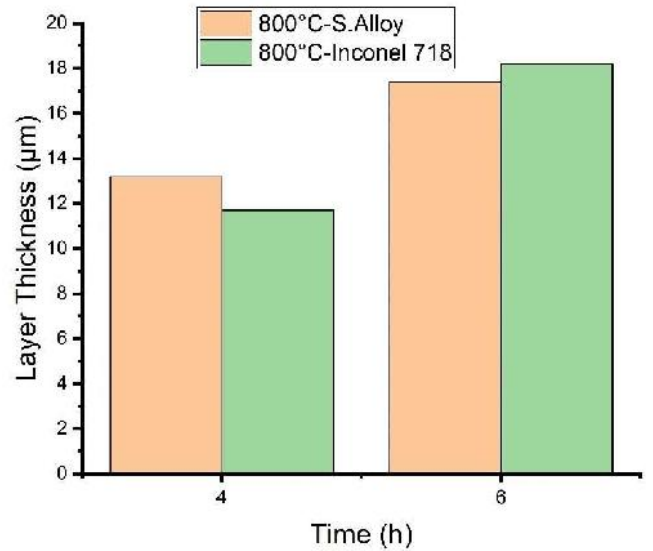


Figure 6. Variation of aluminizing layer thickness of Super alloy and Inconel 718 versus time

2.3. XRD Analyses

The results of the XRD analyses for both coating types are summarised in Figure 7. The XRD analyses confirms both the coatings were composed of aluminide phase. Compared with super alloy and inconel samples aluminised at 800°C-4h, the peaks of Inconel consist of Al_3Ni_2 , $AlFeMo$, $AlCr_2$ where as Super alloy has Fe_3Al , Al_8Cr_5 , $(SiAl)_2Cr$ phases.

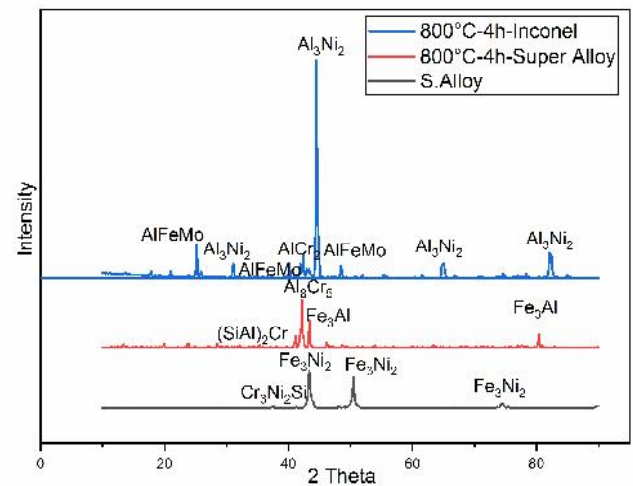


Figure 7. XRD Analyses of Inconel 718 and Super Alloy Samples Aluminised and Chromised at 800°C-4h

2.4. Conclusions

In this study Al-Cr coating on two type of super alloys has been studied at 800 °C for 4 and 6 hours in a powder pack containing 20% Al, 10% metallic Cr, 5% NH₄Cl, 65% Al₂O₃ using pack cementation method on a superalloy and Inconel 718 alloy. The following conclusions can be drawn from this work:

- Fully dense and uniform aluminide coating was obtained on the Fe-Cr-Ni and Inconel 718 type superalloy substrate. Almost no cracks, holes or other defects were observed in substrate/coating interface and inside the coating.
- 800°C -4 and 6 hours are sufficient for aluminide coating formation. According to XRD analyses; Inconel 718 alloy contains Al₃Ni₂, AlFeMo, AlCr₂ phases, whereas super alloys coating has Fe₃Al, Al₈Cr₅, (SiAl)₂Cr phases.
- Depending on the increase in the time, the coating layer increased from 13,2 µm to 17,4 µm for super alloy and from 11,7 to 18,2 µm for Inconel 718.
- Hardness values of coating layer formed on the surface of aluminised super alloy measured as 900 and 1000 HV respectively for Fe-Cr-Ni Super alloy and Inconel 718 at 800°C for 6h whereas hardness of matrix is at about 350 HV.

ACKNOWLEDGMENTS

The author thanks to expert Fuat Kayis and Murat Kazanci for performing XRD and SEM-EDS studies and special appreciation is extended to Prof.Dr.Sakin ZEYTIN for his notable support.

REFERENCES

- [1] I. Schoukens, I. Vandendael, J. De Strycker, A. A. Saleh, H. Terry, and I. De Graeve, "Effect of surface composition and microstructure of aluminised steel on the formation of a titanium-based conversion layer," *Surface and Coatings Technology*, vol. 235, pp. 628–636, Nov. 2013.
- [2] Z. D. Xiang and P. K. Datta, "Relationship between pack chemistry and aluminide coating formation for low-temperature aluminisation of alloy steels," *Acta Materialia*, vol. 54, pp. 4453–4463, 2006.
- [3] R. Pillai et al., "Carbides in an aluminised single crystal superalloy: Tracing the source of carbon," *Surface and Coatings Technology*, vol. 288, pp. 15–24, 2016.
- [4] A. Erdogan, "Investigation of high temperature dry sliding behavior of borided H13 hot work tool steel with nanoboron powder," *Surface & Coatings Technology*, 2018.
- [5] M. Sabri, A. Erdogan, M. Öge, and A. Günen, "Dry sliding wear behavior of borided hot-work tool steel at elevated temperatures," *Surface & Coatings Technology*, vol. 328, pp. 54–62, 2017.
- [6] D. Chaliampalias et al., "The effect of Al and Cr additions on pack cementation zinc coatings," *Applied Surface Science*, vol. 256, no. 11, pp. 3618–3623, Mar. 2010.
- [7] Y. F. Yang, C. Y. Jiang, Z. B. Bao, S. L. Zhu, and F. H. Wang, "Effect of aluminisation characteristics on the microstructure of single phase β -(Ni,Pt)Al coating and the isothermal oxidation behaviour," *Corrosion Science*, vol. 106, pp. 43–54, 2016.
- [8] K. Nikolov, P. Kaestner, C. P. Klages, S. Puls, and B. Schuhmacher, "Low-pressure diffusion chromising of thin low-carbon steel sheet for improved surface and bulk properties," *Journal of Alloys and Compounds*, vol. 692, pp. 101–107, 2017.
- [9] F. J. Pérez, F. Pedraza, M. P. Hierro, M. C. Carpintero, and C. Gómez, "Chromising of stainless steels by the use of the CVD-FBR technology," *Surface and Coatings Technology*, vol. 184, no. 1, pp. 47–54, 2004.
- [10] X. J. Lu and Z. D. Xiang, "Formation of chromium nitride coatings on carbon steels by pack cementation process," *Surface and Coatings Technology*, vol. 309, pp. 994–1000, Jan. 2017.

- [11] Z. D. Xiang and P. K. Datta, "Pack aluminisation of low alloy steels at temperatures below 700 °C," *Surface and Coatings Technology*, vol. 184, no. 1, pp. 108–115, Jun. 2004.
- [12] Yener, Tuba. 2019. "Low Temperature Aluminising of Fe-Cr-Ni Super Alloy by Pack Cementation." *Vacuum* 162 (September 2018). Elsevier: 114–20. doi:10.1016/j.vacuum.2019.01.040.

JOURNAL OF SCIENCE



SAKARYA UNIVERSITY

Sakarya University Journal of Science

ISSN 1301-4048 | e-ISSN 2147-835X | Period Bimonthly | Founded: 1997 | Publisher Sakarya University |
<http://www.saujs.sakarya.edu.tr/>

Title: Determination of Anticancer And Antibacterial Activities of Disubstituted Tacrine Derivatives

Authors: Salih Ökten, Ali Aydın, Ahmet Tutar

Received: 2018-10-10 21:34:27

Accepted: 2019-04-08 16:22:28

Article Type: Research Article

Volume: 23

Issue: 5

Month: October

Year: 2019

Pages: 824-830

How to cite

Salih Ökten, Ali Aydın, Ahmet Tutar; (2019), Determination of Anticancer And Antibacterial Activities of Disubstituted Tacrine Derivatives. Sakarya University Journal of Science, 23(5), 824-830, DOI: 10.16984/saufenbilder.469273

Access link

<http://www.saujs.sakarya.edu.tr/issue/44066/469273>

New submission to SAUJS

<http://dergipark.gov.tr/journal/1115/submission/start>

Determination of anticancer and antibacterial activities of disubstituted tacrine derivatives

Salih Ökten^{*1}, Ali Aydin², Ahmet Tutar³

Abstract

The present study describes the biological features of disubstituted tacrine derivatives using cell proliferation and cell cytotoxicity assays. The abilities of tacrine derivatives to inhibit microbial growth and to interact with DNA were also investigated. Here, the tested compounds (**1-4**) exhibited selective antiproliferative activity against the cancer cell lines (IC₅₀ values 1.1 – 38.9 µg/mL) and showed a similar non-toxic property to cells such as positive control (percent cytotoxicity 7% - 27%). Studies on human pathogenic bacteria showed that the novel tacrine analogues exhibited significant antimicrobial activities between concentrations of 31.25 µg/mL and 250 µg/mL. The data show that they can bind to DNA with the groove binding mode with K_b range of 7.4 × 10⁴ - 2.9 × 10⁴ M⁻¹. As a result, the preliminary data showed that disubstituted tacrine derivatives exhibited effective pharmacological properties.

Keywords: tacrine; anticancer; cytotoxicity; antibacterial

1. INTRODUCTION

Cancer is an enormous threatening problem for the human health in the World due to lead to uncontrolled growth and division of cells to invade other tissues and organs by spreading to the body through blood [1].

Tacrine (**1**, 9-amino-1,2,3,4-tetrahydroacridine) and its derivatives, the class of well-known bioactive compounds, have been commonly used as antimalarial and antibacterial agents [2-4]. Also tacrine has reversibly inhibited the acetylcholinesterase enzyme and was the first approved cholinesterase inhibitor drug, tested clinically for the treatment of Alzheimer's disease (AD) [5-8]. However, tacrine was withdrawn due to its hepatotoxicity and serious side effects on Alzheimer's patients. [9-13]. In recent years, some studies have been focused on determining the anticancer effects of tacrines due to that its derivatives

can inhibit topoisomerase enzyme and block the transcription of DNA [4].

Tacrine is similar to the planar acridine moiety [14-15] and has a cyclohexyl-fused quinoline structure. Its pharmacophore is known ability of to interact with DNA [16] and its platinum(II) complexes might be potential telomerase inhibitors [17-20] and have been reported to trigger cell senescence and apoptosis [21-25]. Some reports showed different substituted tacrines bearing penta or hepta hydrocycle have antitumor activity. For example, a pentacyclic acridine, RHPS4 (3,11-difluoro-6,8,13-trimethyl(8H)-quino[4,3,2-kl]acridinium methylsulfate) was reported to induce tumor cell apoptosis via inhibiting the telomerase activity [22-23]. Tacrine is a quindoline derivative with a large planar aromatic conjugated system [26-27]. In addition, the natural product quindolines were determined as a potent telomerase inhibitor [24,28].

* Corresponding Author: salihokten@kku.edu.tr

¹ Kırıkkale University Department of Maths and Science Education, Yahşıhan, Kırıkkale. ORCID: 0000-0001-9656-1803

² Institution of Gene Engineering and Biotechnology, Tübitak MAM, Gebze, Kocaeli ORCID: 0000-0002-9550-9111

³ Sakarya University Department of Chemistry, Serdivan, Sakarya, Turkey ORCID: 0000-0001-5524-8001

In our recent studies, a series of disubstituted tacrine derivatives were prepared by Friedlander reaction and metal induced substitution reaction [29] and we reported their cholinesterase and carbonic anhydrase enzymes' inhibition activities [30-31]. In this study, prepared disubstituted tacrines bearing six and seven membered hydrocycle were tested for anticancer activities against HT29 (Human colorectal adenocarcinoma), HeLa (Human cervix adenocarcinoma), MCF7 (Human breast adenocarcinoma), A549 (Human lung carcinoma), and Hep3B (Human hepatocellular carcinoma) cancer cell lines and FL (Human amnion cells) normal cell line by MTT cell proliferation assay and also determined their antibacterial activities by microdilution assay.

2. MATERIALS AND METHODS

2.1. Synthesis of compounds (1-4)

This study was carried out with disubstituted tacrine derivatives (1-4) according to our previous paper [29].

2.2. MTT Cell Proliferation Assay

HT29 (Human colorectal adenocarcinoma), HeLa (Human cervix adenocarcinoma), MCF7 (Human breast adenocarcinoma), A549 (Human lung carcinoma), and Hep3B (Human hepatocellular carcinoma) cancer cell lines and FL (Human amnion cells) normal cell line were maintained in a suitable medium containing fetal bovine serum and antibiotic solution. A Cell suspension was adjusted 1×10^6 cells in 10 mL and transferred 100 μ L into each well of culture plates. The compounds were dissolved in sterile DMSO at final concentrations of 10-200 μ g/mL and transferred the cells at 37 °C with 5% CO₂ for overnight. The antitumor activities of the compounds were determined using MTT cell proliferation assay. In MTT assay, the percent inhibitions of test and control molecules were determined. The percent inhibition was equal % inhabitations with following formula;

$$1- \frac{\text{Absorbance of Treatments}}{\text{Absorbance of DMSO}} \times 100$$

The IC₅₀ values (half maximal inhibitory concentration) of the compounds were obtained by using Excel software and noted in μ g/mL at 95 % confidence intervals. The dose response parameters (GI₅₀, TGI, LC₅₀) were calculated according to the following formulas using an Excel software. Growth inhibition of 50% (GI₅₀) was calculated from following equation:

$$\frac{(Ti-Tz)}{(C-Tz)} \times 100 = 50$$

This formula is the drug concentration resulting in a 50% reduction in the net growth increase in control cells during the drug incubation. The total growth inhibition (TGI) was calculated from Ti = Tz. The LC₅₀ indicating a net loss of treated cells was calculated from following equation:

$$\frac{(Ti-Tz)}{Tz} \times 100 = -50$$

2.3. Cytotoxicity Assay

The cytotoxic potentials of the compounds were determined by cytosolic LDH measurement kit according to manufacturer's procedures. Briefly, 5×10^3 cells were conveyed into each well as triplicates and exposed with IC₅₀ concentrations of the compounds at 37 °C with 5% CO₂ for overnight. The percentage cytotoxicities were obtained by using the following equation,

$$\frac{(\text{experimental value} - \text{low control})}{(\text{high control} - \text{low control})} \times 100$$

where experimental value is the cells treated with test compound, high control (maximum LDH release) is Triton X-100 treated cells, low control (spontaneous LDH release) is the untreated cells.

2.4. DNA binding studies

The binding constants (K_b) against calf thymus DNA and physiological interactions of disubstituted tacrine derivatives were examined by using UV-visible absorption spectroscopy technique. To prepare stock calf thymus DNA solution, a 2.5 mg DNA was dissolved in 10.0 mL Tris-HCl buffer (20 mM Tris-HCl, 20 mM NaCl, pH 7.0) and store at +4 °C for up to seven days. DNA concentration in solution was calculated by using ϵ value ($6600 \text{ M}^{-1} \text{ cm}^{-1}$ at 260 nm) that belong to DNA. In addition, the purity of calf thymus DNA solution was controlled with the help of change of absorbance obtained from the ratio of A₂₆₀/A₂₈₀. Since the value was equal to 1.87, the DNA was considered to be sufficiently pure. To obtain 25 μ M of working solution, disubstituted tacrine derivatives were diluted with Tris-HCl buffer and then all of the compounds were incubated at 24 °C for 30 min before the measurement. To ensure sufficient solubility in solution throughout measurement were prepared a special solvent system (1/9 DMSO/Tris-HCl buffer). Eight measurement points at room temperature for disubstituted tacrine derivatives were

recorded by using 1-cm-path quartz cuvettes. The amount of disubstituted tacrine derivatives was kept constant while increasing the CT-DNA concentrations (6.5-800 μM) in the UV absorption titrations.

2.5. Microdilution assay

The minimal inhibitory concentration (MIC) values of disubstituted tacrine derivatives towards some human bacterial strains were examined with the help of a micro-well dilution method. According to this method, inocula of bacteria were obtained using 12 h LB broth cultures. The optical density at 600 nm (OD600) was adjusted to 0.08–0.1 and 0.5 McFarland bacterial suspensions were obtained. Each disubstituted tacrine derivative was dissolved in dimethyl sulfoxide (20 mg/mL). A concentration gradient range from 7.81–1000 $\mu\text{g/mL}$ in uncovered microplate wells containing nutrient broth was made by using serial two-fold dilutions of these compounds. This plate was inoculated with bacteria and incubated at 35 °C for 24 hours. At the end of this period, the growth of microorganisms was determined visually and the point where no visible growth was accepted as the MIC.

2.6. Statistical Analysis

For the statistical analysis, SPSS (Statistical Package for Social Sciences) for Windows computer program was used and standard deviation, *P value*, using means, one-way analysis of variance (ANOVA) followed by Tukey test.

3. RESULTS AND DISCUSSION

3.1. Antiproliferative activities of the compounds

Many anticancer drug candidates have been withdrawn from market due to their serious side effects, loss of sensitivity to drugs, and limited use for many cancer types. In the present study, the disubstituted tacrine derivatives (Table 1) were prepared according to reported procedure by our research group [29] and investigated for their anticancer and cytotoxicities against A549, HeLa, Hep3B, HT29, MCF7 and FL cell lines according to the MTT protocol. Growth inhibition (GI_{50}), total growth inhibition (TGI), and lethal concentration (LC_{50}) parameters of the compounds were evaluated according to NCI screening method and half-maximal inhibitory concentration (IC_{50}) of these molecules were calculated using Four-Parameter Logistic Function, as well. When TGI and IC_{50} values of the compounds were examined, it was found that

tested compounds caused selective antitumor properties against all tested cell lines (Table 1 and 2). Although compound **2** has antiproliferative effect (IC_{50} values between 4.5 and 20.7 $\mu\text{g/mL}$; TGI values between 4.4 and 20.9 $\mu\text{g/mL}$) against FL, HeLa and Hep3B cell lines (Table 1 and 2), compound **4** showed high antitumoral properties (IC_{50} values between 7.8 and 38.9 $\mu\text{g/mL}$; TGI values between 7.9 and 40.1 $\mu\text{g/mL}$) against FL, HeLa, HT29, and MCF7 cell lines (Table 1 and 2). Compound **1** depicted significant antiproliferative effect (IC_{50} value 1.1 and TGI value 1.1 $\mu\text{g/mL}$) against FL cells (Table 1). In Hep3B cells, compound **1** (IC_{50} value 10.4 and TGI value 10.6 $\mu\text{g/mL}$) and **2** (IC_{50} value 9.5 and TGI value 9.6 $\mu\text{g/mL}$) showed a potent antitumor effect (Table 2). When the IC_{50} and TGI values of all the above-mentioned compounds are considered, effective ones have better antiproliferative effects compared to the positive control group, cisplatin and 5-FU (Tables 1 and 2). In addition, the active compounds can be used in advanced pharmacological studies when the low GI_{50} values ($\sim 1 - 2 \mu\text{g/mL}$) and the high LC_{50} values ($\sim 40 - 400 \mu\text{g/mL}$) are considered (Table 1 and 2). Overall, the GI_{50} , TGI and LC_{50} parameters of the respective molecules are at the desired level and meet the NCI criteria.

3.2. Cytotoxic activity of compounds.

That the toxic effect against normal cells should be minimal is important for a substance. For this reason, antitumor and cytotoxic properties of these compounds should be compared in order to find the forward pharmacological capacity of each. The cytotoxicities of the compounds in cells were tested by the LDH cytotoxicity assay, indirectly demonstrating membrane damage. When cytoplasmic LDH activity measurement results are evaluated for these compounds, it has been found that the compounds **1-4** for A549 and Hep3B cell lines, compounds **1** and **4** for MCF7 and HeLa cell, compounds **1** and **3** for HT29 cell lines, and compound **2** and **4** for FL cell lines causes approximately 7% to 27% membrane damage at their IC_{50} concentration (Tables 3). If the compounds are compared to controls (5-FU and cisplatin) for this evaluation, the toxicity of molecules above-mentioned is very close to the cytotoxicity values of 5-FU and cisplatin. Therefore, they may be suitable for advanced pharmacological assays (Table 3).

3.3. Antibacterial activities of the compounds

The effects of the compounds on some pathogenic bacteria causing disease in the human body have been

Table 1. GI₅₀, TGI, LC₅₀ and IC₅₀ of test compounds against A549, FL, and HeLa cell line

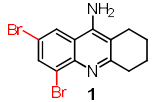
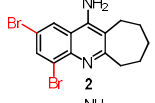
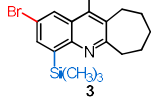
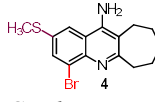
Compounds ($\mu\text{g/mL}$)	A549				FL				HeLa			
	GI ₅₀	TGI	LC ₅₀	IC ₅₀	GI ₅₀	TGI	LC ₅₀	IC ₅₀	GI ₅₀	TGI	LC ₅₀	IC ₅₀
 1	7.4	>1000	>1000	>1000	1.0	1.1	4.4	1.1	5.7	>1000	>1000	>1000
 2	12.1	>1000	>1000	>1000	4.5	20.9	452.8	20.7	2.1	4.4	22.1	4.5
 3	8.8	>1000	>1000	>1000	4.6	>1000	>1000	>1000	4.2	461.1	>1000	416.9
 4	593.7	>1000	>1000	>1000	3.6	40.1	>1000	38.9	2.8	7.9	61.8	7.8
<i>Cisplatin</i>				60.49				52.79				50.29
<i>5FU</i>				69.79				59.09				61.59

Table 2. GI₅₀, TGI, LC₅₀ and IC₅₀ of test compounds against Hep3B, HT29, and MCF7 cell

Compounds ($\mu\text{g/mL}$)	Hep3B				HT29				MCF7			
	GI ₅₀	TGI	LC ₅₀	IC ₅₀	GI ₅₀	TGI	LC ₅₀	IC ₅₀	GI ₅₀	TGI	LC ₅₀	IC ₅₀
1	2.7	10.6	243.2	10.4	1.6	>1000	>1000	>1000	1.6	135.3	>1000	106.9
2	2.8	9.6	127.3	9.5	3.5	229.4	>1000	100.2	3.5	>1000	>1000	>1000
3	4.3	>1000	>1000	>1000	9.9	>1000	>1000	>1000	1.5	>1000	>1000	>1000
4	3.9	192.8	>1000	176.6	3.8	17.6	465.1	15.2	2.4	32.1	>1000	29.6
<i>Cisplatin</i>				48.69				40.39				63.79
<i>5FU</i>				62.89				65.19				74.19

Table 3. % Cytotoxicity of these compounds and positive controls against A549, Hep3B, MCF7, HeLa, HT29, and FL at IC₅₀ concentrations

Comp.	A549	Hep3B	MCF7	HeLa	HT29	FL
1	19.5	21.8	24.8	25.1	20.3	24.7
2	19.1	26.9	29.2	34.3	38.3	17.1
3	19.3	26.9	31.7	30.7	15.8	25.3
4	16.2	24.7	17.4	27.1	38.5	14.6
<i>Cisplatin</i>	8.63	8.46	10.71	9.85	11.23	8.33
<i>5FU</i>	9.19	9.67	7.69	8.83	7.91	8.44

Table 4. Minimum-inhibitory concentrations (MIC, in $\mu\text{g/mL}$) of these compounds

Compounds	<i>E. faecalis</i>	<i>E. faecalis</i>	<i>S. aureus</i>	<i>S. aureus</i>	<i>S. aureus</i>	<i>E. coli</i>	<i>E. coli</i>	<i>P. eruginosa</i>
	ATCC 19433	ATCC 29212	ATCC 25923	ATCC 29213	ATCC 46300	ATCC 25922	ATCC 35218	ATCC 27853
1	250	250	62.50	125	125	500	500	500
2	62.50	500	31.25	125	62.50	500	500	500
3	500	>1000	62.50	>1000	1000	125	500	500
4	>1000	>1000	>1000	250	250	250	250	250
SCF	250	62.5	250	62.5	250	15.62	31.25	250

SCF. sulbactam (30 μg) + cefoperazone (75 μg), as a positive control

evaluated using the Minimum Inhibition Concentration (MIC) method. We considered our test molecules to be antibacterial at 250 µg/mL and below the MIC values.

The MIC values of the compounds were compared with the values of antimicrobial drugs used as positive controls. When the MIC values of recently prepared molecules shows on Gram (+) bacteria were tested, the antibacterial effect of compounds **1** and **2** against *E. faecalis* (VRE) ATCC 19433 (62.5 – 250 µg/mL), compound **1** against *E. faecalis* ATCC 29212 (250 µg/mL), compounds **1-3** against *S. aureus* ATCC 25923 (31.25 – 62.50 µg/mL), compounds **1, 2** and **4** against *S. aureus* (MSSA) ATCC 29213 (125 – 250 µg/mL), and compounds **1, 2** and **4** against *S. aureus* MRSA ATCC 46300 (62.50 – 250 µg/mL) are more or similar to the antibiotic used as a positive control (SCF) (Table 4). According to the MIC values exhibited by the recently synthesized molecules on Gram (-) bacteria, the antibacterial effect of compounds **3** and **4** against the *E. coli* ATCC 25922

(125 – 250 µg/mL), compound **4** against *E. coli* ATCC 35218 (250 µg/mL), and compound **4** against *P. aeruginosa* ATCC27853 (250 µg/mL) strain are more or similar to the SCF (positive control) (Table 4).

As a result, it is obvious that compounds **1** and **2** have promising activity for future studies. In general, tacrines bearing seven membered hydrocycle had higher activity than tacrines bearing six membered hydrocycle in our previous work [30]. Especially, dibromo tacrine bearing seven membered hydrocycle **2** was more active against microorganisms than its silyl **3** and thiomethyl **4** derivatives.

3.4. DNA binding properties of the compounds

DNA binding properties of the compounds were determined using UV-Vis spectrophotometer. Binding type and the binding constants of the compounds were tried to be explained below. These compounds have no clear redshifts or blue shifts at their maximum absorption peak. When CT-DNA was added to the reaction mixture, the decreasing in the absorption intensity of compounds **2** and **4** showed hypochromic effect and the increasing in the absorption intensity of compounds **2** and **4** caused hyperchromic appearance. The binding constants (K_b), showing the affinity of the complex to DNA, of the compounds with the aid of the Benesi-Hildebrand equation. When the binding constants given in Table 5 are evaluated, it can be seen that the K_b values of the compounds are between 2.9×10^4 and $7.4 \times 10^4 \text{ M}^{-1}$. The binding constants of the

compounds are ordered from large to small as follows: $2 > 4 > 3$. According to data in Table, the compound **3** bind DNA much more strongly than others. However, the binding constants of the compound **1** could not be calculated using UV-Vis spectrophotometric method.

Table 5. The binding constants (K_b) of these compounds

Compound	K_b (M^{-1})
2	2.9×10^4
3	7.4×10^4
4	4.6×10^4

4. CONCLUSION

Recently synthesized disubstituted tacrine bearing six or seven membered hydrocycle were tested for their antibacterial and anticancer activities *in vitro*. We have showed that disubstituted tacrines have significant potential as being antitumor and antibacterial agents. The test results describe both a good antiproliferative effect and a low cytotoxic effect, depending on substitution group on tacrine ring. The *in vitro* studies also displayed that mono silyl substituted seven membered tacrine analogue **3** was found to bind the DNA of cancer cells. According to our results, it is suggested that four disubstituted tacrine derivatives are promising anticancer and antibacterial drug candidates but further pharmacological tests should be worked.

ACKNOWLEDGMENTS

Financial support from the Sakarya University Research Fund (Project number: 2014-02-04-008) is gratefully acknowledged.

REFERENCES

- [1] M. Tugrak, H. I. Gul, H. Sakagami, I. Gulcin and C. T. Supuran, "New azafluorenones with cytotoxic and carbonic anhydrase inhibitory properties: 2-Aryl-4-(4-hydroxyphenyl)-5H-indeno[1,2-b]pyridin-5-ones," *Bioorganic Chemistry*, vol. 81, pp. 433–439, 2018.
- [2] C. Boulanger, C. Giorgio and P. Vierling. "Synthesis of acridine-nuclear localization signal (NLS) conjugates and evaluation of their impact on lipoplex and polyplex-based transfection," *European Journal of Medicinal Chemistry*, vol. 40, no. 12, pp 1295-1306, 2005.
- [3] M. J. B. Moore, C. M. Schultes, J. Cuesta, F. Cuenca, M. Gunaratnam, F. A. Tanius, W. D. Wilson and S. Neidle, "Trisubstituted Acridines

- as G-quadruplex Telomere Targeting Agents. Effects of Extensions of the 3,6- and 9-Side Chains on Quadruplex Binding, Telomerase Activity, and Cell Proliferation,” *Journal of Medicinal Chemistry*, vol. 49, no. 2, pp. 582-599, 2006.
- [4] G. F. Han, R. H. Wang, W. T. Zhang, Y. Y. Zhao, Z. Xing and W. Dai, “Synthesis and Crystal Structure of 7,8-Dihydroquinolino[2,3-a]acridine Derivatives,” *Synthetic Communication*, vol. 39; no.14, pp. 2492-2505, 2009.
- [5] M. Recanatini, A. Cavalli, F. Belluti, L. Piazzzi, A. Rampa, A. Bisi, S. Gobbi, P. Valenti, V. Andrisano, M. Bartolini and V. Cavrini, “SAR of 9-Amino-1,2,3,4-tetrahydroacridine-Based Acetylcholinesterase Inhibitors: Synthesis, Enzyme Inhibitory Activity, QSAR, and Structure-Based CoMFA of Tacrine Analogues,” *Journal of Medicinal Chemistry*, vol. 43, no.10, pp. 2007-2018, 2000.
- [6] E. P. Peçanha, C. A. M. Fraga, E. J. Barreiro, M. F. M. Braga, E. F. R. Pereira and E. X. Albuquerque, “Synthesis and Pharmacological Evaluation of a New 2-Azabicyclo[3.3.0]octane Derivative,” *Journal of Brazilian Chemical Society*, vol. 12, no. 3, pp. 408-412, 2001
- [7] R. N. Katzman, “Alzheimer's Disease,” *The New England Journal of Medicine*, vol. 314, no.15, pp. 964-973, 1986.
- [8] G. M. Shutske, F. A. Pierrat, M. L. Cornfeldt, M. R. Szewczak, F. P. Huger, G. M. Bores, V. Haroutunian and K. L. Davis, “(.+.-)-9-Amino-1,2,3,4-tetrahydroacridin-1-ol. A potential Alzheimer's disease therapeutic of low toxicity,” *Journal of Medicinal Chemistry*, vol. 31, no 7, pp. 1278-1279, 1988.
- [9] M. T. McKenna, G. R. Proctor, L. C. Young and A. L. Harvey, “Novel Tacrine Analogues for Potential Use against Alzheimer's Disease: Potent and Selective Acetylcholinesterase Inhibitors and 5-HT Uptake Inhibitors,” *Journal of Medicinal Chemistry*, vol. 40 no. 22, pp. 3516-3523, 1997.
- [10] J. S. da Costa, D. S. Pisoni, C. B. da Silva, C. L. Petzhold, D. Russowsky and M. A. Ceschi, “Lewis Acid Promoted Friedländer Condensation Reactions between Anthranilonitrile and Ketones for the Synthesis of Tacrine and its Analogues,” *Journal of Brazilian Chemical Society*, vol. 20, no. 8, pp. 1448-1454, 2009.
- [11] G. Li, G. Hong, X. Li, Y. Zhang, Z. Xu, L. Mao, X. Feng and T. Liu, “Synthesis and activity towards Alzheimer's disease in vitro: Tacrine, phenolic acid and ligustrazine hybrids,” *European Journal of Medicinal Chemistry*, vol. 148, pp. 238-254, 2018.
- [12] L. Ismaili, B. Refouvet, M. Benchekroun, S. Brogi, M. Brindisi, S. Gemma, G. Campiani, S. Filipic, D. Agbaba, G. Esteban, M. Unzeta, K. Nikolic, S. Butini and J. Marco-Contelles, “Multitarget compounds bearing tacrine- and donepezil like structural and functional motifs for the potential treatment of Alzheimer's disease,” *Progress in Neurobiology*, vol. 151, pp. 4-34, 2017.
- [13] N. Guzior, A. Wieckowska, D. Panek and B. Malawska, “Recent development of multifunctional agents as potential drug candidates for the treatment of Alzheimer's disease,” *Current Medicinal Chemistry*, vol. 22, pp. 373-404, 2015.
- [14] J. Ruiz, J. Lorenzo, C. Vicente, G. Lopez, J. M. Lopez-de-Luzuriaga, M. Monge, F. X. Aviles, D. Bautista, V. Moreno and A. Laguna, “New palladium(II) and platinum(II) complexes with 9-aminoacridine: structures, luminiscence, theoretical calculations, and antitumor activity,” *Inorganic Chemistry*, vol. 47 pp. 6990-7001, 2008.
- [15] X. Chen, K. Zenger, A. Lupp, B. Kling, J. Heilmann, C. Fleck, B. Kraus and M. Decker, “Tacrine-silibinin codrug shows neuro- and hepatoprotective effects in vitro and pro-cognitive and hepatoprotective effects in vivo,” *Journal of Medicinal Chemistry*, vol. 55, pp. 5231-5242, 2012.
- [16] H. M. Kuan, “Synthesis and in-vitro anticancer evaluation of bistacrine congeners,” *Journal of Pharmacy and Pharmacology*, vol. 53: pp. 83-88, 2001.
- [17] L. H. Hurley, “DNA and its associated processes as targets for cancer therapy,” *Nature Reviews Cancer*, vol. 2, pp. 188-200, 2002.
- [18] Q. Cao, Y. Li, E. Freisinger, P. Z. Qin, R. K. O. Sigel and Z. W. Mao, “G-quadruplex DNA targeted metal complexes acting as potential

- anticancer drugs,” *Inorganic Chemistry Frontiers*, vol. 4, pp. 10-32, 2017.
- [19] H. H. Zou, L. Wang, Z. X. Long, Q. P. Qin, Z. K. Song, T. Xie, S. H. Zhang, Y. C. Liu, B. Lin and Z. F. Chen, “Preparation of 4-([2, 20: 60, 200-terpyridin]-40-yl)-N, Ndiethylaniline NiII and PtII complexes and exploration of their in vitro cytotoxic activities,” *European Journal of Medicinal Chemistry*, vol. 108: pp. 1-12, 2016.
- [20] Z. F. Chen, Q. P. Qin, J. L. Qin, Y. C. Liu, K. B. Huang, Y. L. Li, T. Meng, G. H. Zhang, Y. Peng, X. J. Luo and H. Liang, “Stabilization of G-quadruplex DNA, inhibition of telomerase activity and tumor cell apoptosis of organoplatinum(II) complexes with oxoisoaporphine,” *Journal of Medicinal Chemistry*, vol. 58, pp. 2159-2179, 2015.
- [21] M. J. B. Moore, C. M. Schultes, J. Cuesta, F. Cuenca, M. Gunaratnam, F. A. Tanious, W. D. Wilson and S. Neidle, “Trisubstituted acridines as G-quadruplex telomere targeting agents. Effects of extensions of the 3, 6-and 9-side chains on quadruplex binding, telomerase activity, and cell proliferation,” *Journal of Medicinal Chemistry*, vol. 49 pp. 582-599, 2006.
- [22] S. M. Gowan, R. Heald, M. F. G. Stevens and L. R. Kelland, “Potent inhibition of telomerase by small-molecule pentacyclic acridines capable of interacting with G-quadruplexes,” *Molecular Pharmacology*, vol. 60 pp. 981-988, 2001.
- [23] R. A. Heald, C. Modi, J. C. Cookson, I. Hutchinson, C. A. Laughton, S. M. Gowan, L. R. Kelland and M. F. G. Stevens, “Antitumor polycyclic acridines. 8. Synthesis and telomerase-inhibitory activity of methylated pentacyclic acridinium salts,” *Journal of Medicinal Chemistry*, vol. 45, pp. 590-597, 2002.
- [24] V. Caprio, B. Guyen, Y. O. Boahen, J. Mann, S. M. Gowan, L. M. Kelland, M. A. Read and S. Neidle, “A novel inhibitor of human telomerase derived from 10H-indolo [3, 2-b] quinoline,” *Bioorganic Medicinal Chemistry Letters*, vol. 10, pp. 2063-2066, 2000.
- [25] D. Y. Zeng, G. T. Kuang, S. K. Wang, W. Peng, S. L. Lin, Q. Zhang, X. X. Su, M. H. Hu, H. Wang, J. H. Tan, Z. S. Huang, L. Q. Gu and T. M. Ou, “Discovery of novel 11-triazole substituted benzofuro[3,2-b]quinoline derivatives as c-myc Gquadruplex specific stabilizers via click chemistry,” *Journal of Medicinal Chemistry*, vol. 60, pp. 5407-5423, 2017.
- [26] M. I. F. Bachiller, C. Perez, L. Monjas, J. Rademann and M. I. R. Franco, “New Tacrinee4-Oxo-4H-chromene hybrids as multifunctional agents for the treatment of Alzheimer's disease, with cholinergic, antioxidant, and b-amyloid-reducing properties,” *Journal of Medicinal Chemistry*, vol. 55, pp. 1303-1317, 2012.
- [27] E. H. Rydberg, B. Brumshstein, H. M. Greenblatt, D. M. Wong, D. Shaya, L. D. Williams, P. R. Carlier, Y. P. Pang, I. Silman and J. L. Sussman, “Complexes of alkylene-linked Tacrine dimers with torpedo californica acetylcholinesterase: binding of bis(5)-tacrine produces a dramatic rearrangement in the active-site gorge,” *Journal of Medicinal Chemistry*, vol. 49, pp. 5491-5500, 2006.
- [28] T. M. Ou, Y. J. Lu, J. H. Tan, Z. S. Huang, K. Y. Wong and L. Q. Gu, “G-quadruplexes: targets in anticancer drug design,” *ChemMedChem* vol. 3, pp. 690-713, 2008.
- [29] M. Ekiz, A. Tutar, S. Ökten, “Convenient Synthesis of Disubstituted Tacrine Derivatives via Electrophilic and Copper Induced Reactions,” *Tetrahedron*. vol. 72, pp. 5323-5330, 2016.
- [30] S. Ökten, M. Ekiz, A. Tutar, Ü. M. Koçyiğit, B. Bütün, G. Topçu, İ. Gülçin, “SAR Evaluation of Disubstituted Tacrine Analogues as Promising Cholinesterase and Carbonic Anhydrase Inhibitors,” *Indian Journal of Pharmaceutical Education and Research*, vol. 53, pp. 268-275, 2019.
- [31] S. Ökten, M. Ekiz, Ü. M. Koçyiğit, A. Tutar, İ. Çelik, M. Akkurt, F. Gökalp, P. Taslimi, İ. Gülçin, “Synthesis, Characterization, Crystal Structures, Theoretical Calculations and Biological Evaluations of Novel Substituted Tacrine Derivatives as Cholinesterase and Carbonic Anhydrase Enzymes Inhibitors,” *Journal of Molecular Structure*, vol. 1175, pp. 906-915, 2019.

JOURNAL OF SCIENCE



SAKARYA UNIVERSITY

Sakarya University Journal of Science

ISSN 1301-4048 | e-ISSN 2147-835X | Period Bimonthly | Founded: 1997 | Publisher Sakarya University |
<http://www.saujs.sakarya.edu.tr/>

Title: Key Mechanical Design Performance Features And Mechanical Characterization of Poly-Crystallized Bi_{2.1}Sr_{2.0}-Xtixca_{1.1}Cu_{2.0}Oy Superconducting Ceramic Cuprates

Authors: Tahsin Turgay, Yusuf Zalaoglu, Gurcan Yildirim

Received: 2019-02-13 20:18:19

Accepted: 2019-04-11 10:32:12

Article Type: Research Article

Volume: 23

Issue: 5

Month: October

Year: 2019

Pages: 831-839

How to cite

Tahsin Turgay, Yusuf Zalaoglu, Gurcan Yildirim; (2019), Key Mechanical Design Performance Features And Mechanical Characterization of Poly-Crystallized Bi_{2.1}Sr_{2.0}-Xtixca_{1.1}Cu_{2.0}Oy Superconducting Ceramic Cuprates. Sakarya University Journal of Science, 23(5), 831-839, DOI: 10.16984/saufenbilder.526830

Access link

<http://www.saujs.sakarya.edu.tr/issue/44066/526830>

New submission to SAUJS

<http://dergipark.gov.tr/journal/1115/submission/start>



Key mechanical Design Performance Features and Mechanical Characterization of Poly-crystallized $Bi_{2.1}Sr_{2.0-x}Ti_xCa_{1.1}Cu_{2.0}O_y$ Superconducting Ceramic Cuprates

Tahsin Turgay^{*1}, Yusuf Zalaoglu², Gurcan Yildirim³

Abstract

The primary scope of this study is to examine the variations of key mechanical design performance features and mechanical characterization of $Bi_{2.1}Sr_{2.0-x}Ti_xCa_{1.1}Cu_{2.0}O_y$ superconductors via Vickers hardness tests performed at different test loads between 0.245 N and 2.940 N. The materials are prepared within the molar ratios of $0 \leq x \leq 0.10$ by using the ceramic method in the atmospheric air. The measurement findings obtained indicate that the increment of Sr/Ti partial substitution level regresses remarkably the key design mechanical performances namely mechanical strength, stability, stiffness, critical stress, toughness, flexural strengths and mechanical durability. This means that the existence of Ti impurity matrix leads to the enhancement in the problematic defects, crack initiation sites and stress raisers based on the crack-producing omnipresent flaws. Accordingly, the propagation of the problematic defects accelerates considerably at lower indentation test loads applied, and the problematic defects locate easily in their critical propagation speed. All in all, the crystal defects are out of control, and the Sr/Ti partial substituted $Bi_{2.1}Sr_{2.0-x}Ti_xCa_{1.1}Cu_{2.0}O_y$ superconductors are much easier broken. Additionally, it is noted that every material produced show the typical indentation size effect but in diminish trend with enhancing Sr/Ti partial replacement level. The load-dependent mechanical parameters such as Young's modulus, yield strength, fracture toughness, brittleness index and elastic stiffness coefficients are also discussed in the text.

Keywords: $Bi_{2.1}Sr_{2.0-x}Ti_xCa_{1.1}Cu_{2.0}O_y$ cuprate, Mechanical performance, Mechanical characterization, Vickers hardness, Indentation size effect

* Corresponding Author: tahsinturgay@gmail.com

¹ Sakarya University, Department of Architecture, Sakarya, Turkey. ORCID:0000-0003-0304-1097

² Osmaniye Korkut Ata University, Department of Physics, Osmaniye, Turkey. ORCID:0000-0003-2191-8112

³ Abant Izzet Baysal University, Depart. of Mechanical Engineering, Bolu, Turkey. ORCID:0000-0002-5177-3703

1. INTRODUCTION

In the Leiden University Heike Kamerlingh Onnes discovered the superconductivity phenomenon on 8th April in the year of 1911 when measuring the dc electrical resistivity over temperature of the mercury metal [1]. As well known that the superconductivity exerts in case of two main conditions. These are no electrical resistivity below such a low temperature called as critical transition temperature, and expulsion of magnetic flux fields above a critical applied magnetic field [2]. After the discovery of phenomenon, several scientists have extensively researched to find a new material exhibiting the superconductivity nature. As a matter of fact, the phenomenon has been observed in the following years for the materials such as organic compounds, elements (metals, metalloids, nonmetals: halogens and noble gases), dielectric materials, alloys, rutheno-cuprates, chalcogens, heavy fermions, silicon-based materials, pyrochlore oxides, rare-earth borocarbides, carbon-based compounds, A-15 materials, chevre-phase compounds and cuprates (copper oxide layered samples) that drive the superconductivity nature [3]. Among all the compounds studied for a number of years, the cuprate-layered perovskite superconducting materials have widely attracted remarkable attention of academic researchers due to relatively larger critical temperatures higher than the liquid nitrogen temperature value [4–6]. Moreover, the other appealing characteristic features including much larger pinning ability, operating temperature, current and external magnetic field carrying capacity, smaller energy losses, heat dissipations and power consumptions enable the high temperature cuprate superconductors to use in the metallurgical and materials engineering, material science, energy sectors, particle accelerators, levitated trains, energy sectors, power transmission, sensitive process control, heavy-industrial technological and mechanical engineering-based applications such as generators, transformers and motor fields [7–14]. Besides, the cuprate materials with superior optical and electronic properties as well as much easier phase formation, lower material cost lighter weight/size, simpler availability of chemicals,

harmless powder contents and especially environmental benefits can be much more encountered in the usages in the application fields of future refrigeration, innovative energy infrastructure, industrial, spintronics, medical diagnosis, sensitive process control and hydrogen society [15–18]. In the present work, we investigate the role of partial aliovalent replacement of Sr²⁺ impurities for the Ti⁴⁺ foreign additives in the Bi-2212 superconducting cuprate materials (from the parents of cuprate-layered perovskite superconducting materials) on the practicability and feasibility of Bi-2212 cuprates in the application fields by means of Vickers microhardness experimental measurement methods performed at the various applied test loads between the lowest value of 0.245 N and the highest value of 2.940. We also define the load-dependent key mechanical design performance and mechanical characteristic parameters as regards Young's modulus (E), yield strength (Y), fracture toughness (KIC), brittleness index (B) and elastic stiffness coefficient (C11) parameters throughout the full-text for the first time.

2. EXPERIMENTAL PREPARATION DETAILS AND MEASUREMENTS FOR BULK POLY-CRYSTALLIZED $Bi_{2.1}Sr_{2.0-x}Ti_xCa_{1.1}Cu_{2.0}O_y$ MATERIALS

This part of the paper can be divided into two main parts. The first part is about how we produce the pure and Sr/Ti partial substituted $Bi_{2.1}Sr_{2.0-x}Ti_xCa_{1.1}Cu_{2.0}O_y$ superconducting materials in the molar ratios of $0 \leq x \leq 0.10$ while the second part is interested in the variations of load-dependent key mechanical design performance and mechanical characteristic parameters of Bi-2212 cuprate-layered perovskite superconducting materials using Vickers hardness experimental measurement techniques. All the materials are prepared by using the solid-state reaction method. The chemicals of Bi₂O₃, SrCO₃, CaCO₃, CuO and TiO₂ within the high purity are purchased a distributor. For the first part, all the powder of chemicals is weighed with respect to the stoichiometric ratios (x= 0.00, 0.01, 0.03, 0.05, 0.07 and 0.10) with the assistant of the electronic scales and right after subjected to the milling

process for six hours in medium of air conditions both to get more and more homogeneous powder and to minimize the particle sizes of chemicals. The homogeneous powder of mixture is ground in the agate via the grinder for thirty minutes so that the formation of chemicals reaches to the desired particle sizes. After that, the homogeneous mixture is calcinated for the thirty-six hours at 800 °C in the porcelain crucibles with the 5 °C per min heating-cooling rates under medium of air. The powder mixture is re-milled again for nearly thirty minutes in the agate by means of grinder. The chemical powder in the blackish color is pelletized into volume of 1.5x0.5x0.2 mm³ (rectangular bars) under 300 MPa load in the atmospheric air. The next process is annealing for the solidified powders at 850 °C for twenty-four hours. The bulk samples annealed are shown to be the pure or un-substituted, Ti-1, Ti-2, Ti-3, Ti-4 and Ti-5 in terms of mole-to-mole ratio changing of $x = 0.00, 0.01, 0.03, 0.05, 0.07$ and 0.10 , respectively. As for the second part, the microhardness tests are conducted in the different load intervals of 0.245N-2.940N using SHIMADZU HVM-2 tester in the atmospheric air conditions for 10 seconds within the accuracy of about $\pm 0.1 \mu\text{m}$. The indentation tracks in the diagonal forms are recorded with the calibrated microscope. The measurements (distances between two diagonals) are collected from the different locations on the smooth surfaces of materials both to prevent the hardening problem effects on the accurate values. Accordingly, we calculate the load-dependent key mechanical design performance and mechanical characteristic parameters including elastic modulus (abbreviated as E), fracture toughness (known as K_{IC}), yield strength (called as Y), brittleness index (abbreviated as B) and elastic stiffness coefficient (identified as C_{II}) parameters by the help of the experimental Vickers hardness data gathered. At the same time, the experimental curves enable us to discuss the differentiation of mechanical characterizations features (typical indentation size effect, *ISE* or reverse indentation size effect, *RISE* behavior) with the aliovalent Sr/Ti partial substitution level in the Bi-2212 crystal structure. The former is in the relation to the inverse dependence reduction of true Vickers microhardness parameters whereas *RISE* nature is

related to the direct dependence augmentation in the original Vickers hardness values with increasing the external test load [19–21].

3. RESULTS AND DISCUSSION

3.1. Sr/Ti partial replacement effect on key design mechanical performances of $\text{Bi}_{2.1}\text{Sr}_{2.0-x}\text{Ti}_x\text{Ca}_{1.1}\text{Cu}_{2.0}\text{O}_y$ superconducting materials

The role of Ti dopant on the main mechanical performances of bulk Bi-2212 ceramic materials is surveyed by the microhardness measurements conducted at various applied indentation loads between 0.245 N and 2.940 N. The microhardness experimental curves collected are displayed in Fig. 1.

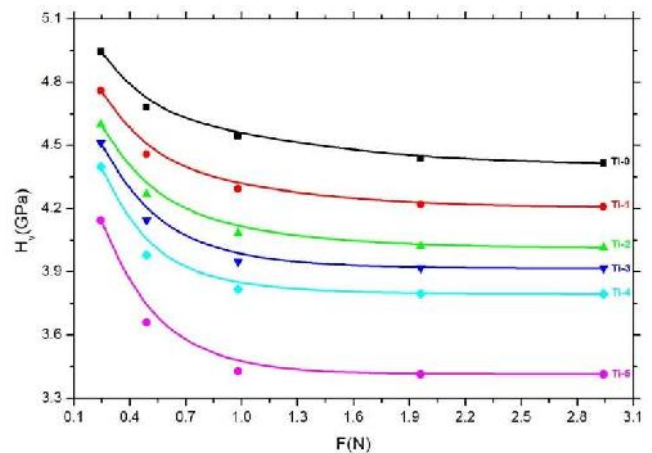


Figure 1. Differentiation of Vickers hardness parameters as a function of external indentation test loads.

It is shown that the key design mechanical performances are found to truncate remarkably with ascending the aliovalent $\text{Sr}^{2+}/\text{Ti}^{4+}$ replacement level in the Bi-2212 superconducting system. This is because the presence of Ti impurity in the main matrix lead to increase harshly the permanent crystal structural problems, cracks, distortions, structural defects, porosity, disorders, voids, misorientations, lattice strains,

inhomogeneity distributions, crack-producing omnipresent flaws, texturing, grain boundary couplings and strength quality of interaction between the superconducting grains in the active Cu-O₂ consecutively stacked layers of multi-layered perovskite Bi-2212 structure. In this regard, the experimental findings in the curves of Fig. 1 confirm that the existence of titanium atoms in the superconducting matrix damages seriously the tetragonal phase and especially critical stress value because of the rapid augmentation of crack initiation regions and stress raisers founded on the crack-producing omnipresent flaws in the distorted crystal lattice. In other words, the damage of aliovalent Sr/Ti partial substitution is explained that the propagation of the problematic defects such as the crack-initiating flaws, voids, cracks and dislocations accelerates significantly under such a relativistic low applied test load value. Thus, the problematic defects easily reach to their critical propagation speed. This is attributed to the fact that the defects are out of control, and the compounds are much easier broken in comparison with before. It is to be mentioned here that the microhardness values provided in Fig. 1 are determined from the following scientific relation:

$$H_v = 1854.4 \left(\frac{F_{load}}{d^2} \right) \quad (1)$$

where the abbreviation of H_v shows the microhardness parameter (in the GPa unit) for the material studied in this work when F_{load} depicts the external indentation test loads. Also, d demonstrates the mean indentation track lengths in the diagonal forms. One can see all the calculations in the curves given in Fig. 1. Further, we numerically tabulate the values in Table 1. Based on the findings, for every material prepared in the current work the augmentation of Sr/Ti partial replacement level as well as the increase of test load results in the degradation of H_v parameters. The decrement trend in the H_v parameters with the load stems from the considerable reduction of active and independent slip systems founded on new-induced strain fields, stress concentrations and stress raisers in the Bi-2212 crystal lattice. On this basis, the highest value of H_v value is found to be about

4.94504 GPa at the test load of 0.245N for the pure sample while the value decreases towards to the smallest value of 4.14537 GPa at 2.940N. Moreover, the microhardness value is found to decrease to minimum value of 3.41318 GPa (for the poly-crystallized Ti-5 sample) at 2.940N applied load. It is very important to note that the penetration of titanium is ploughed to improve the general mechanical properties for the Bi-2212 cuprate materials. The mechanical curves in Fig. 1 also confirm that all the bulk poly-crystallized $Bi_{2.1}Sr_{2.0-x}Ti_xCa_{1.1}Cu_{2.0}O_y$ ceramic materials demonstrate typical indentation size effect (abbreviated as *ISE*) behavior. Namely, there is an inverse dependence (non-linear diminish) of real Vickers hardness values on the test loads. For example, the Ti-2 superconductor presents 0.245N, 4.59865 GPa, 4.26889 GPa, 4.08407 GPa, 4.421 GPa, 4.02184 GPa and 4.01588 GPa at the applied indentation test load of 0.49N, 0.98N, 1.96N and 2.94N, respectively (Table 1).

It is to be stressed here that the *ISE* feature-dependent seems to degrade with the dopant level. This means that the titanium impurity favors the formation of problematic defects in the Bi-2212 crystal structure [22–24]. At the same time, it is to be mentioned here that the main characteristics of the *ISE* nature is formation of reversible and irreversible deformations together in the Bi-2212 system. In this regard, in the poly-crystallized $Bi_{2.1}Sr_{2.0-x}Ti_xCa_{1.1}Cu_{2.0}O_y$ ceramic materials both the elastic and plastic deformations for immediately but in the decrement trend.

Moreover, there is a significant trick associated with the decrement trend on the microhardness curves as given in Fig. 1. Namely, the load-dependent microhardness values degrade dramatically with increasing indentation test loads until 2 N, after which the microhardness values nearly keep on the positions due the presence of saturation limit (or plateau) regions for all the ceramic superconducting materials. As well-known, even if the magnitude of test load increases, Vickers hardness values could not vary meaningfully. In the current study, the microhardness values for the bulk poly-crystallized Ti-6 cuprate ceramic compound reside in the plateau regions at relative lower applied test loads in comparison with those for the

Table 1. Change of original mechanical parameters as regards Young's modulus, yield strength, fracture toughness, brittleness index and elastic stiffness coefficients for the pure and Sr-site Ti partial replaced Bi-2212 cuprate ceramic compounds

<i>Samples</i>	<i>F (N)</i>	<i>H_v (GPa)</i>	<i>E (GPa)</i>	<i>Y (GPa)</i>	<i>K_{IC} (MPam^{1/2})</i>	<i>C_{II} (GPa)^{7/4}</i>	<i>B (m^{-1/2})</i>
<i>Ti-0</i>	0.245	4.94504	405.313	1.648	9.609	16.398	514.633
	0.490	4.68095	383.667	1.560	9.349	14.897	500.703
	0.980	4.54448	372.481	1.515	9.211	14.145	493.350
	1.960	4.43642	363.625	1.479	9.101	13.561	487.449
	2.940	4.41546	361.907	1.472	9.080	13.450	486.296
<i>Ti-1</i>	0.245	4.75976	390.127	1.587	9.423	15.338	505.122
	0.490	4.45794	365.388	1.486	9.119	13.677	488.844
	0.980	4.29511	352.042	1.432	8.951	12.815	479.834
	1.960	4.21798	345.720	1.406	8.871	12.415	475.506
	2.940	4.20866	344.957	1.403	8.861	12.367	474.980
<i>Ti-2</i>	0.245	4.59865	376.921	1.533	9.475	14.441	485.327
	0.490	4.26889	349.893	1.423	9.129	12.678	467.602
	0.980	4.08407	334.745	1.361	8.930	11.733	457.368
	1.960	4.02184	329.644	1.341	8.861	11.422	453.870
	2.940	4.01588	329.156	1.339	8.855	11.392	453.533
<i>Ti-3</i>	0.245	4.51057	369.702	1.504	9.233	13.961	488.513
	0.490	4.14435	339.685	1.381	8.851	12.038	468.261
	0.980	3.94718	323.525	1.316	8.637	11.054	456.987
	1.960	3.91775	321.113	1.306	8.605	10.910	455.280
	2.940	3.91663	321.021	1.305	8.604	10.904	455.215
<i>Ti-4</i>	0.245	4.39828	360.498	1.466	8.962	13.358	490.765
	0.490	3.97946	326.170	1.326	8.525	11.212	466.814
	0.980	3.81743	312.890	1.272	8.349	10.426	457.212
	1.960	3.79576	311.114	1.265	8.326	10.322	455.913
	2.940	3.79502	311.053	1.264	8.325	10.319	455.868
<i>Ti-5</i>	0.245	4.14537	339.769	1.382	9.782	12.043	423.794
	0.490	3.66098	300.067	1.220	9.192	9.689	398.265
	0.980	3.42855	281.016	1.143	8.896	8.639	385.415
	1.960	3.41504	279.909	1.138	8.878	8.579	384.655
	2.940	3.41448	279.863	1.137	8.877	8.577	384.623

Table 2. Fitting parameters for all the bulk poly-crystallized $Bi_{2.1}Sr_{2.0-x}Ti_xCa_{1.1}Cu_{2.0}O_y$ materials

<i>Materials</i>	<i>Fitting relations for the pure and Sr/Ti partial substituted Bi-2212 superconducting cuprates</i>
<i>Pure</i>	$y = 0.2001x^4 - 1.3028x^3 + 2.9015x^2 - 2.7073x + 5.4526$
<i>Ti-1</i>	$y = 0.2067x^4 - 1.3727x^3 + 3.1439x^2 - 3.0115x + 5.3283$
<i>Ti-2</i>	$y = 0.2111x^4 - 1.4200x^3 + 3.3098x^2 - 3.2286x + 5.2111$
<i>Ti-3</i>	$y = 0.2306x^4 - 1.5665x^3 + 3.6882x^2 - 3.5983x + 5.1930$
<i>Ti-4</i>	$y = 0.3303x^4 - 2.1853x^3 + 4.9298x^2 - 4.4875x + 5.2328$
<i>Ti-5</i>	$y = 0.3281x^4 - 2.2154x^3 + 5.1546x^2 - 4.9073x + 5.0696$

other superconducting materials prepared (Fig. 1). The rapid decrement in the H_v value at the test load of 0.245N is thought to be the other clue for the Ti-6 superconducts material. On the other hand, the variation of the H_v value at the test load of 0.245N is noted to be the least decrement as provide in Fig. 1. The different characteristic behavior can be explained by the rapid degradation in the mechanical strength, stability, stiffness, critical stress, toughness, flexural strengths and mechanical durability with the Ti dopant.

Additionally, we point out the negative influence of Sr/Ti substitution in main matrices of ceramic cuprates via the determination of fitting equations between F_{load} and H_v values. One can see the fitting parameters deduced in Table 2.

According to the parameters obtained, it can be summarized that the term of x^4 is calculated to increase systematically from the value of 0.2001 until 0.3281 with enhancing the Sr/Ti substitution level. The value is obviously related to the mechanical sensitivity to the applied test loads due to the increment in the problematic defects in the Bi-2212 cuprate-layered perovskite superconducting materials. Thus, it is derived on the findings that the value of 0.3281 belonging to the bulk Ti-6 superconducting material confirms the least resistant of the material to the applied test load. In other words, the propagation of the problematic defects appeared in the crystal matrix accelerates to locate in their critical propagation speed.

3.2. Role of Sr/Ti replacement on original mechanical performances of $Bi_{2.1}Sr_{2.0-x}Ti_xCa_{1.1}Cu_{2.0}O_y$ cuprate ceramic materials

By using some mathematical relations (arranged below), we determine the crucial variations in the load-dependent key design mechanical performances including the elastic modulus (abbreviated as E), fracture toughness (known as K_{IC}), yield strength (called as Y), brittleness index (abbreviated as B) and elastic stiffness coefficient

(identified as C_{11}) parameters with the different Sr/Ti replacement level [2, 25, 26].

$$E = 81.9635H_v \quad (2)$$

$$Y \approx \frac{H_v}{3} \quad (3)$$

$$K_{IC} = \sqrt{2E\alpha} \quad (4)$$

(α shows surface energy)

$$C_{11} = H_v^{7/4} \quad (5)$$

$$B = \frac{H_v}{K_{IC}} \quad (6)$$

One can encounter all the real mechanical performance parameters in Table 1, also. According to the table, it would be more precise to confirm that the parameters determined are noted to depend sensitively on both the indentation test loads and substitution mechanism. This is attributed to the rapid increment in the problematic defects in the superconducting crystal system. The increment causes to degrade remarkably in mechanical strength, stability, stiffness, critical stress, toughness, flexural strengths and mechanical durability. As for the numerical values for the elastic (Young's) modulus, the maximum value of 405.313 GPa is noted for the pristine material at the constant test load of 0.245N while the minimum value of 279.863 GPa ascribes to the bulk Ti-5 superconducting material at 2.940 N test load. The other values between 360.498 GPa-390.127 GPa are obtained for the moderate dopant levels at 0.245N. The reduction in the Young's modulus verifies the negative influence of titanium foreign additives on polycrystallized Bi-2212 main matrix. Similar results (decrease of Young's modulus with the augmentation of test loads applied) are obtained. On this basis, the smallest elastic modulus value related to the stiffness is observed to be about 279.863 GPa for the Ti-5 cuprate ceramic material at the applied indentation test load of 2.940 N. Likewise, the deepest value for the yield strength is calculated to be about 1.137 GPa for the bulk Ti-5 material

at 2.940 N external indentation test load. Conversely, the maximum yield strength value of 1.648 GPa is observed for the pure sample when 0.245N indentation test load is applied to the sample. Namely, it is found that the Sr/Ti partial replacement in the Bi-2212 crystal lattice harms strongly on the yield strength parameters among the key mechanical design properties. As for the variation of fracture toughness parameters with the Sr/Ti partial substitution, the increase of both dopant level and applied test load leads to degrade the values. Accordingly, the maximum fracture toughness value of 9.609 GPa is noticed for the un-substituted superconducting material at 0.245N applied load while 877 GPa is determined to be the smallest value for the Ti-5 sample. The similar results are observed for the results of brittleness index and elastic stiffness coefficients. All the differentiations of key mechanical design properties discussed above show that the Sr/Ti partial replacement in the main matrix diminishes the mechanical strength, stability, stiffness, critical stress, toughness, flexural strengths and mechanical durability of Bi-2212 superconducting materials.

4. CONCLUSION

In the present work, we investigate the vital role of Sr/Ti partial substitution in the main matrix on the key mechanical design performance parameters and mechanical characterizations of poly-crystallized $Bi_{2.1}Sr_{2.0-x}Ti_xCa_{1.1}Cu_{2.0}O_y$ ceramic materials prepared within the molar ratios of $0 \leq x \leq 0.10$ by means of micro hardness tests conducted at the varied external loads between the value of 0.245 N and 2.940 N in the atmospheric air conditions. It is observed that the key design mechanical performances tend to degrade constantly with increasing the Sr/Ti partial replacement level in superconducting crystal due to the rapid augmentation of problematic defects, crack initiation sites and stress raisers based on the crack-producing omnipresent flaws. Moreover, the durable tetragonal phase and critical stress value are damaged significantly, and hence, the Sr/Ti partial substituted $Bi_{2.1}Sr_{2.0-x}Ti_xCa_{1.1}Cu_{2.0}O_y$ superconducting materials are

much easier broken because of the increased problematic defects in the crystal lattice. Similarly, the Ti dopant level truncates dramatically the typical ISE feature. It is another valuable finding that the existence of excess Ti dopant in the crystal system makes the Bi-2212 material reach to the plateau regions at relative lower applied test loads.

REFERENCES

- [1] H.K. Onnes, Further experiments with Liquid Helium. D. On the change of Electrical Resistance of Pure Metals at very low Temperatures, etc. V. The Disappearance of the resistance of mercury, Koninklijke Nederlandsche Akademie van Wetenschappen Proceedings, vol.14, pp. 113-115, 2011.
- [2] T. Turgay, G. Yildirim, Effect of Diffusion Annealing Temperature on Crack-initiating Omnipresent Flaws, Void/crack Propagation and Dislocation Movements Along Ni Surface-layered Bi-2223 Crystal Structure, Sakarya University Journal of Science, vol. 22, pp.1211-1220, 2018.
- [3] A.T Ulgen, T. Turgay, C. Terzioglu, G. Yildirim, M. Oz, Role of Bi/Tm substitution in Bi-2212 system on crystal structure quality, pair wave function and polaronic states, Journal of Alloys and Compd.vol.764, pp.755–766, 2018.
- [4] S.Y. Oh, H.R. Kim, Y.H. Jeong, O.B. Hyun, C.J. Kim, Joining of Bi-2212 high-T-c superconductors and metals using indium solders, Physica C pp.463–465, pp.464–467, 2007.
- [5] M. Chen, W. Paul, M. Lakner, L. Donzel, M. Hoidis, P. Unternaehrer, R. Weder, M. Mendik, 6.4 MVA resistive fault current limiter based on Bi-2212 superconductor, Physica C vol..372, pp.1657–1663, 2002.
- [6] J.D. Hodge, H. Muller, D.S. Applegate, Q. Huang, A resistive fault current limiter based on high temperature superconductors, Appl. Supercond. vol.3, pp.469–482, 1995.

- [7] K.Y. Choi, I.S. Jo, S.C. Han, Y.H. Han, T.H. Sung, M.H. Jung, G.S. Park, S.I. Lee, High and uniform critical current density for large-size $\text{YBa}_2\text{Cu}_3\text{O}_{7-y}$ single crystals, *Curr. Appl. Phys.* vol.11, pp. 1020–1023, 2011.
- [8] M. Runde, Application of high- T_c superconductors in aluminum electrolysis plants, *IEEE T. Appl. Supercond.* vol. 5, pp.813–816, 1995.
- [9] A.T. Ulgen, I. Belenli, The Effect of Fe Diffusion on Some Physical and Superconducting Properties of MgB_2 , *J. Supercond. Nov. Magn.* vol.30, pp.1089–1095, 2017.
- [10] S. Nagaya, N. Hirano, M. Naruse, T. Watanabe, T. Tamada, Development of a high-efficiency conduction cooling technology for SMES coils, *IEEE T. Appl. Supercond.* vol.23, pp.5602804–5602807, 2013.
- [11] H.H. Xu, L. Cheng, S.B. Yan, D.J. Yu, L.S. Guo, X. Yao, Recycling failed bulk YBCO superconductors using the $\text{NdBCO}/\text{YBCO}/\text{MgO}$ film-seeded top-seeded melt growth method, *J. Appl. Phys.* vol.111, pp.103910, 2012.
- [12] A.T. Ulgen, I. Belenli, Sintering time dependence of iron diffusion in MgB_2 and its effect on superconducting properties, *AIP Conference Proceedings*, no.1815, pp.040008, 2017.
- [13] T.A. Coombs, A finite element model of magnetization of superconducting bulks using a solid-state flux pump, *IEEE T. Appl. Supercond.* vol.21, pp.3581–3586, 2011.
- [14] S.B. Guner, Y. Zalaoglu, T. Turgay, O. Ozyurt, A.T. Ulgen, M. Dogruer, G. Yildirim, A detailed research for determination of Bi/Ga partial substitution effect in Bi-2212 superconducting matrix on crucial characteristic features, *J. Alloy. Compd.* vol.722, pp.388–398, 2019.
- [15] A.T. Ulgen, F. Karaboga, M. Karakaya, R. Podila, A.M. Rao, I. Belenli, Improved transport properties of MgB_2 superconducting round wires via minute addition of gold nanoparticles, *Ceram. Int.*, vol.45, pp.1031–1036, 2019.
- [16] F. Karaboga, A.T. Ulgen, H. Yetis, M. Akdogan, M. Pakdil, I. Belenli, Mechanical properties and uniformity of Fe- MgB_2 wires upon various wire drawing steps, *Mat. Sci. Eng. A-Struct.* vol.721 pp.89–95, 2018.
- [17] W. Buckel, R. Kleiner, *Superconductivity: Fundamentals and Applications*, 2nd ed., Wiley-VCH Verlag, Weinheim, 2004.
- [18] A.T. Ulgen, I. Belenli, Time-Dependent Diffusion Coefficient of Fe in MgB_2 Superconductors, *J. Supercond. Nov. Magn.* vol.30, pp.3367–3375, 2017.
- [19] K. Sangwal, On the reverse indentation size effect and microhardness measurement of solids, *Mat. Chem. Phys.* vol.63, pp.145–152, 2000.
- [20] R. Awad, A.I. Abou-Aly, M. Kamal, M. Anas, Mechanical properties of $(\text{Cu}_{0.5}\text{Tl}_{0.5})\text{-1223}$ substituted by Pr, *J. Supercond. Nov. Magn.* vol.24, pp.1947–1956, 2011.
- [21] A.A. Elmustafa, D.S. Stone, Nanoindentation and the indentation size effect: Kinetics of deformation and strain gradient plasticity, *J. Mech. Phys. Solid.* vol.5, pp.357–381, 2003.
- [22] M.M. Pasare, M.I. Petrescu, A theoretical model for the true hardness determination of Ni-P/SiC electroplated composites, *Mater. Plast.* vol.45, pp. 87–90, 2008.
- [23] F. Poehl, S. Huth, W. Theisen, Detection of the indentation-size-effect (ISE) and surface hardening by analysis of the loading curvature C, *Int. J. Solids Struct.* vol.84, pp.160–166, 2016.

- [24] R.K. Abu Al-Rub, Prediction of micro and nanoindentation size effect from conical and pyramidal indentation, *Mech. Mater.* vol.39, pp.787–802, 2007
- [25] Y. Zalaoglu, B. Akkurt, M. Oz, G. Yildirim, Transgranular region preference of crack propagation along Bi-2212 crystal structure due to Au nanoparticle diffusion and modeling of new systems, *J. Mater. Sci: Mater. El.* vol.28, pp.12839–12850, 2017.
- [26] B. Akkurt, G. Yildirim, Change of mechanical performance and characterization with replacement of Ca by Gd nanoparticles in Bi-2212 system and suppression of durable tetragonal phase by Gd, *J. Mater. Sci: Mater. El.* vol.27, pp.13034–13043, 2016.

JOURNAL OF SCIENCE



SAKARYA UNIVERSITY

Sakarya University Journal of Science

ISSN 1301-4048 | e-ISSN 2147-835X | Period Bimonthly | Founded: 1997 | Publisher Sakarya University |
<http://www.saujs.sakarya.edu.tr/>

Title: Mechanochemical Conversion of Domestic Celestite Mineral To SrCO_3 in The Ammonium Oxalate Media

Authors: Mert Zorađa

Received: 2019-03-05 00:11:51

Accepted: 2019-04-12 16:14:46

Article Type: Research Article

Volume: 23

Issue: 5

Month: October

Year: 2019

Pages: 840-847

How to cite

Mert Zorađa; (2019), Mechanochemical Conversion of Domestic Celestite Mineral To SrCO_3 in The Ammonium Oxalate Media. Sakarya University Journal of Science, 23(5), 840-847, DOI: 10.16984/saufenbilder.535643

Access link

<http://www.saujs.sakarya.edu.tr/issue/44066/535643>

New submission to SAUJS

<http://dergipark.gov.tr/journal/1115/submission/start>

Mechanochemical Conversion of Domestic Celestite Mineral to SrC_2O_4 in The Ammonium Oxalate Media

Mert Zoraga ^{*1}

Abstract

The main raw material used in the production of Sr metal and its compounds is SrSO_4 (celestite) mineral and Turkey has valuable Sr mineral deposits. One of the important steps in the production of Sr compounds is the production of strontium oxalate compound that does not contain alkali compounds as contamination. Strontium is used as a primary raw material in the production of oxalate superconducting material and luminescence.

In this study, in situ conversion of SrSO_4 into $\text{SrC}_2\text{O}_4 \cdot \text{H}_2\text{O}$ by ammonium oxalate is investigated and the effects of rotational speed, ball / sample ratio and $(\text{NH}_4)_2\text{C}_2\text{O}_4 / \text{SrSO}_4$ mole ratio on the conversion reaction were determined. It was found that the conversion of SrSO_4 to $\text{SrC}_2\text{O}_4 \cdot \text{H}_2\text{O}$ was increased with increasing mole ratio of $(\text{NH}_4)_2\text{C}_2\text{O}_4$ to SrSO_4 . The maximum conversion, above 70 %, was achieved by using $(\text{NH}_4)_2\text{C}_2\text{O}_4 / \text{SrSO}_4$ mole ratio: 1.5, rotation speed: 500 rpm and ball / sample ratio: 13.

Keywords: Celestite, strontium oxalate, mechanochemistry

1. INTRODUCTION

The main raw material used in the production of Sr metal and its compounds is the celestite mineral with the basic component of SrSO_4 . Turkey has approximately 2.5 million tons of celestite reserves, which is one of the world's highest percentage of strontium-containing mineral deposits. The celestite mineral is enriched by Barit Maden Turk A.S. and converted into

celestite concentrate containing 95-97 % SrSO_4 [1].

One of the important steps in the production of Sr compounds is to obtain the strontium oxalate compound without any alkali contamination. Strontium oxalate, Bi - Sr - Ca - Cu - oxide (BiSCCO) is used as a primary raw material for the production of superconducting and luminescent materials. Depending on the pH of the reagent solution used, there are different types of strontium oxalate such as anhydrous (SrC_2O_4),

* Corresponding Author: mzoraga@istanbul.edu.tr

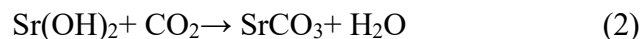
¹ Istanbul University-Cerrahpasa, Engineering Faculty, Metallurgical and Materials Engineering Department, Istanbul, Turkey. ORCID: 0000-0002-7723-728X

monohydrate (SrC₂O₄.H₂O), dihydrate (SrC₂O₄.2H₂O) and acid (Sr (HC₂O₄) (C₂O₄) 0.5.H₂O). The studies in the literature have focused on the conversion of SrSO₄ to SrCO₃ by using different carbonate sources [2, 3]. There are few studies on the conversion of strontium oxalate. The current studies have focused on the thermal decomposition of strontium oxalate, co-precipitation of H₂C₂O₄ and (NH₄)₂C₂O₄ solutions from nitrate solutions and production of superconducting materials [4-6].

Kobe and Deiglmeier [7] examined the conversion of SrSO₄ to SrCO₃ using Na₂CO₃ and K₂CO₃ solutions. It was determined that 96 % conversion was obtained depending on the experimental conditions. Iwai and Toguri [2] studied the conversion of SrSO₄ in Na₂CO₃ solution. They determined that SrCO₃ is formed on the surface of SrSO₄ particles and the rate of diffusion of the reactant from this porous product layer had controlled the reaction rate. Castillejos et al. [3] examined the effect of the solid - liquid ratio, pH value of the solution, temperature, stirring speed on conversion of the celestite concentrate to SrCO₃ by using Na₂CO₃ solution. It was reported that the reaction rate was controlled by the rate of diffusion of the CO₃²⁻ ions between the pores of the product layer.

During the application of the mechanochemical method defined as the progression of the chemical reaction with the help of mechanical energy, the dense product layer surrounding the reactant grains is broken and the new solid reactant surfaces are exposed. Thereby, the chemical reactions progresses in a shorter period. Obut et al. [8], Erdemoglu et al. [9] and Setoudeh et al. [10] showed that this situation was possible when Na₂CO₃ solutions were used. Bingol et al. [11,12] compared the conversion of SrSO₄ to SrCO₃ by using (NH₄)₂CO₃ reactant in both aqueous and anhydrous mechanochemical methods. It was found that 99.10 % and 98.10 % conversion values were achieved with aqueous and anhydrous mechanochemical method, respectively. Zhang and Saito [13] studied the production of Sr(OH)₂ from SrSO₄ by anhydrous mechanochemical method using NaOH. They determined that Sr(OH)₂, obtained as a result of

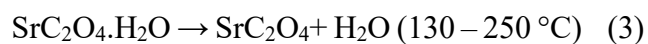
the reaction according to Reaction 1, transformed into SrCO₃ easily with CO₂ in air according to Reaction 2.



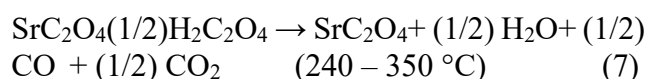
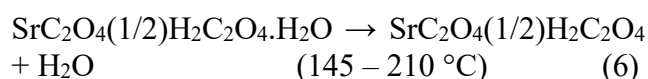
Setoudeh and Welham [14, 15] investigated the reduction of SrSO₄ by using Al and Mg. In these highly exothermic reactions, when Mg was used, the reaction products were SrS and MgO. On the other hand, when Al was used, they determined that Sr₃Al₃₂O₅₁, SrAl₄O₇ and SrAl₂O₄ compounds were formed depending on the grinding time of the mill as well as the SrS and Al₂O₃ compounds.

Selim et al. [16] studied the precipitation of SrC₂O₄.H₂O by using SrCl₂ and Na₂C₂O₄ compounds. In their study, they examined the thermal decomposition of SrC₂O₄.H₂O in different gas atmospheres (air, H₂, N₂ and CO₂) and found that dehydration occurred in two stages. The majority of the water was released at 180 °C and 5 % at 270 °C. They stated that the decomposition reaction of SrC₂O₄ to SrCO₃ occurred at a temperature range of 400 - 480 °C and the reaction was affected by the particle size and morphology of SrCO₃. Dollimore [6] studied the thermal decomposition of SrC₂O₄.2,5H₂O and SrC₂O₄.H₂O in N₂ atmosphere. The samples were prepared by Sr(NO₃)₂ and H₂C₂O₄ solutions. It was reported that the dehydration reaction of SrC₂O₄.H₂O occurred in one stage, but the dehydration reaction of SrC₂O₄.2,5H₂O was occurred gradually due to the crystal symmetry.

Knaepen et al. [4] used Sr(NO₃)₂, H₂C₂O₄.2H₂O and (NH₄)₂C₂O₄.H₂O solutions for the synthesis of different structures of strontium oxalate. They determined that two different forms of neutral strontium oxalate (SrC₂O₄.xH₂O) and acid strontium oxalate (SrC₂O₄.yH₂C₂O₄.xH₂O) were obtained depending on the concentration of H₂C₂O₄ or (NH₄)₂C₂O₄. They stated that the thermal degradation of SrC₂O₄.H₂O in the Ar atmosphere was carried out according to Reactions 3-5. The weight decreases as a result of the degradation where 9.50 %, 14.10 % and 22.70 % theoretical values were calculated, respectively for the Reactions 3-5.

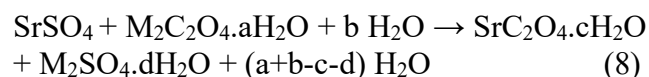


When the thermal decomposition of acid strontium oxalate under the same conditions were examined, they stated that the degradation reactions were carried out in four stages according to Reactions 6, 7, 4 and 5 respectively and the weight decrease was in accordance with the theoretical values of 7.90 %, 18.50 %, 11.40 % and 18.80 % respectively for the Reactions 6-7 and 4-5.



Christensen and Hazell [5] studied the thermal decomposition and crystal structures of the tetragonal SrC₂O₄·2D₂O and triclinic SrC₂O₄·D₂O prepared with Sr(NO₃)₂, H₂C₂O₄·2H₂O and 99.70 % D₂O. They determined that the dehydration step of the SrC₂O₄·xD₂O compound was carried out at two temperatures: 180 °C and 300 °C while the SrC₂O₄·H₂O compound was dehydrated at 150 °C. When they examined the crystal structures of SrC₂O₄·2D₂O and SrC₂O₄·D₂O, they found that SrC₂O₄·2D₂O was in tetragonal structure and that the Sr atom coordinated with eight O atoms from 6 oxalate and 2 water molecules. In addition, they determined that SrC₂O₄·D₂O was triclinic, and that Sr atom coordinated with eight O atoms, 7 of which were oxalate and 1 was the water molecule. Price et al. [17] studied non-aqueous SrC₂O₄ single crystal yield at 240 °C by hydrothermal method using FeC₂O₄·2H₂O and SrCl₂·6H₂O to provide a sufficiently large single crystal formation suitable for crystal structure analysis instead of Na₂C₂O₄ and H₂C₂O₄·2H₂O as oxalate source. As a result of their experimental studies, they stated that each Sr atom coordinates with eight O atoms and that the SrO₈ structure is in the square antiprism geometry. Bacce et al. [18] examined the thermal decomposition of SrC₂O₄·H₂O and the effect of Eu³⁺ addition by using conventional and ultrasonic mixing at 80 °C

using SrCl₂ and (NH₄)₂C₂O₄ solutions. They stated that the ultrasonic mixing and Eu³⁺ admixture reduced the particle size, provided uniform grains, and that the final reaction product was composed of SrCO₃, SrO and Sr(OH)₂ mixture due to the fact that the water could not completely dissociate as a result of the decomposition in the air atmosphere at 1050 °C. Zhang et al. [19] studied the production of strontium oxalate and morphology in polymethacrylic acid (PMAA) solution at room temperature using SrCl₂ and Na₂C₂O₄. In these experimental conditions, they determined that SrC₂O₄ is formed in 6 – 7 μm dimensions and it has a biomimetic growth. Yu et al. [20] investigated the effect of polystyrenmaleic acid (PSMA) on the production of SrC₂O₄·2H₂O using SrCl₂ and Na₂C₂O₄ solutions. They stated that the crystals of SrC₂O₄·2H₂O collapsed in the double pyramid structure at room temperature without using PSMA and when the PSMA was used, due to the concentration of the Sr²⁺ ion with PSMA, the precipitation time increased and the morphology turned into a peanut structure by increasing the PSMA concentration. Obut [21] examined the effect of H₂C₂O₄, Na₂C₂O₄ and (NH₄)₂C₂O₄ solutions on the strontium oxalate conversion by using chemical purity SrSO₄ and concentrated celestite. They found that H₂C₂O₄ and Na₂C₂O₄ had no effect on the conversion of SrSO₄ by using a stoichiometric amount of oxalate ion source according to the Reaction 8, but when using (NH₄)₂C₂O₄, SrCO₄ and celestite concentrate of chemical purity were obtained with 84.60 % and 74.70 % conversion respectively.



The mechanochemical method is more effective than chemical conversion owing to uncover new reaction areas on particle surface especially when a protective layer forms on the surface of solid particles. The aim of this study is to investigate the conversion of celestite to SrC₂O₄·H₂O by using mechanochemical method and to determine the effects of rotational speed, ball to sample ratio and concentration of the solution on the conversion reaction.

2. MATERIALS AND METHODS

2.1. Materials and Techniques

Celestite concentrate was obtained from Barite Maden Turk A.S. (Turkey). The celestite concentrate was wet sieved (Octagon 200) and -75 + 53 μm particle size fraction was collected. $(\text{NH}_4)_2\text{C}_2\text{O}_4$ solutions, which were prepared by dissolving of chemically pure $(\text{NH}_4)_2\text{C}_2\text{O}_4$ (Merck) in distilled water, were used in the conversion experiments. The simultaneous TG - DTA (TA - SDT Q600) device was used to determine the conversion of the solid reaction products. The characterization of the solid reaction products was carried out with X-ray powder diffractometer (XRD) (X Pert Pro) using Cu-K α ($\lambda = 1.54056 \text{ \AA}$) monochromatic X-ray. The results of the quantitative analysis of the celestite concentrate with the XRF device (Panalytical Axios - Minerals) are shown in Table 1.

Table 1. Chemical composition of celestite concentrate

Compound	Composition (wt %)
SrSO ₄	94.82
BaSO ₄	2.85
CaCO ₃	1.52
SiO ₂	0.43
Fe ₂ O ₃	0.21
Al ₂ O ₃	0.08
PbSO ₄	0.06
CuO, ZnO	< 0.02

2.2. Experimental Procedure

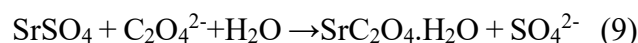
The experiments were carried out in MSE brand mills using 500 mL volumetric ceramic reaction chamber, 200 mm diameter ceramic balls and 250 mL $(\text{NH}_4)_2\text{C}_2\text{O}_4$ solution (AOX) and celestite concentrate. The MSE brand mill has rotating rollers that can be adjusted according to the chamber diameter to be used. It also provides effective milling and mixing by adjusting the rotation speed according to the chamber and ball diameter. SrSO₄ to SrCO₃ conversion reaction yield were investigated by the following parameters: milling time: 3 - 8 h, ball / sample ratio: 9, 11 and 13; $(\text{NH}_4)_2\text{C}_2\text{O}_4$ / SrSO₄ mole ratio: 1.1, 1.3 and 1.5; and the rotational speed of

300, 400 and 500 rpm. After the conversion experiments, the solid-liquid separation was carried out by filtration and the solid reaction products were dried at 80 °C for 8 h. TG - DTA diagrams were obtained with 50 mg sample in alumina crucible and a blank alumina crucible as reference material, with a linear heating rate of 10 °C min⁻¹ and a flow rate of 100 mL min⁻¹ linear air flow.

3. RESULTS AND DISCUSSION

3.1. The conversion reaction mechanism of SrSO₄ to SrCO₃

The conversion reaction of SrSO₄ to SrCO₃ is a solid - liquid heterogeneous type reaction (Reaction 9):



The solubility product of SrSO₄ ($K_{\text{Sp},\text{SrSO}_4} = 2.8 \times 10^{-7}$) is greater than the solids product of SrCO₃ ($K_{\text{Sp},\text{SrCO}_3} = 5.6 \times 10^{-8}$) [9,21]. In this case, the solubility of SrCO₃ in aqueous solutions ($2.37 \times 10^{-4} \text{ mol L}^{-1}$) is less compared to the solubility of SrSO₄ ($5.29 \times 10^{-4} \text{ mol L}^{-1}$), and this is the driving force for the conversion reaction. The molar volumes of SrSO₄ and SrCO₃ calculated by taking into account the densities and molar weights of $46.38 \times 10^{-3} \text{ m}^3 \text{ kmol}^{-1}$ and $71.18 \times 10^{-3} \text{ m}^3 \text{ kmol}^{-1}$ respectively. Since the molar volume of SrCO₃ is greater than that of SrSO₄, SrCO₃, which forms the solid reaction product and surround the surfaces of unreacted SrSO₄ grains, is non-porous. When the solid product layer completely surrounds the surface of the solid reactant particles, it shows a protective behavior and does not allow ion diffusion, and as a result, the conversion reaction comes to a standstill and stops.

By applying the mechanochemical method, this protective product layer is broken, and a new unreacted surface is formed and thus the progression of the conversion reaction is ensured.

3.2. The Effects of Experimental Parameters

(NH₄)₂C₂O₄ (AOX) in the solution of the reaction rate of SrSO₄ to SrC₂O₄ conversion to determine the effect of rotational speed of 300, 400, 500 rpm and (NH₄)₂C₂O₄ (AOX) / SrSO₄ = 1.1, 1.3 and 1.5 experiments for 8 hours were performed. In the experiments, 13.81, 11.69 and 10.13 g of concentrated celestite in the particle size range of -75 + 53 μm, 0.08 mol (NH₄)₂C₂O₄ by using 250 mL of solution obtained by dissolving the ball / sample = 9, 11 and 13 were studied. As shown in Figure 1, the rotational speed of 500 rpm is sufficient to break the protective SrC₂O₄.H₂O layer formed on the surface of SrSO₄ grains and under these conditions, the conversion rate has reached the highest value. In the experiments performed to determine the effects of other parameters on the conversion reaction rate, the rotational speed was kept constant at 500 rpm.

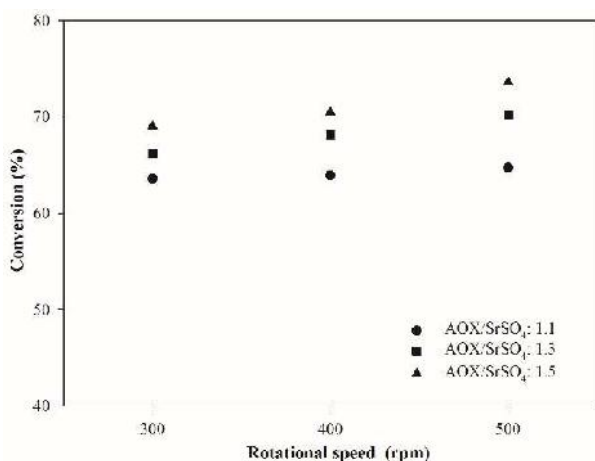


Figure 1. The effect of rotational speed on the conversion reaction to SrSO₄ in SrC₂O₄

In order to determine the effect of AOX on the conversion of SrSO₄ to SrC₂O₄, experiments with AOX / SrSO₄ = 1.1, 1.3 and 1.5 were carried out. As shown in Figure 2, the conversion at 1.5 molar ratio was found to be over 70 %. The reaction takes place as a result of direct contact between the surface of the SrSO₄ and the AOX. Due to the high concentration of C₂O₄²⁻ ions, ion exchange increases and the conversion of SrO₄ to SrC₂O₄.H₂O is also increased with the increase in the AOX / SrSO₄ molar ratio

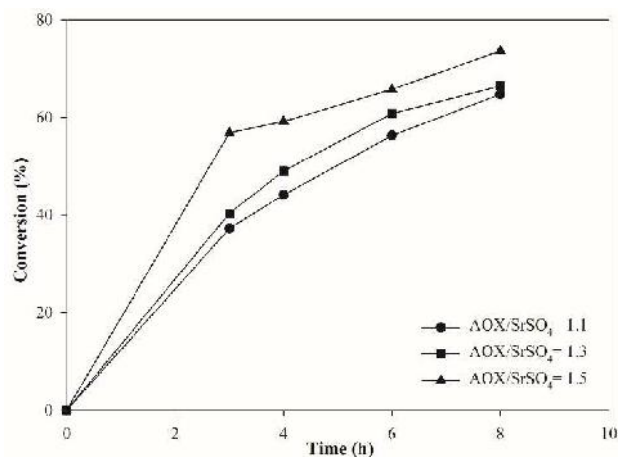


Figure 2. Effect of mole ratio of AOX / SrSO₄ on conversion reaction of SrSO₄ to SrC₂O₄

Experiments were carried out for 8 h to determine the effect of ball / sample ratio of 9, 11 and 13 and (NH₄)₂C₂O₄ (AOX) / SrSO₄ = 1.1, 1.3 and 1.5 on the reaction rate of SrSO₄ to SrC₂O₄ conversion. As shown in Figure 3, the conversion value increased with increasing the ball / sample and AOX/SrSO₄ ratios. In addition, AOX/SrSO₄ ratio has more significant effect on the conversion value at lower ball/sample ratios.

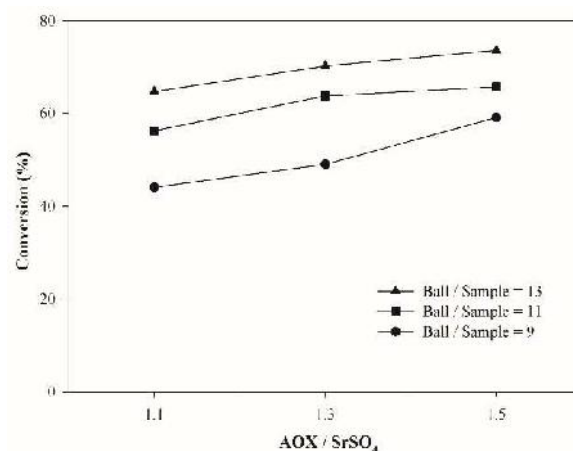


Figure 3. The effect of ball / sample ratio on the conversion reaction to SrSO₄ in SrC₂O₄

3.3. TG-DTA and XRD Analyzes

The conversion reaction of SrSO₄ to SrC₂O₄ were carried out to determine the effects of AOX on AOX / SrSO₄ = 1.1, 1.3 and 1.5 at different reaction times (3, 4, 6 and 8 hours) at 500 rpm rotational speed. The diagrams obtained from the simultaneous TG - DTA analysis of the solid

reaction products obtained are shown in Figures 4 and 5.

TGA analysis carried out in air atmosphere shows three weight loss steps (Figure 4). First weight loss step is between 90 - 305 °C due to the formation of SrC₂O₄, which was achieved by losing the crystal water of SrC₂O₄·H₂O (Reaction 3). The second weight loss between 370 - 595 °C (Reaction 4), the third weight loss between 615 - 1100 °C show that SrCO₃ released CO₂ and converted into SrO (Reaction 5). Weight loss values are shown in Table 2. These values are different from the theoretical values. This difference shows that the sample is not composed only of SrC₂O₄·H₂O, and some of the SrSO₄ remained unchanged.

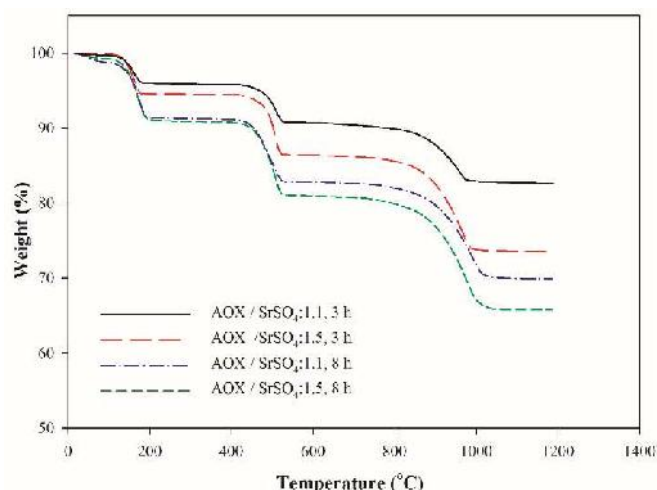


Figure 4. TG analyses of reaction products from conversion of SrSO₄ to SrC₂O₄

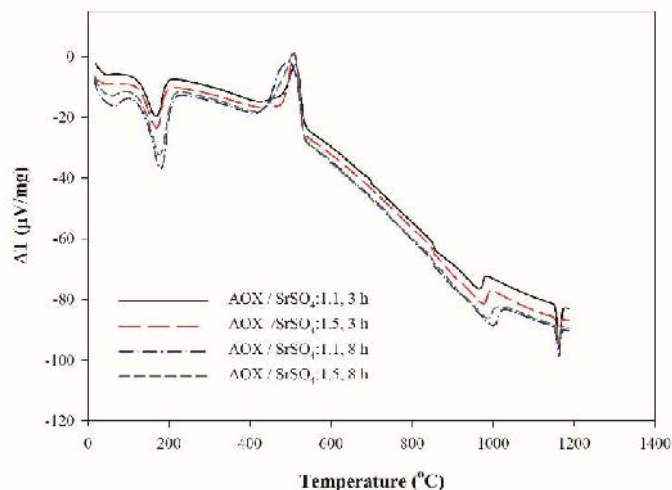


Figure 5. DTA analyses of reaction products from conversion of SrSO₄ to SrC₂O₄

The DTA diagram taken in the air atmosphere (Figure 5) shows the presence of three reactions. Peaks at 171 °C (endothermic peak), 502 °C (exothermic peak) and 980 °C (endothermic peak) are those of Reactions 3, 4 and 5, respectively. It belongs to the reversible allotropic transformation of unreacted SrSO₄ in the severe and sharp endothermic peak sample seen at 1156 °C in the DTA diagram [22]. XRD diagram in Figure 6 shows that the substance consists of a mixture of SrC₂O₄·H₂O (ICDD 20-1203) which is the reaction product of the unreacted SrSO₄ (ICDD 05-0593).

Table 2. The weight loss values obtained from the TG

Sample	Weight loss, %			
	First reaction step	Second reaction step	Third reaction step	Conversion, %
AOX / SrSO ₄ : 1.5, 3 h	5.33	8.41	12.62	56.71
AOX / SrSO ₄ : 1.5, 8 h	8.66	9.63	15.12	71.88
AOX / SrSO ₄ : 1.1, 8 h	7.61	8.49	12.78	62.13
AOX / SrSO ₄ : 1.1, 3 h	3.79	4.77	7.84	35.28
Theoric Value	9.30	23.76	46.48	

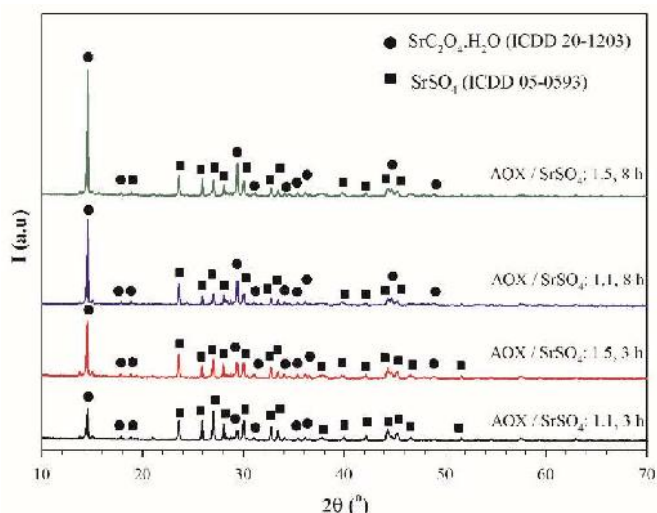


Figure 6. XRD analyses of reaction products

4. CONCLUSIONS

The solubility of SrC₂O₄.H₂O in aqueous solutions is less compared to the solubility of SrSO₄, and this is the driving force for the conversion reaction.

Since the molar volume of SrC₂O₄.H₂O is greater than that of SrSO₄, non-porous SrC₂O₄.H₂O solid product layer formed on the surface of SrSO₄ particles which shows a protective layer characteristic when it completely surrounds the surface of solid reactant grains. This layer, which does not allow ion diffusion, was broken by application of the mechanochemical method, where the formation of new reaction surface resulted in the progression of the conversion reaction.

The conversion of SrSO₄ to SrC₂O₄.H₂O reached the highest value (above 70 %) under the relevant test conditions when working at a rotational speed of 500 rpm. When the reaction time or ball / sample ratio is increased according to the obtained test results, it is expected that the conversion will reach higher values.

Since the reaction was the result of direct contact between the AOX and SrSO₄, it was determined that the conversion of SrSO₄ to SrC₂O₄.H₂O increased with the increase in mole ratio of AOX to SrSO₄. The highest conversion value was above 70 % at AOX / SrSO₄: 1.5 mole ratio.

REFERENCES

- [1] MTA, "Sivas ili maden ve enerji kaynakları," Retrieved 17 September 2018, from http://www.mta.gov.tr/v3.0/sayfalar/bilgimerkezi/maden_potansiyel_2010/sivas_madenler.pdf. 2010.
- [2] M. Iwai and J.M. Toguri, "The leaching of celestite in sodium carbonate solution," *Hydrometallurgy*, vol. 22, no. 1–2, pp. 87–100, 1989.
- [3] A.H. Castillejos, B. De La Cruz Del and S. Uribe, "The direct conversion of celestite to strontium carbonate in sodium carbonate aqueous media," *Hydrometallurgy*, vol. 40, no. 1–2, pp. 207–222, 1996.
- [4] E. Knaepen, J. Mullens, J. Yperman and L.C. Van Poucke, "Preparation and thermal decomposition of various forms of strontium oxalate1". *Thermochim. Acta*, vol. 284, no. 1, pp. 213–227, 1996.
- [5] A.N. Chritensen and R.G. Hazell, "Thermal analysis and crystal structure of tetragonal strontium oxalate dehydrate and of triclinic strontium oxalate hydrate," *Acta Chem. Scandin.*, vol. 52, pp. 508–512, 1998.
- [6] D. Dollimore, "The thermal analysis of strontium oxalate," *Thermochimica Acta*, vol. 92, no. 15, pp. 543–546, 1985.
- [7] A.K. Kobe and N.J. Deiglmeier, "Conversion from strontium sulfate by metathesis with alkali carbonate solution," *Ind. and Eng. Chem.*, vol. 35, no. 3, pp. 323–325, 1943.
- [8] A. Obut, P. Balaz and I. Girgin I, "Direct mechanochemical conversion of celestite to SrCO₃," *Miner. Eng.*, vol. 19, no. 11, pp. 1185–1190, 2006.
- [9] M. Erdemoglu, S. Aydogan and M. Canbazoglu, "A kinetic study on the conversion of celestite (SrSO₄) to SrCO₃ by mechanochemical processing,

- Hydrometallurgy, vol. 86, no. 1–2, pp.1–5, 2007.
- [10] N. Setoudeh, N.J. Welham and S.M. Azami, “Dry mechanochemical conversion of SrSO₄ to SrCO₃,” J. Alloys Compd., vol. 492, no. 1–2, pp. 389–391, 2010.
- [11] D. Bingol, S. Aydogan and S.K. Bozbaş, “Optimization of the wet mechanochemical process conditions of SrSO₄ to SrCO₃ and (NH₄)₂SO₄ by using response surface methodology,” Metall. Trans. B, vol. 43B, pp. 1214–1219, 2012.
- [12] D. Bingol, S. Aydogan and S.K. Bozbaş, “Production of SrCO₃ and (NH₄)₂SO₄ by dry mechanochemical processing of celestite,” J. Ind. Eng. Chem., vol. 18, no. 2, pp. 834–838, 2012.
- [13] Q. Zhang and F. Saito, “Mechanochemical processing of celestine,” Chem. Eng. J., vol. 66, no: 1, pp. 79–82, 1997.
- [14] N. Steoudeh and N.J. Welham, “Ball milling induced reduction of SrSO₄ by Al,” Int. J. Miner. Process., vol. 98, no: 3–4, pp. 214–218, 2011.
- [15] N. Steoudeh and N.J. Welham, “Ball milling induced reduction of SrSO₄ by Mg,” Int. J. Miner. Process., vol. 104, pp. 49–52, 2012.
- [16] A.S. Selim and M. Abd-El-Khalik, “Thermal decomposition of strontium oxalate-effect of various atmospheres,” Powder Technol., vol. 20, no: 1, pp. 53–59, 1978.
- [17] D. J. Price, A.K. Powell and P.T. Wood, Hydrothermal crystallisation and X-ray structure of anhydrous strontium oxalate., Polyhedron, vol. 18, no: 19, pp. 2499–2503, 1999.
- [18] E. D. Bacce, A.M. Pires, M.R. Davalos and M. Jacelicci Jr, “Thermal decomposition and rehydration of strontium oxalate: morphological evolution,” Int. J. Inorg. Mater., vol. 3, no: 6, pp. 443–452, 2001.
- [19] D. Zhang, L. Qi, J. Ma and H. Cheng, “Biomimetic growth of strontium oxalate aggregates with unusual morphologies in the presence of poly(methacrylic acid),” Cryst. Eng. Comm., vol. 4, no: 88, pp. 536–538, 2002.
- [20] J. Yu, H. Tang and B. Cheng, “Morphological control of strontium oxalate particles by PSMA-mediated precipitation reaction,” Mater. Chem. Phys., vol. 9, no: 1, pp. 134–139, 2005.
- [21] A. Obut, “Interaction of celestine concentrate and reagent grade SrSO₄ with oxalate solution,” Acta Montan. Slovaca, vol. 17, no: 2, pp. 126–131, 2012.
- [22] J. Torres, J. Mendez and M. Sukiennik, “Transformation enthalpy of alkali-earth sulfates (SrSO₄, CaSO₄, MgSO₄, BaSO₄),” Thermochim. Acta, vol. 334, no: 1–2, pp. 57–66, 1999.

JOURNAL OF SCIENCE



SAKARYA UNIVERSITY

Sakarya University Journal of Science

ISSN 1301-4048 | e-ISSN 2147-835X | Period Bimonthly | Founded: 1997 | Publisher Sakarya University |
<http://www.saujs.sakarya.edu.tr/>

Title: Heat Transfer Analysis of Different Thermal Oils in Parabolic Trough Solar Collectors With Longitudinal Sinusoidal Internal Fin

Authors: Burak Kurşun

Received: 2018-12-07 17:47:51

Accepted: 2019-04-15 14:21:27

Article Type: Research Article

Volume: 23

Issue: 5

Month: October

Year: 2019

Pages: 848-858

How to cite

Burak Kurşun; (2019), Heat Transfer Analysis of Different Thermal Oils in Parabolic Trough Solar Collectors With Longitudinal Sinusoidal Internal Fin.

Sakarya University Journal of Science, 23(5), 848-858, DOI:

10.16984/saufenbilder.493707

Access link

<http://www.saujs.sakarya.edu.tr/issue/44066/493707>

New submission to SAUJS

<http://dergipark.gov.tr/journal/1115/submission/start>

Heat transfer analysis of different thermal oils in parabolic trough solar collectors with longitudinal sinusoidal internal fin

Burak Kurşun^{*1}

Abstract

Parabolic trough solar collectors (PTSC) plays an important role in the heating of fluids and in the generation of electricity . In this study, heat transfer and temperature distribution analysis was carried out for the use of internal longitudinal fins with different geometries in a parabolic trough solar collector. Numerical analyzes were carried out for different Reynolds (Re) numbers (2×10^4 - 8×10^4) at steady-state conditions and three different thermal oils were used as heat transfer fluid (HTF). The use of the internal fin with sinusoidal lateral surface for all types of thermal oil increased the heat transfer and made the temperature distribution in the fluid more uniform. The highest thermal enhancement factor was occurred for Syltherm 800 oil and sinusoidal fin geometry. With the use of Syltherm 800 oil, the thermal enhancement factor (ψ) increased by 40% and 44% respectively according to the Therminol VP1 and D12 oil type for the case with sinusoidal fin.

Keywords: Longitudinal fin, Parabolic trough, Sinusoidal fin, Thermal oil

1. INTRODUCTION

Renewable energy sources are nowadays widely used as an alternative to energy sources that create air pollution and negatively affect ecological life. Renewable energy can be classified as energies of solar, wind, hydrogen and biomass. Concentrated solar power (CSP) systems play an important role in the heating of fluids and in the generation of electricity. This study focused on parabolic trough solar collectors (PTSC) used in medium temperature (100-400°C) applications [2].

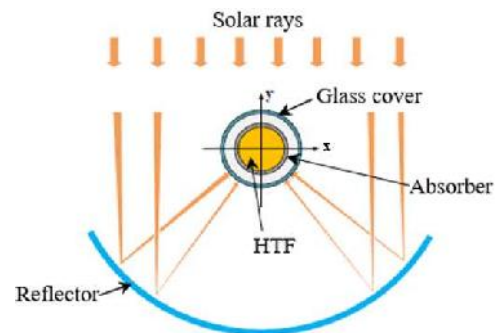


Figure 1. Parabolic trough collector[1]

PTSCs are composed of a parabolic reflector, glass cover and a circular shaped absorber through which the fluid passes. The sun rays are focused on the absorber by reflectors and the fluid in the absorber is heated (Figure 1). There are many experimental and numerical studies to increase the thermal performance of PTSCs.

* Corresponding Author: burak.kursun@amasya.edu.tr

¹ Amasya University, Mechanical Engineering, Amasya, Turkey, ORCID: 0000-0001-5878-3894

Inserts for absorber have been widely applied in these studies [2]. Cheng et al. investigated the effect of an absorber with unilateral milt-longitudinal vortex generators on thermal performance, numerically [3]. Numerical study showed that the vortex generators increased heat transfer by 2.23-13.62%. The use of the twisted tape insert with different nanofluids in the absorber was presented by Waghole et al. [4]. Experimental study revealed that the heat transfer and the pressure loss increase by 1.5-2.10 times and 1-1.75 times respectively. In the study carried out by Kumar and Reddy, perforated disc usage in the absorber was investigated, numerically [5]. For the optimal configuration of the porous disc, it was observed that the heat transfer and the pressure loss increased by 221 watt and 13.5%, respectively. The effect of inserting metal foam in the absorber on the heat transfer was analysed by Wang et al. [6]. The geometry and the porosity of the metal foam were investigated. It was reported that the increase in the Nusselt number (Nu) and the friction coefficient were 10-20 times and 400-700 times, respectively. Investigating of the use of a louvered twisted-tape and the typical plain twisted-tape inserts in the absorber performed by Ghadirijafarbeigloo et al. [7]. For the fully developed turbulent conditions, the louvered twisted-tape inserts significantly increased the heat transfer and pressure loss compared to typical plain twisted-tape inserts. Jaramillo et al. investigated thermal performance by using twisted-tape inserts in a parabolic trough collector for low enthalpy processes [8]. It was revealed that the higher increase in the heat transfer occurred for the low twist ratio and the Reynolds number (Re) values. For a tubular absorber, using of the dimples, protrusions and internal helical fins on the heat transfer were determined by Huang et al. [9]. The highest enhancement in the Nu and friction coefficient by 44-64% and 56-77%, respectively, by using a dimpled tube. In the presented study by Gong et al., the heat transfer enhancement was provided by using an absorber with pin fin inserts [10]. It was reported, the Nu and overall heat transfer performance factor were increased by 9% and 12% respectively for the pin fin usage. Bellos et al. presented a study including the effect of the internal fin with different length and thickness on the thermal performance for the parabolic trough collector [11]. Numerical study showed that increase in the fin thickness and length increased the pressure loss and heat transfer.

It is clear from the literature that the use of inserts for absorber tube increases the heat transfer. Although there are many experimental and numerical studies for inserts with different geometries, there are few studies on the effect of lateral surface geometry of the inserts on heat transfer. In this study, thermal performance analysis was carried out for the use of internal longitudinal fins with sinusoidal lateral surfaces in a parabolic trough solar collector. Sinusoidal geometry are widely used in compact heat exchangers due to the higher thermal performance [12-14]. Thus, sinusoidal geometry was preferred for the numerical analyses. The main aim of the study is to investigate the effect of different types of thermal oil on heat transfer and pressure drop for sinusoidal internal finned absorber. For this purpose, three different types of thermal oil: Syltherm 800, Therminol D12 and Therminol VP1 were used. Numerical analyzes were performed for the conditions with flat fin, sinusoidal fin and without fin and the findings obtained were compared with each other.

2. PHYSICAL MODEL

Absorber geometry used for numerical analysis was given in Figure 2. Figure 2a and 2b represent the flat and the sinusoidal fin geometries, respectively. In Figure 2c, the amplitude value (a) of sinusoidal geometry is $a=6\text{mm}$, periodic length (p) is $p=10\text{mm}$ and thickness (t) is $t=5\text{mm}$. The fin heights (H) are $H=5\text{mm}$ for all conditions.

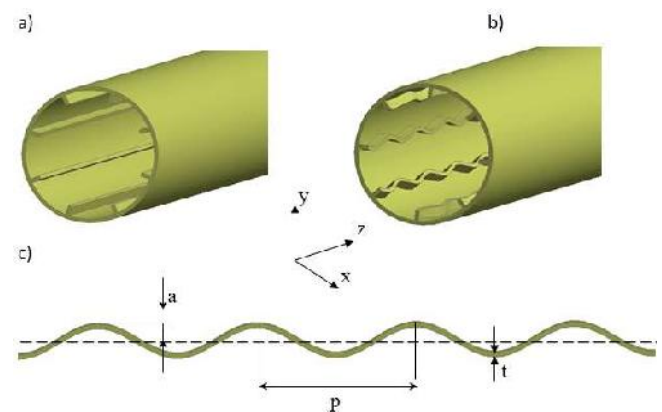


Figure 2. LS-2 absorber and fin geometry, a) flat fin, b) sinusoidal fin, c) sinusoidal geometry

The absorber geometry was modeled according to the LS-2 type receiver dimensions [15] and the absorber material was 316L steel [16]. The values of the absorber dimensions and the thermal properties of the absorber material are given in Table 1. The inlet

temperature of the thermal oils (T_{in}) to the absorber was determined by taking into account the thermal properties such as boiling and autoignition temperature ($T_{in}=400$ K). The thermal properties of Syltherm 800, Therminol D12 and VP1 oils for 400 K temperature were taken from References [11] and [25] respectively (Table 2). Because the absorbing geometry was symmetrical with respect to the y-z plane, half of the absorber was modeled for numerical analysis.

Table 1. Dimension values of LS-2 absorber and thermal properties of absorber material

Absorber	316L steel		
D_i (m)	0.066	λ (W/m.K)	24.92
D_0 (m)	0.070	ρ (kg/m ³)	8030
L (m)	7.8	C_p (J/kg.K)	502.48

Table 2. Thermal properties of oils (T=400K)

Oil type	λ (W/m.K)	ρ (kg/m ³)	C_p (J/kg.K)	μ (Pa.s)
Slyth800	0.1149	840.3	1791	0.00222
VP1	0.1243	977	1850	0.000731
D12	0.0917	681	2520	0.000356

3. MATHEMATICAL MODEL

In the numerical analysis, it was assumed that the fluids were incompressible and their thermal properties were constant. The analyzes were performed under steady-state and turbulent flow conditions. The three-dimensional governing equations are given below. Equations 1, 2 and 3 are the conservation of mass, momentum and energy, respectively.

$$\frac{\partial}{\partial x_i}(\rho u_i) = 0 \tag{1}$$

$$\frac{\partial}{\partial x_j}(\rho u_i u_j) = -\frac{\partial P}{\partial x_i} + \frac{\partial}{\partial x_j} \left[\mu \left(\frac{\partial u_i}{\partial x_j} + \frac{\partial u_j}{\partial x_i} \right) - \frac{2}{3} \mu \frac{\partial u_i}{\partial x_i} \delta_{ij} - \overline{\rho u_i' u_j'} \right] \tag{2}$$

$$\frac{\partial}{\partial x_j}(\rho u_j C_p T) = \frac{\partial}{\partial x_j} \left(\lambda \frac{\partial T}{\partial x_j} + \frac{\mu_t}{\sigma_{h,t}} \frac{\partial (C_p T)}{\partial x_j} \right) + u_j \frac{\partial P}{\partial x_j} + \left[\mu \left(\frac{\partial u_i}{\partial x_j} + \frac{\partial u_j}{\partial x_i} \right) - \frac{2}{3} \mu \frac{\partial u_i}{\partial x_i} \delta_{ij} - \overline{\rho u_i' u_j'} \right] \frac{\partial u_i}{\partial x_j} \tag{3}$$

Where, u_i and u_j are the time-averaged velocity components in the i and j directions, $\overline{\rho u_i' u_j'}$ are the Reynolds stresses, P is the time-averaged pressure, T is

the time-averaged temperature, λ is the fluid thermal conductivity, ρ is the density, μ_t is the turbulent viscosity and $\sigma_{h,t}$ is the turbulent Prandtl number for energy. The Reynolds stresses can be expressed by the following equation depending on the Boussinesq hypothesis to include velocity gradients [19],

$$\overline{\rho u_i' u_j'} = \mu \left(\frac{\partial u_i}{\partial x_j} + \frac{\partial u_j}{\partial x_i} \right) - \frac{2}{3} \mu \left(\rho k + \mu_t \frac{\partial u_k}{\partial x_k} \right) \delta_{ij} \tag{4}$$

Where δ_{ij} is the linear deformation rate of a fluid element, k is the turbulent kinetic energy per unit mass. δ_{ij} and k are given by Equations 5 and 6,

$$\delta_{ij} = \frac{1}{2} \left(\frac{\partial u_i}{\partial x_j} + \frac{\partial u_j}{\partial x_i} \right) \tag{5}$$

$$k = \frac{1}{2} \left(\overline{u'^2} + \overline{v'^2} + \overline{w'^2} \right) \tag{6}$$

k - ϵ model is widely used in flow calculations [19,20]. Realisable k - ϵ model was selected in the present study. In the Realisable k - ϵ model, the two additional equations used for the transport of turbulence kinetic energy (k) and turbulent dissipation rates (ϵ) are given below,

k equation:

$$\frac{\partial}{\partial x_j}(\rho k u_j) = \frac{\partial}{\partial x_i} \mu \left[\left(\mu + \frac{\mu_t}{\sigma_k} \right) \frac{\partial k}{\partial x_j} \right] + G_k - \rho \epsilon \tag{7}$$

ϵ equation:

$$\frac{\partial}{\partial x_j}(\rho \epsilon u_j) = \frac{\partial}{\partial x_i} \mu \left[\left(\mu + \frac{\mu_t}{\sigma_\epsilon} \right) \frac{\partial \epsilon}{\partial x_j} \right] + \rho C_1 S \epsilon - \rho C_2 \frac{\epsilon^2}{k + \sqrt{v \epsilon}} \tag{8}$$

Where σ_k and σ_ϵ are the turbulent Prandtl number for k and ϵ , respectively. G_k is the production of turbulent kinetic energy and calculated by Equation 9,

$$G_k = -\overline{\rho u_i' u_j'} \frac{\partial u_j}{\partial x_i} \tag{9}$$

When the G_k equation is evaluated together with the Equation 4, the following equation can be written,

$$G_k = \mu_t S^2 \tag{10}$$

Turbulent viscosity is given by Equation 11,

$$\mu_t = \rho C_\mu \frac{k^2}{\epsilon} \tag{11}$$

Constants used in the Realisable k - ϵ model are given below,

$$C_1 = \max \left[0.43, \frac{\eta}{\eta+5} \right], \eta = S \frac{k}{\varepsilon}, S \equiv \sqrt{S_{ij}S_{ij}}, C_2 = 1.9, \sigma_k = 1, \sigma_\varepsilon = 1.2$$

C_μ is a function of the mean strain and rotation rates, the angular velocity, and the turbulence fields. Calculation of C_μ function is given in Reference [19].

3.1. Boundary Conditions

The uniform velocity distribution was accepted at the inlet of the absorber and the inlet velocity values were assigned in the z-axis direction depending on the variable Reynolds numbers (Re). At the absorber outlet, the pressure was taken equal to the gauge pressure value (Pressure outlet condition). The boundary conditions at the inlet and outlet of the channel for the symmetric model were expressed by Equations 12 and 13 respectively,

$$u = v = 0, w = w_{in}, T = T_{in}, 90^\circ \leq \theta \leq 270^\circ \quad (12)$$

$$P_{out} = P_{gage} = 0 \quad 90^\circ \leq \theta \leq 270^\circ \quad (13)$$

In parabolic trough collectors, a non-uniform heat flux distribution occurs on the outer surface of the absorber due to the parabolic reflector. The heat flux values on the outer wall of the absorber were determined by multiplying the direct normal irradiation (I) by local concentration ratio (LCR) ($q''_{wall} = I \cdot LCR$). Direct normal irradiance (I) was taken as $I = 1000 \text{ W/m}^2$. The LCR values for the commercial LS-2 parabolic trough solar collector is taken from Reference [6]. The curve was fitted to the LCR values and assigned to the absorber outer surface as a boundary condition by the user-defined function (UDF). In Figure 3a and 3b, LCR and the heat flux distribution on the outer wall of the absorber for the rim angle (θ_r) of $\theta_r = 70^\circ$ were given. In parabolic trough solar collectors, the outer surface of the absorber is surrounded by vacuumed cover glass. Therefore, conduction and convection heat losses from the absorber can be neglected. In this study, it was focused on the thermal performance and pressure losses. Therefore, the radiation heat transfer loss on the outer surface of the absorber was not taken into account as in the References [6] and [21].

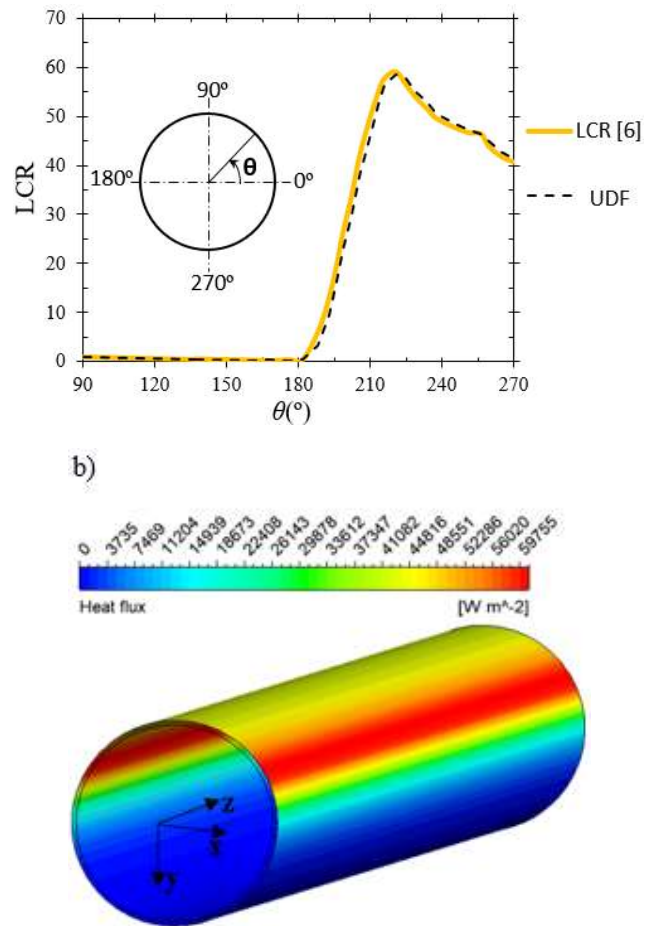


Figure 3. LCR and heat flux distribution on the outer wall of the absorber

Absorber inlet and outlet surfaces on the x-y plane were assumed to be adiabatic ($q'' = 0$). The no-slip boundary condition was defined on all solid surfaces in the fluid zone ($u=0, v=0, w=0$). In the y-z plane, the symmetry condition was applied such that the normal gradients of all flow variables were zero.

4. NUMERICAL METHOD

The Finite Volume Method was used to solve differential governing equations. It was utilized from ANSYS Fluent commercial package program to solve the analyzes. The SIMPLE algorithm was adopted for pressure and velocity coupling. The Second Order Upwind method was selected for the solution of discretized governing equations. Enhanced wall treatment [19] was applied in the flow analysis of the areas near the inner wall of the absorber. Residual value ($\phi_{new} - \phi_{old}$) was given by Equation 14 for the continuity equation, momentum equation, turbulent kinetic energy, turbulent dissipation rate, and energy equation.

$$|\varphi_{new} - \varphi_{old}| \leq 10^{-6} \quad (14)$$

Where, φ represents any variable.

5. REDUCTION OF NUMERICAL DATA

In the assessment of thermal performance, it was utilized from the dimensionless variables given below.

Reynolds number (Re) was determined by Equation 15,

$$Re = \frac{w_{in} D_i}{\nu} \quad (15)$$

Where w_{in} is the fluid inlet velocity in the z-direction, ν is the kinematic viscosity of the fluid and D_i is the inner diameter of the absorber.

For the heat transfer analysis, the average Nu are given by the following equation,

$$Nu = h \frac{D_i}{\lambda} \quad (16)$$

In the equation, λ and h represent thermal conductivity of the fluid and convection heat transfer coefficient, respectively.

Heat transfer coefficient can be calculated by following equation,

$$h = \frac{q''}{(T_{wi} - T_b)} \quad (17)$$

Where T_{wi} is the average inner wall temperature of the absorber, T_b is the average fluid temperature and q'' is the average heat flux on the receiver wall.

Friction coefficient (f) was calculated with Equation 18,

$$f = \frac{\Delta P (D_i/L)}{\rho w_{in}^2/2} \quad (18)$$

Where, ΔP and f are the pressure loss and friction coefficient, respectively

Petukhov and Gnielinski correlations [17] were used for f and Nu , respectively for the validation of pipe flow. Gnielinski correlation is valid in the range of $3 \times 10^3 \leq Re \leq 5 \times 10^6$.

Petukhov correlation:

$$f = (0.790 \ln Re - 1.64)^{-2} \quad (19)$$

Gnielinski correlation:

$$Nu = \frac{\left(\frac{f}{8}\right)^{1/4} (Re - 1000) Pr}{1 + 12.7 \left(\frac{f}{8}\right)^{1/4} \left(Pr^{2/3} - 1\right)} \quad (20)$$

Equation 21 [21] was used to compare thermal performance between different conditions for identical pumping power,

$$\psi = (Nu_{800}/Nu)/(f_{800}/f)^{1/3} \quad (21)$$

Where, Nu_{800} and f_{800} denote the Nusselt number and friction coefficient for the Syltherm 800 oil in any condition. Nu and f are Nusselt number and friction coefficient values which are formed according to other thermal oil types. The non-uniform heat flux distribution on the absorber outer surface increases the circumferential temperature difference on the absorber. This leads to the formation of bending stresses and damage to the vacuumed glass cover [23,24]. With the following equation, the maximum circumferential temperature difference ratios (Γ) on the absorber were determined.

$$\Gamma = \frac{\Delta T_{max}}{\Delta T_{max,800}} \quad (22)$$

Where, $\Delta T_{max,800}$ is the maximum circumferential temperature difference for Syltherm 800 oil, ΔT_{max} is used for other thermal oil types. ΔT_{max} was calculated by Equation 24,

$$\Delta T_{max} = T_{max,o} - T_{min,o} \quad (24)$$

Where, $T_{max,o}$ and $T_{min,o}$ represent the maximum and minimum outer surface average temperature of the absorber.

6. VALIDATION OF NUMERICAL RESULTS

To verify the numerical results, the grid size independence test was performed first. Table 2 shows a grid size comparison for the case without fin and the case with flat fin. For both conditions, the deviation in the values of the variables is approximately 1% for the grid dimensions below 2.5 mm. Thus, 2.5 mm grid size was selected for numerical analysis.

Table 3. Grid size independence test results ($Re=4 \times 10^4$, $T_{in}=300K$, Syltherm 800 oil)

Absorber without fin				
Grid size	f	Deviation(%)	Nu	Deviation(%)
6mm	0.02269	-	809.75	-
4mm	0.02266	0.110743	794.37	1.89873
2.5mm	0.02288	0.957665	776	2.31338
1.25mm	0.02296	0.335939	770	0.77196
Absorber with flat fin				
6mm	0.01925	-	1104.45	-
4mm	0.01850	3.886995	1162.58	5.26315
2.5mm	0.01831	1.033374	1039.48	10.58823
1.25mm	0.01831	0.021484	1027.395	1.16279

The grid structure for the 2,5 mm grid size was shown in Figure 4. The unstructured grid was used in the fluid zone and the grid structure was concentrated in areas close to the solid surfaces. For the absorber tube, however, structured grid was used with uniform distribution. For the grid density on solid surfaces, the y^+ value is approximately $y^+ = 1$ for all analyzes. y^+ is expressed by Equation 25,

$$y^+ = \sqrt{y u_t / \nu} \tag{25}$$

Where, y represents the distance from the solid surface, ν represents the kinematic viscosity, and u_t represents the friction velocity. u_t is determined by following equation,

$$u_t = \sqrt{\tau_w / \rho} \tag{26}$$

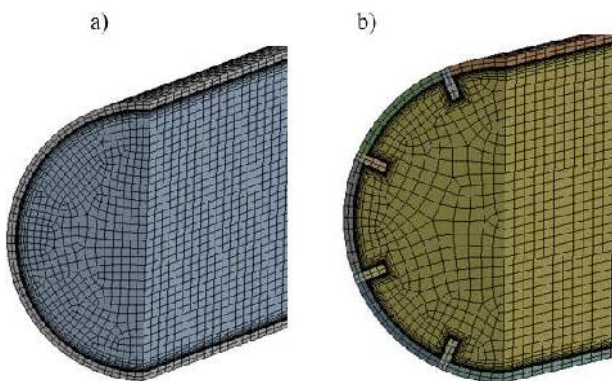


Figure 4. Grid structure a) without fin, b) flat/sinusoidal fin

The comparison of f and Nu values with literature studies was carried out for the case with and without fin. The results of f and Nu were compared with Petukhov and Gnielinski correlations, respectively. In literature studies, it was stated that 20% error was acceptable in industrial applications for these correlations [3,21]. In addition, these correlations are affected at negligible level from the heat flux distribution outside the absorber [17]. Figures 5a and 5b show comparisons of Nu and f for the case without fin. For Nu and f , the highest deviation was observed 8% and 10% respectively.

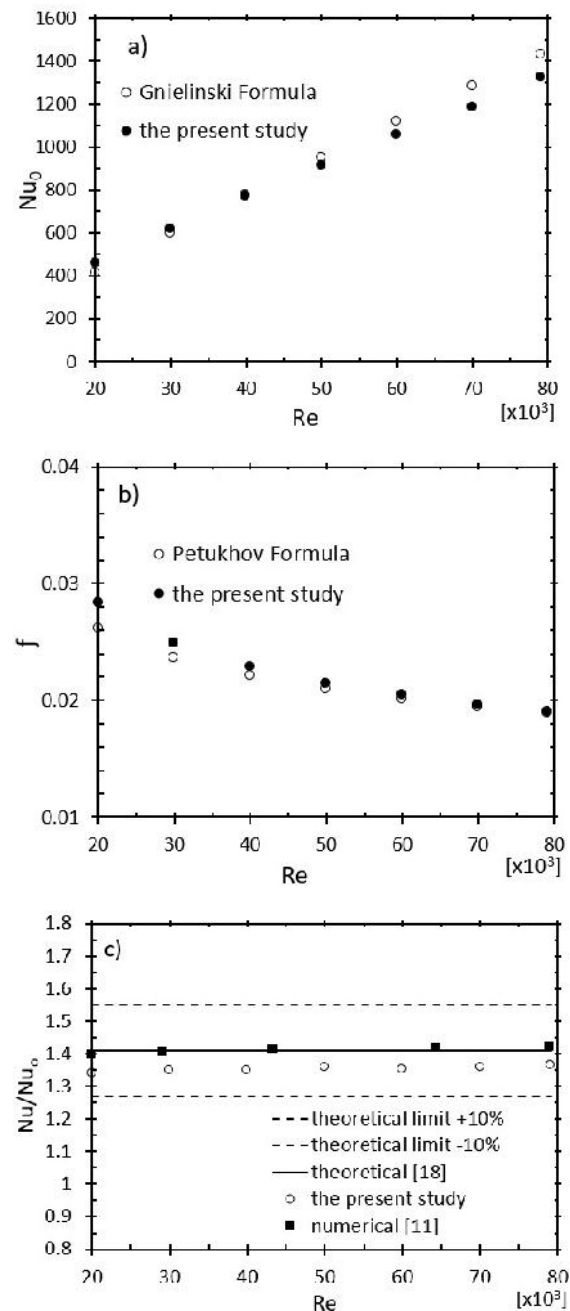


Figure 5. Validation of numerical results a) Nu , without fin, b) f , without fin, c) Nu/Nu_{flat} ratio

The results of the theoretical and numerical study in the literature have been used for the validation of flat fin condition (Figure 5c). The Nu ratios in the cases with and without fin were given in Figure 5c. The deviation between the results in this study and the literature studies was found to be around 4%. These findings indicate that the applied mathematical model and numerical analysis are in good agreement with the results of the literature studies.

7. RESULTS AND DISCUSSIONS

Numerical analyzes were carried out for turbulent flow conditions in the range of $Re=2 \times 10^4-8 \times 10^4$. The results were presented below as graphs containing velocity vectors, temperature contours, circumferential temperature difference and thermal enhancement factor.

7.1. Velocity and Temperature Distribution

In the study, it was aimed to increase the convection around the fin with sinusoidal lateral surface structure in the absorber. In addition, the interaction of different thermal oils types with fin geometries was investigated. In Figure 6b, velocity vectors formed in flat and sinusoidal fin structure were given. As shown in Figure 6, the sinusoidal lateral structure of the fin caused the fluid to change direction. Thus, it was provided increase in convection. Figure 7 shows the velocity vectors formed by the use of sinusoidal fins for different types of thermal oil. Due to the different thermophysical properties of the thermal oils, different fluid velocities occurred in the absorber for the certain Re value. It was observed that the highest and lowest fluid velocity values were formed for Syltherm 800 and Therminol D12 thermal oils, respectively. The increase in fluid velocity also increased the convection around the fin.

The effect of the fin geometry and fluid type on the temperature distribution can be examined with Figures 8 and 9. Figure 8 shows the effect of the use of the internal longitudinal fin on the fluid temperature. As seen in Fig. 8a, a non-uniform temperature distribution occurred in the case without fin and this increased the temperature difference in the absorber depending on the heat flux density. With the use of the fins, the heat transfer surface area increased and the absorber temperatures decreased (Figures 8b and 8c). Furthermore, with the sinusoidal fin surface, fluid

motion increased and a more uniform temperature distribution was obtained (Figure 8c).

The effects of different thermal oil types on the temperature distribution for the sinusoidal fin type was given in Figure 9. The lowest absorber temperature and the most uniform temperature distribution were obtained for Syltherm 800 thermal oil (Figure 9c). On the other hand, the lowest heat transfer was observed for Therminol D12 thermal oil type.

a)

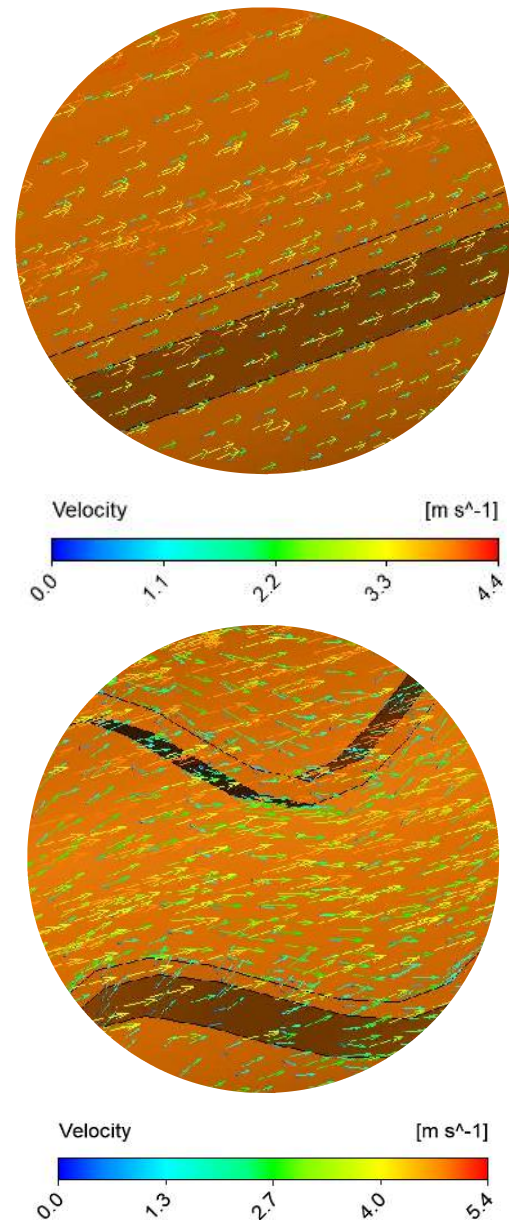


Figure 6. Velocity vectors ($Re=60000$, Syltherm 800 oil) a) flat fin, b) sinusoidal fin

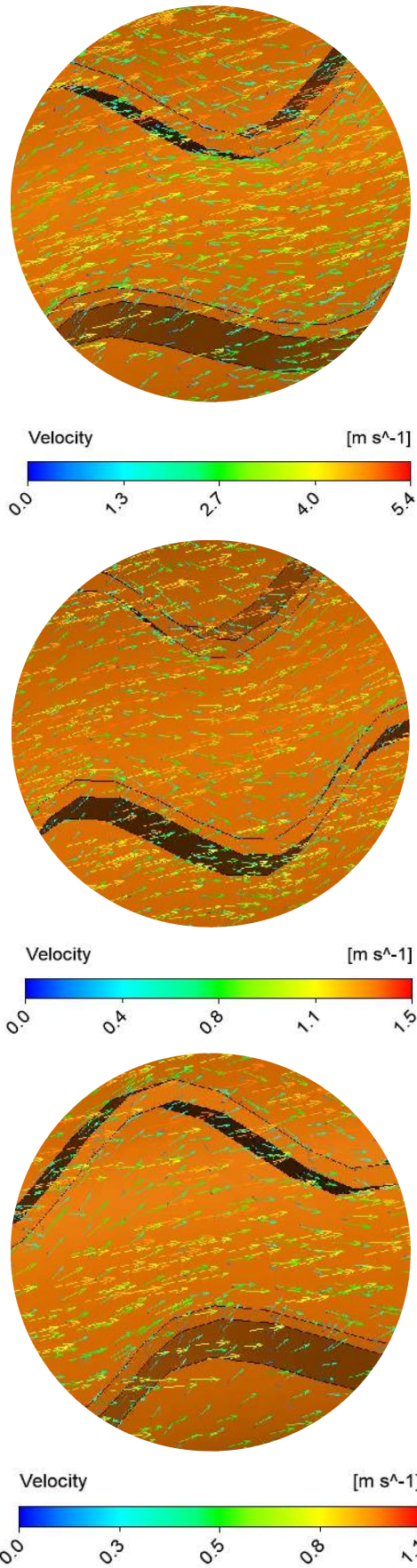


Figure 7. Velocity vectors (Re=60000, Sinusoidal fin) a) Syltherm 800, b) Therminol VP1, c) Therminol D12

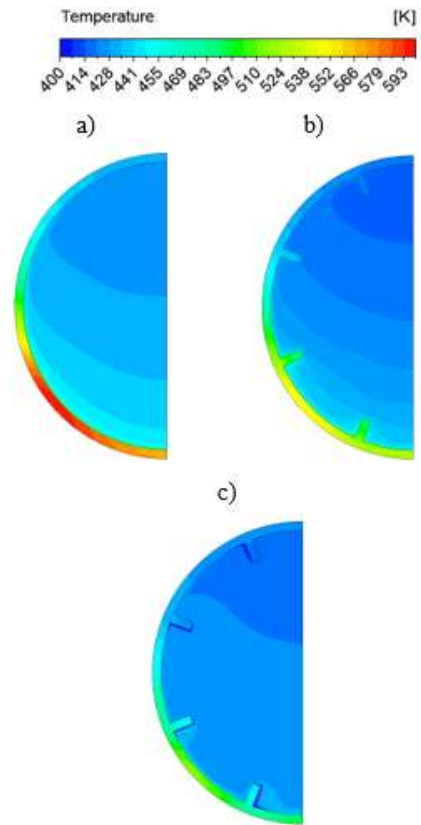


Figure 8. Temperature contours (Re=20000, Therminol VP1) a) without fin, b) flat fin, c) sinusoidal fin

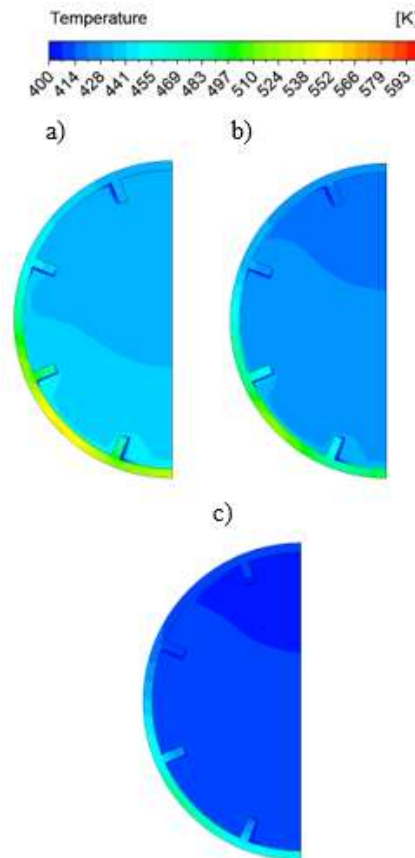


Figure 9. Temperature contours (Re=20000, sinusoidal fins) a) Therminol D12, b) Therminol VP1, c) Syltherm 800

Figure 10 shows the temperature distributions of the fluid and absorber depending on the absorber length in the use of different types of oil for the sinusoidal fin type. For all oil types, heat transfer was obtained the highest in the fluid inlet zone and lowest in the outlet zone. Therefore, the absorber temperature began to increase towards the absorber outlet. In the fluid zone, the oil temperature increased with the effect of convection towards the absorber outlet. The highest convection around the fin was occurred for the Syltherm800 oil and the lowest absorber temperatures were obtained.

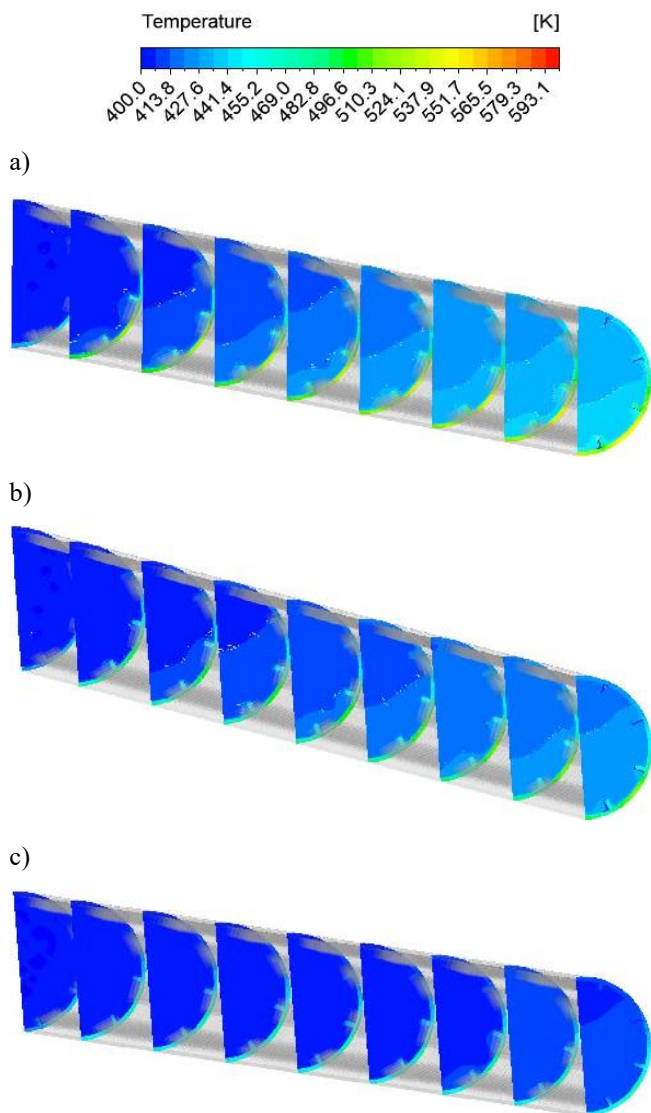


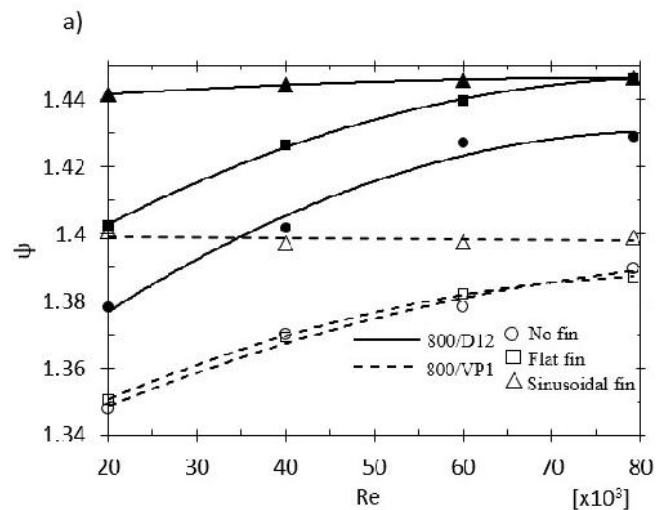
Figure 10. Temperature variations with absorber length (Re=20000, sinusoidal fins) a) Therminol D12, b) Therminol VP1, c) Syltherm 800

7.2. Thermal Performance Analysis

Thermal performance evaluation of thermal oil types was made with reference to Syltherm 800 thermal oil

for all conditions with and without fin usage (Figure 11a). Figure 11a shows the thermal performance curves of the Therminol D12 and VP1 type thermal oils with respect to the Syltherm 800 type thermal oil at variable Re values for an identical pumping power. With the increase in the Re, the heat transfer in the use of Syltherm 800 oil for the cases with flat fin and without fin increased with respect to the heat transfer in the Therminol D12 and VP1 oil use. The highest thermal enhancement factor was achieved in the use of fin with sinusoidal lateral surface, and the heat transfer ratio between the oils remained nearly constant in all the Re values. With the use of Syltherm 800 oil, the thermal enhancement factor increased by 1.4 and 1.44 times respectively according to the Therminol VP1 and D12 oil type for the case with sinusoidal fin. This revealed that the highest and lowest thermal performance occurred for Syltherm 800 and Therminol D12 type thermal oils, respectively.

Figure 11b indicates the ratios of the maximum circumferential temperature differences on the absorber outer surface for different oil types. With the increase in the Re and the use of sinusoidal fin, the temperature difference ratios decreased. When oil types were compared, it was observed that the highest absorber temperatures occurred in Therminol D12 oil usage. For the Therminol D12 oil usage, the maximum circumferential temperature difference ratio increased in the range of 1.73-1.90 according to the use of Syltherm 800 oil.



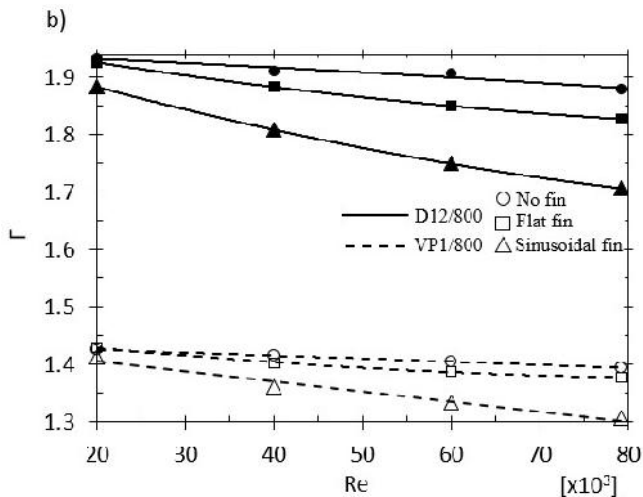


Figure 11. Comparison of thermal oils a) Thermal enhancement factor, b) Maximum circumferential temperature difference ratio

8. CONCLUSIONS

In a parabolic trough solar collector, the analysis of the internal longitudinal fin use with different geometries for different types of thermal oil was carried out and the results obtained were summarized below.

The use of the internal fin with sinusoidal lateral surface for all types of thermal oil increased the convection by directing the fluid. This situation increased the heat transfer to the fluid compared to the flat fin and finless conditions and decreased the absorber temperature. Furthermore, the sinusoidal fin made the temperature distribution in the fluid more uniform.

The highest thermal enhancement factor was obtained for Syltherm 800 oil. With the use of Syltherm 800 oil, the thermal enhancement factor increased by 40% and 44% respectively according to the Therminol VP1 and D12 oil type for the case with sinusoidal fin. Parallel to the results of thermal performance, the highest absorber temperatures occurred in the use of Therminol D12 oil. For the Therminol D12 oil usage, the maximum circumferential temperature difference ratio increased in the range of 73-90% according to the use of Syltherm 800 oil.

REFERENCES

[1] W. Fuqiang, T. Zhexiang, G. Xiangtao, T. Jianyu, H. Huaizhi and L. Bingxi, "Heat transfer performance enhancement and thermal strain restrain of tube receiver for parabolic trough solar collector by using asymmetric outward

convex corrugated tube," *Energy*, vol. 114, pp. 275-292, 2016.

- [2] W. Fuqiang, C. Ziming, T. Jianyu, Y. Yuan, S. Yong and L. Linhua, "Progress in concentrated solar power technology with parabolic trough collector system: A comprehensive review," *Renewable and Sustainable Energy Reviews*, vol. 79, pp. 1314-1328, 2017.
- [3] Z. D. Cheng, Y. L. He and F. Q. Cui, "Numerical study of heat transfer enhancement by unilateral longitudinal vortex generators inside parabolic trough solar receivers," *International journal of heat and mass transfer*, vol. 55, no. 21-22, pp. 5631-5641, 2012.
- [4] D. R. Waghole, R. M. Warkhedkar and R. K. Shrivastva, "Experimental investigations on heat transfer and friction factor of silver nanofluid in absorber/receiver of parabolic trough collector with twisted tape inserts," *Energy Procedia*, vol. 45, pp. 558-567, 2014.
- [5] K. R. Kumar and K. S. Reddy, "Effect of porous disc receiver configurations on performance of solar parabolic trough concentrator," *Heat and Mass Transfer*, vol. 48, no. 3, pp. 555-571, 2012.
- [6] P. Wang, D. Y. Liu and C. Xu, "Numerical study of heat transfer enhancement in the receiver tube of direct steam generation with parabolic trough by inserting metal foams," *Applied energy*, vol. 102, pp. 449-460, 2013.
- [7] S. Ghadirijafarbigloo, A. H. Zamzamin and M. Yaghoubi, "3-D numerical simulation of heat transfer and turbulent flow in a receiver tube of solar parabolic trough concentrator with louvered twisted-tape inserts," *Energy procedia*, vol. 49, pp. 373-380, 2014.
- [8] O. A. Jaramillo, M. Borunda, K. M. Velazquez-Lucho and M. Robles, "Parabolic trough solar collector for low enthalpy processes: An analysis of the efficiency enhancement by using twisted tape inserts," *Renewable Energy*, vol. 93, pp. 125-141, 2016.
- [9] Z. Huang, G. L. Yu, Z. Y. Li and W. Q. Tao, "Numerical study on heat transfer enhancement in a receiver tube of parabolic trough solar collector with dimples, protrusions and helical

- pins,” *Energy Procedia*, vol. 69, pp. 1306-1316, 2015.
- [10] X. Gong, F. Wang, H. Wang, J. Tan, Q. Lai and H. Han, “Heat transfer enhancement analysis of tube receiver for parabolic trough solar collector with pin fin arrays inserting,” *Solar Energy*, vol. 144, pp. 185-202, 2017.
- [11] E. Bellos, C. Tzivanidis and D. Tsimpoukis, “Thermal enhancement of parabolic trough collector with internally finned absorbers,” *Solar Energy*, vol. 157, pp. 514-531, 2017.
- [12] Y. Demagh, I. Bordja, Y. Kabar and H. Benmoussa, “A design method of an S-curved parabolic trough collector absorber with a three-dimensional heat flux density distribution,” *Solar Energy*, vol. 122, pp. 873-884, 2015.
- [13] N. R. Rosaguti, D. F. Fletcher and B. S. Haynes, “Low-Reynolds number heat transfer enhancement in sinusoidal channels,” *Chemical engineering science*, vol. 62, no. 3, pp. 694-702, 2007.
- [14] Y. Sui, C. J. Teo and P. S. Lee, “Direct numerical simulation of fluid flow and heat transfer in periodic wavy channels with rectangular cross-sections,” *International Journal of Heat and Mass Transfer*, vol. 55, no. 1-3, pp. 73-88, 2012.
- [15] A. Fernández-García, E. Zarza, L. Valenzuela, and M. Pérez, “Parabolic-trough solar collectors and their applications,” *Renewable and Sustainable Energy Reviews*, vol. 14, no. 7, pp. 1695-1721, 2010.
- [16] R. Forristall, “Heat transfer analysis and modeling of a parabolic trough solar receiver implemented in engineering equation solver (No. NREL/TP-550-34169),” *National Renewable Energy Lab.*, Golden, CO.(US), 2003.
- [17] Y. A. Cengel, and A. J. Ghajar, “Heat and mass transfer (a practical approach, SI version).”, 2011.
- [18] M. K. Jensen and A. Vlakancic, “Technical Note Experimental investigation of turbulent heat transfer and fluid flow in internally finned tubes,” *International Journal of Heat and Mass Transfer*, vol. 42, no. 7, pp. 1343-1351, 1999.
- [19] Ansys Inc., “ANSYS FLUENT 14.0 Theory Guide,” 2011.
- [20] H. K. Versteeg and W. Malalasekera, “An introduction to computational fluid dynamics: the finite volume method,” Pearson Education, 2007.
- [21] Z. Huang, Z. Y. Li, G. L. Yu and W. Q. Tao, “Numerical investigations on fully-developed mixed turbulent convection in dimpled parabolic trough receiver tubes,” *Applied Thermal Engineering*, vol. 114, pp.1287-1299, 2017.
- [22] R. L. Webb, “Performance evaluation criteria for use of enhanced heat transfer surfaces in heat exchanger design,” *International Journal of Heat and Mass Transfer*, vol. 24, no. 4, pp. 715-726, 1981.
- [23] S. Khanna, S. B. Kedare and S. Singh, “Deflection and stresses in absorber tube of solar parabolic trough due to circumferential and axial flux variations on absorber tube supported at multiple points,” *Solar Energy*, vol. 99, pp. 134-151, 2014.
- [24] S. Khanna, V. Sharma, S. B. Kedare and S. Singh, “Experimental investigation of the bending of absorber tube of solar parabolic trough concentrator and comparison with analytical results,” *Solar Energy*, vol. 125, pp. 1-11, 2016.
- [25] Eastman Therminol® heat transfer fluids, <https://www.therminol.com> (Accessed 2018-12-7).

JOURNAL OF SCIENCE



SAKARYA UNIVERSITY

Sakarya University Journal of Science

ISSN 1301-4048 | e-ISSN 2147-835X | Period Bimonthly | Founded: 1997 | Publisher Sakarya University |
<http://www.saujs.sakarya.edu.tr/>

Title: Implementation of Dormand-Prince Based Chaotic Oscillator Designs in Different Iq-Math Number Standards on Fpga

Authors: İsmail Koyuncu, Halil İbrahim Şeker

Received: 2018-12-30 22:41:28

Accepted: 2019-04-16 11:44:53

Article Type: Research Article

Volume: 23

Issue: 5

Month: October

Year: 2019

Pages: 859-868

How to cite

İsmail Koyuncu, Halil İbrahim Şeker; (2019), Implementation of Dormand-Prince Based Chaotic Oscillator Designs in Different Iq-Math Number Standards on Fpga.

Sakarya University Journal of Science, 23(5), 859-868, DOI:

10.16984/saufenbilder.505497

Access link

<http://www.saujs.sakarya.edu.tr/issue/44066/505497>

New submission to SAUJS

<http://dergipark.gov.tr/journal/1115/submission/start>

Implementation of Dormand-Prince based chaotic oscillator designs in different IQ-Math number standards on FPGA

İsmail KOYUNCU¹, Halil İbrahim ŞEKER^{*2}

Abstract

Chaos and chaotic systems, one of the most important work areas in recent years, are used in areas such as cryptology and secure communication, industrial control, artificial neural networks, random number generators and image processing. The most basic structure used in these studies is a chaotic oscillator design that produces a chaotic signal. Chaotic oscillators are expressed by using differential equations. Numerical algorithms such as Euler, Heun, fourth order Runge-Kutta-4 (RK4), fifth order RK5-Butcher and Dormand-Prince are used for solving these differential equations. When the current literature is searched, chaotic oscillator designs are found by Euler, Heun, RK4 and RK5- Butcher method. However, FPGA-based chaotic oscillator design studies have not been found using the Dormand-Prince method, which produces more accurate solutions than other methods. In this work, self-excited attractor chaotic system was first designed in 16I-16Q, 14I-14Q, 12I-12Q, 10I_10Q, 8I-8Q IQ-Math number standards on FPGA using Dormand-Prince numerical algorithm and encoded in VHDL language. Xilinx ISE Design Tools were used to design the chaotic system. The design was synthesized and tested for the Xilinx Virtex-6 FPGA chip. Using the Xilinx ISE design tool, the chip statistics and maximum operating frequency obtained after the "Route-Place" operation are presented. In future work, safe communication and real random number generator applications can be realized by using the Dormand-Prince based oscillator design presented in this study.

Keywords: Dormand-Prince algorithm, FPGA, chaotic oscillator, VHDL.

1. INTRODUCTION

This Chaos and chaotic systems are one of the working areas on which many national and international studies have been conducted in the recent years. Chaotic systems, for the first time, were discovered by the mathematician and meteorologist Edward Norton Lorenz in 1963. Lorenz has revealed in his study that

even the smallest change in initial conditions can cause unpredictable results after a while. The foundations of chaotic systems were laid with this study [1]. Then Sprott, Rössler, Rikitake, Burke-Shaw, Pehlivan-Wei, Abooe and Deng have proposed chaotic systems to the literature. Chaos and chaotic systems are those that are very tied to initial conditions, demonstrate random, nonlinear, disorganized looking forms but have a unique layout system in itself. These systems are

* Corresponding Author: hseker5@gmail.com

¹ Afyon Kocatepe University, Department of Electrical and Electronics Engineering, Faculty of Technology, Afyon, Turkey, ORCID: <https://orcid.org/0000-0003-4725-4879>.

^{2*} Afyon Kocatepe University, Department of Electrical and Electronics Engineering, Institute of Science and Technology, Afyon, Turkey, ORCID: <https://orcid.org/0000-0002-5343-2419>.

variable and non-periodic structures producing noise-like signs. Chaotic systems are composed of simple differential equations even if they seem like complex structures [2]. A lot of research have been done in many research areas thanks to these properties of chaotic systems. These research areas include such fields as control [3, 4], image processing [5, 6], cryptology and secure communication [7, 8], artificial neural networks [9, 10], biomedical [11], industrial control [12, 13], and random number generators [14, 15]. In the literature, chaotic signal generators can be designed in different platforms. As an example of these platforms, digital signal processors (DSP) for the chaotic signal processor and chaotic communication systems was designed as a software-based and hardware-based by Dmitriev et al. [16]. Akgül et al., in their study, have carried out electronic circuit implementation of non-equilibrium point chaotic system, and produced phase portraits and oscilloscope outputs. This chaotic system has been made with LabVIEW based Field Programmable Gate Array (FPGA) chip and 32-bit floating-point number standard as FPGA based chaotic oscillator design. Then the results of FPGA-based design and LabVIEW-based design have been compared [17]. In the study of Pehlivan et al., chaotic oscillator design has been implemented for synchronization and masking communication circuits by using Matlab-Simulink and Orcad-PSpice programs with Rucklidge chaotic generator [18]. Rajagopalan et al., in their study, have stated that real random number generators can be used in secure communication thanks to their importance for cryptographic communication. It is also indicated in this study that in compliance with CMOS (Complementary Metal Oxide Semiconductor) Boolean chaotic generator, real random number generator design has been modeled using the Cadence virtuoso tool based on the 45 nm CMOS technology with ASIC (Application Integrated Circuit) approach [19]. In the study of Ge et al., they have proved Lyapunov asymptotic stability and worked on a Quantum-CNN (Cellular Neural Network) oscillator design of a special type of generalized synchronization of different order systems synchronized with three different layouts [20]. Chiub et al., in their study, have implemented microprocessor based design of Lorenz chaotic system [21]. Tuna et al, in their study, have designed three dimensional chaotic core as FPGA chip as discrete-time by using Heun algorithm with 32-bit IQ-Math fixed-point number standard [22]. Koyuncu et al., in their study, have designed analog circuit model in PSpice program and digital integrated circuit model on FPGA chip using VHDL (Very High Speed Integrated Circuit Hardware Description Language) language and fourth order Runge-Kutta method and Sundarapandian-Pehlivan chaotic system. The results

of the study have been compared [23]. By using Euler numerical algorithm, Azzaz et al., in their study, have implemented tree dimensional chaotic system with 32-bit (16Q-16I) fixed-point number format on Xilinx Virtex-II FPGA chip with VHDL language. The operation frequency of the design is specified as 38.86 MHz [24]. A chaotic signal generator generating chaotic signal is the most basic structure which is requisite for all these studies. Chaotic oscillators are expressed by using differential equations and these equations can be modeled with different numerical algorithms. Euler [25], Heun [26], the fourth order Runge Kutta (RK4) [27], and fifth order Runge Kutta Butcher (RK5-Butcher) [28] can be given as an example.

In this study, unlike from the before mentioned methods, the self-excited attractor (SEA) chaotic system is modeled using Dormand-Prince (DP) method for the first time. There was not such study when current literature was searched. In the second part of this study, some information about DP numerical algorithm and SEA chaotic system are given. In the third part, FPGA chips are briefly mentioned. In the fourth chapter, DP-based chaotic system's model and chip statistics are presented on FPGA chip. In the last section, the results obtained from the study have been evaluated.

2. DORMAND-PRINCE NUMERICAL ALGORITHM AND SEA CHAOTIC SYSTEM

In the literature, chaotic systems can be modeled using numerical algorithms like Euler, Heun, fourth order Runge-Kutta and fifth order Runge-Kutta-Butcher. The chaotic system presented in this study has been modeled using DP method for the first time. DP algorithm is given in equation (1). DP algorithm consists of seven steps of k_1 , k_2 , k_3 , k_4 , k_5 , k_6 and k_7 . In order to calculate the value of the algorithm, seven steps must be already calculated. Here, k_1 is the result obtained from initial conditions and h step number, k_2 value is the result obtained from h step number and k_1 value, k_3 value is the result obtained from h step number, k_1 and k_2 values, k_4 value is the result obtained from h step number, k_1 , k_2 , and k_3 values, k_5 value is the result obtained from h step number, k_1 , k_2 , k_3 , and k_4 values, k_6 value is the result obtained from h step number, k_1 , k_2 , k_3 , k_4 , and k_5 values, k_7 value is the result obtained from h step number, k_1 , k_2 , k_3 , k_4 , k_5 , and k_6 values. y_i value and h step number are used to calculate the next y_{i+1} value for numerical solution. In this equation, step interval of DP algorithm is taken

as $h=0.01$ and the initial conditions $x_0=-1.8$, $y_0=-1.5$, $z_0=-2.5$ [29].

$$\begin{aligned}
 y_{i+1} &= y_i + h \left(\frac{35}{384} k_1 + \frac{500}{1113} k_3 + \frac{125}{192} k_4 - \frac{2187}{6784} k_5 + \frac{11}{84} k_6 \right) \\
 k_1 &= F(x_i, y_i) \\
 k_2 &= F\left(x_i + \frac{h}{5}, y_i + \frac{h}{5} k_1\right) \\
 k_3 &= F\left(x_i + \frac{3}{10} h, y_i + \frac{3}{40} k_1 + \frac{9}{40} k_2\right) * h \\
 k_4 &= F\left(x_i + \frac{4}{5} h, y_i + \frac{44}{45} k_1 - \frac{56}{15} k_2 + \frac{32}{9} k_3\right) * h \\
 k_5 &= F\left(x_i + \frac{8}{9} h, y_i + \frac{19372}{6561} k_1 - \frac{25360}{2187} k_2 + \frac{64448}{6561} k_3 - \frac{212}{729} k_4\right) * h \\
 k_6 &= F\left(x_i + 1 * h, y_i + \frac{9017}{3168} k_1 - \frac{355}{33} k_2 + \frac{46732}{5247} k_3 + \frac{49}{176} k_4 - \frac{5103}{18656} k_5\right) * h \\
 k_7 &= F\left(x_i + 1 * h, y_i + \frac{35}{384} k_1 + 0 * k_2 + \frac{500}{1113} k_3 + \frac{125}{192} k_4 - \frac{2187}{6784} k_5 + \frac{11}{84} k_6\right) * h
 \end{aligned} \tag{1}$$

The mathematical expression of the chaotic system, expressed in the form of differential equations, is given in equation (2). Here, x , y , and z refer to the state variables of chaotic system, a , b , c , d , e , f and g refer to system parameters, and x_0 , y_0 , and z_0 refer to initial conditions. The values of parameters and initial conditions of submitted chaotic system are represented in equation (3).

$$\begin{aligned}
 dx/dt &= gz \\
 dy/dt &= dx^2 + ey^2 - f \\
 dz/dt &= -ax - bx^2 + cy^2 \\
 a = f &= 4, b = c = d = e = g = 1, \\
 x_0 = -1.8, y_0 &= -1.5, z_0 = -2.5
 \end{aligned} \tag{2}$$

Xu et al. has presented a new chaotic system with a self-excited attractor (SEA) to literature. In the study, they have introduced that is used for an engineering application of the signal encryption. In addition, a random number generator application has been performed using real circuit of SEA chaotic system. Parameter estimation procedure is based on the attractor distribution modeling in the state space. The results of presented study show the success of the parameter estimation method [30]. The selected chaotic system was first modeled as Matlab-based. In consequence of Matlab analysis, time series are presented in Figure 1 and phase portraits are presented in Figure 2.

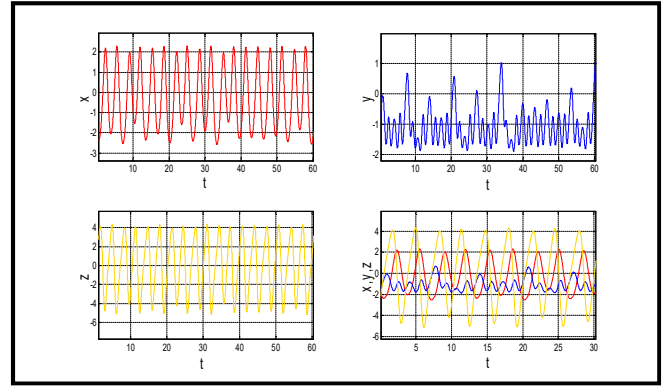


Figure 1. DP-based SEA chaotic oscillator time series

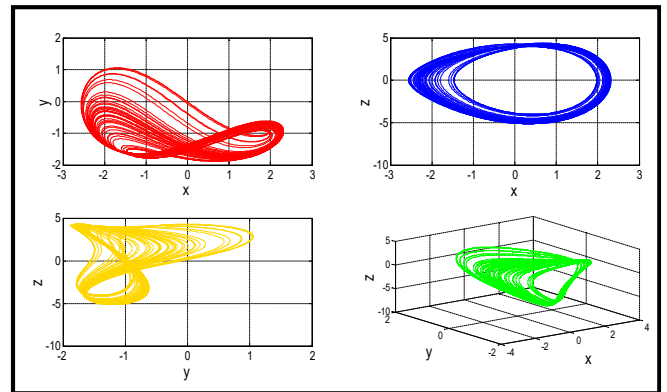


Figure 2. DP-based SEA chaotic oscillator phase series

The analysis of time series of the chaotic system's y variable belonging to Heun, RK-4, RK5B, and DP is presented in Fig. 3. DP method produces more accurate results compared to other algorithms [31, 32]. Furthermore, since the previous value is used to calculate the next step of the system, it is seen that the difference between DP and other algorithms is increasing.

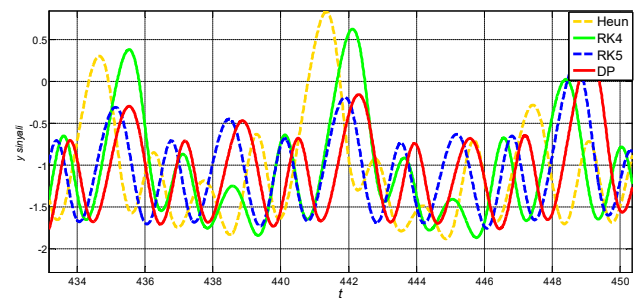


Figure 3. Time series of Heun, RK-4, RK5-Butcher and DP algorithms for the SEA chaotic system.

3. FPGA CHIPS

FPGA chips are digital integrated circuits that can be programmed in the field repeatedly, producing the hardware structure according to the logical function required by the designer. Interconnections, logical

blocks, and input/output blocks can be programmed in the field in compliance with the logical circuit that the designer makes. According to the logical circuit the designer makes, interconnections, logical blocks and input / output blocks can be programmed in the field. FPGA chips have gained popularity due to their real-time, high-frequency, and parallel processing capability and even the ability to take processor into them. Recently, there are FPGA chips starting from a few MHz and operating frequency up to a few GHz. Another advantage of FPGA chips is that it allows the faster design of the desired design by using IP core (Intellectual Properties-core) structures. FPGA chips have three main structures, namely input-output blocks (I-O blocks), configurable logical blocks (CLB), and interconnection network [33, 34].

Input-Output Blocks; I/O blocks are programmable pins of *FPGA*. These pins can be programmed as input, output or both input and output according to the designer's request. I / O pins also allow external data to reach inside the chip. There are also many input output pins on the *FPGA* chip, such as power pins, clock pins, configuration pins and user pins [35].

Configurable Logic Blocks (CLB); They consist of LUT (Look-up table) that is also called logic cell where logical functions are created, Flip-Flop where one bit of information is held, and Mux that manages information flow. LUTs are small memories that perform a logic process [36].

Interconnections; these connections have a flexible programmable structure. Their main task is to establish connections between logical blocks or to establish connections between logical blocks and input/output pins [37].

4. DORMAND-PRINCE-BASED CHAOTIC OSCILLATOR DESIGN ON FPGA

The chaotic system presented in this study was modeled to work on *FPGA* with IQ-Math fixed point number standard using DP numerical algorithm. The design was coded using VHDL language which is a hardware description language. The top level block diagram of this designed chaotic oscillator obtained by using Xilinx ISE 14.7 is shown in Fig. 4.

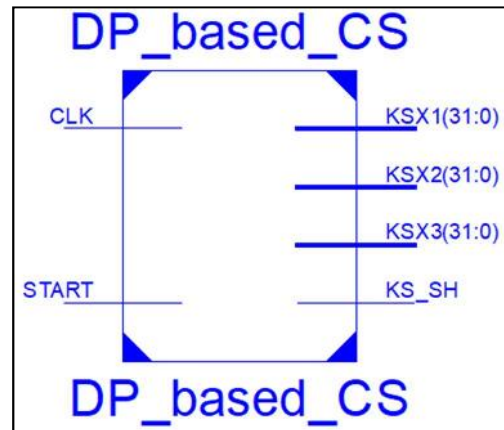


Figure 4. The top level block diagram of DP-based SEA chaotic system on *FPGA*

The 1-bit *START* signal on the designed chaotic system refers to the control signal required to operate the system and the 1-bit *CLK* signal refers to the synchronization signal of the system. At the system output, there are 1-bit *KS_SH* signal indicating the unit produces a result and *KSX1*, *KSX2*, and *KSX3* signals carrying chaotic signal value. The second sub-block structure of the design consists of the most basic elements such as multiplexer unit (*MUX*), chaotic oscillator unit and filter unit as shown in Fig. 5.

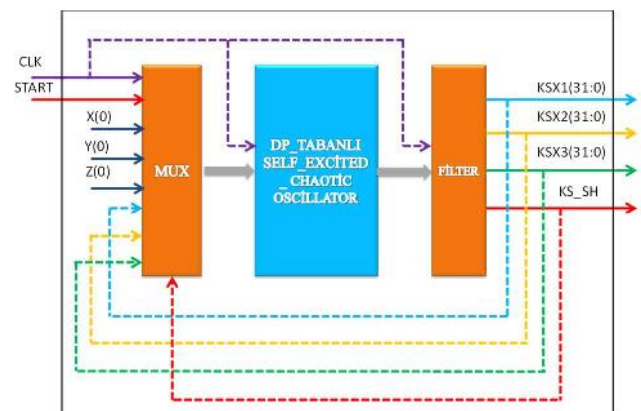


Figure 5. The second sub-level block diagram of *FPGA*-based chaotic oscillator

In this study, the design purpose of multiplexer unit is to take user-assigned initial conditions $X(0)$, $Y(0)$, $Z(0)$ values at the first run and to take these values from filter output at the next stages. 1-bit *KS_SH* signal becomes '1' when the system produces the first result and the system sends this signal to the mux unit, allowing the results produced by the chaotic system to be used instead of the initial values that were originally assigned. The purpose of the filter is to design the chaotic oscillator to filter out unwanted signals. The purpose of DP-based SEA chaotic oscillator structure is to calculate the differential equations of chaotic

system using DP numerical algorithm. Figure 6 shows the third level block diagram of DP-based SEA chaotic oscillator. The basic units used in the chaotic system, such as the multiplier, collector, divider and extraction, were created using the IP-Core Generator, which is compliant with the fixed-point number standards. This

implemented chaotic oscillator was tested by creating test bench unit in VHDL language. Figure 7-11. shows the simulation results obtained by using Xilinx ISE Design Tools program of DP-based SEA chaotic system.

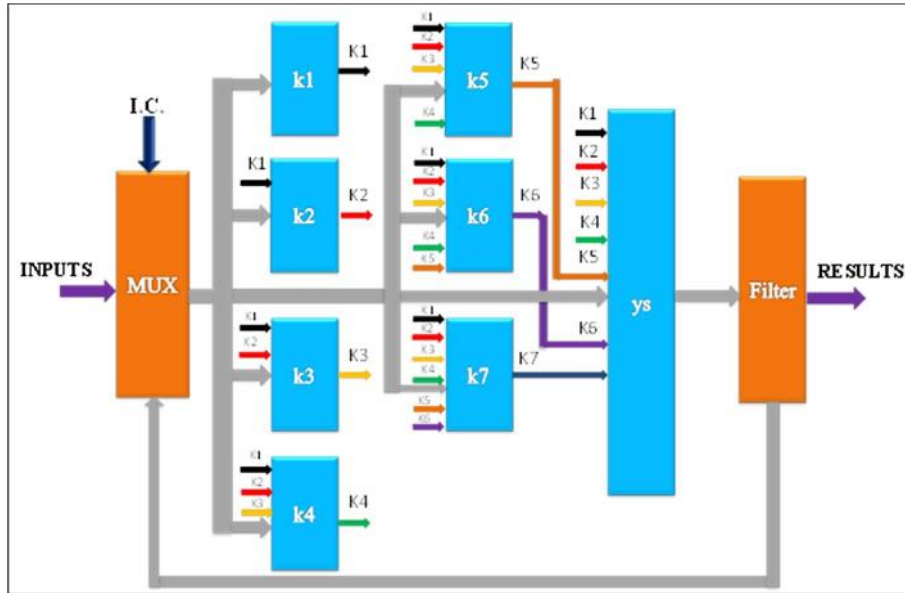


Figure 6. The third level block diagram of DP-based SEA chaotic oscillator

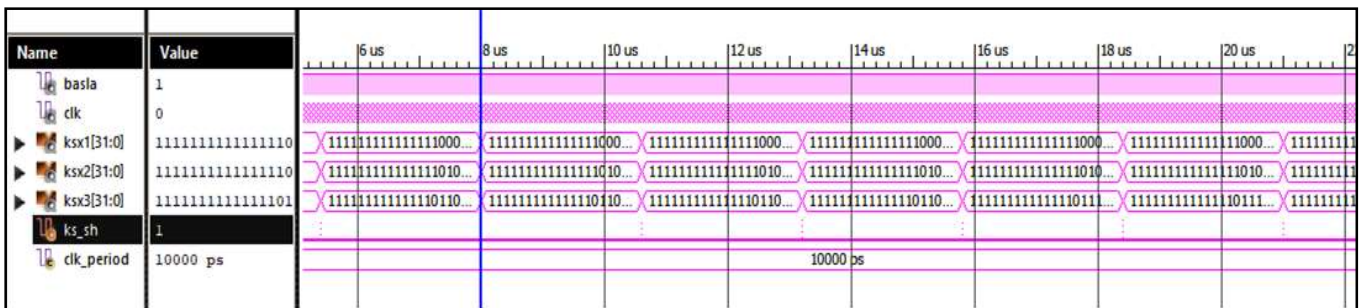


Figure 7. Simulation results of Xilinx ISE 14.7 of DP-based 16I-16Q fixed-point number standard SEA chaotic oscillator

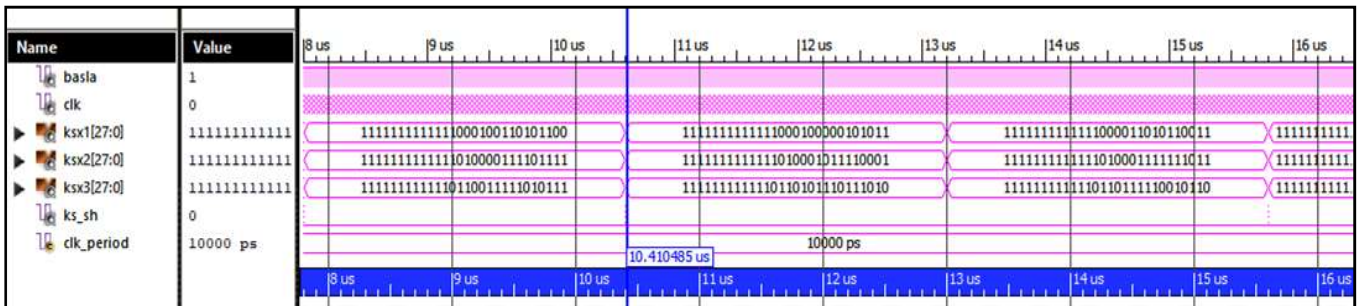


Figure 8. Simulation results of Xilinx ISE 14.7 of DP-based 14I-14Q fixed-point number standard SEA oscillator

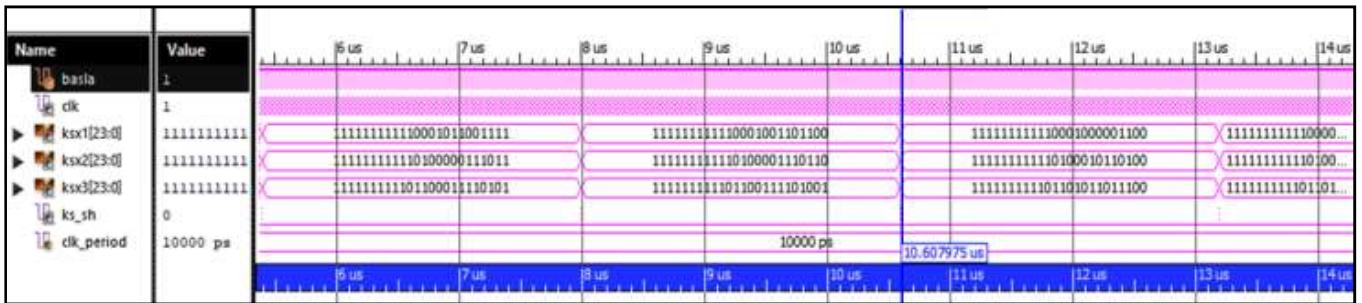


Figure 9. Simulation results of Xilinx ISE 14.7 of DP-based 12I-12Q fixed-point number standard SEA oscillator

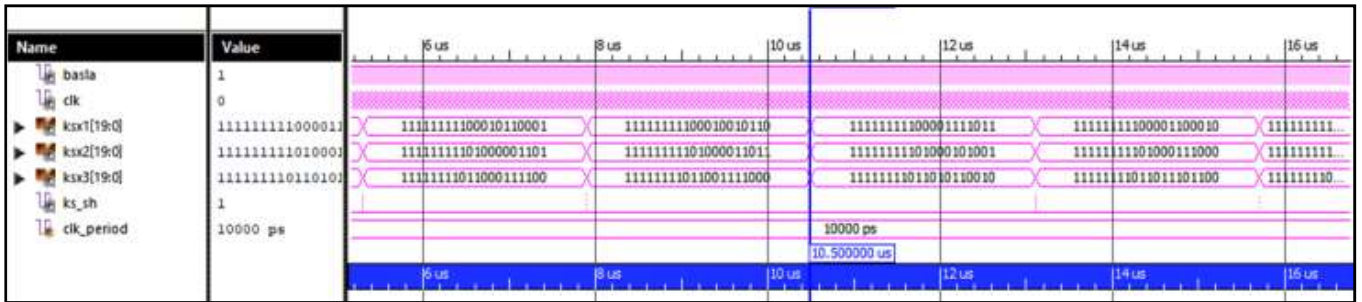


Figure 10. Simulation results of Xilinx ISE 14.7 of DP-based 10I-10Q fixed-point number standard SEA oscillator



Figure 11. Simulation results of Xilinx ISE 14.7 of DP-based 8I-8Q fixed-point number standard SEA oscillator

SEA chaotic systems in the designed 16I-16Q, 14I-14Q, 12I-12Q, 10I-10Q, 8I-8Q IQ-Math number standards were tested by loading the XC6LVX240T chip of the Virtex-6 family of Xilinx, respectively. Then the chip statistics obtained after Place & Route operations are presented in table 1. Table 1 shows the use of chip hardware resources in different number standards. According to this table, the chaotic system in the 16I-16Q IQ-Math number standard used more chip hardware resources than the chaotic system in the 8I-8Q IQ-Math number standard. In addition, the chaotic system with the 8I-8Q number standard has the highest operating frequency. The lowest operating frequency was found to have the chaotic system of the 16I-16Q number standard. The design of the 16I-16Q,

14I-14Q, 12I-12Q, 10I-10Q, 8I-8Q IQ-Math number standards of the SEA chaotic systems produced by FPGA-based 3x100 data set has been recorded in the excel file. According to the recorded data, the system outputs of the chaos systems KXS1, KXS2 and KXS3 and the results of the Matlab-based chaotic system were analyzed for individual MSE and RMSE errors. As a result of these analyzes, the minimum error values for the SEA chaotic system are in the chaotic system of the 16I-16Q IQ-Math number standard and the highest error is in the chaotic system of the IQ-Math number standard 8I-8Q. Mean squared error (MSE) and root mean squared error (RMSE) error analyzes were made by comparing Matlab-based results with FPGA-based results and given in table 2.

Table 1. FPGA chip usage statistics of DP-based SEA chaotic system

Device Utilization Summary (estimated values)	16I-16Q Chaotic sis.	14I-14Q Chaotic sis.	12I-12Q Chaotic sis.	10I-10Q Chaotic sis.	8I-8Q Chaotic sis.
Number of Slice Registers	18280/301440 6%	16529/301440 5%	13888/301440 4%	11575/301440 3%	12747/301440 4%
Number of Slice LUTs	14473/150720 9%	13020/150720 8%	11773/150720 7%	10260/150720 6%	13550/150720 8%
Number used as Memory	7953/58400 13%	7247/58400 12%	6747/58400 11%	6144/58400 10%	10169/58400 17%
Number of BUFG/BUFGCTRLs	1/32 3%	1/32 3%	1/32 3%	1/32 3%	1/32 3%
Number of DSP48E1s	712/768 92%	712/768 92%	356/768 46%	356/768 46%	178/768 23%
Max. Operating Frequency (MHz)	344.585 MHz	349.599 MHz	354.762 MHz	360.080 MHz	365.559 MHz

Table 2. MSE ve RMSE error analysis DP-based SEA chaotic oscillator

IQ-Math Fixed point	OUTPUT	MSE	RMSE
16I-16Q	X	1,23E-05	3,52E-03
	Y	7,08E-06	2,66E-03
	Z	1,75E-05	4,19E-03
14I-14Q	X	2,82E-04	1,68E-02
	Y	1,38E-04	1,17E-02
	Z	5,99E-04	2,45E-02
12I-12Q	X	4,38E-03	6,62E-02
	Y	1,90E-03	4,36E-02
	Z	1,04E-02	1,02E-01
10I-10Q	X	4,93E-02	2,22E-01
	Y	3,94E-02	1,99E-01
	Z	6,24E-02	2,50E-01
8I-8Q	X	8,79E-01	9,38E-01
	Y	4,60E-01	6,78E-01
	Z	1,7756069	1,33252

5. RESULTS AND DISCUSSIONS

A chaotic oscillator structure producing chaotic signal is the most basic structure used in chaos-based applications such as cryptology, secure

communications, industrial control, artificial neural networks, random number generators, and image processing. Because chaotic systems are expressed by differential equations, Euler, Heun, fourth order Runge-Kutta and fifth order Runge-Kutta-Butcher

based solutions have been proposed for numerical solutions of chaotic systems in the literature. In this study, unlike the numerical methods presented in the literature, SEA chaotic system has been designed on FPGA with IQ-Math fixed-point number standard using DP numerical algorithm. The operating frequencies of chaotic oscillator designs were obtained between 344.585 MHz and 365.559 MHz. The design has been coded in VHDL language by using Xilinx ISE Design Tools. It has been synthesized and tested for Xilinx Virtex-6 FPGA chip. In future work, safe communication and real random number generator applications can be realized by using the DP-based oscillator design presented in this study.

ACKNOWLEDGMENTS

This research has been supported by grant number 18.FEN.BİL.50 from Afyon Kocatepe University Scientific Research Projects Coordination Unit.

REFERENCES

- [1] Tuna, M., Fidan, C.B., "A Study on the importance of chaotic oscillators based on FPGA for true random number generating (TRNG) and chaotic systems", *Journal of the Faculty of Engineering and Architecture of Gazi University*, 33(2), pp: 469-486, 2018.
- [2] Yılmaz D., Güler N.F., A Study on the Chaotic Time Series Analysis, *Journal of the Faculty of Engineering and Architecture of Gazi University*, 21 (4), 759-779, 2006.
- [3] Yassen, M. T., Chaos synchronization between two different chaotic systems using active control," *Chaos, Solitons & Fractals*, 23(1): 131-140, 2005.
- [4] Park, J. H., and Kwon, O. M., "A novel criterion for delayed feedback control of time-delay chaotic systems". *Chaos, Solitons & Fractals*, 23.2: 495-501, 2005.
- [5] Chen, G., Mao, Y., & Chui, C. K. "A symmetric image encryption scheme based on 3D chaotic cat maps", *Chaos, Solitons & Fractals*, 21(3), 749-761, 2004.
- [6] Pareek, Narendra K., Vinod, Patidar, and Krishan, K. Sud. "Image encryption using chaotic logistic map", *Image and vision computing*, 24: 9926-934, 2006.
- [7] Pehlivan, İ., Uyaroğlu, Y., Yalçın, M. A., & Ferikoğlu, A. "Sprött_94_A Kaotik Sisteminin Senkronizasyonu ve Bilgi Gizlemede Kullanılması," *Uluslararası Katılımlı Bilgi güvenliği ve Kriptoloji Konferansı*, 2007.
- [8] Çavuşoğlu, Ü., Zengin, A., Pehlivan, I., & Kaçar, S. (2017). A novel approach for strong S-Box generation algorithm design based on chaotic scaled Zhongtang system. *Nonlinear Dynamics*, 87(2), 1081-1094.
- [9] Alçın, M., "The Effect on Modelling Performance of Different Activation Functions for Feed Forward and Feedback Network Structures in Modeling of Chen Chaotic System," *International Journal of Scientific and Technological Research*, ISSN 2422-8702 (Online), Vol 3, No.7, 2017.
- [10] Karunasinghe, Dulakshi SK, and Shie-Yui Liong., "Chaotic time series prediction with a global model: Artificial neural network," *Journal of Hydrology*, 323.1-4: 92-105, 2006.
- [11] Lin, J. S., & Huang, S. M. "An FPGA-based brain-computer interface for wireless electric wheelchairs," *In Applied Mechanics and Materials*, (Vol. 284, pp. 1616-1621). Trans Tech Publications, 2013.
- [12] dos Santos C.L., "Tuning of PID controller for an automatic regulator voltage system using chaotic optimization approach," *Chaos, Solitons & Fractals*, 39(4): 1504-1514, 2009.
- [13] Lu, J., Xinghuo Y., and Guanrong C., "Generating chaotic attractors with multiple merged basins of attraction: A switching piecewise-linear control approach," *IEEE Transactions on Circuits and Systems I: Fundamental Theory and Applications*, 50.2: 198-207, 2003.
- [14] Kaçar, S. (2016). Analog circuit and microcontroller based RNG application of a new easy realizable 4D chaotic system. *Optik*, 127(20), 9551-9561.
- [15] Çavuşoğlu, Ü., Kaçar, S., Pehlivan, I., & Zengin, A. (2017). Secure image encryption algorithm design using a novel chaos based S-Box. *Chaos, Solitons & Fractals*, 95, 92-101.
- [16] Dmitriev, A., Starkov, S., and Yemetz, S., "Chaotic communication using digital signal processors," *Nonlinear Theory and Applications*, 3: 1093-1096, 2000.
- [17] Alçın, M., Tuna, M., Koyuncu, İ., "IQ-Math Based Designing of Fourth Order Runge-Kutta Algorithm on FPGA and Performance Analysis

- According to ANN Approximation,” *International Journal of Advanced Research in Science Engineering and Technology*, 5(8): 6523–6530, 2018.
- [18] Pehlivan, İ., Uyaroğlu, Y. ve Yoğun, M., “Chaotic oscillator design and realizations of the Rucklidge attractor and its synchronization and masking simulations,” *Scientific Research and Essays*, 5(16): 2210-2219, 2010.
- [19] Rajagopalan, S., Rethinam, S., Deepika, A. N., Priyadarshini, A., Jyothirmai, M., Rengarajan, A., Rajagopalan, Sundararaman, et al. “Design of boolean chaotic oscillator using CMOS technology for true random number generation,” *Microelectronic Devices, Circuits and Systems (ICMDCS)*, International conference on: 1-6, 2017.
- [20] Ge, Z. M. ve Yang, C. H., “The generalized synchronization of a Quantum-CNN chaotic oscillator with different order system,” *Chaos, Solitons and Fractals*, 35: 980–990, 2008.
- [21] Chiuab, R., Gonzaleza, M. M., Mancillaa, D. L., “Implementation of a Chaotic Oscillator into a Simple Microcontroller,” *IERI Procedia* 4: 247–252, 2013.
- [22] Tuna, M., Fidan, C. B., Koyuncu, İ., & Pehlivan, İ., “Real time hardware implementation of the 3D chaotic oscillator which having golden-section equilibria,” *24th IEEE In Signal Processing and Communication Application Conference (SIU)*, pp. 1309-1312, 2016.
- [23] Alcin, M., Koyuncu, I., Tuna, M., Varan, M., & Pehlivan, I., “A novel high speed Artificial Neural Network-based chaotic True Random Number Generator on Field Programmable Gate Array,” *International Journal of Circuit Theory and Applications*, 47(3), 365-398, 2019.
- [24] Azzaz, M.S., Taugast, C., Sadoudi, S., Fellah, R., Dandache, A., “A new auto-switched chaotic system and its FPGA implementation,” *Communications in Nonlinear Science and Numerical Simulation*, 18 (7), 1792-1804, 2013.
- [25] Lee, S. H., Kapila, V., Porfiri, M., & Panda, A., “Master-slave synchronization of continuously and intermittently coupled sampled-data chaotic oscillators,” *Communications in Nonlinear Science and Numerical Simulation*, 15(12), 4100-4113, 2010.
- [26] Tuna, M., & Fidan, C. B. “Electronic circuit design, implementation and FPGA-based realization of a new 3D chaotic system with single equilibrium point,” *Optik-International Journal for Light and Electron Optics*, 127(24), 11786-11799, 2016.
- [27] Tlelo-Cuautle, E., Rangel-Magdaleno, J. J., Pano-Azucena, A. D., Obeso-Rodelo, P. J., & Nuñez-Perez, J. C. “FPGA realization of multi-scroll chaotic oscillators,” *Communications in Nonlinear Science and Numerical Simulation*, 27(1-3), 66-80, 2015.
- [28] Koyuncu, İ., Şahin, İ., Gloster, C., & Sarıtekin, N. K. “A Neuron Library for Rapid Realization of Artificial Neural Networks on FPGA: A Case Study of Rössler Chaotic System,” *Journal of Circuits, Systems and Computers*, 26(01), 1750015. 2017.
- [29] Alçın, M., Pehlivan, İ., & Koyuncu, İ. “Hardware design and implementation of a novel ANN-based chaotic generator in FPGA,” *Optik-International Journal for Light and Electron Optics*, 127(13), 5500-5505, 2016.
- [30] Xu, G., Shekofteh, Y., Akgül, A., Li, C., & Panahi, S., “A new chaotic system with a self-excited attractor: entropy measurement, signal encryption, and parameter estimation,” *Entropy*, 20(2), 86, 2018.
- [31] Tuna, M., Koyuncu, İ., & Alçın, M., “Fixed and floating point-based high-speed chaotic oscillator design with different numerical algorithms on FPGA,” *Int J Adv Res Electr Electron Instrum Eng*, 7(7), 3179-3187, 2018.
- [32] Tuna, M., Alçın, M., Koyuncu, İ., Fidan, C. B., & Pehlivan, İ., “High Speed FPGA-based Chaotic Oscillator Design,” *Microprocessors and Microsystems*, 66, 72-80, 2019.
- [33] Jin, C., Herder, C., Ren, L., Nguyen, P. H., Fuller, B., Devadas, S., & van Dijk, M. “Fpga implementation of a cryptographically-secure puf based on learning parity with noise,” *Cryptography*, 1(3), 23, 2017.
- [34] Ratnayake, K., & Amer, A. “Embedded architecture for noise-adaptive video object detection using parameter-compressed background modeling,” *Journal of Real-Time Image Processing*, 13(2), 397-414, 2017.
- [35] Koyuncu I, “Implementation of High Speed Tangent Sigmoid Transfer Function Approximations for Artificial Neural Network Applications on FPGA,” *Advances in Electrical and Computer Engineering*, 18, 79–86, 2018.

- [36] Rajagopal, K., Guessas, L., Vaidyanathan, S., Karthikeyan, A., & Srinivasan, A. “Dynamical analysis and FPGA implementation of a novel hyperchaotic system and its synchronization using adaptive sliding mode control and genetically optimized PID control,” *Mathematical Problems in Engineering*, 2017.
- [37] Chinna, S., Dharmar, S., & Shanmugavel, K. L. “Hardware Implementation of Road Network Extraction Using Simplified Gabor Wavelet in Field Programmable Gate Array,” *International Journal of Engineering and Technology Innovation*, 8(3), 200-216, 2018.

JOURNAL OF SCIENCE



SAKARYA UNIVERSITY

Sakarya University Journal of Science

ISSN 1301-4048 | e-ISSN 2147-835X | Period Bimonthly | Founded: 1997 | Publisher Sakarya University |
<http://www.saujs.sakarya.edu.tr/>

Title: Experimental Research of Energy Consumption of Austenitizing Heat-Treated Casting Fittings in Pipe Threading

Authors: Burak Öztürk

Received: 2019-01-16 01:15:59

Accepted: 2019-04-17 22:54:36

Article Type: Research Article

Volume: 23

Issue: 5

Month: October

Year: 2019

Pages: 869-878

How to cite

Burak Öztürk; (2019), Experimental Research of Energy Consumption of Austenitizing Heat-Treated Casting Fittings in Pipe Threading. Sakarya University Journal of Science, 23(5), 869-878, DOI: 10.16984/saufenbilder.513294

Access link

<http://www.saujs.sakarya.edu.tr/issue/44066/513294>

New submission to SAUJS

<http://dergipark.gov.tr/journal/1115/submission/start>



Investigation of the Effects of Austenitizing Heat Treatment on Energy Consumption of Pipe Threading

Burak Öztürk*¹

Abstract

Energy consumption is an important part of the production cost of mass production industrial enterprises. The casting, heat treatment and threading processes involved in the industrial production of fittings result in high energy consumption. In serial production, the threading of pipe fittings is carried out using high torque and low speed. The thin-walled designs of the fittings lead to rapid cooling, causing the formation of a high rate of pearlite microstructures and subsequent low or extremely hard machinability. Heat treatment with long austenitizing time in the furnace reduces the pearlite ratio, thus enabling a ferritic microstructure to be obtained. In this study, the ½-inch BSP threading process was applied to materials having both microstructures after casting and heat treatment. As in the mass production pipe threading process, fittings were threaded in a multi-threading process using a universal lathe and in a single threading process using a CNC mill. The Power Index (PI) was measured during the metal removal process and the energy consumption of the products was calculated via energy/power conversion equations. In addition, a new model was proposed that takes into consideration the energy consumption per product (ECPP) in the mass production machining process. As a result of combining the energy consumption and energy - power transformation theory with an experimental investigation, 39% optimization was achieved. That's a result of this experimental study resulted in energy savings of 8755 kWh annually.

Keywords: Austenitizing, cast iron, energy consumption, fittings, heat treatment

1. INTRODUCTION

Considering the current economy and competitive conditions, sustainability in energy consumption has become one of the most important research topics carried out in the manufacturing sector [1-3]. In order to obtain both semi-finished and completed products, energy consumption is required for the production processes. A significant increase in energy costs has emerged as a result of the continuous increase in energy

consumption worldwide along with the inadequate supply of new energy resources. Moreover, due to rising production and energy consumption, the resulting increased environmental pollution has arisen as a causal factor for climate change [4,5]. Therefore, energy saving has emerged as a permanent issue for the global economy. One of the industrial areas where energy is consumed is that of the metal cutting sector. Sustainable production as a global concept encompasses important elements of many

* Corresponding Author: burak.ozturk@bilecik.edu.tr

¹ Bilecik University, Metallurgy and Materials Engineering, Bilecik, Turkey. ORCID: 0000-0002-1018-6545

engineering areas and applications, especially in the processes of manufacturing [6,7]. The adoption of sustainable production practices allows companies to increase their economic as well as their environmental performance. Reduction of the energy consumption of machine tools and investigation of measures to be taken to realize clean production are of great importance in those production processes where a large amount of energy is consumed. In order to achieve this, it is necessary to calculate the energy consumption in the computerized numerically controlled (CNC) machine center [8,9]. The relationship between electrical energy consumption of the machine tool and the cutting process should be examined with the aim of achieving better energy efficiency associated with the production process.

2. ENERGY CONSUMPTION IN MACHINING APPLICATIONS

Chip removal using a CNC machine is a common process in the manufacturing industry. Based on this process, a number of studies have been published concerning the optimization of cutting parameters. In most of these studies, surface roughness, cutting force, power index (PI), tool life, and material removal rate (MRR) were used as optimization criteria. In particular, energy consumption during the machining process has previously been the subject of many types of research [10-18]. Mori et al. applied drilling and milling to S45 carbon steel using a CNC milling center. The effect of chip removal conditions on the PI was measured by attaching a clamp-type ammeter¹⁰. In addition, energy consumption in chip removal operations on different steels has also been investigated. The milling of ASSAB 760 steel was performed via CNC milling and the resulting forces were measured by a dynamometer. However, the power consumption was measured by a Power Meter and a new machining energy consumption model was presented in this study [11]. Negrete explored the hard turning of AISI 6061-T6 aluminum materials [12]. As a result, optimum cutting parameter values were obtained to minimize chip removal and achieve the best surface quality.

In the work carried out by Oda et al., the optimized angle of inclination of a 5-axis CNC milling machine was determined and consequently, reduced energy consumption was achieved [13]. Shokoohi et al. turned AISI1045 steel using a universal lathe and observed that the heat produced in the cutting zones during turning played an important role in the final quality of the workpiece and power consumption [14]. Neugebauer et al. drilled holes in gray cast iron and examined energy consumption changes [15]. Escalona et al. investigated the energy consumption of metal cutting on 303 stainless materials [16]. The PI was determined by an ammeter assembly during chip removal from a spheroidal workpiece and the machining process for two different cutting tools was optimized using Taguchi methodology in the study of Nas and Öztürk [17]. Liu et al. presented a new model for estimating the surface roughness of an aluminum alloy during milling. The model was developed using a hybrid approach combining analytical calculation of specific cutting energy consumption (SCEC) and experimental characterization of the correlation between surface roughness and SCEC [18].

3. CAST IRON FITTINGS

The process of manufacturing fittings consumes a great amount of energy due to the high temperature required for casting and subsequent long-term heat treatment in addition to the requirements for threading and coating, thus making sustainable production very difficult. In order to prevent water and gas leaks and other faults in the system, pipes must exhibit high mechanical properties [19]. In addition, secondary processing (e.g., heat treatment and galvanizing) is needed when cast iron fittings are to be used in plumbing. The cast iron fittings fabricated in Central Asian and Balkan countries are thin-walled, fragile and extremely vulnerable to corrosion. The chief problem of these fittings is due to their thin walls (5, 10, 15 and 20 mm), which are responsible for very high cooling rates (1.66 – 2.85 °C/s) [20] (Fig. 1.). The cooling rate following casting leads to ferrite, pearlite and bainite microstructure formation (Fig. 2.), which reduces the workability.

The hardness is increased as the fragility is reduced by austempering heat treatment application. Öktem et al. reported that processability was negatively affected by austempering heat treatment [21]. In serial production using a lathe, pipe threading is applied via multi-operation threading. However, this process is carried out with tap tools by a single operation on a CNC milling bench. There has been no exemplary study in the literature to date on this type of machining.

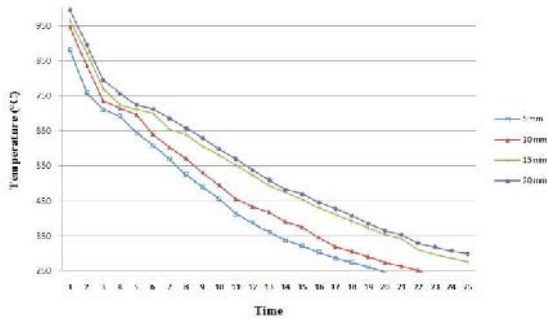


Figure 1. Microstructure changes due to the cooling rate of fittings [20]

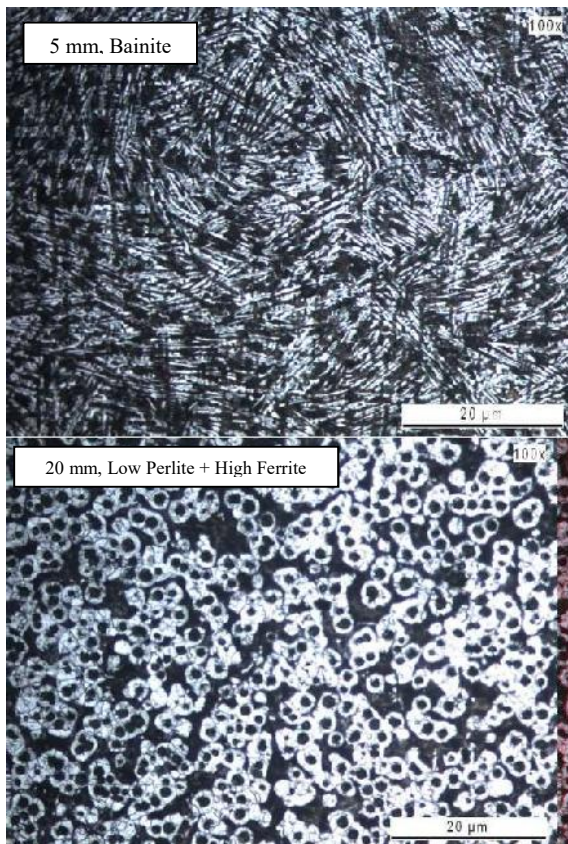


Figure 2. Hardness changes due to the cooling rate of fittings [20]

In this study, we examined the internal threading process of 15 mm-thick $1\frac{1}{2} - \frac{1}{2}$ inch reduction products at a high cooling rate. In order to determine the machinability of these products under different production conditions, this study investigated the energy consumption of two different types of pipe threading processes used in mass production. Optimal conditions for energy conservation and sustainability were determined for the processing of fitting materials responsible for high energy consumption.

4. MATERIAL AND METHOD

4.1. Design of experiment (DOE)

Spherical graphite cast iron fittings are manufactured in the industry using two different types of machining: the multi-operation threading process using a lathe and the single operation threading process using a CNC machining center. In industrial serial production, the threading process is accelerated by the number of revolutions. With the lathe machine, the threading of the fittings starts with turning at the bottom of the teeth, followed by the threading process performed at depths of 0.5, 0.25 and 0.1 mm. As shown in Figure 3, different in-feed shapes can be applied in the multi-operation threading process, including radial, flank and alternate flank in-feed [22].

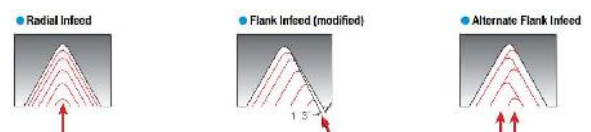


Figure 3. Multi-operation threading in-feed shapes

In this study, the radial type threading process was applied to fittings for a total of five operations. In addition, the single operation CNC milling process was carried out at low speed and high torque using a tap tool. The process of threading at 90, 125 and 180 RPM was selected for both of these machines. Turning was carried out for the first operation of the lathe at 500, 710 and 1000 RPM, respectively.

This experimental design is summarized in Table 1. All operations were applied under dry cutting

conditions. The average flow indices (PI (A)) were calculated by repeating the experiment three times for each sample.

Table 1. Fitting pipe threading process design of experimental (DOE)

Trial No	Process type	Machine Type	Thread Turning Speed (RPM)
1	Casting	Lathe	90
2	Casting	Lathe	125
3	Casting	Lathe	180
4	Casting	CNC Mill	90
5	Casting	CNC Mill	125
6	Casting	CNC Mill	180
7	Austempering	Lathe	90
8	Austempering	Lathe	125
9	Austempering	Lathe	180
10	Austempering	CNC Mill	90
11	Austempering	CNC Mill	125
12	Austempering	CNC Mill	180

4.2. Production of experimental samples by casting process and austempering heat treatment

In this study, the reduction ($3/4 - 1/2$ " product was designed according to TS 11 - EN 10242 standards. Table 3 shows the design features of the reduction fitting material. In addition, Table 4 shows the chemical analysis of the materials used in the experimental study measured after casting using the Oxford Foundry Master Pro spectrometer.

Table 3. Design features

Design Volume (mL)	Chip Volume (mL)	Internal Thread Chip Rate (%)	Pitch Diameter (mm)	Thread Length (mm)	Thread Size
10.097	0.302	3	1.814	20	1/2" BSP

Table 4. Chemical analysis of fittings

Element	Fe	C	Si	Mn	P	S
After spheroidal (%)	93.3	3.58	2.64	0.14	0.03	0.015

The austempering heat treatment was carried out in the heat treatment furnace at 950 °C temperatures for 12 h and cooling was applied to the fitting products under ambient conditions. The object was to obtain a microstructure having a high ferrite content at the end of this heat treatment.

4.3. Threading of test samples and measurement of Power Index (PI (A))

The materials were divided into groups in order to repeat the experiment three times. A Wellcut tap tool was used for the pipe threading on the CNC milling center. As tool wear was not observed during the threading process in the 36 experiments, each test specimen was threaded with the same tap tool (Fig. 4).



Figure 4. Wellcut 1/2 inch BSP tap tool

The tap tool used was 17.5 mm in diameter and 40 mm in length (L/D <3). Using the chuck assembly, the threading operation was carried out on the reduction materials attached to the CNC work bench. Table 5 presents the technical features of the Fanuc Microcut 1000 CNC vertical machining center used in the experimental study (Fig. 5) [23].



Figure 5. Fanuc Microcut 1000 CNC vertical machining center

Table 5 CNC milling machinery specifications

CNC Model	Motor Power	Machine Spindle Rotations (rpm)	Spindle Cos α	Spindle Voltage (V)	Maximum Torque (Nm)
Microcut 1000	15 kW	10.000	0.6	380	103

With the lathe, two different tools were used and a total of five operations were applied under dry cutting conditions. Figure 6 shows the Korloy DCMT-HMP NC 5330 turning tool and Figure 7 shows illustrations of the Korloy 14W IR 14 pipe threading insert.



Fig. 6 Korloy DCMT-HMP, NC 5330 internal hole turning diamond insert [22]

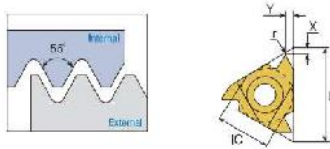


Fig. 7 Korloy 14W IR 55° internal threading diamond insert [22]

The multi-threading process was performed on the TOS SN 50 universal lathe machine. The PI was measured in the range 0.07–200 A (± 1 A) by connecting the Entes EPM 4C digital ammeter and the Entes CT-25 current transformer to each asynchronous motor in the lathe and the three-phase input of the motor drive in the CNC milling machine [24].

4.4. Machining process specific energy consumption model

There are many academic researches about energy in the literature [25-27]. Equation (1) presents the model of energy consumption P (Wh) for a machine tool during operation [10].

$$P = P_1 \times (T_1 + T_2) + P_2 \times T_2 + P_3 \times T_3 \quad (1)$$

In order to determine the energy required during chip removal ($P_{cutting}$), the power consumed when the chips are not being removed (P_{loss}) is deducted from the total power dissipated (P_{total}) (Eq. 2). The P includes the empty bearing power losses together with the power consumption of the spindle motor operating at the desired rpm [17].

$$P_{cutting} = P_{total} - P_{loss} \quad (2)$$

During chip removal, the power index measurement (A) of the spindle servo motor driver was converted to kW using an ammeter via the 3 - phase motor power conversion as presented in Equation (3) [14]. The power factor value was that specified in the Microcut CNC Mill technical specification manual. Here, V = spindle motor voltage value (V, 0.38), I = energy load measured by ammeter (A), $\cos \sigma$ = power factor (servo, 0.60; asynchronous motor, 0.85) [24].

$$P_{total} = \sqrt{3} \cdot V \cdot I \cdot \cos \sigma \quad (3)$$

Following a review of the literature, significant cutting parameters such as material removal rate (MRR), SCEC and material removal volume (Q) can be calculated using the energy power conversion equations and machining operations. The MRR is defined as the amount of chip (mm^3) removed from the workpiece in one second and Q as the total amount of chip processed during manufacturing. The MRR is calculated using Equation (4) given below. The SCEC is the cutting energy used to remove 1 mm^3 of material from the workpiece (Eq. 5) [18]. The SEC is the total amount of energy consumed to remove 1 mm^3 of chip and is calculated by the formula in Equation (6).

$$MRR = (ap * ae * F) / 1000 \quad (4)$$

$$SCEC \left(\frac{J}{\text{mm}^3} \right) = \frac{P_{cutting} (W)}{MRR \left(\frac{\text{mm}^3}{s} \right)} \quad (5)$$

$$SEC \left(\frac{J}{\text{mm}^3} \right) = \frac{P_{total} (W)}{MRR \left(\frac{\text{mm}^3}{s} \right)} \quad (6)$$

A number of studies in the literature deal with production conditions for metal cutting such as machine type and process parameters. For mass production, such as for pipe fittings, new definitions are needed for the energy consumption of short-time processing of materials. In this study, the amount of energy consumed is shown for the hourly production of a fitting material (Eq. 7). Thus, energy consumption for real-time production has been demonstrated. Moreover, energy consumed during the processing of different fittings can be examined and compared.

$$ECPP (Wh) = \frac{P_{total}(W)(inlet)}{\text{Numbers of Production (h)}} + \frac{P_{idle}(W)(outlet)}{\text{Numbers of Production (h)}} \quad (7)$$

5. RESULTS AND DISCUSSION

5.1. Examination of microstructure and mechanical properties

Images of the microstructures after casting and austenitizing heat treatment were obtained using an optical microscope (Fig. 8). When these microstructures were examined, it was observed that a pearlitic microstructure was formed after casting. Although the graphite was not fully spheroidal in some regions, it can be said that the *spheroidization* was generally close to ideal. However, peak infusion caused a low incidence of vermicular structures. A high rate of α -Ferrite was observed after the heat treatment. However, while the graphite was often diffused within the parent matrix, the spherical structures had become distorted and lamella formation was observed. The reduction materials produced after casting and heat treatment were cut and tensile specimens were obtained. The mechanical properties of each product in terms of hardness changes are given in Table 6. The tensile strength results showed that after heat treatment, the hardness decreased, while there was an increase in the elongation % rate.

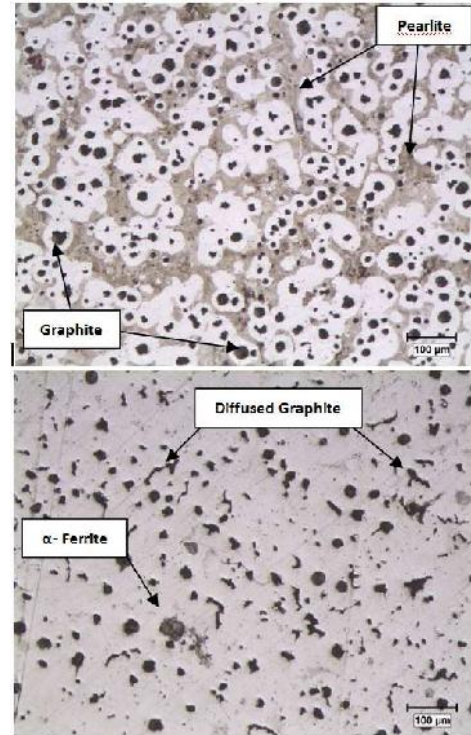


Figure 8. Microstructure: (down) after casting; (up) after heat treatment

Table 6. Tensile test results

	Max. Stress (N/mm ²)	Strain %	Energy (J)	Elongation (mm)	Hardness (HB)
Casting	536.4	27.6	131.3	5.53	162
Heat Treatment	359.9	41.9	180.5	8.38	95

5.2. Energy consumption results

The threading process and PI were measured for the determined experimental design. Total power (P_{total}) was calculated by using the energy/power conversion equations. In addition to the P_{total} , the total chip removal rate and material removal rate (MRR) are given in Table 7. 3.80 to 3.93 kWh energy consumption in the range of the manufacturing process was performed on the universal lathe. However, 10.2 to 15.6 kWh energy consumption in the CNC milling machine thread cutting process is made. The amount of MRR of the universal lathe was 20.6 mm³ on the other hand, CNC mills removed 82 mm³ chip. The results of the instantaneous power measurement showed that the CNC milling machine consumed

more energy. On the other hand, the MRR of CNC milling machine tools was more.

The ECPP and SEC results graph for these twelve different test samples is given in Figure 9. According to these results, although the energy required for the threading process on the CNC milling machine was much higher than the instantaneous energy consumption, the ECPP and SEC values were lower since the amount of chip removed is more and production time is shorter. In other words, the manual lathe consumes less P_{total} , but the production time and number of operations are much higher than the CNC mill.

Table 7. Main production data

No	P_{total} (kWh)	MRR (mm ³ /s)
1	3.86	10.30
2	3.91	14.30
3	3.93	20.60
4	13.3	41.08
5	14.8	57.08
6	15.6	82.06
7	3.8	10.30
8	3.9	14.30
9	3.9	20.60
10	10.26	41.08
11	10.33	57.08
12	10.49	82.06

Regarding the thread milling operations performed via CNC milling, the lowest values of ECPP after casting and heat treatment were calculated as 32 and 21.4 Wh.

According to this result, an energy saving of 49% was provided after the austempering process was applied to the fittings materials. In Table 7, P_{total} results showed similar results with ECPP values. According to these results, Energy consumption was reduced from 10.6 kW to 15.6 kW by the heat treatment applied. The most probable reason for this is that the perlitic microstructure can be converted into a ferritic structure, the hardness value decreases and the tensile strength can be decreased.

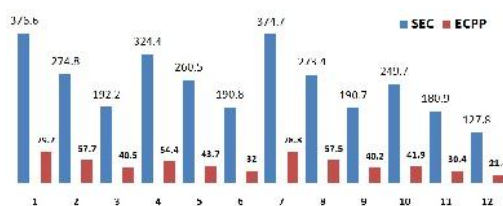


Figure 9. Changes of SEC and ECPP results

The SCEC and $P_{cutting}$ results (Table 8) provide information on the workability of the materials. The changes resulting from the applied heat treatment for these two parameters were examined. Accordingly, the results of measurements for 90, 125 and 180 RPM showed that workability was increased by 49%, 74% and 84%. According to these results, it was determined that the austenitizing heat treatment had a significant effect on the machinability. However, the effect increased as the number of revolutions increased.

Table 8. Machining results in CNC milling

Trial No	$P_{cutting}$ (kW)	MRR	SCEC
4	9.35	41.08	227.60
5	10.65	57.08	186.58
6	11.28	82.06	137.46
10	6.27	41.08	152.63
11	6.11	57.08	107.04
12	6.11	82.06	74.46

The ECPP results were determined by surface plots generated using RPM, production method, MRR and SEC values (Fig. 10). When these results are examined, it can be said that both the ECPP and the SEC values increased in parallel with the MRR values. At the same time, the energy consumption decreased as the number of revolutions increased.

No proportional change was observed between production time and energy consumption. The intensity of the effect of each production parameter determined in the experimental design on the SEC and ECPP results is shown in Tables 9 and 10. According to these findings, the tap tool affected SEC results at the rate of 63%. In addition, the type of machine affected the ECPP results by 58%.

Table 9 Analysis of variance for SEC using adjusted SS for tests

Source	DF	Seq SS	Adj SS	F	F%	P
Production Method	1	4110	4110	5.27	11	0.055
Machine Type	1	10110	10110	12.96	26	0.009
Cycles	2	48771	48771	31.26	63	0.000
Error	7	5460	5460			
Total	11	68451				

Table 10 Analysis of variance for ECPP using adjusted SS for tests

Source	DF	Seq SS	Adj SS	F	F%	P
Production Method	1	115.94	115.94	3.16	5	0.119
Machine Type	1	1410.50	1410.50	38.45	58	0.000
Cycles	2	1810.01	905	24.67	37	0.001
Error	7	256.80	36.69			
Total	11	3593.25				

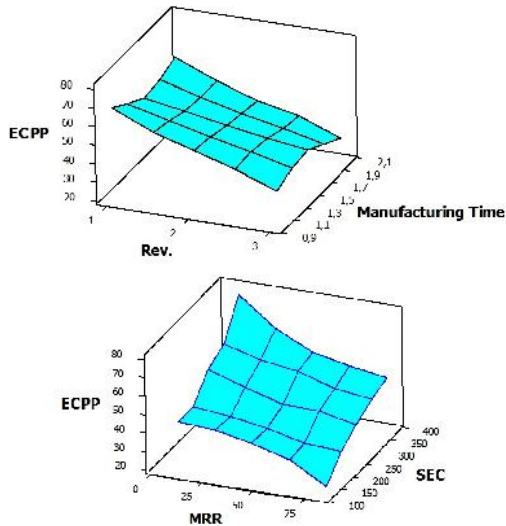


Figure 10. ECPP surface plot results

6. CONCLUSION

The amount of research into energy consumption has increased in recent years along with the rising energy production costs and growing inadequacy of available energy resources [9-18]. As the serial production conditions for reduction fittings involve different microstructure and hardness values, two different internal threading process methods were examined in this study. The threading process is applied in many manufacturing areas, including the aviation, automotive, and machine production industries, while sustainability and energy saving constitute important topics in these sectors.

This study may therefore serve as an important reference source for energy consumption surveys and pipe threading in metal cutting processes. Escalona et al. observed a maximum of 1.8 kWh of energy consumption when machining 304 grade stainless steel 16.

In their studies, Neugebauer et al. measured 6 kWh of power consumption in the drilling of EN-GJL-250 gray cast iron 15. When three different types of treatment methods were examined by Negrete in the turning of 6061 aluminum, the maximum energy expenditure of 5.8 kWh was observed in hole drilling 12. In addition, Öktem et al. researched the threading processes of cast and austempered fitting materials and observed that a total power consumption of 16.5 kWh was needed for the threading of cast iron fittings 21. The process of threading the cast material was carried out at 170 RPM on the same CNC milling machine using a $\frac{3}{4}$ inch tap tool with an instantaneous power consumption of 13.3 – 15.6 kW.

As a result of the austenitizing heat treatment applied in the current study, the threading process was performed with a $\frac{1}{2}$ -inch tap tool at expended energy in the range of 10.26–10.49 kW, making it possible to optimize energy consumption by an average of 39%. After casting, a pearlitic microstructure was observed, and following the heat treatment, the ferritic structure was transformed into α -ferrite.

However, it was determined that the spheroidized graphite was mostly diffused in the main matrix. The tensile strength and hardness decreased after the heat treatment, whereas an increase in the elongation percentage rate was observed. When the P_{total} results were examined, these changes in the microstructural and mechanical features resulted in energy savings of 3040 Wh using the CNC milling machine, which amount to an annual savings of 8755 kWh. Thus, by improving the material properties, high energy savings can be achieved in production, while at the same time yielding products which exhibit superior engineering properties.

Acknowledgements

I would like to thank Bilecik Şeyh Edebali University Scientific Research Projects Unit for their support for the project " 2018-02.BSEU.03-07 ".

7. REFERENCES

- [1] K. Weinert, I. Inasaki, J. W. Sutherland, and T. Wakabayashi, "Dry Machining and Minimum Quantity Lubrication," *CIRP Ann.*, Vol. 53. No. 2, pp. 511–537, 2004.
- [2] I. Düzdar, B. Kantoğlu, and B. Öztürk, "A New Product Design after Benchmarking Analysis of Helix Gear Pumps and Optimization in Energy Consumption," *Düzce Üniversitesi Bilim ve Teknoloji Dergisi*, Vol. 6, pp. 610-617, 2017.
- [3] G. Ingarao, D. R. Lorenzo and F. Micari, "Sustainability issues in sheet metal forming processes. An overview," *J. Clean. Prod.*, Vol. 19, No. 4, pp. 337-347, 2011.
- [4] V. A. Balogun, and P. T. Mativenga, "Modelling of direct energy requirements in mechanical machining processes," *J. Clean. Prod.*, Vol. 41, pp. 179-186, 2013.
- [5] R. K. Bhushan "Optimization of cutting parameters for minimizing power consumption and maximizing tool life during machining of Al alloy SiC particle composites," *J. Clean. Prod.*, Vol. 39, pp. 242-254, 2013.
- [6] I. Hanafi, A. Khamlichi, F. M. Cabrera, E. Almansa, and A. Jabbouri, "Optimization of cutting conditions for sustainable machining of PEEK-CF30 using TiN tools," *J. Clean. Prod.*, Vol. 33, pp. 1-9, 2012.
- [7] C. W. Park, K. S. Kwon, W. B. Kim, B.K. Min, S. J. Park, I.H. Sung, W.S. K.S. Yoon, Lee, J.H. Lee, and J. Seok, "Energy Consumption Reduction Technology in Manufacturing – A Selective Review of Policies, Standards, and Research," *Int. J. Precis. Eng. Man.*, Vol. 10, No. 5, pp. 151-173, 2009.
- [8] H. Akkuş, H. Yaka, "Optimization of Turning Process By Using Taguchi Method". *Sakarya University Journal of Science* vol. 22, pp. 1444-1448, 2018
- [9] N. Özsoy, M. Özsoy, "Optimization of Surface Roughness of AISI 1040 Stainless Steel in Milling Process Using Taguchi Method". *Sakarya University Journal of Science* vol. 23 pp. 113-120, 2019 <<http://www.saujs.sakarya.edu.tr/issue/31265/409502>>
- [10] M. Mori, M. Fujishima, Y. Inamasu, and Y. Oda, "A study on energy efficiency improvement for machine tools," *CIRP Annals – Manuf. Technol.*, Vol. 60, pp. 145–148, 2011.
- [11] N. Liu, Y. F. Zhang and W.F. Lu, "A hybrid approach to energy consumption modelling based on cutting power: A milling case," *J. Clean. Prod.*, Vol. 104, pp. 264-272, 2015.
- [12] C. C. Negrete, "Optimization of cutting parameters for minimizing energy consumption in turning of AISI 6061 T6 using Taguchi methodology and ANOVA," *J. Clean. Prod.*, Vol. 53, pp.195-203, 2013.
- [13] Y. Oda, M. Mori, K. Ogawa, S. Nishida, M. Fujishima and T. Kawamura, "Study of optimal cutting condition for energy efficiency improvement in ball end milling with tool-workpiece inclination," *CIRP Ann.- Manuf. Techn.*, Vol. 61, No. 1, pp. 119–122, 2012.
- [14] Y. Shokoohi, E. Khosrojerdi, and R. Shiadhi, "Machining and ecological effects of a new developed cutting fluid in combination with different cooling techniques on turning operation," *J. Clean. Prod.*, Vol. 94, pp. 330-339, 2015.
- [15] R. Neugebauer, A. Schubert, B. Reichmann, and M., Dix, "Influence exerted by tool properties on the energy efficiency during drilling and turning operations," *CIRP J. Manuf. Sci. Technol.*, Vol. 4, pp. 161–169, 2011.

- [16] P.M. Escalona, A. Shokrani and S.T. Newman, "Influence of cutting environments on surface integrity and power consumption of austenitic stainless steel," *Robot. Cim.-Int. Manuf.*, Vol. 36, pp. 60–69, 2015.
- [17] E. Nas, and B. Öztürk, "Optimization of surface roughness via the Taguchi method and investigation of energy consumption when milling spheroidal graphite cast iron materials," *Mater. Test.*, Vol. 60, No. 5, pp. 519-524, 2018.
- [18] N. Liu, S. B. Wang, Y. F. Zhang and W. F. Lu, , "A novel approach to predicting surface roughness based on specific cutting energy consumption when slot milling Al-7075," *Int. J. Mech. Sci.*, Vol. 118, pp. 13–20, 2016.
- [19] B. Öztürk, Ö. Küçük, İ. Düzdar and Y. S. Altınbilek, "Exploring the economical reasons of the usage of unhealthy & low resisting Far-East products in the water pipe systems," *The Turkish Journal of Occupational/Environmental Medicine and Safety*, Vol. 2, pp. 60-72, 2017.
- [20] B. Öztürk, H. Öktem, G. Said, H. A. Çetindağ, and F. Erzincanlı, "Investigation of Cooling Rate on Hardness and Microstructure in Casting Fittings Materials," in 4th International Symposium on Innovative Technologies in Engineering and Science, ISITES2016, 3-5 November, Alanya/Antalya, Turkey, pp. 1279-1285, 2016.
- [21] H. Öktem, B. Öztürk and S. Akincioğlu, "Investigation of energy consumption on thread machining of austempered ductile cast iron materials," 5th International Conference and Exhibition on Mechanical & Aerospace Engineering, October 02-04, Las Vegas, USA, 2017. DOI: 10.4172/2168-9792-C1-01
- [22] Korloy, "Korloy cutting tool technical specifications catalogue," 2018.
- [23] Fanuc, "Fanuc 1000 CNC user guide," 2012.
- [24] Entes, "Entes current transformer and ammeters technical specifications catalogue," 2018.
- [25] M. H. Shih, W. P. Sung, and C. G. Go, "A Design Concept With a Displacement Dependent Semi Active Hydraulic Damper Energy Dissipation" *Exp Tech* vol. 27, no. 53., 2003, <https://doi.org/10.1111/j.1747-1567.2003.tb00139.x>
- [26] F. Kara and B. Öztürk, "Comparison and optimization of PVD and CVD method on surface roughness and flank wear in hard machining of DIN 1.2738 mold steel," *Sensor Review*, vol. 39 No. 1, 2019 <https://doi.org/10.1108/SR-12-2017-0266>
- [27] G. Simić, V. Lučanin, J. Tanasković, et al., "Experimental Research of Characteristics of Shock Absorbers of Impact Energy of Passenger Coaches" *Exp Tech* vol. 33, 2009

JOURNAL OF SCIENCE



SAKARYA UNIVERSITY

Sakarya University Journal of Science

ISSN 1301-4048 | e-ISSN 2147-835X | Period Bimonthly | Founded: 1997 | Publisher Sakarya University |
<http://www.saujs.sakarya.edu.tr/>

Title: A Study of Symmetrical And Unsymmetrical Short Circuit Fault Analyses in Power Systems

Authors: Faruk Yalçın, Yılmaz Yıldırım

Received: 2019-03-15 19:14:15

Accepted: 2019-04-19 15:28:14

Article Type: Research Article

Volume: 23

Issue: 5

Month: October

Year: 2019

Pages: 879-895

How to cite

Faruk Yalçın, Yılmaz Yıldırım; (2019), A Study of Symmetrical And Unsymmetrical Short Circuit Fault Analyses in Power Systems. Sakarya University Journal of Science, 23(5), 879-895, DOI: 10.16984/saufenbilder.540294

Access link

<http://www.saujs.sakarya.edu.tr/issue/44066/540294>

New submission to SAUJS

<http://dergipark.gov.tr/journal/1115/submission/start>

A Study of Symmetrical and Unsymmetrical Short Circuit Fault Analyses in Power Systems

Faruk Yalçın^{*1}, Yılmaz Yıldırım²

Abstract

In this study, the common symmetrical and unsymmetrical short circuit faults in power systems are analyzed detailed. Unlike the similar studies in the literature, metallic fault conditions for unsymmetrical faults are also given in the paper additionally. For this aim, a short circuit analysis algorithm is created for the analysis of both three phase short circuit, line-to-line short circuit with fault impedance, metallic line-to-line short circuit, double line-to-ground short circuit with fault impedance, metallic double line-to-ground short circuit, line-to-ground short circuit with fault impedance and metallic line-to-ground short circuit. The obtained algorithm is established as software in MATLAB. The algorithm is applied on a sample power test system and the results are given.

Keywords: electric power system, short circuit analysis, symmetrical components, symmetrical faults, unsymmetrical faults

1. INTRODUCTION

The providing of the electrical energy continuously and healthy is very important for both the consumers and the power system. This situation depends on the continuity of the system operation in normal operation conditions [1]. The removing of all of the effects that force the system operate in abnormal operation conditions from the system as soon as possible is very important [2]. There are many situations that force a power system operate in abnormal operation conditions. The significant ones of these are the short circuit

faults [3]. Any short circuit fault causes many undesirable situations in power systems such as thermal-mechanic forces and power system instability [4]. Thus, it is required to remove the short circuit fault from the system as soon as possible. Removing of the short circuit faults from the systems is provided by the circuit breakers in power systems. The circuit breakers remove the short circuit currents caused by the short circuit faults from the system by opening via the relays [5]. The amplitude of the short circuit current occurred by a fault in any point of the system depends on the system parameters, the fault point and the fault type [6]. So, the short circuit

* Corresponding Author: farukyalcin@subu.edu.tr / farukyalcin@sakarya.edu.tr

¹ Sakarya Uni. of Appl. Sciences, Mechatronics Engineering, Sakarya, Turkey. ORCID: 0000-0003-2672-216X

² Sakarya Uni. of Appl. Sciences, Graduate Education Institute, Sakarya, Turkey. ORCID: 0000-0002-8114-6399

analyses in power systems are too important to determine the short circuit powers of the circuit breakers that are located in power systems [7]. On the other hand, it is required to know the voltage values in the buses where there is no fault during the short circuit fault. Because of these reasons, short circuit analyses in power systems are essential in terms of system security and control [8-10].

Different type short circuit faults occur in three phase power systems. These faults are generally divided into two types as symmetrical faults and unsymmetrical faults. [11,12]. Three phase short circuit is a symmetrical fault [13]. The faults through metallic or a fault impedance, line-to-line short circuit, double line-to-ground short circuit and line-to-ground short circuit are unsymmetrical faults [14-16]. In the literature, the short circuit calculations are generally done considering the power systems operate in balanced operation conditions before a fault occurs. Although the positive, negative and zero sequence circuits are independent in balanced normal operation conditions, during a short circuit fault, more precisely during unsymmetrical faults, the sequence circuits connect to each other in the fault point and they cannot be independent. [17]. So, symmetrical components method is useful and essential in short circuit analyses [18].

In this study, the analysis of the short circuit faults in electric power systems is aimed considering the general assumptions used in the literature [19]. For this aim, an algorithm that can calculate the short circuit currents in the fault point and the voltage values in the buses where there is no fault during fault condition by analyzing all of the symmetrical and unsymmetrical faults in power systems mentioned above is built. A software is done in MATLAB for the algorithm. The algorithm is applied on a sample test power system and all of the short circuit faults mentioned above are analyzed.

2. THE SHORT CIRCUIT FAULTS

2.1. General Short Circuit Model

All kind of short circuit faults can be analyzed through the Thevenin equivalent sequence circuits seen from the fault point in power systems. These Thevenin equivalent sequence circuits in a balanced three phase power system can be given in Fig. 1 [19].

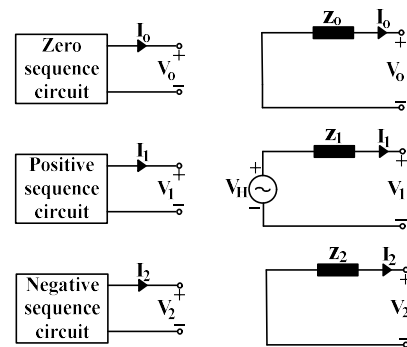


Figure 1. Thevenin equivalent sequence circuits in balanced three phase power system

In Fig. 1, V_0 , V_1 and V_2 define the sequence voltages (zero, positive and negative, respectively). I_0 , I_1 and I_2 define the sequence currents (zero, positive and negative, respectively). V_H defines the Thevenin voltage seen from the fault point. In this study, as the short circuit analyses are considered in balanced power systems, only the positive sequence circuit includes a voltage source. On the other hand, the load currents prior to short circuit faults are ignored in fault analysis. And, as the synchronous generators generate balanced EMFs, V_H equals to EMF value of the synchronous generators. As “n” represents the bus number of the fault point in the system, z_0 , z_1 and z_2 define the (n,n) components of the sequence bus impedance matrices (zero, positive and negative bus impedance matrices, respectively).

The sequence voltages at the fault point can be generalized from Fig. 1 as;

$$\begin{bmatrix} V_o \\ V_1 \\ V_2 \end{bmatrix} = \begin{bmatrix} 0 \\ V_H \\ 0 \end{bmatrix} - \begin{bmatrix} z_o & 0 & 0 \\ 0 & z_1 & 0 \\ 0 & 0 & z_2 \end{bmatrix} \begin{bmatrix} I_o \\ I_1 \\ I_2 \end{bmatrix} \quad (1)$$

In symmetrical short circuit faults, the sequence circuits given in Fig.1 keep independent. But in unsymmetrical short circuit faults, the sequence circuits connect to each other at the fault point.

2.2. Symmetrical Faults

The metallic three phase short circuit fault in a power system is a symmetrical fault. Although three phase short circuit is balanced, symmetrical components method is useful to analyze this short circuit.

2.2.1. Three Phase Short Circuit

The metallic three phase short circuit in a power system is given as schematic in Fig. 2 [20].

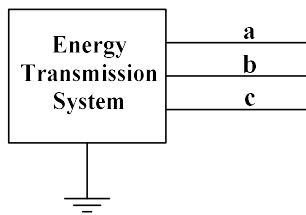


Figure 2. Schematic representation of three phase short circuit fault in power system

In Fig. 2, a, b and c represent the three phases. As seen in Fig. 2, the fault is symmetrical when a direct metallic short circuit occurs between the three phases (a, b, c) in any point of the power system. Thus, the phase voltages at the fault point are equal and zero.

$$V_a = V_b = V_c = 0 \quad (2)$$

Considering the phase “a” as reference, the sequence voltages of this phase can be given as;

$$\begin{bmatrix} V_o \\ V_1 \\ V_2 \end{bmatrix} = \frac{1}{3} \begin{bmatrix} 1 & 1 & 1 \\ 1 & a & a^2 \\ 1 & a^2 & a \end{bmatrix} \begin{bmatrix} V_a \\ V_b \\ V_c \end{bmatrix} = \begin{bmatrix} 0 \\ 0 \\ 0 \end{bmatrix} \quad (3)$$

By using the results of Eq. (3) in Eq. (1), the sequence currents are derived as;

$$\begin{bmatrix} I_o \\ I_1 \\ I_2 \end{bmatrix} = \begin{bmatrix} 0 \\ \frac{V_H}{z_1} \\ 0 \end{bmatrix} \quad (4)$$

By using the results of Eq. (4) in Fig. 1, the sequence circuits connections for three phase short circuit fault can be given in Fig. 3 [21].

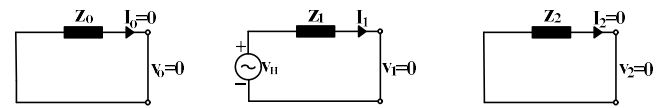


Figure 3. Sequence circuits connections for three phase short circuit fault in power system

The phase currents flowing through phase “a”, “b” and “c” at the fault point can be derived using Eq. (4) as;

$$\begin{bmatrix} I_a \\ I_b \\ I_c \end{bmatrix} = \begin{bmatrix} 1 & 1 & 1 \\ 1 & a^2 & a \\ 0 & a & a^2 \end{bmatrix} \begin{bmatrix} I_o \\ I_1 \\ I_2 \end{bmatrix} = \begin{bmatrix} \frac{V_H}{z_1} \\ a^2 \frac{V_H}{z_1} \\ a \frac{V_H}{z_1} \end{bmatrix} \quad (5)$$

The sequence voltage values of the buses where there is no fault can be derived as [21];

$$\begin{bmatrix} V_{o-k} \\ V_{1-k} \\ V_{2-k} \end{bmatrix} = \begin{bmatrix} 0 \\ V_H \\ 0 \end{bmatrix} - \begin{bmatrix} z_{o-kn} & 0 & 0 \\ 0 & z_{1-kn} & 0 \\ 0 & 0 & z_{2-kn} \end{bmatrix} \begin{bmatrix} I_{o-n} \\ I_{1-n} \\ I_{2-n} \end{bmatrix} \quad (6)$$

In Eq. (6), “k” represents the bus number where there is no fault. z_{o-kn} , z_{1-kn} and z_{2-kn} define the (k,n) components of the sequence bus impedance matrices (zero, positive and negative bus impedance matrices, respectively). The phase voltage values of the buses where there is no fault can be derived from Eq. (6) as;

$$\begin{bmatrix} V_{a-k} \\ V_{b-k} \\ V_{c-k} \end{bmatrix} = \begin{bmatrix} 1 & 1 & 1 \\ 1 & a^2 & a \\ 1 & a & a^2 \end{bmatrix} \begin{bmatrix} V_{o-k} \\ V_{1-k} \\ V_{2-k} \end{bmatrix} \quad (7)$$

2.3. Unsymmetrical Faults

The faults in three phase power systems through metallic or a fault impedance, line-to-line short circuit, double line-to-ground short circuit and line-to-ground short circuit are unsymmetrical faults. The sequence circuits cannot be independent and connect to each other according to the fault type when a short circuit fault occurs in a balanced three phase power system.

2.3.1. Line-to-Line Short Circuit with Fault Impedance

The line-to-line short circuit with a fault impedance in a power system is given as schematic in Fig. 4 [22].

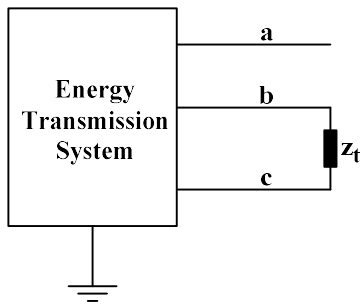


Figure 4. Schematic representation of line-to-line short circuit with a fault impedance in power system

In Fig. 4, z_t defines the fault impedance. From Fig. 4, the phase voltages and currents equations at the fault point can be derived as below:

$$V_b - V_c = z_t I_b \quad (8)$$

$$I_c = -I_b \quad (9)$$

$$I_a = 0 \quad (10)$$

Considering the phase “a” as reference, sequence currents can be defined from Eq. (9) and (10) as;

$$\begin{bmatrix} I_o \\ I_1 \\ I_2 \end{bmatrix} = \frac{1}{3} \begin{bmatrix} 1 & 1 & 1 \\ 1 & a & a^2 \\ 1 & a^2 & a \end{bmatrix} \begin{bmatrix} 0 \\ I_b \\ -I_b \end{bmatrix} = \begin{bmatrix} 0 \\ \frac{1}{3}(a - a^2)I_b \\ \frac{1}{3}(a^2 - a)I_b \end{bmatrix} \quad (11)$$

From Eq. (11), the sequence currents can be written as;

$$I_o = 0, \quad I_2 = -I_1 \quad (12)$$

Considering the phase “a” as reference, sequence voltages can be defined from Eq. (8) as;

$$\begin{aligned} & (V_o + a^2 V_1 + a V_2) - (V_o + a V_1 + a^2 V_2) \\ & = z_t (I_o + a^2 I_1 + a I_2) \end{aligned} \quad (13)$$

From Eq. (12) and (13), the equation below is derived:

$$V_1 - V_2 = z_t I_1 \quad (14)$$

By using the results of Eq. (12) and (14), the sequence circuits connections for the line-to-line short circuit with a fault impedance can be given in Fig. 5 [23].

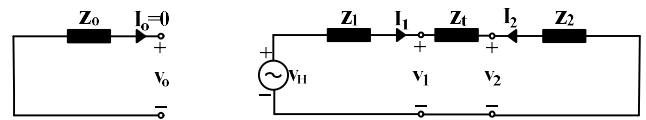


Figure 5. Sequence circuits connections for line-to-line short circuit with a fault impedance in power system

From Fig. 5, the sequence currents can be calculated as below;

$$I_o = 0 \quad (15)$$

$$I_1 = -I_2 = \frac{V_H}{(z_1 + z_2 + z_t)} \quad (16)$$

By using Eq. (15) and (16), the short circuit phase currents flowing through phase “b” and “c” at the fault point can be derived as;

$$I_b = I_o + a^2 I_1 + a I_2 = (a^2 - a) I_1$$

$$= -\frac{j\sqrt{3}V_H}{(z_1 + z_2 + z_i)} \quad (17)$$

$$I_c = I_o + a I_1 + a^2 I_2 = (a - a^2) I_1 = -I_b$$

$$= \frac{j\sqrt{3}V_H}{(z_1 + z_2 + z_i)} \quad (18)$$

The sequence and phase voltage values of the buses where there is no fault can be derived from Eq. (6) and (7) respectively given before.

2.3.2. Metallic Line-to-Line Short Circuit

The metallic line-to-line short circuit fault in a power system is given as schematic in Fig. 6.

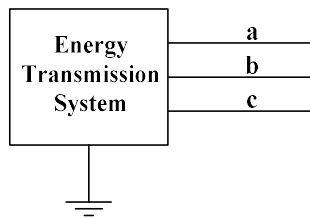


Figure 6. Schematic representation of metallic line-to-line short circuit fault in power system

From Fig. 6, the phase voltages and currents equations at the fault point can be derived as below:

$$V_b = V_c \quad (19)$$

$$I_c = -I_b \quad (20)$$

$$I_a = 0 \quad (21)$$

Considering the phase “a” as reference, sequence currents can be defined from Eq. (20) and (21) as;

$$\begin{bmatrix} I_o \\ I_1 \\ I_2 \end{bmatrix} = \frac{1}{3} \begin{bmatrix} 1 & 1 & 1 \\ 1 & a & a^2 \\ 1 & a^2 & a \end{bmatrix} \begin{bmatrix} 0 \\ I_b \\ -I_b \end{bmatrix} = \begin{bmatrix} 0 \\ \frac{1}{3}(a - a^2)I_b \\ \frac{1}{3}(a^2 - a)I_b \end{bmatrix} \quad (22)$$

From Eq. (22), the sequence currents can be written as;

$$I_o = 0, \quad I_2 = -I_1 \quad (23)$$

Considering the phase “a” as reference, sequence voltages can be defined from Eq. (19) as;

$$(V_o + a^2 V_1 + a V_2) = (V_o + a V_1 + a^2 V_2)$$

$$\implies (a^2 - a) V_1 = (a^2 - a) V_2 \quad (24)$$

From Eq. (24), the equation below is derived:

$$V_1 - V_2 = 0 \quad (25)$$

By using the results of Eq. (23) and (25), the sequence circuits connections for the metallic line-to-line short circuit fault can be given in Fig. 7.

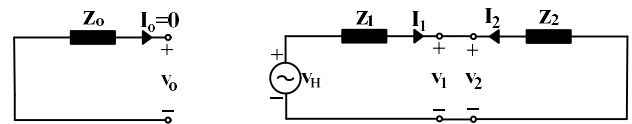


Figure 7. Sequence circuits connections for metallic line-to-line short circuit fault in power system

From Fig. 7, the sequence currents can be calculated as below;

$$I_o = 0 \quad (26)$$

$$I_1 = -I_2 = \frac{V_H}{(z_1 + z_2)} \quad (27)$$

By using Eq. (26) and (27), the short circuit phase currents flowing through phase “b” and “c” at the fault point can be derived as;

$$I_b = I_o + a^2 I_1 + a I_2 = (a^2 - a) I_1$$

$$= -\frac{j\sqrt{3}V_H}{(z_1 + z_2)} \quad (28)$$

$$I_c = I_o + a I_1 + a^2 I_2 = (a - a^2) I_1 = -I_b$$

$$= \frac{j\sqrt{3}V_H}{(z_1 + z_2)} \quad (29)$$

The sequence and phase voltage values of the buses where there is no fault can be derived from Eq. (6) and (7) respectively given before.

2.3.3. Double Line-to-Ground Short Circuit with Fault Impedance

The double line-to-ground short circuit with fault impedance in a power system is given as schematic in Fig. 8 [24].

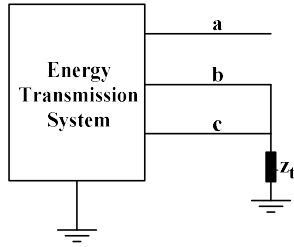


Figure 8. Schematic representation of double line-to-ground short circuit with a fault impedance in power system

From Fig. 8, the phase voltages and currents equations at the fault point can be derived as below:

$$V_b = V_c = z_t (I_b + I_c) \quad (30)$$

$$I_a = 0 \quad (31)$$

Considering the phase “a” as reference, the relation between the sequence currents can be defined from Eq. (31) as;

$$I_a = I_o + I_1 + I_2 = 0 \implies -I_1 - I_2 = I_o \quad (32)$$

Considering the phase “a” as reference, sequence voltages can be defined from Eq. (30) as;

$$\begin{aligned} (V_o + a^2V_1 + aV_2) &= (V_o + aV_1 + a^2V_2) \\ \implies (a^2 - a)V_1 &= (a^2 - a)V_2 \implies V_1 = V_2 \end{aligned} \quad (33)$$

By reorganizing Eq. (33), the equation below can be written:

$$V_1 - V_2 = 0 \quad (34)$$

Eq. (30) can also be rewritten as;

$$\begin{aligned} (V_o + a^2V_1 + aV_2) \\ = z_t (I_o + a^2I_1 + aI_2 + I_o + aI_1 + a^2I_2) \end{aligned} \quad (35)$$

By using Eq. (34) in Eq. (35), the equation below can be derived;

$$(V_o - V_1) = z_t (2I_o - I_1 - I_2) \quad (36)$$

By using Eq. (32) in Eq. (36), the equation below can be derived;

$$(V_o - V_1) = 3z_t I_o \quad (37)$$

By using the results of Eq. (32), (34) and (37), the sequence circuits connections for the double line-to-ground short circuit with fault impedance can be given in Fig. 9 [25].

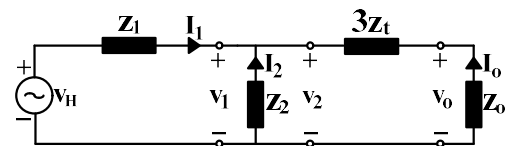


Figure 9. Sequence circuits connections for double line-to-ground short circuit with a fault impedance in power system

From Fig. 9, the positive sequence current can be calculated as;

$$\begin{aligned} I_1 &= \frac{V_H}{z_1 + [z_2 // (z_o + 3z_t)]} \\ &= \frac{V_H}{z_1 + \left[\frac{z_2(z_o + 3z_t)}{z_2 + z_o + 3z_t} \right]} \end{aligned} \quad (38)$$

By applying the current divider formula to the circuit given in Fig. 9, the zero and negative sequence currents can be derived as below;

$$\begin{aligned} I_o &= (-I_1) \left(\frac{z_2}{z_2 + z_o + 3z_t} \right) \\ &= - \frac{V_H}{\left[z_1 + \left(\frac{z_2(z_o + 3z_t)}{z_2 + z_o + 3z_t} \right) \right] \left(\frac{z_2 + z_o + 3z_t}{z_2} \right)} \end{aligned} \quad (39)$$

$$I_2 = (-I_1) \left(\frac{z_o + 3z_t}{z_2 + z_o + 3z_t} \right) = - \frac{V_H}{\left[z_1 + \left(\frac{z_2(z_o + 3z_t)}{z_2 + z_o + 3z_t} \right) \right] \left(\frac{z_2 + z_o + 3z_t}{z_o + 3z_t} \right)} \quad (40)$$

By using Eq. (38)-(40), the short circuit phase currents flowing through phase “b” and “c” at the fault point can be derived as;

$$I_b = - \frac{V_H}{\left[z_1 + \left(\frac{z_2(z_o + 3z_t)}{z_2 + z_o + 3z_t} \right) \right] \left(\frac{z_2 + z_o + 3z_t}{z_2} \right)} + a^2 \frac{V_H}{z_1 + \left[\frac{z_2(z_o + 3z_t)}{z_2 + z_o + 3z_t} \right]} - a \frac{V_H}{\left[z_1 + \left(\frac{z_2(z_o + 3z_t)}{z_2 + z_o + 3z_t} \right) \right] \left(\frac{z_2 + z_o + 3z_t}{z_o + 3z_t} \right)} \quad (41)$$

$$I_c = - \frac{V_H}{\left[z_1 + \left(\frac{z_2(z_o + 3z_t)}{z_2 + z_o + 3z_t} \right) \right] \left(\frac{z_2 + z_o + 3z_t}{z_2} \right)} + a \frac{V_H}{z_1 + \left[\frac{z_2(z_o + 3z_t)}{z_2 + z_o + 3z_t} \right]} - a^2 \frac{V_H}{\left[z_1 + \left(\frac{z_2(z_o + 3z_t)}{z_2 + z_o + 3z_t} \right) \right] \left(\frac{z_2 + z_o + 3z_t}{z_o + 3z_t} \right)} \quad (42)$$

The sequence and phase voltage values of the buses where there is no fault can be derived from Eq. (6) and (7) respectively given before.

2.3.4. Metallic Double Line-to-Ground Short Circuit

The metallic double line-to-ground short circuit fault in a power system is given as schematic in Fig. 10.

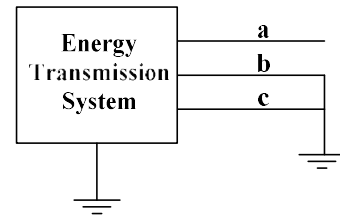


Figure 10. Schematic representation of metallic double line-to-ground short circuit fault in power system

From Fig. 10, the phase voltages and currents equations at the fault point can be derived as below:

$$V_b = V_c = 0 \quad (43)$$

$$I_a = 0 \quad (44)$$

Considering the phase “a” as reference, the relation between the sequence currents can be defined from Eq. (44) as;

$$I_a = I_o + I_1 + I_2 = 0 \quad (45)$$

Considering the phase “a” as reference, sequence voltages can be defined from Eq. (43) as;

$$(V_o + a^2V_1 + aV_2) = (V_o + aV_1 + a^2V_2) \implies (a^2 - a)V_1 = (a^2 - a)V_2 \implies V_1 = V_2 \quad (46)$$

By reorganizing Eq. (46), the equation below can be written:

$$V_1 - V_2 = 0 \quad (47)$$

By considering the equations given by Eq. (47) and (43) together, the equation below is derived;

$$(V_o + a^2V_1 + aV_2) = V_o + (a^2V_1 + aV_1) = V_o - V_1 = 0 \implies V_o = V_1 \quad (48)$$

From Eq. (46) and (48), the relation between the sequence voltages can be derived as;

$$V_o = V_1 = V_2 \quad (49)$$

By using the results of Eq. (45) and (49), the sequence circuits connections for the metallic

double line-to-ground short circuit fault can be given in Fig. 11.

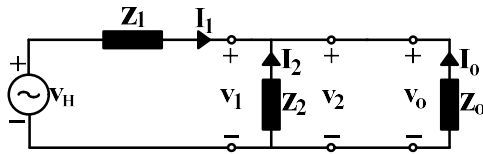


Figure 11. Sequence circuits connections for metallic double line-to-ground short circuit fault in power system

From Fig. 11, the positive sequence current can be calculated as;

$$I_1 = \frac{V_H}{z_1 + (z_2 // z_o)} = \frac{V_H}{z_1 + \frac{z_2 z_o}{z_2 + z_o}} \quad (50)$$

By applying the current divider formula to the circuit given in Fig. 11, the zero and negative sequence currents can be derived as below;

$$I_o = (-I_1) \left(\frac{z_2}{z_2 + z_o} \right) = - \frac{V_H}{\left(z_1 + \frac{z_2 z_o}{z_2 + z_o} \right) \left(\frac{z_2 + z_o}{z_2} \right)} \quad (51)$$

$$I_2 = (-I_1) \left(\frac{z_o}{z_2 + z_o} \right) = - \frac{V_H}{\left(z_1 + \frac{z_2 z_o}{z_2 + z_o} \right) \left(\frac{z_2 + z_o}{z_o} \right)} \quad (52)$$

By using Eq. (50)-(52), the short circuit phase currents flowing through phase “b” and “c” at the fault point can be derived as;

$$I_b = - \frac{V_H}{\left(z_1 + \frac{z_2 z_o}{z_2 + z_o} \right) \left(\frac{z_2 + z_o}{z_2} \right)} + a^2 \frac{V_H}{z_1 + \frac{z_2 z_o}{z_2 + z_o}} - a \frac{V_H}{\left(z_1 + \frac{z_2 z_o}{z_2 + z_o} \right) \left(\frac{z_2 + z_o}{z_o} \right)} \quad (53)$$

$$I_c = - \frac{V_H}{\left(z_1 + \frac{z_2 z_o}{z_2 + z_o} \right) \left(\frac{z_2 + z_o}{z_2} \right)} + a \frac{V_H}{z_1 + \frac{z_2 z_o}{z_2 + z_o}} - a^2 \frac{V_H}{\left(z_1 + \frac{z_2 z_o}{z_2 + z_o} \right) \left(\frac{z_2 + z_o}{z_o} \right)} \quad (54)$$

The sequence and phase voltage values of the buses where there is no fault can be derived from Eq. (6) and (7) respectively given before.

2.3.5. Line-to-Ground Short Circuit with Fault Impedance

The line-to-ground short circuit with fault impedance in a power system is given as schematic in Fig. 12 [26].

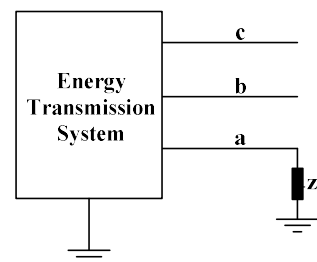


Figure 12. Schematic representation of line-to-ground short circuit with a fault impedance in power system

From Fig. 12, the phase voltages and currents equations at the fault point can be derived as below:

$$V_a = z_t I_a \tag{55}$$

$$I_b = I_c = 0 \tag{56}$$

Considering the phase “a” as reference, the relation between the sequence currents can be defined from Eq. (56) as;

$$\begin{bmatrix} I_o \\ I_1 \\ I_2 \end{bmatrix} = \frac{1}{3} \begin{bmatrix} 1 & 1 & 1 \\ 1 & a & a^2 \\ 1 & a^2 & a \end{bmatrix} \begin{bmatrix} I_a \\ 0 \\ 0 \end{bmatrix} = \frac{1}{3} \begin{bmatrix} I_a \\ I_a \\ I_a \end{bmatrix} \tag{57}$$

From Eq. (57), the sequence currents are derived as below;

$$I_o = I_1 = I_2 \tag{58}$$

Considering the phase “a” as reference, the relation between the sequence voltages can be defined from Eq. (55) as;

$$(V_o + V_1 + V_2) = z_t (I_o + I_1 + I_2) \tag{59}$$

By using Eq. (58) in Eq. (59), the equation below can be derived;

$$(V_o + V_1 + V_2) = 3z_t I_1 \tag{60}$$

By using the results of Eq. (58) and (60), the sequence circuits connections for the line-to-ground short circuit with fault impedance can be given in Fig. 13 [27].

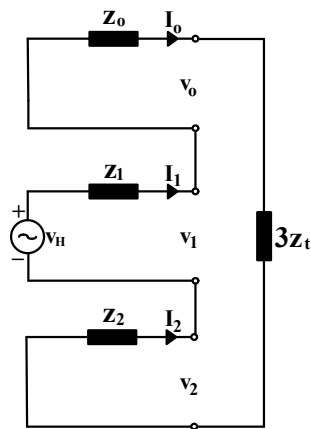


Figure 13. Sequence circuits connections for line-to-ground short circuit with a fault impedance in power system

The sequence currents can be calculated from Fig. 13 as;

$$I_o = I_1 = I_2 = \frac{V_H}{z_o + z_1 + z_2 + 3z_t} \tag{61}$$

By using Eq. (61), the short circuit phase current flowing through phase “a” at the fault point can be derived as;

$$I_a = \frac{3V_H}{z_o + z_1 + z_2 + 3z_t} \tag{62}$$

The sequence and phase voltage values of the buses where there is no fault can be derived from Eq. (6) and (7) respectively given before.

2.3.6. Metallic Line-to-Ground Short Circuit

The metallic line-to-ground short circuit fault in a power system is given as schematic in Fig. 14.

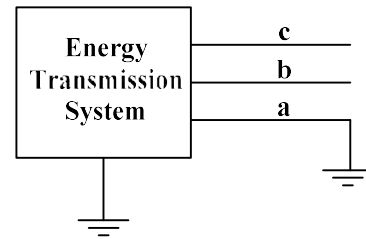


Figure 14. Schematic representation of metallic line-to-ground short circuit fault in power system

From Fig. 14, the phase voltages and currents equations at the fault point can be derived as below:

$$V_a = 0 \tag{63}$$

$$I_b = I_c = 0 \tag{64}$$

Considering the phase “a” as reference, the relation between the sequence currents can be defined from Eq. (64) as;

$$\begin{bmatrix} I_o \\ I_1 \\ I_2 \end{bmatrix} = \frac{1}{3} \begin{bmatrix} 1 & 1 & 1 \\ 1 & a & a^2 \\ 1 & a^2 & a \end{bmatrix} \begin{bmatrix} I_a \\ 0 \\ 0 \end{bmatrix} = \frac{1}{3} \begin{bmatrix} I_a \\ I_a \\ I_a \end{bmatrix} \tag{65}$$

From Eq. (65), the sequence currents are derived as below;

$$I_o = I_1 = I_2 \quad (66)$$

Considering the phase “a” as reference, the relation between the sequence voltages can be defined from Eq. (63) as;

$$(V_o + V_1 + V_2) = 0 \quad (67)$$

By using the results of Eq. (66) and (67), the sequence circuits connections for the metallic line-to-ground short circuit fault can be given in Fig. 15.

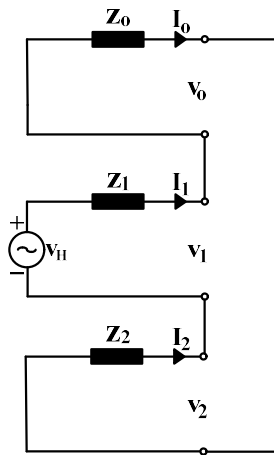


Figure 15. Sequence circuits connections for metallic line-to-ground short circuit fault in power system

The sequence currents can be calculated from Fig. 15 as;

$$I_o = I_1 = I_2 = \frac{V_H}{z_o + z_1 + z_2} \quad (68)$$

By using Eq. (68), the short circuit phase current flowing through phase “a” at the fault point can be derived as;

$$I_a = \frac{3V_H}{z_o + z_1 + z_2} \quad (69)$$

The sequence and phase voltage values of the buses where there is no fault can be derived from Eq. (6) and (7) respectively given before.

3. THE SHORT CIRCUIT ANALYSIS ALGORITHM

In this section, a short circuit analysis algorithm that can analyze all of the short circuit faults given in section 2. The algorithm is written as software in MATLAB. The algorithm can calculate the short currents and the voltage values of the buses where there is no fault in power systems by analyzing the short circuit faults. The schematic representation of the proposed algorithm is given in Fig. 16 and the details of the steps in Fig. 16 are given below the figure.

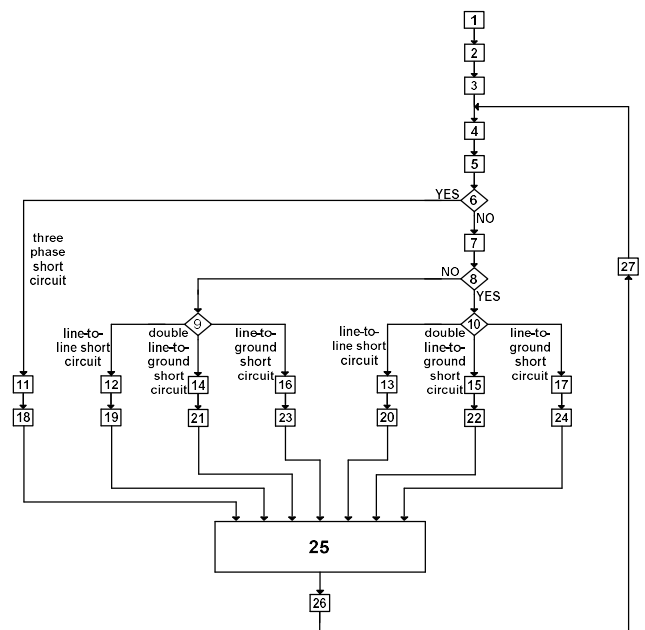


Figure 16. Schematic representation of the proposed short circuit analysis algorithm

Step 1: Read the p.u. values of the power system parameters that are used in the short circuit analysis (Read the Thevenin equivalent voltage value at the fault point, sequence impedances of all of the synchronous generators, sequence impedances of the synchronous and asynchronous motors that have higher powers than 40 kW, serial sequence impedances and the neutral-ground impedances that are in the wye side of the transformers and the serial sequence impedances of the transmission lines. Consider only the reactance values and ignore the resistance values of the read ones).

Step 2: Create the sequence bus admittance matrices (y_{bus-0} , y_{bus-1} and y_{bus-2}) by using the read values in step 1.

Step 3: Create the sequence bus impedance matrices (z_{bus-0} , z_{bus-1} and z_{bus-2}) by inverting the sequence admittance matrices derived in step 2.

Step 4: Enter the bus number where the short circuit fault occurs.

Step 5: Select the short circuit fault type that is required to analyze (three phase short circuit fault? line-to-line short circuit fault? double line-to-ground short circuit fault? line-to-ground short circuit fault?).

Step 6: Is the selected fault in step 5 three phase short circuit fault?

Step 7: Enter the value of the short circuit fault impedance z_f .

Step 8: Is the value of the short circuit fault impedance $z_f = 0$?

Step 9: Is the selected fault type line-to-line short circuit fault, double line-to-ground short circuit fault or line-to-ground short circuit fault?

Step 10: Is the selected fault type line-to-line short circuit fault, double line-to-ground short circuit fault or line-to-ground short circuit fault?

Step 11: Calculate the short circuit currents I_a , I_b ve I_c that occur at the fault point by using Eq. (5).

Step 12: Calculate the short circuit currents I_b and I_c that occur at the fault point by using Eq. (17) and (18).

Step 13: Calculate the short circuit currents I_b and I_c that occur at the fault point by using Eq. (28) and (29).

Step 14: Calculate the short circuit currents I_b and I_c that occur at the fault point by using Eq. (41) and (42).

Step 15: Calculate the short circuit currents I_b and I_c that occur at the fault point by using Eq. (53) and (54).

Step 16: Calculate the short circuit current I_a that occurs at the fault point by using Eq. (62).

Step 17: Calculate the short circuit current I_a that occurs at the fault point by using Eq. (69).

Step 18: Calculate the sequence currents at the fault point by using Eq. (4).

Step 19: Calculate the sequence currents at the fault point by using Eq. (11).

Step 20: Calculate the sequence currents at the fault point by using Eq. (22).

Step 21: Calculate the sequence currents at the fault point by using Eq. (38)-(40).

Step 22: Calculate the sequence currents at the fault point by using Eq. (50)-(52).

Step 23: Calculate the sequence currents at the fault point by using Eq. (57).

Step 24: Calculate the sequence currents at the fault point by using Eq. (65).

Step 25: Calculate the sequence and phase voltage values of the buses where there is no fault by using Eq. (6) and (7).

Step 26: Calculate the real values of the short circuit phase currents and the phase voltage values of the buses where there is no fault through the p.u. values of them calculated in the previous steps.

Step 27: Return to step 4 for a new short circuit analysis.

4. RESULTS

The proposed short circuit analysis algorithm given in section 3 is applied to a sample 14-bus test power system given in Fig. 17.

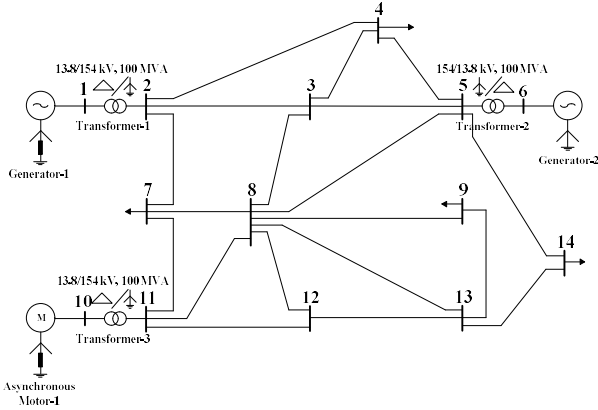


Figure 17. The 14-bus sample test power system

The system parameters of the test system shown in Fig. 17 are given in Table 1, 2 and 3.

Table 1. Transmission line parameters of the 14-bus sample test power system

Transmission Line bus-(i) – bus-(j)	Xh-0 (p.u.)	Xh-1 (p.u.)	Xh-2 (p.u.)
2 – 3	0.69	0.23	0.23
2 – 4	2.13	0.71	0.71
2 – 7	1.74	0.58	0.58
3 – 4	2.52	0.84	0.84
3 – 5	1.08	0.36	0.36
3 – 8	1.41	0.47	0.47
4 – 5	2.79	0.93	0.93
5 – 8	1.98	0.66	0.66
5 – 14	2.07	0.69	0.69
7 – 8	0.87	0.29	0.29
7 – 11	2.70	0.90	0.90
8 – 9	2.31	0.77	0.77
8 – 11	2.43	0.81	0.81
8 – 12	1.77	0.59	0.59
8 – 13	1.26	0.42	0.42
9 – 13	1.17	0.39	0.39
11 – 12	1.95	0.65	0.65
12 – 13	0.87	0.29	0.29
13 – 14	1.05	0.35	0.35

Table 2. Rotating machine parameters of the 14-bus sample test power system

Rotating Machine	Xg-0 (p.u.)	Xg-1 (p.u.)	Xg-2 (p.u.)	Xt (p.u.)
Generator-1	0.035	0.95	0.95	0.045
Generator-2	0.045	0.98	0.98	0
Asynchronous Motor-1	0.04	1.00	1.00	0.05

Table 3. Transformer parameters of the 14-bus sample test power system

Transformer	Xt-0 (p.u.)	Xt-1 (p.u.)	Xt-2 (p.u.)
Transformer -1	0.035	0.95	0.95
Transformer -2	0.045	0.98	0.98
Transformer -3	0.04	1.00	1.00

The proposed algorithm is applied to the test system to analyze a three phase short circuit fault at bus 4. The short circuit currents I_a , I_b and I_c at the fault point (bus-4) and the phase voltages at the buses where there is no fault are given in Table 4. Thevenin equivalent voltage value at the fault point is considered as $v_H=1.02\angle 0^\circ$. The base power is considered as $S_{base}=100$ MVA.

Table 4. The analysis results for three phase short circuit fault at bus 4

Bus No.	Short Current Currents (kA)		
	I_a	I_b	I_c
4 (fault point)	0.5574	0.5574	0.5574
Bus No.	Bus Voltages (kV)		
	V_a	V_b	V_c
1	6.6659	6.6659	6.6659
2	62.2017	62.2017	62.2017
3	58.3281	58.3281	58.3281
5	66.9003	66.9003	66.9003
6	6.8765	6.8765	6.8765
7	72.2971	72.2971	72.2971
8	71.8567	71.8567	71.8567
9	72.8860	72.8860	72.8860
10	8.7033	8.7033	8.7033
11	89.3293	89.3293	89.3293
12	76.6800	76.6800	76.6800
13	73.4073	73.4073	73.4073
14	71.2174	71.2174	71.2174

The proposed algorithm is applied to the test system to analyze a line-to-line short circuit with a fault impedance at bus 7. The short circuit

currents I_b and I_c at the fault point (bus-7) and the phase voltages at the buses where there is no fault are given in Table 5. Thevenin equivalent voltage value at the fault point is considered as $v_H=1.05\angle 0^\circ$. The fault impedance is selected as $z_f=(0.01+j0.025)$ (p.u.). The base power is considered as $S_{base}=100$ MVA.

To compare the results of the line-to-line short circuit with a fault impedance with the metallic line-to-line short circuit fault, the proposed algorithm is applied to the test system to analyze a metallic line-to-line short circuit fault considering the same fault point and the parameters of the previous analysis for the line-to-line short circuit with a fault impedance. So, for the metallic line-to-line short circuit fault analysis, the fault point is selected as bus 7, Thevenin equivalent voltage value at the fault point is considered as $v_H=1.05\angle 0^\circ$ and the base power is considered as $S_{base}=100$ MVA. The short circuit currents I_b and I_c at the fault point (bus-7) and the phase voltages at the buses where there is no fault for the metallic line-to-line short circuit fault analysis are given in Table 6.

Table 5. The analysis results for line-to-line short circuit with a fault impedance at bus 7

Bus No.	Short Current Currents (kA)		
	I_a	I_b	I_c
7 (fault point)	0	0.5838	0.5838
Bus No.	Bus Voltages (kV)		
	V_a	V_b	V_c
1	14.4900	9.1372	9.0408
2	161.7000	95.5293	94.2098
3	161.7000	94.9664	93.6225
4	161.7000	96.3633	95.0788
5	161.7000	99.1421	97.9664
6	14.4900	9.3679	9.2790
8	161.7000	88.7399	87.0778
9	161.7000	90.1935	88.6157
10	14.4900	9.0312	8.9312
11	161.7000	95.0676	93.7282
12	161.7000	91.2428	89.7214
13	161.7000	90.9767	89.4413
14	161.7000	93.4855	92.0748

Table 6. The analysis results for metallic line-to-line short circuit fault at bus 7

Bus No.	Short Current Currents (kA)		
	I_a	I_b	I_c
7 (fault point)	0	0.5966	0.5966
Bus No.	Bus Voltages (kV)		
	V_a	V_b	V_c
1	14.4900	8.9962	8.9962
2	161.7000	93.8457	93.8457
3	161.7000	93.2757	93.2757
4	161.7000	94.6911	94.6911
5	161.7000	97.5146	97.5146
6	14.4900	9.2318	9.2318
8	161.7000	87.0248	87.0248
9	161.7000	88.4724	88.4724
10	14.4900	8.8881	8.8881
11	161.7000	93.3782	93.3782
12	161.7000	89.5228	89.5228
13	161.7000	89.2560	89.2560
14	161.7000	91.7792	91.7792

The proposed algorithm is applied to the test system to analyze a double line-to-ground short circuit with a fault impedance at bus 10. The short circuit currents I_b and I_c at the fault point (bus-10) and the phase voltages at the buses where there is no fault are given in Table 7. Thevenin equivalent voltage value at the fault point is considered as $v_H=1.03\angle 0^\circ$. The fault impedance is selected as $z_f=(j0.03)$ (p.u.). The base power is considered as $S_{base}=100$ MVA.

Table 7. The analysis results for double line-to-ground short circuit with a fault impedance at bus 10

Bus No.	Short Current Currents (kA)		
	I_a	I_b	I_c
10 (fault point)	0	9.1924	9.1924
Bus No.	Bus Voltages (kV)		
	V_a	V_b	V_c
1	11.3247	9.1351	9.1351
2	121.6260	93.8962	93.8962
3	118.9253	89.3844	89.3844
4	120.5505	92.0936	92.0936
5	120.9413	92.7477	92.7477
6	11.2059	8.9328	8.9328
7	109.6299	74.3261	74.3261
8	109.8653	74.6960	74.6960
9	109.3119	73.8273	73.8273
11	90.2851	47.8193	47.8193
12	104.9267	67.0965	67.0965
13	109.0316	73.3888	73.3888
14	113.0397	79.7503	79.7503

Table 8. The analysis results for metallic double line-to-ground short circuit fault at bus 10

Bus No.	Short Current Currents (kA)		
	I_a	I_b	I_c
10 (fault point)	0	9.9872	9.9872
Bus No.	Bus Voltages (kV)		
	V_a	V_b	V_c
1	10.7538	8.9610	8.9610
2	114.3163	91.5714	91.5714
3	111.0820	86.8250	86.8250
4	113.0284	89.6771	89.6771
5	113.4963	90.3647	90.3647
6	10.6116	8.7495	8.7495
7	99.9500	70.8321	70.8321
8	100.2318	71.2285	71.2285
9	99.5691	70.2972	70.2972
11	76.7828	41.5058	41.5058
12	94.3174	63.0356	63.0356
13	99.2334	69.8266	69.8266
14	104.0334	76.6247	76.6247

To compare the results of the double line-to-ground short circuit with a fault impedance with the metallic double line-to-ground short circuit fault, the proposed algorithm is applied to the test system to analyze a metallic double line-to-ground short circuit fault considering the same fault point and the parameters of the previous analysis for the double line-to-ground short circuit with a fault impedance. So, for the metallic double line-to-ground short circuit fault analysis, the fault point is selected as bus 10, Thevenin equivalent voltage value at the fault point is considered as $V_H=1.03\angle 0^\circ$ and the base power is considered as $S_{base}=100$ MVA. The short circuit currents I_b and I_c at the fault point (bus-10) and the phase voltages at the buses where there is no fault for the metallic double line-to-ground short circuit fault analysis are given in Table 8.

The proposed algorithm is applied to the test system to analyze a line-to-ground short circuit with a fault impedance at bus 13. The short circuit current I_a at the fault point (bus-13) and the phase voltages at the buses where there is no fault are given in Table 9. Thevenin equivalent voltage value at the fault point is considered as $V_H=1.04\angle 0^\circ$. The fault impedance is selected as $z_f=(0.012+j0.035)$ (p.u.). The base power is considered as $S_{base}=100$ MVA.

Table 9. The analysis results for line-to-ground short circuit with a fault impedance at bus 13

Bus No.	Short Current Currents (kA)		
	I_a	I_b	I_c
13 (fault point)	0.5637	0	0
Bus No.	Bus Voltages (kV)		
	V_a	V_b	V_c
1	10.2111	13.4037	13.4701
2	104.9152	149.1129	149.8948
3	94.0718	150.0880	150.7865
4	99.3828	149.2976	150.0634
5	98.0165	148.6847	149.5045
6	9.6931	13.3030	13.3783
7	80.9176	151.9723	152.5195
8	63.7993	154.7565	155.0999
9	26.9525	161.9901	161.8861
10	9.6352	13.2920	13.3683
11	96.8210	148.4980	149.3345
12	42.7253	158.5593	158.6549
14	38.4504	159.4778	159.5180

To compare the results of the line-to-ground short circuit with a fault impedance with the metallic line-to-ground short circuit fault, the proposed algorithm is applied to the test system to analyze a metallic line-to-ground short circuit fault considering the same fault point and the parameters of the previous analysis for the line-to-ground short circuit with a fault impedance. So, for the metallic line-to-ground short circuit fault analysis, the fault point is selected as bus 13, Thevenin equivalent voltage value at the fault point is considered as $V_H=1.04\angle 0^\circ$ and the base power is considered as $S_{base}=100$ MVA. The short circuit current I_a at the fault point (bus-13) and the phase voltages at the buses where there is no fault for the metallic line-to-ground short circuit fault analysis are given in Table 10.

Table 10. The analysis results for metallic line-to-ground short circuit fault at bus 13

Bus No.	Short Current Currents (kA)		
	I_a	I_b	I_c
13 (fault point)	0.5938	0	0
Bus No.	Bus Voltages (kV)		
	V_a	V_b	V_c
1	9.9888	13.3951	13.3951
2	101.9482	149.0227	149.0227
3	90.5206	149.9878	149.9878
4	96.1178	149.2051	149.2051
5	94.6779	148.6004	148.6004
6	9.4429	13.2958	13.2958
7	76.6561	151.8655	151.8655
8	58.6090	154.6650	154.6650
9	19.7048	162.0350	162.0350
10	9.3819	13.2850	13.2850
11	93.4180	148.4167	148.4167
12	36.3768	158.5252	158.5252
14	31.8628	159.4626	159.4626

5. CONCLUSION

This paper presents a study to analyze the common symmetrical and unsymmetrical short circuit faults in electric power systems. For this aim, all kind of short circuit faults are studied detailed and their short circuit fault models are derived considering the assumptions commonly used in the literature. Apart from the similar studies in the literature, metallic fault conditions for unsymmetrical short circuit faults are also analyzed in the study additionally. Then, an algorithm for the power systems to analyze these short circuit fault types to determine the short circuit currents at the fault points and the voltages of the buses where there is no fault in the system. A software is created for the proposed algorithm in MATLAB. The proposed short circuit analysis algorithm is applied to a sample 14-bus test power system and each symmetrical and unsymmetrical short circuit faults are analyzed. The obtained results have shown that the algorithm is efficient and accurate.

REFERENCES

- [1] Y. Shu and Y. Tang, "Analysis and recommendations for the adaptability of China's power system security and stability relevant standards," *CSEE Journal of Power and Energy Systems*, vol. 3, no. 4, pp. 334–339, 2017.
- [2] W. Du, Q. Fu, and Y. Wang, "Small-signal stability of an AC/MTDC power system as affected by open-loop modal coupling between the VSCs," *IEEE Transactions on Power Systems*, vol. 33, no. 3, pp. 3143–3152, 2018.
- [3] C. Huang, B. Zhang, Y. Ma, F. Zhou, and J. He, "Analysis of short-circuit current characteristics and its distribution of artificial grounding faults on DC transmission lines," *IEEE Transactions on Power Delivery*, vol. 33, no. 1, pp. 520–528, 2018.
- [4] J. Ma, S. Wang, Y. Qiu, Y. Li, Z. Wang, and J. S. Thorp, "Angle stability analysis of power system with multiple operating conditions considering cascading failure," *IEEE Transactions on Power Systems*, vol. 32, no. 2, pp. 873–882, 2017.
- [5] P. M. Anderson, *Power System Protection*, IEEE Press Marketing, 1999.
- [6] J. Teng, "Systematic short-circuit-analysis method for unbalanced distribution systems," *IEE Proceedings - Generation, Transmission and Distribution*, vol. 152, no. 4, pp. 549–555, 2005.
- [7] R. M. Ciric, L. F. Ochoa, A. Padilla-Feltrin, and H. Nouri, "Fault analysis in four-wire distribution networks," *IEE Proceedings - Generation, Transmission and Distribution*, vol. 152, no. 6, pp. 977–982, 2005.
- [8] G. H. Kjolle, O. Gjerde, B. T. Hjartsjo, H. Engen, L. Haarla, L. Koivisto, and P. Lindblad, "Protection system faults -- a comparative review of fault statistics," *International Conference on Probabilistic*

- Methods Applied to Power Systems, Stockholm, pp. 1–7, 2006.
- [9] Y. Zhang, J. Zhang, J. Ma, and Z. Wang, “Fault detection based on discriminant analysis theory in electric power system,” International Conference on Sustainable Power Generation and Supply, Nanjing, pp. 1–5, 2009.
- [10] C. I. Ciontea, C. Leth Bak, F. Blaabjerg, K. K. Madsen, and C. H. Sterregaard, “Fault analysis for protection purposes in maritime applications,” 13th International Conference on Development in Power System Protection, Edinburgh, pp. 1–6, 2016.
- [11] B. Mahamedi and J. G. Zhu, “A novel approach to detect symmetrical faults occurring during power swings by using frequency components of instantaneous three-phase active power,” IEEE Transactions on Power Delivery, vol. 27, no. 3, pp. 1368–1376, 2012.
- [12] E. H. Badawy and M. K. El-Sherbiny, A. A. Ibrahim, and M. S. Farghaly, “A method of analyzing unsymmetrical faults on six-phase power systems,” IEEE Transactions on Power Delivery, vol. 6, no. 3, pp. 1139–1145, 1991.
- [13] D. Dufournet and G. Montillet, “Three-phase short circuit testing of high-voltage circuit breakers using synthetic circuits,” IEEE Transactions on Power Delivery, vol. 15, no. 1, pp. 142–147, 2000.
- [14] S. Wang, Y. Sun, Z. Huang, and S. Mu, “Analysis of stator internal phase-to-phase short circuit in the 12-phase synchronous generator with rectifier-load system,” IEEE Transactions on Energy Conversion, vol. 33, no. 1, pp. 299–311, 2018.
- [15] R. Korab and E. Siwy, “Statistical analysis of the double line-to-ground short-circuit current in MV urban network for the power cable metallic screen rating,” International Conference on Probabilistic Methods Applied to Power Systems, Stockholm, pp. 1–6, 2006.
- [16] S. Shimizu, H. Kado, Y. Uriu, and T. Ishigohka, “Single-line-to-ground fault test of a 3-phase superconducting fault current limiting reactor,” IEEE Transactions on Magnetics, vol. 28, no.1, pp. 442–445, 1992.
- [17] L. Shi, C. Shan, X. Wu, and H. Wang, “Short circuit current calculation and analysis of shipboard medium frequency power system,” International Conference on Electrical Machines and Systems, Beijing, pp. 1–5, 2011.
- [18] S. Kulkarni, A. B. Parit, Pulavarthi, B. V R S V, and S. S. Patil, “Comparative analysis of three phase, five phase and six phase symmetrical components with MATLAB,” International Conference on Data Management, Analytics and Innovation, Pune, pp. 182–186, 2017.
- [19] J. D. Glover, M. S. Sarma, and T. J. Overbye, Power System Analysis and Design, Cengage Learning, 2012.
- [20] A. A. Sallam and O. P. Malik, Electric Distribution Systems, Wiley-IEEE Press, 2019.
- [21] U. Arifoglu, Güç Sistemlerinin Bilgisayar Destekli Analizi, Alfa Yayınları, 2002.
- [22] M. S. Choi, S. J. Lee, S. I. Lim, D. S. Lee, and X. Yang, “A direct three-phase circuit analysis-based fault location for line-to-line fault,” IEEE Transactions on Power Delivery, vol. 22, no. 4, pp. 2541–2547, 2007.
- [23] M. Alwash, M. Sweet, and E. M. S. Narayanan, “Analysis of voltage source converters under DC line-to-line short-circuit fault conditions,” IEEE 26th International Symposium on Industrial Electronics, Edinburgh, pp. 1801–1806, 2017.

- [24] S. N. Pashkovskiy, R. A. Vainstein, and S. M. Yudin, "Transformation of zero-sequence electric quantities for protection against line-to-ground fault in the networks with various neutral grounding modes," 2nd International Conference on Industrial Engineering, Applications and Manufacturing, Chelyabinsk, pp. 1–5, 2016.
- [25] A. Dubey, H. Sun, D. Nikovski, T. Takano, Y. Kojima, and T. Ohno, "Locating double-line-to-ground faults using hybrid current profile approach," IEEE Power & Energy Society Innovative Smart Grid Technologies Conference, Washington, pp. 1–5, 2015.
- [26] A. Birajdar and S. Tajane, "Modelling and simulation of transmission line to detect single line to ground fault location," IEEE 1st International Conference on Power Electronics, Intelligent Control and Energy Systems, Delhi, pp. 1–4, 2016.
- [27] X. Liang, S. A. Wallace, and X. Zhao, "A technique for detecting wide-area single-line-to-ground faults," IEEE Conference on Technologies for Sustainability, Portland, pp. 121–124, 2011.

JOURNAL OF SCIENCE



SAKARYA UNIVERSITY

Sakarya University Journal of Science

ISSN 1301-4048 | e-ISSN 2147-835X | Period Bimonthly | Founded: 1997 | Publisher Sakarya University |
<http://www.saujs.sakarya.edu.tr/>

Title: X-Ray Radiography of Micro-Alloyed Steel Joined By Submerged Arc Welding

Authors: Mustafa Türkmen

Received: 2019-03-29 23:56:46

Accepted: 2019-04-22 16:46:09

Article Type: Research Article

Volume: 23

Issue: 5

Month: October

Year: 2019

Pages: 896-901

How to cite

Mustafa Türkmen; (2019), X-Ray Radiography of Micro-Alloyed Steel Joined By Submerged Arc Welding . Sakarya University Journal of Science, 23(5), 896-901, DOI: 10.16984/saufenbilder.546992

Access link

<http://www.saujs.sakarya.edu.tr/issue/44066/546992>

New submission to SAUJS

<http://dergipark.gov.tr/journal/1115/submission/start>

X-Ray Radiography of Micro-alloyed Steel Joined by Submerged Arc Welding

Mustafa Türkmen¹

Abstract

In this study, micro-alloyed steels were welded by using submerged arc welding method. Different welding current values in experimental studies were carried out according to Table 3. After welding process, the radiographic tests were examined by using X-Ray. The experimental results indicated that microalloyed steel could be joined by using the submerged arc welding technique with sufficient strength. The results of the radiographic tests indicated that with increasing welding current, the amount of deep penetration increased in all samples.

Keywords: Micro-alloyed Steel, Submerged Arc Welding, Radiographic Test.

1. INTRODUCTION

Welding technology is used commonly in many areas. Non-destructive testing methods are important for quality control strategies related to the wear since it is aimed to provide high and constant quality in manufacturing sector and in products,. Accordingly, the non-destructive testing of welded joints has become a part of total quality system [1-2].

Being one of the most important parts of quality control, non-destructive material testing method is the complementary part of the manufacturing. Non-destructive method is the common name of testing methods which ensures to obtain the static and dynamic information of the materials by testing them without giving any damage. By means of the non-destructive testing method, the defects such as cracks occurring during manufacturing or after used for a while, space in

internal structure, edge reduction etc. are detected [Table 1].

The methods applied in non-destructive testing are visual testing, liquid-penetrant testing, eddy current testing, magnetic particle inspection, ultrasonic inspection, and radiographic inspection respectively [3-6]. Radiography method is applied to ferromagnetic metals, non-ferromagnetic metals, and other all materials. Because X-ray provides the opportunity to analyse the microstructure of the materials without giving any damage, it is widely used in non-destructive testing. Thickness changes, structural changes, inner defects, and installation details can be determined through X-ray or gamma ray [7-11]. The inspection requires method of the radiographic images to be first-rate and consequently controlled by standard. However; being carried out subjectively by inspectors the radiographic inspection requires great experience and there are interpretation errors due to non-detection of defects [6-12-14].

¹ Faculty of Basic Sciences Departments Mathematics turkmen@gtu.edu.tr

Table 1. Non-destructive testing experiments in industry application areas [3].

Practice Area	Function	Application Examples
Research and Development	Structural evaluation of materials, Comparison of production and assembly methods and evaluation findings.	Examination of fatigue and microstructure of metals and the detection of cracks in the welding seam.
Production Control Method	Determination of the variable production method and to control.	Radiographic and ultrasonic thickness measuring method and determination of the manufacturing parameters.
Quality Control	Defective parts and the detection of abnormalities, Manufacturing assembly defects, place and method of evaluation.	Poor adhesion, cracking in welding, metal in the non-uniform pores and the determination of material defects.
During the service evaluation	Wear and use during the early identification of abnormalities.	Corrosion in pipes and location of warehouses and detection, Variety of early warning systems in vehicles.

The advantages of radiography method may be listed as follows; the result is shown with an image, permanent records seen outside of the test area can be obtained, the sensitivity is shown on every film, and the method may be applied to any kind of material. As for its disadvantages, they may be mentioned as follows; it is not suitable for thick pieces, it may be harmful to health, direct calorific energy is needed for two-dimensional faults, it is not suitable for automation, and surface defects, and it does not give information about the depth of the defect under the surface. The equipment used is rather expensive compared to other methods and mostly needs careful work concerning the radiation safety [15].

In this study, X-Ray radiographic test of micro-alloyed steel joined by using Submerged Arc Welding (SAW) was investigated.

2. EXPERIMENTAL PART

Microalloy steel having 400x200x6 mm dimensions was used to join the samples which Table 2 shows the chemical compositions in this study.

The welding process was performed as two passes by using Oerlikon Magmaweld brand ZD5-1000 B model saw machine. S690QL steels were applied to pre-annealing at 100 °C before the welding. Temperature of pre-annealing was determined by being controlled with heat chalk. Three different welded joints specified in Table 3

were performed by using test materials at 300 A, 350 A and 450 A welding current. Oerlikon-S2 submerged arc welding wire, whose chemical composition is shown in Table 2, and SF-104 submerged arc welding powder, proper to this wire, were used in the welding process. Table 3 illustrates welding parameters used in the experimental studies. Table 4 illustrates physical properties of microalloyed steel.

Table 2. Compositions of test materials

Materials	C	Si	Mn	Cr	Ni	Mo	V	Ti
Micro-alloyed Steel	0,13	0,8	1,0	1,5	1,1	0,3	0,1	0,05
Oerlikon S2 (SAW wire)	0,08	0,6	1,3	-	-	-	-	-

Table 3. The welding parameters

Sample Number	Current (A)	Voltage (V)	Welding Speed (cm/min)	Input Heat (kJ/mm)
S1	300	30-32	46	1,34
S2	350	30-32	46	1,53
S3	450	30-32	46	1,73

Table 4. Physical properties microalloyed steel.

Materials	α 10^{-6}	λ W/m °C	Ω nΩm	E kN/mm ²
Microalloyed Steel	11.5	44	140	226

During controlling of the weld seam, radiographic testing among the non-destructive methods was chosen and X-ray tube was chosen as the radiation source since the thickness was 6 mm. Figure 1 shows the principle [16-17]. TS 5127 and EN 1435 Testing standards were applied. According to these standards, the investigated area covers the weld and heat-affected zone (Figure 2).

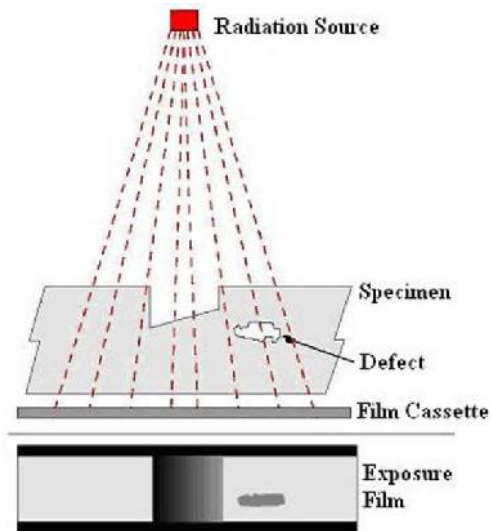


Figure 1. Principle of radiographic test

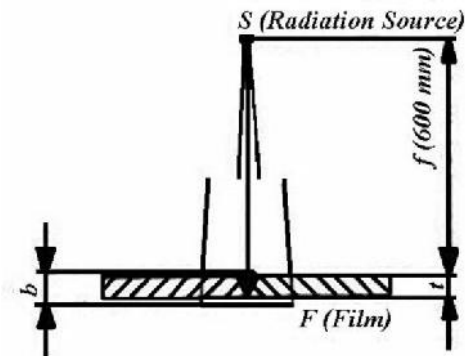


Figure 2. Test preparation for plane wall and one wall.

The X-ray tension chosen according to the thickness of the material was 130 kV (Figure 3) [18-20]. The X-ray device, Rigaku Radioflex-300EGS3 type, having the capacity of 300KV was used (Figure 4a-b). C4 type 100x240 mm Kodak film as well as front and back lead screens with the thickness of 0.125 mm were used. The weld seam applied to the 6-thick material was filmed by sending beam to pose diagram for 48 seconds.

The distance between the X-ray device and film was 600 mm. Figure 5 shows placement of the film.

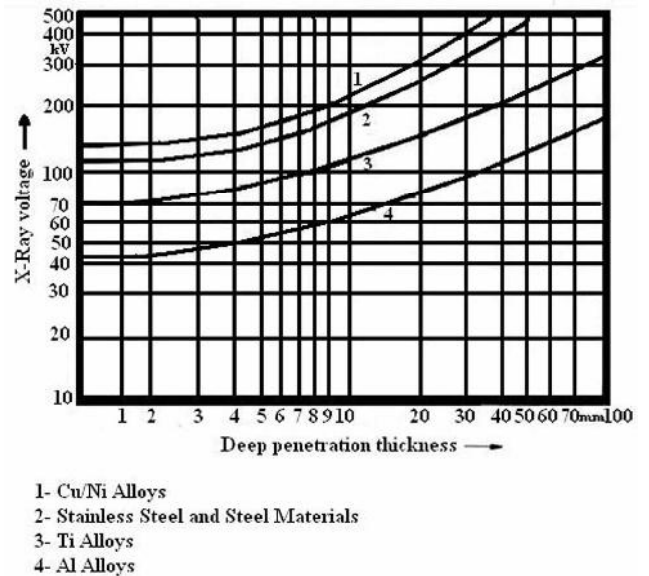


Figure 3. The deep penetration thickness and material as a function 500 kV up to radiography

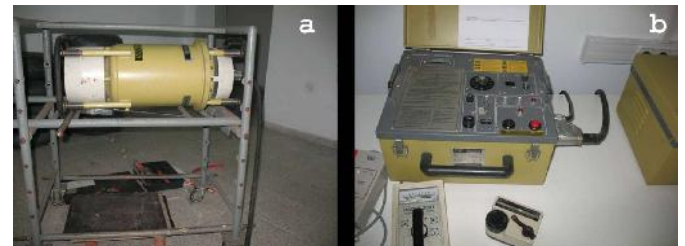


Figure 4. Rigaku mark Radioflex -300EGS3 type device (a) and control panel (b)



Figure 5. Film, penetrometer, stenciling pattern and setting the beam

3. RESULTS AND DISCUSSION

S690QL microalloyed steel was joined by using SAW process at 300, 350, 450 A welding current and 46 cm/min constant welding speeds. According to the International Institute of Welding, welding defects and the explanations of the radiographic images were defined as in Table 5 [18-20]. The image was assessed according to Table 5. It was determined that there was lack of penetration among the most common welding defects shown in Table 5 according to the definitions of welding defects and the radiographic images (D) (Sample No: 1 and 2). No defect was observed in the other sample.

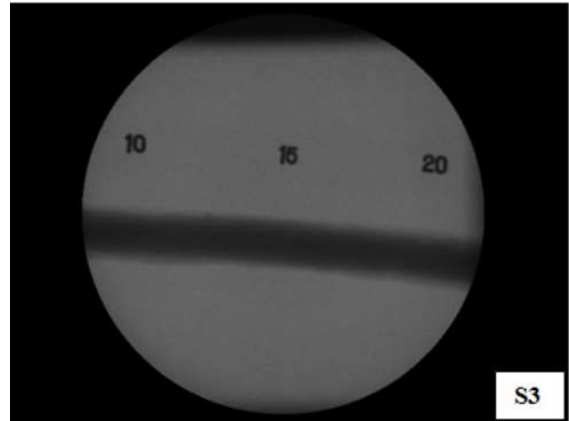
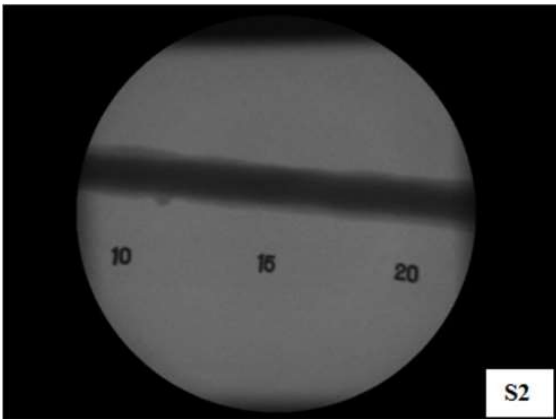
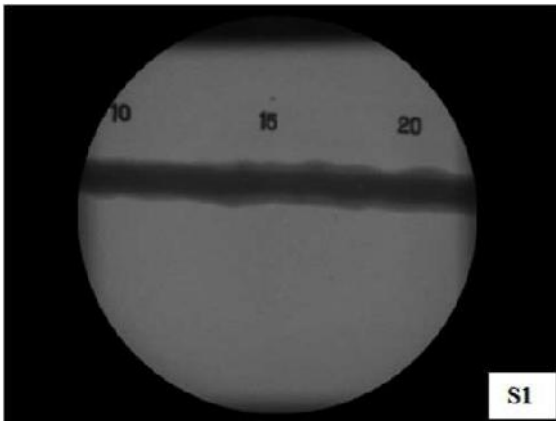


Figure 6. Radiographic-test-images-of-specimens

Figure 6 shows radiographic testing images of all the samples. The experimental results indicated that microalloyed steel could be joined by using the submerged arc welding technique in order to sufficient strength. The radiographic test results demonstrated that as the welding current increased, the amount of deep penetration increased in all samples (Figure 6). The best joining was observed in number S3. The joining decreased in the other samples.

Table 5. Definition of weld defects and radiographic image [18-19].

A: Gas gaps	Description	* Because the captured gas bubbles are formed. * Gas channels or long gaps
Aa: Porosity		
Ab: Gas bubbles	Radiographic Image	* Sharp black shadows around the circle. * Sharp black depending on the round or the long shadows
B: Slag	Description	* Slag or other foreign materials during the welding. * Captured within gaps slag or foreign matter.
Ba: Slag		
Bb: Slag errors	Radiographic Image	* Dark shadows or random shapes. * Continuous dark lines parallel to the seam edge welding.
C: Insufficient Welding	Description	Welding seam merger due to lack of two-dimensional error.
	Radiographic Image	Sharp-edged thin dark line.
D: Insufficient Deep Penetration	Description	The lack of sewing filled fully with the welding or root.
	Radiographic Image	The middle of the dark seam continuous or discrete line
E: Cracks	Description	Local tensile strength of metal exceeded.
Ea: Vertical Cracks		
Eb: Horizontal Cracks	Radiographic Image	Flat thin dark line.
F: Swelter Channel	Description	Welding material on the surface along the seam formed channel or groove.
	Radiographic Image	Welding are spread wide and dark line along the seam.

4. CONCLUSIONS

In this study, X-Ray radiographic test of microalloyed steel joined by using submerged arc welding was investigated. The following results were obtained;

- Submerged arc welding experiments were carried out according to Table 5. This study concluded that microalloyed steel could be joined by using the submerged arc welding technique. The best joining was observed in number S3. The joining decreased in the other samples.
- The microstructural changes took place in HAZs. An increase in the contraction of the samples was observed after increasing the welding current. The width of HAZ was mainly affected by welding current and heat input.
- It was determined that there was lack of penetration among the most common

welding defects shown in Table 5 according to the definitions of welding defects and the radiographic images (D) (Samples No: 1 and 2). No defect was observed in the other sample. The radiographic test results showed that as the welding current increased, the amount of deep penetration increased in all samples. The best properties were observed at the samples welded at 450 A welding current and 1.73 kJ/mm heat input. (Figure 6-S3).

5. REFERENCES

- [1] M. Taskin, U. Caligulu, M. Türkmen, "X-Ray Tests of AISI 430 and 304 Stainless Steels and AISI 1010 Low Carbon Steel Welded by CO₂ Laser Beam Welding," MP-Materials Testing-Materials and Components Technology and Application, 53, pp. 741-747, 2011.

- [2] H. Dikbas, U. Caligulu, M. Taskin, M. Türkmen, "X-Ray Radiography of Ti6Al4V Welded by Plasma Tungsten Arc (PTA) Welding," *Mp-Materials Testing-Materials and Components Technology and Application*, 2013, 03, 197-202, 2013.
- [3] Non-Destructive Testing for Plant Life Assessment IAEA, Vienna, IAEA-TCS-26 ISSN 1018-5518, 2005.
- [4] J. Holmstrom, "Quantitative radiography of welds - dose rate, dose and contrast of X-ray equipment and films," *NDT & E International*, 29 p. 182, 1996.
- [5] E.A. Gusev, V.G. Firstov, "Quality control of welded joints by high-current pulsed X-ray apparatus," *Soviet Journal of Nondestructive Testing*, 24, pp. 376-378, 1989.
- [6] R.R. Da Silva, L. P. Caloba, M.H.S. Siqueira, J.M.A. Rebello, "Patternrecognition of weld defects detected by radiographic test," *NDT&E International* , 37, pp. 461-470, 2004.
- [7] Y. Tekiz, "The Non-destructive Testings," *ITU Faculty of Mechanical Engineering, Istanbul*, 1984.
- [8] M. Albayrak, "The Control and Inspection of the Welding Seams," *IGDAS*, 1997.
- [9] T. Sarayanan, B.B. Lahiria, K. Arunmuthua, S. Bagayathiappana, A. S. Sekharb, V.P.M. Pillaib, J. Philipa, B.P.C. Raoa, T. Jayakumara, "Non-destructive Evaluation of Friction Stir Welded Joints by X-ray" *Radiography and Infrared Thermography*, 86 pp. 469-475, 2014.
- [10] S.I. Rokhlin, K. Cho, A.C. Guu, "Closed-loop process control of weld penetration using real-time radiography," *NDT International*, 23, p. 167, 1990.
- [11] TS EN ISO 5579 Standart, 2014.
- [12] K. Aoki; Y. Suga, "Intelligent image processing for abstraction and discrimination of defect image in radiographic film" In: *Proceedings of the Seventh International Offshore and Polar Engineering Conference, Honolulu, USA*, p. 527, 1997.
- [13] A. Kehoe; G. A. Parker, "Image processing for industrial radiographic inspection: image enhancement," *British Journal of NDT*, 32, pp. 183-190, 1990.
- [14] Y. Cherfa; Y. Kabir; R. Draï, "X-rays image segmentation for NDT of welding defects," In: *7th European Conference on Non Destructive Testing, Copenhagen*, pp. 2782, 1998.
- [15] C. R. Clayton; K. G. Martin, *Conf. Proceedings High Nitrogen Steels, The Institute of Metals, Lille*, pp. 256, 1989.
- [16] Ş. Ekinçi, "The Evaluation of the Welding Seam Errors with Digital Radiographic Methods," *The Atom Energy Foundation of Turkey, Istanbul*
- [17] R. Singh, "Radiography," *Applied Welding Engineering*, 3, pp. 253-274, 2012.
- [18] N. Ozakin; H. Baycık, "The Radiographic Inspection of the Welding Seam of the Body of Ship," *The 4th Iron-Steel Congress, Karabük*, pp. 289, 2007.
- [19] A. Topuz, "The Non-destructive Inspections," *YTU, Istanbul*, 1993.
- [20] U. Caligulu, M. Yalcınöz, M. Turkmen, S. Mercan, "X-Ray radiography of AISI 4340-2205 Steels Welded by friction welding," *Materials-Technology*, 39-45, 2016.

JOURNAL OF SCIENCE



SAKARYA UNIVERSITY

Sakarya University Journal of Science

ISSN 1301-4048 | e-ISSN 2147-835X | Period Bimonthly | Founded: 1997 | Publisher Sakarya University |
<http://www.saujs.sakarya.edu.tr/>

Title: Production and Characterization of Carbon-Kevlar-Aramid Reinforced Layer Composites with VARTM Method

Authors: Yahya Taşgın, Engin Şahin

Received: 2019-04-08 14:52:04

Accepted: 2019-05-02 13:51:55

Article Type: Research Article

Volume: 23

Issue: 5

Month: October

Year: 2019

Pages: 902-907

How to cite

Yahya Taşgın, Engin Şahin; (2019), Production and Characterization of Carbon-Kevlar-Aramid Reinforced Layer Composites with VARTM Method. Sakarya University Journal of Science, 23(5), 902-907, DOI: 10.16984/saufenbilder.550816

Access link

<http://www.saujs.sakarya.edu.tr/issue/44066/550816>

New submission to SAUJS

<http://dergipark.gov.tr/journal/1115/submission/start>

Production and Characterization of Carbon-Kevlar-Aramid Reinforced Layer Composites with VARTM Method

Yahya Tasgin¹, Engin Sahin

ABSTRACT

In this study, laminated composite materials are produced by Vacuum Assisted Resin Transfer Molding (VARTM) Method. Three different reinforcement materials (carbon, kevlar and aramid) are used in the production phase. Tensile test is applied to the samples after the production and in the light of SEM images; fractured surfaces of the samples and their results are evaluated.

It is obvious that the mechanical properties of carbon fiber reinforced samples yield better results.

Keywords: Kevlar, Carbon, Aramid Reinforcement, VARTM Method, Composite.

1. INTRODUCTION

Kevlar reinforcement material is widely used in composite production area thanks to its high impact resistance, high wear resistance and fatigue strength, high chemical resistance and hardness properties. In particular, it is used for carbon aramid reinforced fabric production extensively [1]. Composite materials are designed for high performance applications and their properties are designed according to specific purposes and desired functions [2]. Usage areas of composites are wide and expanding day by day [3]. Vacuum infusion method works with the principle of the progression of the resin in vacuumed media. In this method, are it is aimed to manufacture the product without touching it after production preparation is completed. It is important that the resin impregnated with the materials has an appropriate viscosity. Where narrow gap measurements and long flow paths are involved, the resin needs to be absorbed into its fibers to be strengthened as soon as possible. Generally epoxy, polyester and vinyl ester resins are used.

The infusion (transfer) method consists of four parts: vacuum pump, vacuum tank (resin collection tank), mold and resin bucket. The connections and shapes of these four parts may change, but the overall system is always the same [4].

Gu et al. have produced aramid fabric and epoxy resin composite sample by VARTM method. In order to increase the fiber content, pre-compression method is applied to the ram fabric stack before the epoxy resin is injected into the fiber fabric, and vacuum compression, hot compression with high pressure and temperature are used to compress the fiber bundle, and they have examined the compression reactions of the fabric stack under hot compression conditions. They have stated that hot compression increases the ramie fiber content and the mechanical properties of the composites [5].

Zhang et al. have produced one-way carbon fiber reinforced composite boards in three different processes using the fast curing epoxy resin by VARTM method. They have concluded that the preheating process is suitable for improving the

¹ Munzur Universty, Faculty of Engineering, Department of Machine Engineering, Tunceli, Turkey

processing efficiency in the VARTM method with good mechanical properties [6]. Durgun et al. have produced composite parts with carbon fiber and resin by using vacuum bagging and vacuum infusion method and applied tensile and bending tests to the samples produced by these two production methods. They get the highest results in the vacuum infusion method [7]. Wang et al. have designed a test device to examine the compression behavior and permeability of the preforms during VARTM. In order to examine the resin flow effects and thickness change of preforms, the device has carried out four tests and stated that if the number of layers increases, the permeability of the plane decreases and the preform thickness is influenced by the liquid viscosity and final filling time [8]. Durgun et al. have produced polymer based carbon and glass fiber reinforced composite materials by hand lay-up, vacuum bagging and vacuum infusion methods and compared the mechanical properties of these samples. They obtain the highest values in the vacuum infusion method [7].

Balikoglu et al. have performed a three-point bending test for sandwich composite boards with laminate plans of the hull body provided by Producer Company and produced in the laboratory by the VARTM method [9]. Sevkat et al. have investigated the tensile strength of needle-woven glass-fiber reinforced epoxy composites, fabricated samples using VARTM and hand lay-up methods and tested these samples under tensile load. They report that the samples produced using VARTM method have higher load than the samples produced by hand lay-up [10]. Engine hood is produced by the stagnant vacuum infusion method, the assembled parts are assembled to form the motor assembly and the piece is measured by optical scanning and geometric accuracy analysis is performed [11].

2. MATERIAL AND METHODS

2.1. Workbench production by vacuum infusion

In order to manufacture samples with vacuum assisted resin infusion molding method, a workbench different from the ones previously designed for this method was manufactured with a tempered surface glass and a heat sink dissipating homogenous heat at the bottom (Fig. 1.a,b). The workbench had the sizes of 1.500x1.500x1.00 m and the outer surface and chassis were made of MDF material. The top surface which was the composite production area was made of 10 mm thick tempered (thermos glass) glass resistant to 800°C. This glass surface is heated underneath in a homogeneous manner with a heat sink filled with marble dust and included 5 pieces of 3000 W rod heaters. The vacuum required for infusion was provided by a vacuum pump with a capacity of 130 l/min, vacuum level of maximum 2 Pa and 1/3 HP power. The thermostat sensor was placed at the midpoint of the heat sink at the bottom of the workbench and could control the homogeneously distributed temperature.

2.2 Experimental procedures

In the first stage of our study, we have produced a vacuum infusion machine which has many properties together and will provide our production of layered composites. In order to produce the sample with the vacuum-assisted resin infusion molding method, tempered surface glass, a heat pool radiating from the bottom and a different machine are designed different from the other machines previously designed for this method (Figure 1.a, b). Three different fibers (Kevlar, Carbon and Aramid) are used during production. The production of the composite is performed as shown in Fig. 1 c, d by using the fibers given in Fig. 2.b, c, d,

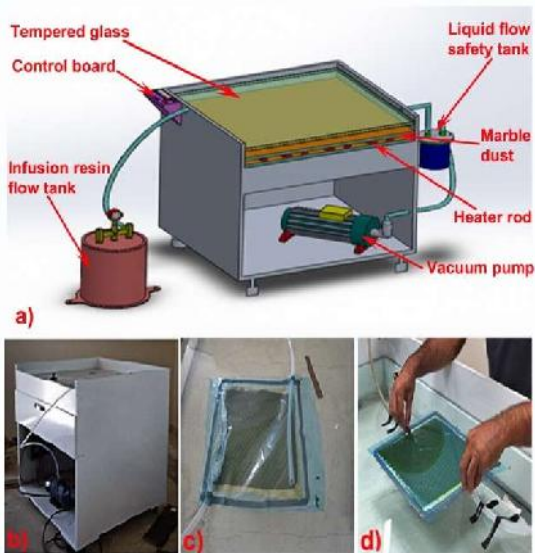


Figure 1. a) Vacuum infusion bench schematic view
b) photograph c-d) Production image.

2.3. Materials used in composite production

Three different fibers as Kevlar, Carbon and Aramid were used during production. Table 1 shows these fibers used. In addition, a total of $300+12+24+18=354$ ml mixture including 300 ml Hexion LR 285 epoxy resin, $300 \times 0.04 = 12$ ml Nutanox M-50 hardener, $300 \times 0.08 = 24$ ml pigment and $300 \times 0.06 = 18$ ml Akcobalt CX1-6 cobalt (accelerator) was used. The mixture which was initially heterogeneous was thoroughly homogenized by mixing for 2 minutes.

2.4. Composite production stages

The temperature for the manufacturing was adjusted by performing the cleaning control of manufacturing surface of the workbench, the control of heat sink, vacuum pump, thermostat, thermometer, cocks and valves; when the bench heated and reached to a constant heat value; it was adhered with double-sided adhesive tapes as shown in Fig. 1.c,d around an area at least 50 mm wider than the sizes wanted to be manufactured. In the area within the tape, three layers of mold release agent were applied with the aid of a non-dusting cloth which was not too soft. The fibers were then cut in the sizes of 310 x 310 mm (if a sheet of 300 x 300 mm size was desired to be manufactured, the fiber should be cut leaving 10 mm margin from the edges). The

fibers cut according to the desired design were laid in the vacuum area. Peel ply was laid on the fibers placed into the waxed (mold release) region (When the peel ply was being cut, it should be cut by leaving 20 mm margins from 3 edges (resin strip) and 60 mm from the other edge). Peel ply facilitated not only the flow of the resin as well as the separation of the produced material from the mold. After the peel ply was laid, a resin line was installed to make resin flow through the resin tank. A spiral hose and a normal transparent hose were used for resin line, the transparent hose was connected to the spiral hose from one end, and this spiral hose is coiled with holes and ensures the balanced progress of the infusion by forming the vacuum through the spiral.

Fig. 1.c shows its form covered with a vacuum-ready vacuum bag. The vacuum line was installed on the opposite side of the resin line. The vacuum indicator was connected to the vacuum infusion mechanism and the vacuum pump was opened. The ports providing resin pass were connected to the mechanism. The workbench was waited until it reached to the desired heating value and the heat setting was kept constant. The hoses were then connected to the ports and the resin flow was started and the process was continued until all the points of the mold were wet with the resin (Fig. 1.d). The last corner of the mold got wet. After all the points were wetted, all resin feed lines were closed with valves or clamps. During this infusion process, heating was continued until the infusion was completed at 50°C and the drying was completed (in our experiments, 2 hours) with the underfloor heating system. The part was then waited for about 2 hours at 50°C until fully hardened under vacuum. After waiting for two hours, the sealing tape was removed, the bag was first removed from the mold and the resin flow lines were cleaned. Then, the part was removed from the mold. It was visually checked if or not there were any air bubbles on the surface of the produced sample and the resin was homogeneously distributed, tensile sample for the tensile test was prepared by marking according to the fiber type used.

3. RESULTS AND DISCUSSION

Tensile stress and strain values of Kevlar, Aramid and Carbon Composite samples are given in Table 1. Tensile tests were carried out in accordance with the EN 100022 standard on the tensile testing device in the Engineering Faculty Laboratory in Munzur University. In both experiments applied to all samples, values are nearly similar. It is seen that the aramid tensile sample value is close to the Kevlar's. Breaking values of the samples depending on stress area are within the range of 65-85 MPa. According to the test results of the composite carbon tensile sample, breaking value is 270MPa in 2.00mm It is obvious that tensile strength of the carbon composite sample is higher than the Kevlar and Aramid samples.

Table 1. Tensile test results

Sample Code	Tensile Strength (MPa)	Elongation (%)
F:1-1 (Kevlar)	60,2464	2,31
F:1-2 (Kevlar)	86,3882	2,57
F:2-1 (Aramid)	67,9012	1,69
F:2-2 (Aramid)	78,5880	1,73
F:3-1 (Carbon)	256,895	2,45
F:3-2 (Carbon)	276,829	2,10

The reinforcing materials used in the sample are shown in Figure 2.

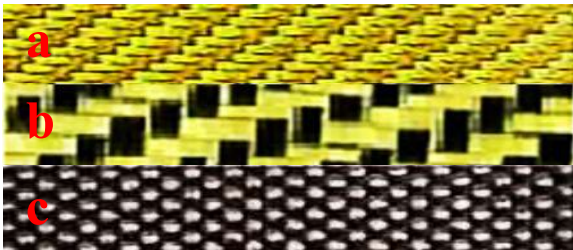


Figure 2. Fibers used in production a)Kevlar b)Aramid c)Carbon

In the SEM analyzes of composite Kevlar tensile sample in Fig 3 the images of resin and fiber structure are examined in detail in different magnifications. It is observed that micro and

macro gaps do not appear and full penetration is achieved in the absorption of the resin to the fiber structure by the infusion method. This is also advantageous in the production of complex shaped structures. Figure 3.a shows the composite Kevlar sample at 40x magnification. Kevlar fabric fibers, epoxy resin and emitter film is shown in the image. In the section mentioned, the boundary between the emitter film and the resin, and the low wall thickness of the sample (1.30 mm) show the estimated dissociation point during cutting for SEM analysis. Figure 3.b shows composite Kevlar sample at 80x magnification. The image (1) shows the horizontal Kevlar fibers, (2) and the vertical Kevlar fibers. In the regions indicated by (3), there are gaps resulting from the separation of the emitter film during the cutting of the sample. Figure 3.c shows composite Kevlar sample at 300x magnification. In the image, horizontal and vertical structure of the Kevlar fabric appears more clearly. Horizontal fibers indicated by (2) are highly void-free and detail (3) is frayed at 300x magnification when the horizontal fibers are cut for SEM images. Fraying is caused by the gap appearing during the separation of the emitter film in the cutting process, which can be eliminated by cutting with higher speed and harder cutting tools, but does not preclude detailed examination of the material. Figure 3.d shows composite Kevlar sample at 1000x magnification.

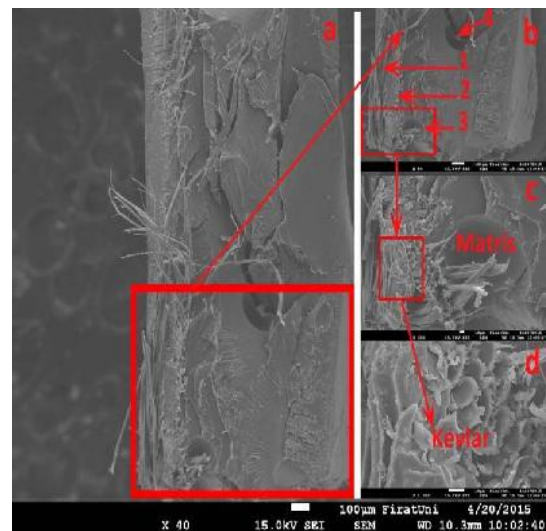


Figure 3. SEM analysis of composite kevlar tensile sample a)27x b)80x c)300x d)1000x

Figure 4.a shows composite Aramid sample at 30x magnification. Figure 4.b shows it at 100x magnification. Image shows the cracking region of Aramid fiber and epoxy resin that appears during cooling. In the sample production method, the appropriate heat value can be determined by examining the crack formation and by trying to increase and decrease the temperature of the machine. Figure 4.c shows the composite Aramid sample at 700x magnification. The image shows the penetration of Aramid fibers with resin. As the structure of Carbon and Kevlar fibers is examined, it is seen that the carbon is more frigid at the cutting points of the cylindrical Kevlar. Figure 4.d shows the composite Aramid sample at 3000x magnification. Carbon and Kevlar surface images show the superiority of hardness and strength properties of carbon.

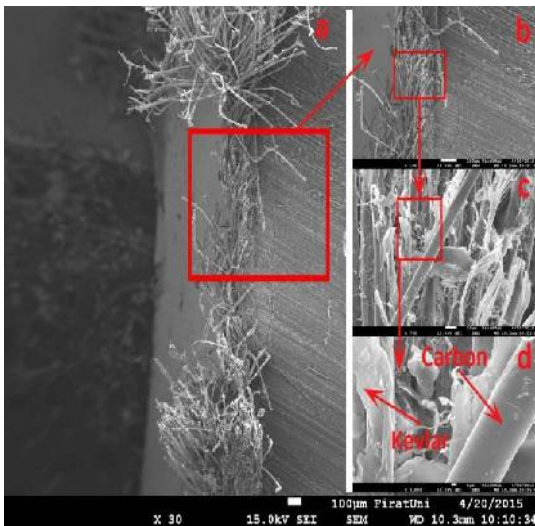


Figure 4. SEM analysis of composite Aramid tensile sample a)30x b)100x c)700x d)3000x

Figure 5.a shows composite Carbon sample at 200x magnification. The image shows the carbon fabric fibers and the epoxy resin. Figure 5.b shows composite Carbon sample at 500x magnification. The image shows horizontal and vertical structure of the carbon fabric fibers. Remarkably, carbon fibers tips are not frayed but they are fragile due to their small particle size. Figure 5.c shows composite Carbon sample at 2.500x magnification. The image shows the horizontal fibers and epoxy resin of the carbon fabric. Carbon fibers have circular cross-section

and no gap. They consist of a dense bundle of fibers and as the fibers are continuous; this structure gives high strength values in terms of tensile strength. Figure 5.d shows composite carbon sample at 10,000x magnification. This image allows very detailed examination of the carbon fabric horizontal fibers. The details of the cross-section and the inner structure of the fiber do not include any cracks or gaps.

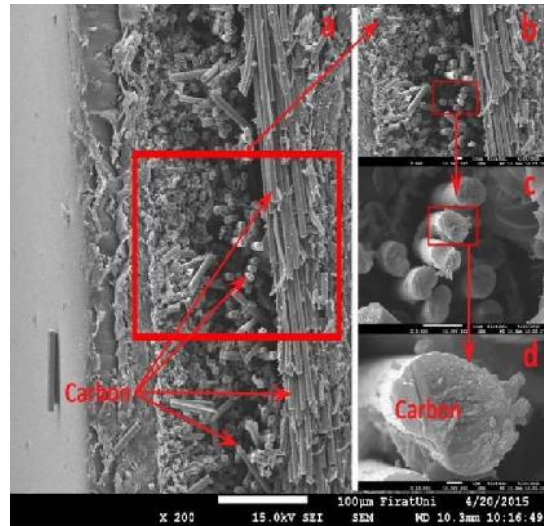


Figure 5. SEM analysis of composite carbon tensile sample a)200x b)900x c)2.500x d)10.000x

4. CONCLUSIONS

In this study, the effects of vacuum assisted resin transfer molding method on composite materials are investigated. The results of the production and improvement of the test set are listed below.

- Vacuum assisted resin infusion molding test set is successfully manufactured.
- Heating of the glass on the intermediate test set on the epoxy tin, used as a resin, by the lower resistances of the glass in order to proceed without forming fluid and air space on the Temper glass results very advantageously during the production phase of the material.
- The differences of the produced materials are compared with the tensile tests. The tensile samples with carbon fiber are more advantageous mechanically and the results are much higher in the samples having the

minimum wall thickness (0.5 mm) in evaluations according to the wall thickness.

ACKNOWLEDGEMENTS

The research was supported by the Munzur University Scientific Research Projects Unit (Project No: MFTUB 013-20)

REFERENCES

- [1] URL-2. 2017. “<http://www.kompozit.net/pinfo.asp?pid=287&diger=tumu>.” Retrieved April 25, 2017 (<http://www.kompozit.net/>).
- [2] Addington, Michelle and Daniel L. Schodek. 2005. Smart Materials and Technologies in Architecture. Retrieved April 25, 2017 (<https://bintian.files.wordpress.com/2013/01/smart-materials-new-technologies-for-the-architecture-design-professions.pdf>).
- [3] URL-1. 2017. “<http://www.bilgiustam.com/kompozit-Malzemeler-Hakkinda-Hersey/>.” Retrieved April 25, 2017 <http://www.bilgiustam.com/?s=kompozit+malzemeler>.
- [4] Ismail, Durgun, Vatansever Onur, Ertan Rukiye, and Yavuz Nurettin. 2014. “The Effect of Production Technique on Mechanical Properties of Polymer Based Fiber Reinforced Composite Materials. 7 th Automotive Technologies Congress.
- [5] Gu, Yizhuo, Xuelin Tan, Zhongjia Yang, Min li, and Zuoguang Zhang. 2014. “Hot Compaction and Mechanical Properties of Ramie Fabric/epoxy Composite Fabricated Using Vacuum Assisted Resin Infusion Molding.” *Materials and Design* 56:852–61. Retrieved (<http://dx.doi.org/10.1016/j.matdes.2013.11.077>).
- [6] Zhang, Kaomin, Yizhuo Gu, Min li, and Zuoguang Zhang. 2014. “Effect of Rapid Curing Process on the Properties of Carbon Fiber/epoxy Composite Fabricated Using Vacuum Assisted Resin Infusion Molding.” *Materials and Design* 54:624–31. Retrieved (<http://dx.doi.org/10.1016/j.matdes.2013.08.065>).
- [7] Ismail, Durgun, Vatansever Onur, Ertan Rukiye, and Yavuz Nurettin. 2013. “The Experimental Comparison of Composite Parts Manufacturing Methods Used in Automotive Sector sel, 2nd National Aegean Composite Materials Symposium.
- [8] Wang, Changchun, Guangquan Yue, Guanghui Bai, Lijian Pan, and Boming Zhang. 2016. “Compaction Behavior and Permeability Property Tests of Preforms in Vacuum-Assisted Resin Transfer Molding Using a Combined Device.” *Measurement: Journal of the International Measurement Confederation* 90:357–64. Retrieved (<http://dx.doi.org/10.1016/j.measurement.2016.04.058>).
- [9] Balikoglu, Fatih, Akin Atas, and Nurettin Arslan. 2012. “Application of Vacuum Infusion and Composite Production Method in Yacht and Boat Manufacturing.” pp. 480–95 in *3rd National Design Manufacturing and Analysis Congress*.
- [10] Sevkat, Ercan and Malek Brahimi. 2011. “The Bearing Strength of Pin Loaded Woven Composites Manufactured by Vacuum Assisted Resin Transfer Moulding and Hand Lay-up Techniques.” *Procedia Engineering* 10:153–58. Retrieved (<http://dx.doi.org/10.1016/j.proeng.2011.04.028>).
- [11] Ismail Durgun. 2013. “Production of Carbon Fiber Engine Hood with Vacuum Infusion Method in II. National Aegean Composite Materials Symposium.

JOURNAL OF SCIENCE



SAKARYA UNIVERSITY

Sakarya University Journal of Science

ISSN 1301-4048 | e-ISSN 2147-835X | Period Bimonthly | Founded: 1997 | Publisher Sakarya University |
<http://www.saujs.sakarya.edu.tr/>

Title: Determination of Fuel Type for Optimal Performance and Emission in a CI Engine Used Biodiesel and its Blends via Multi-Criteria Decision Making

Authors: Sinan Erdoğan, Mustafa Kemal Balki, Cenk Sayın

Received: 2019-02-21 13:14:00

Accepted: 2019-05-06 10:18:59

Article Type: Research Article

Volume: 23

Issue: 5

Month: October

Year: 2019

Pages: 908-915

How to cite

Sinan Erdoğan, Mustafa Kemal Balki, Cenk Sayın; (2019), Determination of Fuel Type for Optimal Performance and Emission in a CI Engine Used Biodiesel and its Blends via Multi-Criteria Decision Making. Sakarya University Journal of Science, 23(5), 908-915, DOI: 10.16984/saufenbilder.530247

Access link

<http://www.saujs.sakarya.edu.tr/issue/44066/530247>

New submission to SAUJS

<http://dergipark.gov.tr/journal/1115/submission/start>

Determination of Fuel Type for Optimal Performance and Emission in a CI Engine Used Biodiesel and its Blends via Multi-Criteria Decision Making

Sinan Erdođan^{*1}, Mustafa Kemal Balki², Cenk Sayın³

Abstract

In this study, fuel type which provides optimum performance and emission in compression ignition (CI) engine used alternative fuel was determined by COPRAS (Complex Proportional Assessment) in multi-criteria decision making (MCDM), and it was ranked from good to bad. Furthermore, the engine performance and emission consequences obtained from the use of fuels are discussed. In the experiments, pure biodiesel, diesel, and biodiesel/diesel blend fuels at a ratio of 5, 20 and 50% by volume were used as an alternative fuel. The performance and exhaust emission characteristics of the engine have been obtained in the tests performed at 7.2 kW power output and 1500 rpm of the constant engine speed. According to experimental results, with the uptrend of the biodiesel ratio in the blended fuel, it has been observed that while the specific fuel consumption (SFC) is enhanced to diesel, the thermal efficiency (η) is partially reduced. At the same time, the emissions of the nitrogen oxide (NO_x), carbon monoxide (CO) hydrocarbon (HC), and carbon monoxide (CO) decreased while the carbon dioxide (CO_2) emission enhanced. According to the COPRAS method, the ranking of fuels from best to worst was calculated as $B5 > B20 > B50 > B0 > B100$.

Keywords: Biodiesel, Optimum performance and emission, MCDM, COPRAS

1. INTRODUCTION

Nowadays, while the energy needs of the developed countries increase, the negative impacts on the environment in the production and use of this energy come into prominence. In our era, vehicles have a large usage area in industrial. World's primary energy demand is expected to increase by 0.9% per year by 2040 [1]. Researchers are developing alternative fuels to

meet the increasing energy needs of human beings and to less harm the environment. Biodiesel is derived from animal fats and vegetable oils as an alternative fuel, and it is used without any change in internal combustion engines. Biofuels obtained by chemical methods are environmentally friendly and renewable liquid fuel.

In the literature research, it was seen that the researchers made motor tests by using biodiesel fuels obtained from vegetable and animal fats.

* Corresponding Author: erdogan.sinan@gmail.com

¹ Ministry of Industry and Technology, KOSGEB, Marmara Directorate, Istanbul, Turkey. ORCID: 0000-0001-8844-0761

² Sinop University, Department of Mechanical Engineering, Sinop, Turkey. ORCID: 0000-0001-9396-5239

³ Marmara University, Department of Mechanical Engineering, Istanbul, Turkey. ORCID: 0000-0001-7286-472X

They evaluated the fuels used in respect of performance and exhaust emissions. When the performance and emission criteria are taken into account, the tested fuels give positive results in some of the evaluation criteria, and some of them have negative results. There is a very limited number of studies to determine the optimum fuel in terms of both performance and emission results, taking into account all evaluation criteria. This study aims to determine the optimum fuel by taking into account all the criteria and by introducing a holistic model.

Some of the experimental study results in the literature are as follows. Imtenan et al. [2] used six different test fuels from diesel and peanut biodiesel fuel mixtures in a 4-cylinder, turbocharged diesel engine. In the study, biodiesel tests showed an increment in SFC after 1500 rpm. When the emission results were examined, CO, CO₂, and HC emissions decreased, except for the amount of NO_x. The reason for the increment in NO_x was interpreted as the healing of combustion because of oxygen (O₂) in the biodiesel and the increase in temperature inside the cylinder. Labeckas and Slavinskas et al. [3] examined the emissions of direct injection and four-cylinder CI engine fueled on pure methyl ester of the rapeseed and its 5, 10, 20 and 35% blend with standard diesel. They stated that CO and HC emissions had reduced whereas NO_x emissions augmented for biodiesel according to diesel. Desantes et al. [4] tested the rapeseed oil biodiesel and diesel fuel mixture in a single cylinder CI engine. They reported that the smoke emissions, NO_x and CO remarkably decreased. In another study [5], it was stated that the SFC increased because of the low latent heat value of palm oil biodiesel. Jeong et al. [6] used methyl ester of the rapeseed and its mixture as a fuel in a CI engine. They expressed that because of the density and low thermal value of biodiesel, SFC increased according to diesel.

Some studies conducted with multi-criteria decision making (MCDM) methods in the energy sector are as follows. Nwokoagbara et al. [7] used AHP and TOPSIS methods from MCDM to determine the best micro algae type for biodiesel production. Durairaj et al. [8], fuzzy AHP and GRA-TOPSIS methods were used to select the

most suitable fuel for biodiesel fuels produced from mahua, cotton, flax, neem, jatropa, meusaferra and pongamia seeds. In another study, it has evaluated biodiesel origin vegetable and animal, and their mixtures with diesel by using MULTIMOORA method in respect of motor performance, combustion and emission characteristics [9]. Yazdani-Chamzini et al. [10] used the COPRAS method to choose the best renewable energy source from wind power, hydroelectric, solar-thermoelectric, biomass, and biofuel. Considering the studies in other areas, Chatterjee and Chakraborty operated the COPRAS method to select the best material [11].

In this study, the impacts of different fuels on the performance and emission characteristics of the engine were empirically investigated. In addition, the fuel type which provides the optimum result for these parameters is determined by COPRAS method. The different results of the experimental results are only possible if the operating and structural conditions of the engine change. In this study, no changes were made to the engine, only fuels with different physical and chemical properties were used.

2. MATERIAL AND METHODS

This section provides information about the equipment and materials used in the experimental study. The theory of the proposed multi-criteria decision-making method is also described.

2.1. Testing Procedure and Method

The tests were performed under constant engine load (7.2 kW). A load bank with resistance connected to the alternator consumes the generated electricity, and the diesel engine is loaded. The engine tests were carried out in a set of diesel generators given in Figure 1.

A technical specification for the alternator and the CI engine are presented in Table 1. A diesel engine with four cylinders, direct-injection, naturally aspirated and water-cooled continuously works at 1500 rpm of the constant speed.

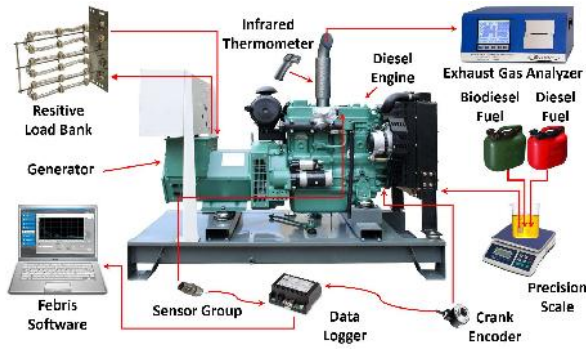


Figure 1. The test setup

Table 1. The specifications for the alternator and diesel engine

Diesel Engine	
Brand - Model	Fawde - 4DW81-23D
Maximum power output	18 kW
Engine speed	1500 rpm
Number of cylinders	4
Compression rate	17:1
Compression system	Direct injection
Number of injectors	4
Injector pressure	400 bar
Injection time	23 °CA bTDC
Cooling system	Water cooled
Cylinder diameter x stroke	85 x 100 mm
Total cylinder volume	2400 cm ³
Alternator	
Model	NWR 22
Standby power	17.5 kW
Phase - Frequency	3 PH - 50 Hz
Power factor	0.8

In order to determine exhaust gas emissions during the use of fuels, the Capelec CAP 3200 exhaust emission measurement device was utilized. In order to gauge the amount of fuel consumed per unit time, a digital scale with 6 kg capacity and 1 gram precision, and a digital stopwatch were used. Raytek Raynger ST4 infrared thermometer with 1 °C sensitivity was preferred to measure the exhaust manifold temperature.

2.2. The Methodology

In this study, COPRAS method has been used in MCDM methods. The criteria have consisted of the engine performance and emission indicators. The ranking degree of the alternatives has

determined by being evaluated these criteria. The elements used in this model are described below.

2.2.1. Test fuels

Biodiesel obtained from the mixture of safflower oil and canola was used in the experiments. The diesel fuel was mixed with 5, 20 and 50% by volume of pure biodiesel fuel and five different fuel with different properties was prepared. The mixtures are designated B5, B20, and B50. The diesel fuel is called B0, and the pure biodiesel is named as B100. The physical and chemical specifications of fuels were measured at TUBITAK Marmara Research Center and presented in Table 2.

Table 2. The physical and chemical properties of the fuels

Properties	Diesel (B0)	Biodiesel (B100)
Density (kg/m ³)	840	883.9
Kinematic viscosity (mm ² /s)	2.800	4.010
Calorific Value (kJ/kg)	43300	38600
Cetane number	52	52,6
Flash point (°C)	78	188
Iodine number (gI/100g)	~0	116
Water content (mg/kg)	~0	202

2.2.2. Evaluation Criteria

The criteria for the proposed model were determined as the specific fuel consumption (SFC), thermal efficiency (η), exhaust manifold temperature (EMT), NO_x, CO₂, CO, and HC.

The SFC is the proportion of the consumed fuel quantity per unit of time to the power output [12]. The SFC calculated with Eq. (1).

$$SFC = \frac{\text{Fuel Consumption}}{V \times I} \times 3600 \quad (1)$$

where I is electric current (A) and V is a voltage (V). The specific energy consumption (SEC) is an important parameter in comparison of fuels with different calorific values (CV). It is the quantity of energy consumed by an engine versus each unit of power output. It is calculated with Eq. (2) [13].

$$SEC = SFC \times CV \quad (2)$$

where calorific value (kJ/kg) and SFC (kg/kWh).

The thermal efficiency (η) is designated as the proportion of energy taken from the engine to the energy consumed and is calculated with Eq. (3).

$$\eta = \frac{3.6 \times 10^6}{SFC_{CV}} \quad (3)$$

The exhaust manifold temperature (EMT) is an important parameter because it is an indicator of the combustion temperatures of the fuels in the tests. The temperature of the exhaust manifold was measured by an infrared thermometer.

The NO_x emission is an evaluation criterion. The nitrogen atoms inside the air turn into NO_x, which is among the exhaust emissions under the high temperatures during the combustion [14]. The CO₂ emission occurs at the end of the chemical reaction within the cylinder in which carbon atoms transform to CO₂. If combustion does not materialize completely, they are discharged from the exhaust as CO. The HC emission represents the fuel that is partially oxidized or not oxidized due to the less of the O₂ in the intake air [15].

2.2.3. COPRAS Method

The COPRAS (Complex Proportional Assessment) method was improved by Zavadskas and Kaklauskas in 1996 [16]. It is a very convenient method for ordering and evaluating decision options considering the maximization and minimization of the criteria [17]. The process steps of the COPRAS method are described as follows [18].

The decision matrix consisting of data on alternatives and criteria is created as Eq. (4).

$$x_{ij} = \begin{bmatrix} x_{11} & x_{12} & \dots & x_{1n} \\ x_{21} & x_{22} & \dots & x_{2n} \\ \vdots & \vdots & \ddots & \vdots \\ x_{m1} & x_{m2} & \dots & x_{mn} \end{bmatrix} \quad (4)$$

where i is alternatives ($i = 1, 2, 3, \dots, m$), and j is criteria ($i = 1, 2, 3, \dots, n$).

By taking into account the weight of the criteria (q_j), the decision matrix is normalized by applying Eq. (5).

$$d_{ij} = \frac{x_{ij} q_j}{\sum_{i=1}^m x_{ij}} \quad (5)$$

The weighted normalized indexes are added by Eq. (6).

$$S_{+i} = \sum_{j=1}^n d_{+ij}; S_{-i} = \sum_{j=1}^n d_{-ij} \quad (6)$$

The relative importance of the alternatives is calculated by Eq. (7).

$$Q_i = S_{+i} + \frac{S_{-min} \sum_{i=1}^m S_{-i}}{S_{-i} \sum_{i=1}^m \frac{S_{-min}}{S_{-i}}} \quad (7)$$

Q_i is sorted in descending order. The higher Q_i is the greater relative importance. The benefit degree of alternatives is determined through Eq. (8).

$$N_i = \left(\frac{Q_i}{Q_{max}} \right) 100\% \quad (8)$$

The alternative with 100 degrees of benefit is the best option. The others are ranked in descending order.

3. RESULTS

3.1. Performance Results

The SFC and SEC were calculated according to the measurement results. That values of the biodiesel and their blends are given in Figure 2.

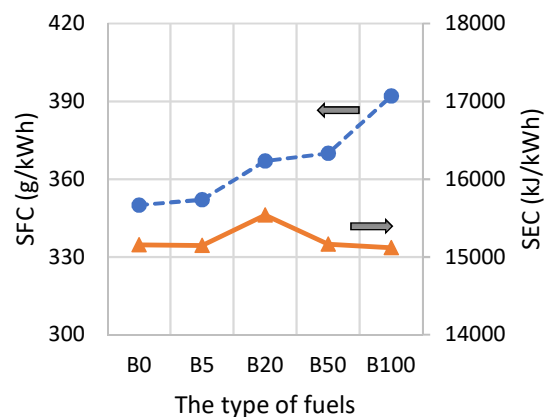


Figure 2. The variations of the SFC and SEC

The main reason for the high SFC of biodiesel and its blends compared to diesel is that the calorific value of biodiesel is lower than diesel. In order to

generate the same amount of energy as diesel, a larger amount of biodiesel fuel must be consumed massively. In addition, the quantity of fuel injected into the cylinder in biodiesel and its mixtures is higher than standard diesel, because the density of biodiesel fuel is higher than standard diesel fuel. SEC is a very important parameter used in the comparison of fuels produced from different raw materials. It is seen that the maximum SEC in the B20 fuel is realized.

Figure 3 shows the thermal efficiency of biodiesel and its blends.

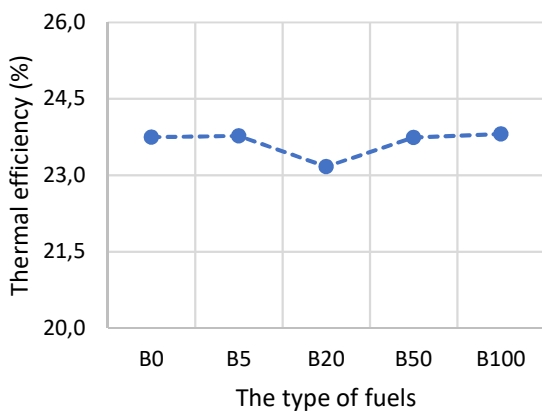


Figure 3. The variations of the thermal efficiency

When the graph is examined, the TE of all fuels is very close to each other. The thermal efficiency of the B20 fuel is slightly lower than the others. Inasmuch as the SEC of the B20 is more than others.

The exhaust manifold temperature (EMT) of biodiesel and their blends are given in Figure 4. The EMT is an important parameter because it is an indicator of the combustion temperatures of the fuels. The combustion within the cylinder improved through the addition of biodiesel to diesel fuel.

There was no regular reduction according to biodiesel rate because the C/H ratio of the fuel mixture and the oxygen content in it are differentiated. Therefore, combustion characteristics can be seen differently. Considering that the SEC of the B20 fuel is higher than the other biodiesel blends, it is normal to be high the EMT of the B20 fuel. It is thought that the temperature of the exhaust gases is increased

for B20 due to the extension of the combustion to the expansion period.

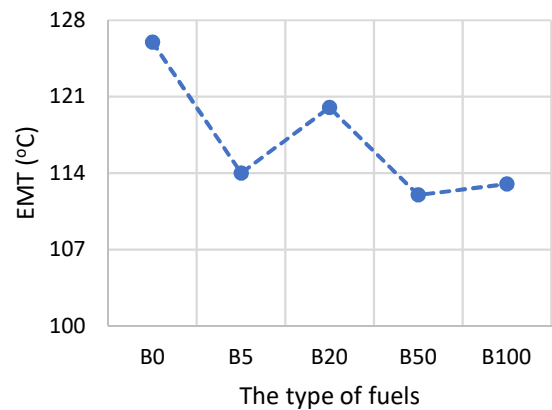


Figure 4. The variations of the EMT

3.2. Emission Results

The CO emission, which is one of the main parameters of exhaust emission, exists the combustion products when the air-fuel ratio is low. If the physical and chemical properties of the fuels, engine load, and spray characteristics change, the amount of CO formation changes. When there is enough O₂ in the burning chamber, the CO changes during combustion and turns into CO₂. The CO emissions and CO₂ emissions of biodiesel and their blends are given in Figure 5.

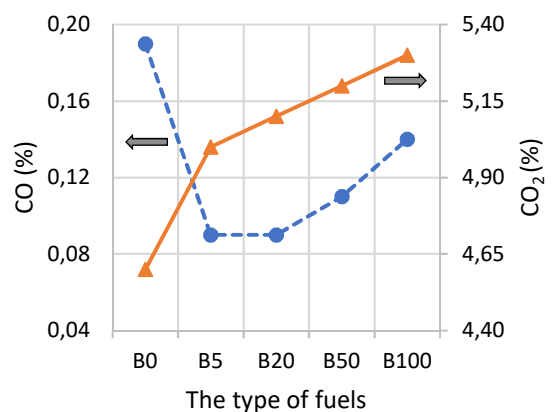


Figure 5. The variations of the CO and CO₂ emissions

The CO emission indicates the lost chemical energy that cannot be used in the engine. B5 and B20 fuels improve combustion and reduce CO emissions. It also increases CO₂ emissions. The positive effect of oxygen in biodiesel decreases

due to the increase in SFC and the decrease in the air-fuel ratio for B50 and B100 fuels.

Figure 6 shows the NO_x and HC emissions of biodiesel and its blends.

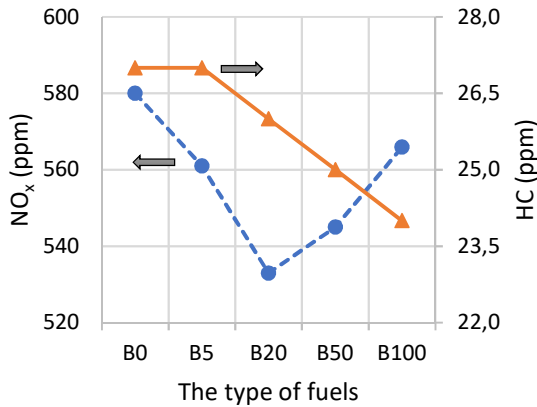


Figure 6. The variations of the HC and NO_x emissions

The main reason for the entity of HC emissions in combustion products is that the fuel starts to burn before the ignition temperature is reached or the oxygen in the environment is insufficient. When the biodiesel rate in the fuel mixtures increases, HC emissions are observed the decrease. The lowest HC emission was viewed in B100.

When the internal temperature within the cylinder rises, NO_x is generated by the reaction of nitrogen in the air with oxygen. Because of the use of biodiesel produced from different raw materials, it has been noticed that NO_x emissions exhibit very different behaviors in the literature research. The lowest NO_x emission was observed in B20 fuel. The TE of B20 fuel is low compared with other fuels. It is estimated that the in-cylinder temperature of the B20 fuel is lower than other fuels.

3.3. Computations of the COPRAS

According to the experimental results, the evaluation criteria for the selection of the fuel that gives the best performance and emission results are determined. These criteria are SFC, TE, EMT, NO_x, CO₂, CO, and HC. The maximization oriented criteria are TE and EMT, while the other criteria are the minimization oriented. The weights of the criteria were calculated using the simple scoring technique, a popular multi-criteria decision method. The most important value was 9 points and the lowest value was chosen as 1. The authors assigned a score of 1-9 to the criteria. Then each criterion was divided into total points and the weights of criteria were calculated as a percentage. The values assigned to the criteria are SFC: 8 points, TE: 9 points, EMT: 2 points, NO_x: 6 points, CO₂: 4 points, CO: 2 points, and HC: 2 points. Multi-criteria decision-making methods such as AHP, SWARA, and ENTROPI may be preferred to determine the weights of the criteria. The weights of the criteria (q_i) and the initial data of the alternatives are given in Table 3.

Table 3. The decision matrix

	SFC	TE	EMT	NO _x	CO ₂	CO	HC
B0	350	23.75	126	580	4.6	0.19	27
B5	352	23.77	114	561	5.0	0.09	27
B20	367	23.17	120	533	5.1	0.09	26
B50	370	23.74	112	545	5.2	0.11	25
B100	392	23.81	113	566	5.3	0.14	24
q_i	24%	27%	6%	19%	12%	6%	6%
	Min.	Max.	Max.	Min.	Min.	Min.	Min.

The decision matrix was normalized and weighted using Eq. (5). It is given in Table 4.

Table 4. The normalized and weighted matrix

	SFC	TE	EMT	NO _x	CO ₂	CO	HC
B0	0.0459	0.0542	0.0129	0.0396	0.0219	0.0184	0.0126
B5	0.0461	0.0543	0.0117	0.0383	0.0238	0.0087	0.0126
B20	0.0481	0.0529	0.0123	0.0364	0.0243	0.0087	0.0121
B50	0.0485	0.0542	0.0115	0.0372	0.0248	0.0106	0.0116
B100	0.0514	0.0544	0.0116	0.0386	0.0252	0.0135	0.0112

The relative importance (Q_i) of alternatives was calculated by Eq. (7). In addition, Eq. (8) was used to determine the benefit degree (N_i) of decision alternatives. S_{+i} , S_{-i} , Q_i , N_i , and the ranking of the fuels are given in the Table 5. According to this order, it is seen that B5 fuel is the first order and B100 fuel is the last order.

Table 5. The ranking of the fuels

	S_{+i}	S_{-i}	Q_i	N_i	Rank
B0	0.0672	0.1383	0.3925	94.9%	4
B5	0.0660	0.1295	0.4134	100.0%	1
B20	0.0652	0.1296	0.4125	99.8%	2
B50	0.0657	0.1327	0.4047	97.9%	3
B100	0.0660	0.1399	0.3875	93.7%	5

4. CONCLUSION

There are numerous studies on the use of biodiesel in the literature. However, few studies have been found in which the results of engine performance and emission tests are optimized with a holistic approach. The most difficult subject as an interpretation of the experimental results is the decision making according to many parameters. In this study, both the experimental results were interpreted separately, and the results were optimized by a multi-criteria decision-making method.

The tests were carried out in a diesel engine operating at 7.2 kW load and at a constant engine speed of 1500 rpm. The pure biodiesel fuel is mixed with 5%, 20% and 50% diesel fuel and named as B5, B20, and B50. The diesel fuel and pure biodiesel fuel are called B0 and B100 respectively. In the tests, SFC, SEC, EMT and TE of the fuels were determined. CO, CO₂, NO_x and HC emissions were also measured.

According to the performance parameters, it has been observed that fuel consumption increases as the biodiesel rate increases within blend fuel. The TE of fuels are close to each other, and EMT has also decreased. In the tests, CO, HC, and NO_x emissions were lower in the fuel mixes with biodiesel and CO₂ emissions increased compared to diesel fuel.

In the optimization study conducted with COPRAS, one of the multi-criteria decision-making methods, fuels are rated according to performance and emission characteristics. Consequently, the best performance emission results in this diesel engine were obtained in B5 fuel. According to the COPRAS optimization method, fuel ranking is B5>B20>B50>B0>B100.

5. REFERENCES

- [1] 2018 Outlook for energy: A view to 2040. Exxon Mobil Corporation, 2018.
- [2] S. Imtenan, H. Masjuki, M. Varman, I. R. Fattah, H. Sajjad, and M. Arbab, "Effect of n-butanol and diethyl ether as oxygenated additives on combustion–emission–performance characteristics of a multiple cylinder diesel engine fuelled with diesel–jatropha biodiesel blend," *Energy Conversion and Management*, vol. 94, pp. 84–94, 2015.
- [3] G. Labeckas and S. Slavinskas, "The effect of rapeseed oil methyl ester on direct injection Diesel engine performance and exhaust emissions," *Energy Conversion and Management*, vol. 47, no. 13-14, pp. 1954–1967, 2006.
- [4] N. Ladommatos, S. M. Adelhalim, H. Zhao, and Z. Hu, "The effects of carbon dioxide in exhaust gas recirculation on diesel engine emissions," *Proceedings of the Institution of Mechanical Engineers, Part D: Journal of Automobile Engineering*, vol. 212, no. 1, pp. 25–42, 1998.
- [5] Y.-C. Lin, W.-J. Lee, and H.-C. Hou, "PAH emissions and energy efficiency of palm-biodiesel blends fueled on diesel generator," *Atmospheric Environment*, vol. 40, no. 21, pp. 3930–3940, 2006.
- [6] M. Aldhaidhawi, R. Chiriac, and V. Badescu, "Ignition delay, combustion and emission characteristics of Diesel engine fueled with rapeseed biodiesel – A literature review," *Renewable and Sustainable*

- Energy Reviews, vol. 73, pp. 178–186, 2017.
- [7] E. Nwokoagbara, A. K. Olaleye, and M. Wang, “Biodiesel from microalgae: The use of multi-criteria decision analysis for strain selection,” *Fuel*, vol. 159, pp. 241–249, 2015.
- [8] S. Durairaj, “Multi - Criteria Decision Model For Biodiesel Selection In An Electrical Power Generator Based On Fapb-Gra-Topsis,” *International Journal of Research in Engineering and Technology*, vol. 03, no. 23, pp. 226–233, 2014.
- [9] S. Erdoğan, M. K. Balki, S. Aydın, and C. Sayin, “The best fuel selection with hybrid multiple-criteria decision making approaches in a CI engine fueled with their blends and pure biodiesels produced from different sources,” *Renewable Energy*, vol. 134, pp. 653–668, 2019.
- [10] A. Yazdani-Chamzini, M. M. Fouladgar, E. K. Zavadskas, and S. H. H. Moini, “Selecting the optimal renewable energy using multi criteria decision making,” *Journal of Business Economics and Management*, vol. 14, no. 5, pp. 957–978, 2013.
- [11] P. Chatterjee and S. Chakraborty, “Materials selection using COPRAS and COPRAS-G methods,” *International Journal of Materials and Structural Integrity*, vol. 6, no. 2/3/4, p. 111, 2012.
- [12] H. A. Rosa, W. T. Wazilewski, D. Secco, L. I. Chaves, G. Veloso, S. N. M. D. Souza, M. J. D. Silva, and R. F. Santos, “Biodiesel produced from crambe oil in Brazil—A study of performance and emissions in a diesel cycle engine generator,” *Renewable and Sustainable Energy Reviews*, vol. 38, pp. 651–655, 2014.
- [13] C. Sayin, M. Gumus, and M. Canakci, “Effect of fuel injection pressure on the injection, combustion and performance characteristics of a DI diesel engine fueled with canola oil methyl esters-diesel fuel blends,” *Biomass and Bioenergy*, vol. 46, pp. 435–446, 2012.
- [14] A. Ashraful, H. Masjuki, M. Kalam, I. R. Fattah, S. Imtenan, S. Shahir, and H. Mobarak, “Production and comparison of fuel properties, engine performance, and emission characteristics of biodiesel from various non-edible vegetable oils: A review,” *Energy Conversion and Management*, vol. 80, pp. 202–228, 2014.
- [15] S. Aydın and C. Sayin, “Impact of thermal barrier coating application on the combustion, performance and emissions of a diesel engine fueled with waste cooking oil biodiesel–diesel blends,” *Fuel*, vol. 136, pp. 334–340, 2014.
- [16] E. Zavadskas, A. Kaklauskas, and Z. Turskis, “Multicriteria decision-making system for building refurbishment,” *Statyba*, vol. 3, no. 12, pp. 62–68, 1997.
- [17] A. Kaklauskas, E. K. Zavadskas, and S. Raslanas, “Multivariant design and multiple criteria analysis of building refurbishments,” *Energy and Buildings*, vol. 37, no. 4, pp. 361–372, 2005.
- [18] D. Pamucar, D. Bozanic, and A. Randjelovic, “Multi-criteria decision making: An example of sensitivity analysis,” *Serbian Journal of Management*, vol. 12, no. 1, pp. 1–27, 2017.

JOURNAL OF SCIENCE



SAKARYA UNIVERSITY

Sakarya University Journal of Science

ISSN 1301-4048 | e-ISSN 2147-835X | Period Bimonthly | Founded: 1997 | Publisher Sakarya University |
<http://www.saujs.sakarya.edu.tr/>

Title: An Experimental Study on Extraction of Sugar From Carob Using With Taguchi Method

Authors: Ufuk Durmaz, Mehmet Berkant Ozel

Received: 2019-03-19 16:18:44

Accepted: 2019-05-07 13:35:45

Article Type: Research Article

Volume: 23

Issue: 5

Month: October

Year: 2019

Pages: 916-923

How to cite

Ufuk Durmaz, Mehmet Berkant Ozel; (2019), An Experimental Study on Extraction of Sugar From Carob Using With Taguchi Method. Sakarya University Journal of Science, 23(5), 916-923, DOI: 10.16984/saufenbilder.541940

Access link

<http://www.saujs.sakarya.edu.tr/issue/44066/541940>

New submission to SAUJS

<http://dergipark.gov.tr/journal/1115/submission/start>

An Experimental Study on Extraction of Sugar from Carob Using by Taguchi Method

Ufuk Durmaz^{*1}, Mehmet Berkant Özel²

Abstract

The carob, a perennial plant, is grown in regions where the Mediterranean climate is dominant. Because of its properties, it is preferred in many sectors especially in food and health sectors. Carob is mostly used as sugar and molasses. Moreover, seeds of carob are also used as thickening material in the food sector and its residue is utilized as animal feeding stuff as well. Molasses are mostly produced from carob, grape, mulberry, apple and pear for many years in Turkey. Molasses production is different from each other with regard to the structure of each fruit. Molasses are produced by pressing in the event of soft. The molasses of hard dried fruits such as carobs which cannot be pressed are obtained by extraction method using water. The parameters which are important for the quality of product such as extraction temperature and duration are not taken into account in the carob molasses obtained by traditional methods. Increasing the amount of water in extraction decreases production efficiency and quality while increasing energy consumption. In this study, the effects of parameters such as water quantity, extraction temperature, duration and batch number that affect quality of molasses were experimentally investigated by using Taguchi method.

Keywords: sugar extraction, mass transfer, batch system, taguchi method.

1. INTRODUCTION

The Latin name of *Ceratonia siliqua* L. is hard carob. The carob has been known for more than 5000 years. Before the production of white sugar, the carob was mostly used in the pastries and desserts. It is grown in regions where the Mediterranean climate dominates such as İzmir, Antalya, Cyprus and Mersin. There are long,

straight and curved types of carob. The carob has 10 to 30 cm longness, 1.5 to 3.5 cm wideness and about 1 cm thickness. Since the carob is consumed as dried, after harvesting, it is desiccated one to two months. The carob is usually consumed as carob molasses in the food industry. The core of carob is also used in ice cream production and in fruit concentrates since it increases its consistency. The carob gum is used in textile field in order to provide an equal

* Corresponding Author: udurmaz@sakarya.edu.tr

¹ Sakarya University, Mechanical Engineering Department, Sakarya, Turkey. ORCID: 0000-0001-5534-8117

² Sakarya University, Mechanical Engineering Department, Sakarya, Turkey.

permeability in cotton fabrics. It is a very effective fruit for allergic asthma. It has many properties such as antioxidant, anti-carcinogenic, antiseptic, and anti-allergic. Due to the chemical and pharmacological properties of carob, it has been known the beneficial and medical properties especially in the digestive system [1]. It is frequently preferred in industry because of its remarkable properties. For this reason, it is aimed to obtain sugar from the carob fruit without waste of energy and resources. There are many studies in the literature on HMF formation, extraction and liquid sugar production.

N. Basak Ozhan [2] examined the kinetics of non-enzymatic browning reactions of carob molasses during storage. She investigated the browning reaction of carob molasses for 4 different grades. As a result of storage in the research, no change was observed in water activity and brix values, whereas the acidity values decreased at 25°C, 35°C and 45°C. It is indicated that the reaction rates of HMF and browning reactions increase with the temperature. S. Khatib and J. Vaya [3] examined the effects of the carob on human health. The carob pulp has been determined that it is rich in soluble fibers and it has reduction ability of total and LDL cholesterol on the hypercholesterolemia patients. A. Mulet et al. [4] investigated the importance of grain size in the extraction of the carob. It was observed that the effect of time and temperature was higher in the use of small grain size in carob extraction. I. Turhan et al. [5] determined soluble quantitative of the total mass transfer coefficient and total phenolic components with carob extraction. The efficiency of the process temperature was determined using the Arrhenius equation. The activation energies were calculated as 5.84 and 0.072×10^{-3} kJ/mol for the diffusion of soluble mass and total phenolic components. Higher concentrations were obtained at higher temperatures. Although it has high temperature, it is stated that it does not cause HMF formation. F. Senay [6] studied the optimum extraction value and the clarification conditions for the production of liquid sugar from the carob. The effects of the amount of water, the extraction temperature, the particle size, the mixing and pressing on the efficiency were investigated. The titration acidity,

pH value, total dry matter and the amount of moisture were also examined. The highest efficiency was obtained at 90 °C, in the rate of 1:4 water, in the small particle size and at 3 hours. It was applied mixing and pressing in the extraction process. O. Demirtas [7] studied on the production of carob gamut from the carob beans and the physical and on chemical properties of these gums. For the production of carob gamut, it was kept in various solutions at 75 °C for an hour and was washed, then it was dried at 30 °C for a day and it was grained in a mill. In order to remove the shell of the carob kernel were used various compounds such as HCl, H₂SO₄ and NaOH. As a result of this, the moisture, protein, ash, insoluble matter in the acid and viscosity values of the carob gamut were compared. The highest viscosity was obtained from HCl, while the content of the insoluble material in the acid was highest in NaOH. The negative effects of these chemicals are also compared. M. Yalcin Yilmaz [8] tried to obtain clear sugar from the carob. The seeds of the carob were removed and carob pods were cut in different sizes. The clarification process was carried out at different water rates and temperatures. Kizelsoldan, bentonite, and gelatin were used in the clarification process. After the removal of color and turbidity, it was concentrated in vacuum evaporation and its rheological properties were determined.

U. Yurdagel and I. Teke [9] examined the roasting trials in different sizes, different temperatures and different times. The carob bean pieces of 3 to 6 mm size were found to be suitable for roasting. After roasting at 160 °C and for 30 minutes, the darkest carob powder was obtained according to Hunterlab measurements. I. Turhan [10] kept constant the carob amount and the solvent flow rate, then extraction of the carob was done depending on temperature. The experiments were carried out at 20 °C, 50 °C, 85 °C with continuous extraction. The increase of soluble dry matter, phenolic compound diffusion and 5-HMF formation were determined in extraction. The titration acidity, crude fiber content, pH value and total amount of nitrogenous substances were analyzed. B. K. Tiwari [11] investigated the ultrasonic extraction method which is used with

the aim of extraction and harmless to the earth. It was indicated that it increases the extraction efficiency and the aqueous extraction process without the use of solvents. For the carob fruit, the conditions of the ultrasound-assisted extraction method are stated as 40 kHz frequency, 45-297 W power, at 30 to 50 °C, 30 to 120 minutes. N. Tetik and E. Yuksel [12] studied on the optimization of extraction conditions of D-pinitol compound by using carob ultrasound and four independent variables. It was stated that these variables are temperature, ultrasonic power, dilution rate and time. As a result of the experiments, the highest D-pinitol concentration was obtained at 50 °C temperature, 207 W ultrasonic power, at 1: 4 dilution rate and at 120 min extraction time. It was stated that ultrasound assisted extraction can be used as an alternative to conventional hot water because of increasing the concentration of D-pinitol by ultrasonic action during extraction. B. A. Sarvin et al. [13] studied on the ultrasound-assisted extraction method for isolation of 17 sugars and sugar alcohols from conifers. The methanol concentration in the extraction solution, the extraction time, the type of plant sample and the extraction temperature was investigated as extraction parameters using Taguchi method. The optimum extraction conditions were obtained as 30% MeOH concentration, 30 minutes, plant sample type-II and 60 °C. The proposed optimum parameters can be used for profiling of sugars and sugar alcohols in a wide range of plant species. A. W. Go et al. [14] studied on Taguchi method to improve the production of sugar which is rich in hydrolysate from non-dilapidated spent coffee grounds. A sugar recovery of %81 to %98 of the available sugars was achieved using 4% v/v sulfuric acid at an SSR of 8 mL/g for a hydrolysis time of 3 to 4 hours at 95 °C. They suggest that their approach allows a potential energy savings as much as 48% according to conventional approaches. There are more studies about the extractions, Taguchi methods, and the heat and mass transfers in the literature [12], [15]–[18].

In this study, it is aimed to obtain maximum sugar from carob by using Taguchi method with optimum level of parameters which are water quantity, temperature, duration, and batch number. Three different levels are determined for

each parameters. At 30 °C, 35 °C, 40 °C, and at 100 (g), 200 (g), 250 (g) water, 30, 60, 90 minutes were studied on the time periods. Batch number is added as a parameter to determine the optimum and sufficient amount. The effects of parameters on the efficiency and the rate of S/N are shown in Fig. 3. At the end of the experiments, the optimum conditions which should be applied according to the efficiency of the sugar amount were determined.

2. MATERIALS AND METHODS

Taguchi method is used to minimize the number of experiments. Thus, the best test results can be obtained without having to do all the experiments. L9 orthogonal array and four parameters were used. Each parameter has three levels. The orthogonal array and the numerical value of each level are shown on Table 1.

Table 1. Controllable factors and their levels

Run	Water(g)	Temp.(°C)	Duration(min.)	Batch
T1	Level 1 100	Level 1 30	Level 1 30	Level 1 4
T2	Level 1 100	Level 2 35	Level 2 60	Level 2 5
T3	Level 1 100	Level 3 40	Level 3 90	Level 3 6
T4	Level 2 200	Level 1 30	Level 2 60	Level 3 6
T5	Level 2 200	Level 2 35	Level 3 90	Level 1 4
T6	Level 2 200	Level 3 40	Level 1 30	Level 2 5
T7	Level 3 250	Level 1 30	Level 3 90	Level 2 5
T8	Level 3 250	Level 2 35	Level 1 30	Level 3 6
T9	Level 3 250	Level 3 40	Level 2 60	Level 1 4

Four batch experiment scheme is shown in Fig. 1 for better understanding of batch system.

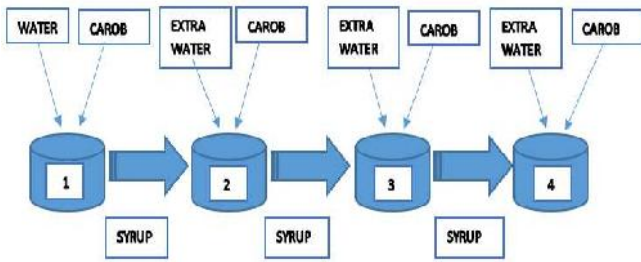
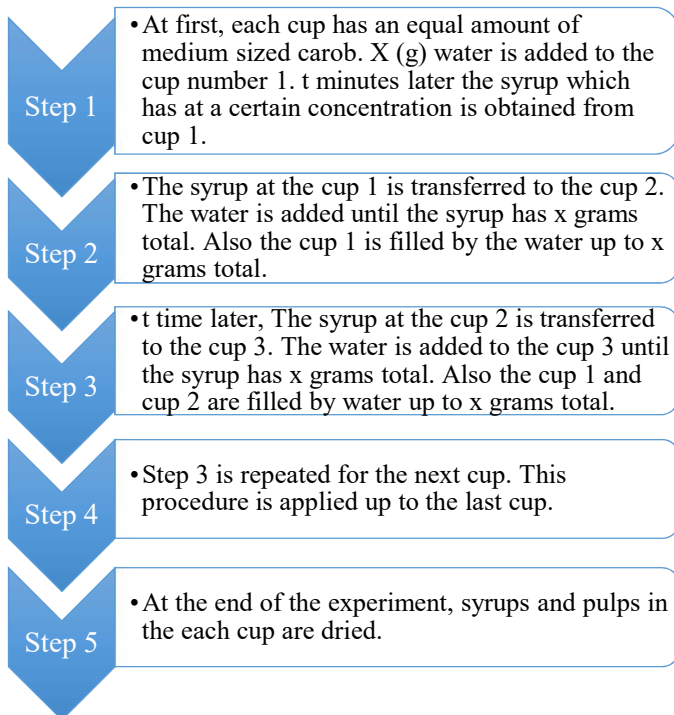


Figure 1. Four batch experiment scheme.

A step-by-step description of a four-batch experiment is shown below. Here, X (water quantity) and t (time) represent any level of the parameters.



During the experiments, thermos cups were held in the styrofoam box to the temperature. At the end of the runs, water of the syrup of each cup was evaporated by drying at 105 °C. The dried syrups for six batches are shown in Fig. 2.



Figure 2. The picture of medium sized carob and the dried syrups for six batches

Errors in temperature measurement: Error due to the structure of the glass thermometer: ±0.25 °C. Error in measuring the temperature of the test environment: ±0.25 °C. Error in temperature measurement in drying oven: ±0.5°C. Error in the mass measurement of the scales: ± 1 g.

According to these error values, uncertainty analysis can be obtained with the following equation [19].

$w_1, w_2, w_3, \dots, w_n$ are uncertainties.

The result R is function of the independent variables ($x_1, x_2, x_3, \dots, x_n$).

$$R = R(x_1, x_2, x_3, \dots, x_n)$$

$$W_R = \left[\left(\frac{\partial R}{\partial x_1} w_1 \right)^2 + \left(\frac{\partial R}{\partial x_2} w_2 \right)^2 + \dots + \left(\frac{\partial R}{\partial x_n} w_n \right)^2 \right]^{1/2} \tag{1}$$

It can be calculated with the equation presented by Kline and Mc. Clintock. Errors according to the total temperature measurement:

$$W_R = [(0.25)^2 + (0.25)^2 + 0.5^2]^{1/2} \tag{2}$$

The total error according to the temperature measurement: ± 0.612 °C

3. RESULTS AND DISCUSSION

As a result of the experiments, the total amount of sugar in each experiment was obtained as follows as in Table 2.

Table 2. The results of experiments

Run	1st Exp.	2nd Exp.	3rd Exp.
1	34	35	30
2	51	52	53
3	63	70	71
4	91	90	89
5	58	60	59
6	65	70	72
7	83	82	81
8	89	91	90
9	58	61	64

According to the Taguchi method, it is necessary to calculate the S / N ratio of each experiment to reach the results. There are 3 equations developed for the S / N ratio.

First equation is ‘Larger is better’.

$$S/N = -10 \times \log \left(\frac{1}{n} \sum_{i=1}^n \frac{1}{y_i^2} \right) \quad (3)$$

‘y_i’ is the yield of sugar extraction.

Second equation is ‘Smaller is better’.

$$S/N = -10 \times \log \left(\frac{\sum_{i=1}^n y_i^2}{n} \right) \quad (4)$$

Third equation is ‘Nominal is best’.

$$S/N = 10 \times \log \left(\frac{y^{-2}}{S^2} \right) \quad (5)$$

The S/N values of the results are calculated from Eq. 3. The calculated S/N ratios for each experiment is shown in Table 3.

Table 3. Yield of the experiments and S / N ratio

Run	1st Exp. (%)	2nd Exp. (%)	3rd Exp. (%)	S/N
1	25.00	25.73	22.05	27.64
2	30.00	30.58	31.17	29.70
3	30.88	34.31	34.80	30.42
4	44.60	44.11	43.62	32.89
5	42.64	44.11	43.38	32.74
6	38.23	41.17	42.35	32.14
7	48.82	48.23	47.64	33.66
8	43.62	44.60	44.11	32.89
9	42.64	44.85	47.05	33.01

Table 4 shows the effects of each parameter on the yield of extraction.

Table 4. Response Table for S/N

Level	Water	Temperature	Duration	Batch
1	29.25	31.40	30.89	31.13
2	32.59	31.78	31.87	31.84
3	33.19	31.86	32.28	32.07
Delta	3.93	0.46	1.39	0.93
Rank	1	4	2	3

According to Table 4, the parameters influenced the sugar extraction, respectively, are water quantity, duration, batch, temperature. If the first level of water quantity is increased to second level (200 g), S/N ratio increases from 29.25 to 32.59. S/N ratio is also achieved 33.19 on third level. In other words, it is clearly that the water quantity is the most effective parameter for the sugar extraction. If the S / N ratios put in equation 3, the effect of parameters on yield can be calculated. For the water quantity; the yield of extraction is determined about % 29 on the first level (100 g). The yields of extraction on the second and third levels, respectively are determined % 42.60 and % 45.65. The yield of extraction for the other parameters can be seen at the Table 5.

Table 5. The effects of the parameters as yield of extraction

Level	Water %	Temperature %	Duration %	Batch %
1	29	37.15	35.03	36.01
2	42.60	38.81	39.21	39.08
3	45.65	39.17	41.11	40.13

Analysis of variance is shown in Table 6.

Table 6. Analysis of variance

Source	DF	Adj SS	Adj MS	F-Value	P-Value
Regression	4	30.4980	7.6245	23.33	0.005
Water	1	25.9905	25.9905	79.52	0.001
Temperature	1	0.3183	0.3183	0.97	0.380
Duration	1	2.8789	2.8789	8.81	0.041
Batch	1	1.3102	1.3102	4.01	0.116
Error	4	1.3074	0.3268		
Total	8	31.8054			

Fig. 3 that shows the effect of the parameters on the extraction was obtained by using Minitab program. Here, the inclinations of each parameter in the graphs show the effect of the level differences of the parameters. According to the Fig. 3, the highest S/N ratio was obtained in the combination of 3.3.3.3 as an expected result because 'larger is better' function was chosen. However, since the inclinations for levels of the parameters in sugar extraction are more important, it is suggested that the optimal combination is 3.1.3.2. The combination of 3.1.3.2 is included in the experiments. Therefore, there is no need to clarification test.

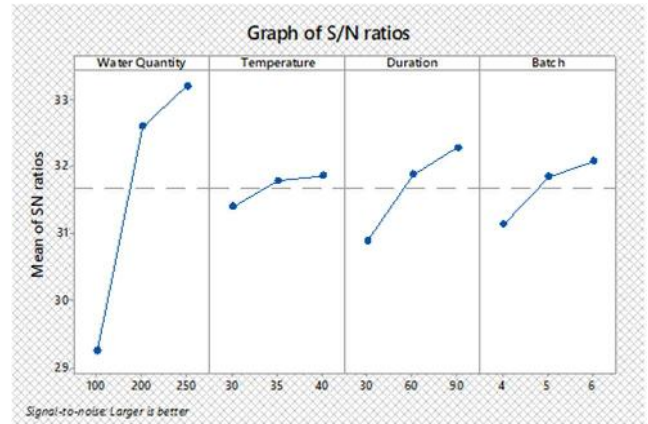


Figure 3. Graph of S/N ratios

The yield and the amount of obtained sugar can be calculated by the below equation which is depending on levels of parameters.

$$F = 3.26786 + 0.11236Water + 0.07200Temperature + 0.08880Duration + 1.51111Batch \quad (6)$$

Here, F is proposed equation. The yield of extraction can be calculated as a percentage by using this equation.

4. CONCLUSION

In this study, the sugar was recovered by extraction method from carob using Taguchi method. It is aimed to determine the optimum extraction conditions in order to consume less energy and resources. The yield of sugar is clearly depending on the extraction conditions. The effects of four parameters which are the water quantity, the temperature, the duration and the batch number were examined as the extraction conditions. It is proposed an equation depending on the parameters to obtain the yield of extraction. According to these results, it was found that the most effective parameter was the water quantity. The duration was found as an important parameter as the water quantity in the experiments. It is seen that the water quantity and duration were more effective than the other two parameters. The batch number was found to be more effective than the temperature. The effects of the temperature and the number of batch also increased the yield of extraction. However, the caramelization of sugar at high temperatures should be taken into consideration. Maximum efficiency of 49.67%

was obtained for the conditions of 250 (g) water, at 40 °C, 90 minutes, 6 batch. On the other hand, of 48.23% efficiency was obtained for the conditions of 250 (g) water, at 30 °C, 90 minutes, 5 batch. Since the difference is very small, the conditions that of 48.23% yield is achieved can be considered as the optimum condition.

5. REFERENCES

- [1] K. Rtibi, S. Selmi, D. Grami, M. Amri, B. Eto, J. El-benna, H. Sebai, and L. Marzouki, "Chemical constituents and pharmacological actions of carob pods and leaves (*Ceratonia siliqua* L.) on the gastrointestinal tract: A review," *Biomed. Pharmacother.*, vol. 93, pp. 522–528, 2017.
- [2] N. B. Ozhan, "Depolama Süresince Keçi boynuzu Pekmezinde Enzimatik Olmayan Esmerleşme Reaksiyonları Kinetiği," Ankara University, 2008.
- [3] S. Khatib and J. Vaya, "Fig, carob, pistachio, and health," *Bioactive Foods in Promoting, Health Fruits and Vegetables*, pp. 245-263, 2010.
- [4] A. Mulet, J. Fernández-Salguero, J. V. García-Pérez, and J. Bon, "Mechanistic modeling to address process analysis: Kibbles of carob (*Ceratonia siliqua*, L.) pod extraction," *J. Food Eng.*, vol. 176, pp. 71–76, 2016.
- [5] I. Turhan, N. Tetik, M. Aksu, M. Karhan, and M. Certel, "Liquid-solid extraction of soluble solids and total phenolic compounds of carob bean (*Ceratonia siliqua* L.)," *J. Food Process Eng.*, vol. 29, no. 5, pp. 498–507, 2006.
- [6] F. Senay, "Keçi boynuzundan sıvı şeker üretimi," Yıldız Technical University, 2009.
- [7] O. Demirtas, "Keçi boynuzu (*Ceratonia Siliqua*) çekirdeklerinden gam üretim yollarının araştırılması," Çukurova University, 2007.
- [8] M. Y. Yılmaz, "Keçi boynuzu Suyu Üretim Teknolojilerinin Geliştirilmesi," Yıldız Technical University, 2009.
- [9] U. Yurdagel and I. Teke, "A Research on Color Changes in Locust Bean during Roasting," 1985.
- [10] I. Turhan, "Sürekli Sistemde Keçi boynuzu Ekstraksiyonu Üzerine Araştırma," Akdeniz University, 2005.
- [11] B. K. Tiwari, "Ultrasound: A Clean, Green Extraction Technology for Bioactives and Contaminants," *Compr. Anal. Chem.*, vol. 76, pp. 111–129, 2017.
- [12] N. Tetik and E. Yuksel, "Ultrasound-assisted extraction of d-pinitol from carob pods using Response Surface Methodology," *Ultrason. Sonochem.*, vol. 21, no. 2, pp. 860–865, 2014.
- [13] B. A. Sarvin, A. P. Seregin, O. A. Shpigun, I. A. Rodin, and A. N. Stavriani, "A novel strategy for isolation and determination of sugars and sugar alcohols from conifers," *J. Chromatogr. B Anal. Technol. Biomed. Life Sci.*, vol. 1092, pp. 138–144, 2018.
- [14] A. W. Go, A. T. Conag, and M. M. N. Bertumen, "Taguchi method to improve the production of sugar-rich hydrolysate from non-delipidated spent coffee grounds, and subsequent recovery of lipids and bioactive compounds," *Biofuels*, vol. 7269, pp. 1–13, 2017.
- [15] R. Ravanfar, A. M. Tamadon, and M. Niakousari, "Optimization of ultrasound assisted extraction of anthocyanins from red cabbage using Taguchi design method," *J. Food Sci. Technol.*, vol. 52, no. 12, pp. 8140–8147, 2015.
- [16] S. Ghasemian, K. Rezaei, R. Abedini, H. Poorazarang, and F. Ghaziani, "Investigation of different parameters on acrylamide production in the fried beef burger using

Taguchi experimental design,” *J. Food Sci. Technol.*, vol. 51, no. 3, pp. 440–448, 2014.

- [17] N. Ozsoy, M. Ozsoy, and A. Mimaroglu, “Taguchi Approach to Tribological Behaviour of Chopped Carbon Fiber-Reinforced Epoxy Composite Materials,” *Acta Phys. Pol. A*, vol. 132, no. 3–II, pp. 846–848, 2017.
- [18] N. Taoualit, F. Z. Azzazi, N. E. Benkadi, and D. E. Hadj-Boussaad, “Extraction and transport of humic acid using supported liquid-membrane containing trioctyl phosphine oxide (TOPO) as the carrier,” *Acta Phys. Pol. A*, vol. 130, no. 1, pp. 115–121, 2016.
- [19] J. P. Holman, “Experimental methods for engineers,” vol. 9, no. 2. 1994.

JOURNAL OF SCIENCE



SAKARYA UNIVERSITY

Sakarya University Journal of Science

ISSN 1301-4048 | e-ISSN 2147-835X | Period Bimonthly | Founded: 1997 | Publisher Sakarya University |
<http://www.saujs.sakarya.edu.tr/>

Title: Effect of Wet Soil on Thermal Performance of Air-Fluid Ground Heat Exchanger For Heating

Authors: Ufuk Durmaz, Orhan Yalçinkaya, Ozlem Bablak Ergun, Mustafa Ozdemir

Received: 2019-03-19 14:02:18

Accepted: 2019-05-07 16:58:30

Article Type: Research Article

Volume: 23

Issue: 5

Month: October

Year: 2019

Pages: 924-928

How to cite

Ufuk Durmaz, Orhan Yalçinkaya, Ozlem Bablak Ergun, Mustafa Ozdemir; (2019), Effect of Wet Soil on Thermal Performance of Air-Fluid Ground Heat Exchanger For Heating. Sakarya University Journal of Science, 23(5), 924-928, DOI:

10.16984/saufenbilder.541815

Access link

<http://www.saujs.sakarya.edu.tr/issue/44066/541815>

New submission to SAUJS

<http://dergipark.gov.tr/journal/1115/submission/start>



Effect of Wet Soil on Thermal Performance of Air-Fluid Ground Heat Exchanger for Heating

Ufuk Durmaz^{*1}, Orhan Yalçınkaya², Mustafa Özdemir³, Özlem Bablak Ergun⁴

Abstract

The energy crises that emerged after the economic problems in the world increased the interest in alternative energy resources. The effects of global warming, which has a serious threat, will be reduced by the more efficient use of these energy resources. In this study, the thermal effects of wet soil were investigated experimentally using a ground source heat exchanger (GHE), which is an alternative energy resource, in an area on the Esentepe campus of Sakarya University. Researches on this subject are mostly directed to dry soil applications. In this study, the thermal performance of GHE was examined in terms of heat transfer. By means of the artificial pool formed under the ground, it is aimed to increase in heat transfer between the soil and the process fluid. In the experiments which are conducted, air is used as the process fluid. The system has a significant advantage in certain temperature ranges due to the passive heating method, in other words, the process fluid can be circulated under the soil without using a compressor. The purpose of this method is to reduce the cost of heating in the winter season. The temperature difference at GHE inlet and outlet is approximately 9.07 °C in the experiments. The heat transfer rate has been increased by 46.28% compared to dry soil application for the same air velocity speed.

Keywords: Ground-Based Heating, Earth-Air Heat Exchanger, Wet Soil.

1. INTRODUCTION

Nowadays, if the average annual price rise of energy resources such as electricity, LPG and diesel is taken into consideration, it will be seen that the renewable energy resources need to be expanded more. In addition, these systems

produce less CO₂ emission than alternative systems. Fluctuations in ambient temperatures do not cause a significant temperature change in the lower layer of the soil. The GHE system, which is installed at a certain depth of the ground, benefits from relatively constant soil temperature. The soil layer temperature is warmer than the air

* Corresponding Author: udurmaz@sakarya.edu.tr

¹ Sakarya University, Mechanical Engineering Department, Sakarya, Turkey. ORCID: 0000-0001-5534-8117

² Sakarya University, Mechanical Engineering Department, Sakarya, Turkey. ORCID: 0000-0003-2380-1727

³ Sakarya University, Mechanical Engineering Department, Sakarya, Turkey.

⁴ Sakarya University, Mechanical Engineering Department, Sakarya, Turkey.

temperature in winter seasons and cooler in summer seasons. This temperature difference can be utilized for cooling purposes in summer months and for heating purposes in winter months. The deepness of soil between 2 m to 3 m is suitable for most applications.

In the literature, there are a great number of studies about GHE systems. Hepbasli, A. et al. [1] examined the coefficient of performance (COP) of U-shaped ground heat exchanger in a 50 m deep soil well in heating process. They also determined the parameters affecting the yield of the ground based heat pump. M. Inalli and H. Esen [2] determined the COP values respectively 2.66 and 2.81 for the deepness of 1 and 2 m by utilizing a horizontal ground based heat pump in April and November. G. Mihalakakou et al. [3] developed a numerical model which is related to the heat and mass transfer to determine the thermal performance of a heat exchanger. Their numerical model is validated with many experimental results. In their study, some parameters such as pipe diameter and fluid velocity were investigated. They also have developed an algorithm to calculate the cooling potential. Y. Song et al. [4] examined the thermal properties of the soil and enhanced a horizontal ground heat exchanger. They investigated the effect of pipe thermal conductivity and the soil type on the system. They used polyethylene pipe as the buried pipe material because of its high density instead of polyvinyl chloride (PVC). The heat transfer rate increases by 100,8% when the thermal conductivity of the soil is increased to 2,5 W/mK. J. Xi et al. [5] investigated the GHE systems in the eastern China area. The variation of the underground thermal area and heat transfer analysis ensure remarkable experimental results. Desideri et al. [6] evaluated the installation costs of the facility in order to match the conventional cooling-heating system and the ground-based heat pump system (GHE). H. Esen et al. [7] examined the economic feasibility of two different systems for cooling and heating processes of a test room and compared the costs of the ground-based heat pump (GCHP) and the air-based heat pump (ACHP) systems using the annual value method. According to the economic analysis as a result of their studies, while the cost of installation of the

ACHP system was more economical and feasible than the GCHP system, the operating expense of the GCHP system was appropriate than the ACHP system. Y. Al-Ameen et al. [8] investigated numerically and experimentally the applicability of recycling some relatively inexpensive industrial materials as probable backfills in horizontal ground heat exchangers. Metal fillers have increased the performance of HGHE by 77%. I. Bulut et al. [9] examined the earth-air heat exchanger (EAHE) consisting of galvanized pipes in winter season in Şanlıurfa. Their investigation is related to the dry soil application. The air outlet temperature, soil temperature, and air velocity measurements were conducted in December and February. The maximum temperature difference at the outlet and inlet of the system is determined as 11.6 °C. They found that the efficiency of the heating process was higher compared to the cooling applications.

The soil is an important characteristic element for GHE since the heat transfer is directly affected by the soil thermal conductivity. One of the best methods for increasing the soil thermal conductivity is to moisturize. The most important point that separates the existing system from other investigations is to examine the influence of wet soil on heat transfer. Durmaz and Ozdemir [10] investigated the GHE system which has an artificial pond where the process fluid is water for cooling applications. In this study, air is determined as the process fluid. The purpose of this study is to heat a test room where is at Sakarya University by using a passive method in January. The outlet and inlet temperatures of the ground heat exchanger were measured by means of a thermocouple and the influence of the artificial pond on heat transfer was investigated experimentally.

2. MATERIALS AND METHODS

The air-fluid is circulated in the GHE system, which has 80 m² area, 0.5 m height, and 2.5 m depth. The thermal influence of wet soil to heat transfer rate is examined in the energy laboratory of Sakarya University. It is aimed to increase the heat transfer between the soil and the process fluid by means of the artificial pond that is set up under

the ground. In order for providing maximum heat transfer, GHE pipes are placed at intervals of 0.3 m [11] and a fan with 20 W, 1800 rpm is used to circulate air flow. In the experiments, inlet and outlet temperatures of 100 mm diameter pipes are measured at 2-minutes intervals by using K type thermocouple.



Figure 1. Artificial pond and underground pipe setup [10]

Figure 1 shows some pictures of the pipe system and artificial pond which are set up to examine the effect of heat transfer [10].

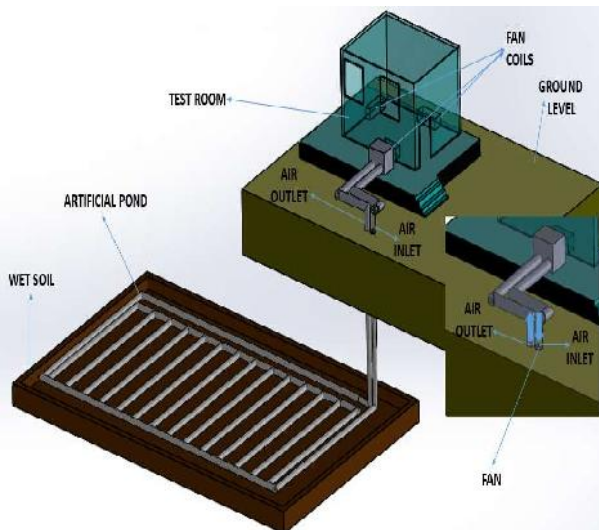


Figure 2. Overview of the GHE system and test room [12]

Figure 2 shows the solid model of the GHE system and the test room. There are three fan coils in the test room. GHE's inlet is the cold air of the environment to be heated. There is relatively hot air at the GHE's outlet. The cold ambient air in the

test room is sent to the pipes of the GHE system with the help of a fan and relatively hot air under the ground is used for heating.

Uncertainty analysis for the measurements and the calculations have been determined according to the J. P. Holman [13].

$$\frac{T_{max}-T_{min}}{T_{average}} = \frac{9.75-9.55}{9.65} = 0.0207 \quad (1)$$

In temperature measurements, the error rate of the thermocouple is taken into consideration ± 0.1 °C. The maximum temperature measurement has been determined as 9.75 °C, the minimum is 9.55 °C and, the average is 9.65 °C in this study. The ratio of percentage change is calculated as 2.07%. As the pipe diameter remains constant, the mass flow rate is constant and local losses are negligible. Therefore, the error rate is not calculated.

3. RESULTS AND DISCUSSION

The soil can be used as a heat sink in summer and a heat source in winter since the soil is not affected by the temperature variations throughout the year. The heat transfer between the air in the pipes of the system and the test room is calculated with the following equation.

$$\dot{Q} = \dot{m} \cdot c_p \cdot \Delta T \quad (2)$$

Considering the first equation, the heat transfer is extremely dependent on temperature difference and mass flow rate. One of the most important factors affecting the temperature difference from these parameters is the moisture content of the soil. There are dry and moist soil applications for GHEs in the literature. The experimental investigation was carried out in the summer months for the dry soil application in Şanlıurfa province and the average GHE inlet and outlet temperature difference were determined as 6.2 °C [9]. In this study, the temperature graphs obtained from the wet soil applications are shown in Figure 3 and Figure 4.

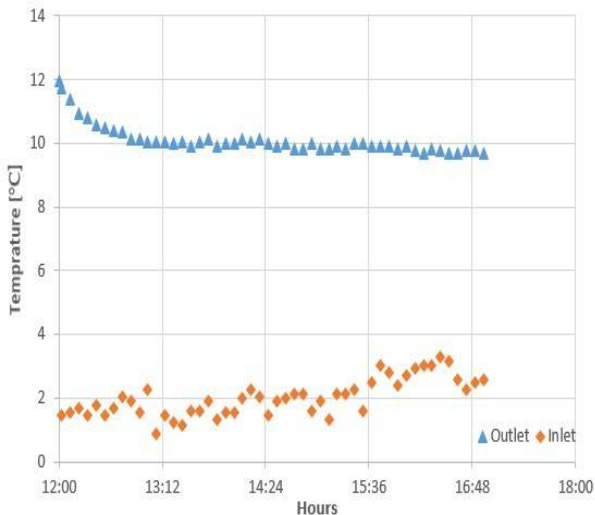


Figure 3. GHE inlet and outlet temperature variation for the first half of January

Figure 3 shows the GHE inlet and outlet temperature measurements. The experimental data in the graph is the average of the measurements in the first half of January. Considering the Figure 3, GHE outlet temperature remains constant at 11 °C on these days. From this experimental data, it is concluded that the soil acts as a heat source and the GHE inlet temperature increased initially from an average of 1 °C to a maximum of 3.5 °C. The average temperature difference during the test time is approximately 9.07 °C. However, if the air circulated under the soil is sent directly to the test room, the room temperature will increase from 1 °C to 11 °C in a short time. This time depends directly on the mass flow rate.

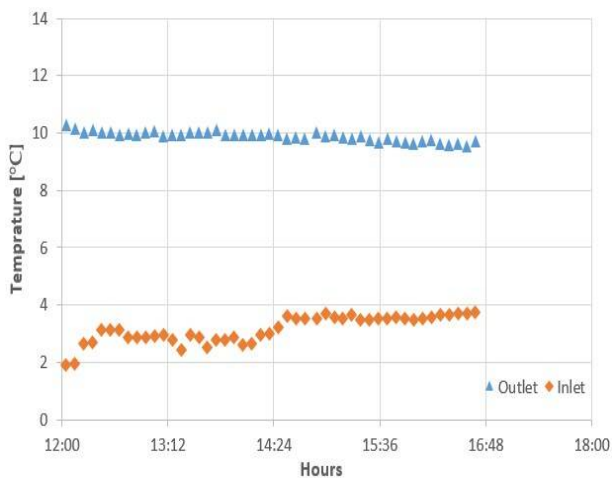


Figure 4. GHE inlet and outlet temperature variation for the second half of January

The temperature measurements at the GHE inlet and outlet in Figure 4 are the data for the average of measurements in the second half of January. Considering the graph, there is a similar characteristic to Figure 3. The soil temperature, in other words, GHE outlet temperature is measured as 10 °C. The GHE inlet temperature is initially 2 °C. This value shows a linear increase of approximately 4°C in four hours. In this case, the temperature difference decreases slightly in the second half of January. The reason for this decrease is due to the increase in the ambient air.

4. CONCLUSION

The annual average soil temperature and soil structure should be examined before the GHE application. Soils with high thermal conductivity and density are more suitable for the GHE systems. It is known that heat transfer increases when the moisture content of the soil improves. Considering the investigation in Sakarya, it is observed that the costs spent on heating processes can be reduced by using a wet ground-source heat exchanger in winter months. It is obvious that this system is more efficient in regions with colder climates. When the annual average soil temperature and soil structure consider before the GHE applications, the yield of the system will increase. In this study, GHE inlet and outlet temperature difference are determined as 9.07 °C. With the wet soil application, the average temperature difference for air fluid increased by 46.28% compared to dry soil in the GHEs. It is expected that energy efficiency will increase by using wet ground heat exchanger systems with other alternative systems. As the air under the ground will be sent directly to the test room, it is also recommended to apply a filtration process such as HEPA filter, taking into account the effect of the subsoil microorganisms on human health.

Acknowledgments

The research is funded by Sakarya University Scientific Research Projects Coordination. under the grant number: 2015-01-06-002.

5. REFERENCES

- [1] A. Hepbasli, "Experimental study of a closed loop vertical ground source heat pump system," *Energy Conversion and Management*, vol. 44, pp. 527–548, 2003.
- [2] M. Inalli and H. Esen, "Experimental thermal performance evaluation of a horizontal ground-source heat pump system," *Appl. Therm. Eng.*, vol. 24, no. 14–15, pp. 2219–2232, 2004.
- [3] G. Mihalakakou, M. Santamouris, D. Asimakopoulos, and I. Tselepidaki, "Parametric prediction of the buried pipes cooling potential for passive cooling applications," *Sol. Energy*, vol. 55, no. 3, pp. 163–173, 1995.
- [4] Y. Song, Y. Yao, and W. Na, "Impacts of soil and pipe thermal conductivity on performance of horizontal pipe in a ground-source heat pump," *Proc. Sixth Int. Conf. Enhanc. Build. Oper.*, no. 2, pp. 2–7, 2006.
- [5] J. Xi, Y. Li, M. Liu, and R.Z. Wang, "Study on the thermal effect of the ground heat exchanger of GSHP in the eastern China area," *Energy*, vol. 141, pp. 56–65. <https://doi.org/10.1016/j.energy.2017.09.060>
- [6] U. Desideri, N. Sorbi, L. Arcioni, and D. Leonardi, "Feasibility study and numerical simulation of a ground source heat pump plant, applied to a residential building," *Appl. Therm. Eng.*, vol. 31, no. 16, pp. 3500–3511, 2011.
- [7] H. Esen, M. Inalli, and M. Esen, "A techno-economic comparison of ground-coupled and air-coupled heat pump system for space cooling," *Build. Environ.*, vol. 42, no. 5, pp. 1955–1965, 2007.
- [8] Y. Al-Ameen, A. Ianakiev, and R. Evans, "Recycling construction and industrial landfill waste material for backfill in horizontal ground heat exchanger systems," *Energy*, vol. 151, pp. 556–568, 2018.
- [9] I. Bulut, H. Demirtas, Y. Karadag, and R. Hilali, "Experimental analysis of an earth tube ventilation system under hot and dry climatic conditions," *8th Mediterr. Congr. Heat. Vent. Air-Conditioning-Climamed*, no. October, 2015.
- [10] U. Durmaz and M. Ozdemir, "An experimental study on the soil-based natural cooling," *Int. J. Environ. Sci. Technol.*, 2018.
- [11] Y. Nam and H. B. Chae, "Numerical simulation for the optimum design of ground source heat pump system using building foundation as horizontal heat exchanger," *Energy*, vol. 73, pp. 933–942, 2014.
- [12] U. Durmaz and O. Yalcinkaya, "Experimental investigation on the ground heat exchanger with air fluid," *Int. J. Environ. Sci. Technol.*, pp. 1–6, 2019.
- [13] J.P. Holman, "Experimental methods for engineers," 7th ed. Hill, McGraw, 2001.

JOURNAL OF SCIENCE



SAKARYA UNIVERSITY

Sakarya University Journal of Science

ISSN 1301-4048 | e-ISSN 2147-835X | Period Bimonthly | Founded: 1997 | Publisher Sakarya University |
<http://www.saujs.sakarya.edu.tr/>

Title: Some Notes on Odd or Even Indexed Fibonacci And Lucas Sequences

Authors: Alparslan Kargin, Emre Kiş, Halim Özdemir

Received: 2019-03-06 18:12:32

Accepted: 2019-05-11 17:49:56

Article Type: Research Article

Volume: 23

Issue: 5

Month: October

Year: 2019

Pages: 929-933

How to cite

Alparslan Kargin, Emre Kiş, Halim Özdemir; (2019), Some Notes on Odd or Even Indexed Fibonacci And Lucas Sequences. Sakarya University Journal of Science, 23(5), 929-933, DOI: 10.16984/saufenbilder.536642

Access link

<http://www.saujs.sakarya.edu.tr/issue/44066/536642>

New submission to SAUJS

<http://dergipark.gov.tr/journal/1115/submission/start>

Some Notes on Odd or Even Indexed Fibonacci and Lucas Sequences

Alparslan Kargin¹, Emre Kişî*¹ and Halim Özdemir¹

Abstract

The uniqueness of the sum of the elements of finite subsets of the odd or even indexed Fibonacci and Lucas sequences are proved. Moreover, it is shown that the odd or even indexed Fibonacci and Lucas sequences are super-increasing sequences. By using the uniqueness properties established, a new cryptology method is presented and exemplified.

Keywords: Fibonacci numbers, Lucas numbers, odd index, even index, cryptology

1. INTRODUCTION

Fibonacci and Lucas sequences have been appearing not only in pure mathematics but also in many applied sciences such as cryptography and coding theory [6-11]. The odd indexed Fibonacci and Lucas sequences are the sequences which consist of odd indexed terms of the Fibonacci and Lucas sequences. Similarly, we can define even indexed Fibonacci and Lucas sequences. In this work, the odd and even indexed Fibonacci and Lucas sequences are mainly considered. The results related to the uniqueness of the sum of the elements of the finite subsets of the odd and even indexed Fibonacci and Lucas sequences are established. By utilizing the results obtained a new cryptology method is developed, and it is illustrated with an example. Moreover, it is shown that the odd or even indexed Fibonacci and Lucas sequences are super-increasing

sequences. The super-increasing sequences are known to be used in the Merkle-Hellman cryptology system [1].

2. PRELIMINARIES

Definition 2.1. Let $F_0 = 0$ and $F_1 = 1$. The sequence $\{F_n\} (n = 1, 2, 3, \dots)$ with the recurrence relation $F_{n+1} = F_n + F_{n-1}$ is called *Fibonacci sequence* [2,3]. The elements of this sequence are called *Fibonacci numbers*.

From now on, the sets of Fibonacci numbers, the even indexed Fibonacci numbers, i.e. $\{F_0, F_2, F_4, \dots, F_{2k}, \dots\}$, and the odd indexed Fibonacci numbers, i.e. $\{F_1, F_3, F_5, \dots, F_{2k+1}, \dots\}$, will be denoted by F , F_E , and F_O , respectively.

* Corresponding Author

¹ Sakarya University, Department of Mathematics, 54100, Sakarya, Turkey akargin@gmail.com, ekisi@sakarya.edu.tr. ORCID: 0000-0001-7763-8932, hozdemir@sakarya.edu.tr. ORCID: 0000-0003-4624-437X

Definition 2.2. Let $L_0=1$ and $L_1=3$. The sequence $\{L_n\}(n=1,2,3,\dots)$ with the recurrence relation $L_{n+1}=L_n+L_{n-1}$ is called *Lucas sequence* [2,3]. The elements of this sequence are called *Lucas numbers*.

Hereafter, the sets of Lucas numbers, the even indexed Lucas numbers, and the odd indexed Lucas numbers will be denoted by L, L_E , and L_O , respectively.

Definition 2.3. Let (b_n) a sequence such that $b_n \in \mathbb{N}$ for every $n \in \mathbb{N}$. (b_n) is said to be a super-increasing sequence if it satisfies the property that $b_n > \sum_{j=1}^{n-1} b_j$ for each $n \geq 2$ [5].

Lemma 2.4. For each $n \in \mathbb{N}$, $\sum_{i=1}^n F_{2i-1} = F_{2n}$ [2].

Lemma 2.5. For each $n \in \mathbb{N}$, $\sum_{i=1}^n F_{2i} = F_{2n+1} - 1$ [2].

3. RESULTS

In this section, the uniqueness of the sum of the elements of finite subsets of the odd or even indexed Fibonacci and Lucas sequences are proved. Moreover, it is shown that the odd and even indexed Fibonacci and Lucas sequences are super-increasing sequences. Since the proofs are similar, the proof will be given only for odd indexed Fibonacci sequence.

Theorem 3.1.

- a) Let A and B be any two finite subsets of F_O such that $A \neq B$. Then $\sum_{F_i \in A} F_i \neq \sum_{F_j \in B} F_j$.

- b) Let A and B be any two finite subsets of L_O such that $A \neq B$. Then $\sum_{L_i \in A} L_i \neq \sum_{L_j \in B} L_j$.

Proof: Since the elements in the intersection of the sets A and B can be eliminated from both sides of the sum, without loss of generality it is assumed that $A \cap B = \emptyset$. Let k be a positive integer such that $F_{2k+1} = \max\{F_i \mid F_i \in A \cup B\}$. Then, either $F_{2k+1} \in A$ or $F_{2k+1} \in B$. If $F_{2k+1} \in A$, then $B \subset \{F_1, F_3, \dots, F_{2k-1}\}$. Hence, we get the following inequality

$$\sum_{F_i \in B} F_i \leq \sum_{i=1}^k F_{2i-1}. \tag{1}$$

From the inequality (1) and Lemma 2.4, we get

$$\sum_{F_i \in B} F_i \leq \sum_{i=1}^k F_{2i-1} = F_{2k} < F_{2k+1} < \sum_{F_j \in A} F_j. \tag{2}$$

It is seen from the inequality (2) that $\sum_{F_i \in B} F_i \neq \sum_{F_j \in A} F_j$.

Hence, the proof is completed. ■

Theorem 3.2.

- a) Let A be a subset of F_O such that $A = \{a_i \in F_O \mid a_1 < a_2 < \dots < a_n, n \in \mathbb{N}\}$. Then, A is a super-increasing sequence.
- b) Let A be a subset of L_O such that $A = \{a_i \in L_O \mid a_1 < a_2 < \dots < a_n, n \in \mathbb{N}\}$. Then, A is a super-increasing sequence.

Proof: Let $F_{2k+1} \in A$ and $F_i \in A$ such that $i < 2k+1$, where k is a positive integer and i is an odd positive integer. Then, we get the inequality

$$\sum_{F_i \in A} F_i \leq \sum_{j=1}^k F_{2j-1}. \tag{3}$$

From the inequality (3) and Lemma 2.4, we obtain

$$\sum_{F_i \in A} F_i \leq \sum_{j=1}^k F_{2j-1} = F_{2k} < F_{2k+1}.$$

Hence, the proof is completed. ■

Corollary 3.3. Since $F_O \subset F_O$ and $L_O \subset L_O$, both F_O and L_O themselves are also super-increasing sequences.

Since the proofs of the Theorems 3.4 and 3.5 given in the following are quite similar with the proofs of the Theorems 3.1 and 3.2, respectively, they will be omitted.

Theorem 3.4.

- a) Let A and B be any two finite subsets of F_E such that $A \neq B$. Then $\sum_{F_i \in A} F_i \neq \sum_{F_j \in B} F_j$.
- b) Let A and B be any two finite subsets of L_E such that $A \neq B$. Then $\sum_{L_i \in A} L_i \neq \sum_{L_j \in B} L_j$.

Theorem 3.5.

- a) Let A be a subset of F_E such that $A = \{a_i \in F_E \mid a_1 < a_2 < \dots < a_n, n \in \mathbb{N}\}$. Then A is a super-increasing sequence.
- b) Let A be a sorted subset of L_E such that $A = \{a_i \in L_E \mid a_1 < a_2 < \dots < a_n, n \in \mathbb{N}\}$. Then A is a super-increasing sequence.

Corollary 3.6. Since $F_E \subset F_E$ and $L_E \subset L_E$, both F_E and L_E themselves are also super-increasing sequences.

4. APPLICATION

Fibonacci and Lucas sequences have been used in many applied sciences such as cryptography and coding theory [6-11]. In this section a new cryptology method, which is based on the uniqueness property of the sum of the elements of the subsets of the odd indexed Fibonacci sequences, is developed, and it is illustrated with an example. The method is presented for odd indexed Fibonacci sequence. Obviously, with a similar manner, it can be also developed for even indexed Fibonacci and odd and even indexed Lucas sequences.

Now we can explain the method. Firstly, each letter is matched with the numerical value of the odd indexed Fibonacci numbers. This match is listed in Table 1. Obviously, this table can be extended according to characters that are wanted to be used.

Table 1: Numerical correspondence of the letters

Letters	Corresponding Fibonacci Numbers	Numerical value
A	F_1	1
B	F_3	2
C	F_5	5
D	F_7	13
E	F_9	34
F	F_{11}	89
G	F_{13}	233
H	F_{15}	610
I	F_{17}	1.597
J	F_{19}	4.181
K	F_{21}	10.946
L	F_{23}	28.657
M	F_{25}	75.025
N	F_{27}	196.418
O	F_{29}	514.229
P	F_{31}	1.346.269
Q	F_{33}	3.524.578
R	F_{35}	9.227.465
S	F_{37}	24.157.817
T	F_{39}	63.245.986
U	F_{41}	165.580.141
V	F_{43}	433.494.437
W	F_{45}	1.134.903.170
X	F_{47}	2.971.215.073
Y	F_{49}	7.778.742.049
Z	F_{51}	20.365.011.074

Encryption Algorithm

Step 1: Determine the different letters in the plaintext.

Step 2: Sort them alphabetically and enumerate them.

Step 3: Sum the numerical values of the corresponding Fibonacci numbers of the letters.

Step 4: Set a sorting code by utilizing the corresponding enumeration of the letters.

Step 5: Set an ordered pair in which the first component is the sum and the second component is the sorting code. This ordered pair is the ciphertext.

Deciphering Algorithm

Step 1: Find the biggest Fibonacci number which is smaller than the sum (the first component of the ordered pair) and subtract it from the sum. Repeat this step until reaching zero.

Step 2: Determine the corresponding letters of the Fibonacci numbers used in step 1.

Step 3: Sort these letters alphabetically and enumerate them.

Step 4: Set the plaintext by utilizing the sorting code (the second component of the ordered pair)

Example 4.1: Let us encrypt the word “HELLO”.

Encryption Algorithm:

Step 1: The different letters in the word are H, E, L, O.

Step 2: The enumeration of the alphabetically ordered letters is listed in Table 2.

Table 2: The enumeration of the alphabetically ordered letters

E	H	L	O
1	2	3	4

Step 3: The sum of the corresponding Fibonacci numbers of the letters is $34 + 610 + 28657 + 514229 = 543530$.

Step 4: The sorting code of the word is 21334.

Step 5: The ciphertext is (543530, 21334).

Deciphering Algorithm:

Step 1: The biggest Fibonacci number which is smaller than 543530 is 514229. The difference of these numbers is $543530 - 514229 = 29301$. By continuing the process similarly, the numbers in the following are obtained: $29301 - 28657 = 644$, $644 - 610 = 34$, and $34 - 34 = 0$.

Step 2: The corresponding letters of the Fibonacci numbers used in previous step are O, L, H, and E, respectively.

Step 3: The alphabetic order of the letters which are determined in step 2 and the corresponding enumeration of them are as in Table 2.

Step 4: By utilizing the sorting code 21334 the plaintext “HELLO” is obtained.

REFERENCES

- [1] Merkle–Hellman knapsack cryptosystem, https://en.wikipedia.org/wiki/Merkle%E2%80%93Hellman_knapsack_cryptosystem.
- [2] Koshy, T., 2001, Fibonacci and Lucas numbers with applications, John Wiley & Sons, New York-Toronto.
- [3] Vajda, S., 1989, Fibonacci and Lucas Numbers and the Golden Section: Theory and Applications, Courier Corporation.
- [4] Brannan, D.A., 2006, A First Course in Mathematical Analysis, Cambridge University Press.
- [5] Mollin, R.A., 2007, An Introduction to Cryptography, Chapman&Hall/CRC, Boca Raton.
- [6] Uçar, S., Taş, N., Özgür, N.Y., A new cryptography model via Fibonacci and Lucas numbers, arXiv: 1709.10355 [cs.CR].
- [7] N Taş, S Uçar, N.Y. Özgür, Ö.Ö. Kaymak, 2018, A new coding/decoding algorithm using Fibonacci numbers, Discrete Mathematics, Algorithms and Applications 10 (02).
- [8] M. Basu, B. Prasad, The generalized relations among the code elements for Fibonacci coding theory, Chaos Solitons Fractals 41 (2009), no. 5, 2517–2525.

- [9] S. Prajapat, A. Jain, R. S. Thakur, A Novel Approach For Information Security With Automatic Variable Key Using Fibonacci Q-Matrix, IJCCT 3 (2012), no. 3, 54–57.
- [10] A. Stakhov, V. Massingue, A. Sluchenkov, Introduction into Fibonacci Coding and Cryptography, Osnova, Kharkov (1999).
- [11] A. P. Stakhov, Fibonacci matrices, a generalization of the Cassini formula and a new coding theory, Chaos Solitons Fractals 30 (2006), no. 1, 56–66.

JOURNAL OF SCIENCE



SAKARYA UNIVERSITY

Sakarya University Journal of Science

ISSN 1301-4048 | e-ISSN 2147-835X | Period Bimonthly | Founded: 1997 | Publisher Sakarya University |
<http://www.saujs.sakarya.edu.tr/>

Title: The Effect of Gibbs Factor on Transient Analysis in Underground Power Cables

Authors: Yılmaz Uyarođlu, Selçuk Emirođlu

Received: 2019-02-19 17:22:09

Accepted: 2019-05-15 10:49:38

Article Type: Research Article

Volume: 23

Issue: 5

Month: October

Year: 2019

Pages: 934-941

How to cite

Yılmaz Uyarođlu, Selçuk Emirođlu; (2019), The Effect of Gibbs Factor on Transient Analysis in Underground Power Cables. Sakarya University Journal of Science, 23(5), 934-941, DOI: 10.16984/saufenbilder.529265

Access link

<http://www.saujs.sakarya.edu.tr/issue/44066/529265>

New submission to SAUJS

<http://dergipark.gov.tr/journal/1115/submission/start>

The Effect of Gibbs Factor on Transient Analysis in Underground Power Cables

Yılmaz Uyaroğlu¹, Selçuk Emiroğlu^{*2}

Abstract

In this work, the transient overvoltage phenomena occurred at 34.5 kV AC underground cable transmission systems during the closure of the underground cables is to be studied and simulated by using the MATLAB program. Then, the transient voltage occurred at the underground cables is analyzed by using a modified Fourier transform. The studied system of underground cables is firstly modeled in the frequency domain. Transient voltages induced at the sending-end and receiving-end terminals of an underground cable of the transmission system are calculated in the frequency domain and using inverse Fourier Transform, the sending end and receiving end voltages are obtained by converting to the time domain. The effects of Gibbs factor on transients overvoltage phenomena considering cable length and source impedance are investigated. Numerical simulations are presented to demonstrate the transient voltages induced at the terminals of sending-end and receiving-end of an underground cable at the transmission system and the effects of Gibbs factor to eliminate Gibbs oscillations.

Keywords: Transient analysis, underground cables, Fourier transforms, Gibbs oscillation

1. INTRODUCTION

Transient network analyzers used to measure and analyze the electromagnetic transients in power systems at early stages [1]. By using a digital computer, the transient analysis and the modeling of underground cables have been a considerably interesting subject in recent years. After using of the digital computer, many methods have been investigated to analyze the transient analysis of underground cables such as Fourier transform [2,3], z transform [4-6], weighting method [7],

discrete wavelet transform [8], orthogonal projection approach [9], state variable approach [10].

Wedepohl who has firstly studied and investigated the transient analysis of cables has used Laplace transform and Bewley – Lattice techniques for transient analysis assuming that all parameters of cable do not depend on frequency [11]. After that, Indulkar and Dang have investigated the transient analysis of a cable

¹ Sakarya University, Electrical and Electronics Engineering, Sakarya, TURKEY. ORCID: 0000-0001-5897-6274

* Corresponding Author: selcukemiroglu@sakarya.edu.tr

² Sakarya University, Electrical and Electronics Engineering, Sakarya, TURKEY. ORCID: 0000-0001-7319-8861

system which has parameters depend on frequency [12].

In this work, the magnitude and waveform of the voltage in any point of the cable have been obtained in the time domain with inverse modified Fourier transform. The integral in inverse Fourier transform goes from minus infinity to infinity. But, the integral of the inverse Fourier transform does not go infinity and goes to the limited final value. So, Gibbs oscillations occur. In order to eliminate Gibbs oscillation, multiplier named as Gibbs factor is inserted in the calculations [13-15].

The transient overvoltages occurred during the switching operations are important phenomena for power system design and protection. To obtain transient voltages, all expressions have been transformed into the frequency domain. The magnitude and waveform of transient voltages have been calculated in the time domain by using the inverse Fourier transform. The cable parameters which depend on frequency such as series impedance, cable length, and effect of ground have been used in calculations.

Switching transient voltages reach the maximum values when the receiving end is open circuit. According to this state, in order to obtain the maximum value of voltage in the studied cable system, the system has been energized when the receiving end terminal of the line is open circuit. Also, the effects of source impedance and cable length on transient voltages have been investigated.

This paper is organized as follows. Section 2 briefly introduced the studied system of underground cables, and the parameter of cable is given. Mathematical formulations of the system are presented in section 3. Fourier transform and sigma factor are presented in section 4 and section 5 respectively. In section 6, simulation results are given. Conclusions are finally given in section 7.

2. ANALYSIS OF CABLE SYSTEM

The geometries of single cable are shown in Fig.1. The underground cable is made of core conductor, inner semiconducting layer, pure XLPE, outer

semiconducting layer, sheath, aluminum foil, inner serving and outer serving as shown in Fig 1.

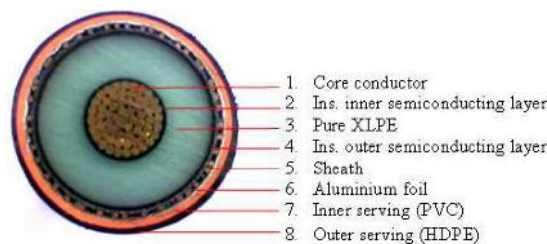


Fig. 1. The geometries of real single cable [16]

The radiuses of the conductor, inner sheath, outer sheath, and cable outer are shown in the cross-section of cable as shown in Fig. 2. Also, the parameters of the underground cable and ground resistivity are given in Table 1. The configuration of the cable system used in simulations is shown in Fig. 3.

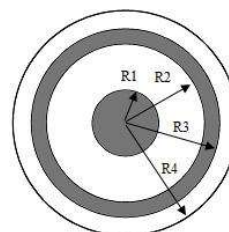


Figure 2. Single cable cross section area [16]

Table 1. The parameters of underground cable [17]

Conductor radius (R1)	3 mm
Sheath inner radius (R2)	14 mm
Sheath outer radius (R3)	15 mm
Cable outer radius (R4)	17 mm
Resistivity of core (ohm-m)	$1.72 \cdot 10^{-8}$
Resistivity of sheath (ohm-m)	$1.72 \cdot 10^{-8}$
Relative permittivity of core insulation	2.3
Relative permittivity of sheath insulation	7
Resistivity of ground (ohm-m)	20

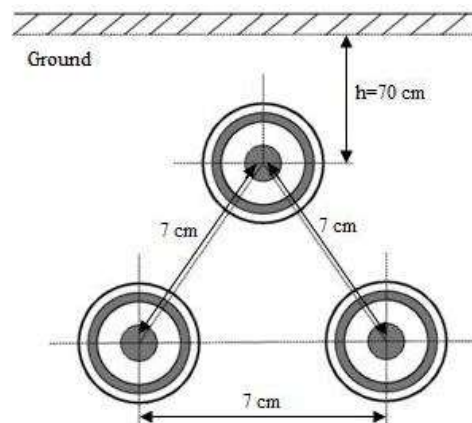


Figure 3. Configuration of cable system [18]

3. MATHEMATICAL FORMULATION OF SYSTEM

The voltage at the equivalent sheath is zero because the cable sheaths at the major part terminals are solidly earthed. So, the row and column elements of the series impedance matrices of cable related to cable sheath may be eliminated. Series impedance matrices are three order square matrices. So, the nodal parameters of two-port system A and B will be a matrix of 3x3 order. As it is shown in Fig. 4, V_S and V_R are sending-end and receiving-end voltage matrices of the 3x1 order. Also, the single line diagram of the studied system is shown in Fig. 5.

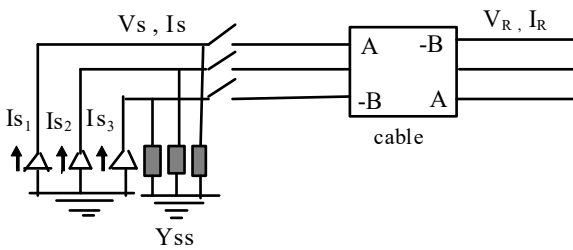


Figure 4. Norton equivalent circuit of cable system

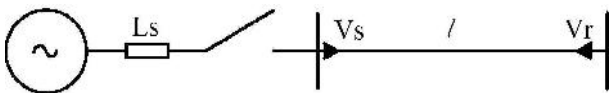


Figure 5. Single line circuit of studied system

The nodal equation of the cable system can be written as equation (1) [1].

$$\begin{bmatrix} I_S \\ I_R \end{bmatrix} = \begin{bmatrix} A & -B \\ -B & A \end{bmatrix} \begin{bmatrix} V_S \\ V_R \end{bmatrix} \quad (1)$$

Writing the Kirchhoff's current law at the sending-end terminal, it gives [1],

$$I_{SS} = I_S + I, I = Y_{SS}V_S \quad (2)$$

Using equation 1 and equation 4, matrix yields as below [1, 17].

$$\begin{bmatrix} I_{SS} \\ I_R \end{bmatrix} = \begin{bmatrix} A+Y_{SS} & -B \\ -B & A \end{bmatrix} \begin{bmatrix} V_S \\ V_R \end{bmatrix} \quad (3)$$

As the receiving end of the cable is not loaded, $I_R=0$. From equation (3),

$$V_R = A^{-1}BV_S \quad (4)$$

Substituting V_R into the matrix (Eq.3), V_S and V_R can be written as [2, 12]

$$V_S = [(A+Y_{SS}) - BA^{-1}B]^{-1}I_{SS} \quad (5)$$

$$V_R = A^{-1}B[(A+Y_{SS}) - BA^{-1}B]^{-1}I_{SS}. \quad (6)$$

As a result, the terminal voltages at receiving-end and sending-end in the cable system are calculated by expressions (5) and (6), respectively [2, 12].

4. FOURIER TRANSFORM

Inverse modified Fourier transform is given below [19].

$$f(t) = \frac{1}{2\pi} \int_{-\infty}^{+\infty} F(\omega)e^{j\omega t} d\omega \quad (7)$$

where $F(\omega)$ is a Fourier transformation and given as

$$F(\omega) = \int_{-\infty}^{+\infty} f(t)e^{-j\omega t} dt. \quad (8)$$

So that all pole of integral expression is real and stable, assume that new angular frequency is ω' . Real axis slipped with ω to the negative side; yields $\omega' = \omega - j\alpha$. So, inverse modified Fourier transform express as below [1, 20].

$$f(t) = \frac{1}{2\pi} \int_{-\infty-j\infty}^{+\infty-j\infty} F(\omega' - j\alpha)e^{j(\omega'-j\alpha)t} d\omega' \quad (9)$$

or

$$f(t) = \frac{e^{\alpha t}}{2\pi} \int_{-\infty-j\infty}^{+\infty-j\infty} F(\omega' - j\alpha)e^{j\omega' t} d\omega' \quad (10)$$

The real part of integral can be written as

$$f(t) = \frac{e^{\alpha t}}{\pi} \text{Re} \int_0^{\infty-j\alpha} F(\omega' - j\alpha)e^{j\omega' t} d\omega'. \quad (11)$$

Writing this integral in the discrete form [15]

$$f(t) = \frac{2\omega_0}{\pi} e^{at} \operatorname{Re} \sum_{n=1}^N F[(2n-1)\omega_0 - j\alpha] e^{j(2n-1)\omega_0 t}. \quad (12)$$

5. GIBBS OSCILLATION AND SIGMA FACTOR

Equation 11 can be calculated with numerical integral (Eq.12) in computer. Frequency harmonics named as Gibbs oscillation have been occurred because of the numerical integral from zero to limited end value.

Lanczos has proposed the method to reduce Gibbs oscillation [13]. So, Gibbs oscillation has been reduced with sigma factor as given below.

$$\sigma = \frac{\sin(\pi\omega/\Omega)}{(\pi\omega/\Omega)} \quad (13)$$

where Ω is cutting frequency of top limit of integral. Including sigma factor to Fourier function,

$$f(t) = \frac{e^{at}}{\pi} \operatorname{Re} \int_0^{\Omega} \sigma F(\omega' - j\alpha) e^{j\omega' t} d\omega' \quad (14)$$

can be written. Sigma factor has a low effect on low frequency and high effect in high frequency for reducing Gibbs oscillation.

6. SYSTEM STUDIES AND SIMULATION RESULTS

The transient voltages induced at the underground cable system on account of simultaneous switching are investigated by using a computer in the MATLAB program [21]. Also, the simulation results are compared with and without the sigma factor. Effects of source impedance and cable length on the transient voltages are also taken into consideration.

6.1. Effect of Cable Length

Effects of cable length on the transient voltage's magnitude owing to simultaneous closure have been investigated by performing three-phase simultaneous switching to the line from the generator which has source impedance.

Sending-end and receiving-end voltage waveforms got with three different cable lengths for low and high source impedances are given in Fig. 6 and Fig. 8. The maximum receiving-end and sending-end voltages for different cable lengths and source impedance are tabulated in Table 2 and Table 3.

As it can be seen from Table 2 and Table 3, the magnitude of the maximum sending-end and receiving-end voltage of the first phase reduces with the rise of cable length.

Table 2. The maximum magnitudes of overvoltages for different cable length ($L_s:0.189$ mH)

Cable length l (m)	Maximum magnitude of the sending-end voltages (p.u)		Maximum magnitude of the receiving-end voltages (p.u)	
	with sigma factor	without sigma factor	with sigma factor	without sigma factor
5000	1.2802	1.4187	1.9817	2.0710
30000	1.0146	1.0880	1.8189	1.8964
80000	1.0079	1.0901	1.5517	1.5694

Table 3. The maximum magnitudes of overvoltages for different cable length ($L_s:9.47$ mH)

Cable length l (m)	Maximum magnitude of the sending-end voltages (p.u)		Maximum magnitude of the receiving-end voltages (p.u)	
	with sigma factor	without sigma factor	with sigma factor	without sigma factor
5000	1.8639	1.8664	2.0699	2.0727
30000	1.5692	1.6022	2.0386	2.1235
80000	1.3168	1.3404	1.6398	1.6677

6.2. Effect of Source Impedance

Sending-end and receiving-end voltage waveforms obtained for low and high source impedance are shown in Fig. 6 and Fig. 8. The maximum receiving-end voltage for low and high source impedance is given in Table 4.

Table 4. Maximum magnitudes of overvoltages for different source inductance ($l=30$ km)

Source inductance (mH)	Maximum sending-end voltage(pu)		Maximum receiving-end voltage(pu)	
	with σ	without σ	with σ	without σ
0.189	1.0146	1.0880	1.8189	1.8964
9.47	1.5692	1.6022	2.0386	2.1235

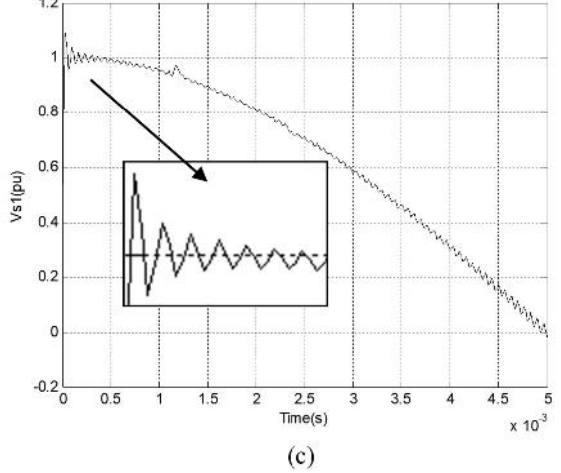
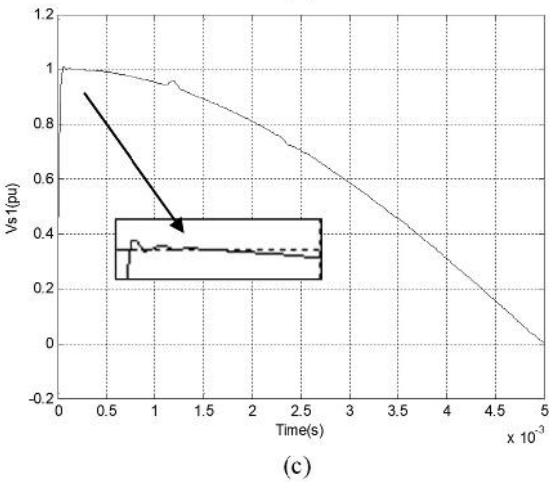
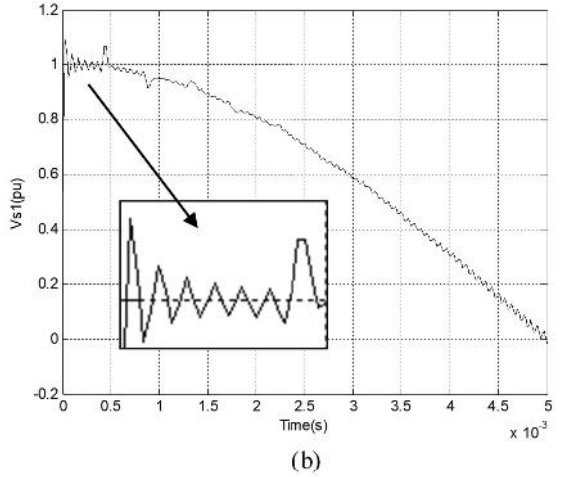
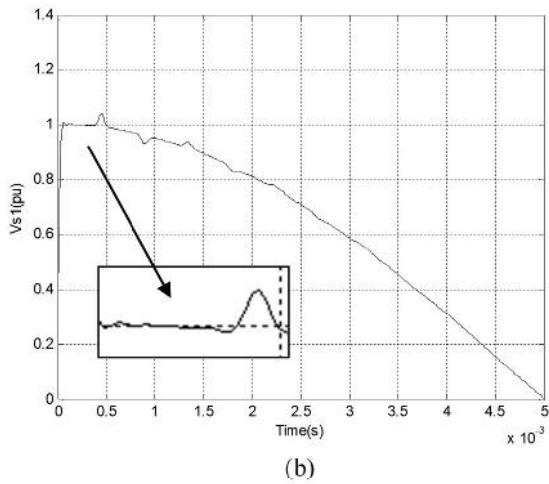
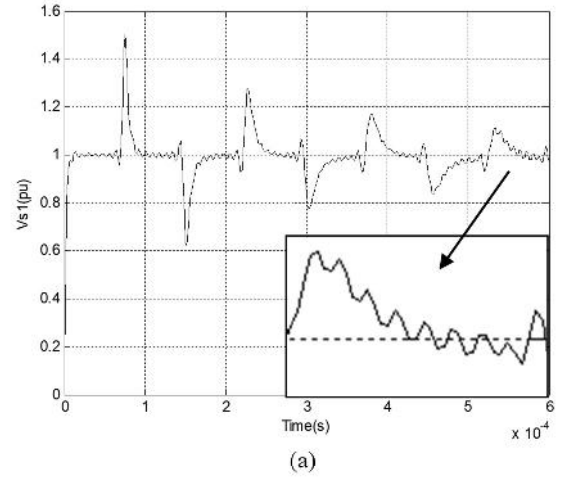
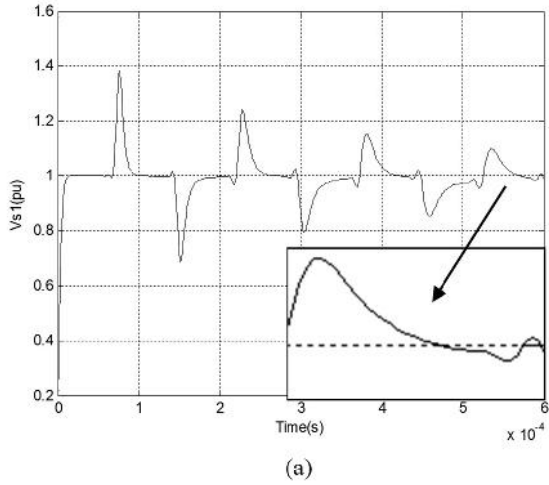
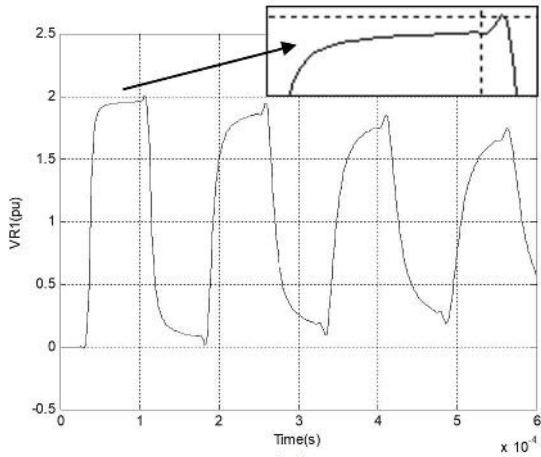


Figure 6. The waveform of transient voltages induced at sending-end with sigma factor when L_S : 0.189 mH \neq a) 5000 m, b) 30000 m, c) 80000 m

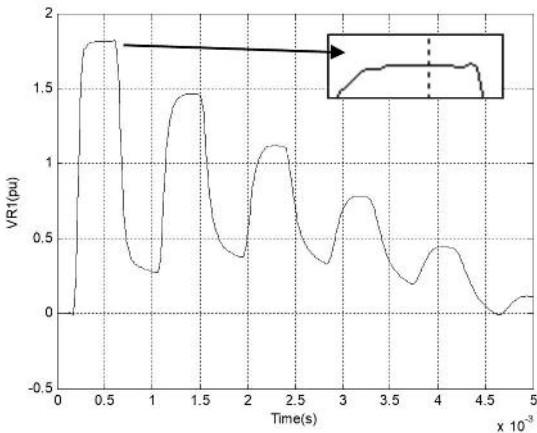
Figure 7. The waveform of transient voltages induced at sending-end without sigma factor when L_S : 0.189 mH \neq a) 5000 m, b) 30000 m, c) 80000 m

The waveform of sending-end and receiving-end voltages including sigma factor when source inductance L_S : 0.189 mH, with cable length (l) 5000 m, 30000 m, and 80000 m are shown in Fig. 6 (a,b,c) and Fig. 8 (a,b,c) respectively.

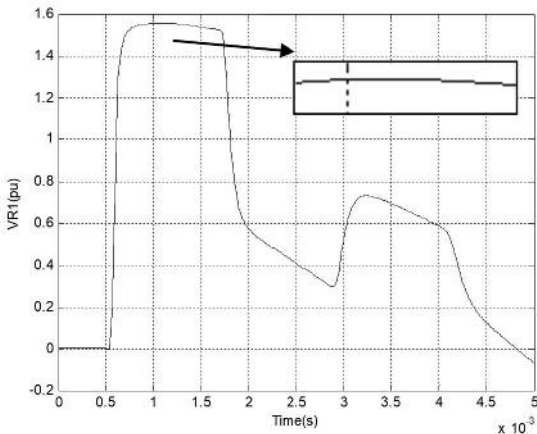
The waveform of sending-end and receiving-end voltages without sigma factor when source inductance L_S : 0.189 mH, with increasing cable length 5000 m, 30000 m, and 80000 m are shown in Fig. 7 (a,b,c) and Fig. 9 (a,b,c) respectively.



(a)



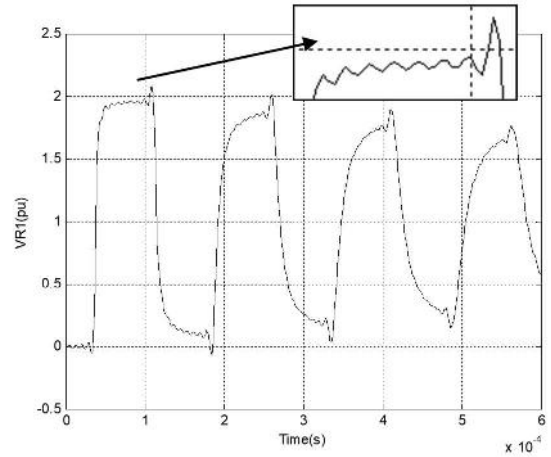
(b)



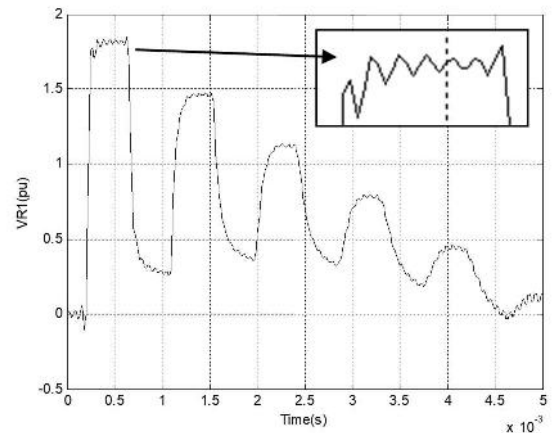
(c)

Figure 8. The waveform of transient voltages induced at receiving-end with sigma factor when L_S : 0.189 mH \neq a) 5000 m, b) 30000 m, c) 80000 m

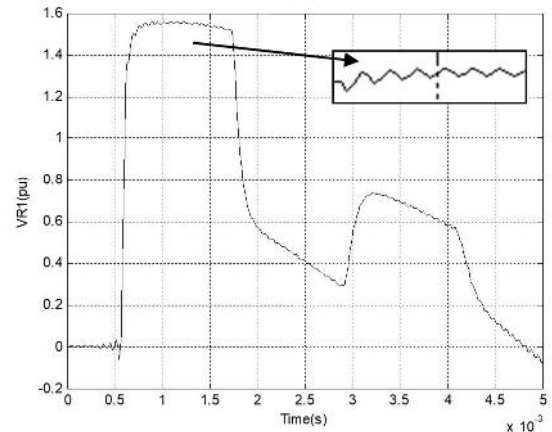
Voltages exponentially increase with a time constant. Besides, it is directly proportional to the source inductance. Also, the frequency of oscillations that are superimposed on nominal voltage frequency reduces with the rising source impedances as shown in Table 5 and Table 6. The voltage frequency of oscillations reduced at receiving-end decreases with the increasing the cable length. Table 5 and Table 6 shows



(a)



(b)



(c)

Figure 9. The waveform of transient voltages induced at receiving-end without sigma factor when L_S : 0.189 mH \neq a) 5000 m, b) 30000 m, c) 80000 m

approximately the voltage frequency of oscillations reduced at receiving-end with source impedance 0.189 mH and 9.47 mH respectively. The approximate values are used in Table 5 and Table 6.

Table 5. The oscillation frequency of the receiving end overvoltages for different cable length ($L_S:0.189$ mH)

Cable Length (m)	Frequency	Oscillation
5000	5 kHz	6.5 cycle (in 1 ms)
30000	1 kHz	5.5 cycle (in 5 ms)
80000	357 Hz	2 cycle (in 5 ms)

Table 6. The oscillation frequency of the receiving end overvoltages for different cable length ($L_S:9.47$ mH)

Cable Length (m)	Frequency	Oscillation
5000	2.5 kHz	2.5cycle (in 1 ms)
30000	835 Hz	4 cycle (in 5 ms)
80000	335 Hz	1.8 cycle (in 5 ms)

7. CONCLUSIONS

In this study, the magnitude and waveform of the transient overvoltages have been obtained using numerical Fourier transform. This paper investigated the source impedance and effect of cable length on the transient voltages induced at terminals of sending end and receiving end. The maximum magnitude transients overvoltages depend on cable length and source impedance etc. Source impedance and cable length have a significant effect on the waveform and magnitude of the transient voltage. Simulation results show that the magnitude of sending end and receiving end voltages decreases with the increasing the cable length. Also, as the source impedance rises, both the sending end and receiving end maximum magnitude of overvoltages rise. Also, the oscillation frequency of overvoltages decreases with the increasing source impedance and increasing the cable length.

This paper also presented the effect of sigma factor on transient analysis. In the transient analysis, because the Fourier integral has a limited final value, the Gibbs oscillation has occurred. Simulation results show that Gibbs oscillations have been reduced and eliminated with including sigma factor in Fourier integral.

8. REFERENCES

- [1] Y. Uyaroğlu, Switching Transients Analysis in Underground Power Cables. M.Sc. Thesis, Sakarya University, 1997. (in Turkish)
- [2] L. M. Wedepohl and C. S. Indulkar, "Switching Overvoltages in Long Crossbonded Cable Systems Using the Fourier Transform," *IEEE Transactions on Power Apparatus and Systems*, pp. 1476-1480, July/August 1979.
- [3] Ana Isabel Brito, V. Maló Machado, M.E. Almeida, M. Guerreiro das Neves, "Skin and proximity effects in the series-impedance of three-phase underground cables," *Electric Power Systems Research*, 130, 132-138, 2016.
- [4] W. D. Humpage, K. P. Wong, T. T. Nguyen, and D. Sutanto, "Z-transform electromagnetic transient analysis in power systems," *Proc. Inst. Elec. Eng., C, Gen. Trans. Dist.*, vol. 127, pp. 370-378, Nov. 1980.
- [5] W. D. Humpage, K. P. Wong, T. T. Nguyen, "Z-transform electromagnetic transient analysis in crossbonded cable transmission systems," *Proc. Inst Elec. Eng, C, Gen. Trans. Dist.*, vol. 128, pp. 55-62, 1981.
- [6] T. Noda, A. Ramirez, "Z-transform based methods for electromagnetic transient simulations," *IEEE Trans.on Delivery*, vol. 22, no. 3, July 2007.
- [7] I. Kocar, J. Mahseredjian, G. Olivier, "Weighting Method for Transient Analysis of Underground Cables," *IEEE Transactions on Power Delivery*, vol. 23, no. 3, July 2008.
- [8] B.A. Suleimanov, O.A. Dyshin, "Application of discrete wavelet transform to the solution of boundary value problems for quasi-linear parabolic equations," *Applied Mathematics and Computation* 219 7036–7047, 2013.
- [9] Heng-Xu Ha, Yu-Zhen Tan, Bo Chen, and Z. Q. Bo, "A Novel Electro-Magnetic Transient Analysis Method Based on

- Orthogonal Projection Approach,” Progress In Electromagnetics Research Symposium Proceedings, Moscow, Russia, August 18 - 21, 2009.
- [10] A. Semlyen and Mansour H. Abdel-Rahman, “A State Variable Approach for the Calculation of Switching Transients on a Power Transmission Line,” IEEE Trans. on Circuits and Systems, vol. cas. 29, no. 9, pp. 624-633, September 1982.
- [11] L.M. Wedepohl, S.E.T. Mohamed, “Multiconductor Transmission Lines, Theory of Natural Modes and Fourier Integral Applied to Transient Analysis,” Proc.IEE, Vol. 116., No 9., September 1969.
- [12] L.M. Wedepohl, C.S. Indulkar, “Switching Overvoltages in Short Crossbonded Cable Systems Using the Fourier Transform,” Proceedings of the Institution of Electrical Engineers, Vol. 122, No 4, 1975.
- [13] C. Lanczos, “Applied Analysis”, Prentice-Hall 539 pp., 1956.
- [14] Ali Abdi, Seyed Mohammad Hosseini, “An investigation of resolution of 2-variate Gibbs phenomenon,” Applied Mathematics and Computation 203, 714–732,2008.
- [15] E. Berriochoa, A. Cachafeiro, J. Díaz, “Gibbs phenomenon in the Hermite interpolation on the circle,” Applied Mathematics and Computation, 253, 274-286, 2015.
- [16] Daud, Muhamad Zalani, Transient behaviour modelling of underground high voltage cable systems, Masters by Research thesis, School of Electrical, Computer and Telecommunications Engineering - Faculty of Informatics, University of Wollongong, 2009. <https://ro.uow.edu.au/theses/2032>
- [17] U. Ünver, “Transient Analysis of Cable Systems Including the effect of Nonlinear Protective Devices,” PhD. Thesis, University of Manchester Institute of Science and Technology, 1979.
- [18] Y. Uyaroğlu, U. Ünver, “Yeraltı Enerji Kablolarında Oluşan Manevra Aşırı Gerilimlerinin Geçici Rejim Analizi: Kablo Uzunluğunun ve Şönt Reaktörlerin Etkisi,” SAÜ Fen Bilimleri Enstitüsü Dergisi, 2, 119-123, 1997.
- [19] N. Mullineux, J. Day, J.R. Reed, “Developments in obtaining transient response using Fourier transforms: use of the modified Fourier transform,” Int. J. Elec. Eng. Educ, 4, pp. 31-40, 1966.
- [20] U. Ünver, “Enerji Nakil Hatlarının Kısa Devre Analizi: Çift Taraftan Beslenen Hatlar,” Elektrik Mühendisliği 6. Ulusal Kongresi, pp. 180-196, 1995.
- [21] The MathWorks. (1993). MATLAB User's Guide. The MathWorks, Inc., Natick, MA

JOURNAL OF SCIENCE



SAKARYA UNIVERSITY

Sakarya University Journal of Science

ISSN 1301-4048 | e-ISSN 2147-835X | Period Bimonthly | Founded: 1997 | Publisher Sakarya University |
<http://www.saujs.sakarya.edu.tr/>

Title: Thermo-Hydraulic Effects of Vortex Generator Pairs in A Crossflow Channel With A Transverse-Jet Flow

Authors: Besir Kok

Received: 2019-04-29 13:53:41

Accepted: 2019-05-21 00:45:52

Article Type: Research Article

Volume: 23

Issue: 5

Month: October

Year: 2019

Pages: 942-963

How to cite

Besir Kok; (2019), Thermo-Hydraulic Effects of Vortex Generator Pairs in A Crossflow Channel With A Transverse-Jet Flow. Sakarya University Journal of Science, 23(5), 942-963, DOI: 10.16984/saufenbilder.558877

Access link

<http://www.saujs.sakarya.edu.tr/issue/44066/558877>

New submission to SAUJS

<http://dergipark.gov.tr/journal/1115/submission/start>

Thermo-hydraulic effects of vortex generator pairs in a crossflow channel with a transverse-jet flow

Besir Kok¹

Abstract

The use of passive obstacles to control the hydraulic and thermal behavior of fluids is an application in many industrial mechanisms. In this study, flow and thermal oscillation behaviors in a crossflow channel with a transverse jet flow were investigated numerically. Passive vortex generator(VG) pairs with different geometric properties were used in the test channel and their thermo-hydraulic effects in the active mixing zone were discussed. In addition, nine boundary conditions, which are the function of velocity and temperature, have been applied to the computational domain. The results showed that VG pairs with different geometric properties do not provide an effective improvement in thermal mixing behavior, but they are very successful in removing thermal oscillations from the channel walls. Momentum and temperature differences between cross flow and jet flow are the secondary parameters of the study. When the jet velocity was gradually increased by keeping the crossflow rate constant, improvements in thermal mixing performance were observed but in this case, it was also seen that thermal oscillations reached the channel walls. As the jet temperature increased, a decrease in thermal mixing performance was observed due to the increased hot fluid dominance in the duct.

Keywords: Transverse jet, Crossflow, Thermal mixing, LES, Vortex generator.

1. INTRODUCTION

During the mixing of fluids at different temperatures, temperature oscillations occur in the mixing zone due to the non-homogeneous thermal mixing. These oscillations may cause thermal stresses on surrounding surfaces of the fluid at certain frequencies. During long working cycles, these stresses occurring on the material surface may cause cracks. Such cracks in industrial mechanisms may cause significant disruptions in the operation of the system. Leakages from such cracks in industrial systems

such as nuclear power plants can cause extremely dangerous consequences for human and environmental health. During the operation of nuclear power plants, there have been many cracks due to the thermal stress that has been detected so far. For instance, a number of cracks were found in the connection pipes of the heat exchanger in the central chamber of the Tsuruga-2 PWR (Japan) nuclear power plant, due to thermal stresses in 1999. Sodium leaks were detected in the purification cycle of the primary circuit of the BN - 600 (Russia) reactor in 1993. Metallurgical analysis showed that the problem

*Corresponding Author: besirkok@gmail.com (B. Kok)

¹ Firat University, Technical Vocational School, Elazığ, TURKEY. ORCID: 0000-0001-7241-952X

was caused by the temperature fluctuations occurring during the mixing of hot and cold sodium[1]. This kind of cracks observed in many industrial applications, particularly in nuclear power plants, led researchers to study on this subject.

Sakai et al. [2] made numerical modeling of angled jet flow in a crossflow channel to examine the cooling effect of the film on the turbine blades. Large Eddy Simulation (LES) turbulence model was used in the analysis. Crossflow and jet velocity ratios are the main parameters of the study. They analyzed the effects of this ratio on jet behavior with film cooling effectiveness and jet trajectory graphics. The results showed that the vertical structure was significantly affected by the rate of velocity. Deng et al. [3], performed a detailed numerical study on shock vector control-SVC in a non-permanent three-dimensional cross flow. Standard $k-\epsilon$, Realizable $k-\epsilon$, $k-\omega$, and LES turbulence models are given in this study. The results showed that LES simulations were more successful in solving non-permanent characteristics of the flow. Liu et al. [4] studied the flow and mixing characteristics of a transverse-jet flow in a supersonic crossflow. In the analysis, LES was used as a turbulence model and the results were verified for comparison with several different numerical methods. LES simulations were confirmed by available experimental data. Chuang et al. [5,6] investigated experimentally the thermal mixing and stripping behavior in a T-junction flow. The Branch flows were positioned at 90 and 45 angles to the main flow. PSD graphs were used to analyze whether the thermal oscillations occurring in the mixture zone create a risk of thermal stress. It was analyzed whether or not the reverse flow conditions occurred in the channel by using the momentum data obtained. McGuinn et al. [7] examined the heat transfer characteristics of six parallel slot jets in a crossflow which can be controlled separately. In the experiment, a system which can detect hot points dynamically and adaptive cooling is used. The jet Reynolds numbers and the distance between the jet and the

The effects of temperature and momentum difference between jets on flow and thermal mixing behaviors are the secondary parameters of these studies. Some of the experimental studies

impact plates are variable. The results showed that the parameters chosen were highly effective on heat transfer. Wang et al. [8,9] experimentally investigated the heat transfer characteristics of jet flow impinging on a heated plate in a crossflow channel. In the experiments, vortex generators(VG) in different geometries were placed in a rectangular test channel. The results show that the VG significantly increase heat transfer. Furthermore, the different geometric ratios of these VGs also affect the heat transfer in all cases. Compared to triple-crossed VG, rectangular VG was found to provide a more heat transfer improvement. As the crossflow flow rate increased, VG was found to significantly affect the heat transfer.

The regions where thermal oscillations are generally seen in industrial mechanisms are T-junctions. When the main pipe/channel flow and the secondary flow connected therein are at different temperatures, cracks can be seen as described above. There are many studies in the literature that demonstrate different thermophysical dynamics in T-junctions. In these studies, the researchers have analyzed whether the temperature oscillations in this region constitute thermomechanical threats. In order to understand this, Power Spectral Density (PSD) graphics are generally considered. These graphs provide information on the frequency and amplitude of the current temperature oscillation[10–15].

Kok et al. have made numerical and experimental studies on the thermal mixing of fluids at different temperatures in confined channels. In these studies, they used two types of jet models, mainly parallel and co-axial. The thermal mixing performance of the fluid in the channel was analyzed with the help of Mixing Index (MI) graphs. In addition, PSD graphs were obtained in order to determine whether the current temperature fluctuations posed a risk of thermal stress. It has been determined whether the thermal oscillations have reached the channel walls by using isotherms. They used velocity profiles to evaluate the turbulence behaviors of jet flows.

have examined the inclination angle of a shallow test channel and the effects of the square and circular passive barriers used in these channels. In another study, an artificial neural network

algorithm was developed using the available experimental data and estimates were made about the parameters not tested. Porous and sequential types of barriers were used in a square cross-section test channel. Large Eddy Simulation (LES) turbulence model was used for numerical modeling of these studies. Experimental data were obtained by using different experimental setups[16–23].

The above literature survey on the effects of temperature oscillations on the mechanisms shows that there are many aspects of this subject. The above literature summary shows how different aspects of this issue are addressed. Every parameter that can be effective on the temperature oscillations in the mixing zone is carefully examined by the researchers. Thermal oscillations occurring in a crossflow are the most common occurrences in industrial applications. In this study, the flow and thermal mixing characteristics of a transverse-jet flow in a crossflow were investigated numerically. LES turbulence model was used with WALE subgrid-scale model to simulate flow area. In the simulations, vortex generators pairs with different geometric properties were used to improve the thermal

mixing efficiency in the mixing zone. The effects of these VGs on flow, thermal mixing behavior and pressure drop in the channel have been extensively discussed. Temperature and momentum differences between cross flow and jet flow are the secondary parameters of the study.

2. COMPUTATIONAL STUDY

Accurate analysis of the thermodynamic and dynamic characteristics of thermal mixing problems is very complicated. Since the sudden temperature oscillations in the mixing zone are random, they are difficult to predict. Therefore, such problems are not problems in which the average temperature oscillation behaviors are examined in large geometries. On the contrary, these are problems in which local behavior is examined in certain sections. As explained above, the cases in which thermal mixing are observed in industrial mechanisms are generally T connections. Therefore, in this study, the flow and thermal mixing behaviors of a jet flow positioned transversely in a cross flow were investigated numerically.

Table 1. Boundary conditions of crossflow and jet flow

	T_j (K)	T_c (K)	U_j (m/s)	U_c (m/s)	Re_j	Re_c
Case 1	318	298	0.5	0.1	8305	13427
Case 2	338	298	0.5	0.1	11316	13427
Case 3	358	298	0.5	0.1	14539	13427
Case 4	318	298	0.75	0.1	12458	13427
Case 5	338	298	0.75	0.1	16974	13427
Case 6	358	298	0.75	0.1	21802	13427
Case 7	318	298	1	0.1	16610	13427
Case 8	338	298	1	0.1	22633	13427
Case 9	358	298	1	0.1	29069	13427

For this purpose, a test channel measuring 15D x 10D x 50D was modeled. Water is used as working fluid in the channel and the jet provides hot fluid to the crossflow channel. In this study, the momentum and temperature values of the crossflow are kept constant while the temperature and momentum values of the jet flow velocities are gradually increased. Detailed information on crossflow and jet flow boundary conditions are

given in Table 1. As shown, there are 9 boundary conditions which are the function of momentum and temperature. As seen in Figure 1, passive Vortex Generator (VG) pairs are placed in the channel. These VGs are two types, Rectangular and Delta, which are shown in Figure 2. When the numerical studies conducted in the past[24] regarding the thermal mixing are examined, it can

be seen that the steady-state studies do not catch the turbulence characteristic.

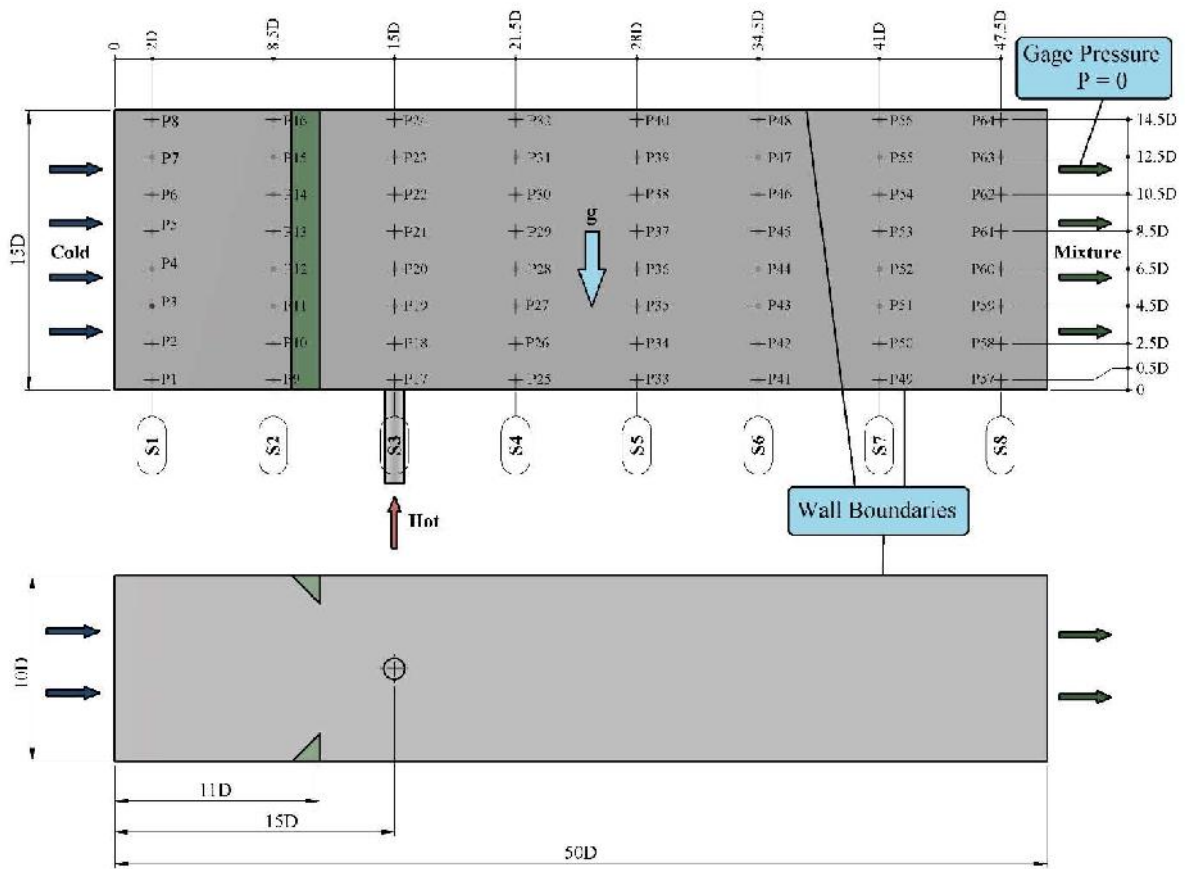


Figure 1. Computational domain and measurement points

In such analyzes, point data is difficult to detect, so the average temperature values over time should be compared. In the literature, it was seen that the LES turbulence model gave quite healthy results compared with experimental findings. Therefore, the LES turbulence model was used for modeling the flow area. In the analyzes, the permanent characteristics of the

fluid were solved using the $k-\epsilon$ turbulence model and the fully developed flow conditions were obtained. Then, time-dependent flow conditions were obtained by using the LES turbulence model. Solutions were made for 4 seconds flow time and the data were collected at 100 Hz frequency.

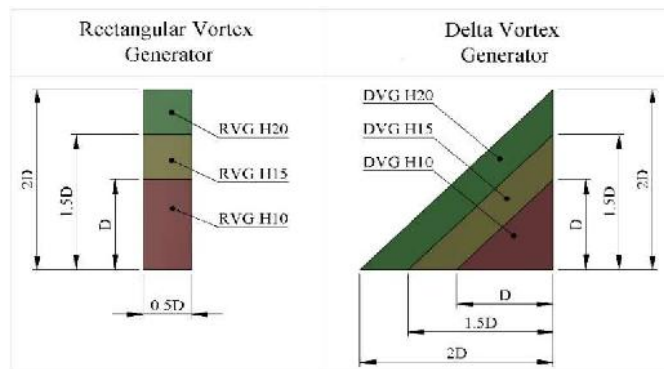


Figure 2. Dimensions of vortex generators

Time steps were defined as 0.01s in transient calculations and 20 iterations were made for each time step. The residuals drop below 8×10^{-5} after 20 iterations. Courant number is under 0.26 in the effective mixing region for all cases.

Mass flow boundary conditions are used for both crossflow and the jet inlet. Wall boundaries were chosen for all the channel walls and pressure outlet boundary condition was defined in the exit of the channel (see Figure 1).

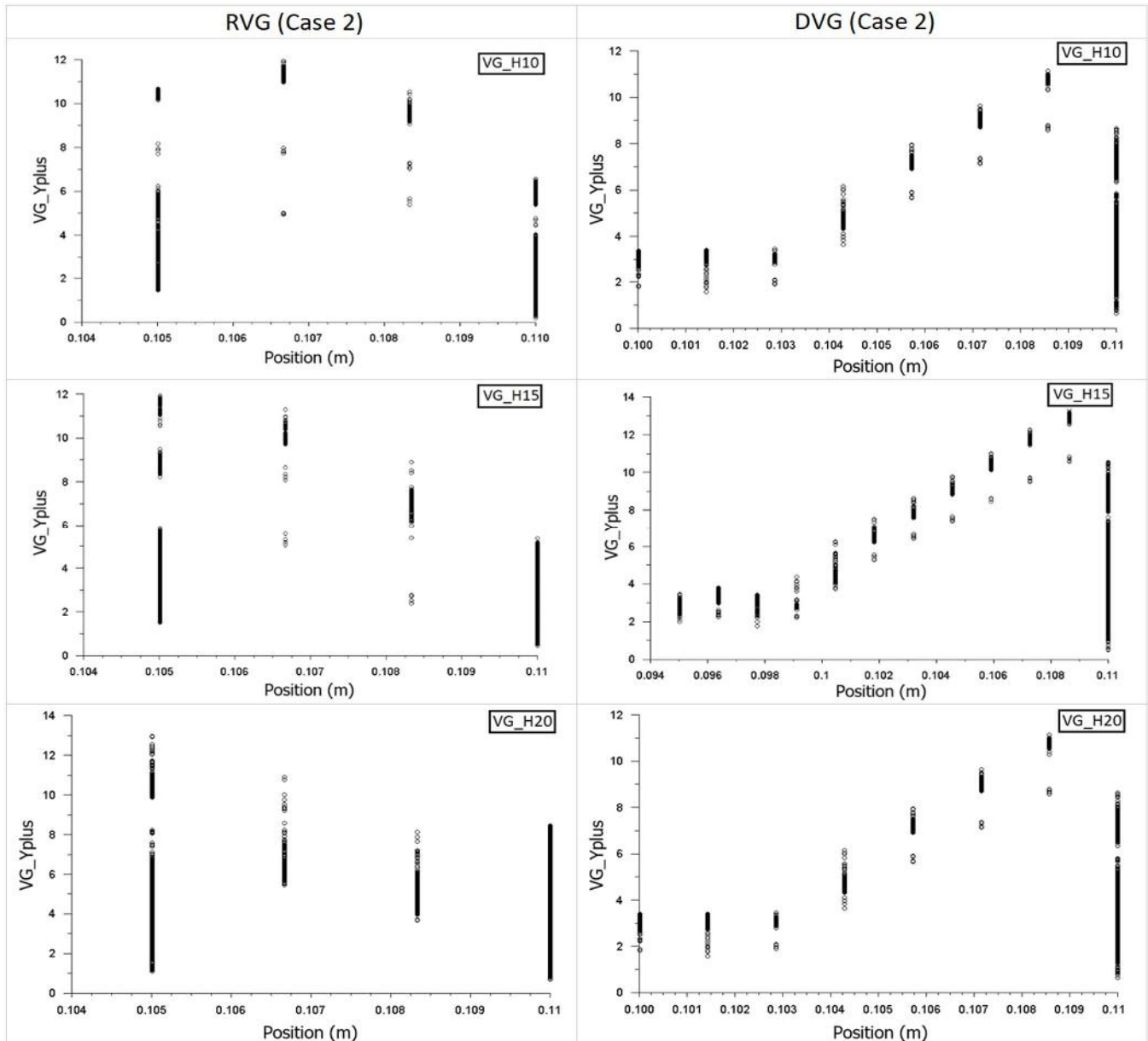


Figure 3. y^+ values of wall boundaries for vortex generator pairs

In the test channel, turbulence is generated by both vortex generator pairs and flow shear. For the turbulence produced by the passive obstacles (VG), the y^+ value must be convenient in order to capture the transition from the viscous layer to the developed layer with the appropriate turbulent energy transfer. The y^+ values for the present

study is given at Figure 3 and as it is seen from the figure y^+ values are under 14 for all cases.

2.1. Mesh Structure

ANSYS Meshing 15.0 software was used to create the mesh structure of the determined

models which are given in Figure 4. The elements must be close to the cubic structure so that the formed mesh structure is suitable for LES simulations. Since small fluctuations are modeled in the LES model, the mesh elements should be as small as possible. However, elements of appropriate sizes must be selected, since the very small dimensions of the elements will extend the calculation time.

Taylor Microscale (TMS) scale was used to determine the correct size of the elements that would not negatively affect the results of the analysis. TMS is often used in the literature in LES analyzes to characterize turbulent fluid flow. Taylor Microscale is an intermediate length scale that gains importance when fluid viscosity significantly affects the movement of turbulence vortices.

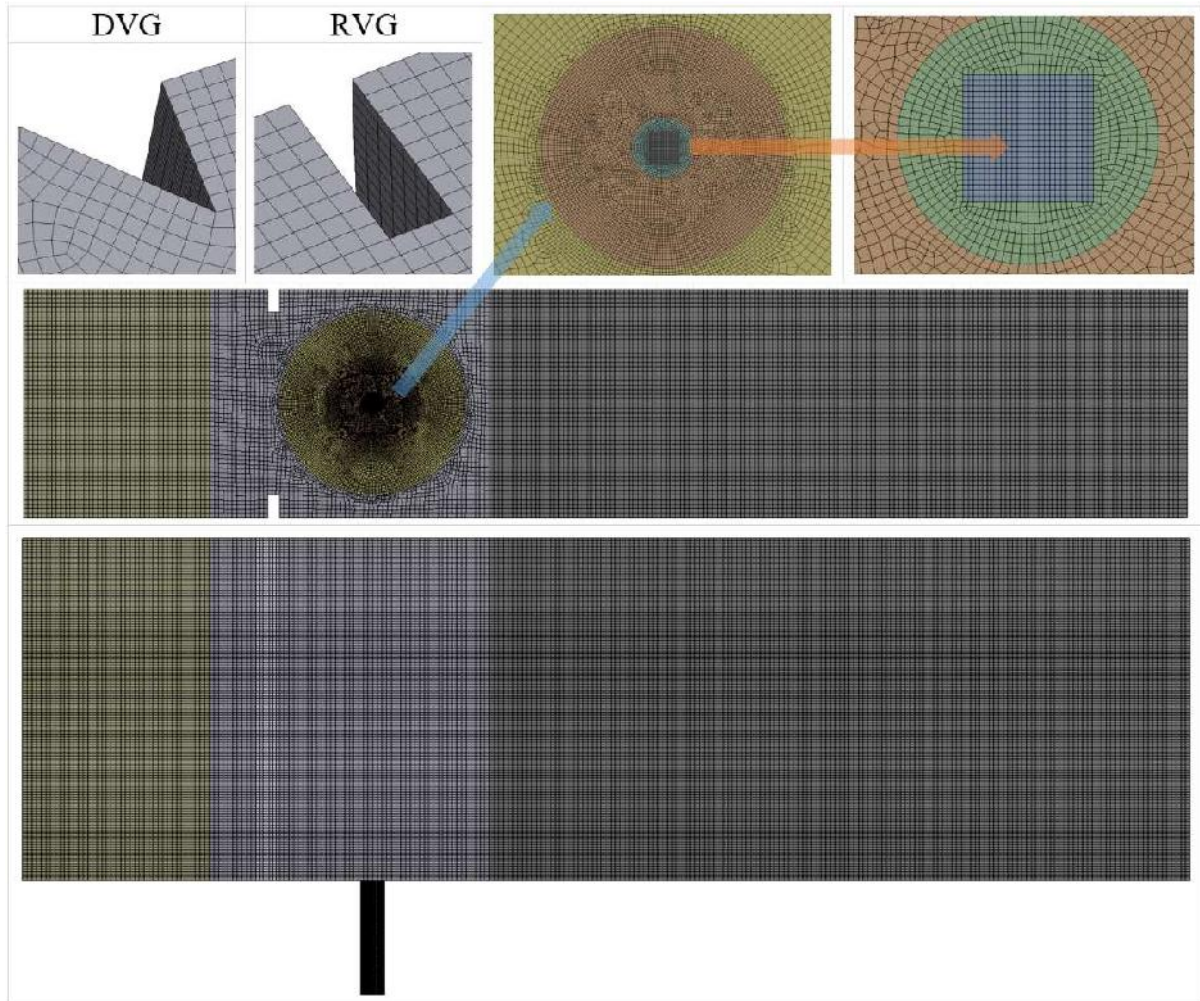


Figure 4. Grid distribution of the computational domain

It is calculated by using $\lambda_T = \sqrt{10\mu_m k / \rho_m \varepsilon}$, where μ_m , k , ρ_m and ε are the molecular viscosity, turbulence kinetic energy, density and turbulence emission rate, respectively. Figure 5. gives a detailed view of the mesh structure. As it is seen from the figure, hexahedral mesh elements were used for accurate resolving of eddies. The generated mesh models consist of 3322740 (Test 2), 3304115, 3322740,

3314240, 3327230, 3214790, 3183540 elements for the Base Channel, RVG_H10, RVG_H15, RVG_H20, DVG_H10, DVG_H15 and DVG_H20 geometric cases, respectively. The TMS values obtained from RANS simulations is about 0.36 mm for jet inlet and 0.78 mm for effective ve mixing region. Element size in the generated model is 0.38 mm for the jet inlet region and 0.82 mm for the effective mixing region.

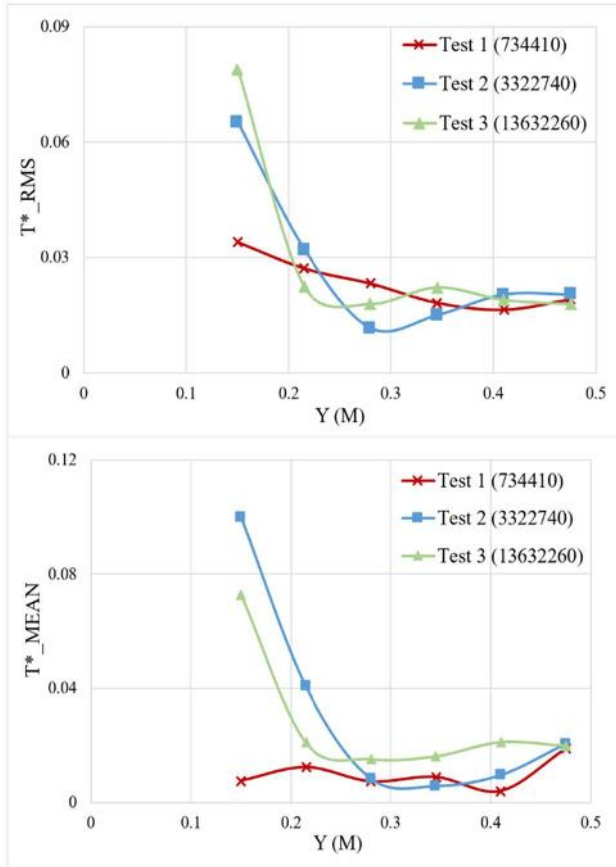


Figure 5. Mesh sensitivity analyses for Case 8 and base channel

To verify the mesh model obtained using TMS, a mesh sensitivity analysis was also performed. For this purpose, 3 test models have been formed in different element sizes. These models are Test 1, Test 2 and Test 3 with 734410, 3322740 and 13632260 element numbers, respectively. The test results shown in Figure 5 show that increasing the number of elements does not significantly change the results, but decreasing the number of elements causes a divergence.

momentum, and energy equations can be written as[25]:

$$\frac{\partial \rho}{\partial t} + \frac{\partial}{\partial x_i} (\rho \bar{u}_i) = 0 \quad (3)$$

$$\frac{\partial}{\partial t} (\rho \bar{u}_i) + \frac{\partial}{\partial x_j} (\rho \bar{u}_i \bar{u}_j) = \frac{\partial \sigma_{ij}}{\partial x_j} - \frac{\partial \bar{p}}{\partial x_i} - \frac{\partial \tau_{ij}}{\partial x_j} + S_{M,i} \quad (4)$$

$$\frac{\partial}{\partial t} (\rho \bar{h}) + \frac{\partial}{\partial x_j} (\rho \bar{h} \bar{u}_j) = \frac{\partial}{\partial x_j} \left(k_{\text{eff}} \frac{\partial \bar{T}}{\partial x_j} \right) \quad (5)$$

2.2.Numerical Method

As it is known in a turbulent flow, small vortices are absorbed into energy, while large vortices are highly influenced by geometric parameters. These properties related to turbulent flows lead researchers to solve large-scale eddies and to model small vortices using the sub-grid scale (SGS) model. The basic feature of the LES model is to filter these vortices using the Navier-Stokes equations according to the size scale. With this method, Navier-Stokers equations are filtered according to their size and the fluctuations below a certain size are modeled. Fluctuations in the filtered size are resolved. Filtration is done by a defined filtering function. Filtering function defined by;

$$G(x-x') = \begin{cases} 1/\Delta, & |x-x'| \leq \Delta/2 \\ 0, & \text{otherwise} \end{cases} \quad (1)$$

Where Δ is the filter width. The wave length of the smallest scale is separated by the filter operator. The filter function decides the dimensions and structures of small scales. The desired variable is filtered by;

$$\bar{\phi}(x) = \int_{D_f} \phi(x') G(x-x') dx \quad (2)$$

where D_f is the fluid domain, and G is the filter function that determines the scale of the resolved eddies. After applying the filter operator, the mass conservation,

where \bar{u}_i , ρ , \bar{p} , $S_{M,i}$, \bar{h} and \bar{T} represent filtered velocity component, the density of fluid, filtered pressure, gravitational body force, filtered enthalpy, and temperature, respectively.

The SGS stress model derived from the filtration processes is unknown and needs to be modeled. The SGS turbulence models in FLUENT apply the Boussinesq hypothesis and are derived using the following equation.

$$\tau_{ij} - \frac{1}{3} \tau_{kk} \delta_{ij} = -2\mu_t \bar{S}_{ij} \quad (6)$$

It should be noted that Wall Adapting Local Eddy Viscosity (WALE) was used as the SGS model. This model is successfully used in modeling turbulent flows that flow through a confined channel. The swirl viscosity in the WALE model,

$$\mu_t = \rho L_s^2 \frac{(S_{ij}^d S_{ij}^d)^{3/2}}{(\overline{S_{ij} S_{ij}})^{5/2} + (S_{ij}^d S_{ij}^d)^{5/4}} \quad (7)$$

where S_{ij}^d is a deviatoric part of rate-of-strain tensor and L_s is the mixing length for sub-grid[25].

3. RESULTS AND DISCUSSION

Since the temperature oscillations in the mixing zone are sudden and random, it is very difficult to predict them. Therefore, such problems should be examined through a system rather than one-to-one point data. In this study, geometric and physical dynamics affecting the thermal mixing were studied extensively. For this purpose, the Mixing Index (MI) graphs, which give the thermal mixing yield in the channel, were plotted. Basically, MI graphs show how much temperature values measured in a given region deviate from the average temperature. MI is calculated by $MI = (S_T / \Delta T) \times 100$, where

$S_T = \sqrt{(\sum_{i=1}^n (T_i - T_{avg})^2) / (n - 1)}$ is the standard deviation of temperature at any measurement point. $MI = 0$ means a flat temperature profile which mean complete thermally mixed flow[26]. As shown in Figure 1, there are 64 temperature measurement points within the test channel. The temperature values are taken from these points for a flow time of 4 seconds at 0.01 second intervals. There are eight temperature measurement columns in the channel from left to right, and each column has eight measuring points. The MI graphs were obtained by using the temperature values of the measurement points in these columns. In MI graphs, the thermal mixing yield of each column is given as percentage. As the MI values approach

zero, the thermal mixture performance increases and $MI = 0$ represents the perfect thermal mixing.

There are two points that should be considered in the analysis of the thermal mixings problems. The first is the analysis of whether or not the temperature oscillations in the system have reached the channel walls. Secondly, if these oscillations reach the channel walls, then it should be determined whether or not this creates a risk of thermal stress. The result of the Power Spectral Density (PSD) determines amplitude of oscillations. It has seen that the PSD results are not much affected by the geometric parameters in similar boundary conditions. In previous studies, we obtained numerically and experimentally that the temperature oscillations in the active mixing zone were at 5 Hz frequency under similar boundary conditions [17,18,22,23].

In order to determine whether or not the temperature oscillations reach the channel walls, it is necessary to look at the isotherms. Also, to analyze the effects of the determined operating parameters on the flow behaviors in the channel, the velocity profiles are given with the streamlines. Consequently, the effects of the VGs used in the channel on the mean pressure behaviors along the channel are discussed in the last part of the findings.

3.1.Effects vortex generator type

In the previous chapters, comprehensive evaluations were made on the effects of thermal oscillations on industrial systems. The main purpose of this study is to control the temperature oscillations occurring in the crossflow- transverse jet combination and to obtain more homogeneous thermal mixtures in the mixing zone. For this purpose, vortex generator pairs were placed in the test channel before the jet entry as shown in Fig 1. Basically, two types of VG (rectangular and triangular) were selected, and their effects in the mixing zone were discussed. In Figure 6, the effects of VG types on the thermal mixing performance are given in comparison with the basic channel using MI graphs. The right and left figures depict MI variations of 2D (H20) and D (H10) for VGs height for Case 2, respectively.

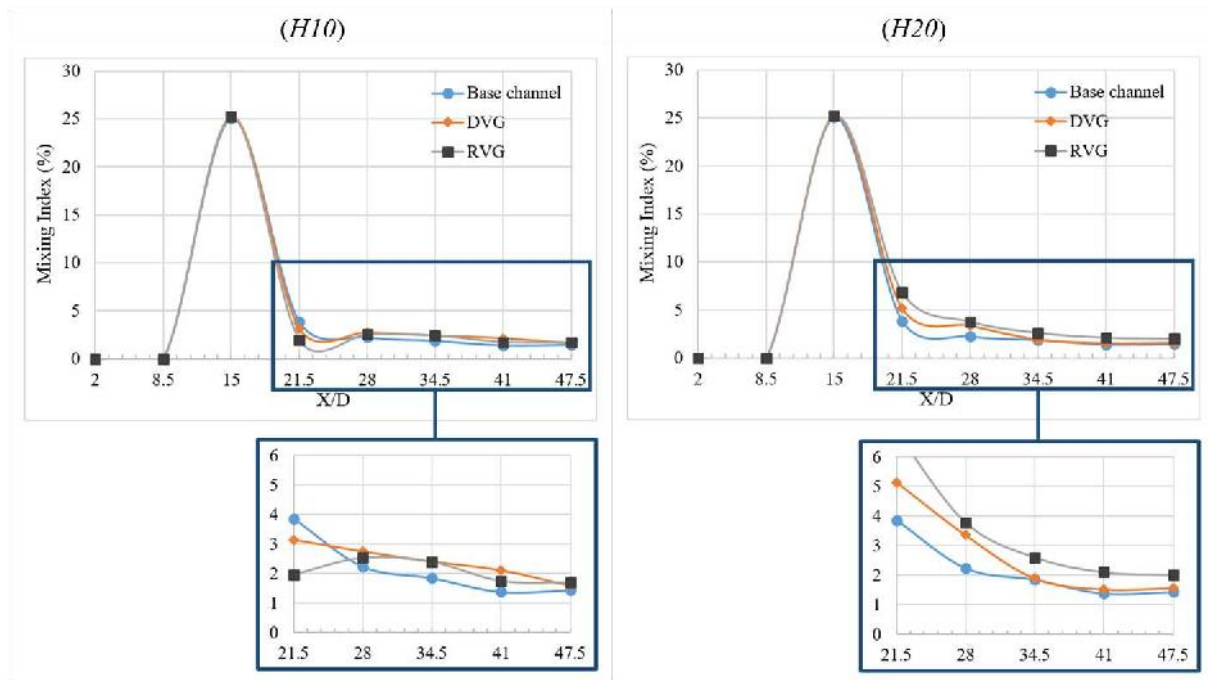


Figure 6. MI variations along the channel for Case 2 and different VG type

Interestingly, in the graphs, it is seen that the lowest MI results are in the basic channel condition in both cases. This indicates that the use of VG does not lead to an improvement in the thermal mixing as expected, but rather a relatively poor mixing performance. The lowest mix performance is seen in at low VG heights (H10) in the DVG case, and at increased VG heights (H20) in RVG case as seen from the figure from left to right, respectively. Figure 7 shows the

isotherms for the same boundary conditions. As seen, in the cases where VG is used, the hot fluid is clustered in the lower half of the channel. In Figure 8, streamlines and velocity profiles are given for the same parameters of Figure 6. In this case, the fluid velocity in the mixing zone increases, especially in increasing VG height conditions (as seen in the right column). This situation partially explains the situation seen above in MI graphs.

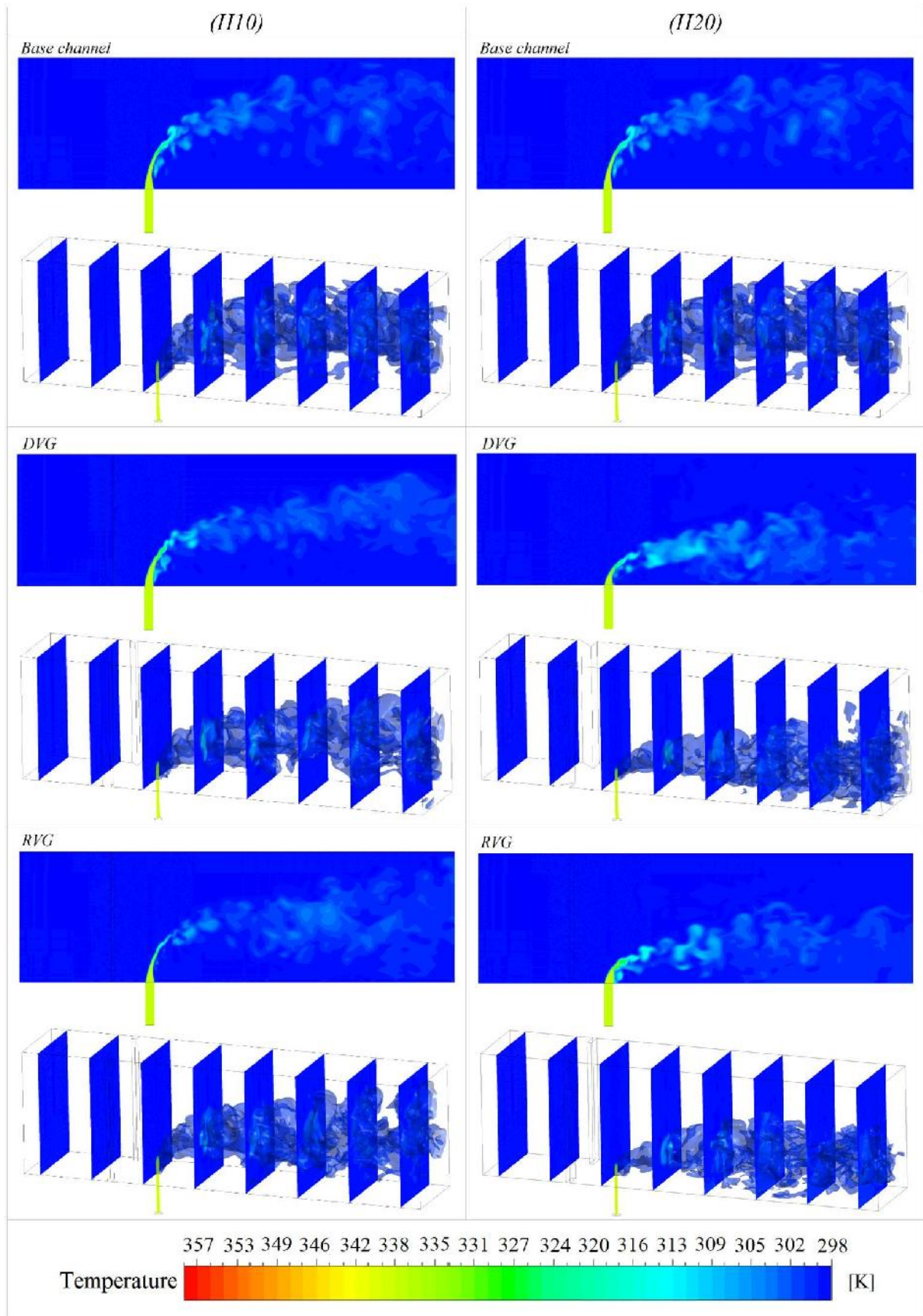


Figure 7. Isotherms for Case 2 and different VG type

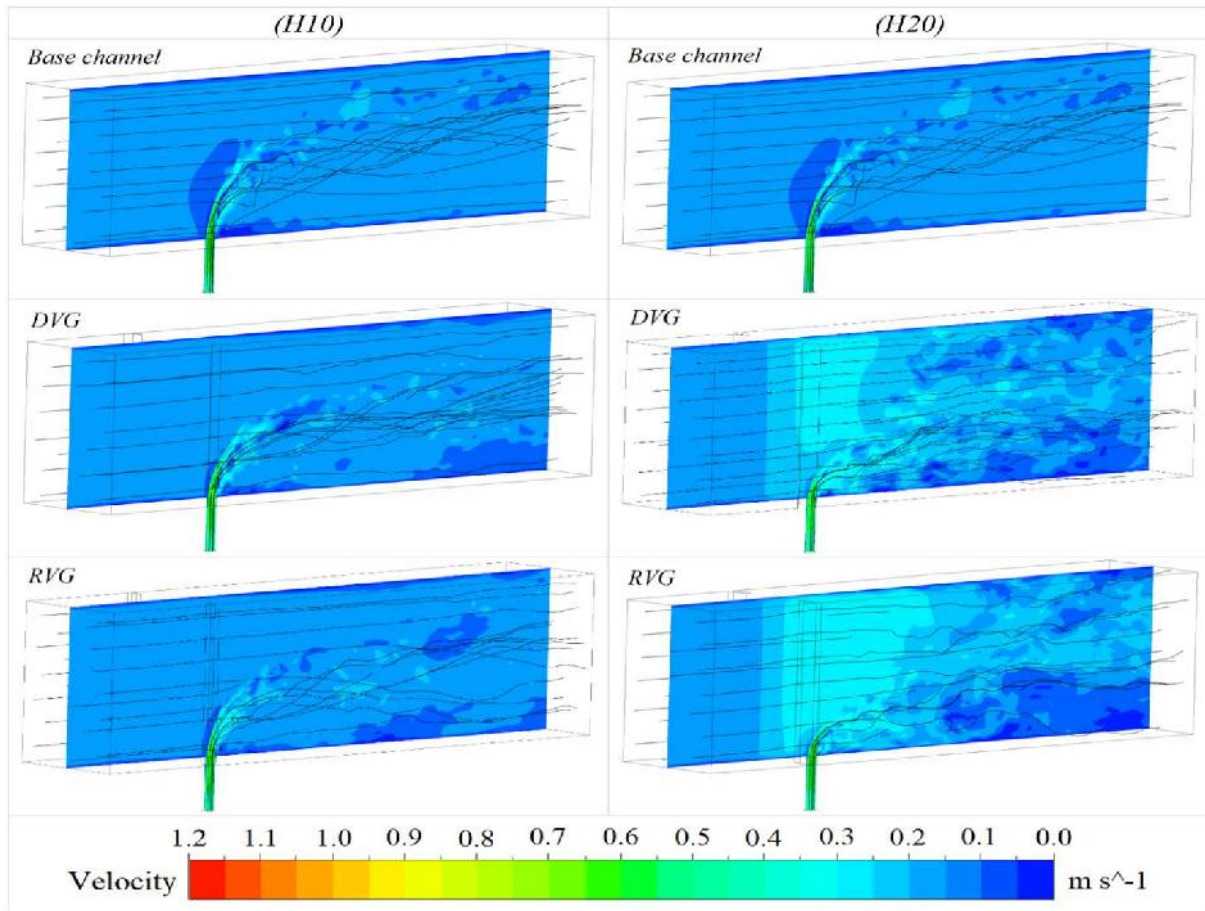


Figure 8. Streamlines and velocity profiles for Case 2 and different VG type

The increasing momentum of the fluid in the mixing zone prevents the hot fluid from being distributed throughout the channel and allows the hot fluid to clump at the bottom of the channel. Considering that the flow of the channel is turbulent as shown in Table 1, the use of VG does not create the expected vortex generation effect in the channel, but rather an extra momentum within the channel due to the narrowing section. Figure 9 shows the average pressure values along the channel for the same parameters. In parallel with the above results, with the use of VG, the fluid momentum has increased due to the narrowing section in the mixing zone and consequently, the pressure has decreased. As the VG height increases, the pressure drop in the mixing zone has increased as expected.

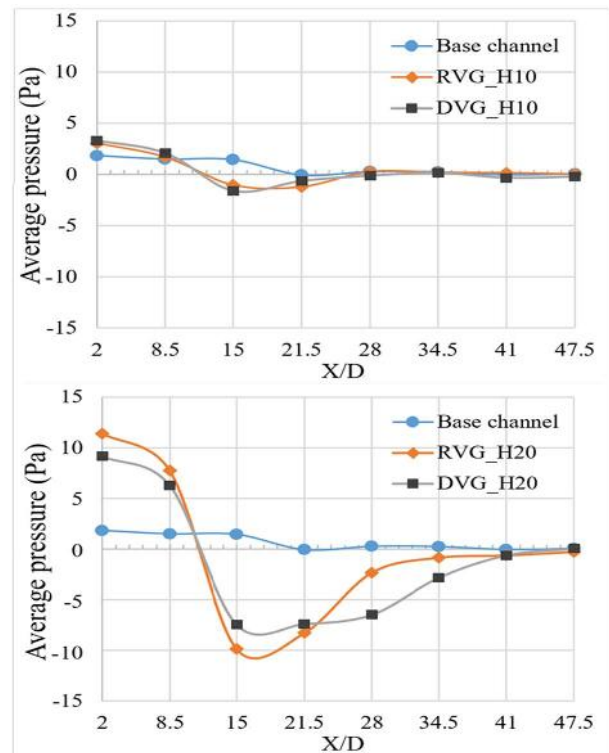


Figure 9. Average pressure along the channel for Case 2 and different VG type

1.1. Effects of vortex generator size

In this section, the height of VG pairs was selected as D (H10), 1.5D (H15) and 2D (H20), respectively, as shown in Figure 2. MI variations of different heights are given for Case 2 (left) and Case 8 (right) in Figure 10. As seen, the increased height of the VGs does not have a significant effect on the thermal mixture yield. In fact, as the VG height increases, a decrease in thermal mixing performance is observed and especially, as shown in the left figure H10 gives the best mixing efficiency. Figure 11 shows the isotherms for the same parameters. As seen, at low VG heights, the hot fluid reaches the opposite wall of the jet and causes thermal oscillations. However, as the VG height increases, due to the increased channel momentum (as seen in Figure 12), the hot fluid is shifting towards the lower regions of the channel.

As can be seen from the figures, the positive effects of VGs on the thermal mixture yield cannot be mentioned. But, with the use of VG, temperature fluctuations can be removed from the duct walls. This allows VGs to be used as a control mechanism in the systems. Figure 13 shows the average pressure changes across the channel for the same parameters of Fig 10. The situation shown here confirms the results given in Figure 12. As the VG height increases in the mixing zone, a decrease in the average pressure is observed. The use of VG gives the possibility of directing the thermal oscillations in the mixing zone. However, this situation clearly shows a pressure loss in the channel. VGs used in industrial mechanisms for controlling thermal oscillations will have an effect on the pump power used in the system. Therefore, these effects should be considered when using these tools.

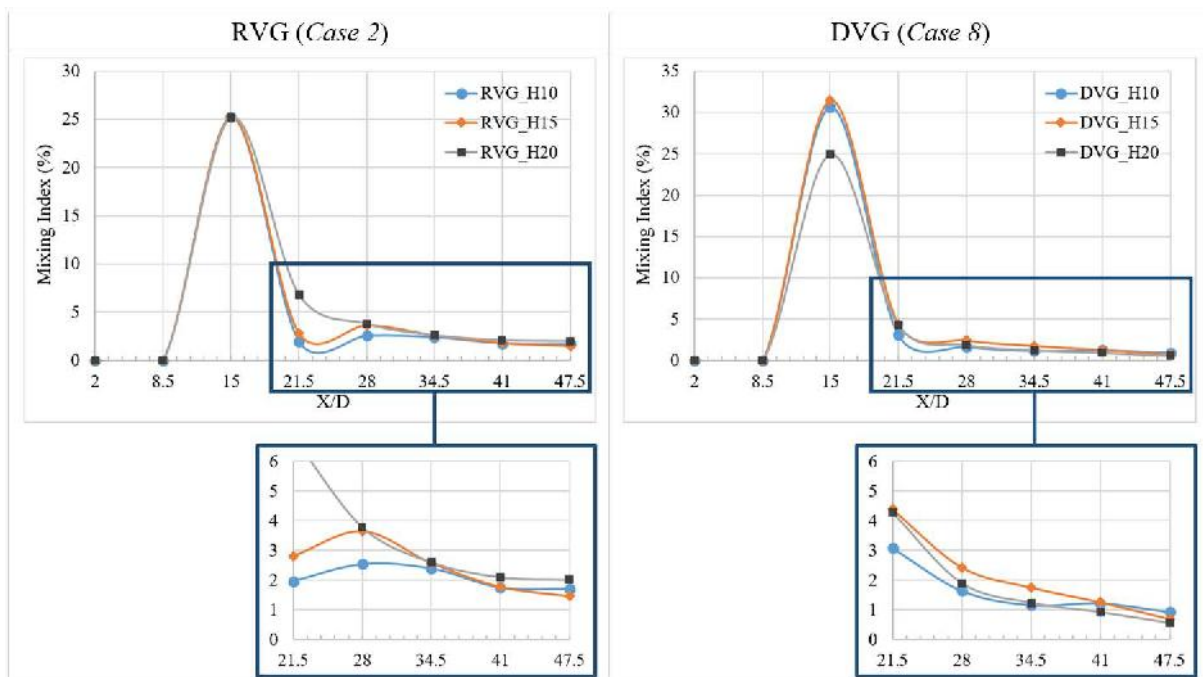


Figure 10. MI variations along the channel for different VG dimensions

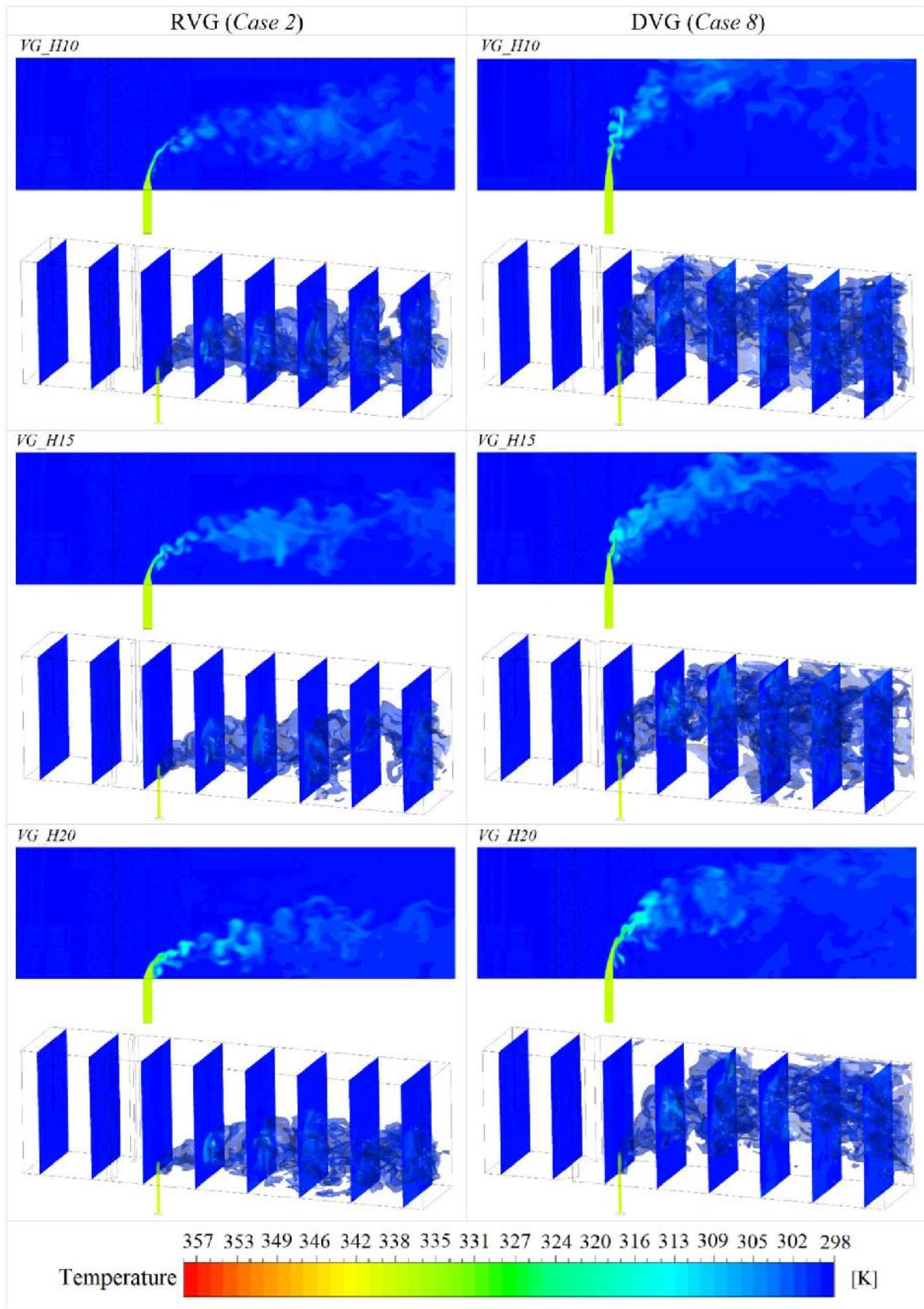


Figure 11. Isotherms for different VG dimensions

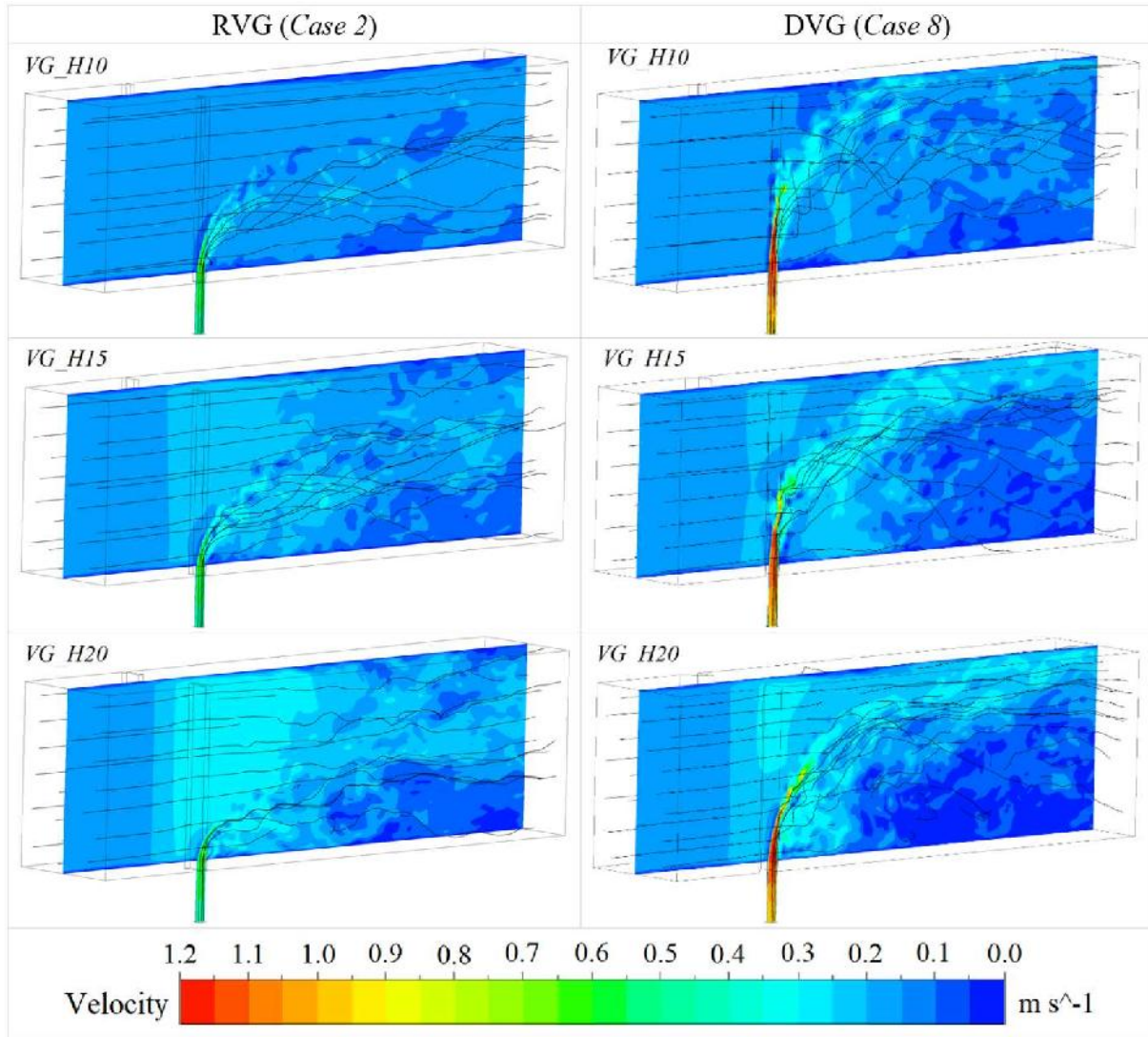


Figure 12. Streamlines and velocity profiles for different VG dimensions

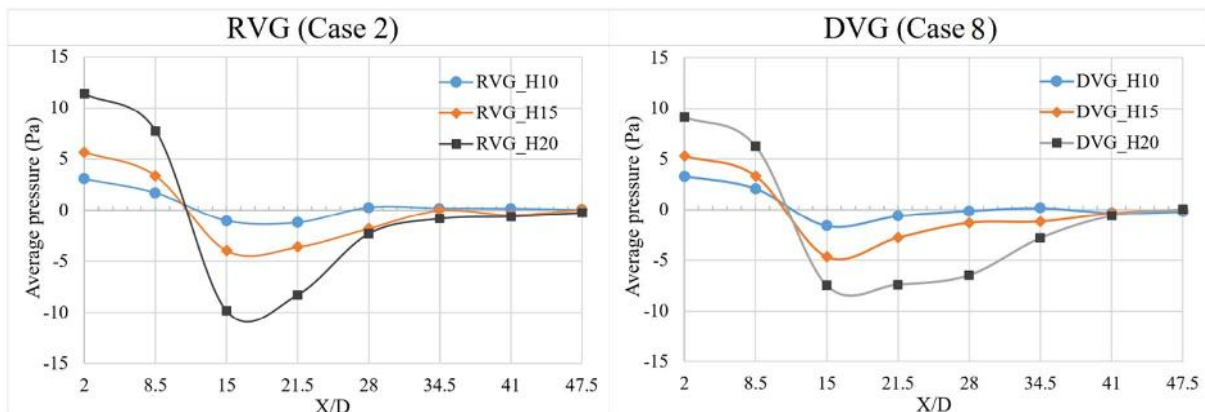


Figure 13. Average pressure along the channel for different VG dimensions

1.2. Effects of the flow rate ratio

There are nine boundary conditions in this study, as seen in Table 1. While the cross flow momentum is kept constant, the jet velocity increases gradually. This leads to the formation of three momentum ratios between the crossflow and the jet flow. Figure 14 shows the effects of different momentum ratios on the MI results for DVG_H20 (left) and Base channel (right). In both cases the results are given for $\Delta T = 40$ K. In the right figure, it is seen that the best thermal mixing yield is at $U_j / U_c = 5$ momentum ratio when the situation related to jet inlet zone is considered. Therefore, the increasing momentum ratio in the jet inlet region did not improve the thermal mixture. However, interestingly, as seen on the

left side, the effect of the momentum ratio in the jet inlet zone decreased to zero with the use of VG. As the jet momentum increases, it is clear that there is an improvement in the thermal mixture. In the continuing part of the channel, it is clear that there is an improvement in the thermal mixing as the jet momentum increases. However, as the jet velocity increases, the hot fluid reaches the channel walls and causes thermal oscillations as seen in Figure 15. It should not be noted that more hot fluid enters the channel as the momentum ratio increases. Therefore, the thermal mixing yield is expected to decrease. But, as seen in Figure 16, as the jet momentum increases, the turbulence density in the mixing zone increases and as a result, an improvement in thermal mixing performance is observed.

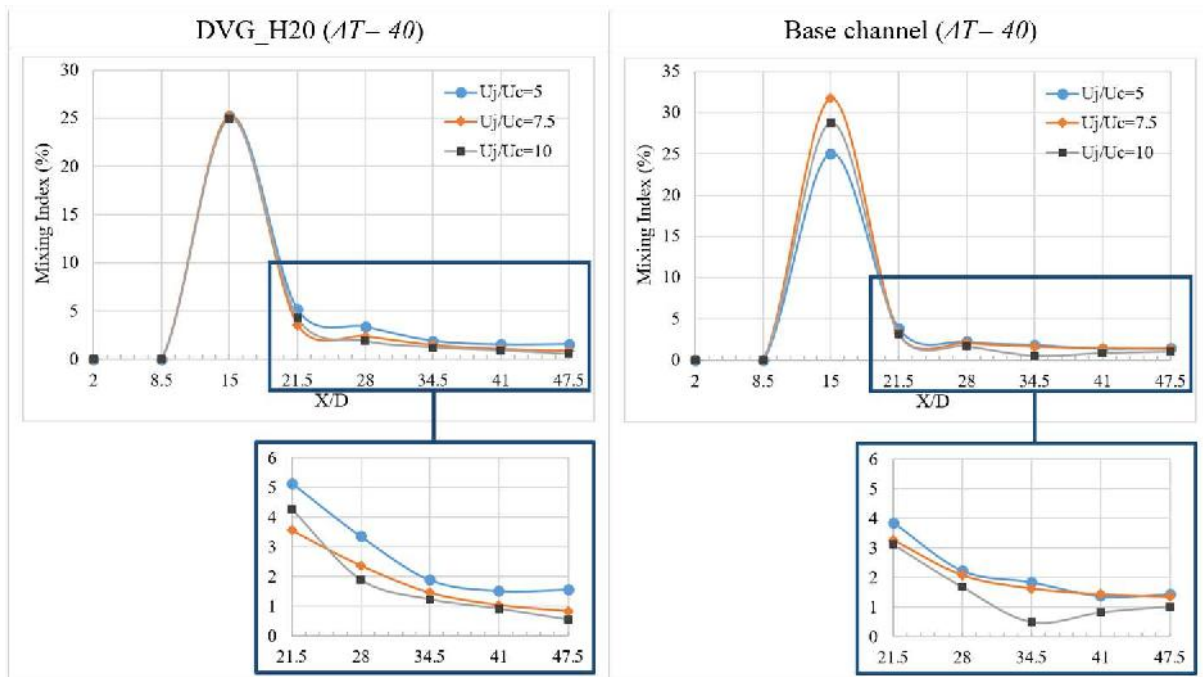


Figure 14. MI variations along the channel for different flow rate ratios

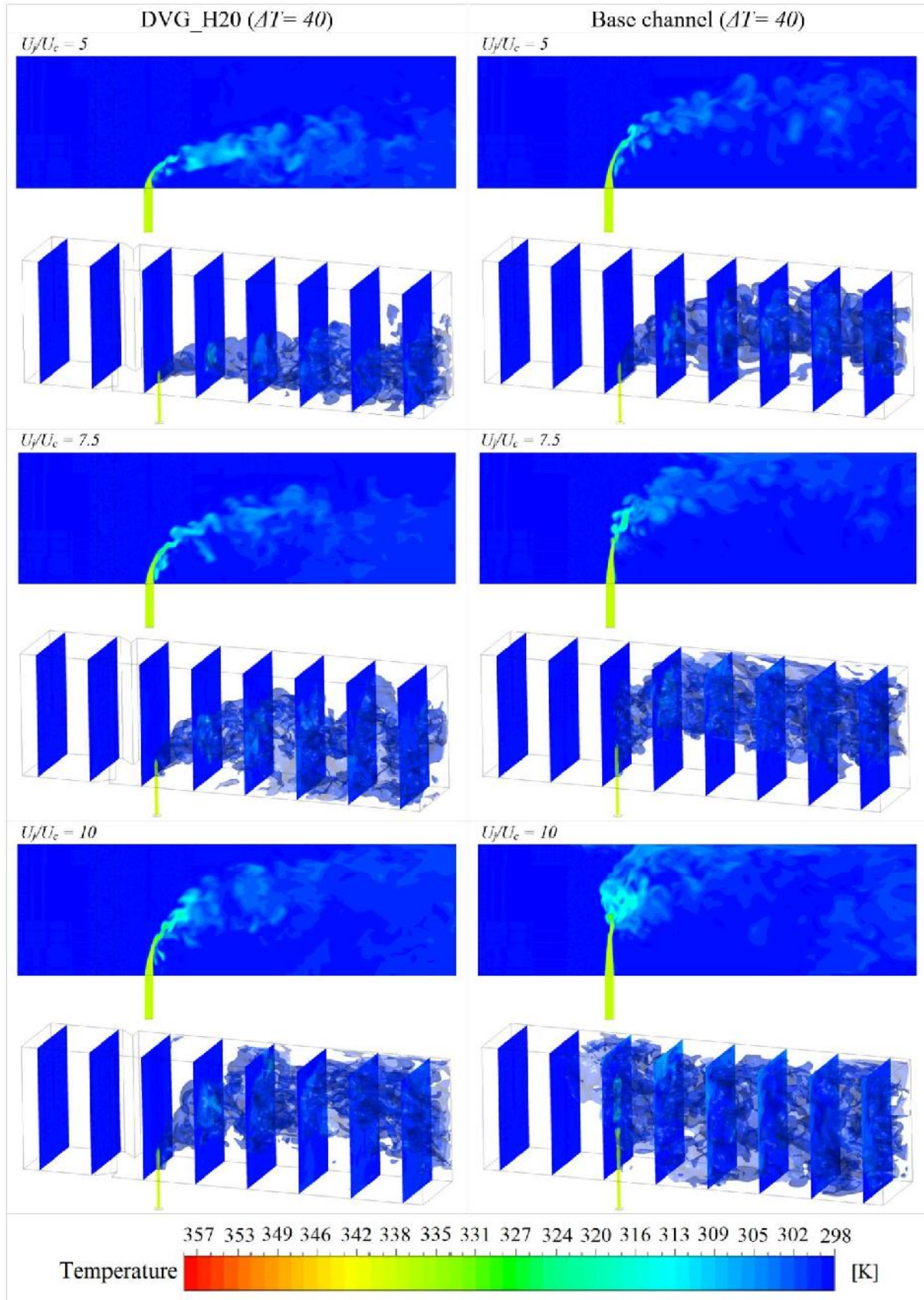


Figure 15. Isotherms for different flow rate ratios

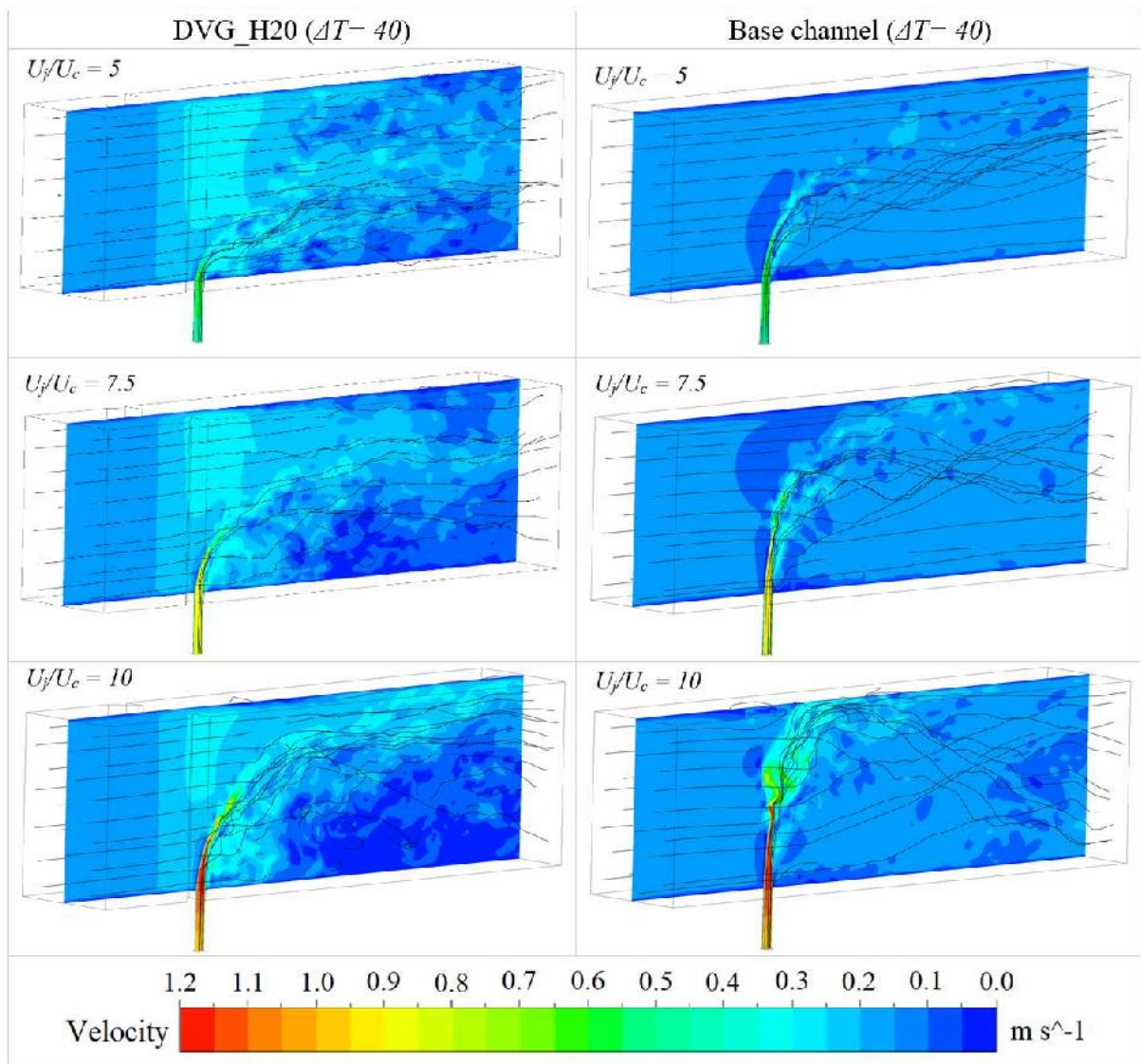


Figure 16. Streamlines and velocity profiles for different flow rate ratios

1.3. Effects of temperature difference

In this section, the effects of the temperature difference between crossflow and jet flow on thermohydraulic behaviors in the active mixing zone are discussed. As shown in Table 1, the crossflow temperature is kept constant while the jet flow temperature is gradually increased. Variations of MI for *DVG_H20* with $U_j/U_c=10$ (left) and Base channel with $U_j/U_c=5$ (right) are given in Figure 17. In both cases, the negative effects of increasing ΔT values

on the thermal mixture yield along the channel are clearly seen. As also seen in Figure 18, as the jet temperature increases, the dominance of the hot fluid increases in the channel, and as a result, a reduction in the thermal mixture yield occurs. Figure 19 shows the streamlines and velocity profiles for the same boundary conditions. As the temperature difference rises, a relative increase is seen in the turbulence density in the mixing zone, especially on the left side, is it due to decreasing viscosity values with temperature rise.

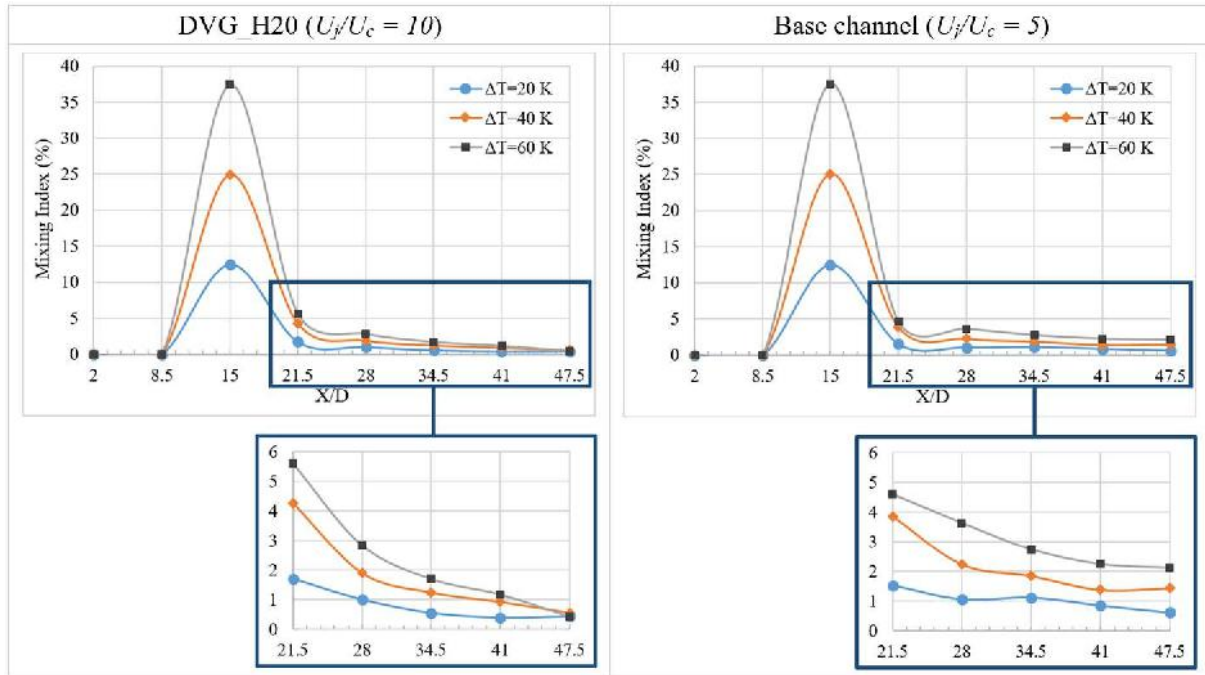


Figure 17. MI variations along the channel for different ΔT

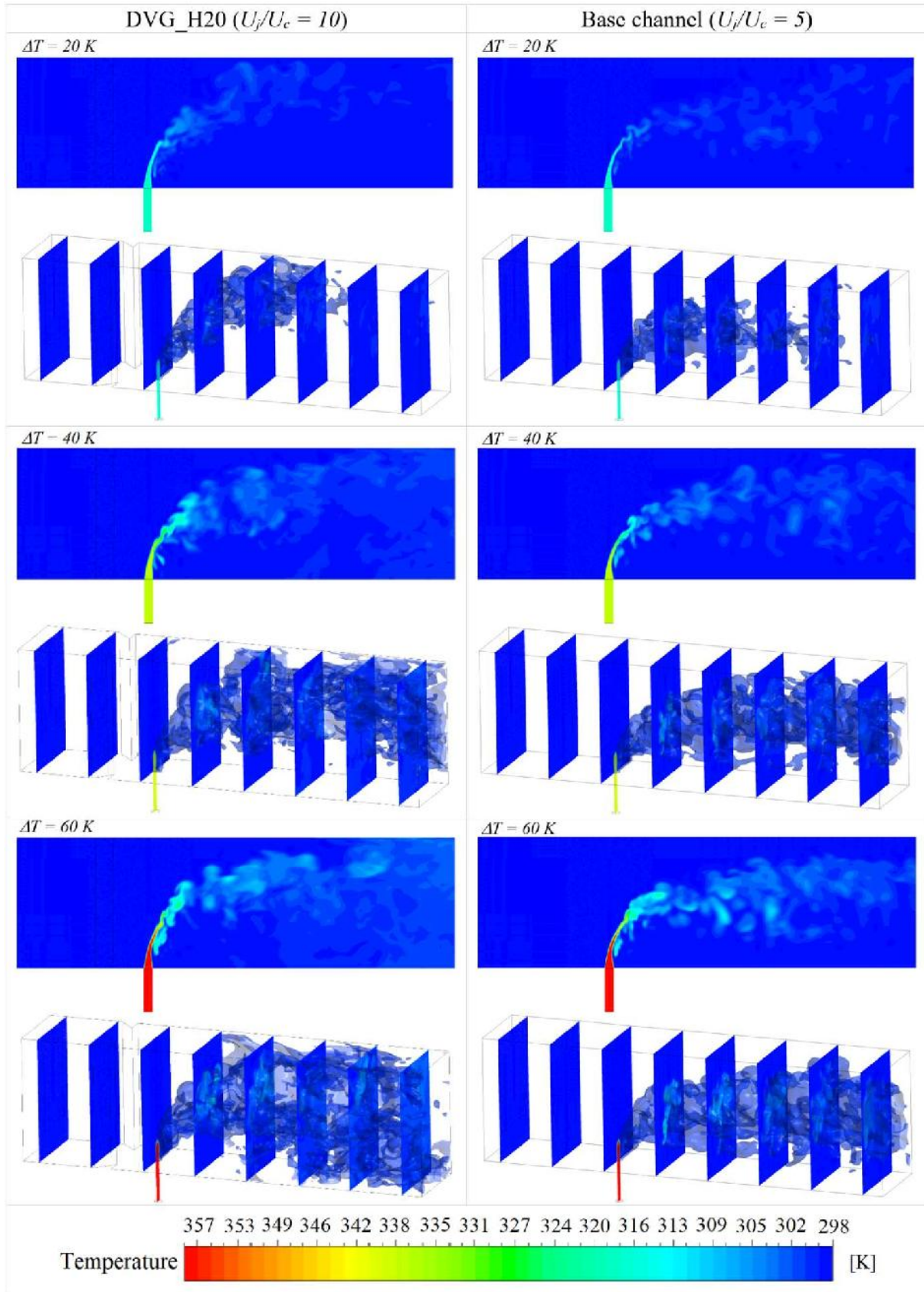


Figure 18. Isotherms for different ΔT

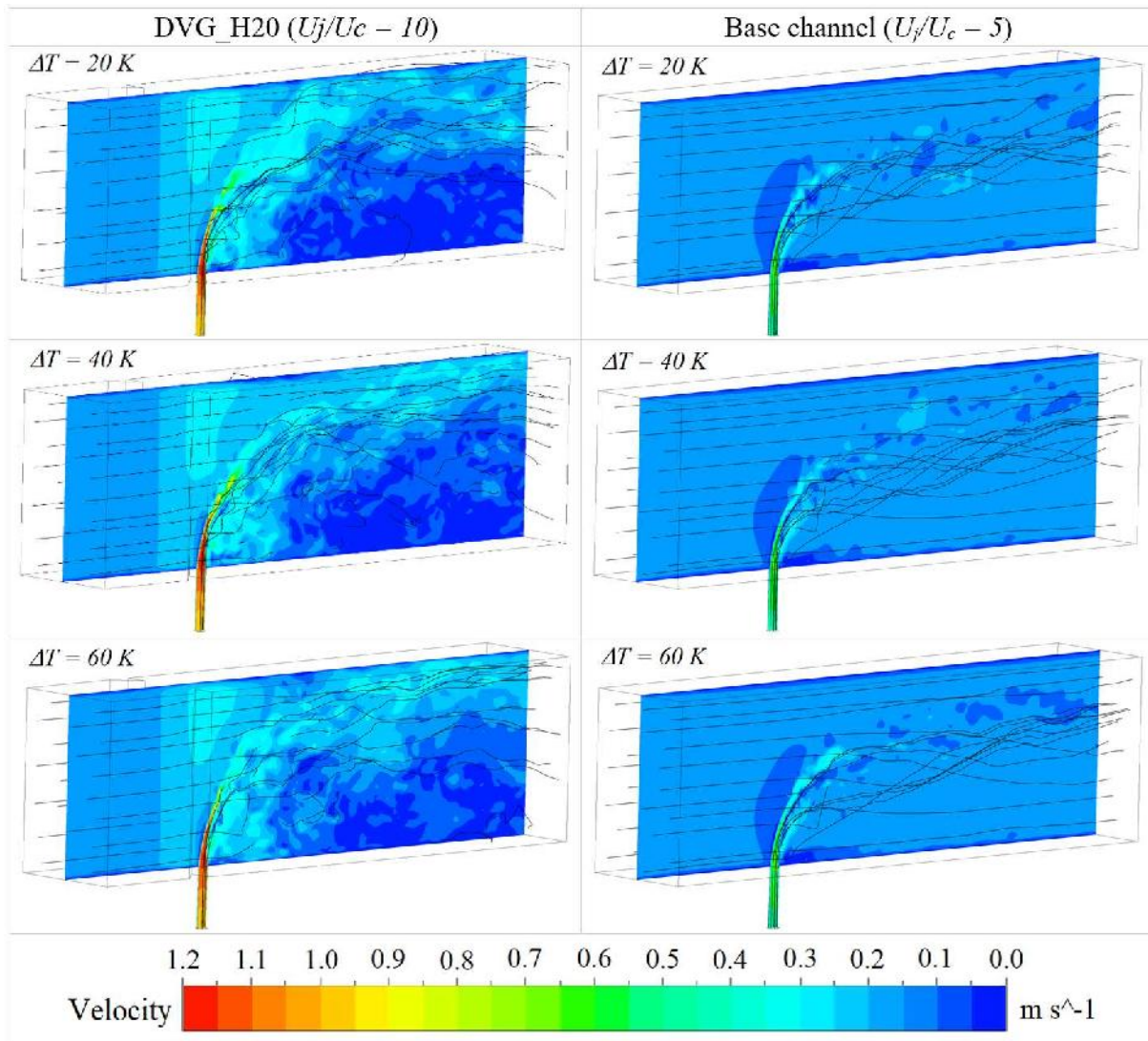


Figure 19. Streamlines and velocity profiles for different ΔT

2. CONCLUSIONS

In this study, the flow and thermal mixing characteristics of a transverse-jet flow in a crossflow channel were investigated using the LES turbulence model. Passive vortex generator (VG) pairs with different geometric properties were used to develop the fluid momentum and to control the thermal mixing performance in the test channel. In addition, nine boundary used in the analyzes. The results are discussed extensively in different aspects for four chapters.

In the first chapter, the effects of different types (rectangular and delta) VGs on the flow and thermal mixture characteristics in the active mixing zone are discussed. The results showed that the use of VG in a crossflow channel does not produce an improvement in the thermal mixing

behavior, as expected. There was no significant difference between the VGs of the same height with different geometric structure in the mixture region. It is thought that the turbulence of the flow regime is significantly effective in these results. In the second part of the results, the effects of VG height are discussed. As the VG height increased, a decrease in the thermal mixing performance was observed. In some analyzes conducted without the use of VG, it was observed that the temperature oscillations reached the channel walls. It was observed that with the use of the VGs, these oscillations shifted downward from the channel walls. This divergence trend continued to increase as the VG height increased. This has led to the idea that VGs can be used as a control parameter to control thermal oscillations. However, with the use of VG, the average pressure within the

channel was reduced as expected. In the third part of the study, the effects of the momentum ratio between the crossflow and the jet flow on the thermohydraulic properties of the fluid are discussed. By keeping the cross flow rate constant, the jet velocity is gradually increased. This increases amount of hot fluid inside the duct and develops turbulence density. This development in turbulence density zone led to an increase in thermal mixing performance in the effective mixing zone. In the last part of the study, the jet temperature was gradually increased while the crossflow temperature was kept constant. This process increased the dominance of the hot water in the channel and caused a decrease in the thermal mixing performance as expected. The turbulence density was relatively increased in the mixing zone due to the reduced viscosity as the jet temperature increased.

REFERENCES

- [1] International Atomic Energy Agency(IAEA), Liquid Metal Cooled Reactors: Experience in Design and Operation, Vienna, Austria, 2007.
- [2] E. Sakai, T. Takahashi, H. Watanabe, "International Journal of Heat and Mass Transfer Large-eddy simulation of an inclined round jet issuing into a crossflow," *International Journal of Heat and Mass Transfer.*, Vol. 69, pp. 300–311, 2014.
- [3] R. Deng, T. Setoguchi, H. Dong, "Large eddy simulation of shock vector control using bypass flow passage," *International Journal of Heat and Fluid Flow.*, Vol. 62, pp. 474–481, 2016.
- [4] C. Liu, Z. Wang, H. Wang, M. Sun, "Mixing characteristics of a transverse jet injection into supersonic crossflows through an expansion wall," *Acta Astronautica.*, Vol. 129, pp. 161–173, 2016.
- [5] G.Y. Chuang, Y.M. Ferng, "Experimentally investigating the thermal mixing and thermal stripping characteristics in a T-junction," *Applied Thermal Engineering.*, Vol. 113, pp. 1585–1595, 2017.
- [6] G.Y. Chuang, Y.M. Ferng, "Investigating effects of injection angles and velocity ratios on thermal-hydraulic behavior and thermal striping in a T-junction," *International Journal of Thermal Sciences.*, Vol. 126, pp. 74–81, 2018.
- [7] A. Mcguinn, D.I. Rylatt, T.S.O. Donovan, "Heat transfer enhancement to an array of synthetic air jets by an induced crossflow," *Applied Thermal Engineering.*, Vol. 103, pp. 996–1003, 2016.
- [8] C. Wang, L. Wang, B. Sundén, "International Journal of Heat and Mass Transfer A novel control of jet impingement heat transfer in cross-flow by a vortex generator pair," *International Journal of Heat and Mass Transfer.*, Vol. 88, pp. 82–90, 2015.
- [9] C. Wang, L. Luo, L. Wang, B. Sundén, "International Journal of Heat and Mass Transfer Effects of vortex generators on the jet impingement heat transfer at different cross-flow Reynolds numbers," *International Journal of Heat and Mass Transfer.*, Vol. 96, pp. 278–286, 2016.
- [10] D.G. Kang, H. Na, C.Y. Lee, "Detached eddy simulation of turbulent and thermal mixing in a T-junction," *Annals of Nuclear Energy.*, Vol. 124, pp. 245–256, 2019.
- [11] M. Zhou, R. Kulenovic, E. Laurien, "T-junction experiments to investigate thermal-mixing pipe flow with combined measurement techniques," *Applied Thermal Engineering.*, Vol. 150, pp. 237–249, 2019.
- [12] M. Kamaya, A. Nakamura, "Thermal stress analysis for fatigue damage evaluation at a mixing tee," *Nuclear Engineering and Design.*, Vol. 241, pp. 2674–2687, 2011.

- [13] J. Galpin, J.P. Simoneau, "Large Eddy Simulation of a thermal mixing tee in order to assess the thermal fatigue," *International Journal of Heat and Fluid Flow.*, Vol. 32, pp. 539–545, 2011.
- [14] Y. Shao, S. Deng, Z. Wang, Y. Zhang, P. Lu, L. Zhao, W. Xu, D. Zhao, "Analysis of pressure drop in T-junction and its effect on thermodynamic cycle efficiency," *Applied Energy.*, Vol. 231, pp. 468–480, 2018.
- [15] H. Ayhan, C.N. Sökmen, "CFD Modeling of Thermal Mixing In T-Junction: Effect of Branch Pipe Diameter Ratio, in: The 15th International Topical Meeting on Nuclear Reactor Thermal - Hydraulics," *NURETH-15*, Italy, p. 12. 2013.
- [16] B. Kok, M. Uyar, Y. Varol, A. Koca, H.F. Oztop, "Analyzing of thermal mixing phenomena in a rectangular channel with twin jets by using artificial neural network," *Nuclear Engineering and Design*. Vol. 265, pp. 554–565, 2013.
- [17] B. Kok, Y. Varol, H. Ayhan, H.F. Oztop, "Experimental and computational analysis of thermal mixing characteristics of a coaxial jet," *Experimental Thermal and Fluid Science.*, Vol. 82, pp. 276–286, 2017.
- [18] B. Kok, Y. Varol, H. Ayhan, H.F. Oztop, S.G. Demiryurek, "Experimental Investigation of Thermal-Mixing Phenomena of a Coaxial Jet with Cylindrical Obstacles," *Journal of Thermophysics and Heat Transfer.*, Vol. 32, pp. 1–11, 2018.
- [19] B. Kok, M. Firat, H.F. Oztop, Y. Varol, "A numerical study on thermal mixing in narrow channels inserted rectangular bodies," *International Communications in Heat and Mass Transfer.*, Vol. 44, pp. 69–76, 2013.
- [20] B. Kok, Y. Varol, H.F. Oztop, A. Koca, "Analysis of thermal mixing in circle shaped body inserted inclined channel," *Experimental Thermal and Fluid Science.*, Vol. 68, pp. 1–10, 2015.
- [21] Y. Varol, B. Kok, H.F. Oztop, I. Turkbay, "An experimental study on thermal mixing in a square body inserted inclined narrow channels," *International Communications in Heat and Mass Transfer.*, Vol. 39, pp. 1245–1252, 2012.
- [22] Y. Varol, B. Kok, H. Ayhan, H.F. Oztop, "Experimental study and Large Eddy Simulation of thermal mixing phenomena of a parallel jet with perforated obstacles," *International Journal of Thermal Sciences.*, Vol. 111, pp. 1–17, 2017.
- [23] B. Kok, Y. Varol, H. Ayhan, H.F. Oztop, "Experimental study and large Eddy simulation of a coaxial jet with perforated obstacles to control thermal mixing characteristics," *Experimental Heat Transfer.*, Vol. 31, pp. 161–182, 2018.
- [24] J. Westin, F. Alavyoon, L. Andersson, P. Veber, M. Henriksson, C. Andersson, "Experiments and Unsteady CFD-Calculations of Thermal Mixing in a T-Junction, Proceedings of OECD/NEA/IAEA Workshop on the Benchmarking of CFD Codes for Application to Nuclear Reactor Safety," *CFD4NRS, Munich Germany.*, Vol. 1, pp. 1–15, 2006.
- [25] I. ANSYS, ANSYS Fluent 15.0 User's Guide, ANSYS, Inc., Canonsburg, 2014. <http://www.ansys.com>.
- [26] S.J. Wang, S. Devahastin, A.S. Mujumdar, "Effect of temperature difference on flow and mixing characteristics of laminar confined opposing jets," *Applied Thermal Engineering.*, Vol. 26, pp. 519–529, 2006.

JOURNAL OF SCIENCE



SAKARYA UNIVERSITY

Sakarya University Journal of Science

ISSN 1301-4048 | e-ISSN 2147-835X | Period Bimonthly | Founded: 1997 | Publisher Sakarya University |
<http://www.saujs.sakarya.edu.tr/>

Title: Imposed Source Current Predictive Control For Battery Charger Applications With Active Damping

Authors: Mustafa Gökdağ, Ozan Gülbudak

Received: 2019-03-21 19:11:05

Accepted: 2019-05-21 13:20:33

Article Type: Research Article

Volume: 23

Issue: 5

Month: October

Year: 2019

Pages: 964-971

How to cite

Mustafa Gökdağ, Ozan Gülbudak; (2019), Imposed Source Current Predictive Control For Battery Charger Applications With Active Damping. Sakarya University Journal of Science, 23(5), 964-971, DOI: 10.16984/saufenbilder.543070

Access link

<http://www.saujs.sakarya.edu.tr/issue/44066/543070>

New submission to SAUJS

<http://dergipark.gov.tr/journal/1115/submission/start>



Imposed Source Current Predictive Control for Battery Charger Applications with Active Damping

Mustafa Gökdağ^{*1}, Ozan Gülbudak²

Abstract

This paper presents an imposed source current control technique based on model predictive control. This proposed control method can be used for battery charger applications fed from three-phase ac grid. The proposed MPC technique allows to charge the battery with a constant current or voltage as what is required for cyclic charge process of batteries. The proposed technique ensures unity input power factor operation for grid side. The single-objective cost function of the predictive control employs the error between supply current reference and supply current prediction and the switching state that makes this user defined cost function minimal is selected among the nine switching vector combinations of the current source rectifier so as to apply for next sampling interval. An active damping current term, that is predicted from the input filter capacitor voltage estimation is included in the cost function to alleviate the resonance phenomenon of input LC filter. The supply current references in phase with grid voltages are generated from grid voltages and the amplitude of this reference currents are generated from the charging requirements of the battery. The input filter model is used to predict the filter capacitor voltages at sampling intervals k and $k+1$ in order to eliminate sensor requirement for them. The control performance of proposed predictive controller is validated by simulation works in terms of steady-state behavior, dynamic response and supply current THD.

Keywords: current source rectifier, battery charger, model predictive control, active damping

1. INTRODUCTION

The three-phase Current Source Rectifier (CSR) can be used as battery charger in electric vehicle and data center applications. LC filters are used for improving input and output current and voltage

qualities by eliminating the unwanted frequency components.

In the control of CSRs, two main objectives are considered:

* Corresponding Author: mgokdag@karabuk.edu.tr

¹ Karabuk Univ., Dept. Of Electr-Electron. Eng., Karabuk, Turkey. ORCID: 0000-0001-5589-2278

² Karabuk Univ., Dept. Of Electr-Electron. Eng., Karabuk, Turkey. ORCID: 0000-0001-9517-3630

- 1) To obtain unity power factor operation with low Total Harmonic Distortion (THD);
- 2) To regulate output voltage or current depending on applications.

The conventional control algorithm of CSR includes two control loops, one as an outer loop to regulate the output voltage and another one as an inner loop to control the output current. The control algorithm with the input filter compensation employs conventional space vector pulse width modulation (SVPWM) with six sectors to obtain regulated output voltage/current for load side and unity power factor with low THD for grid side. The Switching Loss Optimized (SLO) modulation scheme with 12-symmetric sectors has been used in order to reduce switching losses resulting in high converter efficiency [1]. In this rectifier, grid currents can be highly-polluted by any system harmonics as a result of resonance phenomenon of the LC filter placed at the input side of rectifier. To overcome this issue, active damping techniques are included in feedback control strategy of CSRs [2], [3].

The model predictive control (MPC) approach has emerged as an alternative to linear control techniques for power electronics topologies over the last decade [4]–[6]. MPC with imposed sinusoidal input currents is a technique for grid connected topologies such as direct matrix converters and current source rectifiers in order to obtain unity power factor operation. In this strategy the control algorithm imposes the converter to draw a source current having a sinusoidal waveform and being in phase with its respective source voltage [7], [8]. In [9], an MPC approach whose cost function employs dc link current and the supply currents in $\alpha\beta$ coordinates has been proposed. Since the cost function includes two objectives, the use of weighting factor is unavoidable. This method requires the load model to predict the future load currents and requires the sector information for supply current space vector reference. In [10], a predictive control scheme, which is capable to operate the rectifier at very low switching frequency, has been proposed. Supply currents in $\alpha\beta$ coordinates are predicted for next two sampling intervals using the input filter and converter models. Reference source currents are produced from the first harmonic components of

the grid voltage. The amplitudes of these sinusoidal currents are derived from a DC load current error using a PI controller. A Phase Locked Loop (PLL) is employed to predict the supply voltages for next two sampling intervals. In [9], [10] active damping is not included in the proposed control techniques. In [11], a predictive control scheme for a CSR, that does not include output filter capacitor C_o , has been proposed and the cost function involves two terms; the first one is for minimizing reactive power drawn from the grid in order to obtain unity power factor and second term is responsible for the reference load current. Active damping current term is also added to the reference load current. The second term requires the load model to predict the load current at next sampling period. These two goals are combined into a single cost function with weighting factors. In [12], a model predictive PF control scheme for CSRs has been proposed to handle input Power Factor (PF) and LC resonance. The technique is based on the idea that reactive power reference estimator is used to obtain unity power factor and active damping method is adapted for LC resonance mitigation. But a lot of complexity is included for capacitive current compensation in order to eliminate the adverse effect of damping current on input PF regulation.

In this study, a model predictive scheme with active damping to simultaneously compensate the output control variable and input PF of a CSR is presented. The outline of the paper is as follows. The CSR topology and system model are defined in section 2. Proposed model predictive control is presented in section 3 and active damping technique associated with the control strategy is explained in section 4. The simulation results for proposed model predictive control are provided in section 5 in terms of input PF, supply current quality and reference tracking. The paper is concluded by section 6 describing the proposed control scheme and the results in brief.

2. SYSTEM AND PREDICTION MODELS

2.1. Current Source Rectifier Topology

The CSR, shown in Fig. 1, is a three-phase buck-type rectifier, which contains six unidirectional power switches. Output filter is usually used for eliminating high frequency component in order

that output voltage and current will have better quality. The input LC filter is used for get rid of disturbances from three-phase ac grid. Due to constraints in the control of rectifier, there are only nine allowable switching vectors for this topology in which three of them are zero vectors.

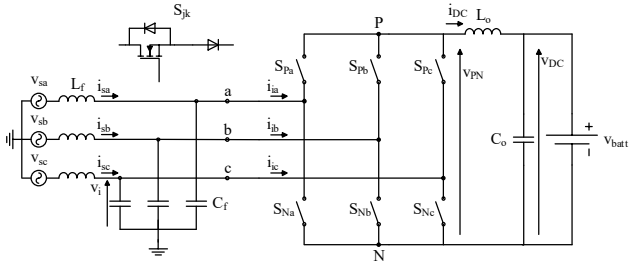


Figure 1. Current Source Rectifier

2.2. Rectifier Model

The output voltage, v_{PN} , and input current, \mathbf{i}_i , are given by (1) and (2).

$$v_{PN} = \begin{bmatrix} S_{pa} - S_{na} & S_{pb} - S_{nb} & S_{pc} - S_{nc} \end{bmatrix} \begin{bmatrix} v_{ia} \\ v_{ib} \\ v_{ic} \end{bmatrix} \quad (1)$$

$$= \mathbf{T}_{CSR} \mathbf{v}_i$$

and

$$\begin{bmatrix} i_{ia} \\ i_{ib} \\ i_{ic} \end{bmatrix} = \begin{bmatrix} S_{pa} - S_{na} & S_{pb} - S_{nb} & S_{pc} - S_{nc} \end{bmatrix}^T i_{DC} \quad (2)$$

$$\mathbf{i}_i = \mathbf{T}_{CSR}^T i_{DC}$$

where \mathbf{T}_{CSR} is the instantaneous transfer function related to CSR topology. This transfer function can be used for describing different electrical quantities. The relationship between DC current and input current is defined in (2).

2.3. Prediction Model

In this work, input filter parameters are used to derive supply current prediction model, and input current and input voltage are measured to predict future behavior of supply current. The discrete-time model of input LC filter is defined in (3).

$$\begin{bmatrix} \mathbf{v}_i(k+1) \\ \mathbf{i}_s(k+1) \end{bmatrix} = \mathbf{\Phi} \begin{bmatrix} \mathbf{v}_i(k) \\ \mathbf{i}_s(k) \end{bmatrix} + \mathbf{\Gamma} \begin{bmatrix} \mathbf{v}_s(k) \\ \mathbf{i}_i(k) \end{bmatrix} \quad (3)$$

The filter model defined in (3) is used to calculate future value of supply current for the next time interval. Supply current prediction is given by (4) and filter capacitor voltage prediction is given by (5).

$$\mathbf{i}_s(k+1) = \mathbf{\Phi}(2,1)\mathbf{v}_i(k) + \mathbf{\Phi}(2,2)\mathbf{i}_s(k) \quad (4)$$

$$+ \mathbf{\Gamma}(2,1)\mathbf{v}_s(k) + \mathbf{\Gamma}(2,2)\mathbf{i}_i(k)$$

$$\mathbf{v}_i(k) = \mathbf{\Phi}(1,1)\mathbf{v}_i(k-1) + \mathbf{\Phi}(1,2)\mathbf{i}_s(k-1) \quad (5)$$

$$+ \mathbf{\Gamma}(1,1)\mathbf{v}_s(k-1) + \mathbf{\Gamma}(1,2)\mathbf{i}_i(k-1)$$

In order to reduce the number of required sensors, the input filter capacitor voltages at sampling interval k can be estimated using the measurements of supply voltages and currents at sampling interval $k-1$. In this case, input currents of the rectifier $\mathbf{i}_i(k-1)$ are calculated from the optimal switching vector and measured output inductor current at sampling interval $k-1$. By this modification, the voltage sensors for input filter capacitors can be eliminated.

2.4. Battery Model

The resistance-capacitance battery model developed at National Renewable Energy Lab. of US is shown in Fig. 2. C_b is the main storage capacity and C_c is the fast charge-discharge capacitance. Values for these parameters are as following: $C_b=82\text{kF}$, $C_c=4.074\text{ kF}$, $R_b=1.1\text{ m}\Omega$, $R_c=0.4\text{ m}\Omega$ and $R=100\text{ m}\Omega$ [13].

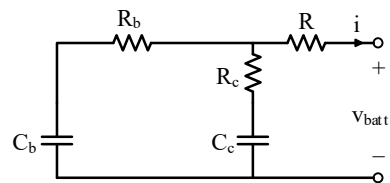


Figure 2. Battery Model

3. MODEL PREDICTIVE CONTROL

The proposed control approach is illustrated in Fig. 3. The supply voltage vector \mathbf{v}_s , supply current

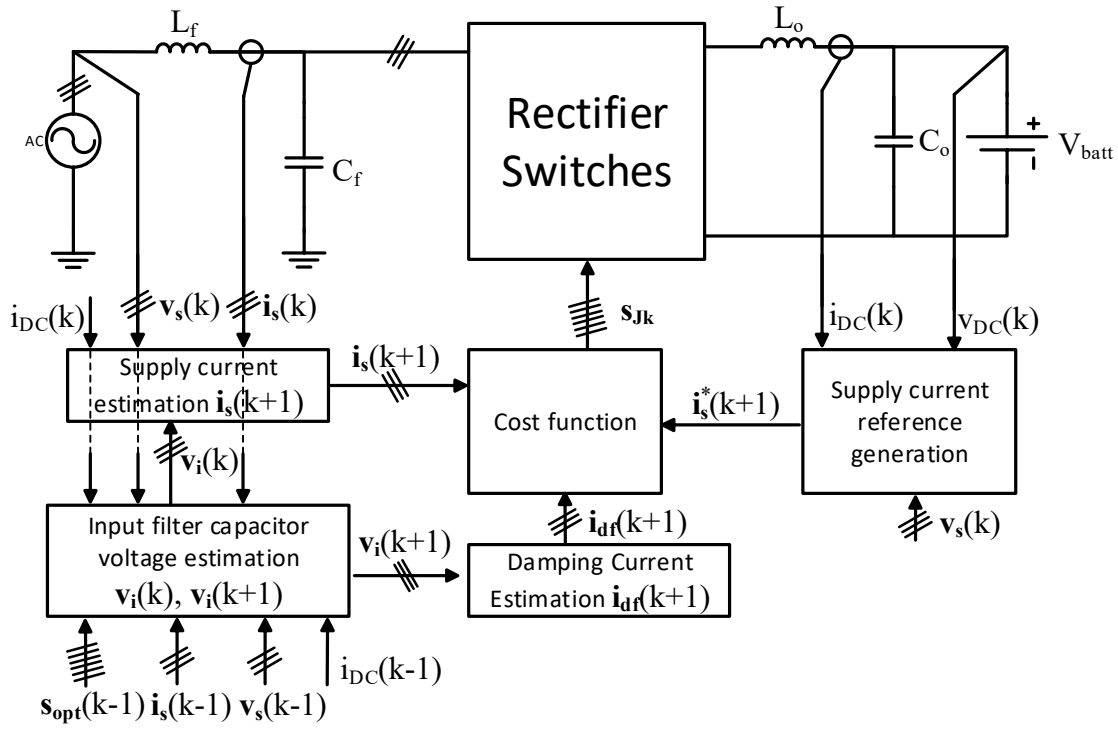


Figure 3. Model Predictive Control Scheme

vector \mathbf{i}_s , load voltage v_{DC} , and the output current i_{DC} are measured at instant k . These measurements are then used for the prediction of input filter capacitor voltages at instants k and $k+1$, and supply currents at instant $k+1$. Active damping term of the proposed control is included in model predictive control strategy and will be explained in the following section. The cost function defined in (6), where $\mathbf{i}_s^*(k+1)$ and $\mathbf{i}_s(k+1)$ reference and predicted supply currents respectively, calculates the error in supply currents with respect to corresponding supply current references which are generated in phase with grid voltages. The most critical point about cost function, any cost term related to the load is not introduced in this cost function. This is significant advantage for controlling the system under unknown load condition. The best switching states that minimizes the user defined cost function, see Eq. (6), is applied to the CSR system. This iterative technique is repeated in every sampling step.

$$g = \sum_{j=a,b,c} |i_{sj}^*(k+1) - i_{sj}(k+1)|^2 \quad (6)$$

In order to generate sinusoidal supply current references in phase with grid voltages, this paper uses the reference generation block shown in Fig.

4. In a cyclic charge process, the battery is either charged by a constant current (CC) or a constant voltage (CV). According to CC or CV charging, the reference charge current or voltage are assumed to be known and these reference commands can be used to generate a constant, m , which is used as a multiplier to convert the supply voltage measurements to current references. In order to eliminate the steady-state errors in charge current or charge voltage, two PI compensators are added to this control scheme. If the battery is charged by CV, the error between reference charge voltage and output voltage v_{DC} is fed to a PI compensator in order to generate a current reference and then another PI compensator, that is fed by error in charge current, is used to generate the constant, m .

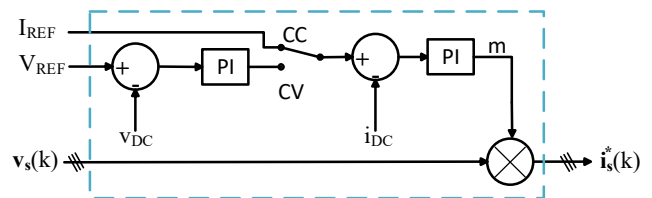


Figure 4. Supply current reference generation block

4. ACTIVE DAMPING

Since the input LC filter of a CSR is lightly damped, resonance mode of this filter can be

excited by any harmonic that interferes from the utility or the rectifier itself and this results in highly polluted grid currents [3]. A damping resistor placed parallel to the input filter capacitor can be used to mitigate this resonance at the expense of a large drop in efficiency. In order to increase the efficiency to a reasonable level, the function of a resistance can be emulated by the rectifier, which is called active damping. Active damping forces the rectifier to draw a current proportional to the filter capacitor voltage. The dc component of the damping current causes an active power flow to the rectifier and has an adverse effect on the active power control. A simple High Pass Filter (HPF) can be used to filter the dc component of the damping current and allows the passage of the fundamental component.

Since the imposed source current method was adopted in MPC scheme of this study, the active damping technique was considered slightly different from the above conventional active damping. Instead of forcing the rectifier to draw high pass filtered current terms, which is proportional to the filter capacitor voltage, these currents were injected into the sinusoidal supply current references. To avoid distorting the active and reactive power components drawn from the grid, dc and fundamental components of these currents must be eliminated using an HPF.

Active damping scheme is depicted in Fig. 5. Since the MPC has a predictive nature, the estimated values for sampling time interval of $k+1$ are used in this scheme. Input filter capacitor voltage at sampling interval of $k+1$ is estimated using the one-step ahead shifted version of (5). This estimated value is then employed in (7) to calculate damping current term $i_d(k+1)$. An HPF, whose 3-dB bandwidth is set to 600 Hz, is used to alleviate dc and fundamental components of the damping currents and to generate the filtered version of damping current term, $i_{df}(k+1)$. In this paper a simple first-order HPF is used. If an HPF with a sharper frequency response (with a stopband of 80 Hz and passband of 100 Hz) is used, a better active damping effect can be achieved to eliminate the third and fifth order components. The transfer function of the HPF in continuous time is given in (8) and discrete version of the filter is provided in (9). The filtered damping current term is then included in the modified cost function as given by

(10) in order to inject damping current term into sinusoidal references.

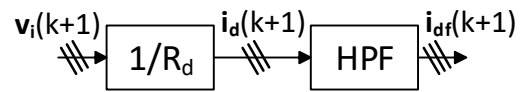


Figure 5. Damping current estimation scheme

$$i_d(k+1) = \frac{v_i(k+1)}{R_d} \quad (7)$$

$$\text{HPF}(s) = \frac{2.6526e-04s}{1 + 2.6526e-04s} \quad (8)$$

$$i_{df}(k+1) = 0.8115 i_{df}(k) + i_d(k+1) - i_d(k) \quad (9)$$

$$g = \sum_{j=a,b,c} |i_{sj}^*(k+1) + i_{df}(k+1) - i_{sj}(k+1)|^2 \quad (10)$$

5. SIMULATION RESULTS

In order to validate the functionality of the proposed framework, several simulation works are performed. All simulation works are done by using Matlab/Simulink. Table 1 lists the parameters used in simulation study.

Table 1. Simulation Parameters

Parameter	Description	Values
T_s	Sampling Period	50 μ s
R_d	Damping Resistance	50 Ω
L_o	Output Inductance	10 mH
L_i	Input Inductance	10 mH
C_o	Output Capacitance	100 μ F
L_r	Input Inductance	2 mH
C_f	Input Capacitance	120 μ F
R_f	Inp. Filt. Damp Resistance	1 Ω
V_s	Supply Peak Voltage	100 V

The results presented in Fig. 6 are obtained when CC charging is used for reference generation. Fig. 6 shows supply voltage and current for phase-a, output current of the rectifier i_{DC} and supply power components for the case in which a 90V-battery is charged from the grid according to the predefined charge current reference command. As it is observed from Fig. 6, the proposed control scheme ensures unity power factor operation and achieves good reference tracking. When CC charging is used for reference generation, the average

switching frequency is measured as 3.06 kHz for 90V – 10A battery charging experiment whereas it is measured as 2.65 kHz for 90V – 5A battery charging experiment.

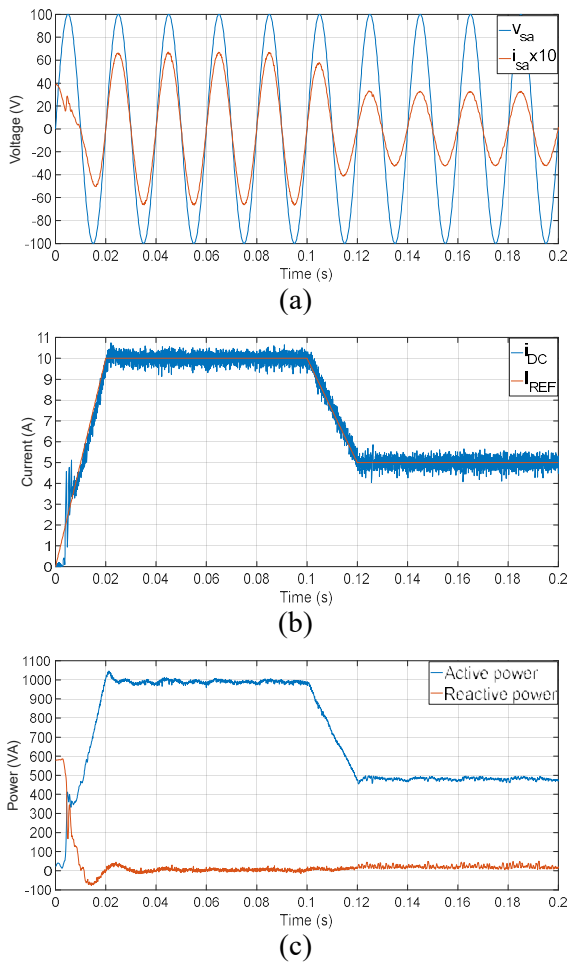


Figure 6. Waveforms for 90V-battery charge and reference generation with PI compensator according to CC charging; (a) Supply voltage and current (x10) for phase-a, (b) charge current command and output current, (c) supply power components

Fig. 7 shows the results of the FFT analysis of the grid current for the case where a 90V-battery is charged with 5A. The total harmonic distortion (THD) in grid current is 4.70% when the damping current term is not included in the cost function whereas THD is decreased to 2.11% with inclusion of damping current term. Comparison results in terms of supply current THD for different operating points are tabulated in Table 2. Although the THD results for the high sampling time are higher as expected, the contribution of the active damping term on THD is more noticeable for low charge current levels at higher sampling periods.

Table 2. THD results obtained under different charge current, battery voltage and sampling period when CC charging is used for reference generation

Sampling Period ↓	$v_{batt} \rightarrow$ $i_{REF} \rightarrow$ Control ↓	48V		90V	
		5A	10A	5A	10A
$T_s=50\mu s$	without damping	4.38%	2.21%	4.70%	1.78%
	with damping	2.24%	1.56%	2.11%	0.88%
$T_s=100\mu s$	without damping	13.09%	5.52%	11.78%	5.25%
	with damping	6.96%	5.17%	8.10%	3.75%

$K_p=0.0001, K_i=10 @T_s=50\mu s, K_i=1 @T_s=100\mu s$

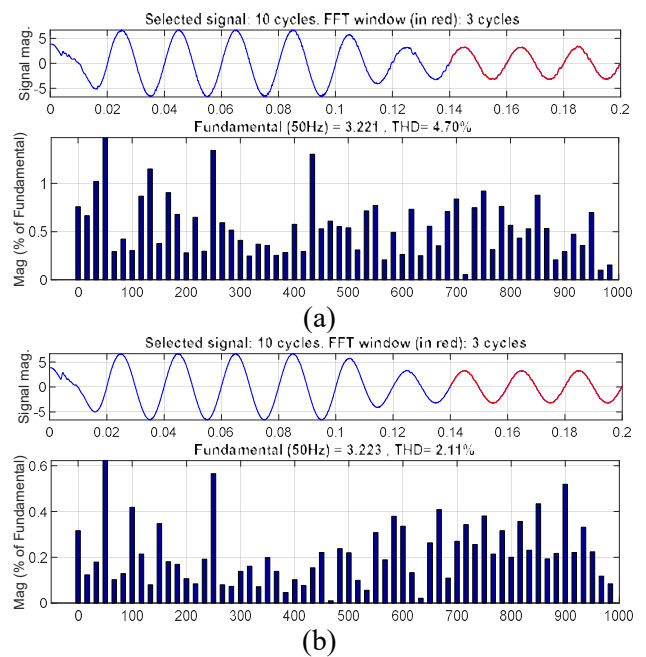


Figure 7. FFT analysis for supply current for $V_{batt}=90$ V and $i_{REF}=5A$; (a) without active damping, (b) with active damping.

The results presented in Fig. 8 are obtained when reference generation according to CV charging is used. The unity power factor operation with low THD at grid side is still achieved while the output voltage reference tracking is quite stable.

6. CONCLUSION

In proposed control method, model predictive strategy is presented to simultaneously control the output variable and input PF of a CSR that is used in a three-phase grid to battery charger application. In the control scheme, the filter capacitor voltages and supply currents are predicted using system

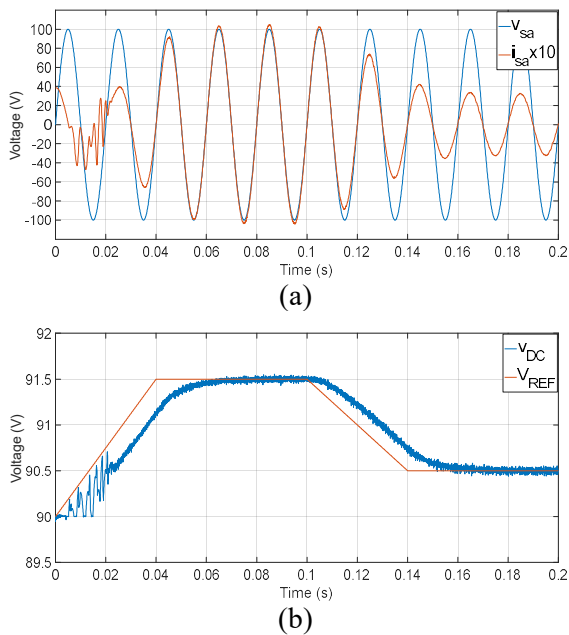


Figure 8. Waveforms for 90V-battery charge and reference generation with PI compensator according to CV charging; (a) Supply voltage and current (x10) for phase-a, (b) Reference charge voltage and output voltage, V_{DC}

model. The sensors measuring the input filter capacitor voltages are eliminated by predicting these voltages from other measurements on the system. The cost function of MPC employs the errors between sinusoidal supply current references and supply current predictions in abc-frame. The cost function is evaluated for all possible switching combinations of the CSR and one that minimizes this cost function is selected and applied to the rectifier for next sampling interval. Sinusoidal supply current references are generated from supply voltages using nested two PI compensators which are fed by errors in charge current or voltage. Active damping method is included into the predictive control scheme in order to mitigate resonance at supply side. High pass filtered active damping current term is added to cost function to force the rectifier to draw a current that has high frequency components responsible to alleviate adverse effect of input filter resonance. As a result, the THD in grid currents are reduced. The proposed method enables the battery to be charged with reference current or voltage according to the charging requirement, simultaneously guarantees the unity PF operation at the grid side and minimizes the THD by active damping method.

7. REFERENCES

- [1] F. Xu, B. Guo, Z. Xu, L. M. Tolbert, F. Wang, and B. J. Blalock, "SiC based current source rectifier paralleling and circulating current suppression," in *2013 Twenty-Eighth Annual IEEE Applied Power Electronics Conference and Exposition (APEC)*, 2013, pp. 402–409.
- [2] H. Yuan and X. Jiang, "A simple active damping method for Active Power Filters," in *Conference Proceedings - IEEE Applied Power Electronics Conference and Exposition - APEC*, 2016, vol. 2016–May, pp. 907–912.
- [3] J. C. Wiseman and B. Wu, "Active damping control of a high-power PWM current-source rectifier for line-current THD reduction," *IEEE Trans. Ind. Electron.*, vol. 52, no. 3, pp. 758–764, 2005.
- [4] J. Munoz, M. Sarbanzadeh, E. Sarebanzadeh, M. Rivera, and M. A. Hosseinzadeh, "Predictive Control in Power Converter Applications: Challenge and Trends," 2019, pp. 1–6.
- [5] S. Vazquez, J. Rodriguez, M. Rivera, L. G. Franquelo, and M. Norambuena, "Model Predictive Control for Power Converters and Drives: Advances and Trends," *IEEE Trans. Ind. Electron.*, vol. 64, no. 2, pp. 935–947, 2017.
- [6] M. Rivera, P. Wheeler, A. Olloqui, and D. A. Khaburi, "A review of predictive control techniques for matrix converters-Part i," in *7th Power Electronics, Drive Systems and Technologies Conference, PEDSTC 2016*, 2016.
- [7] P. Zavala *et al.*, "Predictive control of a current source rectifier with imposed sinusoidal input currents," in *IECON Proceedings (Industrial Electronics Conference)*, 2013, pp. 5842–5847.
- [8] M. Rivera, L. Tarisciotti, and P. Wheeler, "Indirect model predictive control with imposed sinusoidal source currents for a Direct Matrix Converter Working at fixed switching frequency," in *Proceedings - 2017 IEEE Southern Power Electronics Conference, SPEC 2017*, 2018, vol. 2018–Janua, pp. 1–6.

- [9] B. Feng and H. Lin, "Finite control set model predictive control of AC/DC matrix converter for grid-connected battery energy storage application," *J. Power Electron.*, vol. 15, no. 4, pp. 1006–1017, 2015.
- [10] I. Lizama, J. Rodríguez, B. Wu, P. Correa, M. Rivera, and M. Pérez, "Predictive control for current source rectifiers operating at low switching frequency," in *2009 IEEE 6th International Power Electronics and Motion Control Conference, IPEMC '09*, 2009, pp. 1630–1633.
- [11] P. Correa and J. Rodriguez, "A predictive control scheme for current source rectifiers," in *2008 13th International Power Electronics and Motion Control Conference*, 2008, pp. 699–702.
- [12] H. Gao, B. Wu, D. Xu, and N. R. Zargari, "A Model Predictive Power Factor Control Scheme with Active Damping Function for Current Source Rectifiers," *IEEE Trans. Power Electron.*, vol. 33, no. 3, pp. 2655–2667, 2018.
- [13] M. Sitterly, L. Y. Wang, G. G. Yin, and C. Wang, "Enhanced identification of battery models for real-time battery management," *IEEE Trans. Sustain. Energy*, vol. 2, no. 3, pp. 300–308, 2011.

JOURNAL OF SCIENCE



SAKARYA UNIVERSITY

Sakarya University Journal of Science

ISSN 1301-4048 | e-ISSN 2147-835X | Period Bimonthly | Founded: 1997 | Publisher Sakarya University |
<http://www.saujs.sakarya.edu.tr/>

Title: Effect of Reduction Ratio Below Austenite Recrystallization Stop Temperature on Mechanical Properties of An Apı X70M Psl2 Line Pipe Steel

Authors: Ramazan Tütük, Mustafa Merih Arıkan, Eyüp Sabri Kayalı

Received: 2019-02-21 15:54:02

Accepted: 2019-05-24 09:27:00

Article Type: Research Article

Volume: 23

Issue: 5

Month: October

Year: 2019

Pages: 972-981

How to cite

Ramazan Tütük, Mustafa Merih Arıkan, Eyüp Sabri Kayalı; (2019), Effect of Reduction Ratio Below Austenite Recrystallization Stop Temperature on Mechanical Properties of An Apı X70M Psl2 Line Pipe Steel. Sakarya University Journal of Science, 23(5), 972-981, DOI: 10.16984/saufenbilder.530327

Access link

<http://www.saujs.sakarya.edu.tr/issue/44066/530327>

New submission to SAUJS

<http://dergipark.gov.tr/journal/1115/submission/start>

Effect of Reduction Ratio Below Austenite Recrystallization Stop Temperature on Mechanical Properties of an API X70M PSL2 Line Pipe Steel

Ramazan Tütük¹, Mustafa Merih Arıkan^{2*}, Eyüp Sabri Kayalı³

Abstract

Steel grades having high toughness and high strength are required for line pipes since gas and oil should be transported through them at high pressures. Thermo-mechanically controlled rolling processes are used for increasing both toughness and strength at low temperatures since the line pipes are exposed to harsh climatic conditions at full length and rather severe service conditions. Charpy, DWTT and tensile tests were conducted to determine of mechanical properties and measured toughness values were evaluated considering various criteria in this study. Fractured surfaces were examined by means of SEM to distinguish the ductile and brittle fracture areas. Thermo-mechanical rolling trials were performed at the temperature below the non-recrystallization temperature of austenite on an API X70M PSL2 grade steel, to increase the strength without sacrificing the toughness. Different reduction ratios between 60,7% and 72,8% were utilized and the effect of reduction ratios on mechanical properties and microstructures were investigated during the trials. It was observed that final grain size decreased and strength and toughness increased with increasing reduction ratios.

Keywords: X70, thermo-mechanical processing, Charpy impact test, drop weight tear test, toughness

1. INTRODUCTION

High-strength low-alloy (HSLA) steels which are commonly used for different structural applications have been developed by thermo-mechanically controlled hot rolling process to particularly combine high strength with good toughness [1,2]. However, due to recently

increasing demand to use these steels in harsh service conditions, impact toughness at low-temperatures has become a primary concern and key criteria for them.

The demand for natural gas and crude oil rapidly increases with industrial developments. Since many gas and oil fields are located in remote areas, it is necessary to transport the gas and oil

¹ Istanbul Technical University, Graduate School of Science, Engineering and Technology, Materials Science and Eng. Istanbul, Turkiye ORCID: 0000-0002-5791-4976

² Arıkan Engineering Consultancy, Alanya, Turkiye ORCID: 0000-0002-5280-1871

* Corresponding Author: meriharikan@yahoo.com

³ Istanbul Technical University, Metallurgical and Materials Engineering Department Istanbul, Turkiye ORCID: 0000-0002-8646-8274

from these areas to consumption areas economically. In this context, line pipes are considered as the most economical and safe transportation of the gas and oil across distant miles. In order to reduce the transportation costs by long-distance line pipes, higher operating pressures in line pipes are expected, which consequently require higher wall thickness or higher strength steel with excellent combination of high toughness and strength [3-9]. Therefore, the increasing demand for oil and gas transportation is a driving force for the development of specialized and cost-effective line pipe steels with improved toughness, strength, weldability and corrosion resistance [10-13].

Increasing the strength of line pipe material can reduce significantly the wall thickness and consequently weight of the material. Such savings are important especially for the installation of line pipes in distant areas, where any weight reduction can be crucial in reducing the basic costs such as the amount of welding consumables, transportation and manipulation of the pipes during construction [14,15].

In addition to high toughness, resistance to crack-propagation is also extremely important for the development of high strength line pipe steels. Therefore, in practice, appropriate combinations of toughness and strength ensuring resistance to rapid crack propagation are desired [16].

In the line pipe steels, there is no strictly specified elemental composition and microstructure [17,18]. The thermo-mechanically controlled process (TMCP) in hot rolling stage introduces ideal microstructure resulting in desired mechanical properties. In this respect, alloying composition is essentially designed to assist appropriate TMCP.

In TMCP, reheating, rolling and coiling temperatures, distribution of rolling reductions among the rolling passes and cooling rate can be adjusted to get the desired properties [10]. For instance, low finishing temperature and fast cooling rate significantly produces higher strength than high finish rolling temperature and slow cooling rate.

Controlled rolling of heavy gauge material at high temperatures is an exclusive phase of TMCP temperatures, which finally produces various combinations of ferrite–pearlite–bainite in final microstructure.

Generally, controlled rolling of high strength line pipe steels such as API (The American Petroleum Institute) X70 steel consists of two phases [19]:

- Rough rolling, which is carried out at temperatures above non-recrystallization temperature (T_{NR}) of austenite and aims to achieve a recrystallized polygonal austenite microstructure across the thickness.
- Finish rolling, which is carried out below T_{NR} , but above A_{F3} (beginning temperature of transformation from austenite to ferrite during cooling) in order to obtain deformed non-recrystallized in austenitic microstructure.

The T_{NR} can be determined or estimated through many methods. From the literature, T_{NR} can be estimated through empirical formulas and laboratory methods [20-23]. The Boratto's equation [20] given in Equation 1 is the most known empirical formula to estimate T_{NR} ($^{\circ}C$).

$$T_{NR} (^{\circ}C) = 464C + 887 + (6445Nb - 644\sqrt{Nb}) + (732V - 230\sqrt{V}) + 363Al - 357Si + 890Ti \quad (1)$$

where C, Nb, V, Al, Si and Ti are the elements in the steel in weight percent (wt.%).

The accelerated cooling following controlled rolling determines the final microstructure through phase transformation of hot rolled austenite. After controlled rolling, deformed austenite must have high density of dislocations and grain boundaries to permit the nucleation of new phases [24].

The introduction of accelerated cooling after controlled rolling led to the production of higher strength steels [5]. Higher strength line pipe steels have been very successfully exploited worldwide in line pipe construction. These have been produced by accelerated cooling at cooling rates of 10 to 20 $^{\circ}C/s$ finalized with a coiling

temperature of 500-600°C, after which air cooling is used [14].

Additional reduction in grain size of the final microstructure is achievable by increasing the degree of rolling reduction; arranging the final rolling stage and abbreviating the interval between the end of rolling and the onset of cooling [25].

The production of X70 grade for gas and oil line pipes today is based on the controlled rolling with accelerated cooling [26]. Because of the nature of cooling in coil form, non-uniform structures are formed in coil products. Hence, the mechanical properties are non-uniform over the strip length since the external and internal turns in a coil are cooled more rapidly than the middle turns. To avoid a cooling-rate gradient and ensure uniform mechanical properties over the length of the strip, the coils of line pipe steels are subjected to accelerated cooling [26].

Low carbon steels have very good weldability and strength decrease due to carbon content decrease is compensated by the addition of vanadium, niobium and titanium in the micro-scale [27]. Softening caused by the reduction of carbon content is compensated by grain refining and precipitation hardening. The influence of micro-alloying elements on strengthening depends on the controlled rolling and accelerated cooling conditions.

Simultaneous achievement of good weldability, high impact resistance and high strength is possible by keeping carbon, sulfur, phosphorus, nonmetallic inclusions, and gases at the lowest possible level and appropriate selection of micro-alloy additions (Nb, V, Mo, Al, Ti) and Mn assuring achievement of required yield strength after applying meticulously designed TMCP [27]. The most significant reason of keeping low amount of carbon is, to get one-phase microstructure having fine grains after TMCP [20-28].

Line pipes can be suddenly fractured when the cracks initiate and propagate rapidly by explosion, impact or earthquake as they have been used under high pressure and low temperature

conditions [28]. Fracture properties especially at low temperatures of line pipe steels have been widely evaluated by carrying out drop-weight tear tests (DWTT) and Charpy impact tests [4, 5-8, 16, 29-36], and the test results may show variations as the notch shape, dimension and thickness of the test specimens changes [28]. The DWTT has been adopted as the official test condition by the API (American Petroleum Institute) for line pipe steels since DWTT is quite consistent with the fracture appearance transition occurring in actual fracture period of line pipe steels [6].

85 % SATT (shear appearance transition temperature) obtained from the drop weight tear tests is used as a standard to determine FPTT (fracture propagation transition temperature) [5,8]. Chevron Notch (CN) DWTT specimens or Press Notch (PN) DWTT specimens are used for FPTT of line pipe steels according to the API RP 5L3 specification [37]. The absorption energies from the press notch and chevron notch DWT tests and Charpy impacts tests all can be used as the criteria to measure the unstable ductile fracture resistance in line pipe steels [5].

The 85 percent, % SA (shear area) measured from the DWT test is generally known as the “Battelle 85 % Shear Area criterion” [6] to prevent the propagation of brittle fracture: if the measured SA is higher than 85 %, then material is supposed to withstand against the brittle fracture [17].

Crack-tip opening angle (CTOA) method and new approaches to DWT test are also introduced for systematic and more precise analyses as the toughness is greatly improved by ongoing studies on line pipe steels. However, the Charpy impact test being a simple testing method is still most commonly used method to evaluate transition temperature and absorbed energy of line pipe steels [6,16, 17].

As the rolling below T_{NR} is of primary concern to meet high toughness values in TMCP, the effect of hot rolling reduction ratio below T_{NR} on ductile fracture behavior in API X70M PSL2 line pipe steel was investigated in this study. Other rolling parameters and cooling rates were chosen identical in all trials to analyze the effect of hot rolling reduction ratio below T_{NR} . [10-12,16].

2. MATERIALS AND METHODS

An API X70M PSL2 grade steel was used in the industrial trials. Chemical composition of the steel is as follows (wt.%): C:0.052; Si:0.211; Mn:1.63; Cu:0.16; Ni:0.21; Cr:0.13; Mo:0.12; N:0.0063 and Nb+V+Ti:0.089.

Slabs in size of 220 mm (t) x 8500 mm (l) x 1500 mm (w) were hot rolled in one stand 4-high roughing mill with 5 passes and seven stand 4-high finishing mill with 7 passes under thermo-mechanical controlled rolling conditions. Before rolling, all slabs were heated to 1220 °C and soaked for a specific period in the soaking zone of a walking beam type reheating furnace in order to dissolve all the Nb in austenite.

Two different transfer bar thicknesses were used for identical roughing conditions, in which final roughing temperatures were above the calculated T_{NR} . Thicknesses of the slabs were reduced to 73.5 and 56 mm in 5 passes in the roughing mill. Before transferring to the finishing mill, special practice was applied to the transfer bars to obtain a desired homogenous finish rolling temperature below the T_{NR} of material. The T_{NR} for this steel was calculated as 1134 °C according to the Equation 1. Entry of the materials to the finishing mill was conducted at about 1000-980 °C. A primary grain refinement effect was expected by rolling in the non-recrystallized region of austenite with high rolling reduction ratios. Rolling was finished at 800-820 °C (FRT, the temperature at the exit of the last finishing rolling stand). Following finish rolling, the materials were accelerated cooled on run-out table with a cooling rate of ~12-15 °C/s and coiled at 550-600 °C. In the trials, total reduction ratio varied from 60.7 % to 72.8 %.

2.1. Microstructural analysis

The cross-sectional metallographic specimens taken from transversal to rolling direction were polished and etched by a 2 % Nital solution, and microstructures were observed by an optical microscope.

2.2. Tensile and Charpy impact tests

Tensile rectangular specimens with 38 mm gauge width and 50 mm gauge length were prepared in the transversal, diagonal (45° to the rolling direction) and longitudinal directions and were tested at a crosshead speed of 5 mm/min using a 600 kN Zwick tensile test machine at room temperature. Charpy impact tests were performed on Charpy V-notch (CVN) specimens [38] in size of 10 mm × 10mm × 55 mm in transversal orientation in a temperature range from -80 to 0 °C using a Zwick impact tester of 450 J capacity. Ductile and brittle zones on the fracture surfaces of Charpy samples were also investigated by scanning electron microscope (SEM).

2.3. Drop weight tear tests

DWTT specimens were prepared in size of 305 mm × 76.2 mm × 20 mm in transversal direction in accordance with the API 5L3 [37] and ASTM E436-91 [39] specifications, and then a pressed notch was applied on to them. These specimens were tested with a DWT testing machine having a maximum energy capacity of 50,000 J at 0 °C. The special refrigerant was used to cool the DWTT specimens down to 0 °C by putting ethanol in the specimen pool in where specimens were immersed for 20 min. and then immediately tested. The percent shear area (pct. SA) [37] was calculated according to the Equation 2.

$$\text{pct. SA} = \frac{((71-2t)t-(3/4)ab)}{(71-2t)t} \times 100 \quad (2)$$

where a, b and t are the width of cleavage fracture, length of cleavage fracture and full plate thickness respectively [37, 39].

3. RESULTS AND DISCUSSION

Variation of yield strength depending on the reduction ratio is shown in Figure 1. It was observed that yield strength increased as the reduction ratio below T_{NR} increased. The increase is more obvious on the transversal specimens with higher yield strength values, whereas lower yield

strength values were obtained on the longitudinal specimens.

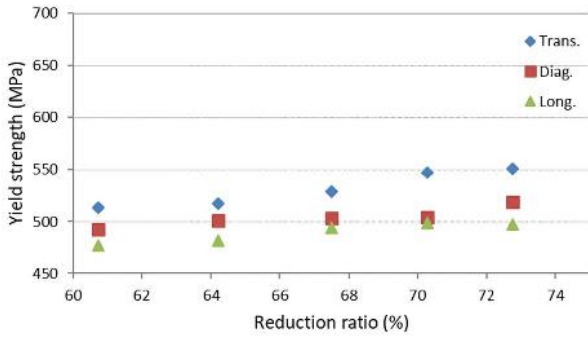


Figure 1. Variation of yield strength with the reduction ratio below T_{NR} .

Compared to yield strength, it was observed that tensile strength slightly increased as the reduction ratio increased (Figure 2). Higher tensile strength values were obtained on the transversal specimens; whereas lower tensile strength values were observed on the longitudinal specimens.

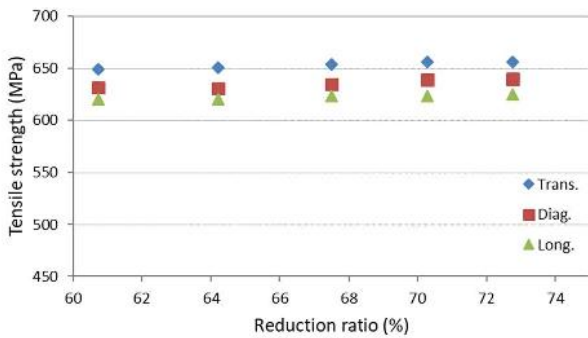


Figure 2. Variation of tensile strength with the reduction ratio below T_{NR} .

It was observed that elongation slightly decreased with increasing reduction ratio (Figure 3).

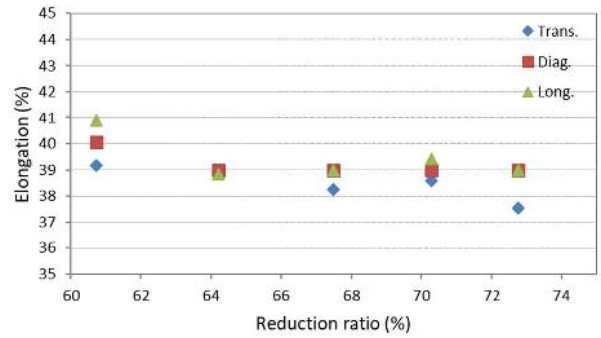


Figure 3. Variation of elongation with the reduction ratio below T_{NR} .

Pct. SA value in DWTT, which is the key property in many line pipe applications increases with the increasing reduction ratio: pct. SA is about 50 at the reduction ratio of 60.7 % and increases up to 90 as the reduction ratio has been increased to 72.8 % (Figures 4 and 5). Here, only the 72.8 % reduction ratio below T_{NR} meets the “Battelle’s criterion” to prevent the brittle fracture propagation.

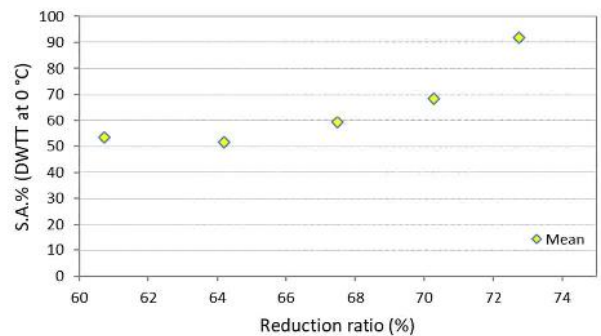


Figure 4. Variation of pct. SA in DWTT with the reduction ratio below T_{NR} .

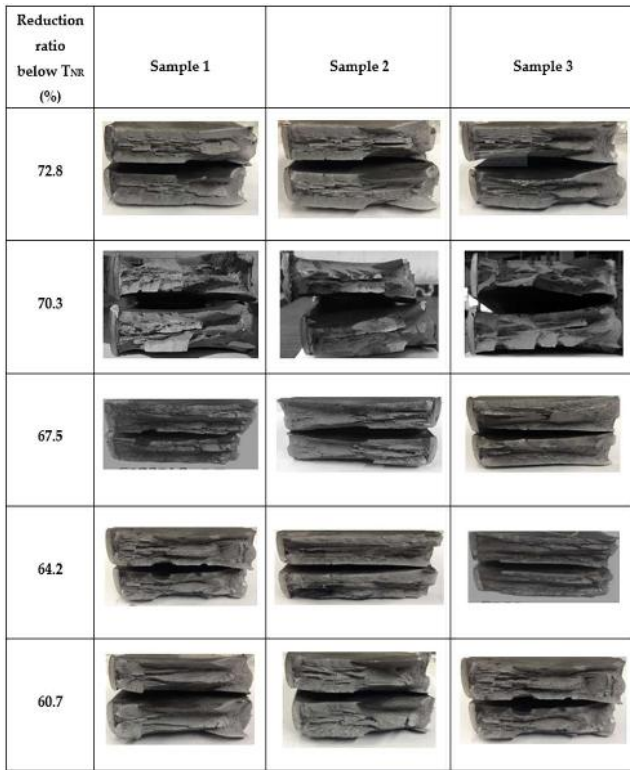


Figure 5. Fracture surfaces of DWTT samples associated with reduction ratio below T_{NR} .

The effect of total % reduction ratio under T_{NR} on the Charpy V notch impact values on different test temperatures is shown in Figure 6. The improving effect of reduction ratio below T_{NR} on the V notched Charpy impact values can significantly be seen at $-80\text{ }^{\circ}\text{C}$ in Figures 6 and 7. Charpy V notch impact values increased and the type of the fracture turns into the ductile fracture from brittle fracture as the reduction ratio increased. The increase in the impact energy values is more obvious on the samples tested at $-80\text{ }^{\circ}\text{C}$ than the samples tested at higher temperatures. The increase of the reduction ratio ensures achieving the desired crack-propagation resistance.

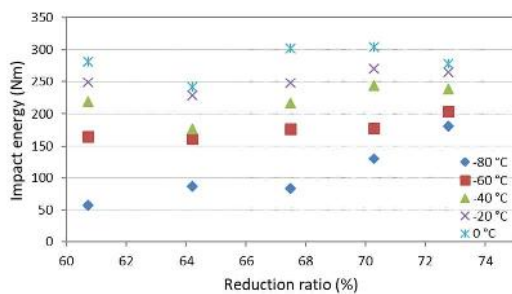


Figure 6. Variation of Charpy V-notch impact values with the reduction ratio below T_{NR} .

Microstructural variations on the investigated steel are shown in Figure 8 depending on the reduction ratio. An obvious decrease in ferrite grain size (from 12 to 13,5 ASTM Grain Size Number according to linear intercept method) is observed in the microstructures with increasing reduction ratio below T_{NR} . Also, acicular ferrite (AF) formations replace pearlite in the microstructure with increasing reduction ratio below T_{NR} while volume fraction of pearlite in the microstructure decreases.

SEM investigations were carried out on Charpy specimens tested at $-80\text{ }^{\circ}\text{C}$ to confirm the nature of fracture depending on the reduction ratio. SEM images of Charpy test specimens tested at $-80\text{ }^{\circ}\text{C}$ are given in Figures 9 and 10 as examples. Totally dimple area which represents ductile fracture is observed at a reduction ratio of 72.8 % and this is clearly visible in Figure 9. Fracture mode is cleavage fracture which is transgranular brittle fracture at a reduction ratio of 60.7 % as can be seen in Figure 10.

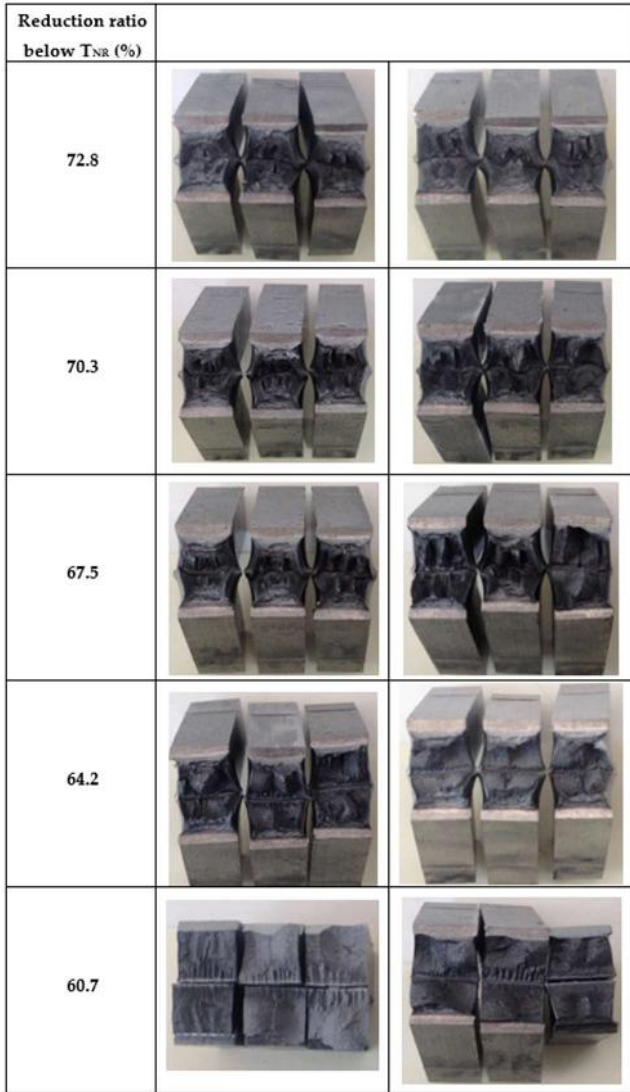


Figure 7. Fracture surfaces of Charpy V-notch impact test samples associated with reduction ratio below T_{NR} (Test temperature -80 °C).

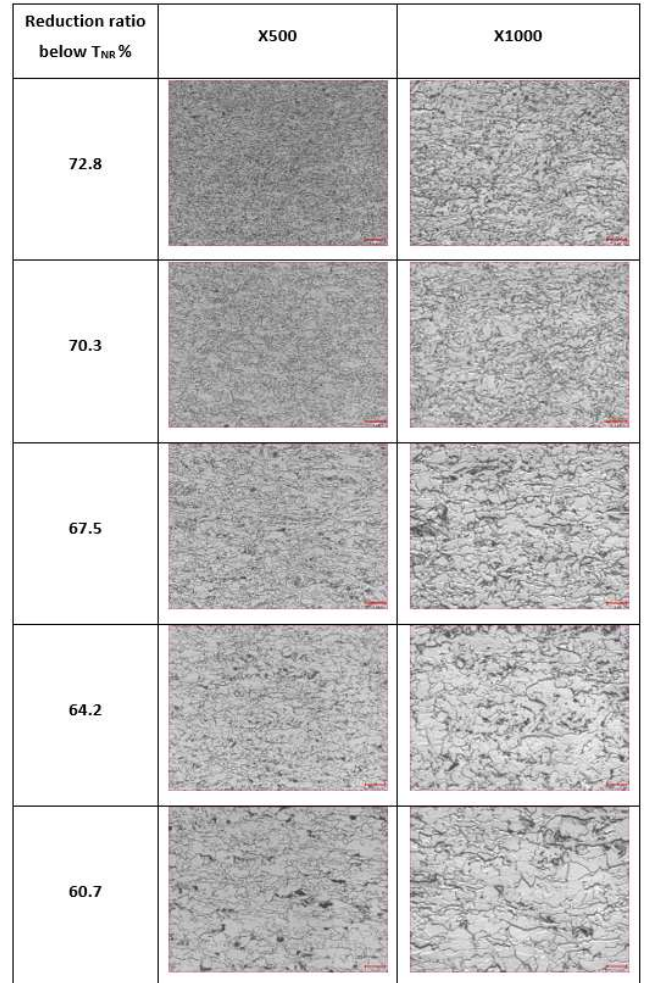


Figure 8. Microstructures associated with reduction ratio below T_{NR} .

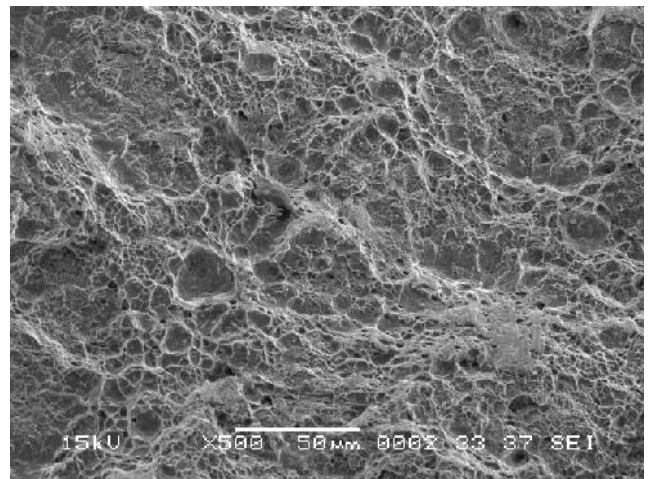


Figure 9. SEM image of Charpy test specimen tested at -80 °C (reduction ratio: 72.8 %).

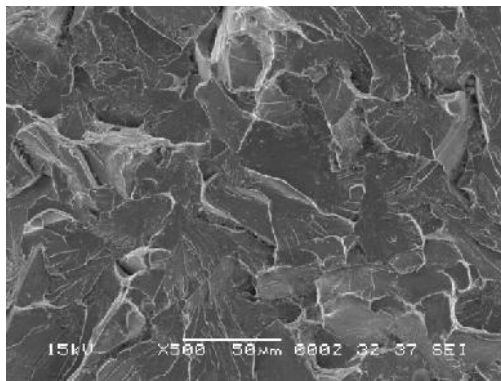


Figure 10. SEM image of Charpy test specimen tested at -80 °C (reduction ratio: 60.7 %).

High dislocation density is generated by the rolling reductions below T_{NR} and some strain energy retains in the austenite, this energy is the mechanical driving force for grain refinement and nucleation of acicular ferrite [24, 25, 26]. It was shown that the rolling deformation prior to the transformation into the acicular ferrite is more effective in increasing the amount of the acicular ferrite phase than chemical alloying and increasing the cooling rate [27]. The dislocations by the rolling reduction do not survive in every case for the transformation into acicular ferrite but the rolling operation induces a finer grained and dislocated “pancaked” austenite before transformation that will provide a high nucleation rate of acicular ferrite during the transformation [3, 27]. Ferrite grain size effects on the yield strength rather than the tensile strength through the Hall-Petch relationship [28, 29]. All of these can hinder the commencement of plastic deformation and cause an increase in the yield strength in the steel.

4. CONCLUSIONS

According to the results achieved in the trials below calculated T_{NR} temperature, it appears that yield strength significantly increases, tensile strength slightly changes, and elongation decreases in some degree. DWTT and impact toughness increases with increasing reduction ratio. Metallographic examinations show that final grain size decreases with increasing deformation ratio, and thereby confirm that fine grain sized microstructure increases toughness and strength together. Based on the trend of the

experimental results of this study, it is expected further improvements on the mechanical properties when the reduction ratio increased beyond to max. reduction ratio (72.8 %) applied in this study.

Acknowledgments

Authors thank to Ali Fikret Gen and Cengiz Şahintürk for their support and encouragement, and Oktay Elkoca for his valuable contribution.

REFERENCES

- [1] W. Yan, W. Sha, L. Zhu, Y. Shan and K. Yang, “Delamination fracture related to tempering in a high-strength low-alloy steel”, *Metall. Mater. Trans. A*, 41A, pp. 159-171, 2010.
- [2] S. Vervynckt, K. Verbeken, P. Thibaux, M. Liebeherr and Y. Houbaert, “Austenite recrystallization-precipitation interaction in niobium microalloyed steels”, *ISIJ Int.*, 49, pp. 911-920, 2009.
- [3] B. Hwang, S. Lee, Y.M. Kim, N.J. Kim, J.Y. Yoo and C.S. Woo, “Analysis of abnormal fracture occurring during drop-weight tear test of high-toughness line-pipe steel”, *Mater. Sci. Eng. A*, 368, pp. 18-27, 2004.
- [4] J. Zhang, W. Sun and H. Sun, “Mechanical properties and microstructure of X120 grade high strength pipeline steel”, *Journal of Iron Steel Int.*, 17(10) pp. 63-67, 2010.
- [5] S. Y. Shin, B. Hwang, S. Lee, N. J. Kim and S. S. Ahn, “Correlation of microstructure and Charpy impact properties in API X70 and X80 line-pipe steels”, *Mater. Sci. Eng. A*, 458, pp. 281-289, 2007.
- [6] B. Hwang, S. Lee, Y. M. Kim and N. J. Kim, “Correlation of rolling condition, microstructure, and low-temperature toughness of X70 pipeline steels”, *Metall. Mater. Trans. A*, 36A, pp. 1793-1805, 2005.

- [7] M. Kang, H. Kim, S. Lee and S. Y. Shin, "Effects of dynamic strain hardening exponent on abnormal cleavage fracture occurring during drop weight tear test of API X70 and X80 linepipe steels", *Metall. Mater. Trans. A*, 45A, pp. 682-697, 2014.
- [8] H. K. Sung, S. S. Sohn, S. Y. Shin, S. Lee, N. J. Kim, S. H. Chon and J. Y. Yoo, "Effects of finish rolling temperature on inverse fracture occurring during drop weight tear test of API X80 pipeline steels", *Mater. Sci. Eng. A*, 541, pp. 181-189, 2012.
- [9] S. S. Sohn, S. Y. Han, J. Bae, H. S. Kim and S. Lee, "Effects of microstructure and pipe forming strain on yield strength before and after spiral pipe forming of API X70 and X80 linepipe steel sheets", *Mater. Sci. Eng. A*, 573, pp. 18-26, 2013.
- [10] V. C. Olalla, V. Bliznuk, N. Sanchez, P. Thibaux, L. A. I. Kestens and R. H. Petrov, "Analysis of strengthening mechanisms in pipeline steels", *Mater. Sci. Eng. A*, 604, pp. 46-56, 2014.
- [11] A. A. Shahrani, N. Yazdipour, A. D. Manshadi and A. A. Gazder, "The effect of processing parameters on the dynamic recrystallization behavior of API-X70 pipeline steel", *Mater. Sci. Eng. A*, 570, pp. 70-81, 2013.
- [12] Y. M. Kim, S. K. Kim, Y. J. Lim and N. J. Kim, "Effect of microstructure on the yield ratio and low temperature toughness of linepipe steels", *ISIJ Int.*, 42, pp. 1571-1577, 2002.
- [13] C. P. Reip, S. Shanmugam and R. D. K. Misra, "High strength microalloyed CMn(V-Nb-Ti) and CMn(V-Nb) pipeline steels processed through CSP thin-slab technology: microstructure, precipitation and mechanical properties", *Mater. Sci. Eng. A*, 424, pp. 307-317, 2006.
- [14] I. D. S. Bott, L. F. G. Souza, J. C. G. Teixeira and P. R. Rios, "High-strength steel development for pipelines: a Brazilian perspective", *Metall. Mater. Trans. A*, 36A, pp. 443-454, 2005.
- [15] S. H. Hashemi and D. Mohammadyani, "Characterization of weldment hardness, impact energy and microstructure in API X65 steel", *Int. J. Pressure Vessels Piping*, 98, pp. 8-15, 2012.
- [16] G. J. Baczynski, J. J. Jonas and L. E. Collins, "The influence of rolling practice on notch toughness and texture development in high-strength linepipe", *Metall. Mater. Trans. A*, 30A, pp. 3045-3054, 1999.
- [17] Specification for line pipe, API specification 5L, forty-fifth edition, December, American Petroleum Institute, 2012.
- [18] D. Clover, B. Kinsella, B. Pejic and R. D. Marco, "The influence of microstructure on the corrosion rate of various carbon steels", *J. App. Electrochem.*, 35, pp. 139-149, 2005.
- [19] P. Korczak, "Influence of controlled rolling condition on microstructure and mechanical properties of low carbon micro-alloyed steels", *J. Mater. Process. Technol.*, 157-158, pp. 553-556, 2004.
- [20] R. Barbosa, F. Boratto, S. Yue and J. J. Jonas, "The influence of chemical composition on the recrystallization behavior of microalloyed steels", *Process. Microstruct. Prop. HSLA Steels*, pp. 51-61, 1988.
- [21] D. Q. Bai, S. Yue, W. P. Sun and J. J. Jonas, "Effect of deformation parameters on the no-crystallization temperature in Nb-bearing steels", *Metall. Mater. Trans. A*, 24, pp. 2151-2159, 1993.
- [22] D. Q. Bai, R. L. Bodnar, J. Ward, J. Dorricott and S. Sanders, "Development of discrete X80 line pipe plate at SSAB Americas", International Symposium on the

- Recent Developments in Plate Steels, pp. 13-22, 2011.
- [23] F. Fletcher, “Meta-analysis of T_{nr} measurements: determining new empirical models based on composition and strain”, Austenite Processing Symposium, pp. 1-14, 2008.
- [24] S. Y. Nastich, S. V. Soya, A. A. Efimov, M. A. Molstov and I. S. Vasil’ev, “Accelerated strip cooling to form ferritic-bainitic microstructure in low-alloy X70 steel strip”, *Steel in Translation*, 42, pp. 357-364, 2012.
- [25] Y. D. Morozov, E. A. Goli-Oglu, S. Y. Nastich, S. V. Denisov and P. A. Stekanov, “Thermomechanical treatment of microalloyed low-carbon steel at a 5000 mill for the production of cold-resistant thick strip”, *Steel in Translation*, 42, pp. 171-176, 2012.
- [26] S. Y. Nastich, N. V. Filatov, Y. D. Morozov, I. V. Lyasotskii and E. V. Shul’ga, “Structuring and deposition of nanoparticles in X70 steel during coiling and subsequent cooling”, *Steel in Translation*, 39, pp. 814-819, 2009.
- [27] P. Korczak, “Modeling of steel microstructure evolution during thermo-mechanical rolling of plate for conveying pipes”, *J. Mater. Process. Technol.*, 153-154, pp. 432-435, 2004.
- [28] Y. Kim, S. Y. Shin, Y. G. Kim and N. J. Kim, “Effects of strain rate and test temperature on torsional deformation behavior of API X70 and X80 linepipe steel”, *Metall. Mater. Trans. A*, 41A, pp. 1961-1972, 2010.
- [29] F. Rivalin, A. Pineau, M. D. Fant and J. Besson, “Ductile tearing of pipeline-steel wide plates I. Dynamic and quasi-static experiments”, *Eng. Fract. Mech.*, 68, pp. 329-345, 2001.
- [30] F. Rivalin, J. Besson, A. Pineau and M. D. Fant, “Ductile tearing of pipeline-steel wide plates II. Modeling of in-plane crack propagation”, *Eng. Fract. Mech.*, 68, pp. 347-364, 2001.
- [31] B. Hwang, Y. G. Kim, S. Lee and N. J. Kim, “Effects of microstructure on inverse fracture occurring during drop-weight tear testing of high-toughness X70 pipeline steels”, *Metall. Mater. Trans. A*, 36A, pp. 371-387, 2005.
- [32] J. Fang, J. Zhang and L. Wang, “Evaluation of cracking behavior or critical CTOA values of pipeline steel from DWTT specimens”, *Eng. Fract. Mech.*, 124-125, pp. 18-29, 2014.
- [33] S. Y. Shin, B. Hwang, S. Kim and S. Lee, “Fracture toughness analysis in transition temperature region of API X70 pipeline steels”, *Mater. Sci. Eng. A*, 429, pp. 196-204, 2006.
- [34] Q. Sha and D. Li, “Microstructure, mechanical properties and hydrogen induced cracking susceptibility of X80 pipeline steel with reduced Mn content”, *Mater. Sci. Eng. A*, 585, pp. 214-221, 2013.
- [35] B. Strnadel, P. Ferfecki and P. Zidlik, “Statistical characteristics of fracture surfaces in high-strength steel drop weight tear test specimens”, *Eng. Fract. Mech.*, 112-113, pp. 1-13, 2013.
- [36] W. Wang, Y. Shan and K. Yang, “Study of high strength pipeline steels with different microstructures”, *Mater. Sci. Eng. A*, 502, pp. 38-44, 2009.
- [37] API recommended practice 5L3, third edition, February, American Petroleum Institute, 1996.
- [38] ASTM A370-17a, Standard test methods and definitions for mechanical testing of steel products, 2017.
- [39] ASTM E436-03(2014), Standard test method for drop-weight tear tests of ferritic steels, 2014.

JOURNAL OF SCIENCE



SAKARYA UNIVERSITY

Sakarya University Journal of Science

ISSN 1301-4048 | e-ISSN 2147-835X | Period Bimonthly | Founded: 1997 | Publisher Sakarya University |
<http://www.saujs.sakarya.edu.tr/>

Title: Some Connections Between Various Classes of Analytic Functions Associated With The Power Series Distribution

Authors: Serkan akmak, Sibel Yalın, Őahsene Altınkaya

Received: 2019-04-12 13:30:42

Accepted: 2019-06-10 11:09:02

Article Type: Research Article

Volume: 23

Issue: 5

Month: October

Year: 2019

Pages: 982-985

How to cite

Serkan akmak, Sibel Yalın, Őahsene Altınkaya; (2019), Some Connections Between Various Classes of Analytic Functions Associated With The Power Series

Distribution. Sakarya University Journal of Science, 23(5), 982-985, DOI: 10.16984/saufenbilder.552957

Access link

<http://www.saujs.sakarya.edu.tr/issue/44066/552957>

New submission to SAUJS

<http://dergipark.gov.tr/journal/1115/submission/start>

Some connections between various classes of analytic functions associated with the power series distribution

Serkan Çakmak¹, Sibel Yalçın², Şahsene Altınkaya^{*3}

Abstract

The primary motivation of the paper is to investigate the power series distribution (Pascal model) for the analytic function classes $T\mathcal{G}(\alpha)$, $T\mathcal{G}\mathcal{S}^*(\alpha, \rho)$ and $T\mathcal{G}\mathcal{C}(\alpha, \rho)$. Furthermore, we give necessary and sufficient conditions for the Pascal distribution series belonging to these classes.

Keywords: Analytic functions, power series distribution

1. INTRODUCTION

The power series distribution is very useful in multivariate data research fields. This family of distributions, particularly is used in survival and reliability studies. However, nowadays, the elementary distributions such as the Poisson, the Pascal, the Logarithmic, the Binomial, the Burr-Weibull have been partially studied in the Geometric Function Theory from a theoretical point of view (see [1], [2], [3], [4]). In this paper, we focus on the Pascal power series distribution.

Let us consider a non-negative discrete random variable \mathcal{X} with a Pascal probability generating function

$$P(\mathcal{X} = j) = \binom{j+t-1}{t-1} p^j (1-p)^t, \quad j \in \{0, 1, 2, 3, \dots\},$$

where p ($0 \leq p \leq 1$), t are called the parameters.

Let \mathcal{A} represent the class of functions f of the form

$$f(z) = z + \sum_{j=2}^{\infty} a_j z^j, \quad (1)$$

which are analytic in the open unit disk $\mathfrak{U} = \{z: z \in \mathbb{C} \text{ and } |z| < 1\}$. Let \mathcal{S} be the subclass of \mathcal{A} consisting of functions which are univalent in \mathfrak{U} and T be the subclass of \mathcal{S} consisting of functions whose coefficients, from the second on, are non-negative given by (see [5])

$$f(z) = z - \sum_{j=2}^{\infty} |a_j| z^j. \quad (2)$$

Furthermore, by $\mathcal{G}(\alpha)$, $\mathcal{G}\mathcal{S}^*(\alpha, \rho)$ we shall denote the class of all functions $f \in \mathcal{A}$ which satisfy the following conditions

$$\operatorname{Re} \left\{ \left(1 + e^{i\theta} \right) \frac{zf'(z)}{f(z)} - e^{i\theta} \right\} \geq \alpha \quad (0 \leq \alpha < 1, \theta \in \mathbb{R}), \quad (3)$$

¹ Bursa Uludag University, Department of Mathematics, Bursa, Turkey. ORCID: 0000-0003-0368-7672

² Bursa Uludag University, Department of Mathematics, Bursa, Turkey. ORCID: 0000-0002-0243-8263

³ Bursa Uludag University, Department of Mathematics, Bursa, Turkey. ORCID: 0000-0002-7950-8450

$$\operatorname{Re} \left\{ \left(1 + \rho e^{i\theta} \right) \frac{zf'(z)}{f(z)} - \rho e^{i\theta} \right\} \geq \alpha \quad (4)$$

$$(0 \leq \alpha < 1, \rho \geq 0, \theta \in \mathbb{R}),$$

respectively.

Let also $\mathcal{GC}(\alpha, \rho)$ denote the class of all functions $f \in \mathcal{A}$ which satisfy the following condition

$$\operatorname{Re} \left\{ \left(1 + \rho e^{i\theta} \right) \left(1 + \frac{zf''(z)}{f'(z)} \right) - \rho e^{i\theta} \right\} \geq \alpha \quad (5)$$

$$(0 \leq \alpha < 1, \rho \geq 0, \theta \in \mathbb{R}).$$

We next must write

$$T\mathcal{G}(\alpha) = \mathcal{G}(\alpha) \cap T,$$

$$T\mathcal{GS}^*(\alpha, \rho) = \mathcal{GS}^*(\alpha, \rho) \cap T$$

and

$$T\mathcal{GC}(\alpha, \rho) = \mathcal{GC}(\alpha, \rho) \cap T.$$

These classes introduced and studied by Ronning [6].

The primary motivation of the paper is to investigate the Pascal power series distribution for the analytic function classes $T\mathcal{G}(\alpha)$, $T\mathcal{GS}^*(\alpha, \rho)$ and $T\mathcal{GC}(\alpha, \rho)$.

2. PASCAL POWER SERIES DISTRIBUTION

We start by stating the Pascal power series and the basis lemmas for our further investigations.

Based upon the Pascal distribution, consider the following power series:

$$P(t, p, z) = z + \sum_{j=2}^{\infty} \binom{j+t-2}{t-1} p^{j-1} (1-p)^t z^j \quad (6)$$

$$(t \geq 0, 0 \leq p \leq 1, z \in \mathcal{U}).$$

Note that, by using ratio test we conclude that the radius of convergence of the above power series is infinity.

Lemma 1. A function $f \in \mathcal{A}$ given by (1) is in the class $\mathcal{G}(\alpha)$ if it satisfies the following condition

$$\sum_{j=1}^{\infty} (2j-1-\alpha) |a_j| \leq 2(1-\alpha). \quad (7)$$

Lemma 2. A function $f \in \mathcal{A}$ given by (1) is in the class $\mathcal{GS}^*(\alpha, \rho)$ if it satisfies the following condition

$$\sum_{j=1}^{\infty} [\rho(j-1) + j - \alpha] |a_j| \leq 2(1-\alpha). \quad (8)$$

Lemma 3. A function $f \in \mathcal{A}$ given by (1) is in the class $\mathcal{GC}(\alpha, \rho)$ if it satisfies the following condition

$$\sum_{j=1}^{\infty} j [\rho(j-1) + j - \alpha] |a_j| \leq 2(1-\alpha). \quad (9)$$

Lemma 4. A function $f \in T$ given by (2) is in the class $T\mathcal{G}(\alpha)$ if and only if it satisfies the following condition (7).

Lemma 5. A function $f \in T$ given by (2) is in the class $T\mathcal{GS}^*(\alpha, \rho)$ if and only if it satisfies the following condition (8).

Lemma 6. A function $f \in T$ given by (2) is in the class $T\mathcal{GC}(\alpha, \rho)$ if and only if it satisfies the following condition (9).

3. APPLICATION

By considering above definitions and lemmas, we have the following necessary and sufficient conditions for the function P .

Theorem 1. For $p \neq 1$, the function P given by (6) is in the class $\mathcal{GTS}^*(\alpha, \rho)$ if and only if

$$\frac{(\rho+1)t p}{(1-p)^{t+1}} \leq 1-\alpha. \quad (10)$$

Proof. According to Lemma 2, we must show that

$$\sum_{j=2}^{\infty} \binom{j+t-2}{t-1} [\rho(j-1) + j - \alpha] p^{j-1} (1-p)^t \leq 1 - \alpha.$$

Therefore, by combining the relation (6) and implication (10), we have the equality

$$\begin{aligned} & \sum_{j=2}^{\infty} \binom{j+t-2}{t-1} [\rho(j-1) + j - \alpha] p^{j-1} (1-p)^t \\ &= (\rho+1)t p (1-p)^t \sum_{j=2}^{\infty} \binom{j+t-2}{t} p^{j-2} \\ &+ (1-\alpha)(1-p)^t \sum_{j=2}^{\infty} \binom{j+t-2}{t-1} p^{j-1} \\ &= (\rho+1)t p (1-p)^t \sum_{j=0}^{\infty} \binom{j+t}{t} p^{j^t} \\ &+ (1-\alpha)(1-p)^t \sum_{j=2}^{\infty} \binom{j+t-1}{t-1} p^j - (1-\alpha)(1-p) \\ &= \frac{(\rho+1)t p}{1-p} + (1-\alpha) - (1-\alpha)(1-p)^t \leq 1 - \alpha. \end{aligned}$$

Thus the proof of Theorem 1 is now completed.

Corollary 1. For $p \neq 1$, the function P given by (6) is in the class $T\mathcal{G}(\alpha)$ if and only if

$$\frac{2tp}{(1-p)^{t+1}} \leq 1 - \alpha.$$

In what follows, we shall give the results for the class $T\mathcal{GC}(\alpha, \rho)$.

Theorem 2. For $p \neq 1$, the function P given by (6) is in the class $T\mathcal{GC}(\alpha, \rho)$ if and only if

$$\frac{(\rho+1)t(t+1)p^2}{(1-p)^{t+2}} + \frac{(3+2\rho-\alpha)t p (1-p)^t}{(1-p)^{t+1}} \leq 1 - \alpha. \quad (11)$$

Proof. According to Lemma 3, we must show that

$$\sum_{j=2}^{\infty} \binom{j+t-2}{t-1} j [1 - \alpha + (\rho+1)(j-1)] p^{j-1} (1-p)^t \leq 1 - \alpha.$$

Therefore, by combining the relation (6) and implication (12), we have the equality

$$\begin{aligned} & \sum_{j=2}^{\infty} \binom{j+t-2}{t-1} j [1 - \alpha + (\rho+1)(j-1)] p^{j-1} (1-p)^t \\ &= (\rho+1)t(t+1)p^2(1-p)^t \sum_{j=3}^{\infty} \binom{j+t-2}{t+1} p^{j-3} \\ &+ (3+2\rho-\alpha)t p (1-p)^t \sum_{j=2}^{\infty} \binom{j+t-2}{t} p^{j-2} \\ &+ (1-\alpha)(1-p)^t \sum_{j=2}^{\infty} \binom{j+t-2}{t-1} p^{j-1} \\ &= (\rho+1)t(t+1)p^2(1-p)^t \sum_{j=0}^{\infty} \binom{j+t+1}{t+1} p^j \\ &+ (3+2\rho-\alpha)t p (1-p)^t \sum_{j=0}^{\infty} \binom{j+t}{t} p^j \\ &+ (1-\alpha)(1-p)^t \sum_{j=0}^{\infty} \binom{j+t-1}{t} p^j - (1-\alpha)(1-p)^t \\ &= \frac{(\rho+1)t(t+1)p^2}{(1-p)^2} + \frac{(3+2\rho-\alpha)t p (1-p)^t}{1-p} \\ &+ (1-\alpha) - (1-\alpha)(1-p)^t \leq 1 - \alpha. \end{aligned}$$

Thus, according to Lemma 3, we conclude that $f \in T\mathcal{GC}(\alpha, \rho)$.

4. REFERENCES

- [1] Ş. Altınkaya and S. Yalçın, “Poisson distribution series for certain subclasses of starlike functions with negative coefficients”, *Annals of Oradea University Mathematics Fascicula*, vol. 24, pp. 5-8, 2017.
- [2] Ş. Altınkaya and S. Yalçın, “Poisson distribution series for analytic univalent functions”, *Complex Analysis and Operator Theory*, vol. 12, pp. 1315-1319, 2018.
- [3] S. Porwal, “An application of a Poisson distribution series on certain analytic functions”, *J. Complex Anal.*, Article ID 984135, vol. 2014, pp. 1-3, 2014.
- [4] W. Nazeer, Q. Mehmood, S.M. Kang and A.U. Haq, “An application of Binomial distribution series on certain analytic functions”, *Journal of Computational Analysis and Applications*, vol. 26, pp. 11-17, 2019.
- [5] H. Silverman, “Univalent functions with negative coefficients”, *Proc. Amer. Math. Soc.*, vol. 51, pp. 109-116, 1975.
- [6] F. Rønning, “Uniformly convex functions and a corresponding class of starlike functions”, *Proc. Amer. Math. Soc.*, vol. 118, pp. 189-196, 1993.
- [7] T. Wei and B. Khoshnevis, “Integration of process planning and scheduling: a review,” *Journal of Intelligent Manufacturing*, vol. 24, no. 6, pp. 51–63, 2000.
- [8] R. Meenakshi Sundaram and S. Fu, “Process planning and scheduling — A method of integration for productivity improvement,” *Computers & Industrial Engineering*, vol. 15, no. 1–4, pp. 296–301, 1988.
- [9] Y. Chu, F. You, J. M. Wassick, and A. Agarwal, “Integrated planning and scheduling under production uncertainties: Bi-level model formulation and hybrid solution method,” *Computers and Chemical Engineering*, vol. 72, pp. 255–272, 2015.
- [10] F. S. Chan, V. Kumar, and M. Tiwari, “Optimizing the Performance of an Integrated Process Planning and Scheduling Problem: An AIS-FLC based Approach,” *2006 IEEE Conference on Cybernetics and Intelligent Systems*, pp. 1–8, 2006.
- [11] W. Tan and B. Khoshnevis, “Integration of process planning and scheduling— a review,” *Journal of Intelligent Manufacturing*, vol. 11, no. 1, pp. 51–63, 2000.
- [12] D. Yip-Hoi and D. Dutta, “A genetic algorithm application for sequencing operations in process planning for parallel machining,” *IIE Transactions (Institute of Industrial Engineers)*, vol. 28, no. 1, pp. 55–68, 1996.
- [13] B. Yuan, C. Zhang, X. Shao, and Z. Jiang, “An effective hybrid honey bee mating optimization algorithm for balancing mixed-model two-sided assembly lines,” *Computers and Operations Research*, vol. 53, no. 5–8, pp. 32–41, 2015.

JOURNAL OF SCIENCE



SAKARYA UNIVERSITY

Sakarya University Journal of Science

ISSN 1301-4048 | e-ISSN 2147-835X | Period Bimonthly | Founded: 1997 | Publisher Sakarya University |
<http://www.saujs.sakarya.edu.tr/>

Title: Optimized Analytical Solution of Platform Panel Radiative Area Dimensioning of Geostationary Communications Satellites: A Practical Approach

Authors: Murat Bulut, Nedim Sözbir

Received: 2019-03-29 21:45:14

Accepted: 2019-06-17 12:53:04

Article Type: Research Article

Volume: 23

Issue: 5

Month: October

Year: 2019

Pages: 986-992

How to cite

Murat Bulut, Nedim Sözbir; (2019), Optimized Analytical Solution of Platform Panel Radiative Area Dimensioning of Geostationary Communications Satellites: A Practical Approach. Sakarya University Journal of Science, 23(5), 986-992, DOI: 10.16984/saufenbilder.546894

Access link

<http://www.saujs.sakarya.edu.tr/issue/44066/546894>

New submission to SAUJS

<http://dergipark.gov.tr/journal/1115/submission/start>



Optimized Analytical Solution of Platform Panel Radiative Area Dimensioning of Geostationary Communications Satellites: A Practical Approach

Murat Bulut^{*1}, Nedim Sözbir^{1,2,3}

Abstract

Determining radiative areas of geostationary satellite are one of the challenging tasks for satellite thermal engineers at the early stage of the project. Radiative areas of geostationary communication satellite for the payload and platform panels are determined based on worst hot case (end-of-life). After calculation of radiative areas, it needs to be optimized according to worst hot and cold scenario at sun acquisition mode, orbit raising mode and geostationary orbit. Authors, in this study, optimized geostationary satellite platform panel. The radiator's dimensions were calculated and then optimized based on sun acquisition mode, orbit raising mode and geostationary orbit. Determining radiative areas of GEO satellite is important task. Radiative areas always are determined based on hot case condition at EOL. On the other hand, these radiative areas needs to be optimized according SAM, ORM, and GEO scenario. Calculated radiative areas both the north panel and the south panel was 1 m². Radiative areas were studied at +/-10% m². It was seen from the analytical results that the surface temperature of the platform panel areas were between -48.5 °C at 1.1 m² of radiative area and 37.7 °C at 0.9 m² of radiative area.

Keywords: geostationary earth orbit satellite, thermal analysis, launcher, solar array

1. INTRODUCTION

The thermal control system (TCS) of a satellite is to maintain temperature of the electronic components of a satellite within acceptable limits during service life. TCS is divided into three parts which are thermal design, analysis, and test.

Based on the results of thermal analysis, thermal design is optimized and verified by the thermal

balance test [1]. Passive and active thermal control techniques are used during TCS. Passive thermal control technique includes in heat pipe (HP), optical solar reflector (OSR), and paintings. Active thermal control technique includes in

* Corresponding Author: bulut44@gmail.com

¹ Turksat Satellite Communication Cable TV and Operations Joint Stock Co., Satellite Programs Directorate, Golbasi, Ankara, Turkey. ORCID: 0000-0002-9024-7722

² Sakarya University, Mechanical Engineering Department, Esentepe, Sakarya, Turkey. ORCID:0000-0003-4633-2521

³ Tübitak MAM, Gebze, Kocaeli, Turkey. ORCID:0000-0003-4633-2521

heaters and thermistors. Thermocouples are used during the thermal test.

Preliminary design review (PDR) and critical design review (CDR) are two main milestones of the satellite project during thermal design and thermal analysis. At PDR phase, radiative areas of the satellite are calculated and then at CDR phase, radiative areas are finalized. Satellite thermal engineers always face the challenge of determining radiative areas at the stage of PDR and CDR phase.

Radiator system optimization is very common subject that many researches have been published numerous studies [2-11] but there is no paper established in optimized platform panel radiative area of three-axis stabilized geostationary communications satellites.

Curran and Lam [2] studied a mathematical model of the spacecraft that had embedded heat pipes in order to optimize radiator area according to payload heat rejection. They calculated the minimum weight configuration based on radiator surface parameters, heat pipe spacing, panel thermal conductives and facesheet thickness [2]. Sam and Deng [3] presented optimization of radiator area of geostationary communications satellite. Optimization of four radiator areas was done by using SINDA/FLUINT commercial software. Analysis results showed that reduction of the total weight was 5.87 kg. Comparing between initial approach and final approach, the weight saved was 1.5 kg. Arslanturk [4] presented the correlation equations to find the optimum dimensions of space radiators in order to maximize the heat transfer per unit radiator mass. Cockfield [5] studied on structural optimization of a radiator area. Kelly et al. [6] studied optimization of a heat pipe radiator area of spacecraft that had high power TWTAs. They developed a detailed analytical model of the radiator to evaluate thermal performance under worst-case environmental and operational conditions. Muraoka et al. [7] developed a simplified thermal model to calculate the optimum radiator/solar absorber areas and then the results of a simplified thermal model were implemented in a detailed thermal model. Their main study was to reduce computational time and

to optimize the radiator areas [7]. Hull et al. [8] presented the development of detailed analysis tool to design radiator area. Kim et al. [9] presented two radiator design optimization methods based on node division of the thermal model. An integrated analysis combining an optimization algorithm with thermal analysis was used at the first method. A radiator node stepwise was added based on a temperature sensitivity at the second method. Kim et al. [10] studied the optimization of a spacecraft radiator. The aim of the study was both enhancing the thermal performance and reducing mass of the spacecraft. Honeycomb core, the distance between heat pipes, facesheet thickness were three parameters during the optimization of the radiator areas. A strategy for a quick determination of the optimum configuration for radiators and solar absorbers in a spacecraft thermal design was presented Muraoka et al. [7]. The aim of the study was to maximize temperature margins and minimize heater power consumption. Hung and Deng [11] presented thermal design and optimization of a heat pipe radiator. A heat pipe radiator consisted of surface mounted heat pipe and embedded heat pipe. After sizing optimization of mounted and embedded heat pipes, minimum weight of the radiator was obtained.

In this study, radiative areas of the platform panels were optimized by analytical solution.

2. SATELLITE DESIGN DESCRIPTION

Figure 1 shows geostationary communication satellite which consists of gregorian antenna, deployable antenna, solar array, main structure and apogee boost motor (ABM) as the main parts. North and south panel outer surface areas are covered by multi layer insulation (MLI) except radiative areas, which are cover with optical solar reflector (OSR). MLI contain multi-layers of metalized mylar or kapton with little contact between each layer (to reduce conduction transfer). MLI has small emittance and absorptance [12]. OSR reflect the sun, but dissipate the heat through surfaces to which they are attached. The optical solar reflector has lower absorptivity value and higher emissivity value. The ratio of absorptivity/emissivity is low.

Therefore, OSR is material to use in space environment as thermal control system hardware [13]. Solar arrays are located at north and south panels in +y and -y directions. Deployable antennas are located at east and west panels in +x and -x directions. ABM is located zenith side in -z direction. Gregorian antenna is located on nadir panel in +z direction.

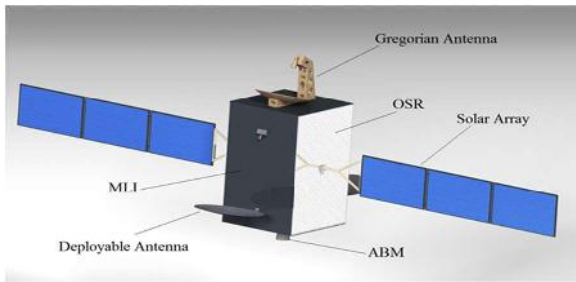


Figure 1. Geostationary communication satellite at GEO

The AOCS has three modes of operation which are sun acquisition mode (SAM), Inertial Attitude Acquisition Mode (IAAM) and Orbit Raising Mode (ORM) during transfer orbit (TO). These modes may be entered automatically or manually by ground control. Figure 2 shows AOCS of the satellite with respect to three modes at TO. SAM brings the satellite from an arbitrary initial condition to a sun pointing attitude, i.e. the desired principal axis is pointed to the sun and the satellite is to rotate around the sunline with a constant rate [14]. At ORM, the solar arrays are folded against two opposite sides of the satellite body which is spinning while the satellite is at SAM and ORM. Figure 3 shows the satellite at ORM and SAM.

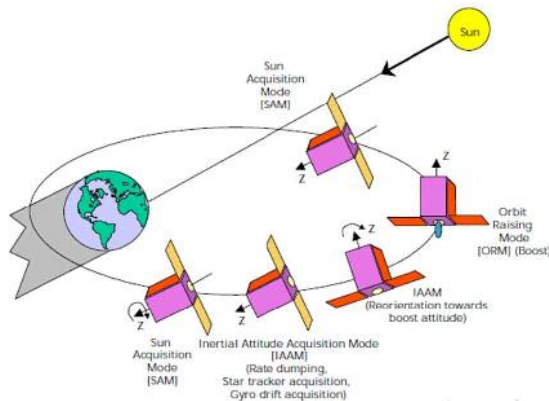


Figure 2. AOCS modes of the satellite at transfer orbit [15]

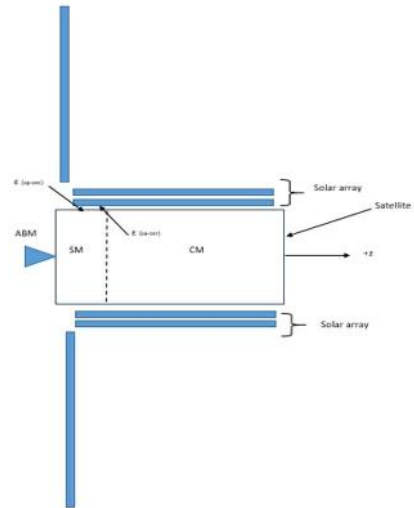


Figure 3. The satellite at ORM and SAM

3. THERMAL ANALYSIS DESCRIPTION

The main goals of TCS is to make sure that the internal components of the satellite remain within their acceptable temperature during the worst hot and cold conditions during service life. A steady-state thermal analysis and a transient thermal analysis are two types of thermal analysis [16-18]. A steady state thermal analysis determines the temperature distribution and other thermal quantities under conditions that a period of time can be ignored [17]. A transient thermal analysis determines the temperature distribution and other thermal quantities under conditions that vary over a period of time [17].

Energy balance for satellite is written as follows in equation (1) and (2).

$$Q_{in} = Q_{out} \quad (1)$$

$$Q_S + Q_A + Q_E + Q_d = Q_{Rad-S} \quad (2)$$

The left side equation (1); Q_S is environmental heat load from solar, Q_A is environmental heat load from albedo, Q_E is environmental heat load from Earth and Q_d is heat dissipation from electronic device. Heat load received by spacecraft (Q_{Rad-S}) is shown on the right side equation.

Equation (3) shows the heat balance between the radiator and the space environment in steady state [19].

$$(A_S q_S + A_A q_A) \alpha + A_E q_E \varepsilon + Q_d = A_{surface} \sigma T^4 \varepsilon \quad (3)$$

where A_S is the projected areas of solar, A_A is the projected area of albedo, A_E is the projected area of Earth, the satellite radiator area is $A_{surface}$. q_S , q_A and q_E are sun flux, albedo flux and Earth flux, respectively. α is absorptivity. ε is emissivity. σ is Stefan-Boltzmann constant σ is $5.699 \times 10^{-8} \text{ W/m}^2\text{K}^4$. T is temperature.

In Figure 4, radiator energy balance is also represented. Radiator areas of the satellite reject heat by infrared (IR) radiation. The radiating power depends on the surface emissivity values and temperature of radiator surface area. Radiative areas were covered by OSR material in order to reject heat from the satellite. Figure 4 shows radiator energy balance.

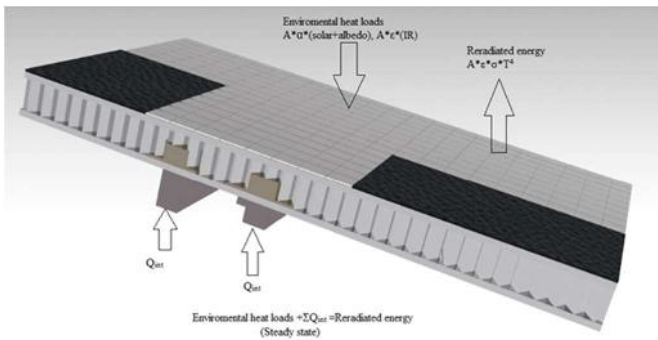


Figure 4. Radiator energy balance

Radiative area is optimized by using the following equation.

$$Q = A_{surface} * \sigma * [\varepsilon_{SP-OSR} * (T_{OSR}^4 - T_{space}^4) + \varepsilon_{SA} * (T_{OSR}^4 - T_{SA}^4)] \quad (4)$$

Q is the total heat loads comes from components and external heat. $A_{surface}$ is the radiative area. ε_{SP-OSR} is emissivity of OSR at structural panel. ε_{SA} is emissivity of solar array backside. T_{OSR} is the temperature of OSR at platform panel. T_{space} is the temperature of space environment which is taken as 4 °K. T_{SA} is the temperature of solar array. $A_{surface}$ would be assumed and T_{OSR} would be calculated. The representation of ε_{SP-OSR} and ε_{SA} is shown in Figure 3.

3.1. Thermal Analysis Input

In this study, the values and properties are taken as follows. At the beginning of life (BOL), The solar absorptivity of the OSR was taken approximately 0.11. The emissivity of the OSR (ε_{SP-OSR}) and the emissivity of solar array back side (ε_{SA}) would be approximately 0.84 and 0.42, respectively at BOL. The space temperature was taken at 4 °K. The solar array temperature of 20 °C at SAM and 60 °C at ORM are selected for the steady state thermal analysis. The intensity of solar radiation is 1418 W/m^2 . The internally generated heat dissipation by components is shown in Table 1.

Table 1. Platform panel heat dissipation

Mode	Case	North panel	South panel
		(W)	(W)
SAM	Cold	93.7	127.1
ORM	Cold	73.2	133.3
	Hot	73.2	133.3
GEO	Cold	189.3	123.7

The radiator's dimensions were determined considering cold scenario at sun acquisition mode (SAM), hot and cold scenario at orbit raising mode (ORM) and cold scenario at geostationary orbit (GEO). Four cases are considered during the analytical solution. Table 1 shows the list of the cases with respect to heat dissipation values. They are three cold cases (SAM, ORM and GEO) and one hot case (ORM). The mission, the orientation, surface properties and the size of the satellite are key parameters to determine the external head loads that are receive from the satellite. Knowing these parameters, the absolute worst hot and cold case conditions are determined [20]. The satellite is in sunlight during hot case conditions. The satellite does not see the Sun during col case condition.

4. RESULTS AND DISCUSSIONS

A steady state analysis was used at SAM, ORM, and GEO as the initial thermal analysis. Table 2

and Table 3 shows OSR area vs OSR temperature at north and south platform panel.

Table 2. OSR area vs OSR temperature at north platform panel

North panel				
Mode	SAM	ORM	GEO	
Case	Cold	Hot	Cold	Cold
SA temperature	20°C	60°C	60°C	60°C
Solar flux (W/m ²)	0	1418	0	0
Dissipation (W)	93.7	73.2	73.2	189.3
OSR area (m ²)	OSR temperature (°C)			
0.9	-2.43	20.81	-39.84	-15.36
0.92	-3.23	20.32	-40.82	-16.78
0.94	-4.01	19.85	-41.77	-18.15
0.96	-4.76	19.4	-42.69	-19.49
0.98	-5.48	18.97	-43.59	-20.79
1	-6.18	18.55	-44.46	-22.06
1.01	-6.52	18.34	-44.88	-22.69
1.02	-6.86	18.14	-45.3	-23.3
1.04	-7.52	17.75	-46.12	-24.51
1.06	-8.15	17.37	-46.92	-25.7
1.08	-8.77	17	-47.7	-26.85
1.1	-9.37	16.65	-48.45	-27.98

In Table 2, at 0.9 m² of radiative areas, the OSR temperatures at north panel is between -39.84 °C and 20.81 °C. The coldest temperature is at ORM (cold case). The hottest temperature is at ORM (hot case). The temperature difference between the coldest temperature and the hottest temperature is 60.61 °C. At 1.1 m² of radiative areas, the OSR temperatures at north panel varies between -48.45 °C and 16.65 °C. The coldest temperature is at ORM (cold case). The hottest temperature is at ORM (hot case). The temperature difference between the coldest temperature and the hottest temperature is 55 °C. OSR temperatures at ORM (cold case) for north panel varies -39.8 °C (0.9 m²) and -48.5 (1.1 m²). The temperatures difference is 8.7 °C.

Table 3. OSR area vs OSR temperature at south platform panel

South panel				
Mode	SAM	ORM	GEO	
Case	Cold	Hot	Cold	Cold
SA temperature	20°C	60°C	60°C	60°C
Solar flux (W/m ²)	0	1418	0	0
Dissipation (W)	127.1	133.3	133.3	123.7
OSR area (m ²)				
0.9	9.8	37.7	-9.49	-17.29
0.92	8.85	36.95	-10.73	-18.69
0.94	7.93	36.22	-11.93	-20.06
0.96	7.04	35.52	-13.1	-21.39
0.98	6.17	34.84	-14.23	-22.68
1	5.34	34.19	-15.34	-23.94
1.01	4.93	33.87	-15.88	-24.56
1.02	4.53	33.56	-16.41	-25.17
1.04	3.74	32.95	-17.46	-26.37
1.06	2.98	32.35	-18.48	-27.55
1.08	2.24	31.78	-19.47	-28.69
1.1	1.52	31.22	-20.44	-29.81

In Table 3, at 0.9 m² of radiative areas, the OSR temperatures at south panel is between -17.29 °C and 37.7 °C. The coldest temperature is at GEO (cold case). The hottest temperature is at ORM (hot case). The temperature difference between the coldest temperature and the hottest temperature is 54.99 °C. At 1.1 m² of radiative areas, the OSR temperatures at south panel is between -29.81 °C and 31.22 °C. The coldest temperature is at ORM (cold case). The hottest temperature is at ORM (hot case). The temperature difference between the coldest temperature and the hottest temperature is 61.03 °C. OSR temperatures at ORM (hot case) for south panel varies 37.7 °C (0.9 m²) and 31.22 °C (1.1 m²). The temperatures difference is 6.58 °C.

5. CONCLUSIONS

Determining radiative areas of GEO satellite is important task at early stage of the project. Radiative areas always are determined based on hot case condition at EOL. On the other hand, these radiative areas needs to be optimized according SAM, ORM, and GEO scenario. In this

study, the analytical solution was carried out to optimize the radiative areas of payload panels (the north and the south panels) that were 1 m^2 for each panel. Radiative areas were studied at $\pm 10\% \text{ m}^2$. Radiative areas of north and south panels from 0.9 m^2 to 1.1 m^2 were studied.

The results showed that OSR temperature of the panels depended on SAM, ORM, and GEO scenario. Increasing the radiative areas from 0.9 m^2 to 1.1 m^2 for the north panel, the coldest temperature decreased from $-39.84 \text{ }^\circ\text{C}$ to $-48.45 \text{ }^\circ\text{C}$. The hottest temperature decreased from $20.81 \text{ }^\circ\text{C}$ to $16.65 \text{ }^\circ\text{C}$. Increasing the radiative areas from 0.9 m^2 to 1.1 m^2 for the south panel, the coldest temperature decreased from $-17.29 \text{ }^\circ\text{C}$ to $-29.81 \text{ }^\circ\text{C}$. The hottest temperature decreased from $37.7 \text{ }^\circ\text{C}$ to $31.22 \text{ }^\circ\text{C}$.

It was seen from the results that at north panel OSR areas (1.1 m^2), the lowest temperature occurred as $-48.45 \text{ }^\circ\text{C}$. That means that north panel needed more heating power in order to maintain equipment within acceptable temperature limit. At south panel OSR areas (0.9 m^2), the highest temperature occurred as $37.7 \text{ }^\circ\text{C}$.

Based on the above results, satellite thermal engineers focus on the optimization of radiative areas based on radiative areas availability and heating power availability in the satellite.

6. REFERENCES

- [1] L. Yang, Q. Li, L. Kong, S. Gu and L. Zhang, "Quasi-all-passive thermal control system design and on-orbit validation of Luojia 1-01 satellite," *Sensors*, vol. 19, pp. 827-18, 2019.
- [2] D. Curran and T.T. Lam, "Weight optimization for honeycomb radiators with embedded heat pipes," *Journal of Spacecraft and Rockets*, vol. 33, pp. 822-828, 1996.
- [3] K.F.C.H. Sam and Z. Deng, "Optimization of a space based radiator," *Applied Thermal Engineering*, vol.31, pp. 2312-2320, 2011.
- [4] C. Arslanturk, "Optimum design of space radiators with temperature-dependent thermal conductivity," *Applied Thermal Engineering*, vol. 26, no. 17-18, pp. 1149-1157, 2006.
- [5] R.D. Cockfield, "Structural optimization of a space radiator," *Journal of Spacecraft and Rockets*, vol. 5, no. 10, pp. 1240-1241, 1968.
- [6] W.H. Kelly and Jr. J.H. Reisenweber 1982, "Optimization of a radiator heat pipe radiator for spacecraft high-power TWTAs," *Advances in Heat Pipe Technology, Proceedings of the IVth International Heat Pipe Conference*, London, UK, 1981.
- [7] I. Muraoka, R.L. Galski, F.L De Sousa and F.M. Ramos, "Stochastic spacecraft thermal design optimization with low computational cost," *Journal of Spacecraft and Rockets*, vol. 43, no. 6, 2006.
- [8] P.V. Hull, M. Tinker, M. SanSoucie, K. Kittredge, Thermal analysis and shape optimization of an in-space radiator using genetic algorithms, *AIP Conference Proceedings 813* (81), 2006.
- [9] H.K. Kim, S. Choi, S.O. Park and K.H. Lee, "Node-based spacecraft radiator design optimization," *Advances in Space Research*, vol. 55, no. 5, pp. 1445-1469, 2015.
- [10] T. Y. Kim, S. Chang and S. S. Young, "Optimizing the design of space radiators for thermal performance and mass reduction," *Journal of Aerospace Engineering*, vol. 30, no. 3, 04016090-1-04016090-6, 2017.
- [11] A.D. Williams and S.E. Palo, "Issues and Implications of the Thermal Control Systems on the 'six day spacecraft'," *in: 4th Responsive Space Conference, RS4-2006-6001*, Los Angeles, California, USA, 2006.

- [12] B. Pattan, *Satellite Systems Principles and Technologies*, New York, NY, Van Nostrand Reinhold; 1993, ISBN-13: 978-0442013578
- [13] M. G. Boato, E.C. Garcia, M.B. Dos Santos and A.F. Beloto, "Assembly and Testing of a Thermal Control Component Developed in Brazil," *Journal of Aerospace Technology and Management*, vol.9. no.2, 2017.
- [14] D.B. DeBra and E. Gottzein "Automatic Control in Aerospace 1992," *the 12th IFAC Symposium*, Ottobrunn, Germany, 1992.
- [15] Alcatel Alenia Space, Space Engineering & Operations University, AOCS Attitude and Orbit Control Subsystem Spacecraft Introduction Session, Ref: 200203304L Issue 1, 2005.
- [16] M. Bulut and N. Sozbir "Analytical investigation of a nanosatellite panel surface temperatures for different altitudes and panel combinations," *Applied Thermal Engineering*, vol. 75, pp. 1076-1083, 2015.
- [17] M. Bulut and N. Sozbir "Thermal Design of a Geostationary Orbit Communications Satellite," *Electronic World*, Pages: 28-32, August 2016.
- [18] M. Bulut, "Thermal simulation software based on excel for spacecraft applications," *Selcuk University Journal of Engineering Science and Technology*, vol. 6, no. 7, pp. 596-600, 2018.
- [19] M. Bulut and N. Sozbir, "Heat rejection capability for geostationary satellites," *9th Ankara International Aerospace Conference (AIAC 2017)*, METU, Ankara, Turkey, 2017.
- [20] K.F.C.H. Sam and D. Zhongmin, "Optimization of a space based radiator," *Applied Thermal Engineering*, vol. 31, pp. 2312-2320, 2011.

JOURNAL OF SCIENCE



SAKARYA UNIVERSITY

Sakarya University Journal of Science

ISSN 1301-4048 | e-ISSN 2147-835X | Period Bimonthly | Founded: 1997 | Publisher Sakarya University |
<http://www.saujs.sakarya.edu.tr/>

Title: Effect of Rapidly Annealing Process on MgB₂ Superconducting Wires

Authors: Firat Karaboğa

Received: 2019-04-11 17:39:31

Accepted: 2019-06-19 11:30:22

Article Type: Research Article

Volume: 23

Issue: 5

Month: October

Year: 2019

Pages: 993-1004

How to cite

Firat Karaboğa; (2019), Effect of Rapidly Annealing Process on MgB₂ Superconducting Wires. Sakarya University Journal of Science, 23(5), 993-1004,
DOI: 10.16984/saufenbilder.552659

Access link

<http://www.saujs.sakarya.edu.tr/issue/44066/552659>

New submission to SAUJS

<http://dergipark.gov.tr/journal/1115/submission/start>

Effect of Rapidly Annealing Process on MgB₂ Superconducting Wires

Firat KARABOĞA*¹

Abstract

The present study has reported the effect of rapidly annealing and cooling process on the transport and morphological properties of Fe/MgB₂ wires. Transport properties like critical transition temperature, transition width and engineering critical current density of the obtained wires at different annealing and durations were determined for superconducting wires. The results show that the annealing temperature is more dominant to accelerate the reaction rate of Mg and B in the wires in comparison with annealing duration. Among the studied wires, a highest J_c ($T = 36K$) value >150 A/cm² was achieved for the wires at 900°C and 1000°C for small durations (15 minutes). In the study, it was investigated whether fast annealing and cooling is a possible candidate to fabricate fast the requested superconducting MgB₂ long length wires for coils by React&Wind method in continuous system or not.

Keywords: MgB₂ wire, critical current density, heat treatment.

1. INTRODUCTION

Critical current density (J_c), critical transition temperature (T_c) and upper critical field (H_{c2}) parameters of superconducting materials are those of the most prominent properties in industrial applications. Since discovery of MgB₂ superconductors [1], has still interesting in terms of higher critical transition temperature than Nb based inter-metallic superconductors and workable above ~ 20 K(liquid hydrogen) as cryogen-free [2]. Many researchers have widely studied on the different application areas such as the materials engineering and heavy-industrial technology of superconducting materials namely, YBCO, BSSCO and especially MgB₂ superconducting materials [3-5]. Besides, nowadays the scientific studies on the wire or tape formations for the intermetallic binary superconductor MgB₂ as Magnetic resonance

imaging [6,7], high power wind turbines [8,9], hydrogen level sensor [10] and space satellite [11].

The fabricated wires commonly by means of powder-in-tube process (PIT) [12-15] have been improved to be applied into industrial by utilizing different preparations such as reactive liquid infiltration(RLI) method [16,17], internal magnesium diffusion (IMD) process [18], cold high pressure densification (CHPD) method [19], and advanced or modified internal magnesium diffusion (AIMD) procedure [20] in according to strengths and weaknesses. The manufacture process is categorized in two main processes as the in-situ and ex-situ MgB₂ method in terms of the initial filling powders. In-situ MgB₂ in the fabrication of superconductor wires has preferred due to the benefit as possible heat treatment at low temperature, comfortable doping, control of particle size, and high critical current density

* Corresponding Author

¹ Bolu Abant İzzet Baysal University-Mehmet Tanrikulu Vocational School of Health Services, Department of Medicine Services and Techniques, BOLU- karabogafirat@ibu.edu.tr ORCID: 0000-0001-8168-3242

under applied external magnetic field [21]. Additionally, there are various parameters that may control and affect the formation rate of the MgB₂ layer as annealing temperature and time [22], cooling and heating rate [23, 24], morphology of the B powder [25] thickness of the B layer [26] and also density of the B layer [27]. The factors affecting J_c performance are weak inter-grain connectivity, porosity, and low MgB₂ core density [28, 29]. Up to now, various manufacture methods [30,31], as several sheath materials [32], efficient dopants [33], and heat treatment conditions [34] have been tested and achieved. Fe sheathed MgB₂ wire or tape has been interested in fabrication due to useful in cold drawing process and relatively high critical current density in comparison with the used other sheaths, etc. [15]. On the other hand, low cost production of a single MgB₂ phase is hard due to the formation of different phases after reaction such as MgB₆, MgB₁₂, and MgO [35]. Heat-treatment, size and purity of constituents, and operational steps affect directly a pure MgB₂ formation. Oxidation and grain connectivity are grave questions in the preparation of MgB₂ samples. Since the critical current density being directly relation with grain connectivity is the most important parameter in applications. The increment of transport critical current density may be possible; however it still requests to diminish several extrinsic factors in the fabrication of wires and other devices [36, 37]. The major challenge is how to overcome the major limitations of inter-grain connectivity in MgB₂ formation to enhance critical current density (J_c). Hence, it is necessary to study the production variables relating to the superconductivity of MgB₂ in detailed. Further studies are needed concerning short annealing steps and short annealing times to obtain the optimum grain structure and to discover and to develop the performance of the MgB₂ sample [38]. The basic studies to deal with difficulties and to transfer gained experience to industrial applications have still been continued.

In the study, the electrical and morphological properties of various superconducting Fe sheathed MgB₂ wires produced with rapidly annealing and cooling via solid state reaction method have been examined by DC electrical

resistivity depending on temperature, critical current values at constant temperature closed to critical transition temperature (T_c) and scanning electron microscopy (SEM). The obtained results showed that the annealing temperature is more dominant according to annealing duration to increase reaction rate between Mg and B. High annealing temperature for small duration is needed to complete formation of MgB₂. The wires annealed at 900°C and 1000°C for small durations (15 minutes) have the highest J_c value >150 A/cm² at 36K temperature closed to critical transition temperature (T_c).

2. EXPERIMENTAL PROCEDURES

A high purity atomized spherical Mg powder (99.0% - 100-200 mesh) and elemental amorphous boron(95-97% pure) bought by Pavezyum Company were weighed in 1:2 ratio as stoichiometric and mixed with a ball milling machine for 3 hours for preparation of in-situ mixture. Then, iron tube OD/12.0mm and ID/9.00mm were cut 200mm in length and cleaned in alcohol with ultrasonic system for 30 minutes. After that, the Fe tube being the aluminium foil was pressed as stopper in both sides of iron tube was filled with densification about 1.30 g/cm³ by weighing 6 g of the obtained mixture by means of powder in tube method. Outer diameter of the prepared iron tube was drawn from 12.0mm to 1.00mm with the diameter 15 percent reduction and intermediate annealing processes. The monocoresh MgB₂/Fe superconducting wires after drawing process were obtained by conventional solid state reaction. The solid state reaction of the drawing wires was performed by annealing at different temperatures(in the range of 650°C and 1000°C) and durations (for 15 and 30 minutes) in a Protherm tube furnace PZF 12/75/700 with suddenly heating and cooling under 5 bar high purity argon pressure. The microstructural properties (grain connectivity, phase formation, densification, and surface morphology) were investigated by a scanning electron microscopy (SEM, JEOL 6390-LV). The DC resistivity measurements ($R-T$) and current carrying capacity measurement($I-V$) of the samples were carried out by the standard dc four probe technique between

10K and 50K and at close to T_c^{offset} values and constant temperature, respectively in CRYO Industries system (closed-cycle cryostat). The nano-voltmeter and the current source were programmable Keithley 2182A and Keithley 220, respectively.

3. RESULTS and DISCUSSIONS

Figure 1 shows the change of the resistivity values depending on temperature of the MgB₂ wires 1.00mm in diameter annealed between 650°C -

1000°C for 15 minutes in the range of 10 to 50 K. It can be said that resistivity value systematically increases with rising of annealing temperature for 15 min. On the other hand, the normal state resistivity of the MgB₂ wires was linearly increased at below 750°C for short time due to the metallic behaviour causing unreacted Mg. Additionally, the critical transition temperature (T_c) of the studied wires at different annealing temperatures for 15 min was the same (about 37.5K) excluding the wire annealed at 650°C for 15 min, because the annealing temperature is not enough for the completely reaction and it has extremely poor connectivity [39].

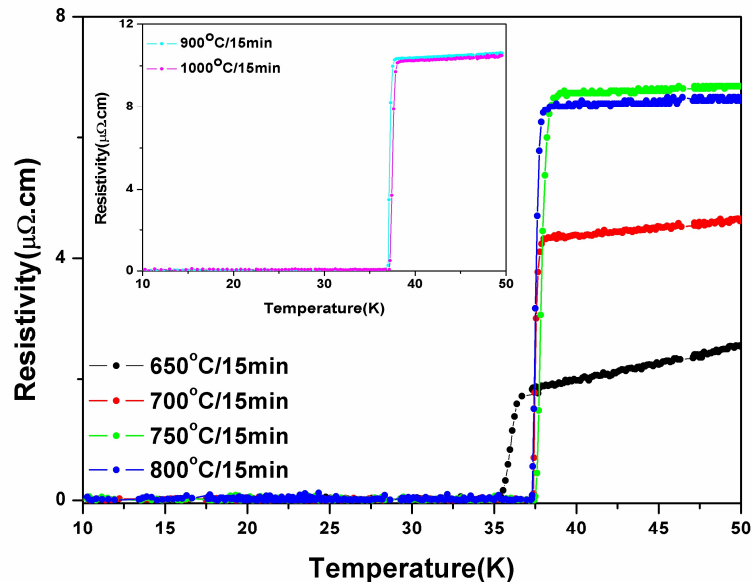


Figure 1. Resistivity vs temperature (ρ - T) curves of superconducting MgB₂/Fe wires obtained at 650 °C/15 min, 700 °C/15 min, 750 °C/15 min and 800 °C/15 min. The inset shows resistivity vs temperature (ρ - T) curves for the wires at 900 °C/15 min, and 1000 °C/15 min.

The resistivity curves depending on temperature of the MgB₂ wires 1.00mm in diameter annealed between 650°C and 800°C for 30 minutes in the range of 10 to 50 K were seen in Figure 2. It can be seen clearly that resistivity value rises with ascending of annealing temperature for 30 min. Furthermore, the normal state resistivity of the MgB₂ wires was also linearly increased due to the unreacted Mg at below 750 °C for 30 min. So, it can be said that the change of the annealing

temperature is more dominant to accelerate the reaction rate of Mg and B in the wires according to annealing duration. In addition, the critical transition temperature (T_c) of the studied wires at different annealing temperatures for 30 min was the same (about 37.5K). The normal state resistivity value (ρ_{40}) was mostly increased with annealing temperature and duration due to the formation of smaller grains.

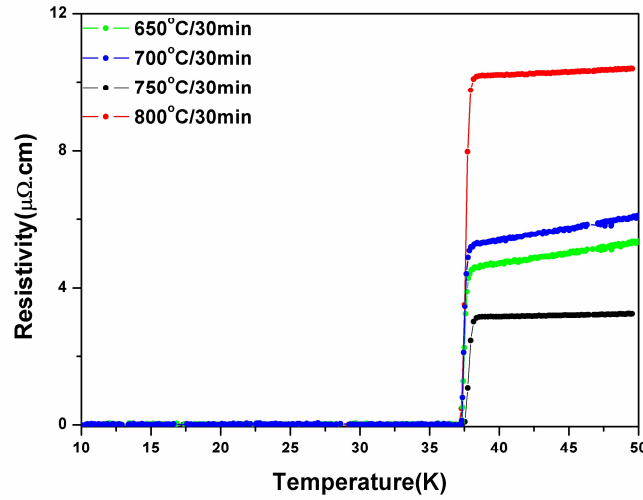


Figure 2. Resistivity vs temperature (ρ - T) curves of superconducting MgB₂/Fe wires obtained at 650 °C/30 min, 700 °C/30 min, 750 °C/30 min and 800 °C/30 min.

As indicated in Table 1, T_c^{onset} , T_c^{offset} , ΔT , T_c , ρ_{40} and slope of the normal state resistivity values of all studied MgB₂ wires can be seen in detailed. T_c values were obtained from the derivative of ρ - T curves. T_c^{offset} and T_c^{onset} values of the wires alter 35.27K to 37.43K and 37.42K to 38.62K, respectively. While T_c^{onset} value does not changes with increment of the annealing duration [38], the change of T_c^{offset} value depending on annealing duration can be significantly seen only at 650°C for 15 min and others are the same, because low annealing temperature(650°C) is near the melting point of Mg [39]. ΔT value being relation with grain connectivity change 0.64 K for the wire at 750°C for 15 min. to 2.15 K for the wire at 650°C for 15min. Also, the obtained results show that the maximum value of the normal state resistivity (ρ_{40}) is 10.38 $\mu\Omega$.cm and ρ_{40} value is approximately the same for greater annealing temperatures than 950°C for 15 min and 800 °C for 30 min. Furthermore, slope of the normal state resistivity altering linearly with temperature is max. 0.0618 $\mu\Omega$.cm/K and 0.0707 $\mu\Omega$.cm/K for the wires 650°C for 30 min. and 700°C for 30 min,

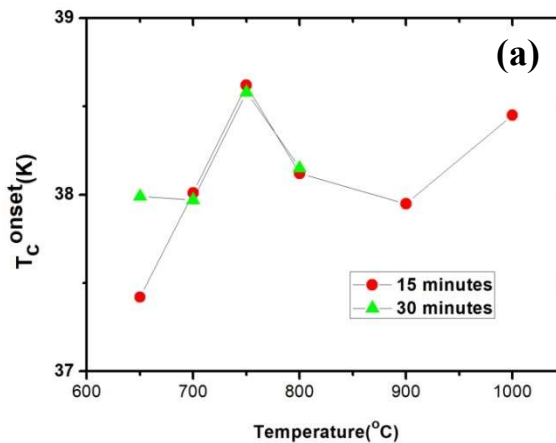
respectively. So, the longer time below 700°C is needed for comparison with the obtained wires at higher annealing temperature. The results indicate that annealing temperature (750 and 800°C) and duration (15 and 30 min.) are suitable for the production of the wires without unreacted Mg. Among the all studied samples, highest resistivity values are the same (10.25 $\mu\Omega$.cm) with negligible deviation (± 0.1 $\mu\Omega$.cm) for the wires at 800°C for 30 min, 900°C for 15 min and 1000°C for 15 min. In the results, it can be said that poor connectivity in the wires obtained at the higher annealing temperature occurs with increment of normal state resistivity as based on formation of the dense filament [40]. Also, increasing of resistivity or reducing of effective cross-section area of the samples is relation with MgO formation in the grain boundaries at high annealing temperature. Moreover, the results indicate that ascending of the annealing temperature and duration increases the normal state resistivity being directly relation with the amount of the grain boundaries and reversely proportional with grain-size.

Table 1. The obtained electrical values from the ρ - T curve of the studied MgB₂/Fe wires.

Samples	T_c^{onset} (K)	T_c^{offset} (K)	ΔT (K)	T_c (K)	ρ_{40} ($\mu\Omega.cm$)	Slope of normal state resistivity ($\mu\Omega.cm/K$)
650 °C/15 min	37.42	35.27	2.15	36.01	1.98	0.0564
700 °C/15 min	38.01	37.37	0.64	37.51	4.39	0.0363
750 °C/15 min	38.62	37.43	1.19	37.84	6.56	0.0144
800 °C/15 min	38.12	37.24	0.88	37.49	6.73	0.0137
900 °C/15 min	37.95	36.63	1.32	37.14	10.38	0.0233
1000 °C/15 min	38.45	37.15	1.30	37.37	10.25	0.0228
650 °C/30 min	37.99	37.29	0.70	37.37	4.68	0.0618
700 °C/30 min	37.97	37.27	0.70	37.47	5.37	0.0707
750 °C/30 min	38.58	37.33	1.25	37.72	3.13	0.0084
800 °C/30 min	38.15	37.12	1.03	37.49	10.19	0.0195

The effect of annealing temperature and short duration on superconducting properties of in situ MgB₂/Fe monocoire wires is investigated. Figure 3a, b presents the T_c^{onset} and T_c^{offset} critical temperature values of the wire samples as a function of annealing temperature and duration. In the results, while the T_c^{offset} values(37.27K with negligible deviation) of the wires obtained for 30 minutes do not depend on the annealing temperature up to 800°C, value of ones for 15 minutes changes significantly at temperature being greater than 800°C(36.63K and 37.15K) and smaller than 700°C(35.27K). Also, the T_c^{offset} values of the wires obtained at temperature between 700°C and 800°C are not different in

annealing durations for 15 and 30 minutes [40]. Moreover, when the Figure 3a,b and c are examined in detailed, the annealing duration in the range of 700°C and 800°C annealing temperature is not effective in terms of the T_c^{onset} , T_c^{offset} , ΔT values. In Figure 3c, the change of ΔT values indicates that the broadening of transition width (2.15K) for the wire at 650°C for 15 min. may be due to the uncompleted MgB₂ formation or inhomogeneity for short time heat treatment. The transition width (ΔT) relation with critical current density (J_c) and grain connectivity of the other wires changes with small variation in the range of 0.64K to 1.32K.



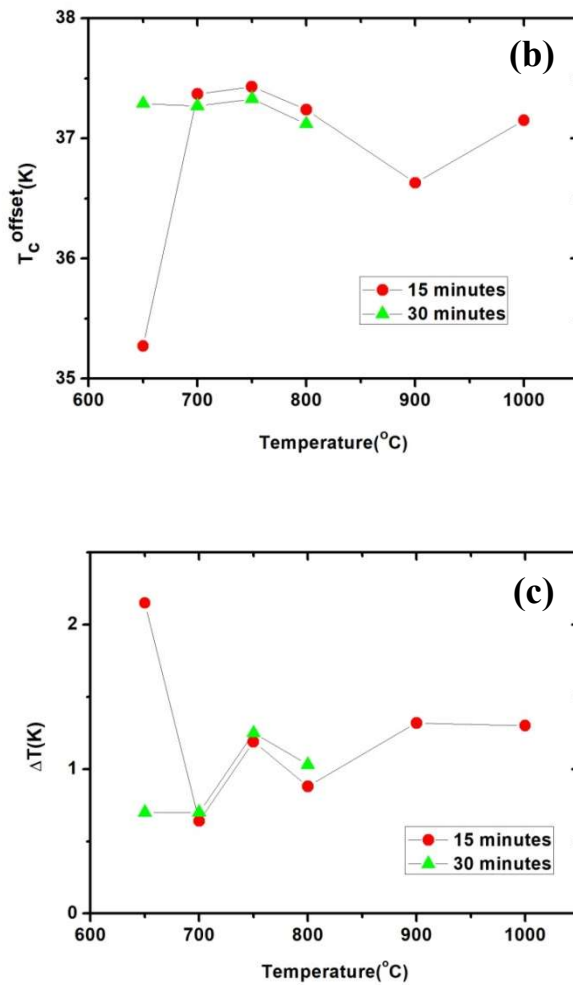


Figure 3. a) T_c^{onset} , b) T_c^{offset} and c) ΔT behaviour of the obtained MgB₂ wires with different annealing temperature and duration.

In the Figure 4, it can be seen that the critical current density (J_c) values of the wires obtained at 750°C and 800°C for 30 min and 900°C and 1000°C for 15 min. were measured at constant temperature (at 36 and 37 K) closed to critical transition temperature (T_c) by applying maximum 1 Amper(A). When the J_c value was measured at a certain temperature range being below 1 K of the T_c value of the studied wire, the result could be analysed easier by applying 1 A. Because, the J_c value of the wire decreases as it gets closer to T_c value. The performed previous our work with heating and cooling rate 5°C/min presents critical current density values in the range of 25A/cm² and 125A/cm² at different temperatures (800 °C - 1000°C) for 1 hour[28]. The results show that the highest J_c values(>150 A/cm²) at 36 K belong to

the wires at the high annealing temperature (900 and 1000°C) for 15 min. although T_c value of the wires at 750°C and 800°C for 30 min. were higher than those of annealed for 15 min. This may be attributed to the increment of J_c value with decrement of T_c value. The J_c values of the wires at 750°C for 30 min, 800°C for 30 min., 900°C for 15 min. and 1000°C for 15 min. were measured 18.88 A/cm², 6.88 A/cm², 32.63 A/cm² and 25.34 A/cm² at 37 K and 69.52 A/cm², 29.11 A/cm², >150 A/cm² and >150 A/cm² at 36 K, respectively. The J_c values decline with increment of annealing temperature at the same duration as Figure 4b, it may be due to the starting formation of Fe₂B phase [41] and MgB₄ phase [35] as impurity. Hence, it can be said that the J_c value decreases with long annealing duration at high

annealing temperature above 900°C due to more impurity phase formation[39].

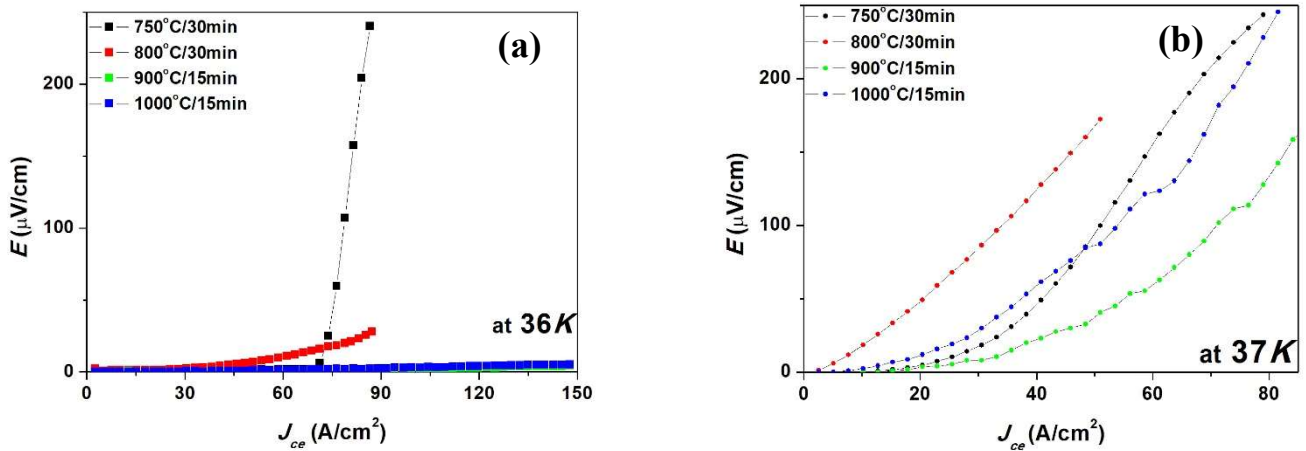


Figure 4. Electric field vs Critical current density ($E-J_c$) graph obtained at constant a-) 36K and b-) 37K for the wires at 750°C and 800°C for 30 min and 900°C and 1000°C for 15 min.

The Figure 5 (a)-(d) shows the cross-sectional SEM images taken from the polished surface of the superconducting wires 1.00mm in diameter at the different annealing temperatures and durations. The amount of the formed holes in the core of the wires mean that reaction between Mg and B is

possible even at 650°C being melting point of Mg for short duration (15 min.) by rapidly heating and cooling. Reaction rate depends on the annealing temperature and duration, however annealing temperature is more effective in accordance with the annealing duration.

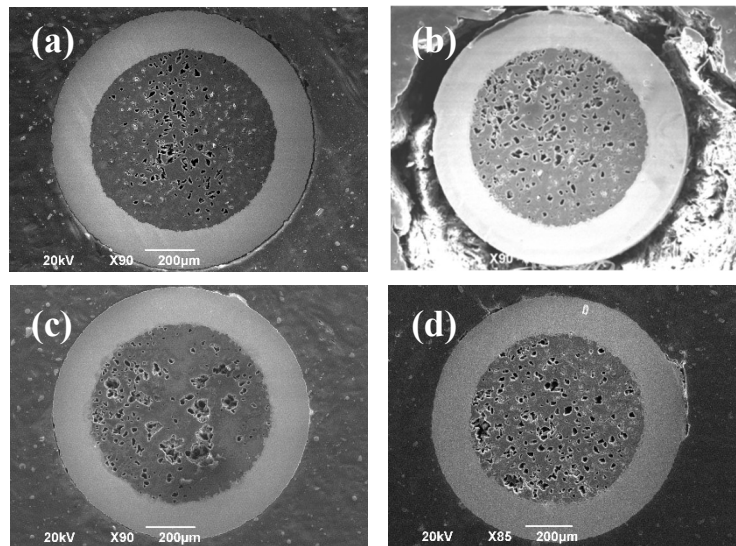


Figure 5. The cross-sectional SEM images of the wires (a) at 650°C-15min, (b) 700°C-15min, (c) 650°C-30min, and (d) 700°C-30min.

In Figure 6, it can be seen the SEM images with x1000 in magnification of the wires at different

annealing temperatures for 15 min. The diameter of the holes in the core of the wire is relation with

reaction process between Mg and B powders. The brightness in the core indicates the uncompleted reaction or the presence of Mg after annealing in the Figure 6 (a), (b) and this is compatible with the behaviour normal state resistivity depending on temperature in the electrical measurements. Also, while the size of the holes formed after reaction changes 10 to 15 μm for the wires at

650°C for 15 min, it alters 15 to 20 μm for the wires at 700°C for 15 min. As the annealing temperature increases 750°C to 900°C for 15 min, the size of the pores raises up to 30 μm . The SEM images shows the completed reaction between Mg and B due to no change significantly of the size of pores above 750°C and no detectible of the brightness at the near to holes.

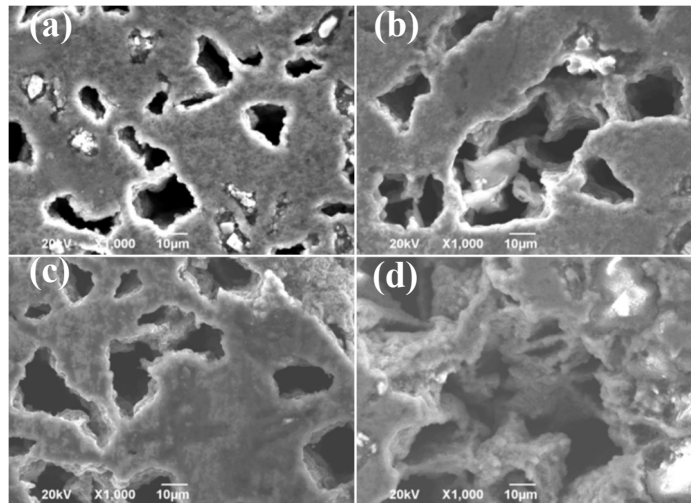
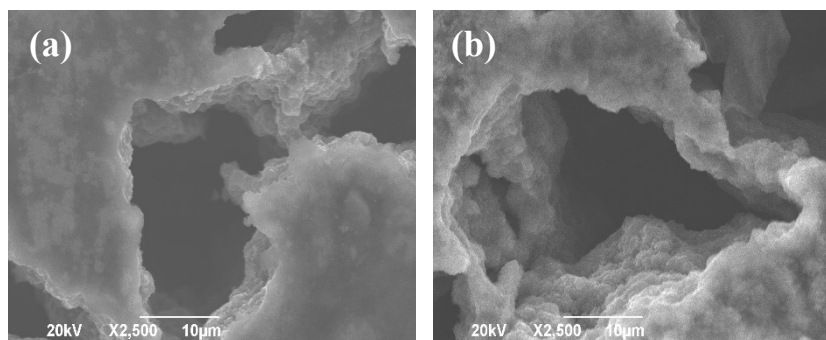


Figure 6. The SEM images of (a) 650 °C -15min, (b) 700 °C -15min, (c) 750 °C -15min, and (d) 900 °C -15min.

Figure 7 presents the SEM images with x2500 in magnification of the wire having high performance. Figure 7 (a) and (b) shows the size of pores does not alter with the short annealing duration at 750°C and it can be said that short annealing duration is recessive according to the annealing temperature. The surface morphology of the wires at the various annealing temperature and duration has almost the same up to 800°C as Figure 7 (a), (b) and (c). Moreover, the smaller

grain size occurs at high annealing temperature above 800°C and this causes more grain boundaries and resistivity. The observations in the SEM images are overlap with the other results. The pore size remains almost constant while the number of voids increases with increasing the annealing temperature. Finally, the structure in Figure 7(d) with well-connected small grains and less porosity supports to be perfect current ways causing high J_c .



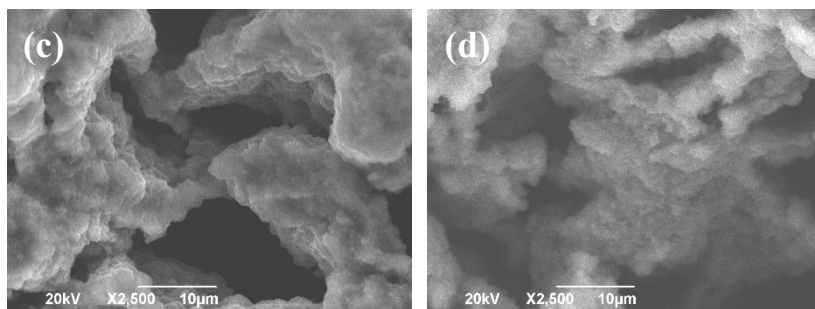


Figure 7. The SEM images of (a) 750 °C -15min, (b) 750 °C -30min, (c) 800 °C -30min, and (d) 900 °C -15min.

4. CONCLUSIONS

The effect of the rapidly annealing process on the superconducting wires was investigated by utilizing electrical and morphological results. The critical transition temperature (T_c) of all wires for 15 min. was about 37.5K excluding the wire annealed at 650°C causing extremely poor connectivity and no completely reaction. The annealing temperature is more dominant to accelerate the reaction rate of Mg and B in the wires in comparison with annealing duration. The wires at the high annealing temperature (900 and 1000°C) for 15 min have the highest J_{ce} values (>150 A/cm²) at 36 K although they were not the highest T_c value among the studied wires. The annealing temperature increases 750°C to 900°C for 15 min, the size of the pores rises up to max. 30 μm and the surface morphology of the wires at the various annealing temperature and duration have almost the same up to 800°C. It can be concluded that the rapidly annealing process has no negative effect on the electrical and morphological properties of the superconducting wires and this process may be possible for coil fabrication by using long wire to anneal rapidly in continuous systems with the React&Wind method.

ACKNOWLEDGEMENT

This study is funded by Bolu Abant Izzet Baysal University, Department of Scientific Research Projects under the contract 2018.32.03.1374.

REFERENCES

- [1] J. Nagamatsu, N. Nakagawa, T. Muranaka, Y. Zenitani, and J. Akimitsu, "Superconductivity at 39K in magnesium diboride," *Nature*, vol. 410, pp. 63-64, 2001.
- [2] Y. Iwasa, D. C. Larbalestier, M. Okada, R. Penco, M. D. Sumption, and X. X. Xi, "A round table discussion on MgB₂ toward a wide market or a niche production? A summary," *IEEE Transaction on Applied Superconductivity*, vol. 16, pp. 1457-1464, 2006.
- [3] S. B. Guner, Y. Zalaoglu, T. Turgay, O. Ozyurt, A. T. Ulgen, M. Dogruer, G. Yildirim, "A detailed research for determination of Bi/Ga partial substitution effect in Bi-2212 superconducting matrix on crucial characteristic features," *Journal of Alloys and Compounds*, vol. 772, pp. 388-398, 2019.
- [4] Y. Zalaoglu, B. Akkurt, M. Oz, G. Yildirim, "Transgranular region preference of crack propagation along Bi-2212 crystal structure due to Au nanoparticle diffusion and modeling of new systems," *Journal of Materials Science: Materials in Electronics*, vol. 28 pp. 12839-12850, 2017.
- [5] B. Akkurt, G. Yildirim, "Change of mechanical performance and

- characterization with replacement of Ca by Gd nanoparticles in Bi-2212 system and suppression of durable tetragonal phase by Gd,” *Journal of Materials Science: Materials in Electronics*, vol. 27 pp. 13034-13043, 2016.
- [6] M. Razeti, S. Angius, L. Bertora, D. Damiani, R. Marabotto, M. Modica, and M. Tassisto, “Construction and installation of cryogen free MgB₂ magnets for open MRI systems,” *IEEE Transactions on Applied Superconductivity*, vol. 18, pp. 882-886, 2008.
- [7] H. S. Kim, C. Kovacs, M. Rindfleisch, J. Yue, D. Doll, M. Tomsic, M. D. Sumption and E. W. Collings, “Demonstration of a Conduction Cooled React and Wind MgB₂ Coil Segment for MRI Applications,” *IEEE Transactions on Applied Superconductivity*, vol. 26 pp. 4400305-4400309, 2016.
- [8] S. Sanz, T. Arlaban, R. Manzanar, M. Tropeano, R. Funke, P. Kováč, Y. Yang, H. Neumann and B. Mondesert, “Superconducting light generator for large offshore wind turbines,” *Journal of physics: Conference Series* vol. 507, 032040, 2014.
- [9] I. Marino, A. Pujana, G. Sarmiento, S. J. M. Merino, M. Tropeano, J. Sun and T. Canosa, “Lightweight MgB₂ superconducting 10 MW wind generator,” *Superconductor Science and Technology*, vol. 29, pp. 024005-024016, 2016.
- [10] C. Haberstroh and G. A. Zick, “superconductive MgB₂ level sensor for liquid hydrogen,” *Advances in Cryogenic Engineering*, vol. 823, pp. 679-684, 2006.
- [11] S. I. Schlachter, W. Goldacker, A. Frank, B. Ringsdorf, H. Orschulko, “Properties of MgB₂ superconductors with regard to space applications,” *Cryogenics*, vol. 46(2-3), pp. 201-2017, 2006.
- [12] G. Grasso, A. Malagoli, C. Ferdeghini, S. Roncallo, V. Braccini, M. R. Cimberle and A. S. Siri, “Large transport critical currents in un-sintered MgB₂ superconducting tapes,” *Applied Physics Letter*, vol. 79, pp. 230-232, 2001.
- [13] H. L. Suo, C. Beneduce, M. Dhalle, N. Musolino, J. Y. Genoud and R. Flukiger “Large transport critical currents in dense Fe- and Ni-clad MgB₂ superconducting tapes,” *Applied Physics Letter*, vol. 79, pp. 3116-3118, 2001.
- [14] S. Soltanian, X. L. Wang, I. Kusevic, E. Babic, A. H. Li, M. J. Qin, J. Horvat, H. K. Liu, E. W. Collings, E. Lee, M. D. Sumption and S. X. Dou, “High transport critical current density above 30 K in pure Fe-clad MgB₂ tape,” *Physica C*, vol. 361, pp. 84-90, 2001.
- [15] S. Jin, H. Mavoori, C. Bower and R. B. van Dover, “High critical currents in iron-clad superconducting MgB₂ wires,” *Nature*, vol. 411, pp. 563-565, 2001.
- [16] G. Giunchi, S. Raineri, R. Wesche and P. Bruzzone, “The voltage-current relations for MgB₂ obtained by reactive liquid infiltration,” *Physica C: Superconductor*, vol. 401, pp. 310–315, 2004.
- [17] P. Badica, D. Batalu, M. Burdusel, M. A. Grigoroscuta, G. V. Aldica, M. Enculescu, R. A. Gabor, Z. Wang, R. Huang and P. Li, “Compressive properties of pristine and SiC-Te added MgB₂ powders, green compacts and spark-plasma-sintered bulks,” *Ceramics International*, vol. 44, pp. 10181–10191, 2018.
- [18] J. Hur, K. Togano, A. Matsumoto, H. Kumakura, H. Wada and K. Kimura, “Fabrication of high-performance MgB₂ wires by an internal Mg diffusion process,” *Superconductor Science and Technology*, vol. 21, pp. 032001, 2008.
- [19] R. Flukiger, M.S.A. Hossain and C. Senatore, “Strong enhancement of J_c and

- B_{irr} in binary in situ MgB₂ wires after cold high pressure densification,” *Superconductor Science and Technology*, vol. 22, pp. 085002, 2009.
- [20] G. Li, M. Sumption, M. Susner, Y. Yang, K. Reddy, M. Rindfleisch, M. Tomsic, C. Thong and E. Collings, “The critical current density of advanced internal-Mg-diffusion-processed MgB₂ wires,” *Superconductor Science and Technology*, vol. 25, pp. 115023, 2012.
- [21] W. K. Yeoh, J. H. Kim, J. Horvat, X. Xu, M. J. Qin, S. Dou, C. Jiang, T. Nakane, H. Kumakura and P. Munreo, “Control of nano carbon substitution for enhancing the critical current density in MgB₂,” *Superconductor Science and Technology*, 19, vol. 596-599, pp. 2006.
- [22] K. Togano, J. Hur, A. Matsumoto and H. Kumakura, “Microstructures and critical currents of single- and multi-filamentary MgB₂ superconducting wires fabricated by an internal Mg diffusion process,” *Superconductor Science and Technology*, vol. 23, pp. 085002, 2010.
- [23] O. V. Shcherbakova, A. V. Pan, S. Soltanian, S. X. Dou and D. Wexler, “Influence of the cooling rate on the main factors affecting current-carrying ability in pure and SiC-doped MgB₂ superconductors,” *Superconductor Science and Technology*, vol. 20, pp. 5-, 2007.
- [24] S. K. Chen, K. S. Tan, B. A. Glowacki, W. K. Yeoh, S. Soltanian, J. Horvat and S. X. Dou, “Effect of heating rates on superconducting properties of pure MgB₂, carbon nanotube- and nano-SiC-doped in situ MgB₂/Fe wires,” *Applied Physics Letters*, vol. 87, pp. 182504-182509, 2005.
- [25] P. Kováč, I. Hušek, A. Rosova, M. Kulich, T. Melišek, L. Kopera and B. Brunner “Properties of MgB₂ wires made by internal magnesium diffusion into different boron powders,” *Superconductor Science and Technology*, vol. 28, pp. 095014, 2015.
- [26] G. Z. Li, M. D. Sumption, M. A. Susner, Y. Yang, K. M. Reddy, M. A. Rindfleisch, M. J. Tomsic, C. J. Thong and E. W. Collings, “The critical current density of advanced internal-Mg-diffusion-processed MgB₂ wires” *Superconductor Science and Technology*, vol. 25, pp. 115023-115031, 2012.
- [27] P. Kováč, I. Hušek, W. Pachla, T. Melišek, M. Kulich, A. Rosová and L. Kopera, “Effect of cold isostatic pressing on the transport current of filamentary MgB₂ wire made by the IMD process,” *Superconductor Science and Technology*, vol. 29, pp. 075004, 2016
- [28] M. A. Senol, F. Karaboga, “Microstructure and transport properties of compaction-modified in situ Fe/MgB₂ wires,” *Journal of Superconductivity and Novel Magnetism*, vol. 29, pp. 2479, 2016.
- [29] A. Kario, A. Morawski, W. Haßler, M. Herrmann, C. Rodig, M. Schubert, K. Nenkov, B. Holzapfel, L. Schultz, B. A. Glowacki, S. C. Hopkins, “Novel ex situ MgB₂ barrier for in situ monofilamentary MgB₂ conductors with Fe and Cu sheath material,” *Superconductor Science and Technology*, vol. 23, pp. 025018, 2010.
- [30] J. M. Hur, K. Togano, A. Matsumoto, H. Kumakura, H. Wada and K. Kimura, “Fabrication of high-performance MgB₂ wires by an internal Mg diffusion process,” *Superconductor Science and Technology*, vol. 21, pp. 032001, 2008.
- [31] Y. E. Shujun and H. Kumakura, “The development of MgB₂ superconducting wires fabricated with an internal Mg diffusion (IMD) process,” *Superconductor Science and Technology*, vol. 29, pp. 113004, 2016.

- [32] T. Holubek, M. Dhalle and P. Kovac, "Current transfer in MgB₂ wires with different sheath materials," *Superconductor Science and Technology*, vol. 20, pp. 123, 2007.
- [33] J. H. Kim and S. Choi, "Carbon doping induced imperfections on MgB₂ superconducting wire," *Journal of Analytical Science and Technology*, vol. 6, pp. 11, 2015.
- [34] G. Bovone, D. Matera, C. Bernini, A. S. Siri, A. Malagoli and M. Vignolo, "The influence of wire heat treatment on PIT MgB₂ conductors manufactured using laboratory-made boron," *IEEE Transaction on Applied Superconductivity*, vol. 25, pp. 6200504, 2015.
- [35] N. N. Kolesnikov and M. P. Kulakov, "Synthesis of MgB₂ from elements," *Physica C*, vol. 363, pp. 166-169, Nov 15 2001.
- [36] R. Flukiger, M. S. A. Hossain, M. Kulich and C. Senatore, "Technical aspects of cold high pressure densification (CHPD) on long lengths of in situ MgB₂ wires with enhanced J_c values," *Advances in Cryogenic Engineering, AIP Conference Proceedings*, vol. 1435, pp. 353, 2012.
- [37] M. S. A. Hossain, A. Motaman, S. Barua, D. Patel, M. Mustapic, J. H. Kim, M. Maeda, M. Rindfleisch, M. Tomsic, O. Cicek, T. Melisek, L. Kopera, A. Kario, B. Ringsdorf, B. Runtsch, A. Jung, S. X. Dou, W. Goldacker and P. Kovac, "The roles of CHPD: superior critical current density and n-value obtained in binary in situ MgB₂ cables," *Superconductor Science and Technology*, vol. 27, pp. 095016, 2014.
- [38] M. Muralidhar, K. Nozaki, H. Kobayashi, X. L. Zeng, A. Koblishka-Veneva, M. R. Koblishka, K. Inoue and M. Murakami, "Optimization of sintering conditions in bulk MgB₂ material for improvement of critical current density," *Journal of Alloys and Compounds*, vol. 649, pp. 833-842, 2015.
- [39] A. Yamamoto, J. Shimoyama, S. Ueda, Y. Katsura, I. Iwayama, S. Horii and K. Kishio, "Effects of sintering conditions on critical current properties and microstructures of MgB₂ bulks," *Physica C*, vol. 426-431, pp. 1220-1224, 2005.
- [40] Y. Zhang, C. Lu, S. H. Zhou, K. C. Chung, Y. K. Kim, and S. X. Dou, "Influence of Heat Treatment on Superconductivity of MgB₂ Bulk Sintered in Flowing Welding Grade Ar Atmosphere," *IEEE Transactions on Magnetics*, vol. 45, pp. 2626-2629, 2009.
- [41] J. C. Grivel, R. Pinholt, N.H. Andersen, P. Kováč, I. Hušek and J. Homeyer, "In situ investigations of phase transformations in Fe-sheathed MgB₂ wires," *Superconductor Science and Technology*, vol. 19, pp. 96, 2006.

JOURNAL OF SCIENCE



SAKARYA UNIVERSITY

Sakarya University Journal of Science

ISSN 1301-4048 | e-ISSN 2147-835X | Period Bimonthly | Founded: 1997 | Publisher Sakarya University |
<http://www.saujs.sakarya.edu.tr/>

Title: Stability And Hopf Bifurcation in Three-Dimensional Predator-Prey Models With Allee Effect

Authors: İlknur Kuşbeyzi Aybar

Received: 2019-03-08 16:16:13

Accepted: 2019-06-21 21:44:53

Article Type: Research Article

Volume: 23

Issue: 5

Month: October

Year: 2019

Pages: 1005-1011

How to cite

İlknur Kuşbeyzi Aybar; (2019), Stability And Hopf Bifurcation in Three-Dimensional Predator-Prey Models With Allee Effect. Sakarya University Journal of Science, 23(5), 1005-1011, DOI: 10.16984/saufenbilder.537485

Access link

<http://www.saujs.sakarya.edu.tr/issue/44066/537485>

New submission to SAUJS

<http://dergipark.gov.tr/journal/1115/submission/start>



Stability and Hopf Bifurcation in Three-Dimensional Predator-Prey Models with Allee Effect

İlknur Kuşbeyzi Aybar ^{*1}

Abstract

In this study, we perform the stability and Hopf bifurcation analysis for two population models with Allee effect. The population models within the scope of this study are the one prey-two predator model with Allee growth in the prey and the two prey-one predator model with Allee growth in the preys. Our procedure for investigating each model is as follows. First, we investigate the singular points where the system is stable. We provide the necessary parameter conditions for the system to be stable at the singular points. Then, we look for Hopf bifurcation at each singular point where a family of limit cycles cycle or oscillate. We provide the parameter conditions for Hopf bifurcation to occur. We apply the algebraic invariants method to fully examine the system. We investigate the algebraic properties of the system by finding all algebraic invariants of degree two and three. We give the conditions for the system to have a first integral.

Keywords: predator-prey model, stability, Hopf bifurcation, algebraic invariants

1. INTRODUCTION

Various generalized predator-prey models that involve quadratic functions which exhibit logistic behaviour [1-3], cubic functions which show different rates of reproduction[4,5], Holling type II functions which state constant consumption[6,7] and Beddington-DeAngelis functions which indicate mutual interference and extinction[8,9] have been shown to overcome some of the biological problems of the original Lotka-Volterra model[10,11]. Population

carrying capacities are introduced into these generalizations by adding the proposed functions to the self-interaction and the coupling terms [12]. Applications of these generalizations have been studied in comparison in order to find suitable functional responses for modeling predation [13].

One of these generalizations include Allee effect which presents a positive relationship between the population size and the individual fitness particularly for invading species [14] and at low population [15-17]. The individual fitness is defined as the per capita population growth rate.

* Corresponding Author: ikusbeyzi@yeditepe.edu.tr

¹ Yeditepe University, Faculty of Education, Department of Computer Education and Instructional Technology, Istanbul, Turkey. ORCID: 0000-0002-5531-0095

Behaviours such as cooperative predation, cooperative defense and environmental and seasonal changes may result in the Allee effect. W. C. Allee first proposed the Allee effect to describe the relationship between the population and the mean of the individual population with the following cubic model [18].

$$\frac{dx}{dt} = ax(1-x)(x-\alpha)$$

Here, x denotes the population density, a denotes the population growth rate and α is the carrying capacity.

Allee effect is defined as a positive correlation between the individual fitness and the population density [19]. Populations with low densities are shown to be more likely to extinct [20] in the population models with the Allee effect. The carrying capacity of the populations may decrease below a critical density threshold in the presence of the Allee effect. In the models representing the spread of the invading organisms, the threshold exposed by the Allee effect may increase the invasion rate [21]. Population models with the Allee effect have various applications in plants and animals, hence it is important to understand the density thresholds to understand the underlying mechanisms of the propagation and extinction of these models. In 2008, Courchamp et.al suggested that Allee effect may even occur at high population levels for some species [22].

The Allee effect can be induced into the system in the prey's growth function. Hence there are two possible versions of inducing Allee effect into a three-dimensional predator-prey system. The differences in the dynamical properties of the two possible three-dimensional predator-prey generalizations with Allee effect have been given in this work. In section 2, we investigate the one prey-two predator system with Allee growth in the prey. In section 3, we investigate the two prey-one predator system with Allee growth in the preys.

2. THE ONE PREY-TWO PREDATOR SYSTEM WITH ALLEE GROWTH IN THE PREY

The one prey- two predator model with Allee growth in the prey is given by the following set of differential equations.

$$\frac{dx}{dt} = ax(1-x)(x-\alpha) - bxy - cxz \quad (1)$$

$$\frac{dy}{dt} = -dy + exy \quad (1)$$

$$\frac{dz}{dt} = -fz + gxz$$

Here x denotes the population density of the prey and y and z denote the population densities of the predators. The parameter a denotes the population growth rate and α is the carrying capacity. b and c are the consumption rates of the predators y and z over the prey. On the other hand, e and g are the growth rates of the predators from the consumption. d and f are the natural death rates of the predators. All parameters are positive since they represent physical values.

Theorem 1. System (1) has at least one stable singular point.

The Jacobian matrix of system (1) is

$$\begin{pmatrix} J_{11} & -bx & -cx \\ ey & ex - d & 0 \\ gz & 0 & gx - f \end{pmatrix},$$

$$J_{11} = a(x(2-3x) + \alpha(2x-1)) - by - cz.$$

Singular points and corresponding eigenvalues of the Jacobian matrix of system (1) are given in Table 1.

Table 1. Singular points and corresponding eigenvalues of the one prey-two predator system with Allee growth in the prey

Singular point	Corresponding eigenvalue
E_0 (0,0,0)	$\{-a\alpha, -d, -f\}$
E_1 (1,0,0)	$\{a(\alpha - 1), \alpha e - d, \alpha g - f\}$
E_2 ($\alpha, 0, 0$)	$\{-a\alpha(\alpha - 1), \alpha e - d, \alpha g - f\}$
E_3 ($\frac{d}{c}, \frac{a(e-d)(d-ae)}{be^2}, 0$)	$\{\frac{dg}{e} - f, \lambda_{3\pm}\}$
E_4 ($\frac{f}{g}, 0, \frac{a(g-f)(f-\alpha g)}{cg^2}$)	$\{\frac{ef}{g} - d, \lambda_{41,42}\}$

where

$$\lambda_{3\pm} = \frac{ad(e(1+\alpha)-2d) \pm \sqrt{ad(4e^2(d-e)(d-ae) + ad(e(1+\alpha)-2d)^2)}}{2e^2}$$

and

$$\lambda_{4\pm} = \frac{af(g(1+\alpha)-2f) \pm \sqrt{af(4g^2(f-g)(f-\alpha g) + af(g(1+\alpha)-2f)^2)}}{2g^2}$$

The eigenvalues of the Jacobian matrix of system (1) at E_0 are all negative which shows that system (1) is always stable at the origin.

According to the eigenvalues of the Jacobian matrix, E_1 is a stable singular point when $e < d$, $g < f$ and $\alpha < 1$ are satisfied together.

According to the eigenvalues of the Jacobian matrix, system (1) is stable at E_2 when $e < d$ and one of the following cases is satisfied.

- i. $g \leq \frac{ef}{d}$ and $1 < \alpha < \frac{d}{e}$
- ii. $\frac{ef}{d} < g < f$ and $1 < \alpha < \frac{f}{g}$

System (1) is stable at E_3 if $e < 2d$, $g < \frac{ef}{d}$ and $\alpha < \frac{2d}{e} - 1$.

E_4 is a stable singular point of system (1) when $e < 2d$, $\frac{ef}{d} < g < 2f$ and $\alpha < \frac{2f}{g} - 1$.

Therefore, system (1) is guaranteed to have at least one stable singular point which is at the origin.

Theorem 2. Hopf bifurcation occurs in system (1) if one of the following conditions is satisfied.

- i. $e < d$
- ii. $d < e < 2d$
- iii. $g < f$
- iv. $f < g < 2f$

According to the eigenvalues of the Jacobian matrix at E_3 , system (1) shows Hopf bifurcation if $\alpha = \frac{2d}{e} - 1$ and one of the cases i or ii is satisfied.

Furthermore, system (1) has Hopf bifurcation at E_4 if $\alpha = \frac{2f}{g} - 1$ and one of the cases iii or iv is satisfied.

Remark 1. The Hopf bifurcation at E_3 is stable if $g < \frac{ef}{d}$ additionally.

Remark 2. The Hopf bifurcation at E_4 is stable if one of the following cases is satisfied additionally.

- i. $e < d$ and $\frac{ef}{d} < g < f$
- ii. $f < g < 2f$
- iii. $d \leq e < 2d$ and $\frac{ef}{d} < g < 2f$

Theorem 3. System (1) has a first integral if one of the following conditions is satisfied.

- i. $a = d = f = 0$
- ii. $a = b = f = 0$
- iii. $a = c = d = 0$
- iv. $a = b = c = 0$
- v. $d = e = 0$
- vi. $e + g = d + f = 0$
- vii. $f = g = 0$

Proof. System (1) has the first integral

$$I_i = 1 + x + \frac{b}{e}y + \frac{c}{g}z + \frac{e}{2b}x^2 + xy + \frac{b}{2e}y^2 + \frac{ce}{bg}xz + \frac{c}{g}yz + \frac{c^2a}{2bg^2}z^2$$

when case i holds. System (1) has the first integrals $I_{ii_1} = 1 + y$, $I_{ii_2} = 1 + z$ and

$$I_{ii_3} = 1 + x + \frac{g}{2c}x^2 + \frac{c}{g}z + xz + \frac{c}{2g}z^2$$

when case ii is satisfied. For case iii, system has the first integral

$$I_{iii} = 1 + x + \frac{e}{2b}x^2 + \frac{b}{e}y + xy + \frac{b}{2e}y^2.$$

The first integrals of the system is

$I_{iv} = 1 + x + x^2$ for case iv and $I_v = 1 + y + y^2$ for case v. System has the first integral $I_{vi} = 1 + yz$ for case vi and $I_{vii} = 1 + z + z^2$ for case vii.

3. THE TWO PREY-ONE PREDATOR SYSTEM WITH ALLEE GROWTH IN THE PREYS

The two prey-one predator system with Allee effect in the preys' growth functions' is given by the following set of equations where x and y denote the population densities of the prey species and z denotes the population density of the predator species.

$$\frac{dx}{dt} = ax(1-x)(x-\alpha) - bxy \tag{2}$$

$$\frac{dy}{dt} = -dy(1-y)(y-\beta) - eyz$$

$$\frac{dz}{dt} = -fz + gxz + hyz$$

The parameters a and d denote the population growth rates and α and β are the carrying capacities of the prey population densities. b and e are the consumption rates of the predator z over the preys. On the other hand, g and h are the growth rates of the predator from the consumption. f is the natural death rate of the predator. All parameters are positive since they represent physical values.

Theorem 4. System (2) can be stable at given singular points.

Proof. The Jacobian matrix of system (2) is

$$J_{11} = \begin{pmatrix} 0 & 0 & -bx \\ 0 & dy(2-3y) + \beta d(2y-1) - ez & -ey \\ gz & hz & hy-f \end{pmatrix},$$

$$J_{11} = a(x(2-3x) + \alpha(2x-1) - bz).$$

The singular points and corresponding eigenvalues of the Jacobian matrix of system (2) is given in Table 2.

Table 2. Singular points and corresponding eigenvalues of the two prey-one predator system with Allee growth in the preys

	Singular point	Corresponding eigenvalue
E_0	(0,0,0)	$\{-a\alpha, -d\beta, -f\}$
E_1	(1,0,0)	$\{a(\alpha-1), -d\beta, g-f\}$
E_2	(0,1,0)	$\{-a\alpha, d(\beta-1), h-f\}$
E_3	(1,1,0)	$\{a(\alpha-1), d(\beta-1), g+h-f\}$
E_4	($\alpha, 0, 0$)	$\{a\alpha(1-\alpha), -d\beta, g\alpha-f\}$
E_5	($\alpha, 1, 0$)	$\{a\alpha(1-\alpha), d(\beta-1), g\alpha+h-f\}$
E_6	(0, $\beta, 0$)	$\{-a\alpha, d\beta(1-\beta), h\beta-f\}$
E_7	(1, $\beta, 0$)	$\{a(\alpha-1), d\beta(1-\beta), g+h\beta-f\}$
E_8	($\alpha, \beta, 0$)	$\{a\alpha(1-\alpha), d\beta(1-\beta), g\alpha+h\beta-f\}$
E_9	($\frac{f}{g}, 0, \frac{a(g-f)(f-\alpha g)}{bg^2}$)	$\{\frac{ae(f-g)(f-g\alpha)}{bg^2} - d\beta, \lambda_{9\pm}\}$
E_{10}	($\frac{f}{g}, 0, \frac{a(g-f)(f-\alpha g)}{bg^2}$)	$\{\frac{bd(f-h)(f-h\beta)}{eh^2} - a\alpha, \lambda_{10\pm}\}$
E_{11}	(x_{11}, y_{11}, z_{11})	($\{A, B \pm iC\}$)
E_{12}	($\bar{x}_{11}, \bar{y}_{11}, \bar{z}_{11}$)	($\{A, B \pm iC\}$)

where

$$\lambda_{9\pm} = \frac{1}{2g^2}(af(g(1+\alpha) - 2f) \pm \sqrt{af(4g^2(f-g)(f-g\alpha) + af(g(1+\alpha) - 2f)^2)})$$

$$\lambda_{10\pm} = \frac{1}{2h^2}(df(h(1+\beta) - 2f) \pm \sqrt{df(4h^2(f-h)(f-h\beta) + df(h(1+\beta) - 2f)^2)})$$

$$x_{11} = \frac{1}{2(bdg^2 - aeh^2)}(bdg(2f - h(1+\beta)) - aeh^2(1+\alpha) - \sqrt{\Delta_1}),$$

$$y_{11} = \frac{1}{2h(bdg^2 - aeh^2)} (h(bdg^2(1 + \beta) + aeh(g(1 + \alpha) - 2f) + g\sqrt{\Delta_1}))$$

$$z_{11} = \frac{ad}{2(bdg^2 - aeh^2)^2} (bdg^2(2(g - f)(f - \alpha g) - h(1 + \beta(g(1 + \alpha) - 2f) - h^2(1 + \beta^2))) - g(g(1 + \alpha) + h(1 + \beta) - 2f)\sqrt{\Delta_2} + aeh^2(2f(g(1 + \alpha) + h(1 + \beta) - 2f^2 - g^2(1 + \alpha^2)) - gh(1 + \alpha)(1 + \beta) - 2\beta h^2))$$

$$\Delta_1 = (aeh^2(1 + \alpha) + bdg(h(1 + \beta) - 2f))^2 - 4(bdg^2 - aeh^2)(bd(f - h)(f - \beta h) - aeah^2),$$

$$\Delta_2 = h^2(bd(bdg^2(\beta - 1)^2 + 4ae(f - g)(f - \alpha g) - 2abdeh(1 + \beta)(2f - g(1 + \alpha)) + ae(4b\beta d + aeh^2(\alpha - 1)^2))$$

E_0 is a stable singular point of system (2) when one of the following set of conditions are satisfied in addition to $\beta < \frac{2f}{h} - 1$.

- i. $h < f, \alpha \leq \frac{bdf(f-h)}{aeh^2}$
and $\frac{f}{h} - \frac{aah^2}{bdh(f-h)} < \beta$
- ii. $h < f$ and $\alpha > \frac{bdf(f-h)}{aeh^2}$
- iii. $f \leq h < 2f$

System (2) is stable at E_1 when $g < f$ and $\alpha < 1$ both hold.

At E_2 system (2) is stable when $g < f, h < f - g, 1 < \alpha < \frac{f-h}{g}$ and $\beta < 1$ hold.

E_3 is a stable singular point if $g < f, h < f - g, \alpha < 1$ and $\beta < 1$ hold.

E_4 is a stable singular point if $g < f$ and $1 < \alpha < \frac{f}{g}$ hold.

System (2) is stable at E_5 when $g < f, h < f - g, 1 < \alpha < \frac{f-h}{g}$ and $\beta < 1$ hold.

The singular point E_6 is stable when $h < f$ and $\beta < 1$ hold.

E_7 is a stable singular point when $g < f, h < f - g, \alpha < 1$ and $1 < \beta < \frac{f-g}{h}$ hold.

System (2) is stable at E_8 when $g < f, h < f - g, 1 < \alpha < \frac{f-h}{g}$ and $1 < \beta < \frac{f-\alpha g}{h}$ are satisfied.

System (2) is stable at E_9 when one of the following cases holds.

- i. $g < f, \alpha \leq \frac{f}{g}$ and
 $\beta > \frac{aef(f-g) - a\alpha eg(f+g)}{bdg^2}$
- ii. $g < f$ and $\frac{f}{g} < \alpha < \frac{2f}{g} - 1$
- iii. $f \leq g < 2f$ and $\alpha < \frac{2f}{g} - 1$

System (2) is stable at E_{10} when $h < f$ and $1 < \beta < \frac{f}{h}$ hold.

Since the expressions of system (2) at E_{11} and E_{12} are complex, it is not possible to calculate the eigenvalues of the Jacobian matrix at these singular points. In order to analyse the system at these points, the method of algebraic invariants can be applied.[23,24]

Theorem 5. Hopf bifurcation at E_0 is stable if it exists.

Proof. System (2) has Hopf bifurcation at E_0 when $\beta = \frac{2f}{h} - 1$ and one of the following conditions is satisfied.

- i. $h < f$
- ii. $f < h < 2f$

These conditions coincide with the stability of Hopf bifurcation.

Theorem 6. System (2) has a first integral when one of the following holds.

- i. $a = d = f = 0$
- ii. $a = f = h = 0$
- iii. $d = f = g = 0$
- iv. $f = g = h = 0$

Proof. For case i, system (2) has the first integral

$$I_i = 1 + \frac{g}{b}x + \frac{h}{e}y + z.$$

The first integral of system (2) for case ii is $I_{ii} = 1 + x + \frac{b}{g}z$.

System (2) has the first integral $I_{iii} = 1 + y + \frac{e}{h}z$ for case iii. When case iv holds, the first integral of system (2) is $I_{iv} = 1 + z$.

Theorem 7. System (2) has an algebraic invariant when $b = 0$ or $e = 0$ holds.

Proof. We look for an algebraic invariant of the form

$$L = a_0 + a_1x + a_2y + a_3z$$

with the corresponding cofactor

$$k = s_0 + s_1x + s_2y + s_3z + s_4x^2 + s_5y^2 + s_6z^2 + s_7xy + s_8xz + s_9yz$$

When $b = 0$ holds, system (2) has the algebraic invariants $l_1 = 1 - x$ with the cofactor $k_1 = aax - ax^2$ and $l_2 = 1 - \frac{x}{\alpha}$ with the cofactor $k_2 = ax - ax^2$. When $e = 0$, The algebraic invariants of system (2) are $l_1 = 1 - y$ with the cofactor $k_1 = \beta dy - dy^2$ and $l_2 = 1 - \frac{y}{\beta}$ with the cofactor $k_2 = dy - dy^2$.

3.1. Acknowledgments

This paper is presented at the 2nd International Conference of Mathematical Sciences (ICMS 2018) Maltepe University, Istanbul, Turkey [25].

4. REFERENCES

- [1] A. A. Berryman, "The origins and evolution of predator-prey theory," *Ecology*, vol. 73, no. 5, pp. 1530 – 1535, 1992.
- [2] H. W. Hethcote, W. D. Wang, L. T. Han and M. Zhiem, "A predator-prey model with infected prey," *Theoretical Population Biology*, vol. 66, no. 3, pp. 259—268, 2004.
- [3] I. Kusbeyzi Aybar, O. O. Aybar, M. Dukaric and B. Fercec, "Dynamical analysis of a two prey-one predator system with quadratic self interaction," *Applied Mathematics and Computation*, vol. 333, pp. 118—132, 2018.
- [4] X. C. Huang, Y. M. Wang and L. M. Zhu, "One and three limit cycles in a cubic predator-prey system," *Mathematical Methods in the Applied Sciences*, vol. 30, no. 5, pp. 501—511, 2007.
- [5] I. Kusbeyzi, O. O. Aybar and A. Hacinliyan, "Stability and bifurcation in two species predator-prey models," *Nonlinear Analysis: Real World Applications*, vol. 12, pp. 377—387, 2011.
- [6] X. N. Liu and L. S. Chen, "Complex dynamics of Holling type II Lotka-Volterra predator-prey system with impulsive perturbations on the predator," *Chaos Solitons and Fractals*, vol. 16, no. 2, pp. 311—320, 2003.
- [7] M. A. Aziz-Alaoui and M. D. Okiye, "Boundedness and global stability for a predator-prey model with modified Leslie-Gower and Holling-type II schemes," *Applied Mathematics Letters*, vol. 16, no. 7, pp. 1069—1075, 2003.
- [8] R. S. Cantrell and C. Cosner, "A predator-prey model with infected prey," *Journal of Mathematical Analysis and Applications*, vol. 257, no. 1, pp. 206—222, 2001.
- [9] M. Fan and Y. Kuang, "Dynamics of a nonautonomous predator-prey system with the Beddington-DeAngelis functional response," *Journal of Mathematical Analysis and Applications*, vol. 295, no. 1, pp. 15—39, 2004.

- [10] A. J. Lotka, *Elements of Physical Biology*, Williams and Wilkins Company, Baltimore, 1925.
- [11] V. Volterra, *Variations and fluctuations of a number of individuals in animal species living together*, in: *Animal Ecology*, Chapman, McGraw-Hill, New York, 1931.
- [12] E. Venturino, “Epidemics in predator-prey models: disease in the predators,” *IMA Journal of Mathematics Applied in Medicine and Biology*, vol. 19, no. 3, pp. 185—205, 2002.
- [13] G. T. Skalski and J. F. Gilliam, “Functional responses with predator interference: viable alternatives to the Holling Type II model,” *Ecology*, vol. 82, no. 11, pp. 3083—3092, 2001.
- [14] C. M. Taylor and A. Hastings, “Allee effects in biological invasions,” *Ecology Letters*, vol. 8, no. 8, pp. 895-908, 2005.
- [15] N. Knowlton, “Thresholds and Multiple Stable States in Coral-Reef Community Dynamics,” *Integrative and Comparative Biology*, vol. 32, no. 6, pp. 674—682, 1992.
- [16] J. A. Hutchings, and J. D. Reynolds, “Marine fish population collapses: Consequences for recovery and extinction risk,” *Bioscience*, vol. 54, no. 4, pp. 297—309, 2004.
- [17] R. A. Myers, N. J. Barrowman, J. A. Hutchings, and A. A. Rosenberg, “Population dynamics of exploited fish stocks at low population levels,” *Science*, vol. 269, no. 5227, pp. 1106—1108, 1995.
- [18] W.C. Allee, *Animal Aggregations: A Study in General Sociology*. University of Chicago Press, Chicago, 1931.
- [19] P. A. Stephens, W. J. Sutherland and R. P. Freckleton, “What is the Allee effect?,” *Oikos*, vol. 87, no. 1, pp. 185—190, 1999.
- [20] F. Courchamp, “Inverse density dependence and the Allee effect,” *Trends in Ecology and Evolution*, vol. 14, no. 10, pp. 405—410, 1999.
- [21] M. Kot, M. A. Lewis and P. vandenDriessche, “Dispersal data and the spread of invading organisms,” *Ecology*, vol. 77, no. 7, pp. 2027—2042, 1996.
- [22] F. Courchamp, J. Berc and J. Gascoigne, *Allee effects in ecology and conservation*, Oxford University Press, New York, 2008.
- [23] V. G. Romanovski and D.S. Shafer, *The Center and Cyclicity Problems: A Computational Algebra Approach*, Birkhauser, Boston-Basel-Berlin, 2009.
- [24] L. Liu, O. O. Aybar, V. G. Romanovski and W. Zhang, “Identifying weak foci and centers in the Maxwell–Bloch system,” *Journal of Mathematical Analysis and Applications*, vol. 430, no. 1, pp. 549—571, 2015.
- [25] I. Kusbeyzi Aybar, “Stability and Hopf bifurcation of 3D predator-prey models with Allee effect via computational algebra”, *International Conference of Mathematical Sciences (ICMS 2018)*, 31 July–06 August 2018, Maltepe University, Istanbul, Turkey.

JOURNAL OF SCIENCE



SAKARYA UNIVERSITY

Sakarya University Journal of Science

ISSN 1301-4048 | e-ISSN 2147-835X | Period Bimonthly | Founded: 1997 | Publisher Sakarya University |
<http://www.saujs.sakarya.edu.tr/>

Title: Hermite-Hadamard Type Inequalities For Exponentially P-Convex Stochastic Processes

Authors: Serap Özcan

Received: 2019-05-06 17:05:47

Accepted: 2019-06-24 11:47:45

Article Type: Research Article

Volume: 23

Issue: 5

Month: October

Year: 2019

Pages: 1012-1018

How to cite

Serap Özcan; (2019), Hermite-Hadamard Type Inequalities For Exponentially P-Convex Stochastic Processes. Sakarya University Journal of Science, 23(5), 1012-1018, DOI: 10.16984/saufenbilder.561040

Access link

<http://www.saujs.sakarya.edu.tr/issue/44066/561040>

New submission to SAUJS

<http://dergipark.gov.tr/journal/1115/submission/start>



Hermite-Hadamard Type Inequalities for Exponentially p -Convex Stochastic Processes

Serap Özcan*¹

Abstract

In this paper, the concept of exponentially p -convex stochastic process is introduced. Several new inequalities of Hermite-Hadamard type for exponentially p -convex stochastic process are established. Some special cases are given which are obtained from our main results. The results obtained in this work are the generalizations of the known results.

Keywords: Convex stochastic processes, p -convex stochastic processes, exponentially p -convex stochastic processes, mean-square integral, Hermite-Hadamard type inequality

1. INTRODUCTION

Stochastic process is a research area in probability theory dealing with probabilistic models that develop over time. It is seen as a branch of mathematics, because it starts with the axioms of probability and gives rise to remarkable results about those axioms. Even though those results are applicable to many areas, at first they are best understood with regard to their mathematical structures.

Stochastic convexity is of great importance in statistics and probability, also in optimization, because it provides numerical approximations when there exist probabilistic quantities.

In 1980, Nikodem [8] defined convex stochastic processes and investigated their properties. In 1988, Shaked et al. [13] defined stochastic

convexity and gave its applications. In 1992, Skowronski [14] introduced some new types of convex stochastic processes and obtained some further results on these processes. In 2012, Kotrys [3] extended classical Hermite-Hadamard inequality to convex stochastic processes.

In recent years, there have been many studies on the above mentioned processes. For recent generalizations and improvements on convex stochastic processes, please refer to [2]-[6], [9]-[12], [15], [16].

2. PRELIMINARIES

Suppose (Ω, ξ, P) be a probability space and $X: \Omega \rightarrow \mathbb{R}$ be a function. If the function X is ξ -measurable it is called a random variable. Suppose $I \subset \mathbb{R}$ be an interval. A function $X: I \times \Omega \rightarrow \mathbb{R}$ is called a stochastic process, if the function $X(s, \cdot)$ is a random variable for all $s \in I$.

* Corresponding Author: serapozcann@yahoo.com

¹ Department of Mathematics, Faculty of Arts and Sciences, Kırklareli University, 39100, Kırklareli, Turkey.
ORCID: 0000-0001-6496-5088

Let $P - \lim$ and $E[X(s, \cdot)]$ denote the limit in probability and the expectation value of random variable $X(t, \cdot)$, respectively. Then, a stochastic process $X: I \times \Omega \rightarrow \mathbb{R}$ has

(1) continuity in probability in I , if for every $s_0 \in I$

$$P - \lim_{s \rightarrow s_0} X(s, \cdot) = X(s_0, \cdot).$$

(2) mean-square continuity in I , if for all $s_0 \in I$

$$\lim_{s \rightarrow s_0} E \left[(X(s, \cdot) - X(s_0, \cdot))^2 \right] = 0.$$

(3) mean-square differentiability at a point $s \in I$ if there exists a random variable $X'(s, \cdot): I \times \Omega \rightarrow \mathbb{R}$ such that

$$X'(s, \cdot) = P - \lim_{s \rightarrow s_0} \frac{X(s, \cdot) - X(s_0, \cdot)}{s - s_0}.$$

Note that if the stochastic process $X: I \times \Omega \rightarrow \mathbb{R}$ has mean-square continuity, then it has continuity in probability, but the converse is not true.

Let $X: I \times \Omega \rightarrow \mathbb{R}$ be a stochastic process with $E \left[(X(s, \cdot))^2 \right] < \infty$ and for all $s \in I$. Let $c = s_0 < s_1 < s_2 < \dots < s_n = d$ be a partition of $[c, d]$, if the identity

$$\lim_{n \rightarrow \infty} E \left[(X(\theta_j)(s_j - s_{j-1}) - Y)^2 \right] = 0$$

holds for all normal sequences of partitions of $[c, d]$ and for all $\theta_j \in [s_{j-1}, s_j]$, $k = 1, 2, \dots, n$. Then, we can write

$$Y(\cdot) = \int_c^d X(t, \cdot) dt \quad (\text{almost everywhere})$$

The assumption of the mean-square continuity of the stochastic process X is enough for the mean-square integral to exist.

Definition 2.1. [8] The stochastic process $X: I \times \Omega \rightarrow \mathbb{R}$ is said to be convex if for all $\theta \in [0, 1]$ and $c, d \in I$ the inequality

$$X(\theta c + (1 - \theta)d, \cdot) \leq \theta X(c, \cdot) + (1 - \theta)X(d, \cdot) \quad (1)$$

is satisfied almost everywhere. If the inequality (1) is assumed only for $\lambda = \frac{1}{2}$, then the stochastic process X is called Jensen-convex or $\frac{1}{2}$ -convex.

Theorem 2.2. [3] Let $X: I \times \Omega \rightarrow \mathbb{R}$ be a Jensen-convex stochastic process and mean-square continuous in I . Then for every $c, d \in I$, $c < d$, the inequality

$$X\left(\frac{c+d}{2}, \cdot\right) \leq \frac{1}{d-c} \int_c^d X(s, \cdot) ds \leq \frac{X(c, \cdot) + X(d, \cdot)}{2} \quad (2)$$

is satisfied almost everywhere.

Definition 2.3. [9] The stochastic process $X: I \times \Omega \rightarrow \mathbb{R}$ is called a p -convex stochastic process if the inequality

$$X\left([\theta c^p + (1 - \theta)d^p]^{\frac{1}{p}}, \cdot\right) \leq \theta X(c, \cdot) + (1 - \theta)X(d, \cdot)$$

holds almost everywhere for all $c, d \in I \subset (0, \infty)$, $\theta \in [0, 1]$ and $p \in \mathbb{R} \setminus \{0\}$.

Theorem 2.4. [9] Let $X: I \subset (0, \infty) \times \Omega \rightarrow \mathbb{R}$ be a p -convex stochastic process and mean-square integrable on $[c, d]$ where $c, d \in I$ and $c < d$. Then

$$X\left(\left[\frac{c^p + d^p}{2}\right]^{\frac{1}{p}}, \cdot\right) \leq \frac{p}{d^p - c^p} \int_c^d \frac{X(s, \cdot)}{s^{1-p}} ds \leq \frac{X(c, \cdot) + X(d, \cdot)}{2} \quad (3)$$

Lemma 2.5. [9] Let $X: I \subset (0, \infty) \times \Omega \rightarrow \mathbb{R}$ be a mean-square differentiable stochastic process on I° (the interior of I) and $c, d \in I$, $c < d$ and $p \in \mathbb{R} \setminus \{0\}$. If X' is mean-square integrable on $[c, d]$, then the following equality holds almost everywhere:

$$\begin{aligned} & \frac{X(c, \cdot) + X(d, \cdot)}{2} - \frac{p}{d^p - c^p} \int_c^d \frac{X(s, \cdot)}{s^{1-p}} ds \\ &= \frac{d^p - c^p}{2p} \int_0^1 \frac{1 - 2\theta}{[\theta c^p + (1 - \theta)d^p]^{1-\frac{1}{p}}} \\ & \quad \times X'([\theta c^p + (1 - \theta)d^p]^{\frac{1}{p}}, \cdot) d\theta. \end{aligned}$$

Definition 2.6. [7] A function $f: I \subset (0, \infty) \rightarrow \mathbb{R}$ is called exponentially p -convex if the inequality

$$f\left([\lambda u^p + (1-\lambda)v^p]^{\frac{1}{p}}\right) \leq \lambda \frac{f(u)}{e^{\alpha u}} + (1-\lambda) \frac{f(v)}{e^{\alpha v}}$$

holds for all $u, v \in I$, $p \in \mathbb{R} \setminus \{0\}$, $\lambda \in [0,1]$ and $\alpha \in \mathbb{R}$.

Now we recall the following special functions (see [1]).

The beta function is defined as:

$$\beta(x, y) = \int_0^1 \lambda^{x-1} (1-\lambda)^{y-1} d\lambda, \quad x > 0, y > 0.$$

The hypergeometric function is as follows:

$$\begin{aligned} & {}_2F_1(a, b; c; z) \\ &= \frac{1}{\beta(b, c-b)} \int_0^1 \lambda^{b-1} (1-\lambda)^{c-b-1} (-z\lambda)^{-a} d\lambda \end{aligned}$$

for $c > b > 0, |z| < 1$.

3. MAIN RESULTS

In this section we introduce a new concept, which is called exponentially p -convex stochastic process. We establish new Hermite-Hadamard type inequalities for exponentially p -convex stochastic process. We also give some special cases obtained from our main results.

Definition 3.1. The stochastic process $X: I \times \Omega \rightarrow \mathbb{R}$ is called exponentially p -convex, if the following inequality holds almost everywhere:

$$\begin{aligned} X\left([\theta c^p + (1-\theta)d^p]^{\frac{1}{p}}, \cdot\right) \\ \leq \theta \frac{X(c, \cdot)}{e^{\alpha c}} + (1-\theta) \frac{X(d, \cdot)}{e^{\alpha d}} \end{aligned} \quad (4)$$

for all $c, d \in I \subset (0, \infty)$, $\theta \in [0,1]$, $p \in \mathbb{R} \setminus \{0\}$ and $\alpha \in \mathbb{R}$. If the inequality (4) is reversed, then the process X is called exponentially p -concave.

It can be easily seen that, an exponentially p -convex stochastic process reduces to p -convex and convex stochastic processes for $\alpha = 0$ and $(\alpha, p) = (0,1)$, respectively.

Theorem 3.2. Let $X: I \subset (0, \infty) \rightarrow \mathbb{R}$ be an exponentially p -convex stochastic process. Let $c, d \in I$ with $c < d$. If X is mean-square integrable on $[c, d]$, then for $p \in \mathbb{R} \setminus \{0\}$ and $\alpha \in \mathbb{R}$, we have almost everywhere

$$\begin{aligned} X\left(\left[\frac{c^p + d^p}{2}\right]^{\frac{1}{p}}, \cdot\right) &\leq \frac{p}{d^p - c^p} \int_c^d \frac{X(s, \cdot)}{s^{1-p} e^{\alpha s}} ds \\ &\leq A_1(\theta) \frac{X(c, \cdot)}{e^{\alpha c}} + A_2(\theta) \frac{X(d, \cdot)}{e^{\alpha d}} \end{aligned} \quad (5)$$

where

$$\begin{aligned} A_1(\theta) &= \int_0^1 \frac{\theta d \theta}{e^{\alpha(\theta c^p + (1-\theta)d^p)^{\frac{1}{p}}}} \\ A_2(\theta) &= \int_0^1 \frac{(1-\theta) d \theta}{e^{\alpha(\lambda c^p + (1-\theta)d^p)^{\frac{1}{p}}}} \end{aligned}$$

Proof. From exponential p -convexity of the stochastic process X , we have

$$2X\left(\left[\frac{s^p + t^p}{2}\right]^{\frac{1}{p}}, \cdot\right) \leq \frac{X(s, \cdot)}{e^{\alpha s}} + \frac{X(t, \cdot)}{e^{\alpha t}}.$$

Let $s^p = \theta c^p + (1-\theta)d^p$ and $t^p = (1-\theta)c^p + \theta d^p$. So, we get

$$\begin{aligned} 2X\left(\left[\frac{c^p + d^p}{2}\right]^{\frac{1}{p}}, \cdot\right) &\leq \frac{X([\theta c^p + (1-\theta)d^p]^{\frac{1}{p}}, \cdot)}{e^{\alpha(\theta c^p + (1-\theta)d^p)^{\frac{1}{p}}}} \\ &\quad + \frac{X([(1-\theta)c^p + \theta d^p]^{\frac{1}{p}}, \cdot)}{e^{\alpha((1-\theta)c^p + \theta d^p)^{\frac{1}{p}}}}. \end{aligned}$$

Integrating with respect to $\theta \in [0,1]$ and applying the change of variable method, we have

$$X\left(\left[\frac{c^p + d^p}{2}\right]^{\frac{1}{p}}, \cdot\right) \leq \frac{p}{d^p - c^p} \int_c^d \frac{X(s, \cdot)}{s^{1-p} e^{\alpha s}} ds. \quad (6)$$

Thus, the left-hand side of the inequality (5) is established. For the right-hand side of the inequality (5), again utilizing the exponential p -convexity of the stochastic process X , we have

$$\frac{X\left([\theta c^p + (1-\theta)d^p]^{\frac{1}{p}}, \cdot\right)}{e^{\alpha(\theta c^p + (1-\theta)d^p)^{\frac{1}{p}}}} \leq \frac{\theta \frac{X(c, \cdot)}{e^{\alpha c}} + (1-\theta) \frac{X(d, \cdot)}{e^{\alpha d}}}{e^{\alpha(\theta c^p + (1-\theta)d^p)^{\frac{1}{p}}}}$$

Integrating with respect to θ on $[0,1]$, we have

$$\begin{aligned} \frac{p}{d^p - c^p} \int_c^d \frac{X(s, \cdot)}{s^{1-p} e^{\alpha s}} ds &\leq \frac{X(c, \cdot)}{e^{\alpha c}} \int_0^1 \frac{\theta d\theta}{e^{\alpha(\theta c^p + (1-\theta)d^p)^{\frac{1}{p}}}} \\ &+ \frac{X(d, \cdot)}{e^{\alpha d}} \int_0^1 \frac{(1-\theta)d\theta}{e^{\alpha(\theta c^p + (1-\theta)d^p)^{\frac{1}{p}}}}. \end{aligned} \quad (7)$$

A combination of inequalities (6) and (7) gives inequality (5).

Remark 3.3. Choosing $\alpha = 0$ in Theorem 3.2, we get inequality (3) in Theorem 2.4.

Remark 3.4. By taking $(\alpha, p) = (0,1)$ in Theorem 3.2, we attain inequality (2) in Theorem 2.2.

Theorem 3.5. Let $X: I \subset (0, \infty) \times \Omega \rightarrow \mathbb{R}$ be a differentiable stochastic process on I° and X' be mean-square integrable on $[c, d]$. If $|X'|^q$ is exponentially p -convex stochastic process on $[c, d]$ for $q \geq 1$, $c, d \in I^\circ$, $c < d$ and $p \in \mathbb{R} \setminus \{0\}$, then the following inequality holds almost everywhere

$$\begin{aligned} &\left| \frac{X(c, \cdot) + X(d, \cdot)}{2} - \frac{p}{d^p - c^p} \int_c^d \frac{X(s, \cdot)}{s^{1-p}} ds \right| \\ &\leq \frac{d^p - c^p}{2p} B_1^{1-\frac{1}{q}} \left[B_2 \left| \frac{X'(c, \cdot)}{e^{\alpha c}} \right|^q + B_3 \left| \frac{X'(d, \cdot)}{e^{\alpha d}} \right|^q \right]^{\frac{1}{q}}, \end{aligned}$$

where

$$\begin{aligned} B_1 = B_1(c, d; p) &= \frac{1}{4} \left(\frac{c^p + d^p}{2} \right)^{\frac{1}{p}-1} \\ &\times \left[{}_2F_1 \left(1 - \frac{1}{p}, 2; 3; \frac{c^p - d^p}{c^p + d^p} \right) + {}_2F_1 \left(1 - \frac{1}{p}, 2; 3; \frac{d^p - c^p}{c^p + d^p} \right) \right], \end{aligned}$$

$$\begin{aligned} B_2 = B_2(c, d; p) &= \frac{1}{24} \left(\frac{c^p + d^p}{2} \right)^{\frac{1}{p}-1} \\ &\times \left[{}_2F_1 \left(1 - \frac{1}{p}, 2; 4; \frac{c^p - d^p}{c^p + d^p} \right) + 6 {}_2F_1 \left(1 - \frac{1}{p}, 2; 3; \frac{d^p - c^p}{c^p + d^p} \right) \right. \\ &\quad \left. + {}_2F_1 \left(1 - \frac{1}{p}, 2; 4; \frac{d^p - c^p}{c^p + d^p} \right) \right] \end{aligned}$$

and

$$B_3 = B_3(c, d; p) = B_1 - B_2.$$

Proof. From Lemma 2.5 and using power-mean integral inequality, we have

$$\begin{aligned} &\left| \frac{X(c, \cdot) + X(d, \cdot)}{2} - \frac{p}{d^p - c^p} \int_c^d \frac{X(s, \cdot)}{s^{1-p}} ds \right| \\ &= \frac{d^p - c^p}{2p} \int_0^1 \frac{1-2\theta}{[\theta c^p + (1-\theta)d^p]^{1-\frac{1}{p}}} X'([\theta c^p + (1-\theta)d^p]^{\frac{1}{p}}, \cdot) d\theta \\ &\leq \frac{d^p - c^p}{2p} \int_0^1 \left| \frac{1-2\theta}{[\theta c^p + (1-\theta)d^p]^{1-\frac{1}{p}}} \right| \\ &\quad \times \left| X'([\theta c^p + (1-\theta)d^p]^{\frac{1}{p}}, \cdot) \right| d\theta \\ &\leq \frac{d^p - c^p}{2p} \left(\int_0^1 \frac{|1-2\theta|}{[\theta c^p + (1-\theta)d^p]^{1-\frac{1}{p}}} d\theta \right)^{1-\frac{1}{q}} \\ &\quad \times \left(\int_0^1 \frac{|1-2\theta|}{[\theta c^p + (1-\theta)d^p]^{1-\frac{1}{p}}} \left| X'([\theta c^p + (1-\theta)d^p]^{\frac{1}{p}}, \cdot) \right|^q d\theta \right)^{\frac{1}{q}}. \end{aligned}$$

Since $|X'|^q$ is exponentially p -convex stochastic process on $[c, d]$, we have almost everywhere

$$\begin{aligned} &\left| \frac{X(c, \cdot) + X(d, \cdot)}{2} - \frac{p}{d^p - c^p} \int_c^d \frac{X(s, \cdot)}{s^{1-p}} ds \right| \\ &\leq \frac{d^p - c^p}{2p} \left(\int_0^1 \frac{|1-2\theta|}{[\theta c^p + (1-\theta)d^p]^{1-\frac{1}{p}}} d\theta \right)^{1-\frac{1}{q}} \\ &\quad \times \left(\int_0^1 \frac{|1-2\theta| \left[\theta \left| \frac{X'(c, \cdot)}{e^{\alpha c}} \right|^q + (1-\theta) \left| \frac{X'(d, \cdot)}{e^{\alpha d}} \right|^q \right]}{[\theta c^p + (1-\theta)d^p]^{1-\frac{1}{p}}} d\theta \right)^{\frac{1}{q}} \\ &\leq \frac{d^p - c^p}{2p} B_1^{1-\frac{1}{q}} \left[B_2 \left| \frac{X(c, \cdot)}{e^{\alpha c}} \right|^q + B_3 \left| \frac{X(d, \cdot)}{e^{\alpha d}} \right|^q \right]^{\frac{1}{q}}. \end{aligned}$$

where

$$\int_0^1 \frac{|1-2\theta|}{[\theta u^p + (1-\theta)v^p]^{1-\frac{1}{p}}} d\theta = B_1(c, d; p),$$

$$\int_0^1 \frac{|1 - 2\theta|\theta}{[\theta c^p + (1 - \theta)d^p]^{1-\frac{1}{p}}} d\theta = B_2(c, d; p),$$

$$\int_0^1 \frac{|1 - 2\theta|(1 - \theta)}{[\theta c^p + (1 - \theta)d^p]^{1-\frac{1}{p}}} d\theta = B_1(c, d; p) - B_2(c, d; p).$$

Thus, the proof is completed.

Remark 3.6. If we choose $\alpha = 0$ in Theorem 3.5, we attain Theorem 4 in [9].

Remark 3.7. By choosing $(\alpha, p) = (0, 1)$ in Theorem 3.5, we attain Theorem 5 in [9].

Corollary 3.8. Under the conditions of Theorem 3.5, if we take $q = 1$, then

$$\left| \frac{X(c, \cdot) + X(d, \cdot)}{2} - \frac{p}{d^p - c^p} \int_c^d \frac{X(s, \cdot)}{s^{1-p}} ds \right|$$

$$\leq \frac{d^p - c^p}{2p} \left[B_2 \left| \frac{X'(c, \cdot)}{e^{\alpha c}} \right| + B_3 \left| \frac{X'(d, \cdot)}{e^{\alpha d}} \right| \right] \quad (\text{a. e.}),$$

where B_2 and B_3 are given in Theorem 3.5.

Remark 3.9. If $\alpha = 0$ in Corollary 3.8, we attain Corollary 4 in [9].

Remark 3.10. By letting $(\alpha, p) = (0, 1)$ in Corollary 3.8, we attain Theorem 5 in [9].

Theorem 3.11. Let $X: I \subset (0, \infty) \times \Omega \rightarrow \mathbb{R}$ be a differentiable stochastic process on I° and X' be mean-square integrable on $[c, d]$. If $|X'|^q$ is exponentially p -convex stochastic process on $[c, d]$ for $q, r > 1, \frac{1}{q} + \frac{1}{r} = 1$, then the following inequality holds almost everywhere

$$\left| \frac{X(c, \cdot) + X(d, \cdot)}{2} - \frac{p}{d^p - c^p} \int_c^d \frac{X(s, \cdot)}{s^{1-p}} ds \right|$$

$$\leq \frac{d^p - c^p}{2p} \left(\frac{1}{r+1} \right)^{\frac{1}{r}} \left[B_4 \left| \frac{X'(c, \cdot)}{e^{\alpha c}} \right|^q + B_5 \left| \frac{X'(d, \cdot)}{e^{\alpha d}} \right|^q \right]^{\frac{1}{q}},$$

where

$$B_4 = B_4(c, d; p; q)$$

$$= \begin{cases} \frac{1}{2c^{qp-q}} {}_2F_1 \left(q - \frac{q}{p}, 1; 3; 1 - \left(\frac{d}{c} \right)^p \right), & p < 0, \\ \frac{1}{2d^{qp-q}} {}_2F_1 \left(q - \frac{q}{p}, 2; 3; 1 - \left(\frac{c}{d} \right)^p \right), & p > 0, \end{cases}$$

$$B_5 = B_5(c, d; p; q)$$

$$= \begin{cases} \frac{1}{2c^{qp-q}} {}_2F_1 \left(q - \frac{q}{p}, 2; 3; 1 - \left(\frac{d}{c} \right)^p \right), & p < 0, \\ \frac{1}{2d^{qp-q}} {}_2F_1 \left(q - \frac{q}{p}, 1; 3; 1 - \left(\frac{c}{d} \right)^p \right), & p > 0. \end{cases}$$

Proof. Using Lemma 2.5, Hölder's integral inequality and exponential p -convexity of the stochastic process $|X'|^q$ on $[c, d]$, we have almost everywhere

$$\left| \frac{X(c, \cdot) + X(d, \cdot)}{2} - \frac{p}{d^p - c^p} \int_c^d \frac{X(s, \cdot)}{s^{1-p}} ds \right|$$

$$\leq \frac{d^p - c^p}{2p} \left(\int_0^1 |1 - 2\theta|^r d\theta \right)^{\frac{1}{r}}$$

$$\times \left(\int_0^1 \frac{1}{[\theta c^p + (1 - \theta)d^p]^{q(1-\frac{1}{p})}} \left| X' \left([\theta c^p + (1 - \theta)d^p]^{\frac{1}{p}}, \cdot \right) \right|^q d\theta \right)^{\frac{1}{q}}$$

$$\leq \frac{d^p - c^p}{2p} \left(\frac{1}{r+1} \right)^{\frac{1}{r}} \left(\frac{\theta \left| \frac{X'(c, \cdot)}{e^{\alpha c}} \right|^q + (1 - \theta) \left| \frac{X'(d, \cdot)}{e^{\alpha d}} \right|^q}{[\theta c^p + (1 - \theta)d^p]^{q(1-\frac{1}{p})}} d\theta \right)^{\frac{1}{q}}$$

$$\leq \frac{d^p - c^p}{2p} \left(\frac{1}{r+1} \right)^{\frac{1}{r}} \left[B_4 \left| \frac{X'(c, \cdot)}{e^{\alpha c}} \right|^q + B_5 \left| \frac{X'(d, \cdot)}{e^{\alpha d}} \right|^q \right]^{\frac{1}{q}},$$

where

$$B_4 = \int_0^1 \frac{\theta}{[\theta c^p + (1 - \theta)d^p]^{q(1-\frac{1}{p})}} d\theta$$

$$= \begin{cases} \frac{1}{2c^{qp-q}} {}_2F_1 \left(q - \frac{q}{p}, 1; 3; 1 - \left(\frac{d}{c} \right)^p \right), & p < 0, \\ \frac{1}{2d^{qp-q}} {}_2F_1 \left(q - \frac{q}{p}, 2; 3; 1 - \left(\frac{c}{d} \right)^p \right), & p > 0, \end{cases}$$

$$B_5 = \int_0^1 \frac{1 - \theta}{[\theta c^p + (1 - \theta)d^p]^{q(1-\frac{1}{p})}} d\theta$$

$$= \begin{cases} \frac{1}{2c^{qp-q}} {}_2F_1 \left(q - \frac{q}{p}, 2; 3; 1 - \left(\frac{d}{c} \right)^p \right), & p < 0, \\ \frac{1}{2d^{qp-q}} {}_2F_1 \left(q - \frac{q}{p}, 1; 3; 1 - \left(\frac{c}{d} \right)^p \right), & p > 0. \end{cases}$$

Remark 3.12. If we take $\alpha = 0$ in Theorem 3.11, we attain Theorem 6 in [9].

Theorem 3.13. Let $X: I \subset (0, \infty) \times \Omega \rightarrow \mathbb{R}$ be a differentiable stochastic process on I° and X' be mean-square integrable on $[c, d]$. If $|X'|^q$ is exponentially p -convex stochastic process on $[c, d]$ for $q, r > 1, \frac{1}{q} + \frac{1}{r} = 1$, then

$$\left| \frac{X(c, \cdot) + X(d, \cdot)}{2} - \frac{p}{d^p - c^p} \int_c^d \frac{X(s, \cdot)}{s^{1-p}} ds \right| \leq \frac{d^p - c^p}{2p} B_6^{\frac{1}{q}} \left(\frac{1}{q+1} \right)^{\frac{1}{q}} \left(\frac{|X'(c, \cdot)|^q + |X'(d, \cdot)|^q}{2} \right)^{\frac{1}{q}},$$

where

$$B_6 = B_6(c, d; p; r)$$

$$= \begin{cases} \frac{1}{2c^{rp-r}} {}_2F_1\left(r - \frac{r}{p}, 1; 2; 1 - \left(\frac{d}{c}\right)^p\right), & p < 0, \\ \frac{1}{2d^{rp-r}} {}_2F_1\left(r - \frac{r}{p}, 1; 2; 1 - \left(\frac{c}{d}\right)^p\right), & p > 0, \end{cases}$$

Proof. From Lemma 2.5, using Hölder’s integral inequality and exponential p -convexity of the stochastic process $|X'|^q$ on $[c, d]$, we have almost everywhere

$$\begin{aligned} & \left| \frac{X(c, \cdot) + X(d, \cdot)}{2} - \frac{p}{d^p - c^p} \int_c^d \frac{X(s, \cdot)}{s^{1-p}} ds \right| \\ &= \frac{d^p - c^p}{2p} \int_0^1 \frac{1 - 2\theta}{[\theta c^p + (1 - \theta)d^p]^{1-\frac{1}{p}}} X'([\theta c^p + (1 - \theta)d^p]^{\frac{1}{p}}, \cdot) d\theta \\ &\leq \frac{d^p - c^p}{2p} \left(\int_0^1 \frac{1}{[\theta c^p + (1 - \theta)d^p]^{r(1-\frac{1}{p})}} d\theta \right)^{\frac{1}{r}} \\ &\quad \times \left(\int_0^1 |1 - 2\theta|^q \left| X'([\theta c^p + (1 - \theta)d^p]^{\frac{1}{p}}, \cdot) \right|^q d\theta \right)^{\frac{1}{q}} \\ &\leq \frac{d^p - c^p}{2p} B_6^{\frac{1}{q}} \left(\frac{1}{q+1} \right)^{\frac{1}{q}} \left(\frac{|X'(c, \cdot)|^q + |X'(d, \cdot)|^q}{2} \right)^{\frac{1}{q}}, \end{aligned}$$

where

$$\begin{aligned} B_6 &= \int_0^1 \frac{1}{[\theta c^p + (1 - \theta)d^p]^{r(1-\frac{1}{p})}} d\theta \\ &= \begin{cases} \frac{1}{2c^{rp-r}} {}_2F_1\left(r - \frac{r}{p}, 1; 2; 1 - \left(\frac{d}{c}\right)^p\right), & p < 0, \\ \frac{1}{2d^{rp-r}} {}_2F_1\left(r - \frac{r}{p}, 1; 2; 1 - \left(\frac{c}{d}\right)^p\right), & p > 0, \end{cases} \end{aligned}$$

and

$$\begin{aligned} \int_0^1 \theta |1 - 2\theta|^q d\theta &= \int_0^1 (1 - \theta) |1 - 2\theta|^q d\theta \\ &= \frac{1}{2(q+1)}. \end{aligned}$$

Remark 3.14. If we take $\alpha = 0$ in Theorem 3.13, we attain Theorem 7 in [9].

REFERENCES

- [1] M. Abramovitz and I. A. Stegun, “Handbook of Mathematical Functions with Formulas, Graphs, and Mathematical Tables”, Dover, New York, 1965.
- [2] L. Gonzalez, N. Merentes and M. Valera-Lopez, “Some estimates on the Hermite-Hadamard inequality through convex and quasi-convex stochastic processes”, *Mathematica Aeterna*, vol. 5, no. 5, pp. 745–767, 2015.
- [3] D. Kotrys, “Hermite-Hadamard inequality for convex stochastic processes”, *Aequationes Mathematicae*, vol. 83, pp. 143–151, 2012.
- [4] D. Kotrys, “Remarks on strongly convex stochastic processes”, *Aequationes Mathematicae*, vol. 86, pp. 91–98, 2013.
- [5] L. Li and Z. Hao, “On Hermite-Hadamard inequality for h-convex stochastic processes”, *Aequationes Mathematicae*, vol. 91, pp. 909–920, 2017.
- [6] S. Maden, M. Tomar and E. Set, “Hermite-Hadamard type inequalities for s-convex stochastic processes in first sense”, *Pure and Applied Mathematics Letters*, vol. 2015, pp. 1–7, 2015.

- [7] N. Mehreen and M. Anwar, “Hermite-Hadamard type inequalities for exponentially p-convex functions and exponentially s-convex functions in the second sense with applications”, *Journal of Inequalities and Applications*, vol. 2019, no. 92, pp. 1–17, 2019.
- [8] K. Nikodem, “On convex stochastic processes”, *Aequationes Mathematicae*, vol. 20, pp. 184–197, 1980.
- [9] N. Okur, İ. İşcan and E. Yuksek Dizdar, “Hermite-Hadamard type inequalities for p-convex stochastic processes”, *An Int. J. Optim. and Cont.*, vol. 9, no. 2, pp. 148–153, 2019.
- [10] M. Z. Sarıkaya, H. Yıldız and H. Budak, “Some integral inequalities for convex stochastic processes”, *Acta Math. Univ. Comenianae*, LXXXV, pp. 155–164, 2016.
- [11] E. Set, M. Tomar and S. Maden, “Hermite-Hadamard type inequalities for s-convex stochastic processes in the second sense”, *Turkish Journal of Analysis and Number Theory*, vol. 2, no. 6, pp. 202–207, 2016.
- [12] E. Set, M. Z. Sarıkaya and M. Tomar, “Hermite-Hadamard type inequalities for coordinates convex stochastic processes”, *Mathematica Aeterna*, vol. 5, no. 2, pp. 363–382, 2015.
- [13] M. Shaked and J. G. Shanthikumar, “Stochastic convexity and its applications”, *Advances in Applied Probability*, vol. 20, pp. 427–446, 1988.
- [14] A. Skowronski, “On some properties of J-convex stochastic processes”, *Aequationes Mathematicae*, vol. 44, pp. 249–258, 1992.
- [15] M. Tomar, E. Set and S. Maden, “Hermite-Hadamard type inequalities for log-convex stochastic processes”, *Journal of New Theory*, vol. 2, pp. 23–32, 2015.
- [16] M. Tomar, E. Set and N. O. Bekar, “Hermite-Hadamard type inequalities for strongly log-convex stochastic processes”, *Journal of Global Engineering Studies*, vol. 1, no. 53–61, 2014.